

97  
8/27/86 JS (2)

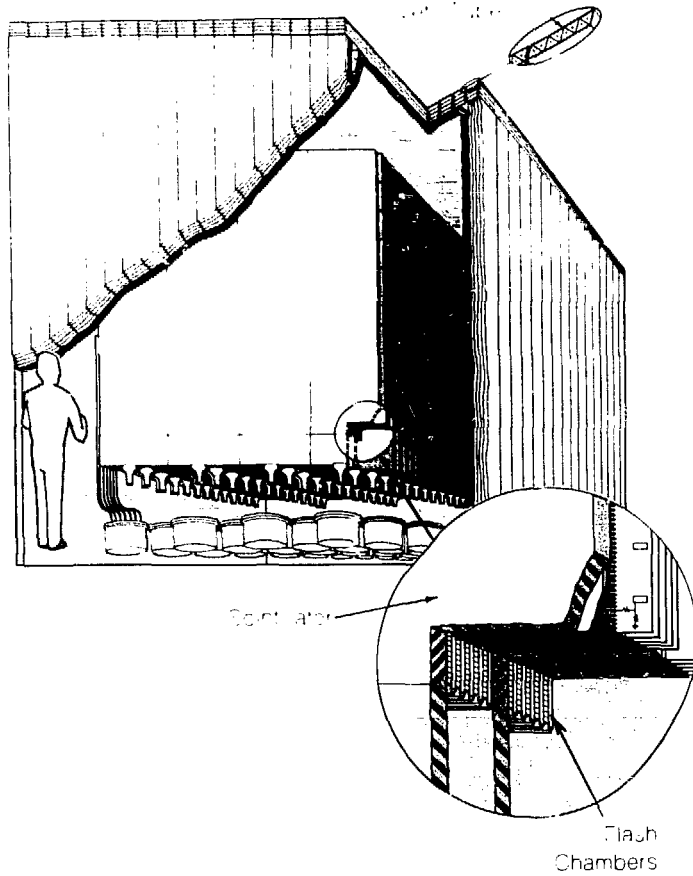
(2.5)

DE-1904-6

I-27690

### Progress at LAMPF

January—December 1985



Clinton P. Anderson  
Meson Physics Facility  
Los Alamos National Laboratory  
LA-10738-PR  
Progress Report

The world's first observation of scattering of electron neutrinos by electrons was made at LAMPF in 1985 (see p. 18). The cover shows a cutaway view of the neutrino detector. The active cosmic-ray veto system (purple) consists of 594 multiwire proportional counters (MWPCs) arranged as shown in four layers covering the walls and roof, with one additional layer on the floor; each counter has eight triangular sections. The central detector is a 40-layer sandwich of alternating scintillator counters and flash-chamber modules (FCMs). The 160 scintillator counters weigh 9.5 tons, and the 208,000 tubes of the FCMs, in alternating horizontal and vertical orientation as shown, weigh 4.5 tons. In the figure the scintillator counters are pale blue, flash chambers are shown as white layers in the central detector sandwich.



LOS ALAMOS SCIENTIFIC LAB

LOS ALAMOS SCIENTIFIC LAB

## DISCLAIMER

This report was prepared as an account of work sponsored by an agency of the United States Government. Neither the United States Government nor any agency thereof, nor any of their employees, makes any warranty, express or implied, or assumes any legal liability or responsibility for the accuracy, completeness, or usefulness of any information, apparatus, product, or process disclosed, or represents that its use would not infringe privately owned rights. Reference herein to any specific commercial product, process, or service by trade name, trademark, manufacturer, or otherwise does not necessarily constitute or imply its endorsement, recommendation, or favoring by the United States Government or any agency thereof. The views and opinions of authors expressed herein do not necessarily state or reflect those of the United States Government or any agency thereof.

LA--10738-PR

DE86 014891

## Progress at LAMPF

LA-10738-PR  
Progress Report

UC-28  
Issued: May 1986

### EDITORS

John C. Allred

Beverly Talley

### SCIENTIFIC EDITORIAL BOARD

Olin B. van Dyck

Richard L. Hutson

Mario E. Schillaci

### DESIGN

Jeff Segler

### INFRARED PHOTOGRAPHY

Jeff Cannon

Mick Greenbank

### PRODUCTION

Lois Rayburn

Chris Weaver

### ABSTRACT

"Progress at LAMPF" is the annual progress report of MP Division of the Los Alamos National Laboratory. Included are brief reports on research done at LAMPF by researchers from other institutions and other Los Alamos Divisions.



**FOREWORD**

The past year has been one of great excitement and change both here at LAMPF and at Los Alamos National Laboratory. Louis Rosen stepped aside as Director of LAMPF on November 11, 1985, and I took over that very challenging assignment. Don Kerr resigned as the Los Alamos National Laboratory Director on October 1, 1985, and Sig Hecker, an outstanding metallurgist and former Director of the Center for Materials Science, was selected by a distinguished search committee to be our next Laboratory Director. He will be an understanding and strong advocate of basic research.

LAMPF has had an outstanding record of reliable and effective operation while delivering the most intense proton beam anywhere in the world. Hence, in the search for a new leader for the Medium-Energy Physics Division (MP), it was only natural to turn to a person who was greatly responsible for this excellent record. So it was that Don Hagerman was selected by Los Alamos management to be the new MP-Division Leader. He and I will be working closely over the coming years to continue to provide the environment and hardware required for a world-class research program.

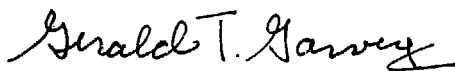
The research output over the past year was outstanding. Among the highlights were results from Exp. 225, the world's first observation of the interference between the neutral and charge-changing weak currents. The present results are consistent with the Standard Model and, after an additional year of running, the results will further test the Standard Model. A new and very strong lower limit has been placed on the lepton family number violating rare decay of the muon into an electron and a photon and the  $\pi, \eta$  reaction has been observed for the first time on a variety of nuclei.

With regard to new facilities and large experiments, we are firmly committed to proceeding with the upgrade of the Nucleon Physics Laboratory. This upgrade will provide unparalleled opportunities for our users to investigate the spin and isospin dependence of nucleon-nucleon and nucleon-

nucleus interactions. A third generation rare decay experiment involving 10 institutions is also just getting under way. We all share a real sense of pride in the rapid commissioning of the Proton Storage Ring (PSR), which reached 30  $\mu$ A, or one third of its design intensity, within the first 6 months of operation. The pulses of the protons from PSR are used to produce a source of pulsed neutrons for studies of the structure of materials both physical and biological. The pulsed neutron facility is referred to as the Los Alamos Neutron Scattering Center (LANSCE).

In addition to the facilities and experiments, LAMPF serves as a center for the discussion and development of new and significant concepts in medium-energy physics. We held 6 workshops and a summer school at which some 50 graduate students were exposed to the frontiers of nuclear theory. It was intellectually stimulating and shows the intellectual attraction of the frontiers of our subject to young scientists.

The foreword would not be complete without mention of developments surrounding our plans for an advanced hadron facility. We will soon be circulating an update of our proposal of December 1984. Considerable advances have been made in every aspect of that original proposal. The physics case has been greatly strengthened, particularly with regard to strong-interaction research. A viable and cost-effective machine design is now more certain and new ideas for producing secondary beams of greater intensity and flexibility have been developed. Thus, our new plan will show higher intensity secondary beams and lower cost. The actual funding to construct any large facilities in basic research remains highly uncertain while the United States deals with the issues surrounding the large federal deficit.



**Gerald T. Garvey**  
Director of LAMPF

**CONTENTS**

|  |             |
|--|-------------|
| <b>Experimental Areas</b> . . . . .  | <i>xiii</i> |
| <b>LAMPF News</b> . . . . .  | 1           |
| Rosen Steps Down . . . . .   | 2           |
| New LAMPF Director . . . . .   | 3           |
| New MP-Division Leader . . . . .   | 4           |
| <b>LAMPF Users Group</b> . . . . .   | 7           |
| Nineteenth Annual Meeting . . . . .  | 8           |
| Committees . . . . .   | 9           |
| Minutes . . . . .  | 12          |
| Workshops . . . . .  | 13          |
| Visitors Center . . . . .  | 14          |
| <b>Research</b> . . . . .  | 17          |
| <b>Nuclear and Particle Physics</b> . . . . .  | 18          |
| EXPERIMENT 225 — Neutrino Area   |             |
| A Study of Neutrino-Electron Elastic Scattering . . . . .  | 18          |
| Cygnus Cosmic-Ray Air-Shower Array . . . . .   | 24          |
| EXPERIMENT 657 — EPICC   |             |
| Pion Inelastic Scattering from the $N=28$ Isotones and<br>Neighbors . . . . .  | 26          |
| EXPERIMENTS 773 and 906 — EPICS  |             |
| Pion Double-Charge-Exchange Angular Distributions for<br>$T=2$ Double-Isobaric-Analog States . . . . .                     | 27          |
| EXPERIMENTS 777, 780 and 826 — EPICS   |             |
| Mass Dependence of Pion Double Charge Exchange . . . . .   | 29          |
| EXPERIMENT 800 — EPICS   |             |
| Inelastic Pion Scattering from $^{22}\text{Ne}$ . . . . .  | 33          |
| EXPERIMENT 833U — EPICC  |             |
| Large-Angle Excitation Functions for Elastic Scattering<br>of $\pi^\pm$ from $^{12}\text{C}$ and $^{16}\text{O}$ . . . . . | 34          |
| EXPERIMENT 836 — EPICS   |             |
| Energy Dependence of Pion Scattering to the<br>Giant Resonance Region of $^{208}\text{Pb}$ . . . . .                       | 38          |
| EXPERIMENT 905 — EPICS   |             |
| New Test of Superratio by $\pi^\pm$ Elastic Scattering<br>on $^3\text{H}$ and $^3\text{He}$ . . . . .                      | 40          |

EXPERIMENT 392 — HRS  
 Measurement of the Wolfenstein Parameters for  $p + p$   
 and  $p + n$  Scattering at 500 and 800 MeV . . . . . 44

EXPERIMENT 686 — HRS  
 Measurement of Third-Order Spin Observables  
 for Elastic  $pd$  Scattering at 800 MeV . . . . . 47

EXPERIMENT 722 — HRS  
 Measurement of Cross Sections and Analyzing Powers  
 for Elastic and Inelastic Scattering of  
 400- to 500-MeV Protons from  $^{14}\text{C}$  . . . . . 52

EXPERIMENT 741 — HRS  
 Continuum Polarization Transfer in 500-MeV  
 Proton Scattering and Pionic Collectivity in Nuclei . . . . . 53

EXPERIMENT 879 — HRS  
 Characteristic Dirac Signature in Large-Angle  
 Elastic Scattering at 500 MeV . . . . . 56

EXPERIMENT 897 — HRS  
 Development of a  $0^\circ$  Focal-Plane Polarimeter at HRS . . . . . 58

EXPERIMENT 907 — HRS  
 Continuum Spin-Flip Cross-Section Measurements  
 from  $^{48}\text{Ca}$  . . . . . 60

EXPERIMENT 7467 — LEP  
 Measurement of the  $E2$  Resonance Effect in Pionic Atoms . . . . . 62

EXPERIMENT 313 — LEP  
 Pion Charge Asymmetries for  $^{13}\text{C}$  at Low Beam Energies  
 on the LEP Spectrometer . . . . . 74

EXPERIMENT 884 — LEP  
 Pion Double Charge Exchange on  $^{14}\text{C}$   
 at Low Energies . . . . . 76

EXPERIMENT 933 — LEP  
 Study of the Mass Dependence of Pion  
 Single Charge Exchange at 20 MeV . . . . . 85

EXPERIMENT 899 — LEP  
 Angular Distributions for the  $^{163}\text{Ho}(\pi^+, \pi^0)^{165}\text{Er}$  Reaction  
 to the Isobaric-Analog State at 100, 165, and 230 MeV . . . . . 89

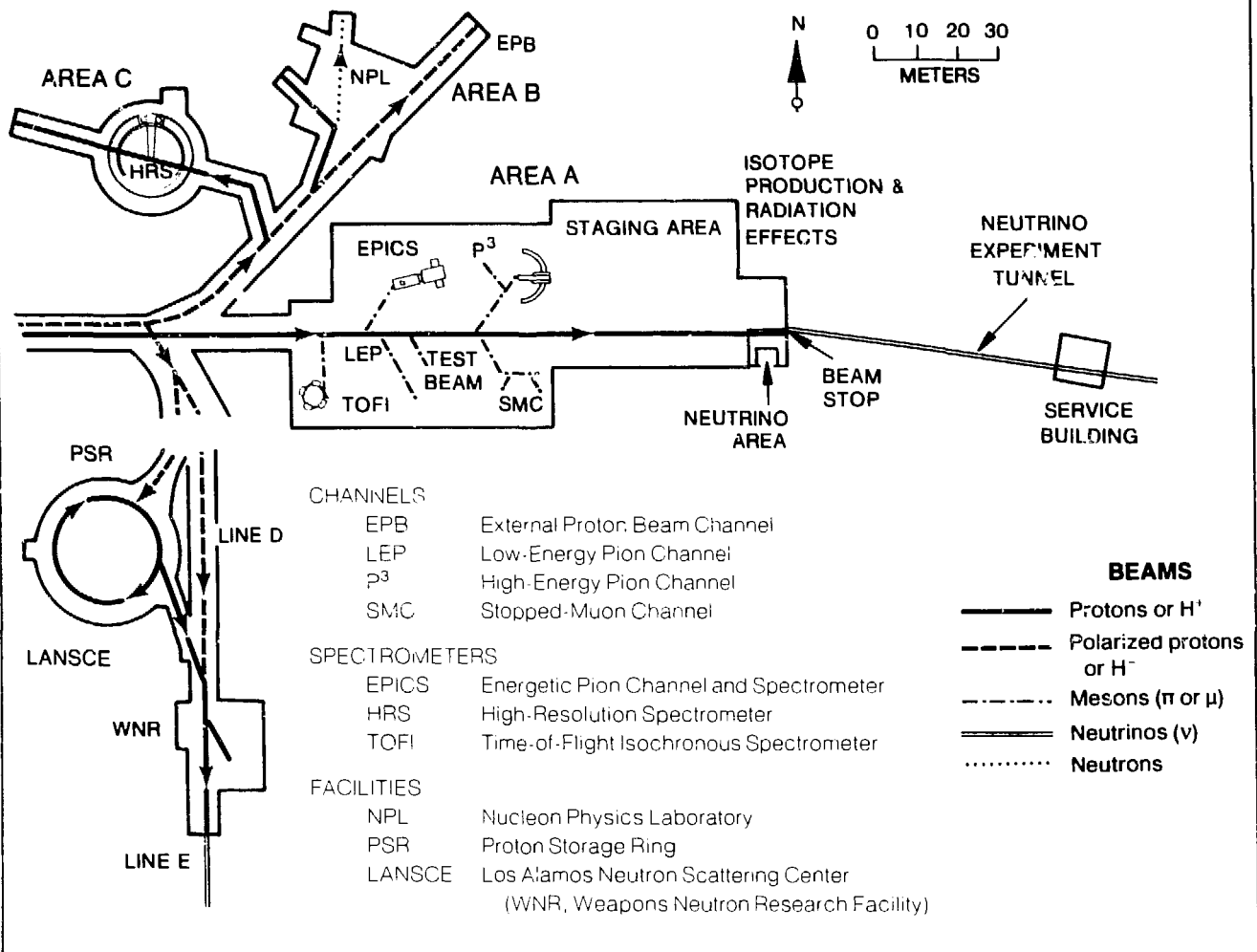


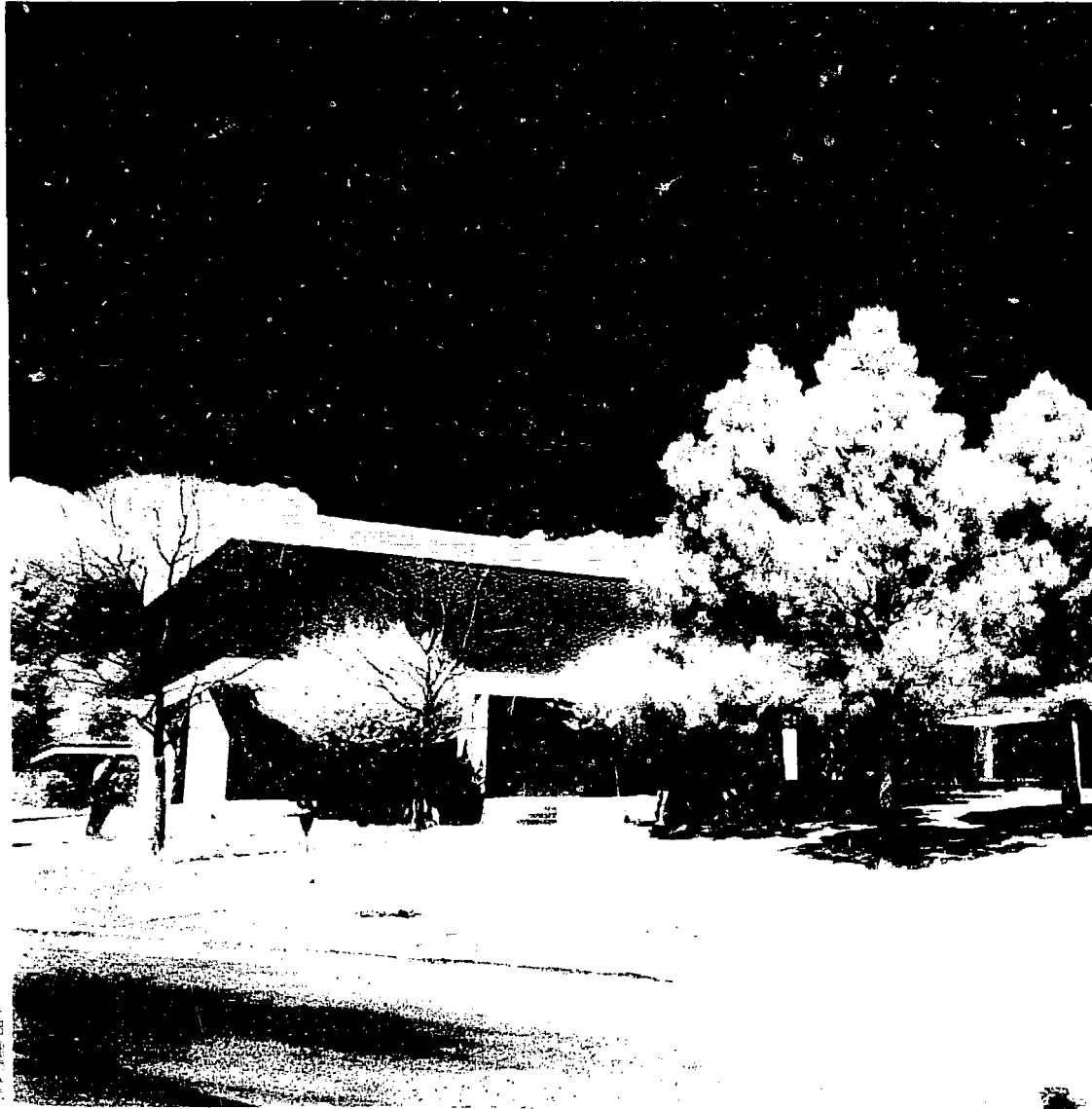
|   |            |
|---|------------|
| EXPERIMENT 745 — Triangle Area<br>Search for Neutrino Oscillations at LAMPF . . . . .   | 92         |
| EXPERIMENTS 704, 750, 950, and 957 — P <sup>3</sup><br>A Dependence of Inclusive Pion Double Charge Exchange . . . . .  | 96         |
| EXPERIMENT 804 — P <sup>3</sup> East<br>Measurement of the Analyzing Power in $\pi^-p \rightarrow \gamma n$<br>and $\pi^-p \rightarrow \pi^0 n$ Using a Transversely Polarized Target . . . . . | 100        |
| EXPERIMENT 827 — P <sup>3</sup><br>Study of Isobaric-Analog-State Transitions with<br>Pion Single Charge Exchange in the<br>300- to 500-MeV Region . . . . .                                    | 106        |
| EXPERIMENT 852 — P <sup>3</sup><br>Measurements of ( $\pi^\pm, \eta$ ) Reactions on Nuclear Targets<br>to Study the Production and Interaction<br>of $\eta$ Mesons with Nuclei . . . . .        | 110        |
| EXPERIMENT 888 — SMC<br>Study of the Decay $\pi^+ \rightarrow e^+ \nu_e \gamma$ . . . . .   | 113        |
| EXPERIMENT 969 — SMC<br>MEGA: Search for the Rare Decay $\mu^+ \rightarrow e^+ \gamma$ . . . . .  | 114        |
| EXPERIMENT 914 — SMC (LAMPF)<br>EXPERIMENT 791 — Beam B5 (Brookhaven)<br>Study of Very Rare $K_L$ Decays . . . . .  | 122        |
| EXPERIMENT 745 — SMC<br><i>E2</i> and <i>E4</i> Deformations in $^{232}\text{Th}$ , $^{233,234,235,236,238}\text{U}$ ,<br>and $^{239,240,242}\text{Pu}$ . . . . .                               | 126        |
| EXPERIMENT 726 — SMC<br>A Search for the <i>C</i> -Noninvariant Decay $\pi^0 \rightarrow 3\gamma$ . . . . .   | 129        |
| EXPERIMENTS 400/445 — SMC<br>Crystal Box Experiments . . . . .  | 131        |
| <b>Atomic and Molecular Physics . . . . .</b>   | <b>134</b> |
| Theory of Muon-Catalyzed Fusion . . . . .   | 134        |
| EXPERIMENT 727 — Biomed and SMC<br>Measurement of the Efficiency of Muon Catalysis in<br>Deuterium-Tritium Mixtures at High Densities . . . . .   | 142        |

|  |     |
|--|-----|
| <b>Materials Science</b> . . . . .   | 150 |
| EXPERIMENT 842 — SMC   |     |
| Muon Spin-Relaxation and Knight-Shift Studies of<br>Itinerant Magnets and Heavy-Fermion Materials . . . . .                                    | 150 |
| EXPERIMENT 839 and 854 — SMC   |     |
| Muon-Spin Relaxation ( $\mu$ SR) in Select Magnetic Oxides<br>and Oxide Spin Glasses . . . . .   | 157 |
| EXPERIMENT 941 — SMC   |     |
| Muon-Spin-Relaxation Studies ( $\mu$ SR) of<br>Disordered Spin Systems . . . . .   | 161 |
| Improvements to the Muon-Spin-Relaxation ( $\mu$ SR)<br>Experimental Facility . . . . .  | 165 |
| EXPERIMENT 787 — Biomed  |     |
| Muon Channeling for Solid-State Physics Information . . . . .  | 166 |
| <b>Radiation-Effects Studies</b> . . . . .   | 172 |
| Operating Experience at the Los Alamos Spallation<br>Radiation-Effects Facility (LASREF) at LAMPF . . . . .                                    | 172 |
| EXPERIMENT 769 — Beam Stop Area  |     |
| Proton-Irradiation Effects on Candidate Materials for the<br>German Spallation Neutron Source (SNQ) . . . . .                                  | 173 |
| Quantitative Study, by Field-Ion Microscopy, of<br>Radiation Damage in Tungsten After Neutron<br>and Proton Irradiation . . . . .              | 174 |
| EXPERIMENT 936 — Radiation Damage  |     |
| Additional Measurements of the Radiation Environment<br>at the Los Alamos Spallation Radiation-Effects<br>Facility (LASREF) at LAMPF . . . . . | 175 |
| EXPERIMENT 943 — Radiation Damage  |     |
| Microstructural Evolution Under Particle Irradiation . . . . .   | 176 |
| <b>Biomedical Research and Instrumentation</b> . . . . .   | 178 |
| Radiobiology of Ultrasoft X Rays . . . . .   | 178 |
| Instrumentation . . . . .  | 179 |
| <b>Nuclear Chemistry</b> . . . . .   | 180 |
| EXPERIMENT 897 — LEP   |     |
| Pion Single Charge Exchange in ${}^7\text{Li}$ to the<br>Isobaric-Analog Ground State of ${}^7\text{Be}$ . . . . .                             | 180 |

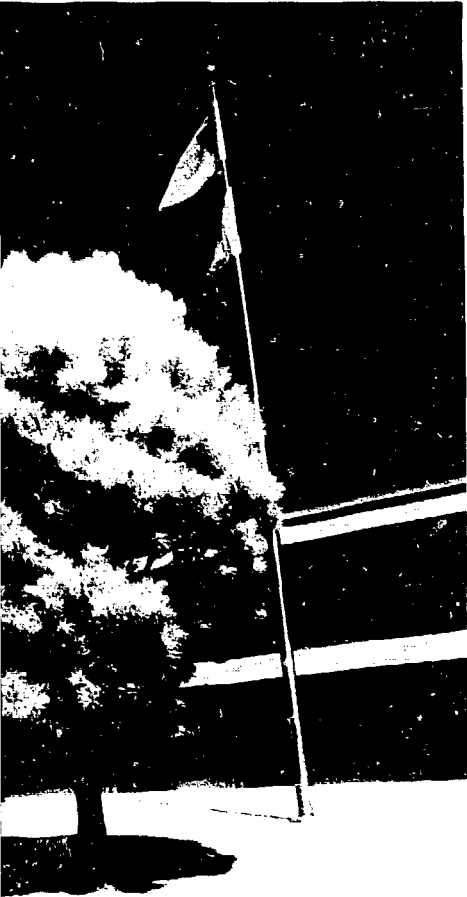
|  |            |
|--|------------|
| EXPERIMENT 752 -- Thin Target Area                       |            |
| Time-of-Flight Isochronous (TOFI) Spectrometer . . . . . | 184        |
| <b>Radioisotope Production . . . . .</b>                 | <b>190</b> |
| Isotope Production and Separation . . . . .              | 190        |
| Radiopharmaceutical Labeling Research . . . . .          | 195        |
| Radioisotope Production Publications . . . . .           | 200        |
| <b>Theory . . . . .</b>                                  | <b>204</b> |
| Nonanalog Pion Double Charge Exchange                    |            |
| Through the $\Delta_{33}$ -Nucleon Interaction . . . . . | 204        |
| Theoretical Evidence for the Existence of the            |            |
| $\eta$ -Mesic Nucleus . . . . .                          | 205        |
| A Self-Consistent Calculation of One-Gluon Exchange      |            |
| in the Friedberg-Lee Soliton Model . . . . .             | 208        |
| The Pion-Nucleon System at Low Energy. . . . .           | 211        |
| Report of the T-5 Theoretical Group . . . . .            | 220        |
| <b>MP-Division Publications . . . . .</b>                | <b>232</b> |
| <b>Status of LAMPF II . . . . .</b>                      | <b>249</b> |
| Accelerator Studies . . . . .                            | 250        |
| <b>Facility Development . . . . .</b>                    | <b>261</b> |
| Nucleon Physics Laboratory (NPL) Upgrade . . . . .       | 262        |
| Spectrometer Calibration at EPICS. . . . .               | 269        |
| Radiation-Effects Facility . . . . .                     | 272        |
| Data-Analysis Center. . . . .                            | 277        |
| LAMPF Computer-Control System . . . . .                  | 279        |
| <b>Accelerator Operations . . . . .</b>                  | <b>283</b> |
| <b>Milestones . . . . .</b>                              | <b>287</b> |
| <b>Appendixes . . . . .</b>                              | <b>295</b> |
| Appendix A:  |            |
| Experiments Run in 1985. . . . .                         | 296        |
| Appendix B:  |            |
| New Proposals During 1985 . . . . .                      | 303        |
| Appendix C:  |            |
| LAMPF Visitors During 1985 . . . . .                     | 311        |
| <b>Information for Contributors. . . . .</b>             | <b>317</b> |

**LAMPF Experimental Areas**





## LAMPF News



Rosen Steps Down

New LAMPF Director

New MP-Division Leader



## Rosen Steps Down

At the November LAMPF Users Meeting, it was announced that Louis Rosen will be succeeded by Gerald Garvey as LAMPF Director. Garvey continues as a Deputy Associate Director of Los Alamos National Laboratory. Rosen has been named a Senior Fellow of the Laboratory, a position that will enable him to pursue several interests that follow from a lifetime of activities in science and public interest.

After teaching physics at the University of Alabama and Pennsylvania State University, Louis Rosen joined the Manhattan Project in Los Alamos

in 1944. Following World War II, Rosen divided his time between basic research in nuclear physics and national defense activities. At Los Alamos he has held the position of group leader of the nuclear microscopy laboratory, alternate division leader of the experimental physics division, and division leader of the Medium-Energy Physics Division.

Rosen was a pioneer in the development and exploitation of techniques for neutral- and charged-particle detection. From this work emerged a clearer understanding of the mechanism of neutron interactions and the first clear evidence that a controlled thermonuclear reactor, operating on the *dt* cycle, might produce more tritium than it consumes. His work gave rise to better phenomenological potentials for describing and predicting nucleon-nucleus interactions and for placing better limits on the validity of microscopic reversibility in nuclear reactions. He was responsible for measuring many of the neutron cross sections in the design of the first thermonuclear weapons.

In 1963 he received the E. O. Lawrence award for these activities from the U.S. Atomic Energy Commission. Other honors include Sesquicentennial Honorary Professor at the University of Alabama, Pennsylvania State Alumni Fellow, and University of New Mexico Honorary Doctor of Science.



Henry Ortega

In 1962 Rosen initiated the meson factory proposal at Los Alamos. Under his leadership LAMPF became the largest nuclear science facility in the world. In addition to promoting basic research, Rosen saw that accelerator beams and technology were made to serve the immediate public interest through production of better radioisotopes for industry and medicine, the study of radiation damage in reactor materials, and cancer therapy.

Rosen is active in the affairs of science and in providing advice on scientific matters to the federal establishment. He served as a member of the National Accelerator Panel on the Future of Nuclear Science, on the panel to recommend a management structure for the administration of the Orbiting Space Telescope Project, and as a member of a committee to advise the General Accounting Office on ground rules for an in-depth audit of high-energy physics. In the American Physical Society (APS), he was Chairman of the Division of Nuclear Physics in 1985. He has also served as a member of the APS Council and as Chairman of the Panel on Public Affairs. He currently serves on the USA-USSR Joint Committee for Collaboration on the Fundamental Properties of Matter and continues to support the role of science as a channel for international understanding.

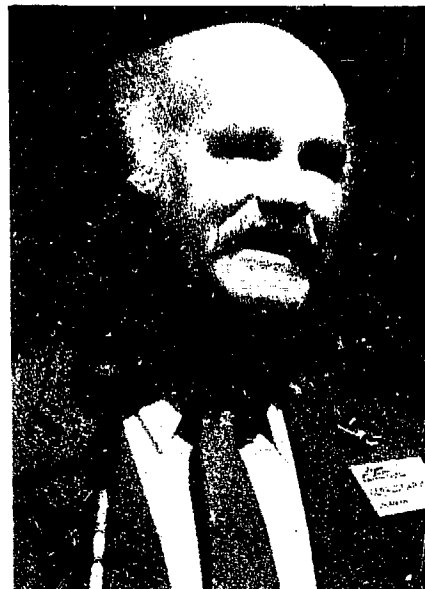
### **Gerald Garvey New LAMPF Director**

New LAMPF Director Gerald T. Garvey joined the Laboratory in 1984 as Deputy Associate Director for Nuclear and Particle Physics Programs. He came to Los Alamos from Argonne National Laboratory in Illinois, where he was also a professor at the University of Chicago. He has taught at Princeton, Oxford, and Yale Universities, and he has been a visiting lecturer at the Weizmann Institute in Israel.

Garvey received his doctorate from Yale University and his undergraduate degree from Fairfield University, Fairfield, Connecticut.

Garvey is currently an editor of *Annual Review of Nuclear and Particle Science* (since 1982) and of *Comments on Nuclear and Particle Physics* (since 1984). He was editor of *Physics Reports* from 1976 to 1979.

Garvey has served on program advisory committees at Nevis, Indiana University, and LAMPF. He is a member of the Visiting Committee of the Physics Department at SUNY, Stony Brook, and has served in a similar capacity at the University of Rochester.





He is presently a member of the Advisory Committee for Physics of the National Science Foundation and is chairman of its subcommittee to review NSF's Nuclear Science Program. He was a member of the High-Energy Advisory Committee at Brookhaven National Laboratory, 1979-1983; the Review Committee for the Nuclear Science Division at Lawrence Berkeley Laboratory, 1981-1984; and the Review Committee on TRIUMF of the National Research Council of Canada, 1983-1984.

Garvey served on the Livingston Panel on Future Electron Accelerators, 1977; the Committee on the Future of Nuclear Science of the National Academy of Sciences, 1976-1977; and the DOE/NSF Nuclear Science Advisory Committee (NSAC), 1977-1980.

Of his successor, Rosen said, "We were fortunate to recruit someone of Garvey's competence, knowledge, and scientific reputation."

Since 1962, he has played a key role in the design, construction, scheduling, operation, and upgrades of LAMPF—a half-mile-long accelerator that has emerged as a world-class research center.

Hagerman received a bachelor's degree in physics (*magna cum laude*) from the University of Colorado in 1951. Four years later he earned a doctorate in physics from Stanford University.

A Fellow of the American Physical Society, he has served as a member of the Department of Energy/National Science Foundation/Nuclear Science Advisory Committee.

In 1983 he was a visiting scientist at MIT and a visitor at the Indiana University Cyclotron Facility.

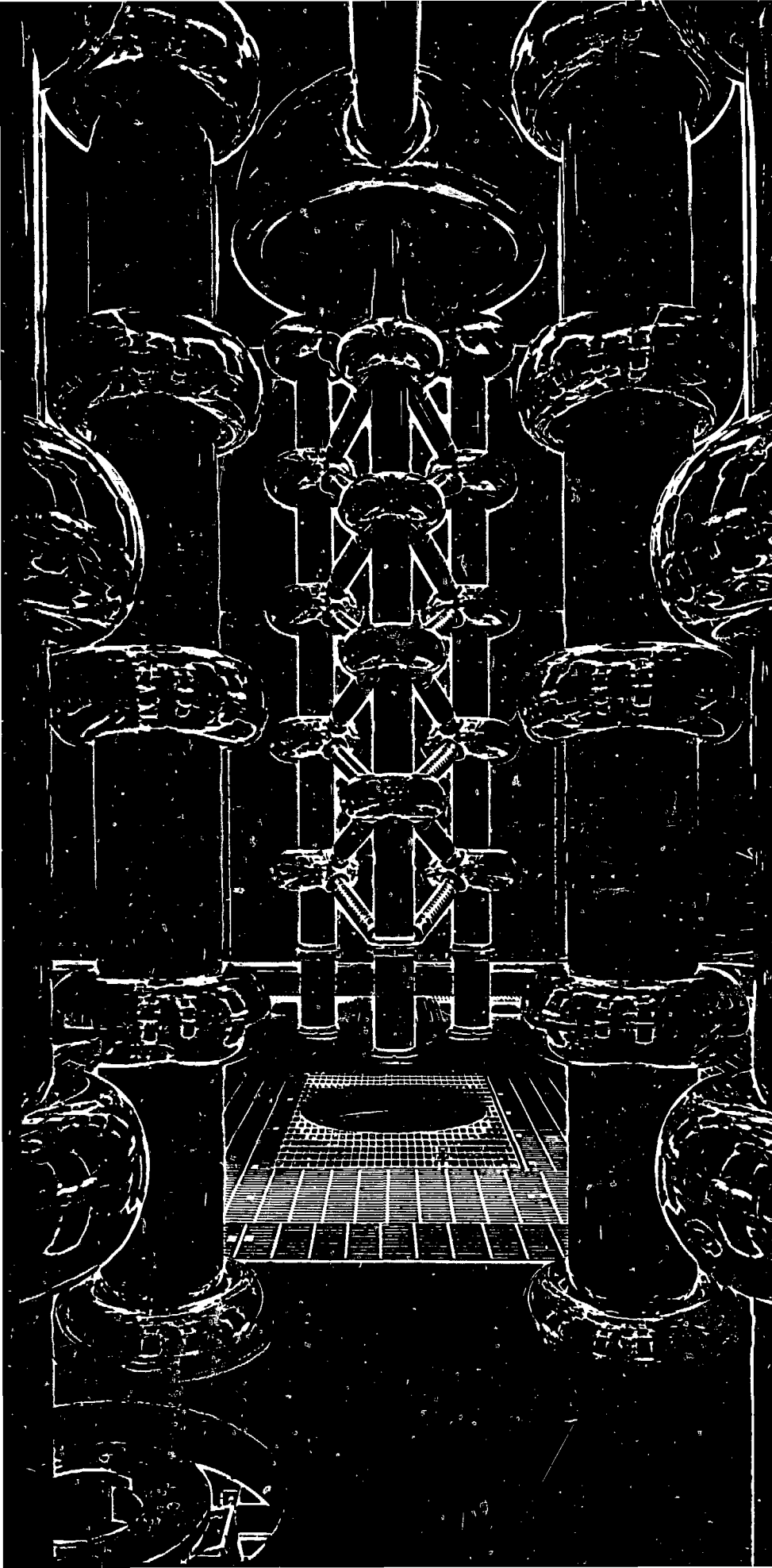


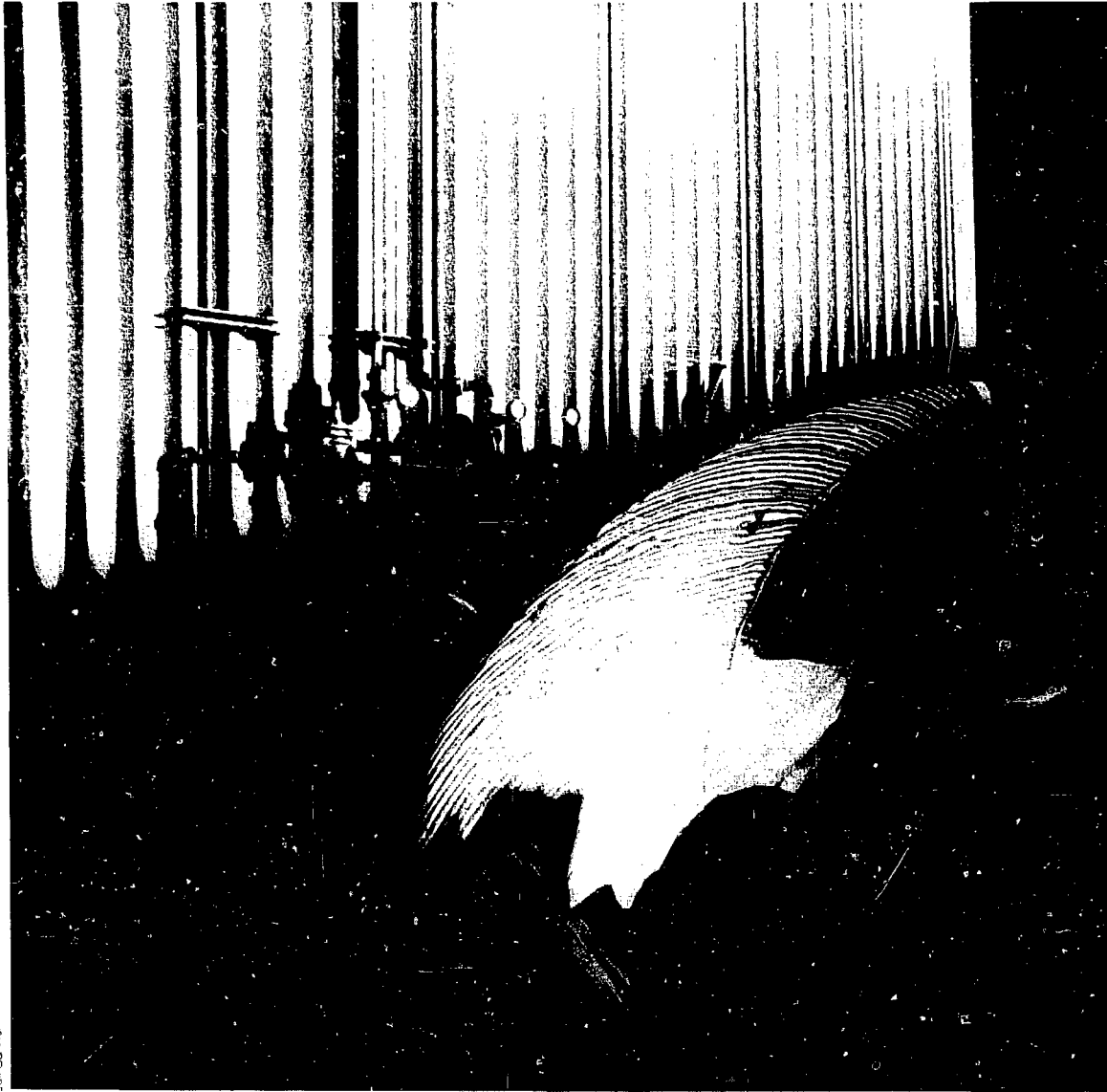
Fred Rick

### **Don Hagerman New MP-Division Leader**

Don Hagerman was appointed April 7, 1986, to lead the Medium-Energy Physics Division. The announcement, which followed a nationwide search launched earlier this year, was made by John Browne, Associate Director for Research.

Hagerman became a staff member at Los Alamos in 1955, conducting research on controlled thermonuclear reactions.





Jeff Gurney

## **LAMPF Users Group**



Nineteenth Annual Meeting

Committees

Minutes

Workshops

Visitors Center

### **Nineteenth Annual Meeting**

The Nineteenth Annual Meeting of the LAMPF Users Group, Inc., was held in Los Alamos on November 4-5, 1985, with 172 attendees. Chairman Robert Redwine (MIT) presided at the first session, which included a welcoming address by Robert Thorn, Acting Laboratory Director, and a Report from Washington by David Hendrie (Department of Energy). The LAMPF Status Report was presented by Louis Rosen, and Gerald Garvey spoke on Future Directions of LAMPF. The LAMPF operations report was delivered by Donald Hagerman.



In the afternoon session, conducted by incoming Chairman Barry Freedom (University of South Carolina), Robert Redwine gave the Annual Users Group Report, which was followed by a presentation of the election results. June Matthews (MIT) is Chairman-Elect of the Board of Directors; new members are Charles Goodman (Indiana University) and Gerald Hoffmann (University of Texas).

The following talks were given during the meeting:

- "A  $\nu_{\mu} - e$  Proposal for LAMPF," Hywel White (Brookhaven);
- "Searching for Muon Number Violation at LAMPF: Current Results and Future Prospects," Martin Cooper (Los Alamos);
- "NPL Upgrade," John McClelland (Los Alamos);
- "The WNR Neutron Source," Paul Lisowski (Los Alamos);
- "New High-Resolution  $\pi^0$  Spectrometer," David Bowman (Los Alamos);
- "Japanese Medium-Energy Program," Toshimitsu Yamazaki (University of Tokyo); and
- "LAMPF II," Henry A. Thiessen (Los Alamos).

## Committees

### Board of Directors

The Board of Directors comprises a Secretary/Treasurer and seven members elected by the LAMPF Users Group, Inc., whose interests they represent and promote. They concern themselves with LAMPF programs, policies, future plans, and especially with how users are treated at LAMPF. Users should address problems and suggestions to individual Board members.

The Board also nominates new members to the Program Advisory Committee (PAC).

The 1986 membership and term expiration dates are listed below.

James Bradbury  
(Secretary/Treasurer)  
Los Alamos

#### Terms Expiring in 1986

Robert Redwine  
(Past Chairman)  
MIT

George Burleson  
New Mexico State University

Donald Geesaman  
Argonne National Laboratory

#### Terms Expiring in 1987

Barry Freedom (Chairman)  
University of South Carolina

Charles Goodman  
Indiana University

Gerald Hoffmann  
University of Texas

#### Terms Expiring in 1988

June Matthews  
(Chairman-Elect)  
MIT

### Technical Advisory Panel

The Technical Advisory Panel (TAP) provides technical recommendations to the Board of Directors and LAMPF management about the development of experimental facilities and support activities. The TAP has 12 members, appointed by the Board of Directors for 3-year staggered terms; the Chairman of the Board of Directors also serves as TAP chairman. The TAP membership and term expiration dates are listed below.

#### Terms Expiring in 1985

Harold A. Enge  
MIT

Richard Hutson  
Los Alamos

Christopher L. Morris  
Los Alamos

Thomas A. Romanowski  
Ohio State University

#### Terms Expiring in 1986

William Briscoe  
George Washington University

Michael A. Oothoudt  
Los Alamos

Gary Sanders  
Los Alamos

Charles A. Whitten  
UCLA

**Terms Expiring in 1987**

David Bowman  
Los Alamos

Gerald Hoffmann  
University of Texas

Roy J. Peterson  
University of Colorado

Robert E. Pollock  
Indiana University

**LAMPF Program Advisory  
Committee**

The Program Advisory Committee (PAC) comprises about 25 members appointed for staggered 3-year terms. Members advise the Director of LAMPF on the priorities they deem appropriate for the commitment of beam time and the allocation of resources for the development of experimental facilities. The PAC meets twice each year for 1 week, during which time all new proposals that have been submitted at least 2 months before the meeting date are considered. Old proposals, and the priorities accorded to them, also may be reviewed.

**Terms Expiring in 1986**

David Axen  
TRIUMF

Barry Barish  
California Institute of Technology

Dietrich Dehnhard  
University of Minnesota

Frieder Lenz  
SIN

Harold M. Spinka, Jr.  
Argonne National Laboratory

Victor E. Viola, Jr.  
Indiana University

Larry Zamick  
Rutgers University

**Terms Expiring in 1987**

Eric G. Adelberger  
University of Washington

Gerard M. Crawley  
Michigan State University

William R. Gibbs  
Los Alamos

Wick C. Haxton  
University of Washington

Stanley B. Kowalski  
MIT

Philip G. Roos  
University of Maryland

Benjamin Zeidman  
Argonne National Laboratory

**Terms Expiring in 1988**

Hall L. Crannell  
Catholic University of America

David J. Ernst  
Texas A&M University

James L. Friar  
Los Alamos

Daniel S. Koltun  
University of Rochester

W. Gary Love  
University of Georgia

Norbert T. Porile  
Purdue University

Willem T. H. Van Oers  
University of Manitoba

D. Hywel White  
Brookhaven National Laboratory

### **Working Groups Chairmen**

**High-Resolution Spectrometer (HRS)**  
Raymond Ferguson  
Rutgers University

**Neutrino Facilities**  
Stuart Freedman  
Argonne National Laboratory

**Stopped-Muon Channel (SMC)**  
Martin Cooper  
Los Alamos

**Nuclear Chemistry**  
Robert Kraus  
Clark University

**Energetic Pion Channel and Spectrometer (EPICS)**  
Kalvir Dhuga  
New Mexico State University

**High-Energy Pion Channel (P<sup>3</sup>)**  
Gordon Mutchler  
Rice University

**Nucleon Physics Laboratory (NPL) Upgrade/Medium-Resolution Spectrometer**  
John Faucett  
New Mexico State University

**Computer Facilities**  
Kok-Heong McNaughton  
University of Texas

**Solid-State Physics and Materials Science**  
Robert Brown  
Los Alamos

**Muon-Spin Relaxation**  
Mario Schillaci  
Los Alamos

**Low-Energy Pion Channel (LEP)**  
James Knudson  
Arizona State University



## Minutes

### Board of Directors

The LAMPF Users Group, Inc. (LUGI), Board of Directors (BOD) met on March 10, July 9, and November 3, 1985. All meetings were chaired by Robert Redwine. Selected topics of discussion are provided below.

There were 172 registrants for the 1985 Annual Users Meeting. The papers presented at the meeting and the minutes of the workshops are given in the Proceedings.

The Program Advisory Committee (PAC) met in February and August 1985. For these 2 sessions 70 new proposals were received. The breakdown follows.


|   |    |
|---|----|
| HRS. . . . .  | 13 |
| EPICS. . . . .  | 19 |
| LEP . . . . .   | 15 |
| Nuclear Chemistry . . . . .                           | 1  |
| NPL . . . . .   | 5  |
| SMC. . . . .  | 4  |
| P <sup>3</sup> . . . . .                              | 6  |
| Solid-State Physics and<br>Materials Science. . . . . | 7  |

The BOD selected William J. Burger (MIT) as the recipient of the Louis Rosen Prize for 1985 for his thesis "An Experimental Study of Pion Absorption in <sup>58</sup>Ni at  $T_{\pi} = 160$  MeV." Because he was out of the country at the time, the award was presented to his advisor, Robert Redwine, and will be forwarded to him later.

### Technical Advisory Panel

The Technical Advisory Panel (TAP) met on February 8 and November 6, 1985. The chief purpose of the February meeting was to provide recommendations for LAMPF management concerning medium-term (next several years), medium-scale (several million dollars) projects and expenditures. After hearing a number of presentations the TAP assigned highest priorities to (1) adequate facilities and support for data acquisition and analysis, (2) the Medium-Resolution Spectrometer (MRS) on Line B, and (3) the Neutron Time-of-Flight (NTOF) facility on Line B.\*

\*LAMPF is fully committed to the Nucleon Physics Laboratory upgrade, including the MRS and NTOF facilities. Design and procurement effort has begun.



At the November meeting the TAP heard presentations on the status of a number of projects, including the High-Resolution Atomic-Beam facility, the Clamshell spectrometer at the LEP, the Data-Acquisition Center, the Nucleon Physics Laboratory upgrade, a rare muon decay detector system, a new neutrino-source possibility, and LAMPF II.

### **Workshops**

The following workshops are scheduled to be held at LAMPF.

**NUCLEAR PHYSICS LABORATORY UPGRADES  
AND MUON-CATALYZED FUSION**  
December 16-17, 1985

**FUNDAMENTAL MUON PHYSICS: ATOMS,  
NUCLEI, AND PARTICLES**  
January 20-22, 1986

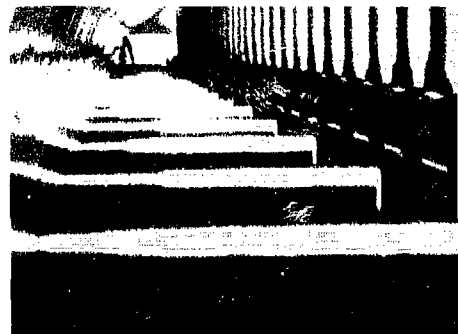
**PHYSICS WITH POLARIZED NUCLEAR  
TARGETS**  
February 6, 1986

**QUARK/GLUON PHENOMENA IN NUCLEAR  
AND PARTICLE PHYSICS**  
February 7-8, 1986

**ANNUAL USERS MEETING**  
October 27-28, 1986

**Visitors Center**

During this report period, 450 research guests worked on LAMPF-related activities or participated in experiments at LAMPF; of these, 132 were foreign visitors.



**LAMPF Users Group Membership**

**Membership**

|                                      |     |
|--------------------------------------|-----|
| Non-Laboratory _____                 | 610 |
| Los Alamos National Laboratory _____ | 182 |
| TOTAL _____                          | 792 |

**Fields of Interest\***

|  |     |
|--|-----|
| Nuclear and Particle Physics _____                             | 655 |
| Nuclear Chemistry _____  | 93  |
| Solid-State Physics and Materials Science _____                | 150 |
| Theory _____   | 164 |
| Biomedical and Biological Applications _____                   | 155 |
| Weapons Neutron Research _____                                 | 128 |
| Data Acquisition and Instrumentation _____                     | 193 |
| Administration, Coordination, Facilities, and Operations _____ | 52  |
| Isotope Production _____                                       | 49  |
| LAMPF II _____   | 397 |

\*These numbers do not add up to total membership because of multiple interests

**Institutional Distribution**

*Membership by Institutions*

|   |     |
|---|-----|
| Los Alamos National Laboratory _____      | 182 |
| National or Government Laboratories _____ | 81  |
| U.S. Universities _____                   | 338 |
| Industry _____                            | 31  |
| Foreign _____                             | 144 |
| Hospitals _____                           | 10  |
| Nonaffiliated _____                       | 6   |
| TOTAL _____                               | 792 |

*Number of Institutions*

|   |     |
|---|-----|
| National or Government Laboratories _____ | 19  |
| U.S. Universities _____                   | 97  |
| Industry _____                            | 27  |
| Foreign _____                             | 80  |
| Hospitals _____                           | 9   |
| Nonaffiliated _____                       | 6   |
| TOTAL _____                               | 238 |

**Regional Breakdown***East*

|  |     |
|--|-----|
| Pennsylvania, New Jersey, Delaware, Washington DC,<br>Massachusetts, New York, Connecticut, Vermont,<br>Rhode Island, New Hampshire, Maine _____ | 102 |
|--|-----|

*Midwest*

|  |    |
|--|----|
| Ohio, Missouri, Kansas, Indiana, Wisconsin, Michigan, Illinois,<br>North Dakota, South Dakota, Nebraska, Iowa, Minnesota _____ | 94 |
|--|----|

*South*

|   |    |
|---|----|
| Maryland, Virginia, Tennessee, Arkansas, West Virginia,<br>Kentucky, North Carolina, Alabama, Mississippi, Louisiana,<br>Georgia, Florida _____ | 70 |
|---|----|

*Southwest, Mountain*

|   |     |
|---|-----|
| Montana, Idaho, Utah, Wyoming, Arizona, Colorado,<br>New Mexico (excluding Los Alamos), Oklahoma, Texas _____ | 113 |
|---|-----|

*West*

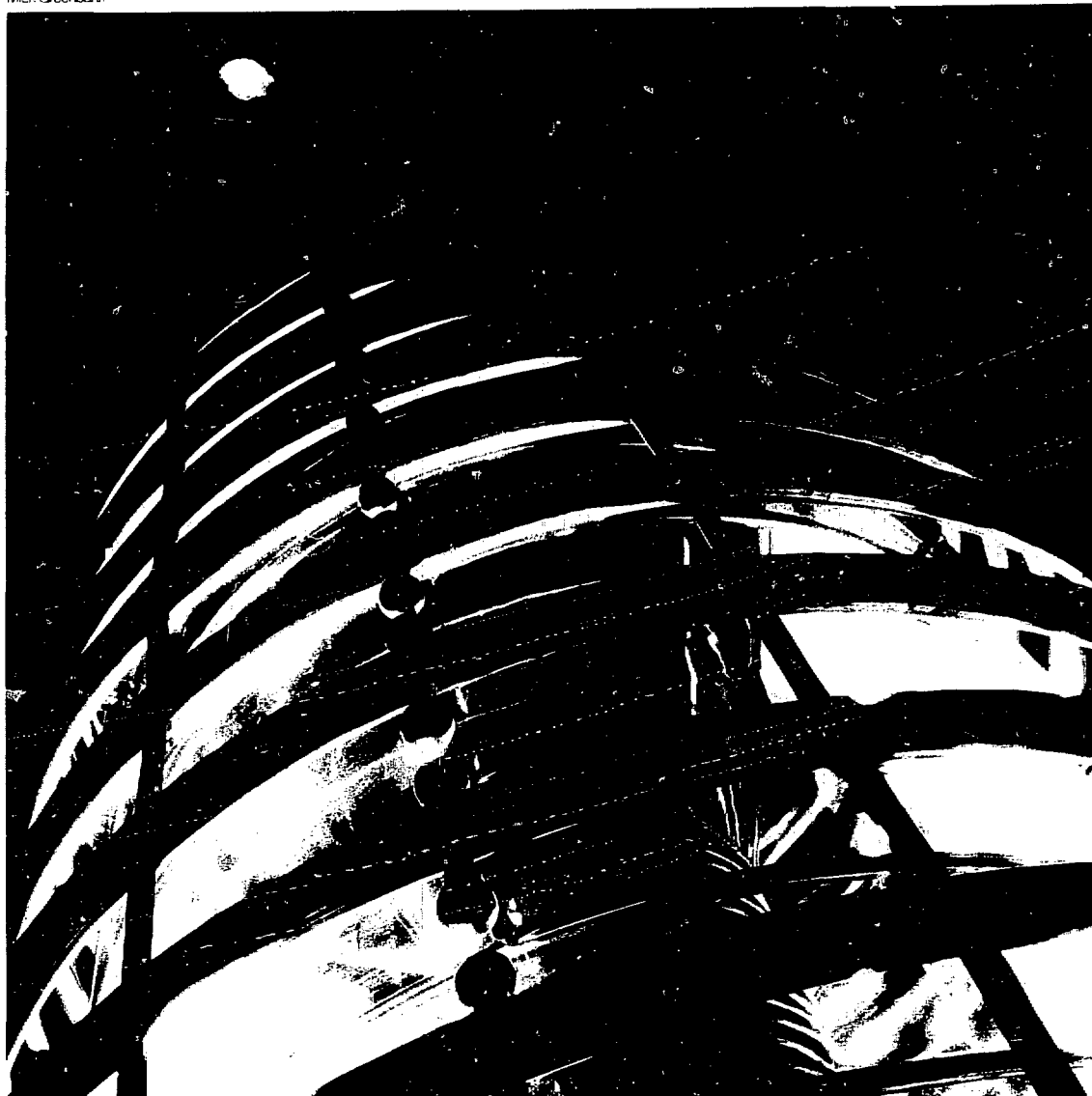
|  |    |
|--|----|
| Alaska, Hawaii, Nevada, Washington, Oregon, California _____ | 86 |
|--|----|

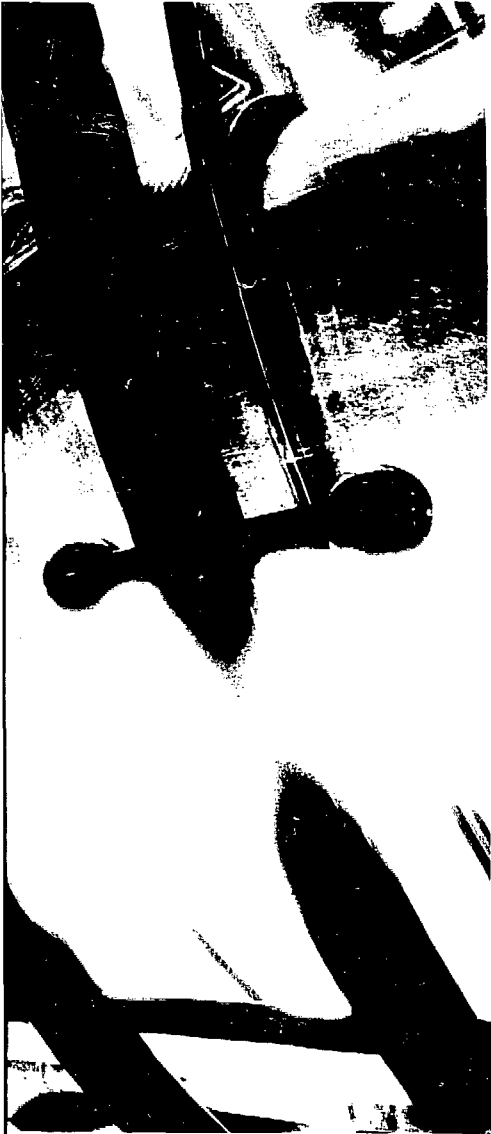
|                      |     |
|----------------------|-----|
| <i>Foreign</i> _____ | 145 |
|----------------------|-----|

|   |     |
|---|-----|
| <i>Los Alamos National Laboratory</i> _____ | 182 |
|---|-----|

|             |     |
|-------------|-----|
| TOTAL _____ | 792 |
|-------------|-----|

Mick Greenbank





## Research

Nuclear and Particle Physics

Atomic and Molecular Physics

Materials Science

Radiation-Effects Studies

Biomedical Research and Instrumentation

Nuclear Chemistry

Radioisotope Production

Theory

MP-Division Publications

## NUCLEAR AND PARTICLE PHYSICS

EXPERIMENT 225 — Neutrino Area

### A Study of Neutrino-Electron Elastic Scattering

Univ. of California at Irvine, Los Alamos,  
Univ. of Maryland

Spokesman: H. H. Chen (Univ. of California,  
Irvine)



LeRoy Sanchez

Bob Burman (MP-4) and Danny Krakauer (University of Maryland) with central detector used in Exp. 225 (see illustration on facing page)

Using the intense 0- to 53-MeV neutrino beam from the LAMPF Line A beam stop, a collaboration from the University of California at Irvine, Los Alamos, and the University of Maryland has made the first observation of  $\nu_e + e^- \rightarrow \nu_e + e^-$  elastic scattering. Measurement of this purely leptonic weak reaction provides a sensitive experimental test of the structure of the electroweak interaction.

The currently popular theories of fundamental forces are gauge theories. Within these theories the gravitational, the electromagnetic, and the strong and weak nuclear forces that operate between fermions are transmitted by the exchange of vector or tensor bosons. A significant advance in the attempt to find a single description of these four forces has been made by the unification of the electromagnetic force and the weak nuclear force. This electroweak gauge theory of Weinberg, Salam, and Glashow (WSG) is described by the interchange of four vector bosons—the photon, the charged  $W^\pm$ , and the neutral  $Z^0$ . To date, the weak interactions have been studied in reactions involving the exchange of  $W^\pm$  and  $Z^0$  bosons and  $Z^0$  photon interference. Now, in this experiment currently under way at LAMPF, evidence is beginning to appear for  $Z^0$ - $W^\pm$  interference.

The first publication of results has now appeared<sup>1</sup> in an article entitled "First Observation and Cross-Section Measurement of  $\nu_e + e^- \rightarrow \nu_e + e^-$ ." At this stage in the experiment the results agree with the standard (WSG) electroweak theory.

The LAMPF Line A beam stop is an intense source of 0- to 53-MeV  $\nu_e$ 's that are produced predominantly from stopped  $\pi^+$  decays leading to  $\nu_\mu$ 's, followed by stopped  $\mu^+$  decays leading to  $\bar{\nu}_\mu$ 's and  $\nu_e$ 's. In the WSG theory,  $\nu_e e^-$  scattering is expected to dominate  $\nu_\mu e^-$  and  $\bar{\nu}_\mu e^-$  scattering. In this energy range,  $\nu_e e^-$  scattering (where  $\nu$  without the subscript refers to any of these neutrinos) is confined within a forward kinematic cone of  $10^\circ$  for a 20-MeV detection threshold. Backgrounds to elastic scattering from cosmic rays, from accelerator-associated neutrons, and from other neutrino reactions are expected to be essentially isotropic. Hence the signature for  $\nu_e e^-$  scattering is a sharp forward peak in the angular distribution of single electron tracks.

Because a fairly detailed description of the detector system was given in the previous LAMPF Progress Report,<sup>2</sup> we give here only a brief summary. The large duty factor of LAMPF (6 to 12%) plus the small anticipated cross section for  $\nu_e e^-$  scattering results in an extremely high cosmic-ray background relative to the  $\nu_e e^-$  scattering signal, even with the high current (up to 1 mA) of the LAMPF beam. To reduce this cosmic-ray background to an acceptable level, three active and passive shields were

used in conjunction with a fine-grained sandwich detector. Figure 1 is a cutaway drawing illustrating the principal components of the active cosmic-ray shield and the sandwich detector used in the experiment.

The outermost cosmic-ray shield consists of steel and concrete with an effective thickness of more than  $900 \text{ g/cm}^2$ . This attenuates hadron fluxes by two orders of magnitude. Within this shield is an active anti-coincidence system consisting of 594 multiwire proportional chambers (MWPCs) that cover all inner surfaces of the massive outer shield. These counters, typically 520 cm long by 20 cm wide by 5 cm thick, are arranged into four layers in the walls and roof and a single layer on the floor. The MWPCs provide a prompt veto to reduce on-line triggers by a factor of  $10^4$  and to tag cosmic-ray muons for off-line analysis. Another inert shield averaging more than  $100 \text{ g/cm}^2$  of steel and lead is used inside the MWPCs to attenuate residual cosmic-ray gammas by a factor of 30.

The central detector, which has a total mass of 15 metric tons arranged in a 40-layer sandwich structure located a mean distance of 900 cm from the beam stop, is shielded by 630 cm of steel to reduce beam-associated neutrons by more than 15 orders of magnitude. The detector is designed to identify electrons by the measurement of  $dE/dx$  and to determine electron track direction in spite of large multiple scattering at these low energies.

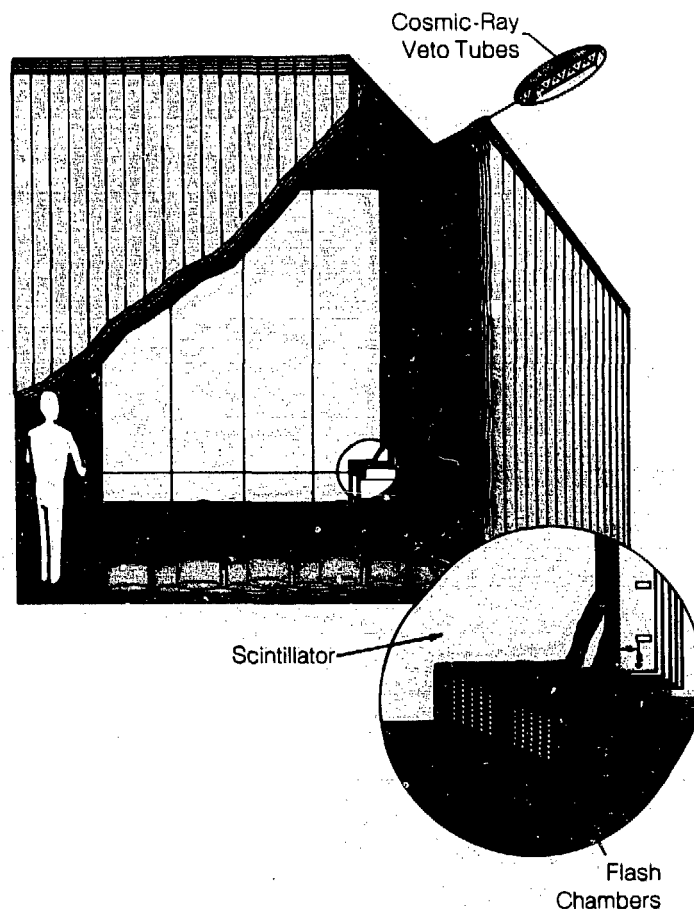


FIGURE 1. Cutaway view of the neutrino detector. The active cosmic-ray veto system (purple) consists of 594 MWPCs arranged as shown in four layers covering the walls and roof, with one additional layer on the floor; each counter has eight triangular sections. The central detector is a 40-layer sandwich of alternating scintillator counters and flash-chamber modules (FCMs). The 160 scintillator counters weigh 9.5 tons, and the 208 000 tubes of the FCMs, in alternating horizontal and vertical orientation as shown, weigh 4.5 tons. In the figure the scintillator counters are pale blue, flash chambers are shown as white layers in the central detector sandwich.



Each of the 40 layers in the detector is 305 cm high by 305 cm wide and consists of a plane of plastic scintillator and a flash-chamber module (FCM). The scintillation plane is constructed from four 2.6-cm-thick pieces, each 76 cm wide and viewed by a 12.7-cm-diam photomultiplier tube, for a total of 160 counters. An FCM, 1.4 g/cm<sup>2</sup> thick, contains 10 panels of polypropylene flash tubes with alternating coordinate readout, 5 horizontal and 5 vertical. Each panel contains 520 flash tubes of dimensions 0.5 by 0.6 by 305 cm for a total of 5200 flash tubes per FCM and 208 000 flash tubes in the entire detector. The average overall operating efficiency of the FCM system is 60% per panel and the angular resolution for short electron tracks including multiple scattering is  $\pm 7^\circ$  per projection.

The trigger is defined by a coincidence between at least three adjacent scintillation planes, with energy deposition between 1 and 16 MeV per plane and no veto from the MWPC system. This cosmic-ray veto is defined by MWPC hits in any two of the four planes of a wall or roof resulting in a veto rate of 7 kHz; a veto of 20  $\mu$ s is required to reduce triggers by electrons from stopped-muon decays. This gives a 15% system dead-time and results in a residual cosmic-ray trigger rate of less than 0.1 per second.

For each trigger, we recorded information from every scintillation counter, FCM, and MWPC. Also, we recorded information from every scintillator and MWPC for 32  $\mu$ s

before the trigger to further suppress backgrounds from stopped-muon decays. Data were taken during the LAMPF beam spill and also during a beam-off gate between spills for a cosmic-ray background subtraction.

Our publication was based on data accumulated between September 1983 and December 1984. The total exposure was 1.95 A · h of protons ( $4.4 \times 10^{22}$ ) on the beam stop, resulting in a sample of 98 558 beam-on and 317 740 beam-off events. The beam-off to beam-on live-time ratio was 4.43. Triggers from cosmic-ray stopped-muon decays and traversing muons were also recorded every 10 min for calibration and efficiency monitoring.

After an off-line analysis that (1) tightened cosmic-ray background identification, (2) imposed fiducial volume restrictions, and (3) required an electron signature in the  $dE/dx$  and tracking information, we were left with 1127 beam-on and 3864 beam-off events. Correction for the 4.43 beam-off to beam-on live-time ratio then gave a net number of  $255 \pm 36$  beam-associated events.

We show in Fig. 2(a) the histogram of the number of events versus  $\cos \theta_e$  for the beam-on and beam-off events, normalized by live time. Here  $\theta_e$  is the reconstructed angle of the upstream part of the recoil electron track relative to the direction of the neutrino. Figure 2(b) shows the histogram of the number of events versus  $\cos \theta_e$  for the difference between these beam-on and beam-off samples. In the forward cone, defined as  $\cos \theta_e \geq 0.96$ , a well-defined peak contains  $74.1 \pm 13.5$  beam-associated events. The  $\cos \theta_e \geq 0.96$  ( $\theta_e \leq 16^\circ$ )

cut is selected with consideration of  $\nu e^-$  kinematics, multiple scattering, and detector angular resolution. Beam-associated background in the forward cone is  $11.4 \pm 7.0$  events.

This result is determined from the number of beam-associated events in the  $\cos \theta_e$  interval between 0.84 and 0.96, assuming a flat distribution and accounting for the fraction of  $\nu e^-$  events outside the forward cone as determined by a Monte Carlo simulation. The extent of the chosen  $\cos \theta_e$  interval for this background subtraction comes from doubling the forward-cone angle; however, varying the extent of the  $\cos \theta_e$  interval in this subtraction does not significantly change this background. The background is due to  $\nu_e$  charged-current interactions with nuclei and possibly the capture of energetic neutrons scattered around the 630-cm-thick iron shield at the beam stop. We attribute the remaining  $62.7 \pm 16.7$  beam-associated events in the forward cone to  $\nu e^-$  scattering.

To determine the cross section, the efficiency for detecting  $\nu e^-$  scattering was evaluated by use of a Monte Carlo simulation. The simulated events were then passed through the data-reduction and data-analysis programs. Cosmic-ray stopped-muon decay events were also simulated and compared with observation to provide confidence in the Monte Carlo analysis. Altogether we assigned a 9% systematic error to the absolute detection efficiency.

The absolute neutrino source intensity depended on an earlier measurement of the number of stopped  $\pi^+$  and  $\mu^+$  decays per incident proton in copper done at the Lawrence

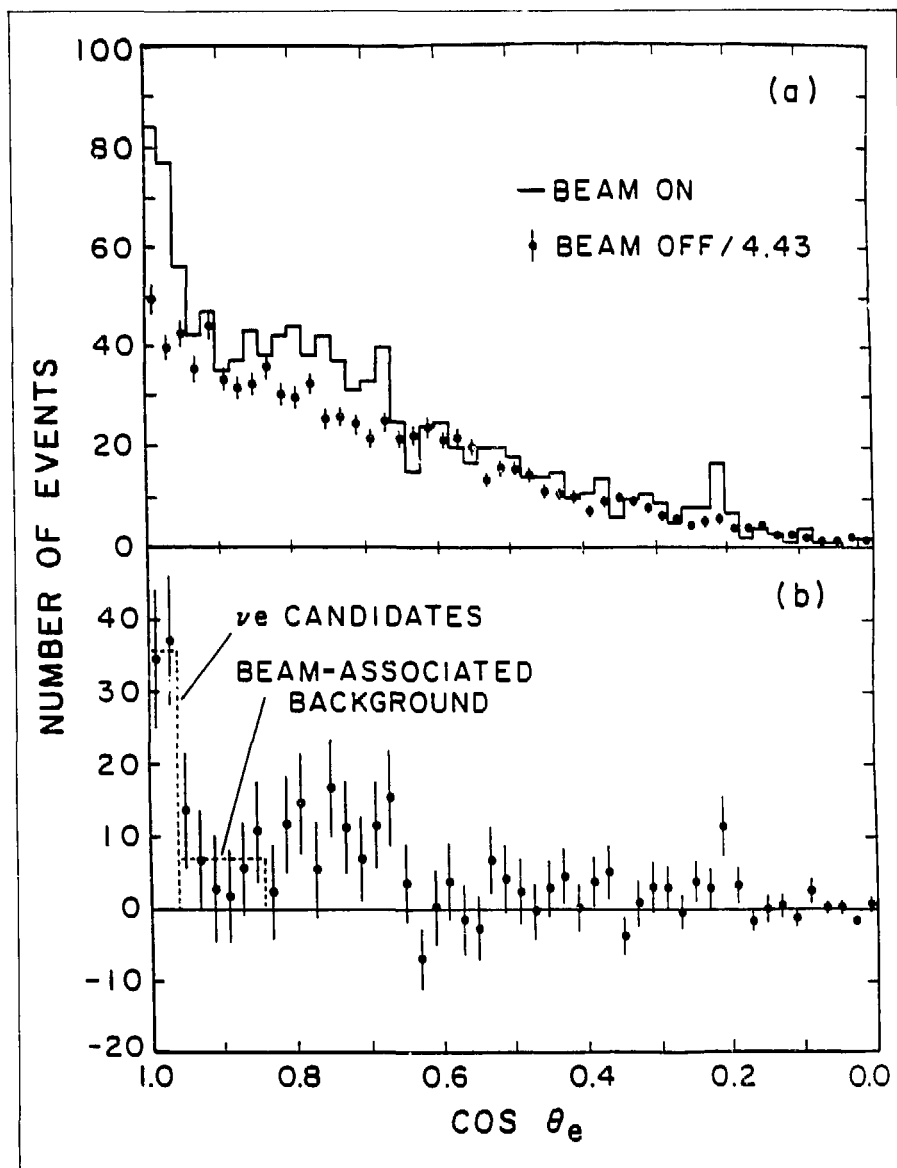


FIGURE 2 Histograms of the number of events versus  $\cos \theta_e$  in bins of 0.02

(a) for beam-on and normalized beam-off events after the analysis described in the text. Here,  $\theta_e$  is the recoil-electron angle relative to the direction of the incident neutrino, and

(b) for the beam-associated events above Events in the forward peak are candidates for  $\nu e^-$  scattering. Beam-associated backgrounds in the forward peak are estimated from outside the forward peak. Only statistical errors are shown

TABLE I The Number of Observed  $\nu_e + e^- \rightarrow \nu_e + e^-$  Events Compared with Several Possibilities Involving Interference Between  $Z^0$  and  $W^\pm$  Exchange. The indicated uncertainties for this measurement are statistical only; for the expected number of events, systematic only

|                                |                  |
|--------------------------------|------------------|
| This measurement               | $51.1 \pm 16.7$  |
| Expected number of events      |                  |
| Destructive interference (WSG) | $53.1 \pm 8.0$   |
| No interference                | $108.0 \pm 16.0$ |
| Constructive interference      | $163.0 \pm 25.0$ |

Berkeley Laboratory 184 in. cyclotron. For the present neutrino experiment, a 20-cm water degrader was inserted in front of the beam stop to increase, by 35%, the number of such decays per proton. A simulation of the effect of differing proton energy and of beam stop composition resulted in  $0.089 \pm 0.011$  stopped  $\pi^+$  decays per incident 765-MeV proton. Combining in quadrature the 9% uncertainty in absolute detection efficiency and the 12% uncertainty in neutrino source intensity results in an overall systematic error of 15%.

The  $62.7 \pm 16.7$  events attributed to  $\nu + e^- \rightarrow \nu + e^-$  contain  $\nu_\mu e^-$  and  $\bar{\nu}_\mu e^-$ , as well as  $\nu_e e^-$  candidates. Using the Monte Carlo simulation, we determined the number of expected  $\nu_\mu e^-$  and  $\bar{\nu}_\mu e^-$  events from measured cross sections and assigned  $4.3 \pm 1.1$  and  $7.3 \pm 1.7$  events, respectively, to these two reactions. The remaining  $51.1 \pm 16.7$  events are thus assigned to  $\nu_e + e^- \rightarrow \nu_e + e^-$ . This number is consistent with the WSG electroweak theory with a  $\nu_e e^-$  cross section of

$$\sigma(\nu_e e^-) = \left\{ \left[ 8.9 \pm 3.2 \text{ (stat)} \pm 1.5 \text{ (syst)} \right] \times 10^{-45} \text{ cm}^2/\text{MeV} \right\} E_\nu$$

The WSG electroweak theory predicts destructive interference between the  $Z^0$  and  $W^\pm$  vector boson exchange for  $\nu_e e^-$  scattering. We show in Table I the observed number of  $\nu_e e^-$  events and the calculated numbers assuming destructive interference (WSG), no interference, and constructive interference. Our result rules out constructive interference by almost 4 std dev and begins to rule out the no-interference case.

Additional data were taken during the period from June to December 1985. The total number of neutrino-electron scattering events collected is now more than double the 51 events presented above and in our paper. A very preliminary analysis of all the data is shown in Fig. 3, where the beam-associated events are plotted against the angle  $\theta_e$  between the recoil electron track and the incident neutrino direction. Improvements now being made in our analyses are expected to markedly reduce the error, both systematic and statistical, in the measurement of the  $\nu_e e^-$  cross section. In an ancillary experiment, 866, we will also improve the systematic error by making a more precise calibration of the neutrino flux. This will be a new measurement of the number of stopped  $\pi^+$  and  $\mu^+$  decays per incident proton.

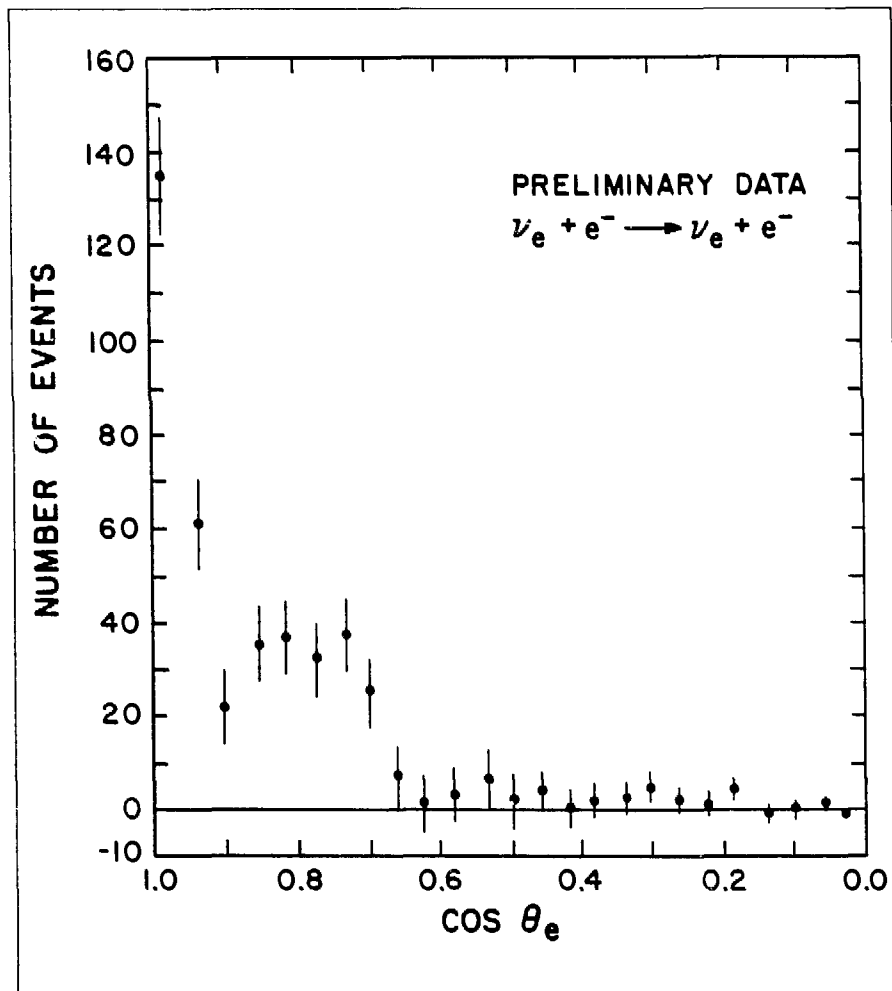


FIGURE 3 Beam-associated events from a preliminary analysis for all data taken from September 1983 to December 1985. As in Fig. 2,  $\theta_e$  is the recoil-electron angle relative to the direction of the incident neutrino. The forward peak now contains about 120 candidate  $\nu_e e^-$  events.

## References

1. R. C. Allen et al., *Physical Review Letters* **55**, 2401 (1985).
2. "Progress at LAMPF," Los Alamos National Laboratory report LA-10429-PR (April 1985), pp. 51-59.

## Cygnus Cosmic-Ray Air-Shower Array

Los Alamos, Univ. of Maryland, George Mason Univ., Univ. of New Mexico, Univ. of California at Irvine

*Spokesmen: D. E. Nagle (Los Alamos) and G. Yodh and J. Goodman (Univ. of Maryland)*

An array of scintillation counters has been deployed around the Exp. 225 detector to search for astrophysical sources of super-high-energy cosmic rays. This search, called the Cygnus project, is a collaborative effort of scientists and technicians from Los Alamos, University of New Mexico, University of California at Irvine, and University of Maryland. It derives its name from Cygnus X-3, a known source of 1012-eV gamma rays located in the direction of the constellation Cygnus.

Cygnus X-3 is thought to be a binary system consisting of a conventional star and a compact object, such as a neutron star or a black hole. It is an intense source of radio, x-ray, and gamma radiations with a 4.8-h periodicity. There are stochastic phenomena associated with its emissions in energy, amplitude, and timing. At this time it is an object of very

active experimental and theoretical interest. Several other gamma-ray sources appear to exist that have similar properties, and studies are under way at laboratories in both the northern and southern hemispheres. The Cygnus project will take high-quality data on gamma sources and make a significant contribution to the understanding of these interesting objects.

The Cygnus array detects super-high-energy gamma rays (greater than  $10^{14}$  eV) by detecting the extensive cosmic-ray air showers they create in the earth's atmosphere. These air showers are thought to be distinguishable from hadron-induced showers by their electron-to-muon ratio. By triggering the Exp. 225 detector (a muon detector with a 3-GeV threshold) on a signal from the array, which is sensitive to both low-energy muons and electrons, we expect to be able to determine the electron-to-muon ratio in the shower core.

The array consists of 40 scintillation counters (later to be upgraded to 80 counters), located on a grid with 10- by 10-m spacing, 60 m in radius, surrounding the Exp. 225 detector. Because of the topography in the beam stop area, the various counters

are located on roofs, hillsides, and parking lots. Each scintillation counter is constructed from a disk of plastic scintillator 1 m<sup>2</sup> in area (salvaged from the Volcano Ranch cosmic-ray array) that is viewed by a 5-cm photomultiplier tube mounted 60 cm above the center of the disk. The disk and photomultiplier tube are enclosed in cone-shaped Fiberglas that is lightproof and weatherproof.

The signals from the photomultiplier tubes are sent through coaxial cables to the central trigger electronics located in the Exp. 225 electronics trailer, where a majority coincidence of scintillation counters in the array triggers the data-acquisition electronics and the detector. The time of the trigger (determined by a 60-kHz WWV clock) and the charge and relative timing from each of the counters are recorded. Preliminary tests lead us to expect better than a 2-ns time resolution for each counter. An off-line analysis will derive the shower front direction from the timing and charge information. The number and density of particles in the shower also will be measured by the charge in each counter.

The past year's efforts were primarily concerned with the physical design and fabrication of the array and its electronics. We plan to devote a substantial effort to developing the analysis in the forthcoming year. We have a preliminary analysis package and are examining different fitting strategies to determine the optimal algorithm. We expect to begin taking data by the end of February 1986.

## EXPERIMENT 657 — EPICS

**Pion Inelastic Scattering from the  $N = 28$  Isotones and Neighbors**

Univ. of Texas, Los Alamos, New Mexico  
 State Univ., Univ. of Pennsylvania,  
 Bradford Univ. in the United Kingdom,  
 Univ. of Minnesota

Spokesman: D. S. Oakley (Univ. of Texas, Austin)

Experiment 657 is one of several EPICS experiments that have centered on the measurements of the differences between the neutron and proton multipole matrix elements  $M_n$  and  $M_p$  (Refs. 1 and 2). Although there have been some theoretical investigations (Ref. 3), the differences between  $M_n$  and  $M_p$  observed in  $(\pi, \pi')$  are still not fully understood.

In this experiment we measured the cross sections for  $\pi^+$  and  $\pi^-$  scattering from  $^{48}\text{Ti}$ ,  $^{50}\text{Ti}$ ,  $^{51}\text{V}$ ,  $^{52}\text{Cr}$ ,  $^{54}\text{Fe}$ , and  $^{56}\text{Fe}$ . Angular distributions were measured for all targets between

$\theta_{\text{lab}} = 18$  and  $55^\circ$  at  $T_\pi = 180$  MeV. In addition,  $^{48}\text{Ti}$ ,  $^{50}\text{Ti}$ ,  $^{54}\text{Fe}$ , and  $^{56}\text{Fe}$  were measured simultaneously as strip targets in the incident beam.

The data have been replayed and are now being analyzed. Distorted-wave impulse approximation (DWIA) calculations using collective-model transition densities have been used to extract the matrix elements for the  $2_1^+$  states in several of these nuclei, but other models will be needed to measure the higher-lying states (Fig. 1).

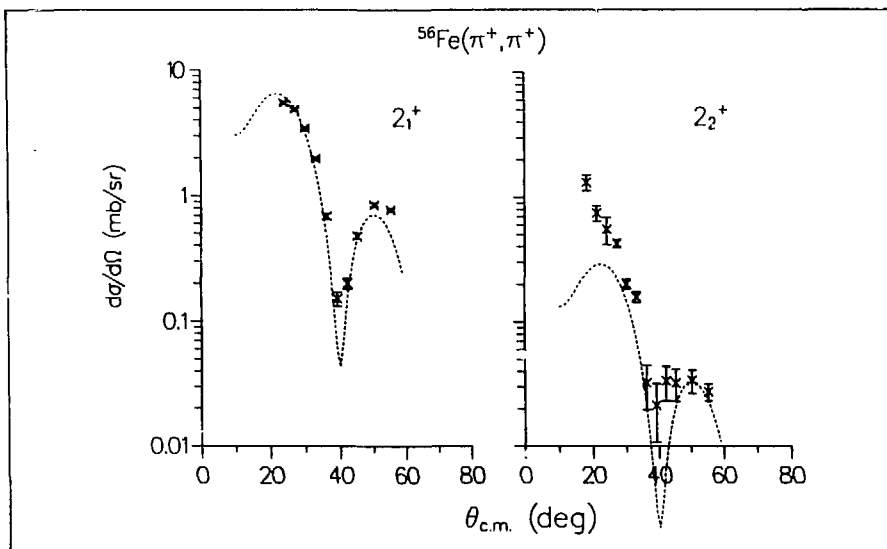


FIGURE 1 Comparison of collective-model DWIA calculations and data for the  $2_1^+$  and  $2_2^+$  states of  $^{56}\text{Fe}$

### References

1. K. G. Boyer et al., *Physical Review C* **24**, 598 (1981).
2. S. J. Seestrom-Morris, in "Progress at LAMPF," Los Alamos National Laboratory report LA-10429-PR (April 1985), p. 20.
3. V. R. Brown, A. M. Bernstein, and V. A. Madsen, *Physics Letters* **164B**, 217 (1985).

Previous experiments at LAMPF have shown that angular distributions on  $T=1$  nuclei in the pion double-charge-exchange (DCX) reaction to residual double-isobaric-analog states (DIASs) do not exhibit minima at the expected diffractive position. There have been different explanations of these data, which are consistent for  $T=1$  nuclei. For  $T=2$  DIAS transitions, however, these various theories predict contradictory results for the angular distribution shapes. Experiments 773 and 906 were designed to measure the shapes of angular distributions on two  $T=2$  nuclei,  $^{44}\text{Ca}$  (Brookhaven Exp. 906) and  $^{56}\text{Fe}$  (LAMPF Exp. 773), thus distinguishing between correct and incorrect theories. The experiments ran at EPICS between October and December 1985 (cycle 44). Replay

and analysis of the data are currently under way. Here we present some on-line results from the experiments, along with predictions of the angular distribution shapes.

A sample spectrum for  $^{56}\text{Fe}(\pi^+, \pi^-)$  is shown in Fig. 1. The spectrum is the sum of all data at 292 MeV and is dominated by the residual DIAS. The resolution (determined by elastic scattering) is about 700 keV (FWHM), whereas the  $^{44}\text{Ca}(\pi^+, \pi^-)$  resolution was only about 1 MeV. In each case the residual DIAS is at an excitation energy of about 9.5 MeV. At lower energies several other states are also strongly excited, including the ground state, a state just below the DIAS (in excitation energy), and one or more states just above the excitation energy of the DIAS.

EXPERIMENTS 773 and 906 —  
EPICS

### Pion Double-Charge-Exchange Angular Distributions for $T=2$ Double-Isobaric-Analog States

Univ. of Texas, Los Alamos, New Mexico  
State Univ., Univ. of Pennsylvania

Spokesmen: G. R. Burlison (New Mexico State Univ.), H. T. Fortune and R. Gilman (Univ. of Pennsylvania), and P. A. Seidl (Univ. of Texas, Austin)

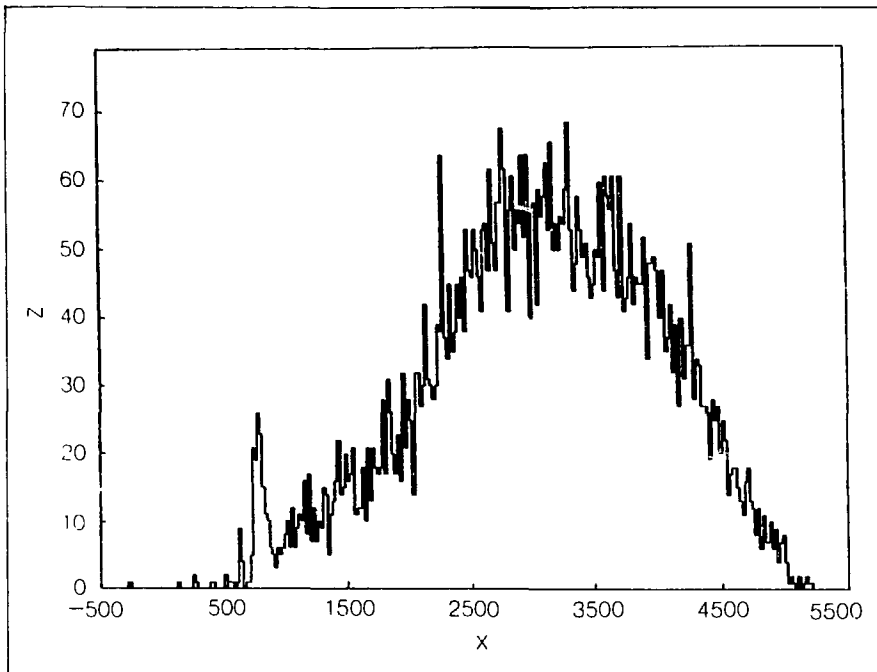


FIGURE 1 Spectrum for double charge exchange (DCX) on  $^{56}\text{Fe}$  at 292 MeV.



A  $5^\circ$  excitation function obtained for  $^{44}\text{Ca}$  is shown in Fig. 2. Both the nonanalog ground-state (g.s.) transition and the DIAS transition exhibit the usual characteristics. The g.s. transition is peaked near 140 MeV, which is very similar to  $^{56}\text{Fe} \rightarrow ^{56}\text{Ni}$  (g.s.) but about 20 MeV lower than in lighter nuclei. The DIAS transition cross section increases monotonically between  $\sim 160$  and  $\sim 300$  MeV, as seen for all DIAS transitions.

Angular distributions are shown in Fig. 3. (A partial angular distribution was also obtained for the  $^{56}\text{Fe}$  DIAS at 164 MeV and for corresponding ground-state transitions.) The curves represent predictions of three different models. The curve with a forward minimum (dot-dashed) predicts no shape difference between DIAS transitions on  $T=1$  and  $T=2$  nuclei. The middle curve (dashed) is a standard lowest-order optical-model calculation, and the curve with the minimum moved outward (solid) is a prediction of the second-order optical-potential theory of Johnson and Siciliano. The cross sections displayed result from

summing area gates (zero background has been assumed). The almost constant results are most similar to the second-order prediction. However, given the  $^{44}\text{Ti}$  and  $^{56}\text{Ni}$  spectra, estimates of the background will have to be made to better estimate the uncertainty in the angular distribution shape.

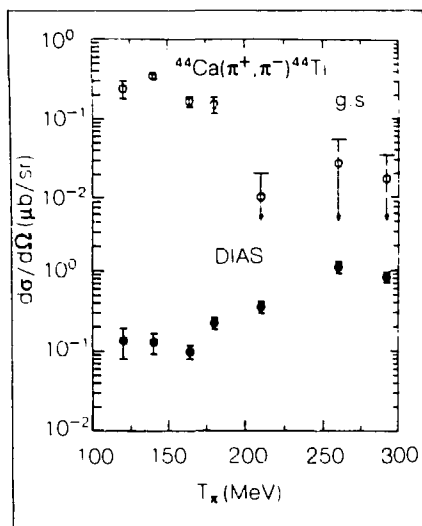


FIGURE 2 Excitation functions for DCX on  $^{44}\text{Ca}$  leading to the residual ground state and DIAS.

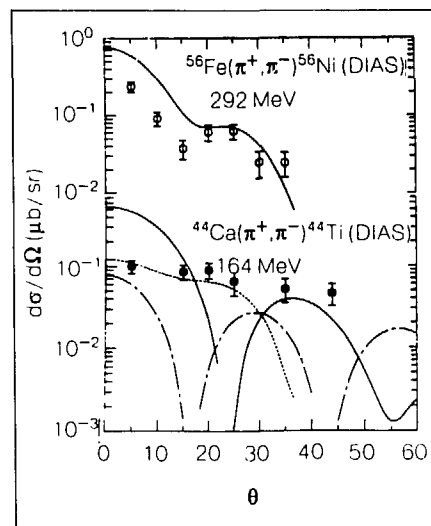


FIGURE 3 Comparison of the angular distribution at 292 MeV for  $^{56}\text{Fe}(\pi^+, \pi^-)^{56}\text{Ni}$  (DIAS) with prediction of the PIESDEX lowest-order calculation, and of the angular distribution at 164 MeV for  $^{44}\text{Ca}(\pi^+, \pi^-)^{44}\text{Ti}$  (DIAS) with predictions of various models. The curves are described in the text.

The amount of data available for investigation of the mass dependence of pion double charge exchange (DCX) has increased several fold over the past few years. Before any experimental evidence became available, Johnson<sup>1</sup> derived the mass dependence of sequential single charge exchange leading to double-isobaric-analog states (DIASs) as

$$\frac{d\sigma}{d\Omega}(q_x=0) \propto (N-Z) \times (N-Z-1)A^{-10/3}.$$

Several subsequent articles have made graphical comparisons of data (typically at  $\theta_{\text{lab}} = 5^\circ$ ) with the above expression.<sup>2,6</sup> No similar expression has been derived for nonanalog g.s.  $\rightarrow$  g.s. (ground-state) DCX, but the mass dependence has been claimed to be  $A^{-1/3}$  in some articles, again based on graphical comparisons. Here, we report results of a numerical comparison of data with some possible DCX expressions.

For both nonanalog and DIAS DCX, we have simultaneously fitted the mass dependence of  $5^\circ_{\text{lab}}$  cross sections at several incident beam energies. We have used three dif-

ferent mass-dependence functions:

1.  $(N-Z)(N-Z-1)A^{-x}$ ,
2.  $A^{-x}$ , and
3.  $N(N-1)A^{-x}$ .

The function  $(N-Z)(N-Z-1)A^{-x}$ , with  $x \sim 10/3$ , represents the expected form of the DIAS mass dependence. The function  $A^{-x}$ , with  $x \sim 4/3$ , has been used previously<sup>2,7</sup> to describe nonanalog DCX. The  $N(N-1)A^{-x}$  mass dependence, with  $x \sim 10/3$ , represents a collective enhancement in the cross sections over the expected  $A^{-10/3}$  because the cross section is proportional to the total number of neutron pairs rather than the number of excess neutron pairs to which we expect DIAS DCX to be sensitive.

The results of these fits are given in Table I. For the nonanalog data, the large  $\chi^2$  for the  $(N-Z)(N-Z-1)A^{-x}$  mass dependence indicates that it is inappropriate. This is to be expected, as there are many nonzero cross sections for  $N=Z$  nuclei. The  $N(N-1)A^{-x}$  and  $A^{-x}$  formulas result in comparable fits. For the large fraction of the nonanalog data that has been measured on  $N=Z$  targets, these two dependences are indistinguishable (given the experimental uncertainties). A reduced  $\chi^2$  value of 2.3 for the  $A^{-x}$  dependence, however,

EXPERIMENTS 777, 780, and 826 — EPICS

## Mass Dependence of Pion Double Charge Exchange

Univ. of Texas, Los Alamos, New Mexico State Univ., Univ. of Pennsylvania

Spokesmen: G. R. Bureson (New Mexico State Univ.), H. T. Fortune and R. Gilman (Univ. of Pennsylvania), C. L. Morris (Los Alamos), and P. A. Seidl (Univ. of Texas, Austin)

TABLE I Simultaneous Fits of the  $A$  Dependence at all Energies

| Type      | Form                 | $\chi^2$ | Exponent         |
|-----------|----------------------|----------|------------------|
| Nonanalog | $A^{-x}$             | 2.30     | $-1.35 \pm 0.06$ |
|           | $(N-Z)(N-Z-1)A^{-x}$ | 15.9     | $-3.25 \pm 0.13$ |
|           | $N(N-1)A^{-x}$       | 2.48     | $-3.51 \pm 0.06$ |
| DIAS      | $A^{-x}$             | 7.48     | $-1.79 \pm 0.07$ |
|           | $(N-Z)(N-Z-1)A^{-x}$ | 3.15     | $-3.29 \pm 0.04$ |
|           | $N(N-1)A^{-x}$       | 7.03     | $-3.72 \pm 0.07$ |

may indicate that this is an inadequate representation of the data. We note that one effect that will increase the  $\chi^2$  is the decrease of the peak energy of the excitation function with increasing target mass. Below the peak energy, this will result in heavier-mass nuclei being closer to the peak and will slow the mass dependence. Above the peak energy, the mass dependence will increase. We return to this point below.

In Table II we present fits to the nonanalog data, done independently at each energy with the  $A^{-x}$  function, and fits of two energy-independent parameters. The quantity  $g$  is a magnitude parameter for fits to the nonanalog excitation-function shapes (all are peaked near 160 MeV and are represented with Breit-Wigner functions). The quantity  $\sigma(T_0)$  is the maximum cross section of the nonanalog excitation functions independent of energy. The energy dependence is consistent with the description given above; a more quantitative comparison is made below. Given the energy-dependent results,

the fits to the energy-independent quantities  $\sigma(T_0)$  and  $g$ , and the simultaneous fit to all energies, we conclude that, on average, an  $A$  dependence of  $A^{-4/3}$  represents nonanalog DCX well.

Fits to DIAS DCX with the various mass dependences are also shown in Table I. The only possibly adequate representation of the DIAS mass dependence is the expected mass dependence formula, for which the exponent agrees with the expected value of  $-10/3$ . Table III presents fits with the expected mass dependence formula at each energy. At every energy the best-fit exponent is consistent with  $-10/3$  within errors. The major energy dependence is the larger  $\chi^2$  at the lower energies that results from the greater scattering in the data.

In Fig. 1 we present the energy dependence of the fitted exponents of Tables II and III. The DIAS exponents are essentially independent of energy, despite a variety of excitation-function behaviors. We know of no simple explanations of the fact

TABLE II. Results of Nonanalog  $A^{-x}$  Fits at Each Energy.<sup>a</sup>

| $T_\pi$       | $\chi^2$ | $f$                  | Exponent            | Constrained $A^{-4/3}$ Fit |                      |
|---------------|----------|----------------------|---------------------|----------------------------|----------------------|
|               |          |                      |                     | $\chi^2$                   | $f$                  |
| 120           | 2.16     | 93( $\pm 12$ )       | -0.77( $\pm 0.16$ ) | 3.58                       | 60( $\pm 6$ )        |
| 130           | 0.01     | 54( $\pm 28$ )       | -0.40( $\pm 0.20$ ) | 3.58                       | 59( $\pm 12$ )       |
| 140           | 0.87     | 133( $\pm 16$ )      | -0.97( $\pm 0.15$ ) | 1.37                       | 105( $\pm 9$ )       |
| 164           | 1.38     | 118( $\pm 8$ )       | -1.42( $\pm 0.09$ ) | 1.36                       | 124( $\pm 6$ )       |
| 180           | 3.15     | 50( $\pm 5$ )        | -1.81( $\pm 0.13$ ) | 3.98                       | 56( $\pm 5$ )        |
| 210           | 1.01     | 53( $\pm 9$ )        | -1.28( $\pm 0.20$ ) | 0.91                       | 51( $\pm 4$ )        |
| $\sigma(T_0)$ | 0.30     | 142( $\pm 29$ )      | -1.11( $\pm 0.22$ ) | 1.19                       | 117( $\pm 12$ )      |
| $g$           | 1.29     | 0.025( $\pm 0.005$ ) | -1.47( $\pm 0.20$ ) | 0.38                       | 0.028( $\pm 0.003$ ) |

<sup>a</sup>The  $d\sigma/d\Omega [A(\text{nb/sr})] = f/A_0^{-x}$ , with  $A_0 = 40$

that at lower energies there is no change to the DIAS mass dependence. Nuclear-structure effects might be expected to only add scattering to the data. The  $p^2$  terms, six-quark bags, and double-isobaric-nonanalog-transition (DINT) mechanisms that have been proposed as important to understanding resonance-energy DIAS DCX, however, might be expected to modify the  $A$  dependence.

The nonanalog exponents, in contrast, have a striking energy dependence, even though the whole data set was simultaneously fitted by an exponent that was about  $-4/3$ . We have estimated the effects of the variation in nonanalog excitation-function shapes with mass on the  $A$  dependence. The result (with error band) is shown as a set of dashed lines in Fig. 1. The variation with energy is similar to that of the fits to the data and agrees with the description given above. This comparison indicates

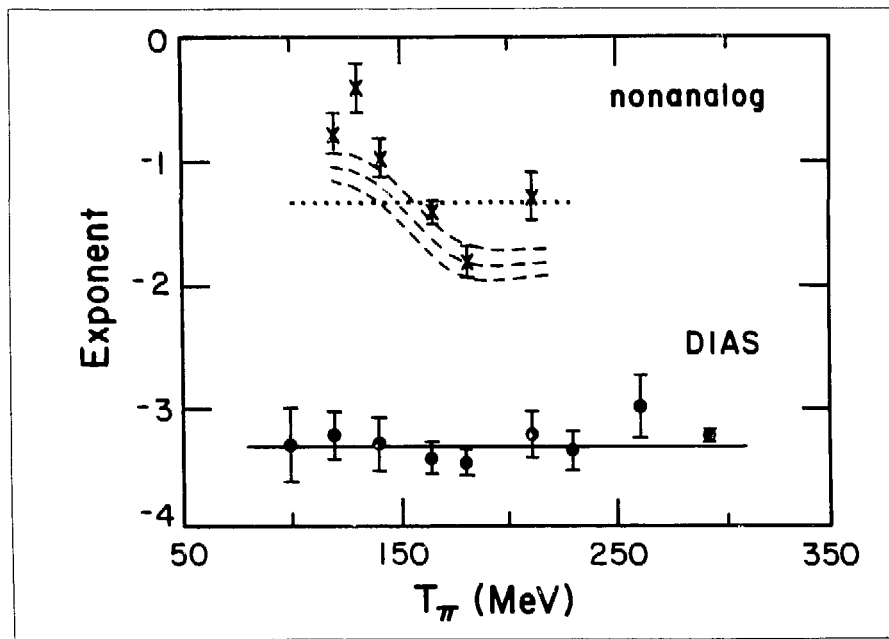


FIGURE 1 Variation with energy of the best-fit exponents for the DIAS and nonanalog mass dependences. The DIAS exponents are compared with the expected value of  $-10/3$  (solid line). The nonanalog exponents are compared with a prediction (see text) based on the Breit-Wigner excitation-function fits. The dashed lines show the prediction and error bands, and the dotted line is at  $-4/3$ .

TABLE III Results of DIAS  $(N - Z)(N - Z - 1)A^{-\lambda}$  Fits at Each Energy <sup>a</sup>

| $T_{\pi}$ | $\chi^2$ | $l$            | Exponent            |
|-----------|----------|----------------|---------------------|
| 100       | 7.9      | 12( $\pm 4$ )  | -3.32( $\pm 0.32$ ) |
| 120       | 6.4      | 24( $\pm 5$ )  | -3.23( $\pm 0.21$ ) |
| 140       | 6.7      | 16( $\pm 4$ )  | -3.31( $\pm 0.23$ ) |
| 164       | 4.0      | 15( $\pm 2$ )  | -3.43( $\pm 0.14$ ) |
| 180       | 3.4      | 18( $\pm 1$ )  | -3.47( $\pm 0.11$ ) |
| 211       | 0.03     | 29( $\pm 4$ )  | -3.23( $\pm 0.20$ ) |
| 230/5     | 2.8      | 39( $\pm 4$ )  | -3.37( $\pm 0.16$ ) |
| 260       | 1.8      | 64( $\pm 13$ ) | -3.00( $\pm 0.26$ ) |
| 292       | 2.1      | 68( $\pm 3$ )  | -3.24( $\pm 0.05$ ) |

<sup>a</sup>The  $d\sigma/d\Omega [A \text{ (nb/sr)}] = l(N - Z)(N - Z - 1)(A/A_0)^{-\lambda}$ , with  $A_0 = 42$

that much of the energy variation of the exponents arises from the fact that the nonanalog energy dependence is slightly different for different nuclei.

In summary, the mass dependences of both analog and nonanalog DCX may be approximated by relatively simple formulas,

$(N - Z)(N - Z - 1)A^{-10/3}$  for DIAS DCX and  $A^{-4/3}$  for nonanalog DCX, that are applicable over a wide range of masses. In both cases the quality of the agreement between data and formula varies with energy. For DIAS DCX the mass-dependence exponent is independent of energy, but the quality of the agreement is much worse at lower energies. For nonanalog DCX the quality of the agreement is fairly good at each energy, but the exponent varies with energy.

---

## References

1. M. B. Johnson, *Physical Review C* **22**, 192 (1980).
2. C. L. Morris et al., *Physical Review C* **25**, 3218 (1982).
3. S. J. Greene et al., *Physical Review C* **25**, 927 (1982).
4. P. A. Seidl et al., *Physical Review Letters* **50**, 1106 (1983).
5. K. K. Seth et al., *Physics Letters* **155B**, 339 (1985).
6. P. A. Seidl et al., *Physical Review C* **30**, 973 (1984).
7. L. C. Bland et al., *Physics Letters* **128B**, 157 (1983).

Measurement of neutron and proton transition amplitudes in  $^{22}\text{Ne}$  using  $\pi^-$  and  $\pi^+$  inelastic scattering allows meaningful comparison with sophisticated shell-model calculations in the lightest  $T=1$  nucleus not plagued by low-lying "intruder" states.

Experiment 800 was run during cycle 43 using the EPICS cooled-gas target with the rare-gas-handling equipment. Spectra were obtained for  $^{22}\text{Ne}(\pi, \pi')$  at an incident pion energy of 180 MeV in the angular range from 14 to 90°.

Figure 1 shows the spectra obtained at  $\theta_{\text{lab}} = 70^\circ$ . The data from this experiment have been replayed and extraction of the angular distributions from the spectra is in progress. Figure 2 shows the angular distributions for the first  $2^+$  and  $3^-$  states in  $^{22}\text{Ne}$ .

## EXPERIMENT 800 — EPICS

### Inelastic Pion Scattering from $^{22}\text{Ne}$

Los Alamos, Michigan State Univ., Univ. of Minnesota, Univ. of Pennsylvania, Univ. of Texas

Spokesmen: H. T. Fortune (Univ. of Pennsylvania) and C. F. Moore (Univ. of Texas, Austin)

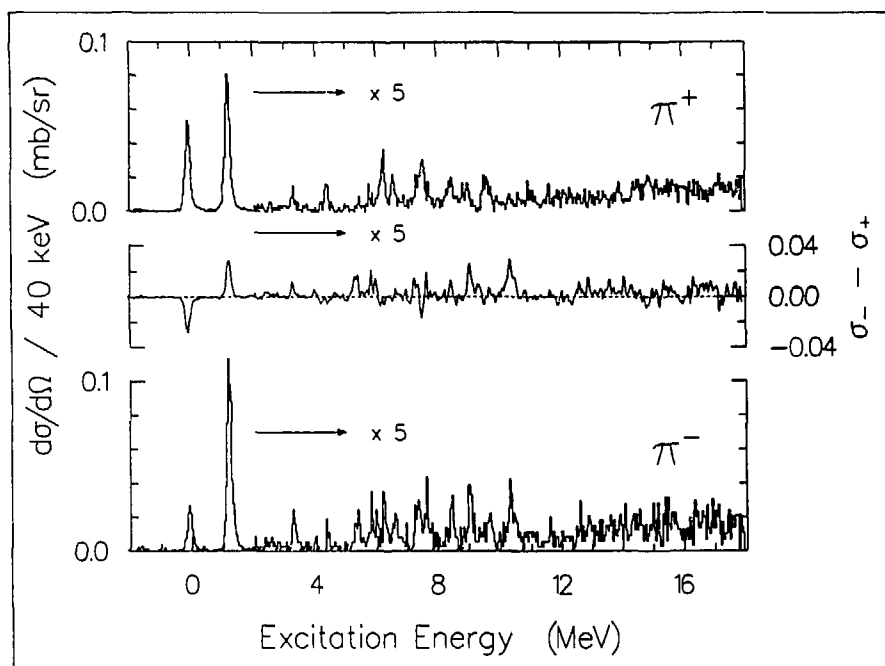


FIGURE 1 The  $\pi^+$  and  $\pi^-$  spectra at  $\theta_{\text{lab}} = 70^\circ$  along with the quantity  $(\sigma_- - \sigma_+)$

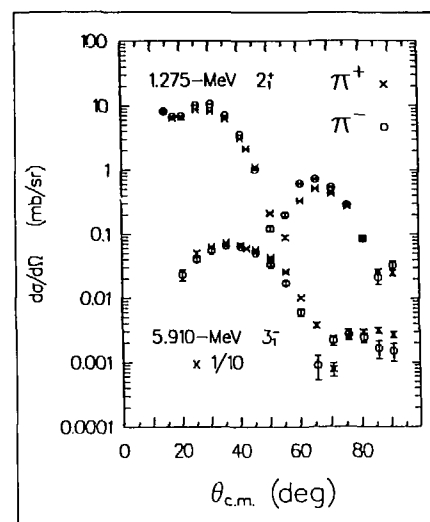


FIGURE 2 The cross sections (c.m.) for  $^{22}\text{Ne}(\pi, \pi')$  to the first  $2^+$  and  $3^-$  states

## EXPERIMENT 833U — EPICS

**Large-Angle Excitation Functions  
for Elastic Scattering of  $\pi^\pm$  from  $^{12}\text{C}$   
and  $^{16}\text{O}$** 

New Mexico State Univ., Univ. of Texas,  
Los Alamos, Univ. of Pennsylvania,  
Univ. of Minnesota

Spokesman: G. R. Burlison (New Mexico State  
Univ.)

Although a great deal has been learned about the pion-nucleus interaction from measurements that have principally involved scattering over the forward hemisphere, very little is known about scattering at angles greater than  $\sim 120^\circ$ . The only published large-angle data, for nuclei with  $A > 4$  and pion energies in the range of the  $\Delta(1232)$  resonance, include angular distributions for  $\pi^\pm$  on

$^{12,13}\text{C}$  at 100 MeV (Ref. 1),  $\pi^\pm$  on  $^{12}\text{C}$  at 162 MeV (Ref. 2),  $\pi^\pm$  on  $^{16}\text{O}$  at 114 MeV (Refs. 3 and 4), and  $\pi^\pm$  on  $^{16}\text{O}$  at 163 and 244 MeV (Ref. 4).

There is much interest in studying elastic scattering in this angular region because the predictions of various theoretical models, which are fairly successful in describing the forward-angle data, diverge considerably beyond  $100^\circ$ .

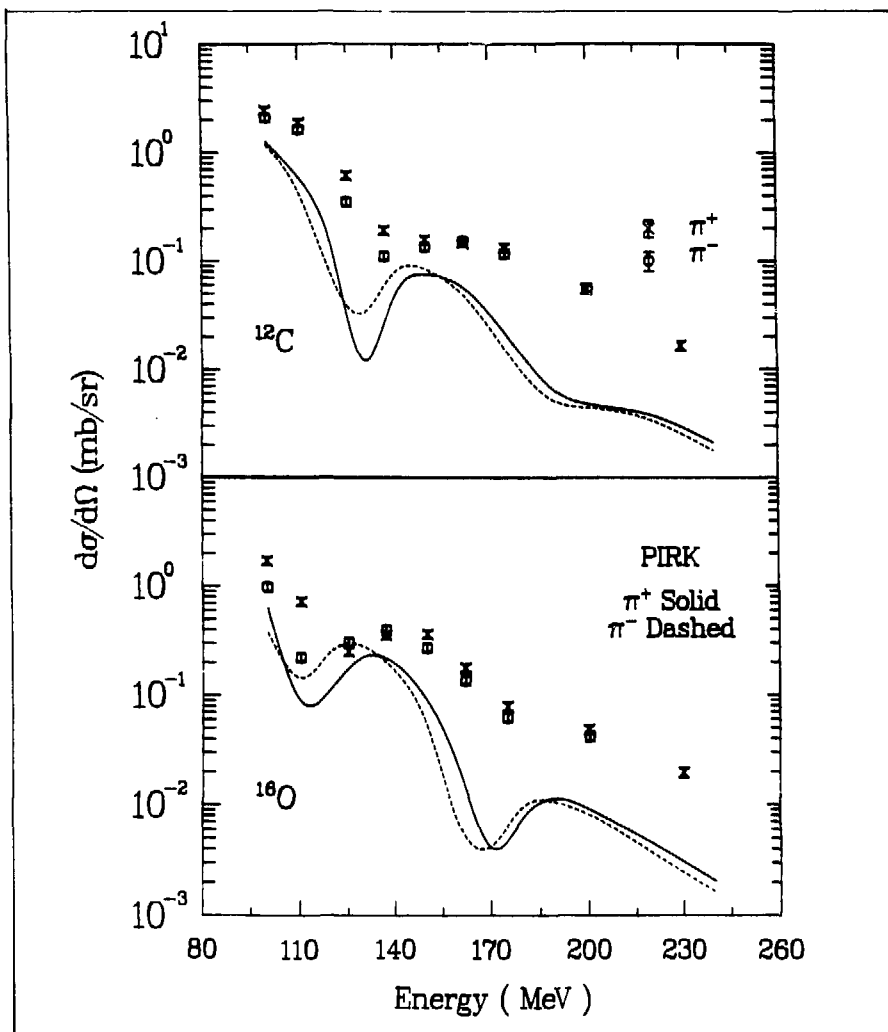


FIGURE 1 Measured excitation functions (at  $175^\circ$ ) for  $\pi^+$  (crosses) and  $\pi^-$  (open circles) on  $^{12}\text{C}$  and  $^{16}\text{O}$ . The lines are optical-model (PIRK) calculations

Recently, measurements showing large differences between  $\pi^+$  and  $\pi^-$  scattering from  $^{16}\text{O}$  at 114 MeV for angles near  $180^\circ$  were reported.<sup>3</sup> Calculations using pion-nucleus scattering models that include the Coulomb interaction and second-order terms were unable to reproduce the data over the full angular region. We feel that it is important to study these differences further, because they may help determine certain features of the nuclear amplitude, as has been found at small angles.<sup>5</sup>

We also feel that measurements of pion-scattering cross sections at large angles will help in understanding second-order effects in the pion-nucleus interaction. For these reasons we have made an experimental determination of the  $\pi^+$  and  $\pi^-$  scattering differences near  $180^\circ$ , as well as a study of the general behavior of large-angle scattering with energy. Here, we report the first measurements of large-angle excitation functions for  $\pi^+$  and  $\pi^-$  scattering on nuclei with  $A > 4$ . The data were measured using  $^{12}\text{C}$  and  $^{16}\text{O}$  targets at  $175^\circ$  for  $\pi^+$  energies between 100 and 230 MeV and  $\pi^-$  energies between 100 and 200 MeV.

The experiment<sup>6</sup> was performed at EPICS. The measurements were carried out with the back-angle EPICS setup, which is described in Ref. 7. Absolute normalizations were accomplished through the comparison of  $\pi^\pm p$  yields, measured with a  $\text{CH}_2$  target of areal density  $211 \text{ mg/cm}^2$ , with the  $\pi^\pm p$  cross sections calculated using the phase shifts from Ref. 8. The normalization uncertainty was  $\pm 10\%$ .

The data are presented in Figs. 1 and 2. All the excitation functions decrease with increasing incident energy and exhibit a broad structure with a minimum between 100 and 150 MeV. The  $\pi^+$  and  $\pi^-$  excitation functions on  $^{12}\text{C}$  are similar in shape and position of the minima and are different by less than 30% in magnitude. For  $^{16}\text{O}$  the  $\pi^+$  and  $\pi^-$  shapes are also similar, but the  $\pi^-$  minimum

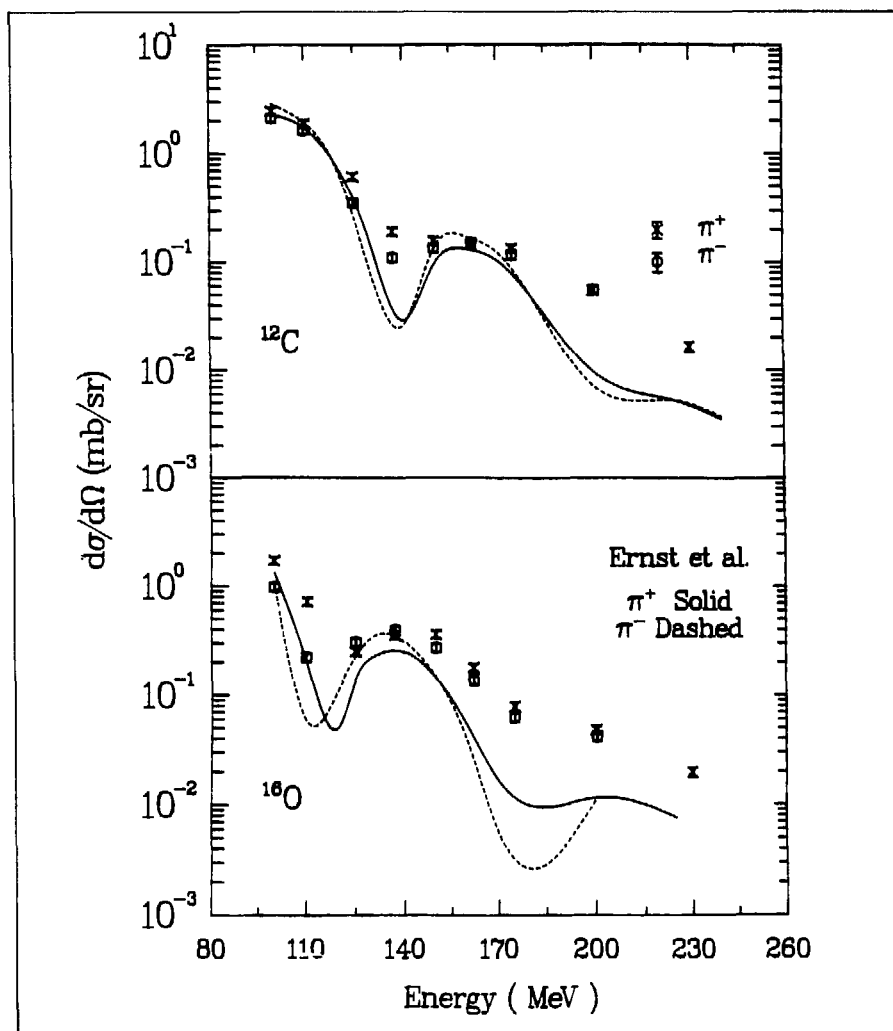


FIGURE 2 Data as in Fig. 1, but with the calculations of Ernst et al. (see text).



occurs about 10 MeV lower than the  $\pi^+$  minimum. The differences in magnitude between the  $\pi^+$  and  $\pi^-$  data are largest near  $\sim 120$  MeV and are greater for  $^{16}\text{O}$  than for  $^{12}\text{C}$ . For  $^{16}\text{O}$  there is a suggestion of a second minimum near 180 MeV, but for  $^{12}\text{C}$  the data appear to vary smoothly in this region.

To investigate the origin of the structure seen in the excitation functions, we have performed various optical-model calculations. One of these used the elastic-scattering code PIRK,<sup>9</sup> as modified by Cottingham and Holtkamp.<sup>10</sup> This code uses a zero-range coordinate-space model with a modern version of the Kisslinger optical potential.<sup>11</sup> The results of the calculations are displayed in Fig. 1. Although these calculations reproduce some features of the excitation functions, the calculated cross sections are generally smaller than those in the data by at least a factor of 2 at lower energies and by an order of magnitude at higher energies. The minima seen in the data are reproduced by PIRK within 15 MeV. At higher energies, however, the calculations indicate similar structures that are not observed in the data, except possibly for  $^{16}\text{O}$  at a reduced level.

We have also used the field-theoretical momentum-space model of Ernst et al.<sup>12</sup> Features of this approach include an exact treatment of relativistic kinematics, the incorporation of the finite range of the pion-nucleon amplitude, and the exact evaluation of the Fermi-averaging integral. This last feature allows the model to incorporate the formation, propagation, and decay of the  $\Delta(1232)$  resonance. The results are shown in Fig. 2. The qualitative features of the measured excitation functions are again reproduced with a noticeable improvement for  $^{12}\text{C}$ . However, the magnitudes of the predicted cross sections at higher energies are still too small.

In summary, the qualitative agreement of the optical-model calculations with the data is encouraging. However, the question of the origin of the generally larger absolute magnitude of the data is still unresolved, as is the disappearance of the predicted minima at the higher energies. As was found in an earlier study,<sup>3</sup> higher-order terms in the optical potential or additional effects not included in the models may be necessary to reproduce the cross sections at large angles. (Calculations along these lines are in progress.) Because the  $\pi^+$  and  $\pi^-$  excitation functions are not reproduced in detail, a better understanding of Coulomb distortions and of the interference of Coulomb and nuclear amplitudes is needed. In this respect, it is clear that large-angle pion-nucleus scattering affords a unique opportunity to explore further the pion-nucleus interaction.

---

## References

1. L. E. Antonuk et al., *Nuclear Physics* **A420**, 435 (1984).
2. B. Chabloz et al., *Physics Letters* **81B**, 143 (1979).
3. K. S. Dhuga et al., *Physical Review C* **32**, 2208 (1985).
4. E. Bason et al., *Physics Letters* **118B**, 319 (1982).
5. J. F. Germond and C. Wilkin, *Annals of Physics (New York)* **121**, 243 (1978).
6. H. A. Thiessen and S. Sobottka, Los Alamos National Laboratory report LA-4534-MS (1970).
7. W. B. Cottingham et al., Los Alamos National Laboratory report LA-10201-MS (1984); and G. R. Bureson et al., "A Large-Angle Pion-Nucleus Scattering Facility for EPICS at LAMPF" (submitted to *Nuclear Instruments & Methods*).
8. G. Rowe, M. Salomon, and R. H. Landau, *Physical Review C* **18**, 584 (1978).
9. R. A. Eisenstein and G. Miller, *Computer Physics Communication* **8**, 130 (1974).
10. W. B. Cottingham and D. B. Holtkamp, *Physical Review Letters* **45**, 1828 (1980).
11. L. S. Kisslinger, *Physical Review* **98**, 761 (1955).
12. D. L. Weiss and D. J. Ernst, *Physical Review C* **26**, 605 (1982); and M. B. Johnson and D. J. Ernst, *Physical Review C* **27**, 709 (1983).

## EXPERIMENT 836 — EPICS

**Energy Dependence of Pion Scattering to the Giant Resonance Region of  $^{208}\text{Pb}$** 

Univ. of Minnesota, Univ. of Pennsylvania,  
Los Alamos, Univ. of Texas, Univ. of  
Colorado, Univ. of Orsay

Spokesperson: Susan Seestrom-Morris (Univ. of  
Minnesota)

Experiment 836 ran at EPICS in July 1985. The objective was to measure the energy dependence of the ratio  $M_n/M_p$  extracted for the giant quadrupole resonance (GQR) in  $^{208}\text{Pb}$  as a function of incident pion energy. We hope that these measurements will be helpful in understanding the large ratios previously observed at  $T_\pi = 162$  MeV in Exp. 672.

Cross sections were measured for  $\pi^+$  and  $\pi^-$  scattering to the GQR at  $T_\pi = 120, 162, 200, 250,$  and  $300$  MeV. The 162-MeV data were measured for an overlap with the existing 162-MeV data as well as to add a new  $\pi^+$  point at 162 MeV. At 120 MeV,  $\pi^+$  data were taken at 23, 26, and 29°, and  $\pi^-$  data were taken at 19 and 24°. At 200 MeV, the  $\pi^+$  point is at 18° and the  $\pi^-$  point is at 16°. At 250 MeV, the  $\pi^+$  data were

taken at 12, 15, and 17°, and the  $\pi^-$  data were taken at 12, 14, and 16°. The 300-MeV  $\pi^+$  point was at 13°; the  $\pi^-$  point was at 12°. In the cases for which only a single angle was measured, this angle was chosen to be at the same momentum transfer as the peak in the 162-MeV angular distributions. The replay and normalization of the data are complete and peak fitting of the spectra is in progress.

The results of the preliminary peak fitting indicate some energy dependence to the ratio of  $\pi^-$  to  $\pi^+$  cross sections. At 120 and 162 MeV this ratio is about 3, whereas from 200 to 300 MeV it is  $\leq 2$ . The preliminary angular distributions have been analyzed by comparing them with distorted-wave impulse approximation (DWIA) calculations using Tassie-model transition densities to extract values for the neutron and proton matrix elements  $M_n$  and  $M_p$ . These are plotted as a function of

pion energy in Fig. 1. There is some evidence for an energy dependence to the extracted  $M_n$ . The  $M_p - M_n$  seems to increase with increasing pion energy, whereas  $M_n$  seems to decrease. However, because of the large uncertainties in these quantities, a straight line would also give a reasonable description of the data. Using the average values of  $M_n$  and  $M_p$  gives a ratio of  $M_n/M_p \approx 2.8$ , which is smaller than that determined at 162 MeV,  $M_n/M_p \approx 3.8$ .

We are investigating the effect of the shapes of the transition densities on both the values and energy dependence of  $M_n$  and  $M_p$ . So far the transition densities studied are limited to Tassie and collective models, with variation in geometry. No significant differences were found between results obtained using Tassie-model transition densities and those obtained using collective-model transition densities. A test was performed by varying the radius parameter of the distribution, whose derivative is used to calculate the

Tassie-model transition density. This essentially moves the peak of the transition density without changing the shape. If this parameter is changed so that there is a 1-fm difference between its value for neutrons and that for protons, the extracted value of  $M_n/M_p$  can be reduced from 3.8 to 1.54 ( $N/Z$ ). This is an unreasonably large difference between the neutron and proton distributions; also, it does not change the energy dependence of the extracted  $M_n$  and  $M_p$ . However, it is still possible that, by use of transition densities for which the neutron and proton shapes are different, a value of  $M_n/M_p$  nearer the theoretically expected value of  $N/Z$  could be obtained. Such shape differences could result from random-phase approximation (RPA) calculations that seem to predict larger tails for the neutron transition densities than for the proton transition densities.

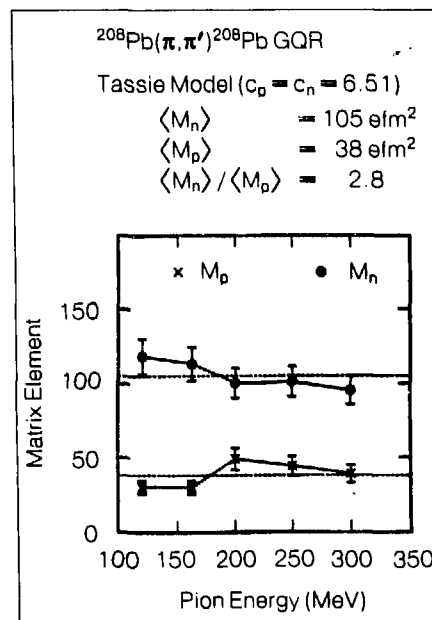


FIGURE 1. Preliminary values of  $M_n$  and  $M_p$  for the GQR in  $^{208}\text{Pb}$  extracted using Tassie-model transition densities

## EXPERIMENT 905 — EPICS

**New Test of Superratio by  $\pi^\pm$  Elastic Scattering on  $^3\text{H}$  and  $^3\text{He}$** 

UCLA, George Washington Univ.,  
Abilene Christian Univ.

Spokesman: B. M. K. Nefkens (UCLA)

Experiment 905 is a new measurement of  $\pi^+$  and  $\pi^-$  scattering on  $^3\text{H}$  and  $^3\text{He}$  to investigate, simultaneously, elastic and inelastic scattering slightly above nuclear breakup. The experiment was done at EPICS at three different energies (142, 180, and 220 MeV) and at five different angles (40, 60, 80, 90, and  $110^\circ$ ). The objectives of the experiment are

1. to probe the nature and extent of charge symmetry breaking as manifested in the deviation from unity of the superratio,

$$R = \left[ \frac{d\sigma(\pi^+ ^3\text{H})}{d\sigma(\pi^- ^3\text{He})} \right] / \left[ \frac{d\sigma(\pi^+ ^3\text{He})}{d\sigma(\pi^- ^3\text{H})} \right] \quad (1)$$

- Our previous result<sup>1</sup> at  $T_\pi = 180$  MeV and  $\theta_\pi = 60^\circ$  for elastic scattering implied that there is a definite intrinsic charge-symmetry violation in the strong interaction; and
2. to compare the  $^3\text{H}$ ,  $^3\text{He}$ , and  $^4\text{He}$  form factors. In the vicinity of  $70^\circ$  a comparison of  $d\sigma(\pi^+ ^3\text{H})$  with  $d\sigma(\pi^- ^3\text{He})$  elastic scattering is a comparison of the unpaired nucleon of  $^3\text{H}$  and  $^3\text{He}$ ; similarly, outside  $70^\circ$  in  $d\sigma(\pi^- ^3\text{H})$  and  $d\sigma(\pi^+ ^3\text{He})$  the mass form factors of the paired nucleons are compared.

Finally, coupling the new results with existing  $d\sigma(\pi^+ ^4\text{He})$  provides an interesting comparison of the form factors and radii of  $^3\text{He}$  and  $^4\text{He}$ .

It has been argued by Weinberg and others<sup>2,4</sup> that quantum chromodynamics (QCD) implies a small intrinsic violation of charge symmetry. Unfortunately, this violation has the same magnitude as that caused by the everywhere-present electromagnetic interaction, which makes it difficult to pin down the intrinsic violation of charge symmetry in any reaction.

A novel test for the validity of charge-symmetry violation can be made by measuring the superratio, which we have defined [see Eq. (1)] as the ratio of ratios of two pairs of charge-conjugate reactions. If the charge symmetry is valid,  $R = 1$  at each angle and at all energies after corrections have been made for electromagnetic effects. Looking at the charge-symmetry violation using the superratio has several distinct advantages.

1. Electromagnetic corrections are small (we estimate, less than a few per cent).
2. The  $\Delta$  resonance plays a major role in pion scattering on light nuclei, specifically the  $\Delta^-$  in the  $\pi^- ^3\text{H}$  scattering and  $\Delta^{++}$  in  $\pi^+ ^3\text{He}$ . Quark-model calculations<sup>5,8</sup> give a mass difference of about 5 MeV between  $\Delta^{++}$  and  $\Delta^-$  leading to  $R = 1$ .
3. Pion scattering covers a large range of four-momentum transfers  $t$ , up to  $10 \text{ fm}^{-2}$  in our case. This permits a measurement of possible differences in the  $^3\text{He}$  and  $^3\text{H}$  matter and spin form factors over a wide range of  $t$ .

4. From an experimental point of view the superratio method is more elegant, mainly because a measurement of  $R$  is completely independent of the absolute beam calibration as well as the efficiency and acceptance of the pion detector.

Our previous results for the superratio<sup>1</sup>  $R$  at pion energies of 142 and 180 MeV deviate very much from unity. Among the suggested explanations for the observed deviations of  $R$  from unity are

1.  $d\sigma(\pi^+p) \neq d\sigma(\pi^-n)$ , which is expected if  $\Delta^{++}$  and  $\Delta^-$  have different masses;
2.  $F(^3\text{H}) \neq F(^3\text{He})$ , where  $F$  is the form factor. Such a difference could in turn be the consequence of different<sup>6</sup> coupling constants,  $g(pp\pi^0) \neq g(nn\pi^0)$ ;
3. a possible charge-symmetry-violating, three-body interaction<sup>9</sup>; and
4. all of the above.

Important insight into the reaction mechanism for the pion-nucleus scattering comes from a comparison of the ratios  $\rho_1 = d\sigma(\pi^+{}^3\text{H})/d\sigma(\pi^+{}^3\text{He})$  and  $\rho_2 = d\sigma(\pi^-{}^3\text{He})/d\sigma(\pi^-{}^3\text{H})$  or elastic and inelastic scattering. These ratios have no special values except that charge symmetry requires that  $\rho_1 = \rho_2$ . They are easily measured without having to worry about absolute beam calibration. Our previous result shows striking dissimilarity between elastic and inelastic scattering. This difference is due mainly to the suppression of the spin-flip con-

tribution in the elastic channel. Thus, measurement of the ratios  $\rho_1$  and  $\rho_2$  for the elastic channel together with the inelastic channel provides a powerful, yet simple, measure of the spin-flip contribution to  $\pi^-{}^3\text{H}$  scattering. Also, the comparison of the superratio for elastic scattering with that for inelastic scattering is a novel probe of the contribution of the electromagnetic interaction.

To differentiate among the above possibilities requires knowledge of  $R$  at various pion energies,  $T_\pi \approx 140$  to 290 MeV, covering the  $\Delta$  resonance and spanning a wide range of angles from 30 to 120°. The various possibilities each have their own signature. If  $R$  at 100° changes sign for high momentum, it is suggestive of explanation 1; if  $R$  depends only on  $t$ , it must be explanation 2.

The experiment was performed at EPICS from June 17 to July 6, 1985. EPICS has the appropriate characteristics for this experiment, namely a large pion flux ( $\sim 10^8$  pions/s), good energy resolution, and a large acceptance for simultaneous measurements of elastic and inelastic scattering. This enabled us to measure the superratio for the elastic and inelastic scattering with a minimum relative error.

We used five targets having a cylindrical shape 12.7 cm in diameter and 22.9 cm high, made of special aluminum (aluminum alloy 2024-T3511), which has a small diffusion coefficient for tritium and a high

tensile strength (65 000 psi minimum). The walls of the cylinders were 1.85 mm thick. The cylinders were tested thoroughly for gas leaks and strength by pressurizing up to 700 psi with helium before being filled with the gases. The gases used were  $T_2$ ,  $H_2$ ,  $^3He$ , and  $D_2$ .

The fifth cylinder was evacuated to make the empty target. The average pressure in the cylinders was 450 psi. The pressure and weight of each cylinder were accurately measured before and after the experiment. The purity of each gas was determined spectroscopically. Because of the high radioactivity involved, a special

tritium enclosure and vent/recapture system was used. The target ladder at EPICS was slightly modified to accommodate the new target system. We used an incident momentum acceptance of 2% for all the runs. The energies of the incident pions ( $\pi^+$  and  $\pi^-$ ) used were 142, 180, and 220 MeV at lab angles of 40, 60, 80, 90, and 110°. At each angle, we measured successively the  $\pi^+$  yield from the tritium,  $^3He$ , and hydrogen targets with the spectrometer tuned for pion-tritium kinematics, yielding

$$\rho_1 = \frac{Y(\pi^+ ^3H \rightarrow \pi^+ ^3H)}{Y(\pi^+ ^3He \rightarrow \pi^+ ^3He)}$$

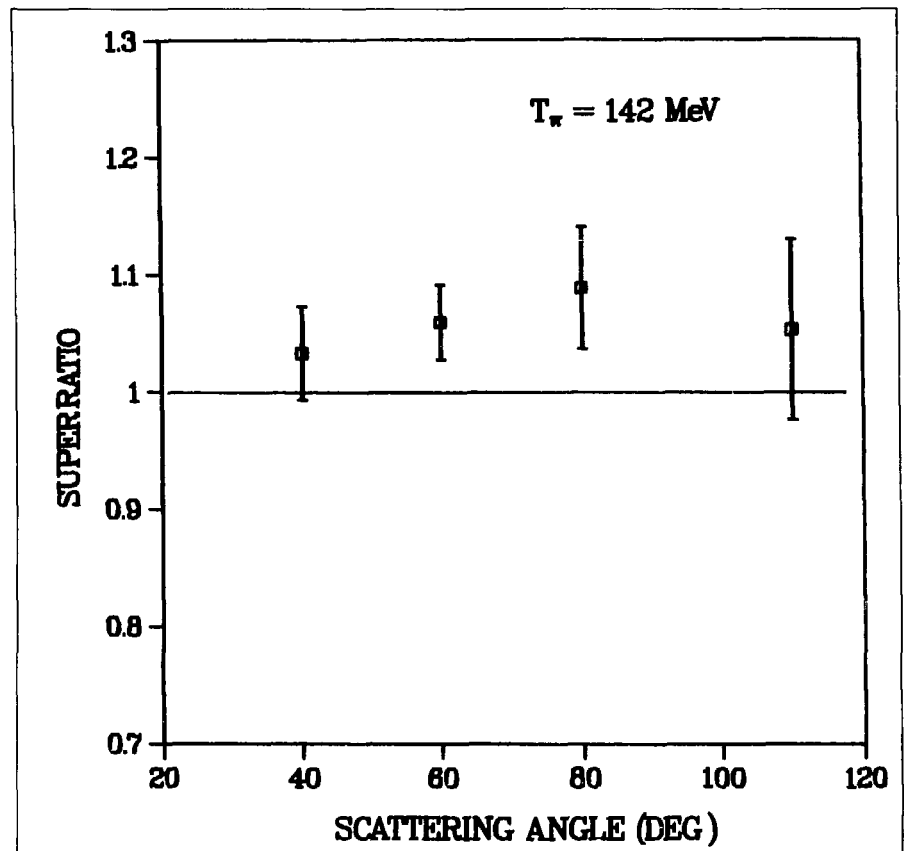


FIGURE 1. Preliminary results for the superratio  $R$  at  $T_\pi = 142$  MeV.

The background was measured using the hydrogen as well as the empty target. The measurement of  $\rho_1$  was followed by data collection on the hydrogen target, deuterium target, and empty target, with the spectrometer tuned to the  $\pi$ -D kinematics. A comparison of these data with the known hydrogen and deuterium cross section will give the normalization that will be used to calculate the absolute cross section. The same sequence with the same kinematics was repeated for the  $\pi^-$  beam to get  $\rho_2$ ,

$$\rho_2 = \frac{Y(\pi^- \text{ } ^3\text{H} \rightarrow \pi^- \text{ } ^3\text{H})}{Y(\pi^- \text{ } ^3\text{He} \rightarrow \pi^- \text{ } ^3\text{He})}$$

Now the superratio is obtained as  $R = \rho_1 \cdot \rho_2$ . Because at large angles the cross sections are small, we were not able in the time allocated for the experiment to collect enough statistics for the  $120^\circ$  angle. Also, we did not look for the dip around  $\theta_\pi = 70^\circ$  very carefully. We plan another experiment in the near future for this purpose.

The analysis of the data is proceeding. Preliminary results for the superratio  $R$  at  $T_\pi = 142$  MeV are shown in Fig. 1.

## References

1. B. M. K. Nefkens, W. J. Brisco, A. D. Eichon, D. H. Fitzgerald, J. A. Holt, A. A. Mokhtari, J. A. Wightman, M. E. Sadler, R. Boudrie, and C. Morris, *Physical Review Letters* **52**, 735 (1984).
2. S. Weinberg, in "A Festschrift for I. Rabi," *Transactions of the New York Academy of Sciences* **1**, 185 (1977).
3. P. Langacker and H. Pagels, *Physical Review D* **19**, 2070 (1979).
4. D. Gross, S. Treiman, and F. Wilczek, *Physical Review D* **19**, 2188 (1979).
5. H. R. Rubenstein, *Physical Review Letters* **17**, 41 (1966).
6. R. P. Bickerstaff and A. W. Thomas, *Physical Review D* **25**, 1869 (1982); and N. G. Deshpande et al., *Physical Review D* **15**, 1885 (1977).
7. K. F. Liu and C. W. Wong, *Physical Review D* **17**, 920 (1978); and N. Isgur, *Physical Review D* **21**, 779 (1980).
8. F. Myhrer and H. Pilkuhn, *Zeitschrift fuer Physik* **29**, 675 (1984).
9. J. Friar et al., *Comments on Nuclear and Particle Physics* **11**, 51 (1983).



## EXPERIMENT 392 — HRS

**Measurement of the Wolfenstein Parameters for  $p + p$  and  $p + n$  Scattering at 500 and 800 MeV**

Univ. of Texas at Austin, Rutgers Univ.,  
Los Alamos

Spokesman: G. W. Hoffmann (Univ. of Texas,  
Austin)

The proton-nucleon scattering amplitudes are necessary first-order ingredients for microscopic descriptions of proton-nucleus scattering that use the impulse approximation (IA) (both the nonrelativistic and relativistic approaches). Lack of sufficient data for  $p$ -nucleon scattering from 500 to 800 MeV, particularly at small momentum transfers, has in the past led to ambiguous or poorly determined scattering amplitudes. The objective of Exp. 392 is to provide additional  $p$ -nucleon scattering data at 500 and 800 MeV that will further constrain the scattering amplitudes at small-to-medium momentum transfers.

The experiment is divided into two phases at each energy: (1) free proton-proton ( $pp$ ) measurements using a liquid-hydrogen target and (2) quasi-elastic proton-proton and proton-neutron ( $pn$ ) measurements using a liquid-deuterium target. In both phases, incident beams of protons, polarized in the  $\hat{n}$  (up, down),  $\hat{s}$  (left, right), and  $\hat{q}$  (parallel-, antiparallel-to-the-beam momentum) direction, are scattered from the target.

The high-energy scattered protons are detected by the HRS and are rescattered at the HRS focal-plane-polarimeter (FPP) carbon analyzer in order to determine the spin components of the outgoing protons (transverse, vertical and transverse, horizontal). Because of the precession of the spin components that are not parallel to the HRS magnetic fields, the spin components de-

termined by the FPP are actually mixtures of the orthogonal set of spin components at the target. This precession facilitates measurements of the outgoing spin components that lie along the momentum of the particles at the target, and it is also the reason that certain spin components cannot be determined over certain angular ranges (at some angles these components precess to longitudinal or nearly longitudinal spins at the focal plane). The polarizations determined at the focal plane, therefore, must be separated into the appropriate polarization components at the target before the triple-scattering parameters can be determined.

In the quasi-elastic phase of the experiment, a second arm, the recoil-particle-detection system, is used to distinguish between  $pp$  and  $pn$  scatterings. By requiring either a recoil proton or a recoil neutron in coincidence with the event detected by the HRS, both quasi-elastic  $pp$  and  $pn$  triple-scattering parameters may be measured. A comparison between elastic and quasi-elastic  $pp$  data is also made to indicate the validity of using quasi-elastic  $pn$  (deuterium target) results to determine free-scattering amplitudes.

Both the 500- and 800-MeV phases of Exp. 392 are complete. The 800-MeV results are published in Refs. 1 and 2, and the 500-MeV data are now in final form. These data are compared with recent phase-shift predictions of Arndt\* in Fig. 1(a)-(e) for  $pp$  data and in Fig. 2(a)-(e) for  $pn$  data. An overall normalization

\*Reference 3, and information on the WIB4 solution provided by Richard A. Arndt, Virginia Polytechnic Institute and State University, 1984

uncertainty of  $\pm 0.01$  ( $\pm 0.02$  for the parameters  $D_{LS}$  and  $D_{LL}$ ) has not been included in the error bars but should be applied to all data. As seen in the figures, the 500-MeV scattering amplitudes appear to be reasonably well determined. The agreement between data and phase-shift solution

also provides further support for the equivalence of free nucleon-nucleon and quasi-elastic (deuterium) nucleon-nucleon measurements at these bombarding energies and in the range of momentum transfer spanned by Exp. 392.

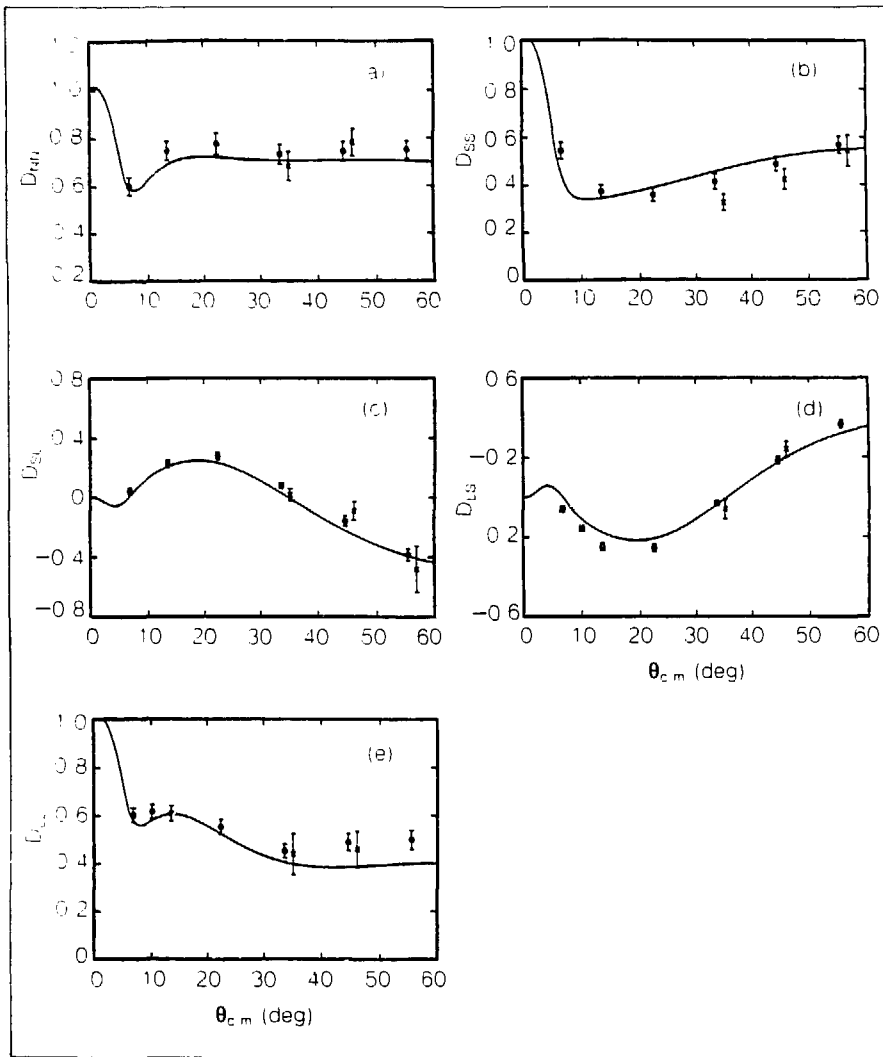


FIGURE 1 The 500-MeV elastic and quasi-elastic  $pp$  triple-scattering parameters (a)  $D_{NN}$ , (b)  $D_{SS}$ , (c)  $D_{SL}$ , (d)  $D_{LS}$ , and (e)  $D_{LL}$ . The solid curves are phase-shift predictions (solution W184). The free  $pp$  data are indicated by solid dots, and the quasi-elastic data are indicated by crosses.

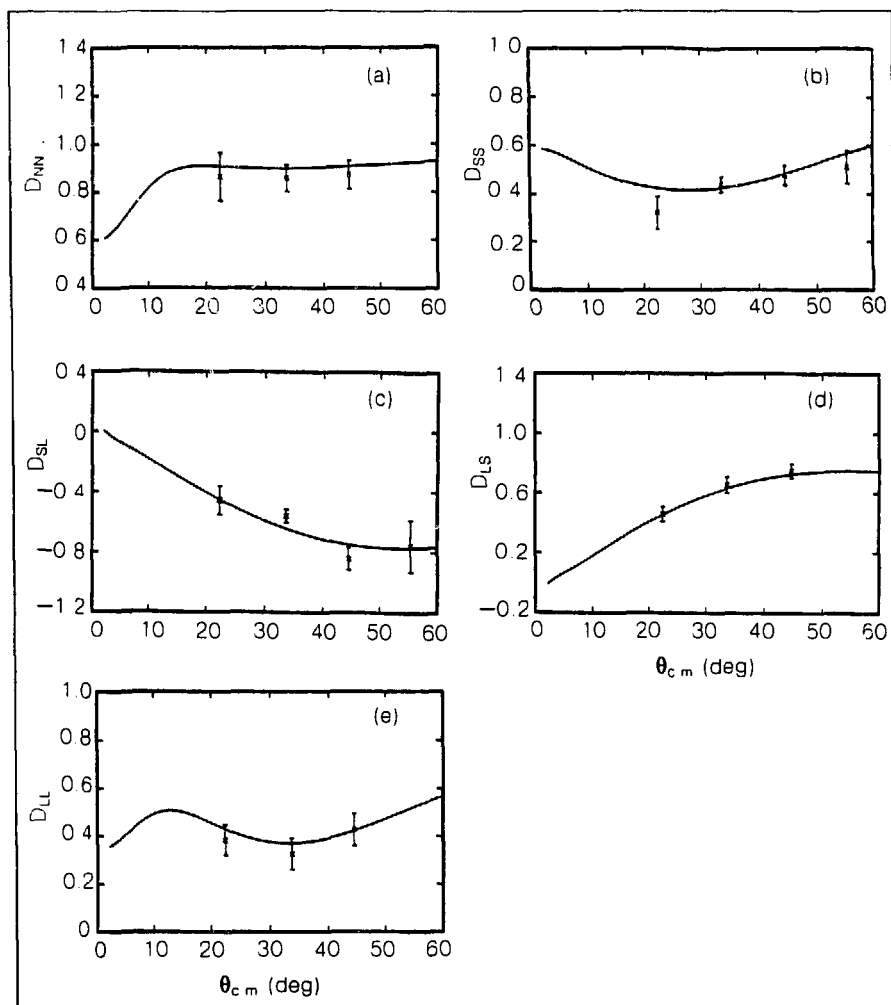


FIGURE 2. The 500-MeV quasi-elastic  $pn$  triple-scattering parameters (a)  $D_{NN}$ , (b)  $D_{SS}$ , (c)  $D_{SL}$ , (d)  $D_{LS}$ , and (e)  $D_{LL}$ . The solid curves are phase-shift predictions (solution W184).

## References

1. M. L. Barlett, G. W. Hoffmann, J. A. McGill, R. W. Ferguson, E. C. Milner, J. A. Marshall, et al., *Physical Review C* **30**, 279 (1984).
2. M. L. Barlett, G. W. Hoffmann, J. A. McGill, B. Hoistad, L. Ray, R. W. Ferguson, et al., *Physical Review C* **32**, 239 (1985).
3. R. A. Arndt, L. D. Roper, R. A. Bryan, R. B. Clark, B. J. VerWest, and P. Signell, *Physical Review D* **28**, 97 (1983).

The analysis of the data taken with the  $\hat{N}$ -type polarized deuterium target at HRS in the summer of 1983 is now complete. The connections between measured and deduced observables can be written

for  $\hat{N}$ -polarized beam:

$$\begin{aligned}
 I/I_0 = 1 &= P_N^B A_N + \frac{3}{2} P_N^T A_N^T + \frac{1}{2} P_{NN}^T A_{NN}^T, \\
 &+ \frac{3}{2} P_N^B P_N^T C_{N,N,0} + \frac{1}{2} P_N^B P_{NN}^T C_{N,NN,0}, \\
 I\langle\sigma N\rangle/I_0 &= P + \frac{1}{2} P_{NN}^T CO,NN,N + \frac{3}{2} P_N^T CO,N,N, \\
 &+ P_N^B C_{N,0,N} + \frac{1}{2} P_N^B P_{NN}^T CN,NN,N, \\
 &+ \frac{3}{2} P_N^B P_N^T CN,N,N;
 \end{aligned}$$

for  $\hat{S}$ -polarized beam:

$$\begin{aligned}
 I/I_0 &= 1 + \frac{3}{2} P_N^T A_N^T + \frac{1}{2} P_{NN}^T A_{NN}^T, \\
 I\langle\sigma S\rangle/I_0 &P_S^B = C_{S,0,S} + \frac{1}{2} P_{NN}^T CS,NN,S + \frac{3}{2} P_N^T CS,N,S, \\
 I\langle\sigma N\rangle/I_0 &= P + \frac{1}{2} P_{NN}^T CO,NN,N + \frac{3}{2} P_N^T CO,N,N, \\
 I\langle\sigma L\rangle/I_0 &P_S^B = C_{S,0,L} + \frac{1}{2} P_{NN}^T CS,NN,L + \frac{3}{2} P_N^T C_{S,N,L};
 \end{aligned}$$

EXPERIMENT 685 — HRS

### Measurement of Third-Order Spin Observables for Elastic $pd$ Scattering at 800 MeV

UCLA, Los Alamos, KEK Laboratory,  
Hiroshima Univ., Kyoto Univ., Univ. of  
Education in Japan, Univ. of  
Minnesota, Univ. of Texas at Austin

Spokesmen: G. J. Igo and M. Bleszynski (UCLA)

and for  $\hat{L}$ -polarized beam:

$$I/I_0 = 1 + \frac{3}{2} P_N^T A_N^T + \frac{1}{2} P_{NN}^T A_{NN}^T ,$$

$$I \langle \sigma S \rangle / I_0 P_L^B = C_{L,0,S} + \frac{1}{2} P_{NN}^T C_{L,NN,S} + \frac{3}{2} P_N^T C_{L,N,S} ,$$

$$I \langle \sigma N \rangle / I_0 = P + \frac{1}{2} P_{NN}^T C_{0,NN,N} + \frac{3}{2} P_N^T C_{0,N,N} ,$$

$$I \langle \sigma L \rangle / I_0 P_L^B = C_{L,0,L} + \frac{1}{2} P_{NN}^T C_{L,NN,L} + \frac{3}{2} P_N^T C_{L,N,L} .$$

Here,  $P_N^B$ ,  $P_N^T$ , and  $P_{NN}^T$  are beam and target, vector and tensor polarization, respectively, in the vertical ( $\hat{N}$ ) direction. The  $A_j^T$ 's are the proton and deuteron analyzing powers and  $P$  is the induced proton polarization.  $I_0$  is the yield one would observe with unpolarized beam and target,  $I$  is the corresponding quantity with polarized beam and target, and  $\langle \sigma i \rangle$  is the polarization of the scattered proton beam as measured with the HRS focal-plane polarimeter ( $S$  = sideways,  $N$  = vertical, and  $L$  = along the beam direction). The  $C_{i,j,k}$ 's are the two- and three-spin observables that one wishes to obtain from the measurement, where  $i$  denotes the polarization direction of the incoming beam;  $j$ , the polarization of the target; and  $k$ , the polarization of the scattered beam ( $i, j$ , or  $k = 0$  denotes unpolarized incoming or unmeasured outgoing polarization).

The polarized-target setup is described in earlier LAMPF Progress Reports. The analysis of the data is distinguished from that of a conventional HRS spin-rotation measurement only by the presence of the 10-kG holding field of the polarized target. This strong magnetic field caused a bend in the horizontal direction of the 800-MeV proton beam of  $5.0^\circ$  and a proton spin precession of about  $17^\circ$ . This spin precession made necessary corrections to the measured values of the  $C_{i,j,k}$ 's of up to 1.0. Figure 1(a)-(g) shows the new variables we were able to extract from the measurement. The solid lines are theoretical predictions from nonrelativistic multiple-scattering calculations by E. and M. Bleszynski.

There are no tensor observables among the deduced quantities. With a deuteron vector polarization of 0.3 or less, the residual tensor polarization is less than 0.07; no tensor observables could be extracted with useful accuracy.

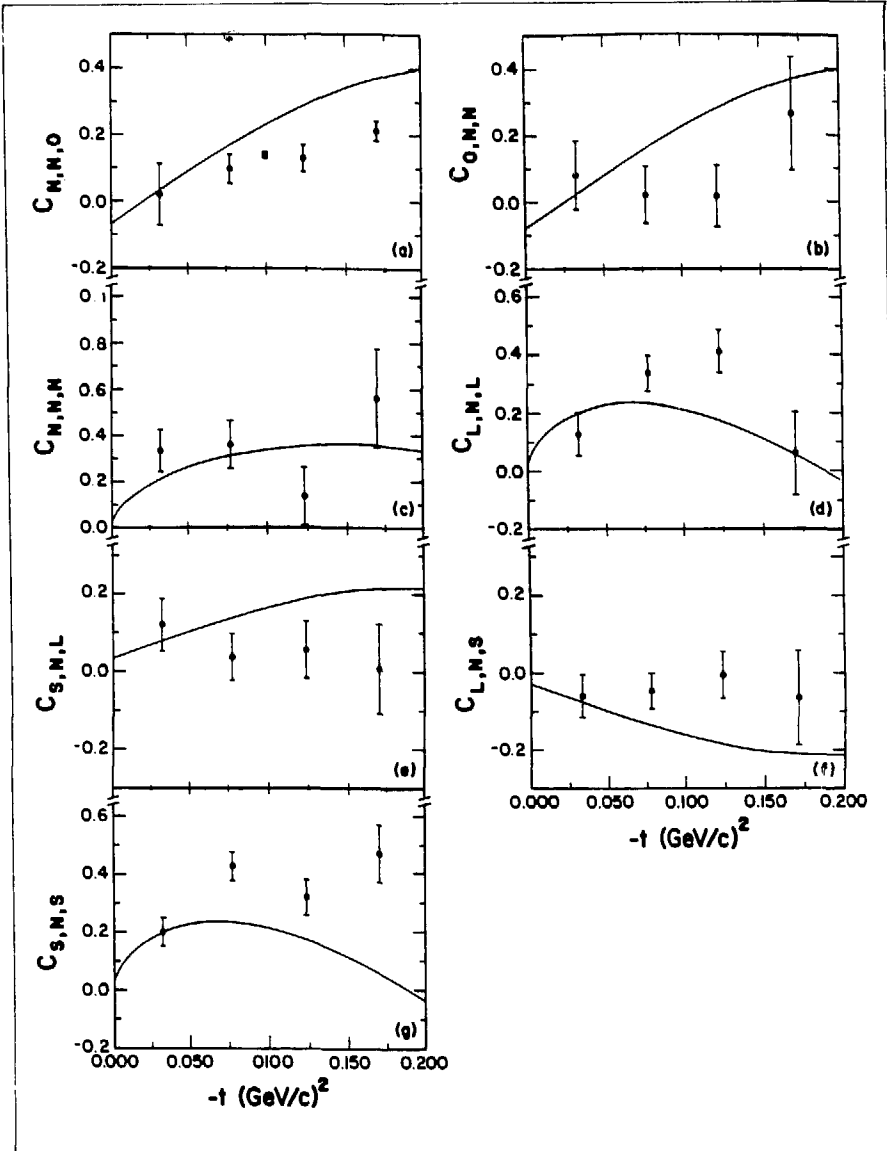


FIGURE 1(a) (g) Deduced two- and three-spin observables for elastic  $pd$  scattering at 800 MeV

### Calibration of the Deuteron Target Polarization by the Deuteron Magnetic Resonance (DMR) Signal Asymmetry

The area of the deuteron magnetic resonance (DMR) signal is (nearly) proportional to the deuteron vector polarization. One way to calibrate the proportionality constant is to exploit the asymmetry of the DMR-signal line shape. This asymmetry determines the intensity ratio of the transitions between the magnetic substates of the deuteron. Assuming that all deuterons have a common spin temperature, the polarization then follows from the measured intensity ratio. Following is a brief description of this method that we developed for determining the deuteron target polarization in Exp. 685.

It has been demonstrated<sup>1</sup> that the assumption of a common spin temperature  $T_s$  for the deuteron spin in the target sample is valid. The relative populations  $p_+$ ,  $p_0$ , and  $p_-$  of the magnetic substates  $m = +1, 0, -1$  are then determined by a Boltzmann distribution,

$$r \equiv \frac{p_+}{p_0} = \frac{p_0}{p_-} = e^{\exp(h\nu/kT_s)} ,$$

where  $\nu$  is the deuteron Larmor frequency and  $h$  and  $k$  are the Planck

and Boltzmann constants, respectively. The ratio  $r$ , defined by this equation, can now be extracted from the DMR-signal line shape thanks to the interaction of the deuteron quadrupole moment with the molecular electric-field gradient. This interaction shifts the substate levels, depending on the orientation of the molecule with respect to the magnetic field. The DMR signal therefore consists of two peaks corresponding to the two transitions

$$m = +1 \rightarrow m = 0$$

and

$$m = 0 \rightarrow m = -1 .$$

The two peaks overlap each other because the molecules are oriented isotropically. The transition intensities  $I_+$  and  $I_-$  are proportional to the population differences  $p_+ - p_0$  and  $p_0 - p_-$ , respectively, and their ratio turns out to be

$$\frac{I_+}{I_-} = \frac{p_+ - p_0}{p_0 - p_-} = \frac{r - 1}{1 - 1/r} = r .$$

Hamada et al.<sup>2</sup> have analyzed the rather complex structure of the DMR signal for fully deuterated propanediol, the target material that we used in our experiments, and derived the general mathematical function for its line shape. One of the parameters of this function is the ratio  $r$ , which thus can be obtained by fitting the DMR signal. The vector

and tensor polarization follow, then, from the normalization

$p_+ + p_0 + p_- = 1$  and from Eq. (1),

$$P_z \equiv p_+ - p_- = \frac{r^2 - 1}{r^2 + r + 1}$$

and

$$P_{zz} \equiv 1 - 3p_0 = \frac{r^2 - 2r + 1}{r^2 + r + 1}$$

A first attempt to fit the DMR signal, following the suggestion of Hamada et al., failed. The fits were quite poor and the results inconsistent (large discrepancies between the area/polarization ratios for positive and negative signals). A detailed analysis finally showed that the line-shape function used in the fitting lacked two essential ingredients:

1. In the paper of Hamada et al., it is implicitly assumed that the DMR signal has the same shape as the absorption part  $\chi''$  of the

magnetic susceptibility, thus neglecting the dispersion part  $\chi'$ . However, it turns out that  $\chi'$  causes quite significant effects on the signal shape, as has also been demonstrated recently by Kiselev et al.<sup>3</sup>

2. To obtain consistently good fits for both positive and negative signals, it was also necessary to account for the coaxial cable (of length  $\lambda/2$ ), which connects the DMR coil at the target sample to the preamplifier.

Figure 2 shows a typical fit to a DMR signal recorded during the 1984 run of Exp. 685, at a magnetic field of 2.5 T (DMR frequency = 16.34 MHz), using a constant-current parallel resonant circuit. The dashed curve represents the base line, that is, the voltage signal in the absence of DMR ( $\chi' = \chi'' = 0$ ). The polarization resulting from this fit is  $p = -0.348$ . We estimate the uncertainty in the polarization, determined by this fitting procedure, to be less than 0.010.

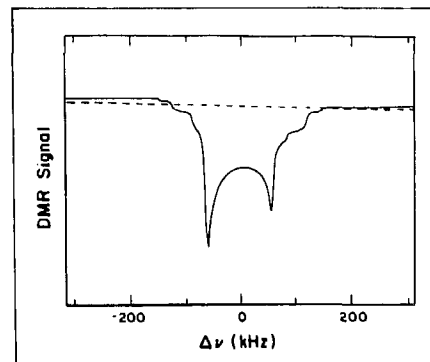


FIGURE 2. Fit to a deuteron magnetic resonance (DMR) signal recorded during the 1984 run of Exp. 685. The dashed curve represents the base line, that is, the voltage signal in the absence of DMR. The deuteron polarization obtained from this fit is  $-0.348$ . The horizontal axis gives the difference to the DMR frequency of 16.34 MHz.

## References

1. M. Borghini and K. Scheffler, *Nuclear Instruments & Methods* **95**, 93 (1971).
2. O. Hamada et al., *Nuclear Instruments & Methods* **189**, 561 (1981).
3. Y. F. Kiselev et al., *Nuclear Instruments & Methods* **220**, 399 (1984).



## EXPERIMENT 722 — HRS

**Measurement of Cross Sections and Analyzing Powers for Elastic and Inelastic Scattering of 400- to 500-MeV Protons from  $^{14}\text{C}$** 

Los Alamos, Univ. of Minnesota, Arizona State Univ., Univ. of South Carolina, Univ. of Pennsylvania, Univ. of Texas

Spokesman: M. Plum (Los Alamos)

During a 1-week period in August 1984,  $^{14}\text{C}(p,p')$  data were obtained for 11 angles,  $3.75^\circ \leq \theta_{\text{lab}} \leq 28.0^\circ$ , at an incident energy of  $E_p = 497$  MeV. The salient features of most types of angular distributions are contained within this angular region. One of the primary objectives of this experiment was to measure an angular distribution for the cross section and analyzing power for the 6.90-MeV

$0^-$  state. However, the thick  $^{14}\text{C}$  target ( $170\text{-mg/cm}^2$   $^{14}\text{C}$ - $^{12}\text{C}$  powder and  $45\text{-mg/cm}^2$   $^{nat}\text{Ni}$  foil windows) limited the resolution to about 280 keV, so a clean observation of this state was not possible. Most other states below 11-MeV excitation are resolved, and data analysis is proceeding for these and all other resolved states.

In addition to the  $^{14}\text{C}$  target,  $^{12}\text{C}$  and  $^{nat}\text{Ni}$  targets were required to subtract these impurities from the  $^{14}\text{C}$  spectra. A sample spectrum, with the  $^{12}\text{C}$  and  $^{nat}\text{Ni}$  subtracted, is shown in Fig. 1. The peaks at  $-0.39$ - and  $5.76$ -MeV excitation are due to unexpected contributions from  $^{16}\text{O}$ .

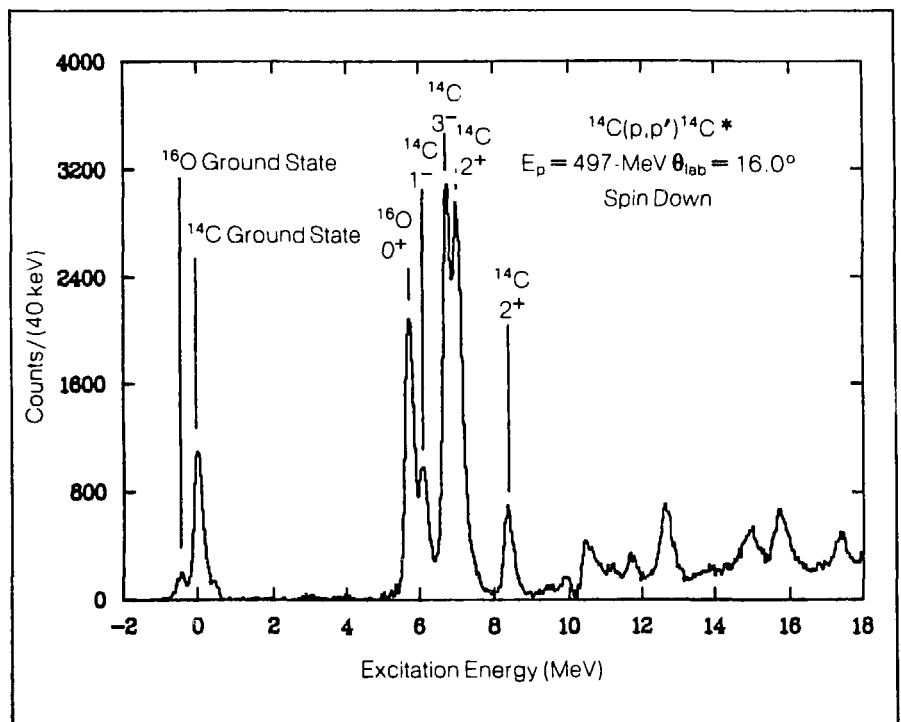


FIGURE 1 Sample spectrum with  $^{12}\text{C}$  and  $^{nat}\text{Ni}$  subtracted.

The response of nuclei to the spin-isospin fields  $\vec{\sigma} \times \vec{q} e^{i\vec{q} \cdot \vec{r}}$  and  $\vec{\sigma} \cdot \vec{q} e^{i\vec{q} \cdot \vec{r}}$  (where  $\vec{q}$  is the momentum transfer) holds general interest for understanding the properties of hadronic matter. The transverse ( $\vec{\sigma} \times \vec{q}$ ) and longitudinal ( $\vec{\sigma} \cdot \vec{q}$ ) response functions have simple connections to the exchanges of  $\rho$  and  $\pi$  mesons between nucleons and between nucleons and  $\Delta$  isobars, and hence are very relevant to current investigations into the effects of the isobar on nuclear properties. Beyond this there are many issues connected with the spin-isospin responses that carry over into the discussion of the role of quarks and gluons in describing nuclear properties and interactions. One such issue is the interpretation of the European Muon Collaboration (EMC) effect.

The experiment reported here uses a new and general technique for the measurement of the spin-dependent response function. It relies on measurement of a complete set of polarization transfer observables and is applicable, in principle, to nucleon inelastic scattering or charge-exchange reactions for the entire  $q$ - $\omega$  response surface, including discrete states and the continuum. In this report we present data derived from 500-MeV proton scattering for both the transverse and spin-longitudinal response functions for calcium and lead at a momentum transfer of  $1.75 \text{ fm}^{-1}$  for a range of  $\omega$  from 20 to 100 MeV. Some of the data have been published in a previous letter.<sup>1</sup>

The principle of the experiment is simple. For targets of  $^2\text{H}$ , Ca (natural), and Pb (natural), one measures spin-flip probabilities (SFPs) that bear a simple, although model-dependent, relation to the spin-isospin response functions. One then looks for differences in these observables between  $^2\text{H}$  and the heavy nuclei. Deuterium is assumed to be a free neutron-plus-proton target and hence free of any collectivity that might occur in the heavy nuclei.

As in the earlier reporting of the experiment, we find no difference in the longitudinal SFP between the heavy targets and deuterium. The new data have higher statistical precision and thus weigh even more heavily against pionic collectivity.

The major theoretical emphasis of this work has been to analyze the data with the best theoretical model available—the semi-infinite slab model of Bertsch, Scholten, and Esbensen.<sup>2,3</sup> Beyond this we have examined several corrections to the model that have been discussed in the literature but not considered quantitatively. Specifically these are

- spin-dependent distortion effects,
- kinematic effects in the  $^2\text{H}$  data, and
- double scattering.

## EXPERIMENT 741 — HRS

### Continuum Polarization Transfer in 500-MeV Proton Scattering and Pionic Collectivity in Nuclei

Los Alamos, Indiana Univ. Cyclotron Facility, Argonne

Spokesmen: T. A. Carey and J. B. McClelland (Los Alamos)

Participants: L. B. Rees, J. M. Moss, K. W. Jones, N. Tanaka, A. D. Bacher, and H. Esbensen

The conclusion based on the complete analysis is that no evidence exists of pionic collectivity in nuclei. A major consequence of this is that there are no excess pions that could account for the low- $x$  EMC effect. This is clear from a comparison of several theoretical calculations to both our data and the EMC data. The nuclear-structure model, identical

for the calculation of both data sets, contains a parameter  $g'$ , which scales the degree of pionic collectivity. Figures 1 and 2 show that the calculation  $g' = 0.55$ , which gives a reasonable account of the EMC experiment, fails completely to account for our data. Thus one is forced to consider more seriously the quark-level models of nuclei that have been proposed to explain the EMC effect.

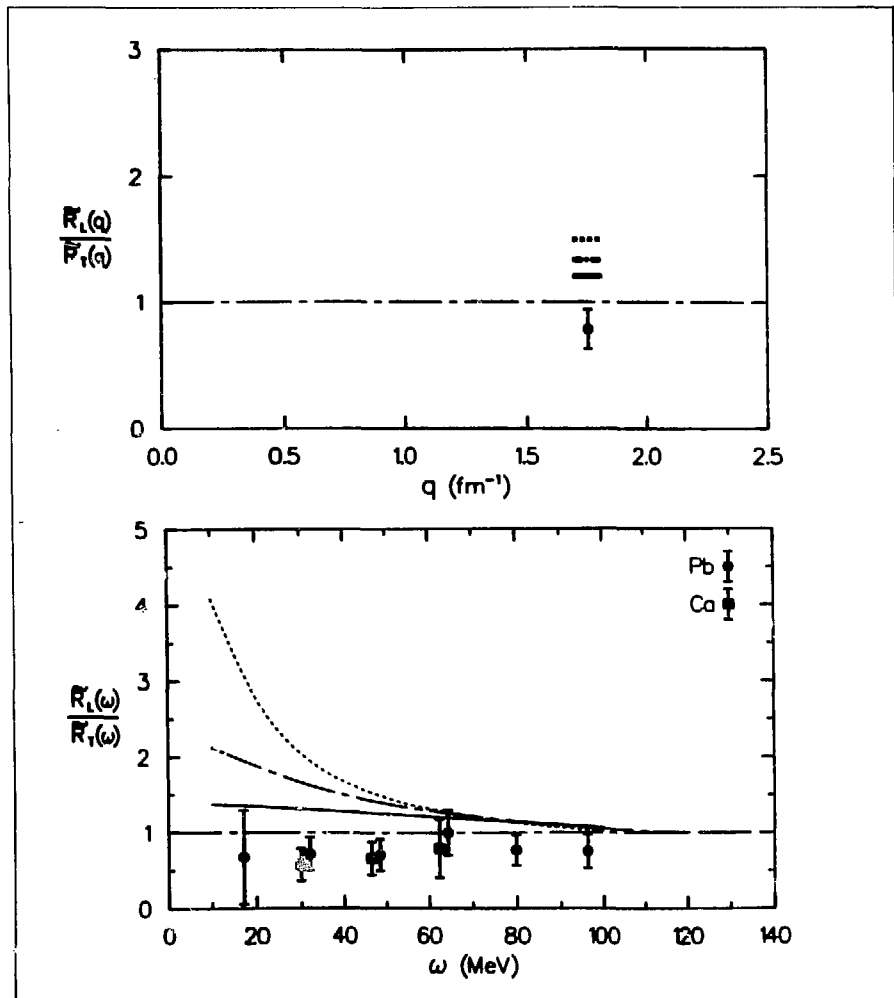


FIGURE 1. The ratio of spin-longitudinal to spin-transverse response functions with  $g' = 0.55$  (dotted line),  $0.7$  (dot-dashed line), and  $0.9$  (solid line).

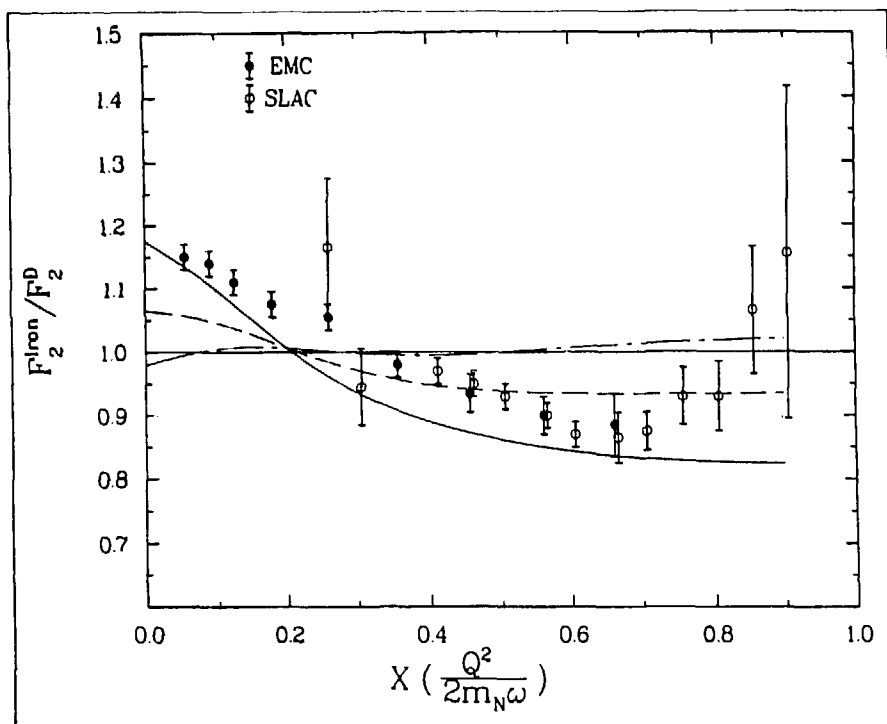


FIGURE 2 The  $A$ -corrected ratio of  $F_2^{\text{Iron}}$  structure functions from the EMC and SLAC as a function of the scaling variable  $x$ . The curves are semi-infinite-slab calculations, as in Fig. 1

## References

1. T. A. Carey et al., *Physical Review Letters* **53**, 144 (1984).
2. G. F. Bertsch and O. Scholten, *Physical Review C* **25**, 804 (1982).
3. H. Esbensen and G. F. Bertsch, *Annals of Physics* **157**, 255 (1984).

EXPERIMENT 879 — HRS

**Characteristic Dirac Signature in Large-Angle Elastic Scattering at 500 MeV**

Los Alamos, Univ. of Texas at Austin

Spokesmen: G. W. Hoffmann and M. L. Barlett  
(Univ. of Texas at Austin)

The success<sup>1-3</sup> of the relativistic impulse approximation (RIA) in describing 500-MeV  $\vec{p}$ -nucleus elastic-scattering observables is due to the automatic inclusion in the Dirac equation of virtual-pair processes involving the beam proton and two target nucleons. This process, sometimes called the Z diagram, is shown schematically in Fig. 1.

Recently, Hynes, Picklesimer, Tandy, and Thaler<sup>4</sup> reported results of momentum-space calculations that suggested a characteristic Dirac signature would be seen in large-angle  $p$ -nucleus elastic analyzing-power data. For the center-of-momentum angular range from 45 to 60°, nonrelativistic and relativistic impulse-approximation (NRIA and

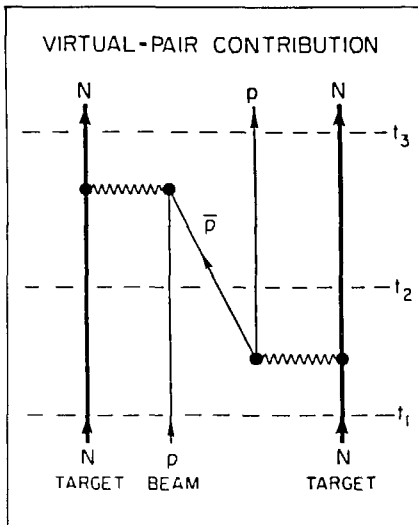


FIGURE 1 Virtual-pair process involving a beam proton and two target nucleons.

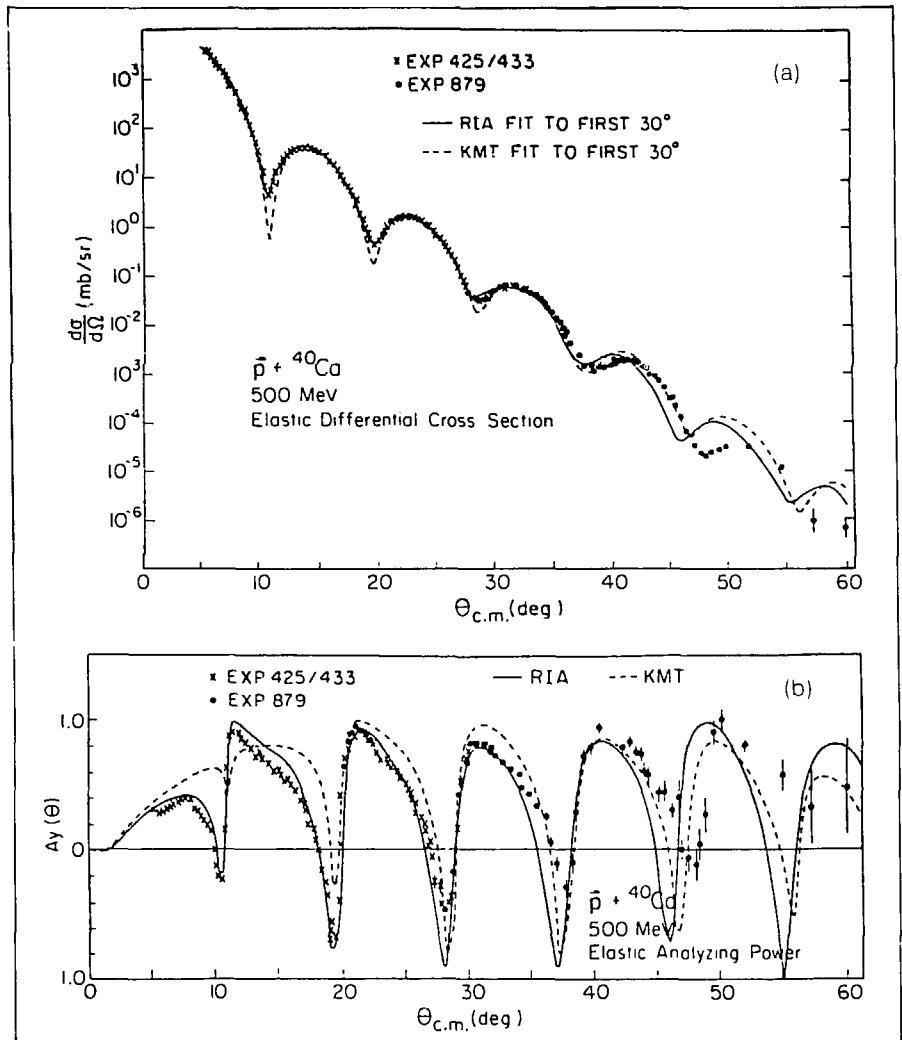


FIGURE 2 Large-angle 500-MeV  $\vec{p}$ - $^{40}\text{Ca}$  (a) cross-section data and (b) analyzing-power data obtained in Exp. 879 compared with RIA (solid curve) and NRIA (dashed curve) predictions. (KMT indicates results from Kerman-McManus-Thaler.)

RIA) approaches predicted extreme differences in  $A_p$ . In fact, near  $55^\circ$  the NRIA analyzing power was approximately  $+1$ , whereas the RIA analyzing power was approximately  $-1$ . This signature was claimed to be insensitive to other uncertainties associated with the calculations.<sup>4</sup>

Experiment 879 extended the 500-MeV  $\vec{p}$ - $^{40}\text{Ca}$  elastic cross-section and analyzing-power data to a center-of-momentum scattering angle of  $60^\circ$  to provide data that would confirm or disclaim the Dirac signature hypothesis. The data are shown in Fig. 2(a) and 2(b). Interestingly, the characteristic diffractive structure seen in both the cross section and analyzing power of the earlier data set (angular range from  $5$  to  $30^\circ$ )

continues out to the largest momentum transfer. This is in contrast to the predictions of Ref. 4, where the predicted diffractive pattern changes abruptly and qualitatively for angles larger than about  $30^\circ$ . The solid and dashed curves are standard RIA and NRIA predictions, respectively, made using coordinate space codes. In this instance, the NRIA and RIA curves are qualitatively similar to each other and to the data at large momentum transfer. Therefore, we conclude that there is no large-angle characteristic Dirac signature in  $\vec{p}$ -nucleus elastic scattering (experimental or theoretical).

---

## References

1. J. Shepard, J. A. McNeil, and S. J. Wallace, *Physical Review Letters* **50**, 1443 (1983).
2. B. C. Clark, S. Hama, R. L. Mercer, L. Ray, and B. D. Serot, *Physical Review Letters* **50**, 1644 (1983).
3. B. C. Clark, S. Hama, R. L. Mercer, L. Ray, G. W. Hoffmann, and B. D. Serot, *Physical Review C* **28**, 1421 (1983).
4. M. V. Hynes, A. Picklesimer, P. C. Tandy, and R. M. Thaler, *Physical Review Letters* **52**, 978 (1984).

## EXPERIMENT 891 — HRS

**Development of a 0° Focal-Plane Polarimeter at HRS**

Los Alamos, Univ. of Minnesota, Rutgers Univ., Université Paris XI

Spokesmen: J. B. McClelland (Los Alamos) and S. K. Nanda (Univ. of Minnesota)

This experiment was to extend inelastic spin-flip measurements,  $S_{nn}$ , to 0°. Our previous work had demonstrated the feasibility of inelastic cross-section measurements at 0° for light- to medium-mass targets. This would be an integral part of the  $M1$  spin-flip measurements now under way to 3° at the HRS.

The considerable spin-flip strength seen in the  $^{90}\text{Zr}(\vec{p}, \vec{p}')$  studies at forward angles has been tentatively identified as being from  $M1$ ,  $M2$ , and  $M3$  contributions, based on multipole decomposition using angular distributions of  $\sigma$  and  $S_{nn}$ . However, the sensitivity of these measurements is compromised because the smallest angle achievable corresponds to the peak in the  $M2$  cross section at 318 MeV. To gain increased sensitivity to  $M1$  contributions, it is necessary to go to smaller momentum transfer.

Angles between 1 and 3° are completely dominated by pole-face scattering, within the spectrometer, of the very strong elastic peak so that 0° is the only other possibility. A tenfold increase in sensitivity to the  $M1$  spin-flip cross section is predicted, based on distorted-wave impulse approximation (DWIA) calculations obtained only if the instrumental background can be maintained at a level as good as at 3°.

Experiment 891 was our first attempt at 0° spin-flip measurements. A completely new detector system was installed at the HRS to accommodate the new requirements. Smaller focal-plane wire chambers, trigger scintillators, and a left/right scintillator system to detect the rescattered protons were installed. An additional beam-profile monitor and beam integrator were added for energy calibration and cross-section normalization. In this configuration, the unscattered beam was clearly delivered through the spectrometer, above all detectors and out a hole in the detector shielding assembly.

The large overhead involved in the installation of new equipment, and the substantial beam preparation and tuning required, allowed time only for measurement of  $^{12}\text{C}$ . Figure 1(a) shows the yield between 11 and 18 MeV; Fig. 1(b) is the spin-flip cross section in arbitrary units. Absolute normalization will be available after further off-line processing.

It is clear from Fig. 1 that instrumental background is almost entirely suppressed in the spin-flip cross section. The preliminary value of  $D_{nn}$  for 15.11-MeV  $1^+$ ,  $T=1$  is  $0.6 \pm 0.1$ , in good agreement with DWIA calculations. Extensive non-0° elastic data were taken for systematic checks.

We feel we have demonstrated the feasibility for 0° inelastic spin-flip measurements using the HRS and plan to continue the program over a large range of target masses in an attempt to cleanly identify  $M1$  strength in nuclei.

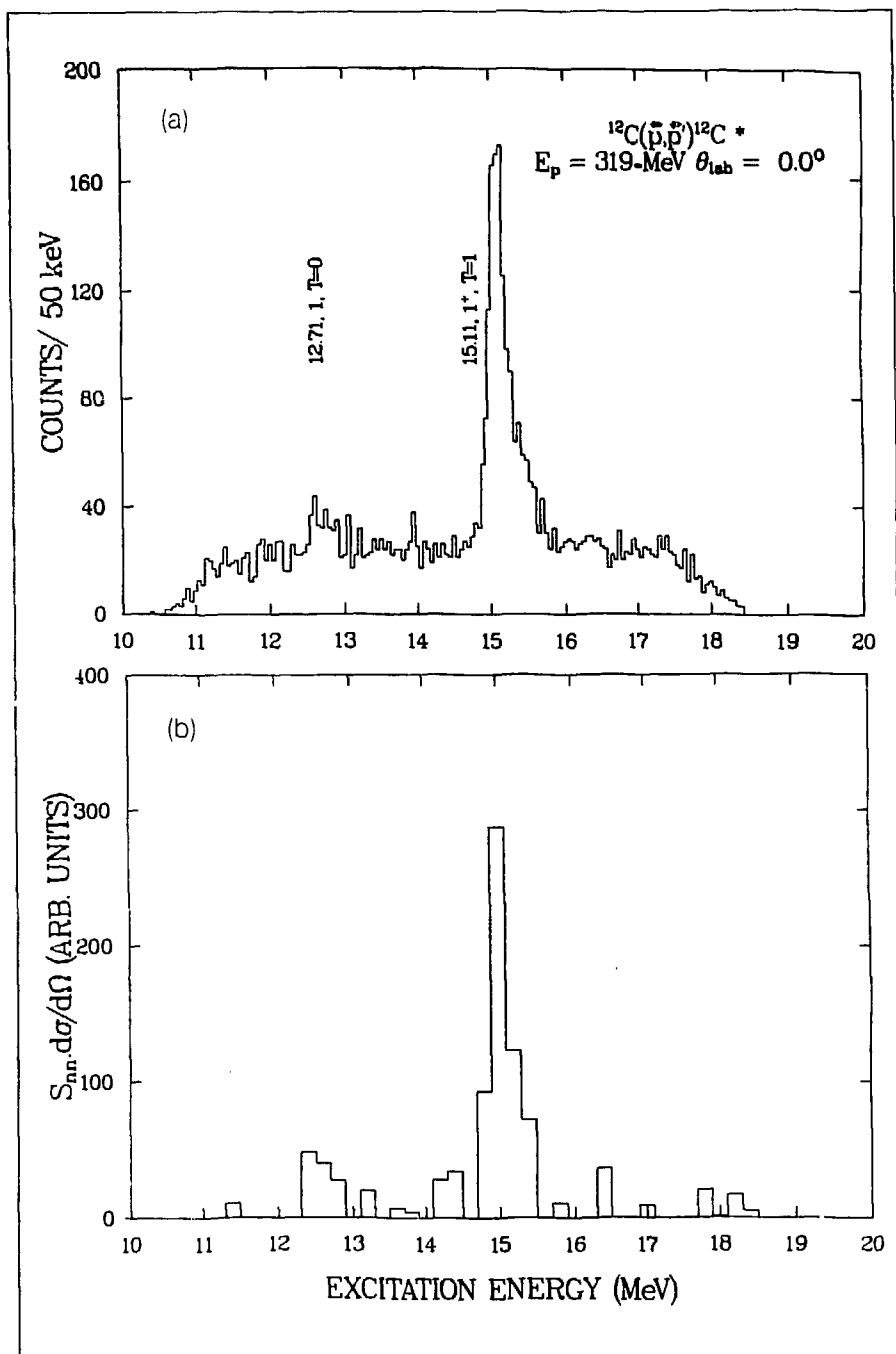


FIGURE 1 (a) Yield between 11 and 18 MeV and (b) spin-flip cross section in arbitrary units



## EXPERIMENT 907 — HRS

**Continuum Spin-Flip Cross-Section Measurements from  $^{40}\text{Ca}$** 

Los Alamos, Univ. of Minnesota, Rutgers Univ., Univ. of Paris XI, Univ. of Georgia, Brigham Young Univ.

Spokesmen: S. K. Nanda (Univ. of Minnesota), C. Glashauser (Rutgers Univ.), and K. W. Jones (Brigham Young Univ.)

The purpose of this experiment is to study the distribution of spin-flip strength at medium excitation energies ( $E_x \leq 40$  MeV) and ground-state correlations in the doubly closed-shell nucleus  $^{40}\text{Ca}$ . Previous measurements on  $^{90}\text{Zr}$ ,  $^{51}\text{V}$ , and  $^{58}\text{Ni}$  indicate unexpectedly large spin-flip probabilities up to an excitation of about 25 MeV at small laboratory scattering angles ( $\theta \leq 5^\circ$ ).

Esbensen and Bertsch have calculated the response of a semi-infinite Fermi liquid to a spin-isospin dependent probe.<sup>1</sup> Collective effects were included using the random phase approximation (RPA); there were no free parameters in the calculation. The results are shown in Fig. 1, where they are compared with data from previous measurements on  $^{90}\text{Zr}$  (Exp. 660).<sup>2</sup> It is noteworthy that the calculations indicate that the spin-flip cross section should be decreasing steadily for excitation energies above 20 MeV.

We have measured the spin-flip cross section from 3 to 12° in the

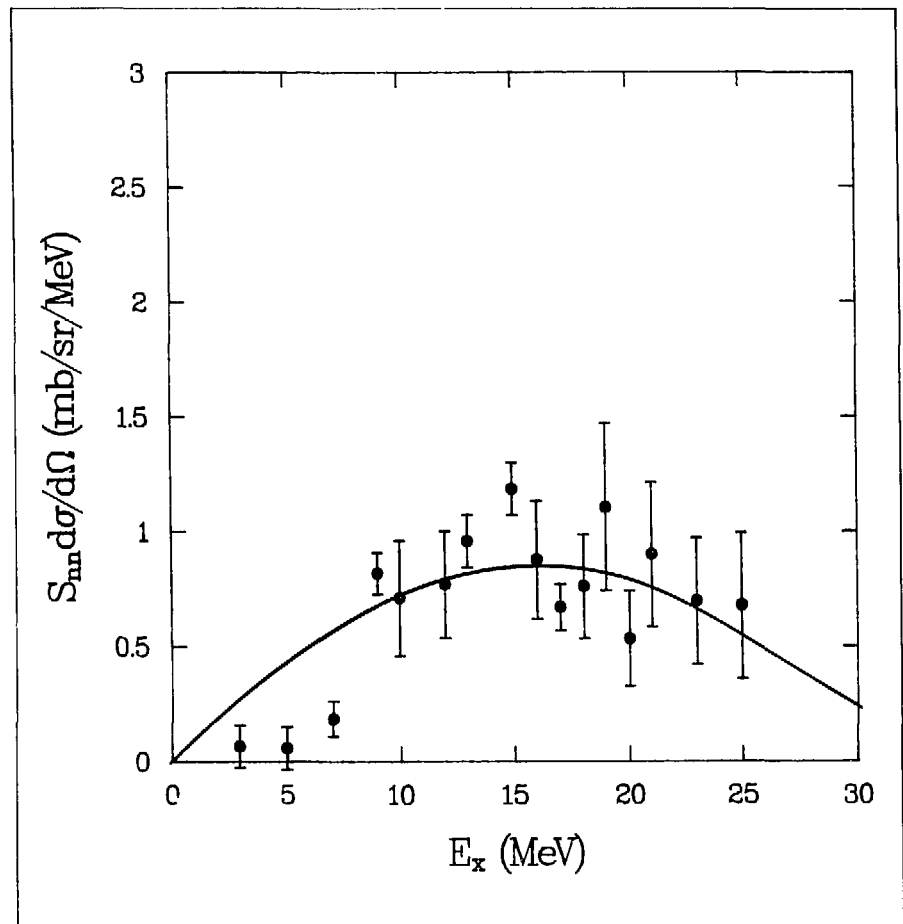


FIGURE 1 Spin-flip cross section for proton scattering from  $^{90}\text{Zr}$  at  $3.5^\circ$ . The curves are the predictions of Esbensen and Bertsch.

laboratory, spanning an excitation energy range from 6 to 40 MeV for proton inelastic scattering from  $^{40}\text{Ca}$ . The HRS focal-plane polarimeter was used for these measurements.

Preliminary on-line data are shown in Fig. 2(a)–(c). It is clear from these figures that the spin-flip cross section is large at small angles, even for excitation energies up to 40 MeV. The known, strong  $2^-$  state in  $^{40}\text{Ca}$  at 8.42 MeV excitation is easily seen in the spectra and has a large spin-flip cross section. The weak  $M1$  transi-

tions at 10.2 and 12.0 MeV were also observed in the small-angle data, and we hope that values of the spin-flip cross section for these states can be extracted from the data during re-play.

Study of these  $0\hbar\omega$  excitations may improve our understanding of  $2p$ - $2h$  correlations in the ground-state wave function of this nucleus. A multipole decomposition of the data is planned to determine the strengths and angular distributions of  $M1$  to  $M3$  spin-flip transitions.

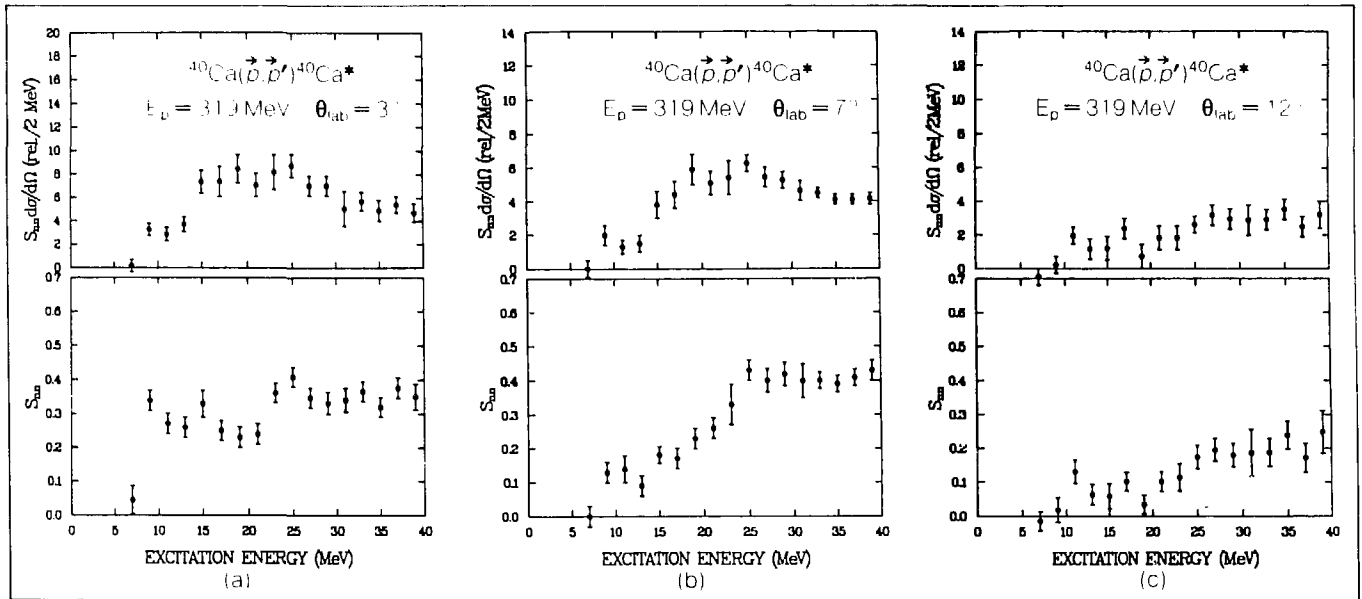


FIGURE 2. Spin-flip probability and relative spin-flip cross section at (a)  $3.0^\circ$ , (b)  $7.0^\circ$ , and (c)  $12.0^\circ$ .

## References

1. H. Esbensen and G. Bertsch, *Annals of Physics* **157**, 255 (1984).
2. S. K. Nand, C. Glashauser, K. W. Jones, J. A. McGill, T. A. Cary, J. B. McClelland, et al., *Physical Review Letters* **51**, 1526 (1983).

## EXPERIMENT 487 — LEP

**Measurement of the E2 Resonance Effect in Pionic Atoms\***

Univ. of Mississippi; Los Alamos,  
Technische Universität in Munich,  
Germany; Univ. of Wyoming

Spokesmen: J. Reidy (Univ. of Mississippi) and  
M. Leon (Los Alamos)

Measurements on the x rays emitted by pionic atoms have provided the principal means of studying the zero-energy pion-nucleus interaction. A negative pion incident on a target slows down and is eventually captured by a target atom. The captured pion then cascades down through the pionic-atom levels, at first emitting Auger electrons and later pionic x rays. Near the end of the cascade the strong short-range pion-nucleus interaction comes into play. This is reflected in changes in the intensities, energies, and widths of the observed x-ray lines compared with what would be observed in a purely electromagnetic cascade. These x-ray data are used for determining semiphenomenological optical potentials that give good agreement with most of the x-ray data and that are consistent with the optical potentials used to describe low-energy pion-nucleus scattering.

However, the strong-interaction information derived from x-ray measurements comes from rather limited regions of  $Z$  for each pionic-atom level ( $1s$  from  $Z \lesssim 11$ ,  $2p$  from  $8 \lesssim Z \lesssim 33$ ,  $3d$  from  $39 \lesssim Z \lesssim 60$ , and  $4f$  from  $Z \gtrsim 67$ ). The reason for this is that for a given nucleus the observable x-ray lines terminate rather abruptly at a "last line" as the overlap with the nucleus and hence the absorption widths increase. Although it clearly would be desirable to test the optical potential for levels with greater overlap with the nucleus, this is not generally possible, so these levels stay hidden.

A method to probe a few examples of such hidden levels, the  $E2$  nuclear-resonance effect, was proposed by Leon. This effect occurs when an atomic deexcitation energy closely matches a nuclear-excitation energy and the electric-quadrupole coupling induces configuration mixing of the two states. A pion in the  $(n, \ell)$  state (with the nucleus in its ground state) is also partly in a  $(n', \ell-2)$  state (with the nucleus in its excited state). Because the  $(n', \ell-2)$  state atomic wave function has a greatly increased overlap with the nucleus, even a very small amount of configuration mixing can result in a significant induced width  $\Gamma_{ind}$  in the  $(n, \ell)$  state, which leads to a reduction of the  $(n, \ell) \rightarrow (n-1, \ell-1)$  x-ray intensity. Measurement of this attenuation allows one to extract information<sup>1,2</sup> about the  $(n', \ell-2)$  pion level. The attenuation may be measured with precision by comparing the intensities of the  $(n, \ell) \rightarrow (n-1, \ell-1)$  lines in the spectra of two isotopes, one of which possesses the resonance.

The purpose of the present work was to make high-precision measurements on a number of pionic atoms where the  $E2$  nuclear-resonance effect is significant. The nuclei studied were  $^{48}\text{Ti}$ ,  $^{104}\text{Ru}$ ,  $^{110}\text{Pd}$ ,  $^{111}\text{Cd}$ ,  $^{112}\text{Cd}$ ,  $^{125}\text{Te}$ , and  $^{150}\text{Sm}$ . We have previously reported results for some of these isotopes,<sup>3,5</sup> but the present work represents new, more precise and accurate results for all cases. Comparisons are made with theoretical estimates.<sup>1,2</sup> Because they give the most intense lines, we deal exclusively with transitions between

\*Published in *Physical Review C* **32**, 1646 (1985)

circular states, for which  $\ell = n-1$ .

This work was motivated in part by the persistent discrepancy between an earlier observation and the predictions of the optical potentials for the  $3p$  level of pionic palladium<sup>3,5</sup> ( $Z = 46$ ); this discrepancy remains, even when comparison is made with the more complete calculations of Dubach et al.<sup>2</sup> instead of the simpler model of Leon.<sup>1</sup> The  $3p$  state is also the lower admixed state in <sup>104</sup>Ru and <sup>125</sup>Te. The highest  $Z$  nucleus where the hadronic contribution to the  $1s$  state can be studied is <sup>48</sup>Ti, and it has the greatest mixing. A more precise determination of the attenuation would provide a sensitive test for this mixing. Dubach et al. have pointed out that pionic <sup>150</sup>Sm is potentially very interesting because a precise determination of the attenuation may allow one to distinguish between two nuclear models for <sup>150</sup>Sm. Of all the pionic examples of the  $E2$  resonance effect, <sup>111</sup>Cd and <sup>112</sup>Cd are the most studied.<sup>3,5</sup> They are important test cases because the lower admixed state is directly observable rather than hidden.

The theoretical description of the  $E2$  nuclear-resonance effect was first given by Leon<sup>1</sup> and later extended by Dubach et al.<sup>2</sup> to include mixing effects that are due to the strong interaction. Let  $|1\rangle$  denote the state consisting of the nucleus in its ground state and the pion in an atomic state  $(n, \ell)$ , and  $|2\rangle$  the state with the nucleus in an  $E2$  excited state and the pion in a lower atomic state  $(n', \ell-2)$ . Denoting the quadrupole-coupling Hamiltonian by  $H' = H'_{strong} + H'_{em}$ , we can write for the eigenstate  $|1'\rangle$

$$|1'\rangle = \sqrt{1-a^2}|1\rangle + a|2\rangle, \quad (1)$$

where  $a$ , the admixture coefficient, is given by

$$a = \frac{\langle 2 | H' | 1 \rangle}{\Delta E}. \quad (2)$$

The complex energy difference  $\Delta E$  is

$$\Delta E = E_{nuc}^{2*} - E_{n', \ell-2} + E_{n, \ell} - \frac{1}{2} i (\Gamma_{n, \ell-2} + \Gamma_{n, \ell}) \equiv \varepsilon - i\gamma, \quad (3)$$

where  $E_{nuc}^{2*}$  is the energy of the  $E2$  excited nuclear state,  $E_{n, \ell}$  is the binding energy of the pion in the  $n, \ell$  pionic-atom state, and  $\Gamma_{n, \ell}$  is the width of this level. From this admixture of the lower level, the upper atomic level now has an induced width  $\Gamma_{ind}$ , which is given by

$$\Gamma_{ind} = |a|^2 \Gamma_{n', \ell-2}. \quad (4)$$

This induced width leads to an attenuation of the x-ray intensity from the  $n, \ell$  state. Conversely, a determination of the x-ray attenuation gives information about the strength of the coupling.

The pionic x-ray transitions that are usually detected are those  $E1$  transitions involving circular orbits

(maximum  $\ell$ ). One determines for a given isotope the intensity ratio of the observed lines

$$r(Z,A) \equiv \left[ \frac{I(n,\ell \rightarrow n-1,\ell-1)}{I(n+1,\ell+1 \rightarrow n,\ell)} \right]_{Z,A}, \quad (5)$$

where  $I(n,\ell \rightarrow n-1,\ell-1)$  represents the measured intensity of the transition between the state  $n,\ell$  and the state  $n-1,\ell-1$ , and where  $Z,A$  represents the isotope. We refer to the isotope where mixing occurs as the resonant isotope. For a nonresonant isotope  $Z,A'$ , one measures the same ratio and then forms the ratio of ratios

$$R = \frac{r(Z,A)}{r(Z,A')}. \quad (6)$$

The attenuation  $A$  is defined as the complement of  $R$ , that is,

$$A = 1 - R, \quad (7)$$

and is a direct measure of the induced pion absorption out of the level  $n,\ell$  (to the extent that unresolved noncircular transitions are absent). One can readily show<sup>1</sup> that contours of fixed attenuation are circles in the  $(\epsilon,\gamma)$  plane (assuming that the mixing-matrix element is fixed)

The energies and widths of the pionic-atom states are obtained by solving numerically the Klein-Gordon equation\* with the nuclear-Coulomb potential plus the hadronic optical potential. The potential of Seki and Masutani,<sup>6</sup> with parameters given in their Table III ( $a = 1R$ ), was chosen. Following Leon,<sup>1</sup> the mixing-matrix elements are calculated using nonrelativistic point-nucleus wave functions (electromagnetic contribution only). One then obtains predictions of the attenuation that can be compared with experiment.

Additional factors can contribute to the induced width, such as nuclear-size effects, isomer shifts, nuclear states above the collective quadrupole state, and the inclusion of a  $p$ -wave optical potential. Dubach et al.<sup>2</sup> have included these.

These experiments were carried out at LAMPF using the  $P^3$  and LEP beams. The experimental arrangement was similar to that described in Ref. 3.

Using the fitted-line intensities and Eqs. (5) and (6), we determined the experimental values of  $R$ . These  $R$  values were then corrected for the fact that the targets were not all isotopically pure.

The relevant x-ray lines are listed in Table I. Columns 3-6 give the lines that were analyzed in order to measure the attenuation. For the cadmium isotopes the reference line is an unresolved doublet; furthermore, two lines,  $5 \rightarrow 4$  and  $4 \rightarrow 3$ , exhibit attenuation. The corresponding  $R$  values are denoted  $R_a$  and  $R_b$ , respectively.

\*Computer program MATOM, from R. Seki, California State University at Northridge, 1985

TABLE I Relevant x-Ray Lines

| Nucleus                | Levels (Mixed) | Attenuated Lines                       | Energy (keV) | Reference Lines                     | Energy (keV) |
|------------------------|----------------|--|--------------|-------------------------------------|--------------|
| $^{48}_{22}\text{Ti}$  | $3d - 1s$      | $3 \rightarrow 2$                      | 254          | $4 \rightarrow 3$                   | 88           |
| $^{104}_{44}\text{Pd}$ | $4f - 3p$      | $4 \rightarrow 3$                      | 355          | $5 \rightarrow 4$                   | 163          |
| $^{110}_{48}\text{Ru}$ | $4f - 3p$      | $4 \rightarrow 3$                      | 389          | $5 \rightarrow 4$                   | 178          |
| $^{111}_{48}\text{Cd}$ | $5g - 3d$      | $5 \rightarrow 4$<br>$4 \rightarrow 3$ | 194<br>424   | $6 \rightarrow 5 + 8 \rightarrow 6$ | 105          |
| $^{125}_{52}\text{Te}$ | $4f - 3p$      | $4 \rightarrow 3$                      | 500          | $5 \rightarrow 4$                   | 227          |
| $^{150}_{62}\text{Sm}$ | $5g - 4d$      | $5 \rightarrow 4$                      | 326          | $6 \rightarrow 5$                   | 176          |

The relevant parameters and calculated results for the induced widths are given in Table II. Row 2 gives the calculated energy difference of the relevant pionic-atom levels using the code MATOM. For the cadmium isotopes the measured value is used. Row 3 lists the energy of the nuclear  $E2$  excited state. The static quadrupole moment of the excited state is listed in row 4; two values are given for  $^{110}\text{Pd}$  that correspond to two possible results from Coulomb-excitation measurements. Row 5 lists the interaction energy of the excited-state quadrupole moment with the lower atomic state. For the odd nuclei, which have spin  $1/2$ , there are two possible orientations with  $j = \ell \pm 1/2$ ; the values for the anti-parallel case are given in brackets. The sum of rows 2, 3, and 5 is presented in row 6; this corresponds to  $\varepsilon = Re\Delta E$  [see Eq. (3)]. The calculated (measured for cadmium) level width of the lower mixed state is listed in row 7. Rows 9, 10, and 11 give the contributions to the uncertainty in  $\Gamma_{\text{nr}}^{\text{nc}}$  that are due to the uncertainties in  $\varepsilon, \Gamma_{\text{nr}}$  and  $B(E2\uparrow)$ , re-

spectively. (For hidden levels we assume a  $\pm 10\%$  uncertainty in the shifts and widths.) Finally, the calculated induced widths, with uncertainties obtained by adding in quadrature the values given in rows 9, 10, and 11, are given in row 12. Even though there are two values for the induced width for the odd nuclei, the smaller value has little effect on the total induced width.

The results of the measurements and comparisons with theory are presented in Table III. Column 1 lists the target composition and chemical form used for the nonresonant and the resonant measurement. Column 2 gives the x-ray line designation for the experimental ratio, which is given in column 3. The values in column 4 have been corrected for the isotopic abundances in the resonant and nonresonant targets. Column 5 presents the resultant attenuation values derived from the values in column 4. Previous measurements are given for

TABLE II Summary of Parameters and Calculated Results for the induced widths

| Row   | $^{48}\text{Tl}$          | $^{104}\text{Pb}$      | $^{110}\text{Po}^a$            | $^{111}\text{Cd}^b$            | $^{114}\text{Cs}$             | $^{125}\text{I}^c$              | $^{150}\text{Sm}$      |
|---|---------------------------|------------------------|--------------------------------|--------------------------------|-------------------------------|---------------------------------|------------------------|
| 1 Mixed levels<br>$n\ell-r\ell'$                        | 3d-1s                     | 4f-3p                  | 4f-3p                          | 5g-3d                          | 5g-3a                         | 4f-3p                           | 5g-4d                  |
| 2 $(E_{n\ell}-E_{r\ell'})_0$ (keV) <sup>d</sup>         | -1029.8 ± 37.5            | -346.01 ± 0.98         | -373.41 ± 1.52                 | -618.711 ± 0.034 <sup>d</sup>  | -618.711 ± 0.034 <sup>d</sup> | -460.36 ± 3.42                  | -336.74 ± 0.59         |
| 3 $E_{nuc}$ (keV)                                       | 983.512 ± 0.002           | 358.02 ± 0.07          | 373.81 ± 0.06                  | 620.2 ± 0.4                    | 617.494 ± 0.097               | 463.387 ± 0.011                 | 333.95 ± 0.01          |
| 4 $Q_{nuc}$   | 0.26 ± 0.08               | -0.70 ± 0.08           | -0.72 ± 0.14<br>(-0.47 ± 0.03) | -0.2 ± 0.2 <sup>e</sup>        | -0.37 ± 0.04                  | 0.2 ± 0.2 <sup>e</sup>          | -1.28 ± 0.11           |
| 5 $E_0$ (keV)   | 0.0                       | -1.45 ± 0.17           | -1.71 ± 0.33<br>(-1.11 ± 0.08) | -0.15 ± 0.15<br>[+0.26 ± 0.26] | -0.285 ± 0.031                | -0.69 ± 0.69<br>[2.19 ± 2.19]   | 0.90 ± 0.08            |
| 6 $\epsilon = \text{Re}\Delta E$ (keV)                  | -46.3 ± 37.5              | 10.56 ± 1.00           | -1.31 ± 1.56<br>(-0.71 ± 1.52) | 1.34 ± 0.43<br>[1.75 ± 0.48]   | -1.502 ± 0.107                | 2.34 ± 3.49<br>[5.22 ± 4.06]    | -3.69 ± 0.60           |
| 7 $-\Gamma_{r\ell'}$ (keV) <sup>f</sup>                 | 84.55 ± 8.46              | 22.28 ± 2.23           | 25.54 ± 2.55                   | 1.638 ± 0.083 <sup>d</sup>     | 1.638 ± 0.083 <sup>d</sup>    | 38.81 ± 3.88                    | 6.67 ± 0.67            |
| 8 $B(E2\uparrow)$ ( $e^2 b^2$ )                         | 0.072 ± 0.003             | 0.834 ± 0.044          | 0.91 ± 0.06                    | 0.126 ± 0.017                  | 0.484 ± 0.004                 | 0.158 ± 0.005                   | 1.33 ± 0.02            |
| 9 $[\delta\Gamma_{n\ell}^{n\ell}]_{\Delta E}$ (eV)      | +0.775<br>-0.387          | +0.11<br>-0.09         | +0.04(+0.0)<br>-0.09(-0.07)    | +1.72[+0.13]<br>-0.98[-0.06]   | +0.56<br>-0.48                | +0.02[+0.006]<br>-0.08[-0.009]  | +0.33<br>-0.26         |
| 10 $[\delta\Gamma_{n\ell}^{n\ell}]\Gamma_{r\ell'}$ (eV) | +0.003<br>-0.010          | +0.01<br>-0.01         | +0.29<br>-0.22                 | 0.06[+0.10]<br>-0.06[-0.05]    | +0.12<br>-0.14                | +0.14[+0.007]<br>-0.11[-0.066]  | +0.01<br>-0.02         |
| 11 $[\delta\Gamma_{n\ell}^{n\ell}]_{B(E2)}$ (eV)        | +0.030<br>-0.030          | +0.06<br>-0.06         | +0.18<br>-0.17                 | +0.40[+0.03]<br>-0.50[-0.02]   | +0.04<br>-0.04                | +0.04[+0.002]<br>-0.04[-0.002]  | +0.03<br>-0.02         |
| 12 $\Gamma_{n\ell}^{n\ell}$ (eV) <sup>g</sup>           | 0.698<br>+0.776<br>-0.388 | 1.13<br>+0.13<br>-0.11 | 2.62<br>+0.34<br>-0.29         | 2.94<br>+1.77<br>-1.10         | 4.73<br>+0.57<br>-0.50        | 1.25 ± 0.15                     | 1.66<br>+0.33<br>-0.26 |
|   |                           |                        | ( 2.65    +0.34<br>-0.29 )     | [ 0.19    +0.17<br>-0.08 ]     |                               | [ 0.079    + 0.009<br>- 0.011 ] |                        |

<sup>a</sup>See Nuclear Data Sheet for explanation of two possible  $Q$  values. values in parentheses correspond to smaller  $Q$  value

<sup>b</sup>Values in brackets correspond to the quadrupole moment and orbital angular momentum being antiparallel, other values are for the parallel case

<sup>c</sup>Uncertainties are assumed to be 10% of the strong-interaction energy except as noted

<sup>d</sup>Measured values are taken from Ref. 7

<sup>e</sup>Assumed value is from systematics of neighboring nuclei

<sup>f</sup>Uncertainties are assumed to be 10% of the width except as noted

<sup>g</sup>Uncertainties are obtained by summing in quadrature rows 9, 10, and 11

TABLE III Results of Measurements and Comparisons with Theory

| Target Pair  | Lines Compared  | Present Results               |                     |                            | Previous Results <sup>a</sup><br>A $\alpha$ (%) | Theory<br>A $\alpha$ (%) |
|--|---|-------------------------------|---------------------|----------------------------|---|--------------------------|
|  |   | $R_{\alpha}^{obs}$            | $R_{\alpha}^{corr}$ | $A_{\alpha}^{corr}$ (%)    |   |                          |
| nat. <sup>48</sup> TiO <sub>2</sub>                | $\frac{3 \rightarrow 2}{4 \rightarrow 3}$                   | $0.955 \pm 0.010$             | $0.941 \pm 0.013$   | $5.9 \pm 1.3$              | $19 \pm 3.2$                                    | $12.0^{+10.3}_{-6.7}$    |
| nat. <sup>104</sup> Ru                             | $\frac{4 \rightarrow 3}{5 \rightarrow 4}$                   | $0.913 \pm 0.014^b$           | $0.897 \pm 0.016$   | $10.3 \pm 1.6$             | $7.2 \pm 10.5$                                  | $10.5 \pm 1.0$           |
| nat. <sup>110</sup> Pd                             | $\frac{4 \rightarrow 3}{5 \rightarrow 4}$                   | $0.860 \pm 0.007$             | $0.840 \pm 0.008$   | $16.0 \pm 0.08$            | $19.4 \pm 2.8$                                  | $15.2 \pm 1.3$           |
| nat. <sup>111</sup> CdL                            | $\frac{4 \rightarrow 3}{6 \rightarrow 5 + 8 \rightarrow 6}$ | $0.908 \pm 0.007$             | $0.780 \pm 0.007$   | $22.0 \pm 0.7$             | $21.5 \pm 3.7$<br>$20.4 \pm 3.6^c$              | $21.1 \pm 3.2$           |
|  | $\frac{5 \rightarrow 4}{6 \rightarrow 5 + 8 \rightarrow 6}$ | $R_{\beta} = 0.922 \pm 0.013$ | $0.818 \pm 0.014$   | $A_{\beta} = 18.2 \pm 1.4$ | $9.2 \pm 5.9$<br>$8.6 \pm 5.7^b$                | $16.4 \pm 2.8$           |
| nat. <sup>112</sup> CdO                            | $\frac{5 \rightarrow 4}{6 \rightarrow 5 + 8 \rightarrow 6}$ | $0.624 \pm 0.005$             | $0.528 \pm 0.006$   | $47.2 \pm 0.5$             | $50.5 \pm 2.9^c$<br>$44.3 \pm 2.2^c$            | $46.0 \pm 1.7$           |
|  | $\frac{4 \rightarrow 3}{6 \rightarrow 5 + 8 \rightarrow 6}$ | $R_{\beta} = 0.710 \pm 0.011$ | $0.623 \pm 0.012$   | $A_{\beta} = 37.7 \pm 1.2$ | $28.5 \pm 5.8$<br>$32.2 \pm 3.7^c$              | $37.4 \pm 1.7$           |
| <sup>130,125</sup> Te                              | $\frac{4 \rightarrow 3}{5 \rightarrow 4}$                   | $0.994 \pm 0.012$             | $0.994 \pm 0.012$   | $0.6 \pm 1.2$              |   | $2.9 \pm 0.3$            |
| nat. <sup>150</sup> Sm <sub>2</sub> O <sub>3</sub> | $\frac{5 \rightarrow 4}{6 \rightarrow 5}$                   | $0.888 \pm 0.007$             | $0.868 \pm 0.008$   | $13.2 \pm 0.8$             | $14.0 \pm 3.4$                                  | $11.1 \pm 1.1$           |

<sup>a</sup>From Ref. 5, except as noted

<sup>b</sup>Corrected for target thickness and density differences

<sup>c</sup>Reference 7

comparison in column 6. Calculated results using the widths from Table II are listed in column 7.

All the parameters used in the calculation of the induced width for <sup>111</sup>Cd and <sup>112</sup>Cd have been measured. In addition, as described in Leon et al.<sup>3</sup> and Batty et al.,<sup>7</sup> x-ray intensity values for transitions from non-circular orbits have been measured. Consequently, one can constrain the initial distribution. Figures 1(a) and 1(b) give a plot of  $R_{\alpha}$  and  $R_{\beta}$  versus the

$$\frac{7 \rightarrow 5}{6 \rightarrow 5 + 8 \rightarrow 6}$$

and

$$\frac{6 \rightarrow 4}{6 \rightarrow 5 + 8 \rightarrow 6}$$

ratios for <sup>111</sup>Cd and <sup>112</sup>Cd, respectively. The ranges for these latter two ratios, determined by Leon et al.<sup>5</sup> and Batty et al.,<sup>7</sup> are indicated. The upper and



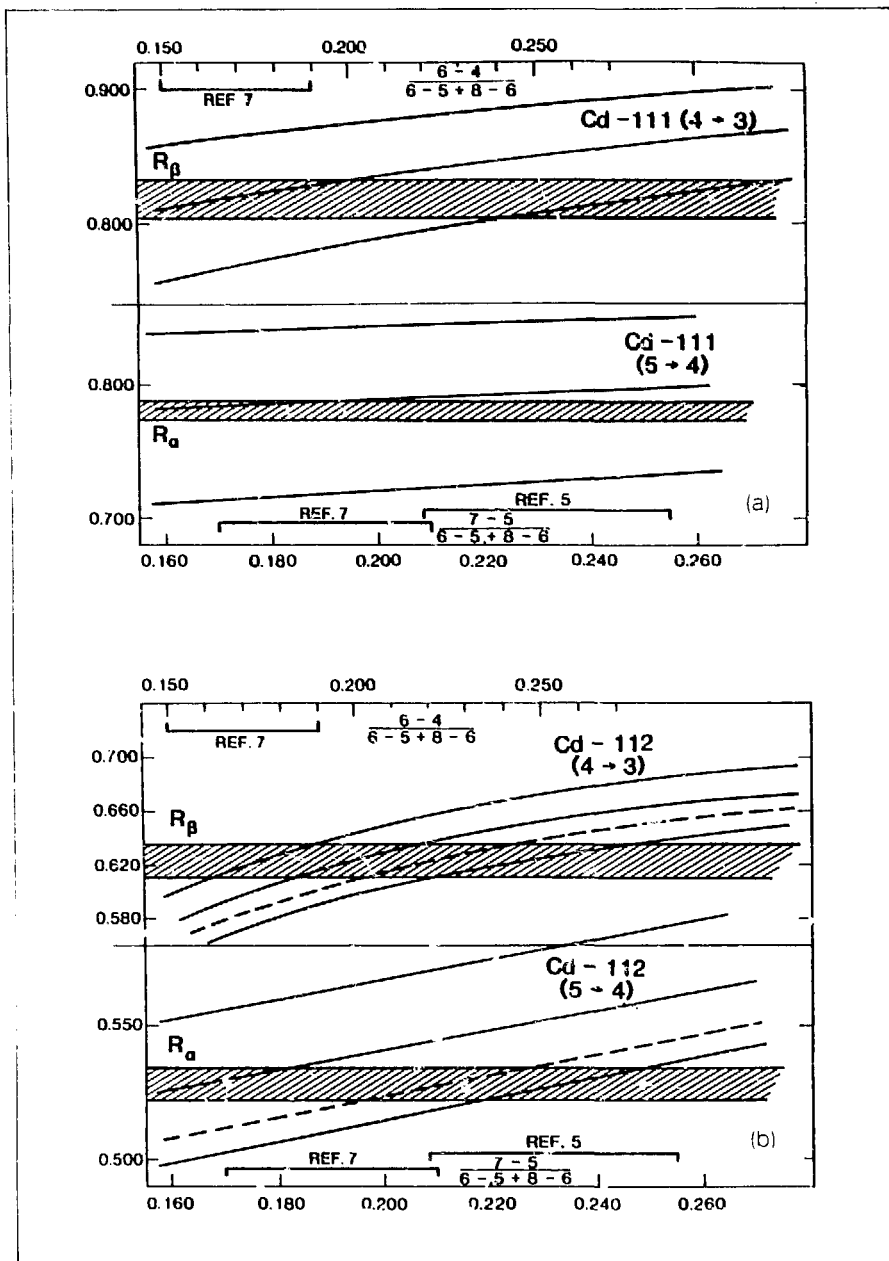


FIGURE 1. Attenuation values  $R_\alpha$  and  $R_\beta$  versus the

$$\frac{7 \rightarrow 5}{6 \rightarrow 5 + 8 \rightarrow 6}$$

x-ray line intensity ratio for (a)  $^{111}\text{Cd}$  and (b)  $^{112}\text{Cd}$

lower bounds for each  $R_\alpha$  and  $R_\beta$  are determined by the range of uncertainty in the induced width. The dashed regions correspond to the measured values. The dotted lines in Fig. 1(b) correspond to the curve obtained by using only calculated values for the x-ray parameters in Table II. The calculated values given in Table III are the weighted averages of the values determined with the three separate measured x-ray intensity ratios.

The excellent agreement between the measured values and calculated values for both  $^{111}\text{Cd}$  and  $^{112}\text{Cd}$  lead us to deduce that the energy of the nuclear-excited state in  $^{111}\text{Cd}$  is most likely  $620.2 \pm 0.2$  keV.

The contour plot for  $^{48}\text{Ti}$  is shown in Fig. 2(a). The attenuation values (in per cent) are given for each contour. The measured attenuation range corresponds to the shaded area. The elongated ellipse bounds the region determined from the induced width value in Table II. We see that the major uncertainty in the calculated value is due to a large uncertainty in  $\epsilon$ . This reflects the assumed 10% uncertainty in the strong-interaction contribution to energy of the  $1s$  state (see Table II). The agreement between the calculated and experimental values is marginal for this case. One expects that strong mixing would be significant for this  $1s$  state, so the treatment of Dubach et al.<sup>2</sup> should be more appropriate. Indeed, including strong mixing could decrease the calculated attenuation value in the present case to approximately 4.5%, in excellent agreement with the experimental value.

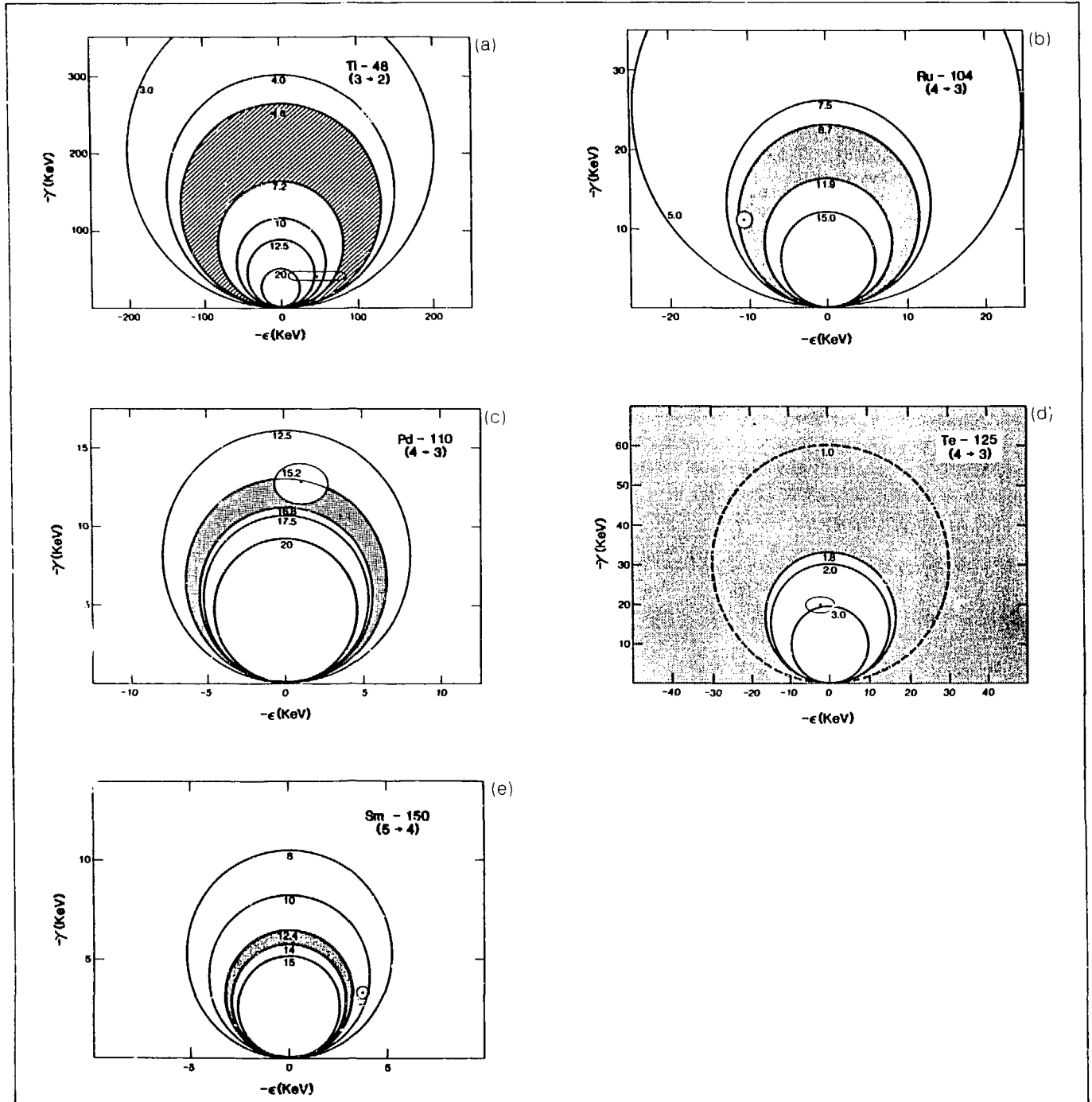


FIGURE 2 Contour plots for (a)  $^{48}\text{Ti}$ , (b)  $^{104}\text{Ru}$ , (c)  $^{110}\text{Pd}$ , (d)  $^{125}\text{Te}$ , and (e)  $^{150}\text{Sm}$ . Each attenuation value is next to its contour. The range of experimental values is represented by the shaded region, and each calculated value with its region of uncertainty is shown by a point and an associated ellipse.

The contour plot for  $^{104}\text{Ru}$  is shown in Fig. 2(b). The striking agreement between the simple theory and experiment is evident. The contour plot for  $^{110}\text{Pd}$  is shown in Fig. 2(c). In the past a great deal of effort has gone into trying to reconcile theory and experiment for this case. The theoretical calculations, even with strong mixing and unequal neutron and proton distributions, gave attenuation values that were too low compared with experiment.<sup>2</sup> However, from Fig. 2(c) we see that even the simple theory now gives excellent agreement with experiment. This is primarily due to the fact that the calculated width of the  $3p$  state using the parameters of Seki and Masutani<sup>6</sup> is somewhat lower than that calculated by Dubach et al.<sup>2</sup> From Fig. 2(c) we see that a given change in  $\gamma$  will lead to a larger change in attenuation than a corresponding change in  $\epsilon$ . Comparison of Table II with the calculations of Dubach et al. shows that the values of  $\gamma$  and  $\epsilon$  used in their work are about 7 keV larger than those used in the present work.

Including strong mixing in the present work would increase the theoretical attenuation, which would lead only to a marginal improvement in the overlap between theory and experiment.

The same atomic levels are involved in  $^{125}\text{Te}$  as for  $^{104}\text{Ru}$  and  $^{110}\text{Pd}$ . The contour plot is presented in Fig. 2(d). For the theoretical region, only the parameters in Table II, which give the larger induced width, are used. Unlike the  $^{104}\text{Ru}$  and  $^{110}\text{Pd}$  cases, the experimentally determined attenuation value is nearly 2 std dev from the theoretical value. This is the heaviest nucleus that involves the  $p$ -wave pion-nucleus interaction on which experiments have been performed, and it is possible that for such a large  $A$  the form of the optical potential or the values of the potential parameters are not appropriate. Neutron-proton density distribution differences would play a greater role for  $^{125}\text{Te}$  than for lower-mass nuclei; this could be another factor leading to the discrepancy between theory and experiment. Dubach et al. did not treat odd- $A$  nuclei, so the effect of strong mixing has not been investigated.

The contour plot for  $^{150}\text{Sm}$  is shown in Fig. 2(e). The experimental value for the attenuation is about

2.5 std dev larger than the theoretical value. Dubach et al. have shown that the attenuation can be increased to 14.6% if a three-level strong-mixing configuration is used. However, this value is still about 1.5 std dev from the experimental value. A two-level calculation produces a decrease in the attenuation.

In conclusion, the agreement of the experimental results for the cadmium isotopes (where the lower mixed level is observable) with simple theory is excellent, and indeed for  $^{111}\text{Cd}$  the data can be used to deduce a more precise value of the  $(5/2)^+$  excitation energy. The persistent discrepancy between theory and experiment for  $^{110}\text{Pd}$ , involving the hidden  $3p$  level, now appears to be resolved, and the  $^{104}\text{Ru}$  result also shows good agreement. However,  $^{125}\text{Te}$ , the last  $3p$  case, does have a discrepancy of 2 std dev. Although the  $^{150}\text{Sm}$  value differs from the simple-theory prediction of Leon<sup>1</sup> by more than 2 std dev, the calculation of Dubach et al.<sup>2</sup> provides much better agreement. Finally, for the potentially very interesting case of  $^{48}\text{Ti}$ , more careful theoretical work is needed for a meaningful comparison.

In summary, the basic  $E2$  resonance mechanism is understood, but it is not clear that the effects of the

strong interaction are properly included. The present work provides experimental values that should enable one to test more rigorously the inclusion of strong-interaction effects.

This work was supported in part by the National Science Foundation. The present work provides an attenuation smaller than a corresponding change in  $\epsilon$ . Comparison of Table II with the calculations of Dubach et al. shows that the values of  $\gamma$  and  $\epsilon$  used in their work are about 7 keV larger than those used in the present work. Including strong mixing in the present work would increase the theoretical attenuation, which would lead only to a marginal improvement in the overlap between theory and experiment.

The same atomic levels are involved in  $^{125}\text{Te}$  as for  $^{104}\text{Ru}$  and  $^{110}\text{Pd}$ . The contour plot is presented in Fig. 2(d). For the theoretical region, only the parameters in Table II, which give the larger induced width, are used. Unlike the  $^{104}\text{Ru}$  and  $^{110}\text{Pd}$  cases, the experimentally determined attenuation value is nearly

2 std dev from the theoretical value. This is the heaviest nucleus that involves the  $p$ -wave pion-nucleus interaction on which experiments have been performed, and it is possible that for such a large  $A$  the form of the optical potential or the values of the potential parameters are not appropriate. Neutron-proton density distribution differences would play a greater role for  $^{125}\text{Te}$  than for lower-

mass nuclei; this could be another factor leading to the discrepancy between theory and experiment. Dubach et al. did not treat odd- $A$  nuclei, so the effect of strong mixing has not been investigated.

The contour plot for  $^{150}\text{Sm}$  is shown in Fig. 2(e). The experimental value for the attenuation is about 2.5 std dev larger than the theoretical value. Dubach et al. have shown that the attenuation can be increased to 14.6% if a three-level strong-mixing configuration is used. However, this value is still about 1.5 std dev from the experimental value. A two-level calculation produces a decrease in the attenuation.

In conclusion, the agreement of the experimental results for the cadmium isotopes (where the lower

mixed level is observable) with simple theory is excellent, and indeed for  $^{111}\text{Cd}$  the data can be used to deduce a more precise value of the  $(5/2)^+$  excitation energy. The persistent discrepancy between theory and experiment for  $^{110}\text{Pd}$ , involving the hidden  $3p$  level, now appears to be resolved, and the  $^{104}\text{Ru}$  result also shows good agreement. However,  $^{125}\text{Te}$ , the last  $3p$  case, does have a discrepancy of 2 std dev. Although the  $^{150}\text{Sm}$  value differs from the simple-theory prediction of Leon<sup>1</sup> by more than 2 std dev, the calculation of Dubach et al.<sup>2</sup> provides much better agreement. Finally, for the potentially very interesting case of  $^{48}\text{Ti}$ , more careful theoretical work is needed for a meaningful comparison.

In summary, the basic  $E2$  resonance mechanism is understood, but it is not clear that the effects of the strong interaction are properly included. The present work provides experimental values that should enable one to test more rigorously the inclusion of strong-interaction effects.

This work was supported in part by the National Science Foundation.

---

## References

1. M. Leon, *Physics Letters* **50B**, 25 (1974), and **53B**, 141 (1974); and —, *Nuclear Physics* **A260**, 461 (1976).
2. J. F. Dubach et al., *Physical Review C* **20**, 725 (1979).
3. M. Leon et al., *Physical Review Letters* **37**, 1135 (1976).
4. J. N. Bradbury et al., *Physical Review Letters* **34**, 303 (1975).
5. M. Leon et al., *Nuclear Physics* **A322**, 397 (1979).
6. R. Seki and K. Masutani, *Physical Review C* **27**, 2799 (1983).
7. C. J. Batty et al., *Nuclear Physics* **A296**, 361 (1978).

## EXPERIMENT 813 — LEP

**Pion Charge Asymmetries for  $^{13}\text{C}$  at Low Beam Energies on the LEP Spectrometer**

Univ. of Colorado, Los Alamos, Univ. of South Carolina, Arizona State Univ., Virginia Polytechnic Institute and State Univ.

Spokesmen: R. J. Peterson and J. J. Kraushaar (Univ. of Colorado)

Previous pion inelastic-scattering experiments at resonance<sup>1</sup> have revealed several transitions in  $^{13}\text{C}$  that exhibit large asymmetries with respect to  $\pi^-$  and  $\pi^+$  scattering. The aim of Exp. 813 was to examine these same transitions at lower beam energies where  $T = 3/2$  amplitudes may not be so dominant. Of particular interest is the  $J = 9/2^+$ ,  $T = 1/2$  state at an excitation of 9.50 MeV. This state is due to a stretched ( $p_{3/2}d_{5/2}$ ) neutron particle-hole configuration.<sup>2</sup> At resonance, the cross section for scattering to this state exhibits a 9/1 ratio for  $\pi^-$  to  $\pi^+$  scattering.<sup>1</sup> Because this state has a simple and known structure, we hope that low-energy data will shed some light on the reaction mechanism for inelastic pion scattering at energies well below (3,3) dominance.

The experiment was performed in September at the LEP channel using the new Clamshell spectrometer. Data were taken at an incident energy of 65 MeV at lab angles of 45, 65, 84, and 105°, with both  $\pi^+$  and  $\pi^-$  beams. In addition, we took a  $\pi^-$  spectrum at 105° with a beam energy of 50 MeV. Characteristic spectra at a lab angle of 84° with an energy resolution of 500 keV are shown in Fig. 1. As can be seen from the figure, we will also be able to obtain information about several other states, especially the quadrupole collective transitions at 3.68 and 7.55 MeV and the monopole transition at 8.86 MeV. Broad, excited states are seen up to 20 MeV in excitation.

The data are currently being replayed and analyzed at the University of Colorado at Boulder. Preliminary results suggest that the ratio of  $\pi^-$  to  $\pi^+$  cross sections at 65 MeV for the 9.50-MeV state is much less than the 9/1 ratio found at resonance. It is perhaps as low as 2 or 3 to 1. At 65 MeV, absolute cross sections will be obtained by normalizing to the  $\pi^\mp D$  measurements of Balestri et al.<sup>3</sup> from our spectra on deuterated polyethylene.

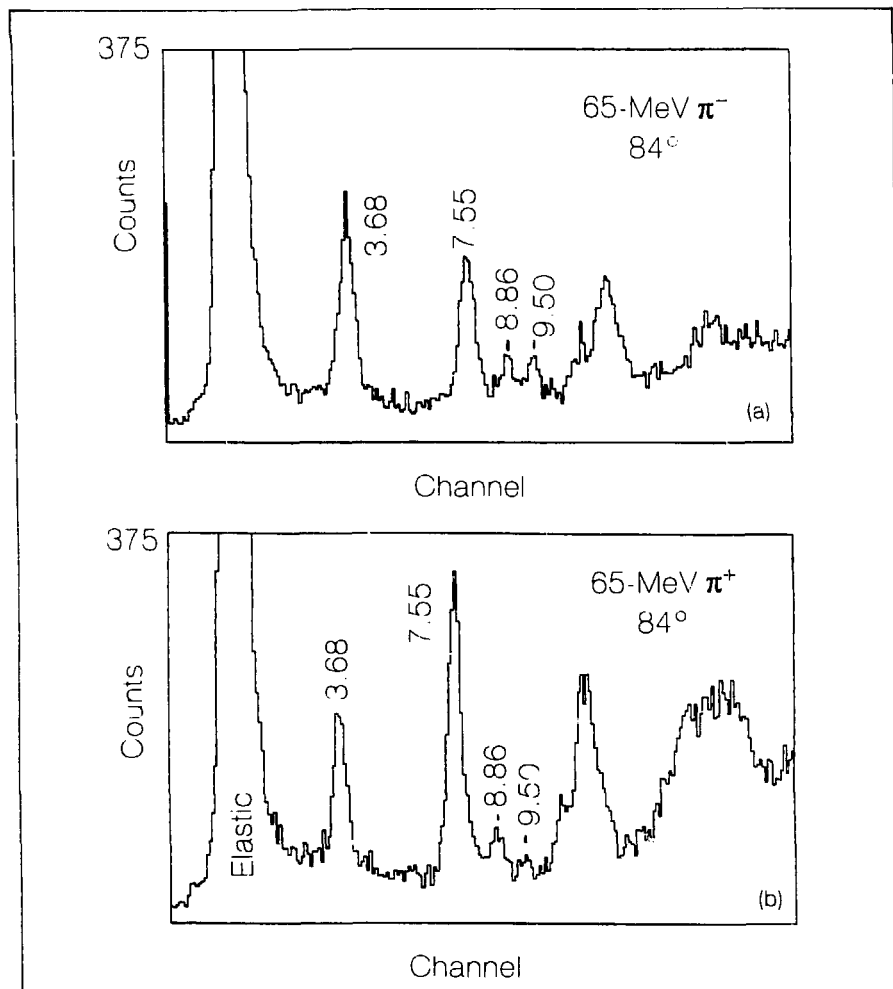


FIGURE 1 Spectra for 65-MeV (a)  $\pi^-$  and (b)  $\pi^+$  scattering on  $^{13}\text{C}$ , obtained with the Clamshell spectrometer. An enhancement of  $\pi^-$  over  $\pi^+$  excitation of the 9.50-MeV M4 transition is observed, but this is not as great as that seen at resonant pion beam energies.

## References

1. S. J. Seestrom-Morris, D. Dehnhard, M. A. Franey, G. S. Kyle, C. L. Morris, R. L. Boudrie, et al., *Physical Review C* **26**, 594 (1982).
2. T. S. Lee and D. Kurath, *Physical Review C* **22**, 1670 (1980).
3. B. Balestri, G. Fournier, A. Gerard, J. Miller, et al., *Nuclear Physics* **A392**, 217 (1983).



## EXPERIMENT 884 — LEP

**Pion Double Charge Exchange on  $^{14}\text{C}$  at Low Energies**

Los Alamos, Arizona State Univ., Virginia  
 Tech. Inst. and State Univ.,  
 Univ. of Pennsylvania

Spokesmen: M. J. Leitch and H. W. Baer (Los  
 Alamos)

Participants: R. L. Burman, M. D. Cooper, J. R.  
 Comfort, A. Cui, B. J. Dropesky, G. C. Giesler,  
 R. Gilman, F. Irom, J. N. Knudson, M. J.  
 Leitch, C. L. Morris, and D. H. Wright

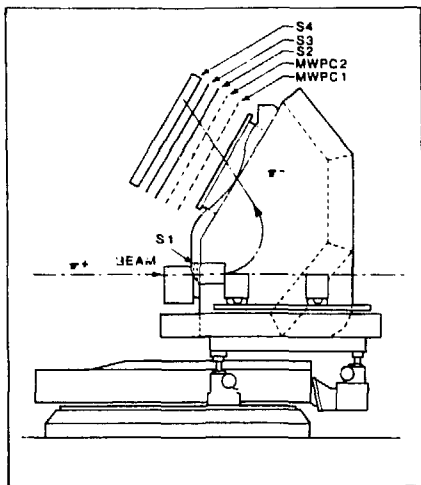


FIGURE 1. Schematic diagram of the Clamshell spectrometer.

**Introduction**

This is the first double-charge-exchange (DCX) experiment performed with the Clamshell spectrometer. The goal is to determine the energy dependence and mass dependence of double-isobaric-analog-state (DIAS) transitions at low pion energies. The few previous measurements at low energies can be found in Refs. 1-3.

In the 1985 runs we measured the  $^{14}\text{C}$  DIAS transition at energies 30, 50, 65, and 80 MeV, and the  $^{48}\text{Ca}$  DIAS transition at 35 MeV. Our measurements cover a much broader angular range (from 20 to 130°) than do the EPICS measurements at higher energies, and therefore we can determine the angle-integrated DIAS cross sections.

A unique feature that distinguishes low-energy (30- to 65-MeV) DCX reactions from higher energy reactions ( $T_\pi \geq 100$  MeV) is the inhibition of the double-forward-scattering mechanism at the low energies. This is due to the small forward-angle, single-charge-exchange (SCX) amplitude near 50 MeV that results from the near cancellation of the  $s$  and  $p$  partial waves in the  $\pi N$  charge-exchange reaction. Calculations by Gibbs et al.<sup>4</sup> show that at 50 MeV successive near-90° scatterings produce most of the forward-angle DIAS cross section, whereas at 180 MeV successive near-0° scatterings produce most

of the 0° DIAS cross section. A consequence is that the average separation distance of the two nucleons participating in the double scattering is significantly less for 50-MeV scattering than for 180-MeV scattering.<sup>4</sup> Thus low-energy DIAS transitions hold some promise for providing a means of study for the short-range  $NN$  dynamics in nuclei.

**Experiment**

The DIAS measurements reported here were made using the Clamshell spectrometer at the LEP channel. The Clamshell spectrometer is a single-dipole spectrometer with nonparallel pole faces and a flight path of about 2 m. It has a solid angle of 40 msr with a resolution of several hundred kiloelectron volts and a maximum momentum of 260 MeV/ $c$ . A schematic diagram<sup>1</sup> is shown in Fig. 1. A trigger is provided by one or more focal-plane scintillators (S2, S3, S4) and, for DCX, a front scintillator (S1) in coincidence. Two x-y drift chambers<sup>5</sup> in the focal plane provide the position and angle in both  $x$  and  $y$  at the focal plane that are used to construct the momentum of each particle. The acceptance curve across the focal plane is shown in Fig. 2. Our group has been extensively involved in the commissioning of this spectrometer and is primarily responsible for developing its DCX capability.

The present DCX capability of the Clamshell rests on the rejection of events with low pulse height in S2

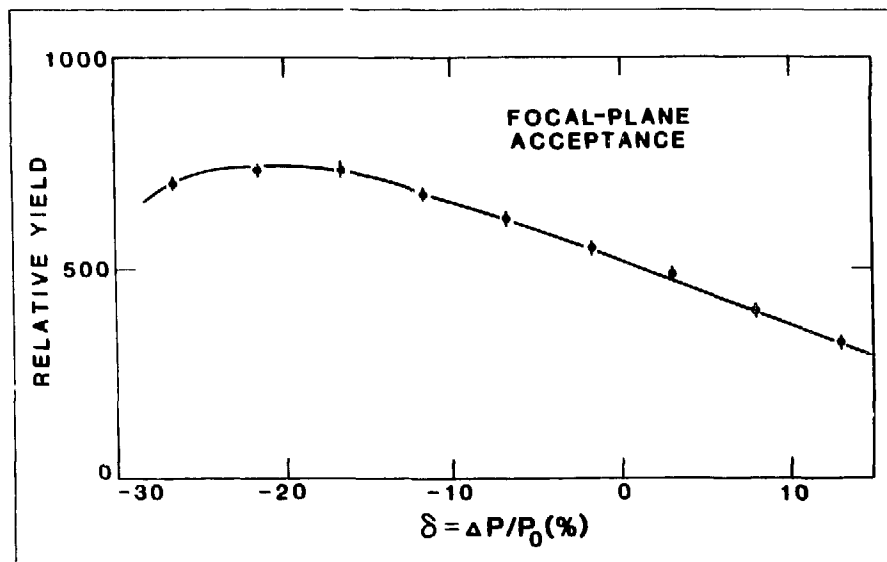


FIGURE 2 A measured focal plane acceptance curve for the Clamshell

and S3 (electrons primarily) and the rejection by time of flight between S1 and S2 (rejection of muons and any electrons surviving the previous rejection). The water Čerenkov detector used in our first runs to reject electrons was unnecessary at low energies because of the excellent electron rejection by pulse height and time of flight. During our most recent run it was replaced with a thick (15-cm) scintillator that stops  $\pi$ 's up to 70 MeV and, along with the other scintillators, gives a total energy determination for the particles.

Figure 3 shows a plot of time of flight versus  $E$  difference, where the  $E$  difference is the difference between the total energy deposited in the scintillators and the energy determined from the bending in the magnetic field as measured by the

wire chambers (assuming a pion mass). The  $\pi$ 's,  $\mu$ 's, and  $e$ 's can be clearly seen as separated groups. For  $\pi^-$ 's, the  $\pi$  group can be smeared in the  $E$ -difference direction because of the possibility of huge energy depositions from stopped  $\pi^-$ 's that "star."

Several deficiencies in this system limit it to angles larger than  $20^\circ$  and to energies  $\geq 15$  MeV. The most serious problem is the necessity for the front scintillator, which provides the excellent time-of-flight information for particle identification (PID). At forward angles its rate becomes excessive because of decay muons and large elastic-scattering cross sections. In test runs without this front

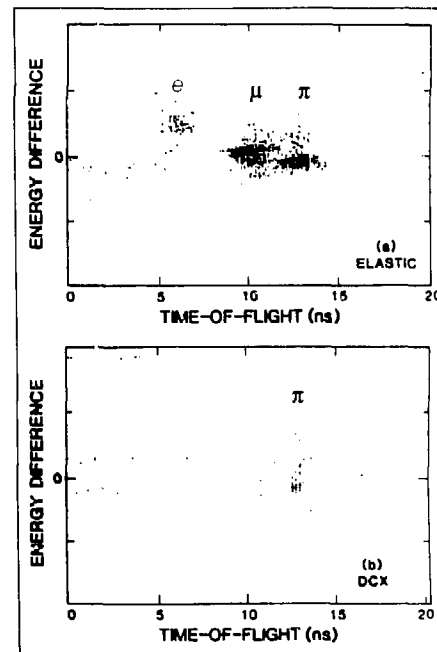


FIGURE 3 Scatter plot of the variable  $E$  difference versus time of flight, where  $E$  difference =  $[\sum E_i$  (scintillation) -  $T_\pi$  (Clamshell)], and time of flight = trajectory-corrected time of flight between S1 (entrance scintillator) and S2 (local-plane scintillator) for  
(a) 22-MeV  $\pi^+$  elastic scattering at  $40^\circ$  and  
(b) 35-MeV DCX on  $^{48}\text{Ca}$  at  $45^\circ$

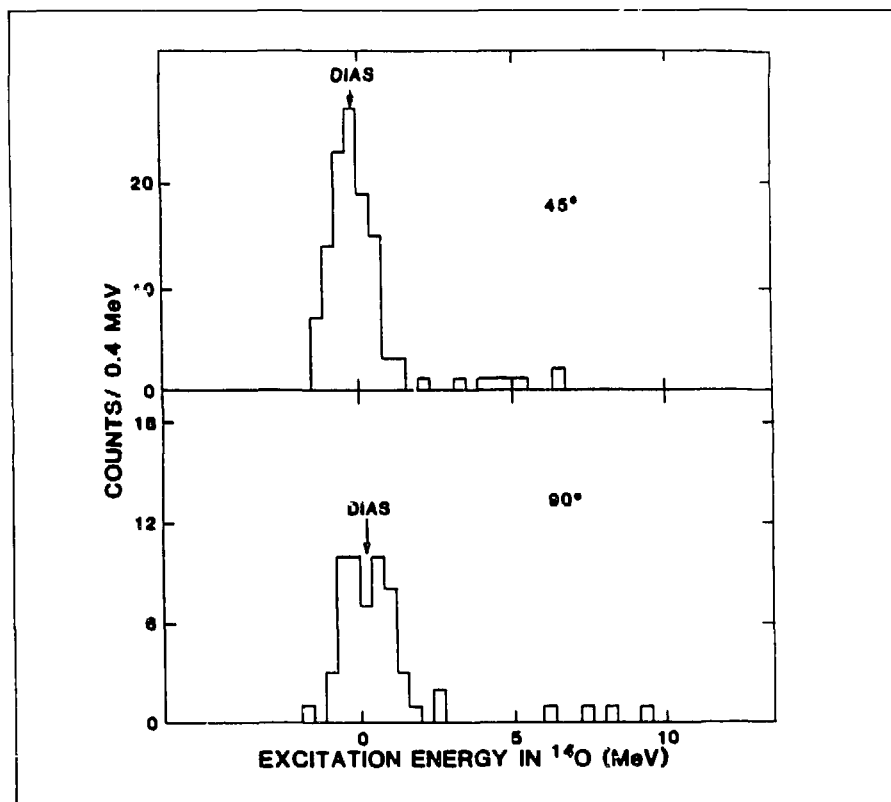


FIGURE 4. Spectra for the  $^{14}\text{C}(\pi^+, \pi^-)$  reaction for 30 MeV at 45 and 90°. The DIAS is virtually the only component in the spectrum.

scintillator we were unable to see even the strong well-separated DIAS transition on  $^{14}\text{C}$  at 50 MeV and 40°. We see two possible solutions to this problem:

1. remove the front scintillator and use, instead, a scintillator placed part way through the spectrometer in the vacuum where particles of the same charge as the beam have been bent out by the magnetic field so that the rate will be much lower. We have already designed this system and could implement it next year; and

2. install a sweeping magnet at the scattering chamber similar to that used at EPICS for forward-angle DCX measurements.

Other more straightforward modifications are also planned to improve the very low energy capability and the  $E$ -difference PID:

1. install a thinner front and a thinner first-focal-plane scintillator to reduce energy loss and multiple-scattering effects for the very low energy pions, and
2. construct a layered and segmented stopping counter in the focal plane to replace the

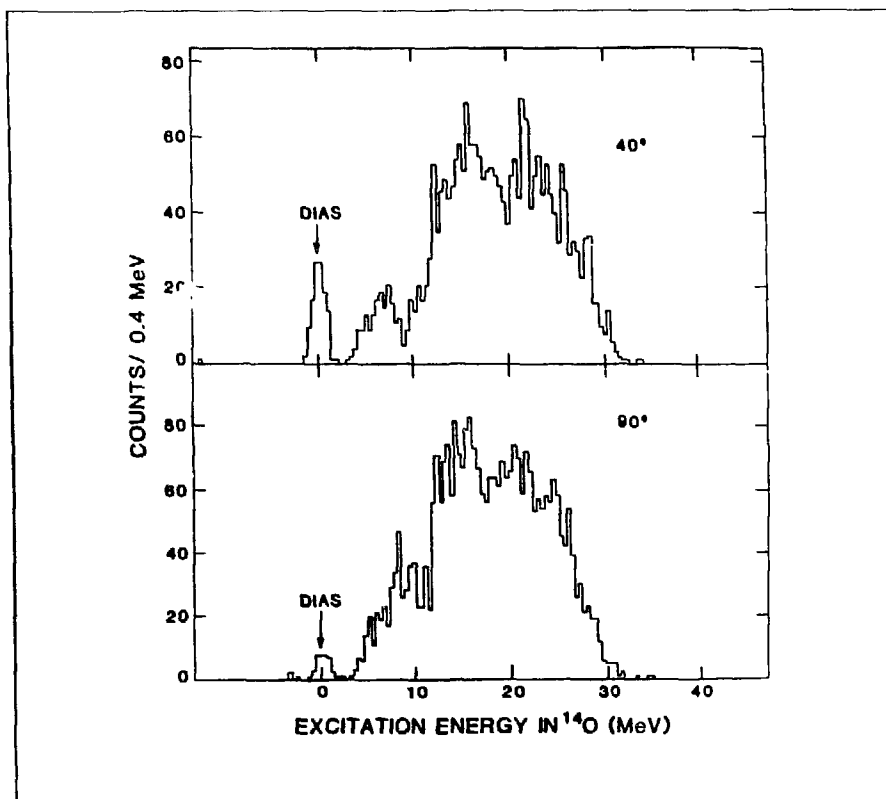


FIGURE 5 Spectra for the  $^{14}\text{C}(\pi^+, \pi^-)$  reaction at 65 MeV (preliminary data, this experiment)

present 15-cm stopping counter. Also, further shielding near the scattering chamber will be added to reduce backgrounds and singles rates.

The results presented here were obtained in September and November of 1985. The  $^{14}\text{C}$  target, which was the same one used in our previous measurements<sup>2</sup> at 50 MeV, had a thickness of  $0.29 \pm 0.02$  g/cm<sup>2</sup>. The data were normalized at each angle and energy to  $^{12}\text{C}$  elastic scattering using the cross sections from Refs. 6-10. The  $^{48}\text{Ca}$  target consisted of a stack of four 3- by 8-cm plates, each approximately 0.115 g/cm<sup>2</sup>

thick. The  $^{48}\text{Ca}$  isotope enrichment was 91%.

## Results

**Carbon-14.** Measurements were made at 30, 50, 65, and 80 MeV. We discuss some of the interesting new results.

1. A new effect we observed was that the states between 5 and 12 MeV are very weakly populated when the beam energy is near 30 MeV, whereas they are strongly populated near 65 and 80 MeV. Spectra measured at 30 and 65 MeV are shown in Figs. 4 and 5. This is not just a momentum

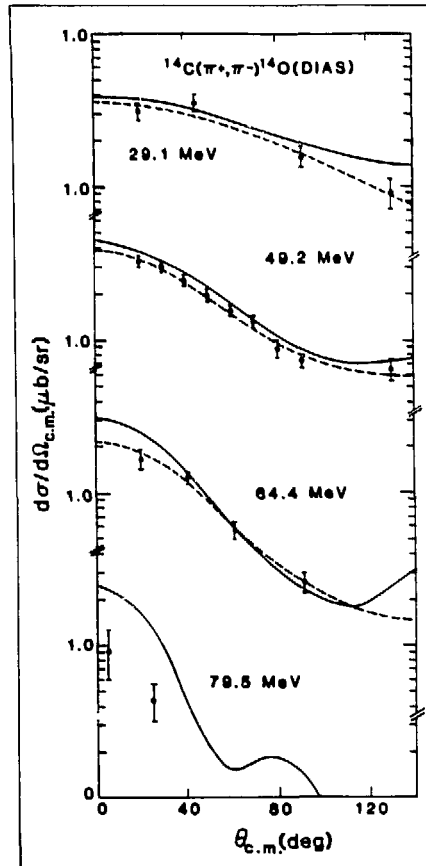


FIGURE 6 The  $^{14}\text{C}$  angular distributions at 30, 50, 60, and 80 MeV compared with PIESDEX calculations (solid lines). The  $5^\circ$  datum at 80 MeV is taken from Ref. 11. \* The dashed lines represent the convenient function discussed in the text used to extract  $0^\circ$  cross sections and integrated cross sections.

transfer ( $q$ ) effect. For a state at 5-MeV excitation in  $^{14}\text{O}$ , we have the following results.

$$\begin{aligned} 30 \text{ MeV: } q &= 131 \text{ MeV}/c \text{ at } 90^\circ \\ 65 \text{ MeV: } q &= 113 \text{ MeV}/c \text{ at } 40^\circ \\ 80 \text{ MeV: } q &= 73 \text{ MeV}/c \text{ at } 25^\circ \end{aligned}$$

Thus there is a larger  $q$  in the  $90^\circ$  data at 30 MeV than in the higher-energy data. Yet, comparison of Figs. 4 and 5 shows that the 5- to 12-MeV region in  $^{14}\text{O}$  is much more populated at 65 and 80 MeV. The large reduction in the nonanalog cross section between 65 and 30 MeV and the near constancy of the forward-angle DIAS cross sections over this energy interval should be useful in determining the relative contributions of the nonanalog and analog intermediate states for DIAS transitions.

2. Figure 6 shows the measured angular distributions together with the fitted function  $Ae^{\lambda(\cos\theta-1)} + B$ . These were used to obtain the  $0^\circ$  cross sections,  $d\sigma/d\Omega_{\text{DIAS}}(0^\circ) = A + B$ , and the angle-integrated cross sections,

$$\sigma_{\text{DIAS}} = 2\pi[2B + A(1 - e^{-2\lambda})/\lambda].$$

Preliminary values are given in the following table:

\*Additional information for Figs. 6-8 is from R. Gilman, University of Pennsylvania, 1965. Information on  $^{14}\text{C}$  is from Refs. 1 and 2, on  $^{48}\text{Ca}$ , from Ref. 12.

| $T_{\pi}$<br>(MeV) | $d\sigma/d\Omega_{\text{DIAS}}(0^{\circ})$<br>( $\mu\text{b}/\text{sr}$ ) | $\sigma_{\text{DIAS}}$<br>( $\mu\text{b}$ ) | $\lambda$ |
|--------------------|---|---|-----------|
| 29.1               | 3.7   | 23.1  | 0.51      |
| 49.2               | 3.9   | 15.0  | 2.31      |
| 64.4               | 2.2   | 6.3   | 2.75      |

The angular distributions become more isotropic ( $\lambda = 0$ ) as the beam energy is lowered.

Also shown in Fig. 6 are calculations with the optical-model program PIESDEX using the 50 MeV parameters described in Ref. 13. It is interesting to note that, although the second-order isoscalar and isovector

parameters used are known to have strong energy dependences that have not been included here, the agreement is quite good for the 30- and 65-MeV data. This may be an indication that the isotensor second-order parameters have little energy dependence.

3. Another interesting result is the forward-angle excitation function. With the addition of our new data points between 30 and 80 MeV, the  $^{14}\text{C}$  excitation is mapped out rather completely between 30 and 300 MeV (Fig. 7). These data exhibit the deep minimum between 100 and 140 MeV that was predicted in some early theoretical calculations (for example, Fig. 8 of Lui and Franco<sup>14</sup>). This minimum is due to the strong absorption of pions near the resonance energy. The rise in  $d\sigma/d\Omega_{\text{DIAS}}(0^{\circ})$  at the lower energies is in part due to the weakening of the optical potential and the consequent higher transparency. In addition, there may be enhancements from short-range  $NN$  correlations.

An important question in the study of DIAS transitions concerns the role of scattering through the intermediate-analog state. At 50 MeV it appears that double scattering through the isobaric-analog state (IAS) is much less than double scattering through nonanalog intermediate states.<sup>15</sup> At 300 MeV, it appears that the analog route dominates.<sup>16</sup> A PIESDEX calculation, similar to those

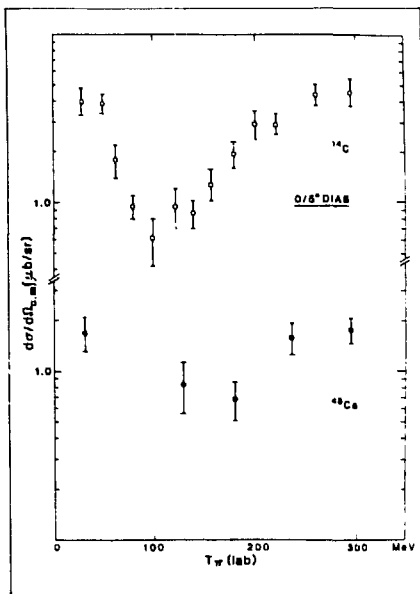


FIGURE 7. Excitation functions at  $0^{\circ}$  for the DIAS states in  $^{14}\text{C}$  and  $^{48}\text{Ca}$ . Data are from Refs. 11 and 12 except for the  $^{48}\text{Ca}$  point at 35 MeV, which is a preliminary result from this experiment.

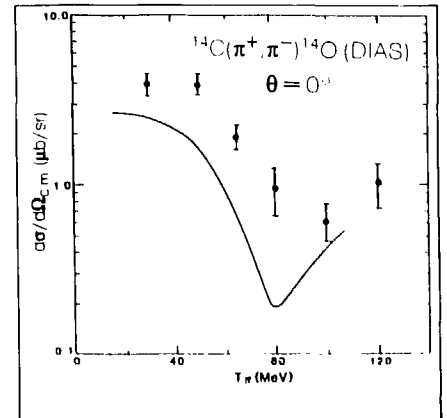


FIGURE 8. Excitation function for  $^{14}\text{C}$  DCX to the DIAS. The data are from Refs. 2 and 11 except for our preliminary points at 30 and 65 MeV. The solid curves are calculations with the optical model program PIESDEX using potential parameters determined in Ref. 13. These calculations include second-order ( $\rho^2$ ) isoscalar and isovector parameters but do not include an isotensor term. Parameters have been adjusted to give a good description of elastic and IAS cross sections at 50 MeV on light nuclei. (No energy dependence in these second-order parameters has been included here.)

in Fig. 6 but with no isotensor  $p^2$  strength, is compared with the  $^{14}\text{C}$  excitation function data in Fig. 8. This curve essentially represents sequential scattering through the IAS and clearly shows a need for sequential scattering through nonanalog intermediate states or for mechanisms involving short-range correlations.

**Calcium-48.** These are the first DIAS cross sections measured at low energies for a nucleus heavier than  $^{26}\text{Mg}$ . Cross sections were determined at 35 MeV and upper limits for 50 MeV.

1. The  $^{48}\text{Ca}$  spectra at 35 and 50 MeV also show the substantial suppression of the nonanalog strength at lower energies, as was discussed above for  $^{14}\text{C}$ . The 35-MeV spectra shown in Fig. 9 can be contrasted with those for 50 MeV in Fig. 10. At 35 MeV the DIAS dominates the spectrum with some nonanalog strength at higher and lower excitation energies. At 50 MeV the nonanalog strength fills the spectrum, making it difficult to observe the DIAS.

2. The angular distribution at 35 MeV is shown in Fig. 11. By comparing it with the  $^{14}\text{C}$  data (Fig. 6) we

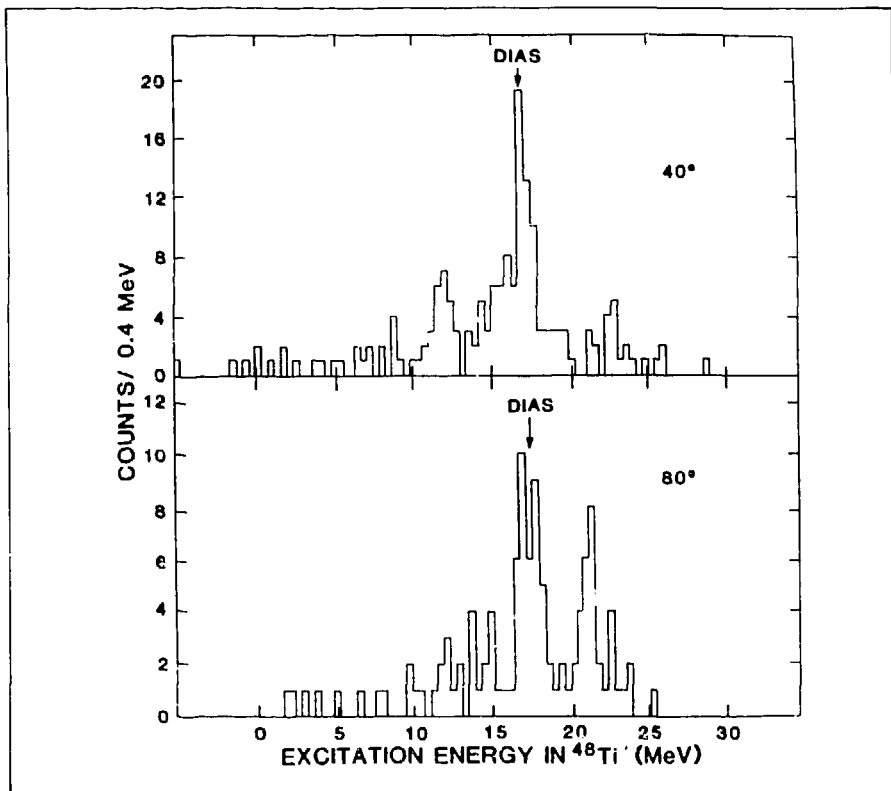


FIGURE 9. Spectra for the  $^{48}\text{Ca}(\pi^+ \pi^-)$  reaction for 35 MeV at 40 and 80°. Peaks at the expected position for the DIAS are clearly visible (preliminary data, this experiment).

see that the  $^{48}\text{Ca}$  cross sections are about 3 times smaller than those for  $^{14}\text{C}$  at 30 MeV. Thus, although there are 4 times as many valence nucleons available in  $^{48}\text{Ca}$ , the cross section is substantially smaller. The solid curve in Fig. 11 is a PIESEX calculation with the same parameters as were used for the comparison with the  $^{14}\text{C}$  angular distributions in Fig. 6. The calculation overestimates the  $^{48}\text{Ca}$  data by a factor of 3. However, this discrepancy cannot be taken too seriously because the isospin-invariant coupled-channel (IICC) approach used cannot take Coulomb effects or  $Q$ -value effects into ac-

count. For  $^{48}\text{Ca}$  ( $Q_{\text{DIAS}} = -12.1$  MeV) at these low beam energies, these effects may be quite important. Siciliano is extending the PIESEX work to include the effects by using a distorted-wave impulse approximation (DWIA) approach that reproduces the IICC well but can also include Coulomb and  $Q$ -value effects.<sup>13</sup>

3. The excitation function for  $^{48}\text{Ca}$  at 35 MeV is compared with that for  $^{14}\text{C}$  in Fig. 7. The  $^{48}\text{Ca}$  data are qualitatively similar in shape but have a broader minimum that appears to be at a higher energy.

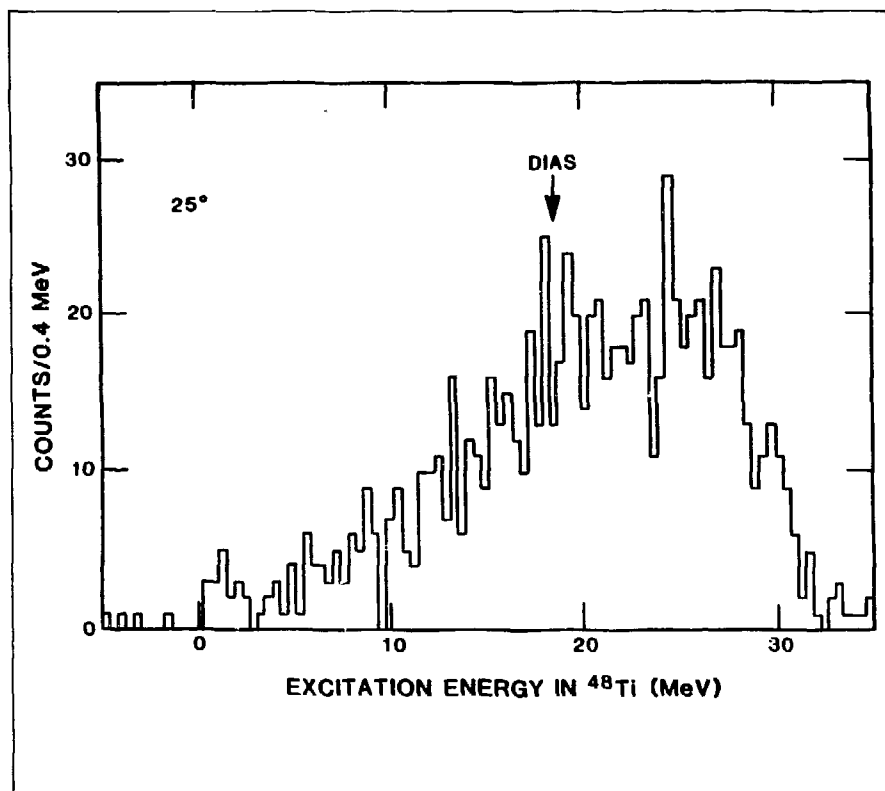


FIGURE 10. Spectrum for the  $^{48}\text{Ca}(\pi^+, \pi^-)$  reaction at 50 MeV. The expected position of the DIAS is indicated by the arrow (preliminary data, this experiment).

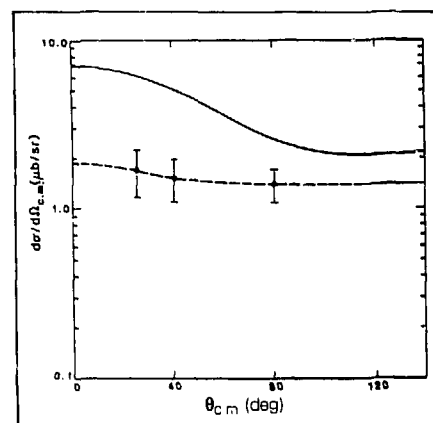


FIGURE 11. Angular distribution for the  $^{48}\text{Ca}(\pi^+, \pi^-)^{48}\text{Ti}$  (DIAS) reaction at 35 MeV. The solid curve is a PIESEX calculation with the same parameters as those used in Fig. 8. The dashed lines represent the convenient function discussed in the text ( $A = 0.493$ ,  $B = 1.38$ ,  $\lambda = 5.85$ ).



---

## References

1. I. Navon et al., *Physical Review Letters* **52**, 105 (1984).
2. M. J. Leitch et al., *Physical Review Letters* **54**, 1482 (1985).
3. A. Altman et al., *Physical Review Letters* **55**, 1273 (1985).
4. W. R. Gibbs, W. B. Kaufman, and P. B. Siegel, "Proceedings of the LAMPF Workshop on Pion Double Charge Exchange," Los Alamos National Laboratory report LA-10550-C (September 1985).
5. L. G. Atencio et al., *Nuclear Instruments & Methods* **187**, 381 (1981).
6. B. Freedom et al., *Physical Review C* **23**, 1134 (1981).
7. M. Blecher et al., *Physical Review C* **20**, 1884 (1979).
8. M. J. Leitch et al., *Physical Review C* **29**, 561 (1984).
9. F. E. Obenshain et al., *Physical Review C* **27**, 2753 (1983).
10. M. Blecher et al., *Physical Review C* **28**, 2033 (1983).
11. P. A. Seidl et al., *Physical Review C* **30**, 973 (1984).
12. M. Kaletka, Ph.D. thesis, Northwestern University, Los Alamos National Laboratory report LA-9947-T (1984).
13. E. R. Siciliano, M. D. Cooper, M. B. Johnson, and M. J. Leitch, "Effects of Nuclear Correlations on Low-Energy Pion Charge-Exchange Scattering" (submitted to *Physical Review C*).
14. L. C. Lui and V. Franco, *Physical Review C* **11**, 760 (1975).
15. T. Karapiperis and M. Kobayashi, *Physical Review Letters* **54**, 1230 (1985).
16. G. A. Miller, *Physical Review C* **24**, 221 (1981).

At the resonance energy, the  $\pi$ -nucleus optical potential is strongly absorbing. The optical absorption dominates true absorption, the  $p$ -wave amplitude dominates the  $s$ -wave amplitude, and the interaction is strong. For the most part the information obtained concerns properties of nuclear surfaces. In the ultra-low-energy region (below 50 MeV) the opposite situation occurs. The  $s$ -wave interaction is larger than the  $p$ -wave interaction, true absorption dominates optical absorption, and the interaction is weak. In this energy region the pion mean free path in the nucleus becomes comparable to the internucleon spacing and the information obtained concerns the nuclear interior.

In the last few years a substantial amount of data for low-energy pion single charge exchange (SCX) to the isobaric-analog state (IAS) has been produced with the  $\pi^0$  spectrometer. In particular, in cycle 41 we succeeded in measuring excitation functions<sup>1,2</sup> for  $^{15}\text{N}(\pi^+, \pi^0)$  (IAS) and  $^{14}\text{C}(\pi^+, \pi^0)$  (IAS) in the range from 35 to 65 MeV. Also, we have measured excitation functions<sup>1</sup> for  $^{39}\text{K}(\pi^+, \pi^0)$  (IAS) and  $^{120}\text{Sn}(\pi^+, \pi^0)$  (IAS) in the range from 40 to 80 MeV. Data have been published for angular distributions for  $^{15}\text{N}$  (Ref. 3),  $^{39}\text{K}$  and  $^{48}\text{Ca}$  at 50 MeV (Ref. 4), and for an excitation function for  $^7\text{Li}$  (Ref. 5).

In this experiment we have measured forward-angle differential cross sections for IASs for  $^7\text{Li}(\pi^+, \pi^0)$ ,  $^{14}\text{C}(\pi^+, \pi^0)$ ,  $^{15}\text{N}(\pi^+, \pi^0)$ ,  $^{60}\text{Ni}(\pi^+, \pi^0)$ , and  $^{120}\text{Sn}(\pi^+, \pi^0)$  at 20 MeV. Also, the dif-

ferential cross sections for the  $^7\text{Li}(\pi^+, \pi^0)$  (IAS) were measured at  $180^\circ$  for 20-MeV incident beam energy. This is the first measurement of pion SCX at  $180^\circ$ .

The experiment was performed at the LEP using the  $\pi^0$  spectrometer,<sup>6</sup> which was set in its two-post configuration. A 1.5-m, crossed-field dc separator was used to obtain nearly pure 20-MeV  $\pi^+$  beam. Sufficient spatial separation of the  $\pi$ ,  $\mu$ , and  $e$  beams was achieved at a mass slit immediately downstream of the separator to remove all but a small part of the beam contaminants at the target position. The pion flux of  $7 \times 10^5 \pi/\text{s}$  was determined directly by a sampling-grid scintillator (SGS), which consists of a number of cylindrical plastic scintillators embedded in a Lucite sheet. The nominal sampling ratio  $R$  for this grid is

$$R = \frac{\text{scintillator area}}{\text{total grid area}}$$

The use of the sampling grid then makes it possible to monitor the intensity of the particle beam by counting individual particles at a sampling fraction, 1:100 in our case, that can be handled by conventional photomultipliers and their associated electronics. The sampling method was independent of beam phase space and divergence. The

## EXPERIMENT 933 — LEP

### Study of the Mass Dependence of Pion Single Charge Exchange at 20 MeV

Los Alamos, George Washington Univ.,  
Abilene Christian Univ., Tel Aviv Univ.,  
Utah State Univ., Arizona State Univ.

Spokesmen: F. Irom and J. D. Bowman (Los Alamos)

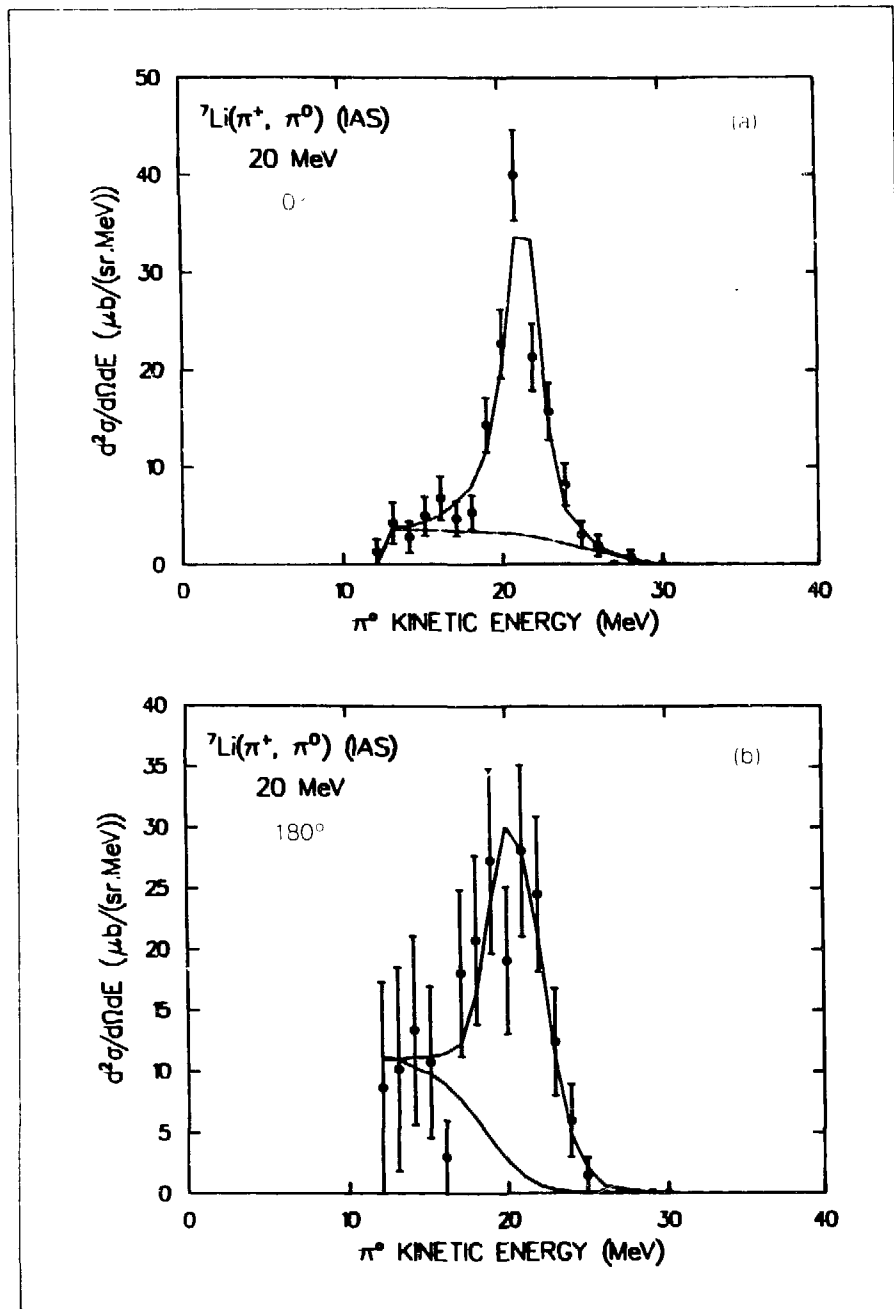


FIGURE 1 Measured  $\pi^0$  spectra for the  ${}^7\text{Li}(\pi^+, \pi^0)$  (IAS) reaction at 20 MeV with the spectrometer setting at (a)  $0^\circ$  and (b)  $180^\circ$ . The solid curve shows a fit to the IAS.

sampling fraction, measured with a low-rate beam, agreed with Monte Carlo calculation to within 5%. The uncertainty in the beam normalization was about 5%.

Typical  $\pi^0$  spectra for the incident beam energy of 20 MeV on the  ${}^7\text{Li}$  target at  $0^\circ$  and  $180^\circ$  spectrometer settings are shown in Fig. 1(a) and 1(b), respectively. The  $\pi^0$  energy resolution (FWHM) in these measurements was 3 to 3.5 MeV. A Monte Carlo simulation of the spectrometer, beam, and target<sup>7</sup> gave the angle-dependent line shapes that were used to fit the data, and described them well. The decomposition of the spectra into background and the IAS peak for the  ${}^7\text{Li}$  measurements can be seen from the solid lines in Fig. 1. The data were fitted by the maximum-likelihood method described in Ref. 7.

In Fig. 2 we present our preliminary results for the measured cross sections at the mean acceptance angle for each bin. The cross section for  ${}^7\text{Li}(\pi^+, \pi^0)$  (IAS) at  $180^\circ$  is as large as the cross section for this reaction at  $0^\circ$ . This result is remarkable and totally unexpected.

The  $A$  dependence of the forward-angle differential cross sections to the IAS is presented in Fig. 3. The shape is well represented by a form  $g(N-Z)A^{-\alpha}$ . The fitted parameters are  $g = 698.4 \mu\text{b}/\text{sr}$  and  $\alpha = 0.92$ . This result is contrary to what one might expect from the transparent limit, which is that the cross section simply scales with the number of excess neutrons ( $N-Z$ ).

Currently, there are no SCX data at  $180^\circ$ , with the exception of our measurement of 20-MeV  ${}^7\text{Li}(\pi^+, \pi^0)$ . Recently, measurements<sup>8</sup> of large-angle elastic scattering at EPICS have demonstrated that the first-order optical model calculations fail to reproduce the large-angle data. These studies show that higher-order terms in the optical potential have their greatest influence at back angles. To understand the effect of the isovector

higher-order terms and to establish the systematics of the back-angle SCX at low energies, a larger body of the data is needed. The present work shows that the  $180^\circ$  SCX cross sections to the IAS are large enough to be measured. Future experiments are planned to further map out the mass and energy dependence of low-energy SCX at back angles.

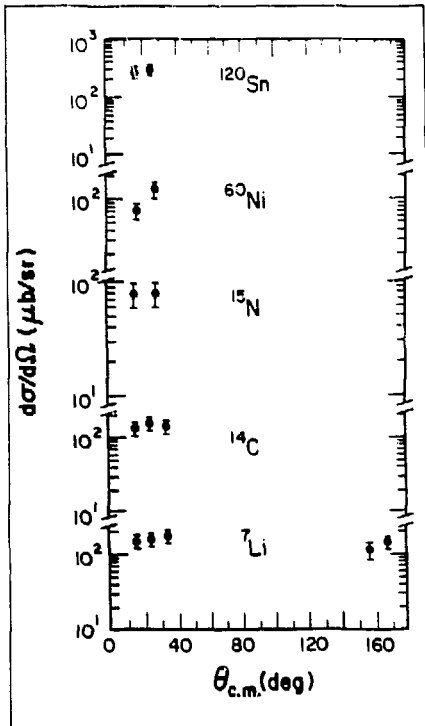


FIGURE 2 Angular distribution for the isobaric-analog states (IAS) of  ${}^7\text{Li}(\pi^+, \pi^0)$ ,  ${}^{14}\text{C}(\pi^+, \pi^0)$ ,  ${}^{15}\text{N}(\pi^+, \pi^0)$ ,  ${}^{60}\text{Ni}(\pi^+, \pi^0)$ , and  ${}^{120}\text{Sn}(\pi^+, \pi^0)$  with a 20-MeV pion beam.

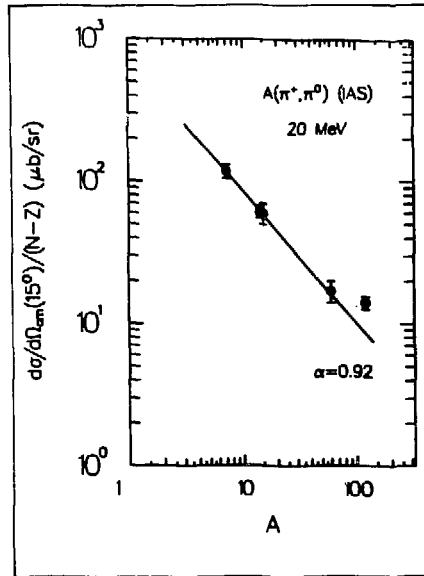


FIGURE 3 The  $A$  dependence of the forward-angle  $(\pi^+, \pi^0)$  differential cross section to the isobaric-analog state normalized with the neutron excess  $(N - Z)$ . The solid line represents a fit to the data with the  $gxA^{-\alpha}$  function.

---

## References

1. F. Irom et al., *Physical Review Letters* **55**, 1862 (1985).
2. J. L. Ullman et al., "Pion Single Charge Exchange on  $^{12}\text{C}$  from 35 to 295 MeV" (submitted to *Physical Review Letters*)
3. M. D. Cooper et al., *Physical Review Letters* **52**, 1100 (1984).
4. M. J. Leitch et al., "Pion Single-Charge-Exchange Angular Distributions at  $T_{\pi} = 48$  MeV," *Physical Review C* **33**, 278-286 (1986).
5. F. Irom et al., *Physical Review C* **31**, 1464 (1985).
6. H. W. Baer et al., *Nuclear Instruments & Methods* **180**, 445 (1981).
7. M. D. Cooper et al., *Physical Review C* **25**, 438 (1982).
8. K. S. Dhuga et al., *Physical Review C* **32**, 2208 (1985).

We have studied the  $^{165}\text{Ho}(\pi^+, \pi^0)^{165}\text{Er}$  isobaric-analog-state (IAS) reaction at energies near the  $\pi N(3,3)$  resonance as a test of the feasibility of the full experiment planned for Exp. 899, which is designed to make a  $<15\%$  determination of the shape of the neutral-matter distribution in  $^{165}\text{Ho}$ . This study also compared the IAS reaction on  $^{165}\text{Ho}$ , which has a very deformed nucleus, to previous work<sup>1</sup> where the systematics of the IAS reaction was established using primarily spherical nuclei. The forward-angle cross sections for  $^{165}\text{Ho}$  are consistent with the systematics, thus supporting the geometric model<sup>2</sup> of pion single charge exchange.

Angular distributions from 0 to about  $20^\circ$  at incident pion energies of 100, 165, and 230 MeV were measured using the  $\pi^0$  spectrometer, which performed well after being refurbished during the 1985 shutdown. The target was amorphous holmium metal with a total areal density of  $2.80\text{ g/cm}^2$ . The technique of target compensation<sup>3</sup> was used to minimize finite target-thickness effects. Although the  $\pi^0$  spectrometer is not capable of resolving excitation to adjacent components of the  $^{165}\text{Ho}$  ground-state rotational band, the observed energy resolution of 3.2 to 3.5 MeV is sufficient to discriminate between a strongly populated IAS transition and one whose isobaric-analog strength is widely dispersed.

The 100- and 165-MeV data were each divided into three angular bins of roughly equal acceptance, but a

lack of statistics for the 230-MeV data allowed only a single bin encompassing the entire acceptance. The forward-angle  $\pi^0$  kinetic-energy spectrum at 165 MeV is shown in Fig. 1. The IAS is strongly populated, as it is for the other two energies. Peak areas were extracted using a fitting-routine<sup>4</sup> method of maximum likelihood based on Poisson statistics, with monoenergetic  $\pi^0$  line shapes calculated by a Monte Carlo routine<sup>5</sup> that also determines the spectrometer solid angle. The results of one such peak extraction are shown in Fig. 1 as two smooth curves representing the background fit and the total fit, respectively. Differential cross sections were calculated in the usual manner.

EXPERIMENT 899 ---- LEP

### Angular Distributions for the $^{165}\text{Ho}(\pi^+, \pi^0)^{165}\text{Er}$ Reaction to the Isobaric-Analog State at 100, 165, and 230 MeV

Arizona State Univ., Los Alamos, National Bureau of Standards

Spokesmen: J. N. Knudson and J. R. Comfort (Arizona State Univ.) and H. W. Baer (Los Alamos)

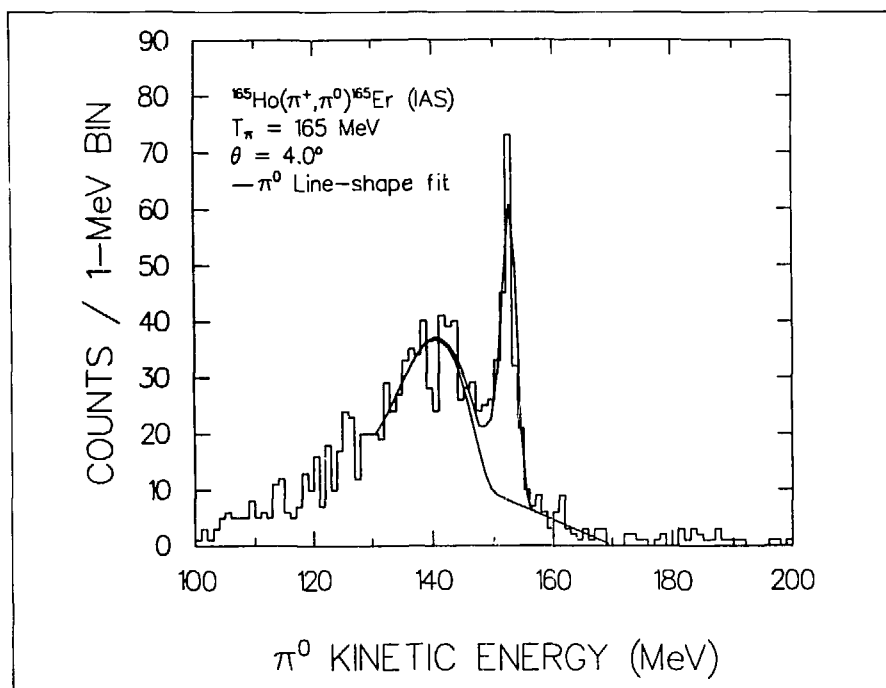


FIGURE 1 Kinetic-energy spectrum of  $\pi^0$ 's produced in  $^{165}\text{Ho}(\pi^+, \pi^0)$  for  $T_\pi = 165\text{ MeV}$ . The smooth curves are the result of a fit using a Monte Carlo-generated line shape

The calculated cross sections are shown in Fig. 2. The error bars represent only the statistical uncertainties in the experiment. Normalization uncertainties are 12% for the 165- and 230-MeV data and 16% for the 100-MeV data. These angular distributions were extrapolated to  $0^\circ$  by fitting them to linear functions of  $q^2$  and  $\cos^2\theta$  and averaging the results at  $\theta = 0^\circ$ .

In Fig. 3 the extrapolated cross sections are shown along with the earlier  $\pi^0$  IAS cross sections<sup>1</sup> at  $0^\circ$ . These earlier data established the

systematic behavior of the IAS reaction on the nuclei as a function of  $N - Z$  and  $A$ . The results of the  $^{165}\text{Ho}$  experiment are consistent with the established systematics. This implies that the same physics applies to both the undeformed nuclei and the highly deformed  $^{165}\text{Ho}$ —that is, that the strong-absorption model,<sup>6</sup> which forms the basis of the single-charge-exchange (SCX) systematics, applies to deformed nuclei as well as to spherical nuclei.

These  $^{165}\text{Ho}$  SCX data also establish the feasibility of the full experiment,

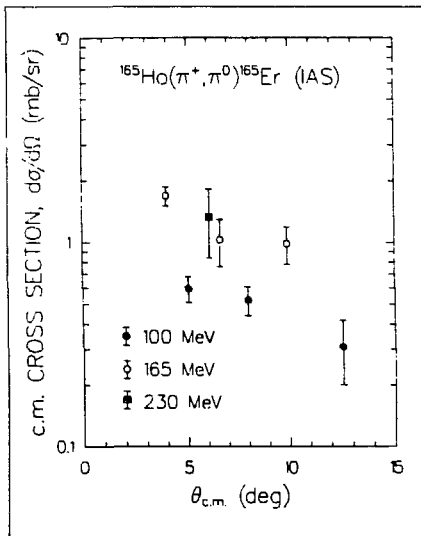


FIGURE 2 Angular distributions of differential cross sections for  $^{165}\text{Ho}(\pi^+, \pi^0)^{165}\text{Er}$  to the isobaric-analog state in  $^{165}\text{Er}$ . Error bars indicate statistical uncertainties.

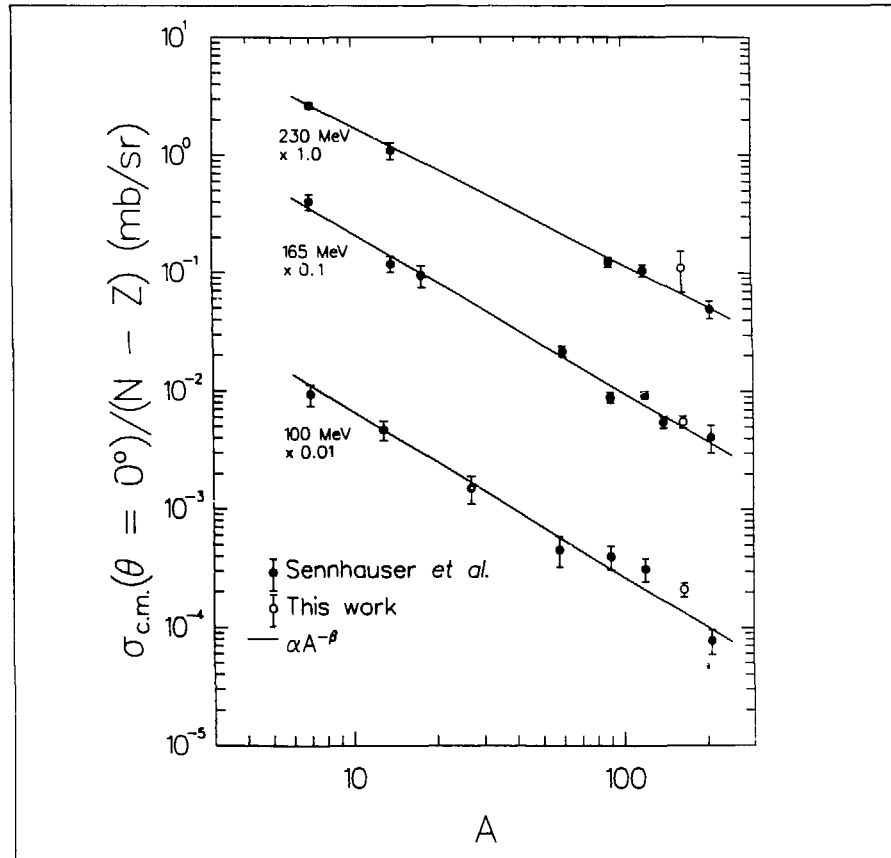


FIGURE 3 Extrapolated  $0^\circ$  cross sections, divided by neutron excess, for previous work (Ref. 4, solid dots) and this work (open circles) as a function of mass number  $A$ . The nuclei reported in Ref. 4 were  $^7\text{Li}$ ,  $^{14}\text{C}$ ,  $^{18}\text{O}$ ,  $^{60}\text{Ni}$ ,  $^{90}\text{Zr}$ ,  $^{120}\text{Sn}$ ,  $^{140}\text{Ce}$ , and  $^{208}\text{Pb}$ . Error bars represent statistical as well as normalization uncertainties.

whose aim is to determine the distribution of neutral matter at the nuclear surface. The full experiment, based on the theoretical work of Chiang and Johnson,<sup>6</sup> will attempt to measure an asymmetry among different orientations of an aligned,

single-crystal <sup>165</sup>Ho sample. The spectrum shown in Fig. 1 is consistent with our ability to measure the asymmetry to <10%, which will allow a determination of the shape of the neutral-matter distribution to <15%.

---

## References

1. U. Sennhauser, F. Piasezky, H. W. Baer, J. D. Bowman, M. D. Cooper, H. S. Matis, H. J. Ziock, J. Alster, A. Erell, M. A. Moinester, and F. Irom, *Physical Review Letters* **51**, 1324 (1983).
2. M. B. Johnson, *Physical Review C* **22**, 192 (1980).
3. S. Gilad, Ph.D. dissertation, Tel Aviv University, 1979 (unpublished).
4. M. D. Cooper, H. W. Baer, J. D. Bowman, F. H. Cverna, R. H. Heffner, C. M. Hoffman, N. S. P. King, J. Piffaretti, J. Alster, A. Doron, S. Gilad, M. A. Moinester, P. R. Bevington, and E. Winkleman, *Physical Review C* **25**, 438 (1982).
5. H. W. Baer, R. D. Bolton, J. D. Bowman, M. D. Cooper, F. H. Cverna, R. H. Heffner, C. M. Hoffman, N. S. P. King, J. Piffaretti, J. Alster, A. Doron, S. Gilad, M. A. Moinester, P. R. Bevington, and E. Winkleman, *Nuclear Instruments & Methods* **180**, 445 (1981).
6. H.-C. Chiang and M. B. Johnson, *Physical Review Letters* **53**, 1996 (1984), and *Physical Review C* **31**, 2140 (1985).



## EXPERIMENT 645 — Neutrino Area

**Search for Neutrino Oscillations at LAMPF**

Ohio State Univ., Argonne National Lab, Caltech, Lawrence Berkeley Lab, Los Alamos, Louisiana State Univ.

*Spokesmen:* T. Y. Ling and T. A. Romanowski (Ohio State Univ.)

*Participants:* R. W. Harper, J. W. Mitchell, E. S. Smith, M. Timko, S. J. Freedman, J. Napolitano, B. K. Fujikawa, R. D. McKeown, K. T. Lesko, E. B. Norman, R. D. Carlini, J. B. Donahue, G. T. Garvey, V. D. Sandberg, W. C. Choi, A. Fazely, R. L. Imlay, and W. J. Metcalf

The decays of stopped pions in the LAMPF beam stop present a unique opportunity to probe neutrino oscillations, in the mass region of  $\delta m^2 \sim 0.1 \text{ eV}^2$ , and mixing parameters as low as  $\sin^2 2\theta \sim 10^{-3}$ . The appearance of  $\bar{\nu}_e$  will be measured with high sensitivity by Exp. 645 during the run cycle that begins in summer 1986.

Intermediate-energy proton accelerators provide neutrino sources in the energy range from 10 to 50 MeV, which is ideal for oscillation searches in the mass region  $\delta m^2 \sim 0.1 \text{ eV}^2$ . In addition, the available beams are very intense, allowing the experiments to be sensitive to mixing parameters as low as  $\sin^2 2\theta \sim 10^{-3}$ . The distance of the detector from the beam stop  $L$  and neutrino energy  $E_\nu$  set a typical oscillation scale of  $L/E_\nu \sim 0.6 \text{ m/MeV}$ , a value intermediate to that obtained in reactors and high-energy experiments.

LAMPF provides a 670- $\mu\text{A}$  proton beam with a kinetic energy of 800 MeV. The beam is absorbed in a copper beam stop, producing on average 0.09 pions for every proton.<sup>1</sup> Although both positive and negative pions are produced,  $\pi^-$  quickly fall into atomic orbitals and are absorbed into the nucleus by strong processes. The  $\pi^+$  come to rest and decay, producing the beam stop neutrino spectra via the decay sequence  $\pi^+ \rightarrow \mu^+ \nu_\mu$ ,  $\mu^+ \rightarrow e^+ \nu_e \bar{\nu}_\mu$ . These decays provide a clean point source of  $\nu_e$ ,  $\bar{\nu}_\mu$ , and  $\nu_\mu$ .

LAMPF Exp. 645 is located 24 m from the beam stop at a polar angle of  $17^\circ$  from the main proton beam. The liquid-scintillator detector is the target for the inverse beta decay reaction  $\bar{\nu}_e p \rightarrow e^+ n$ , which, if seen, would provide a signature for the appearance of  $\bar{\nu}_e$ . The construction phase of the experiment is complete and calibration and cosmic-ray background studies are currently underway. The first data run is expected to begin July 1986.

The design and construction of the experiment are dictated by the expected backgrounds rather than by the signal of a single isolated positron. Because of the long accelerator duty cycle ( $\sim 9\%$ ) and because Los Alamos is 2100 m above sea level, cosmic rays constitute a serious background.

The detector will operate inside a tunnel with an overburden of 3000  $\text{g/cm}^2$ , enough passive material to eliminate the hadronic component in the cosmic-ray flux (see Fig. 1). The estimated integrated muon flux inside the tunnel is 8 kHz. In addition, the central detector is covered by a  $4\pi$  cylindrical cosmic-ray shield,<sup>2</sup> which contains an outer layer of liquid scintillator (15.2 cm) and an inner layer of lead and iron (12.7 and 5.1 cm, respectively). The outer layer is used to veto charged particles. The passive layer is designed, in particular, to eliminate the background of muons stopping outside the active layer, where an electron from the decay radiates a photon that can pass through the scintillator undetected before it converts inside the shield. To minimize inefficiencies in the shield, the scintillator fills only three optically isolated sections: the

TABLE 1 Backgrounds Caused by Interactions in the Detector

| Target           | Mass (Tons) | $\sigma(10^{-41}\text{cm}^2)$ | Rate/Day in Detector<br>( $E_\nu > 35\text{ MeV}$ ) |
|------------------|-------------|-------------------------------|---|
| $^{12}\text{C}$  | 15          | 1.5                           | <0.01   |
| $^{13}\text{C}$  | 0.15        | <5                            | <0.05   |
| $^{27}\text{Al}$ | 0.2         | <5                            | <0.03   |

cylinder and one end cap, the bottom, and the other end cap. The scintillator is viewed by 360 photomultiplier tubes (EMI 4870-B) to provide ample redundancy.

The central detector has 40 layers, each one consisting of a scintillator plane followed by vertical and horizontal proportional drift chambers (see Fig. 2). The liquid scintillator is contained in horizontal Lucite tanks (366 by 30 by 3 cm<sup>3</sup>) and is viewed at both ends by Hamamatsu R878 phototubes. Particles lose 75% of their energy in the scintillator; the rest is deposited in the Lucite and drift-tube walls. The drift-chamber planes consist of 45 wires assembled 8.1 cm apart. Drift-time and pulse-height information are recorded for

every wire. Nuclei with loosely bound neutrons—for example,  $^{27}\text{Al}$  and  $^{13}\text{C}$ —provide a target for  $\nu_e$  interactions and are a source of background because we are not able to distinguish between electrons and positrons (see Table 1). Thus, the drift tubes are constructed of laminated Kraft paper, with only a 25- $\mu\text{m}$  aluminum inner layer to shape the electric field.<sup>3</sup> The detector weight is 20 metric tons, of which 2.3 tons is hydrogen.

We must be able to distinguish protons from electrons with high efficiency in order to eliminate knock-on protons produced in fast-neutron interactions. The granularity of the detector permits such identification

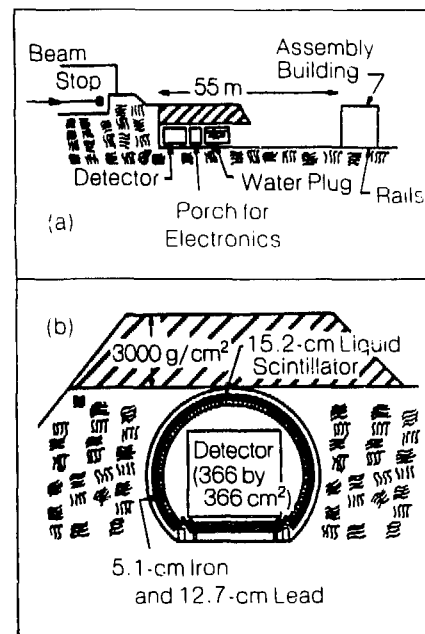


FIGURE 1. Cosmic-ray shielding for the neutrino tunnel (a) side view and (b) front view. The shielding includes 3000 g/cm<sup>2</sup> of overburden, an active charged-particle veto, and an inner layer of lead and iron.

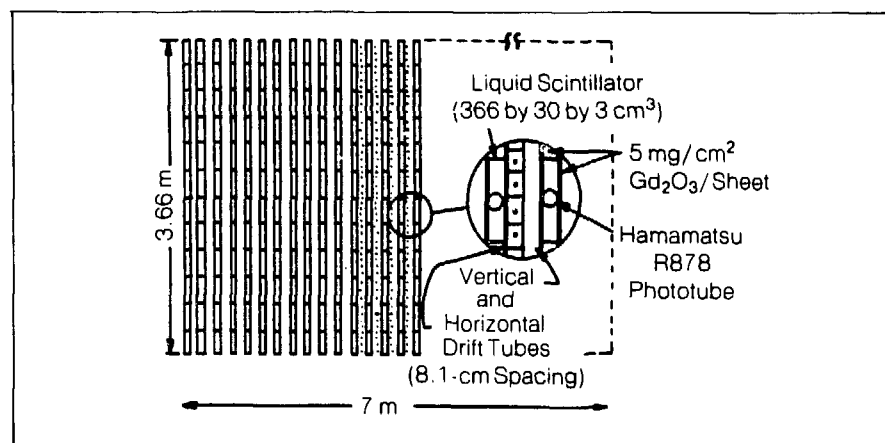


FIGURE 2. Neutrino detector sandwich (elevated view), consisting of 40 scintillator and drift-chamber planes.

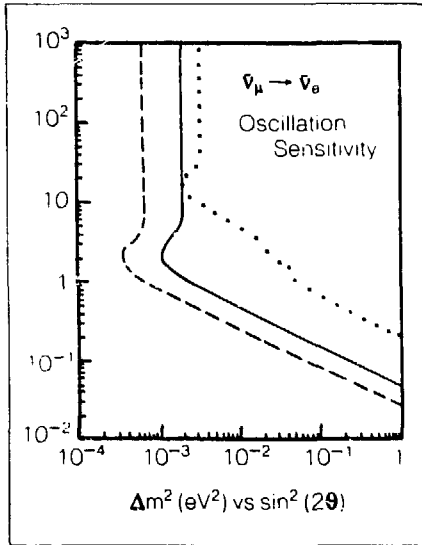


FIGURE 3 Expected sensitivity of Exp. 645 to neutrino oscillations. The dashed curve assumes the experiment is free of background, the full curve assumes a background rate of 0.1 events/day, and the dotted curve shows current oscillation limits.

to be made by comparing the particle range with the energy loss measured in the scintillator. An additional selection can be made based on the  $dE/dx$  measurement in a single scintillator plane. Using these criteria, we have rejected protons by a factor of  $3 \times 10^{-4}$  in a prototype detector studied in the LAMPF test beam channel. Given the present estimates of neutron backgrounds ( $\sim 1000/\text{day}$ ) in our detector, this rejection is adequate to eliminate knock-on protons with kinetic energies greater than 100 MeV.

The signals from the detector and the shield are digitized with flash analog-to-digital converters (ADCs) and stored in cyclic memories containing 150  $\mu\text{s}$  of data. After the positron trigger is flagged by hits in three consecutive planes, data continue to be read into the memories for 100  $\mu\text{s}$ , so that when the data are eventually transferred to the computer, only 50  $\mu\text{s}$  of information are recorded before the event trigger.

The history is used to tag any signals that might be associated with the trigger—for example, a stopping muon. The data recorded after the trigger help identify the neutron that would be present if the event were in fact a  $\bar{\nu}_e$  interaction.

Mylar sheets painted with natural  $\text{Gd}_2\text{O}_3$  are located between all scintillator planes. Neutrons from the interaction may thermalize in the scintillator and capture on gadolinium, which deexcites by emitting 4.5 gamma rays on the average. The detection of these gammas (total energy is 7.9 MeV) provides a neutron signature. The detection efficiency of the neutrons is expected to be about 25%, but depends on requirements imposed on the detection of the resulting gammas.

In Fig. 3 we show the expected sensitivity of Exp. 645 to neutrino oscillations. The  $\bar{\nu}_e p$ -interaction cross section<sup>4</sup> is  $11 \times 10^{-41} \text{ cm}^2$ . Assuming a positron detection efficiency of 50%, the event rate for maximum oscillation is 47 events/day. We hope to keep background rates, which limit the sensitivity of the experiment, to less than 0.1 events/day. For comparison, the best published limits are also shown in the figure.<sup>5</sup>

---

## References

1. R. C. Allen et al., *Physical Review Letters* **55**, 2401 (1985); and H. H. Chen et al., *Nuclear Instruments & Methods* **160**, 393 (1979).
2. S. J. Freedman et al., *Nuclear Instruments & Methods* **215**, 71 (1983).
3. J. Fitch et al., *Nuclear Instruments & Methods* **226**, 373 (1984).
4. S. E. Willis et al., *Physical Review Letters* **44**, 522 (1980); and S. E. Willis et al., *Physical Review Letters* **45**, 1370 (1980).
5. L. A. Anrens et al., *Physical Review D* **31**, 2732 (1985); F. Bergsma et al., *Physics Letters* **142**, 103 (1984); and G. N. Taylor et al., *Physical Review D* **28**, 2705 (1983).

EXPERIMENTS 309, 750, 859,  
and 957 — P<sup>3</sup>

## A Dependence of Inclusive Pion Double Charge Exchange

Los Alamos, MIT, Univ. of Wyoming,  
Univ. of New Mexico, Tel Aviv Univ.,  
Colorado College

Spokespersons: P. A. M. Gram (Los Alamos), J. L.  
Matthews (MIT), and G. A. Rebka, Jr. (Univ. of  
Wyoming)

Participants: C. A. Bordner, D. A. Clark, S.  
Hoibraten, E. R. Kinney, D. W. MacArthur, P.  
Mansky, E. Piasezky, D. A. Roberts, C. R.  
Schermer, T. Soos, S. A. Wood, and H.-J.  
Ziock

The strength of the elementary pion-nucleon interaction suggests, and analysis of pion-nucleus reactions confirms, that multiple scattering plays an important, if often indirect, role in all pion-nucleus reactions.<sup>1</sup> Inclusive pion double charge exchange (DCX) is of special interest because charge conservation alone demands that at least two nucleons within a nucleus explicitly participate in the reaction. Thus DCX provides a way directly to study multiple scattering in pion-nucleus reactions. At present there is no adequate theoretical description of multiple scattering of strongly interacting particles in nuclei. To promote the construction of such a theory it is useful to establish the systematics of the DCX reaction.<sup>2</sup>

Our experimental program, started in 1981, has produced accurate, systematic measurements of the doubly differential cross sections for inclusive DCX, establishing its dependence on the energy and charge of the incoming pion, the outgoing pion energy, the angle of observation, and the target nucleus in nine nuclei<sup>3-6</sup> ranging in atomic weight from 4 to 208. Important information about the reaction mechanism is contained in the dependence of the DCX cross section on the number of neutrons and protons in the target nucleus. We present here a sample of our observations of this dependence in the total-reaction cross sections for both the  $A(\pi^+\pi^-)$  and the  $A(\pi^-\pi^+)$  reactions at two incident pion energies.

In a simple classical picture the DCX reaction proceeds as two successive quasi-free single-charge-exchange (SCX) scatterings. In the  $(\pi^+\pi^-)$  reaction the SCX reactions take place only on the neutrons, whereas in the  $(\pi^-\pi^+)$  reaction the SCX reactions take place only on the protons. In the limit of a weak pion-nucleon interaction, the probability of the first SCX scattering would thus be proportional to  $N$  (the number of neutrons) or  $Z$  (the number of protons), depending on the charge of the incoming pion. The probability of the second scattering would be proportional to  $N-1$  or to  $Z-1$ . Therefore, we might expect the cross section for DCX to be proportional to  $Q(Q-1)$ , where  $Q$  is the number of nucleons of the appropriate type. This picture also suggests that a comparison of  $(\pi^+\pi^-)$  and  $(\pi^-\pi^+)$  on a given nucleus may lead to information on the relative neutron and proton structure of the nucleus.

In these experiments the doubly differential cross section  $\sigma(T,\theta)$  was measured for each target and incident beam at several angles, with complete coverage of the outgoing pion energy spectrum from 10 MeV up to the kinematic cutoff for inclusive DCX. Absolute cross sections were obtained by normalization with respect to  $\pi p$  scattering. The  $\sigma(T,\theta)$  was integrated over outgoing energy at each angle to yield singly differential cross sections  $\sigma(\theta)$ . These were fitted by sums of Legendre polynomials. Total-reaction cross sections were obtained by integrating the fitted functions over angle. The cross sections, given in Tables I and

TABLE I Total Inclusive Double-  
Charge-Exchange Cross Sec-  
tions for the  $A(\pi^+\pi^-)$  X Reac-  
tion in Several Nuclei at 180  
and 240 MeV

| Nucleus           | 180 MeV     | 240 MeV     |
|-------------------|-------------|-------------|
| <sup>4</sup> He   | 0.54 ± 0.05 | 1.09 ± 0.1  |
| <sup>9</sup> Be   |             | 4.84 ± 0.5  |
| <sup>12</sup> C   | 1.92 ± 0.2  | 2.79 ± 0.3  |
| <sup>16</sup> O   | 3.30 ± 0.44 | 5.47 ± 0.54 |
| <sup>40</sup> Ca  | 5.72 ± 0.74 | 9.38 ± 0.9  |
| <sup>103</sup> Rh | 16.2 ± 2.0  | 27.2 ± 3.0  |
| <sup>208</sup> Pb | 33.7 ± 4.0  | 73.4 ± 7.0  |

II, are all preliminary results except those for  $^{16}\text{O}$  and  $^{40}\text{Ca}$ .

Figure 1 presents the variation of the reaction cross section with  $A$  for the  $(\pi^+, \pi^-)$  reaction at 180 and 240 MeV. The monotonic rise of the cross section according to a power law in  $A$  is not unexpected. Only the cross section for  $^9\text{Be}$ , which has an

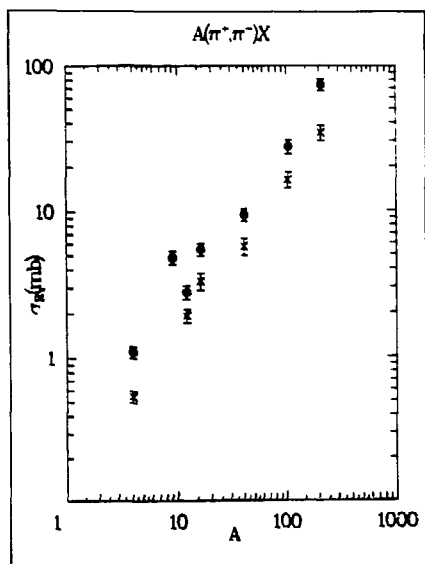


FIGURE 1 Total inclusive DCX cross sections for the  $A(\pi^+, \pi^-)$  reaction at 180 and 240 MeV as a function of  $A$  ( $\circ$ , 240 MeV) and  $X$  (180 MeV)

extra neutron, deviates significantly, lying about a factor of 2 above the general trend. The surprising result is shown in Fig. 2. The cross section for the  $(\pi^-, \pi^+)$  reaction rises approximately parallel to that for the  $(\pi^+, \pi^-)$  reaction up to about  $A = 40$ , where it becomes constant and remains so up to  $A = 208$ , despite the fact that lead has over 4 times as many protons as calcium.

A possible explanation of this effect is that the large neutron excess in heavy nuclei shields the protons from the incoming negative pions. At the  $\Delta$ -resonance energy, negative pions interact strongly with neutrons and relatively weakly with protons, but it is the protons on which DCX takes place. Moreover, there is theoretical

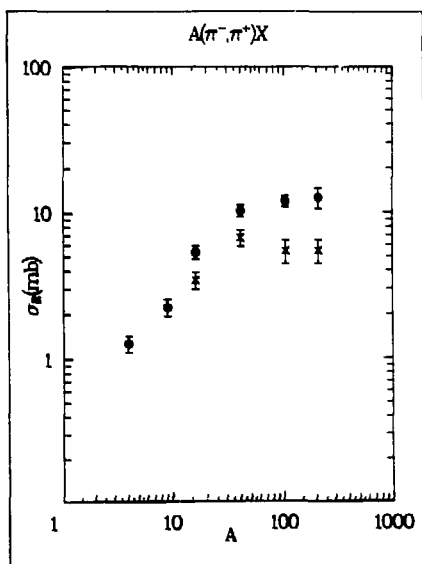


FIGURE 2 Total inclusive DCX cross sections for the  $A(\pi^-, \pi^+)$  reaction at 180 and 240 MeV as a function of  $A$ .

reason to believe that in heavy nuclei a fraction of the neutron distribution lies outside the proton distribution. Therefore, DCX is inhibited by competing reactions that occur on the neutrons. Naturally, neutrons and protons exchange roles for positive incoming pions, but there are no heavy proton-rich nuclei, so the cross section does not saturate at some value of  $A$ . Observation of DCX in  $^3\text{He}$ , planned for the future, will be very interesting.

TABLE II. Total Inclusive Double-Charge-Exchange Cross Sections for the  $A(\pi^-, \pi^+)X$  Reaction in Several Nuclei at 180 and 240 MeV.

| Nucleus           | 180 MeV         | 240 MeV          |
|-------------------|-----------------|------------------|
| $^4\text{He}$     |                 | $1.26 \pm 0.16$  |
| $^9\text{Be}$     |                 | $2.23 \pm 0.3$   |
| $^{16}\text{O}$   | $3.43 \pm 0.44$ | $5.32 \pm 0.54$  |
| $^{40}\text{Ca}$  | $6.69 \pm 0.85$ | $10.22 \pm 0.95$ |
| $^{103}\text{Rh}$ | $5.43 \pm 1.0$  | $11.9 \pm 1.0$   |
| $^{208}\text{Pb}$ | $5.48 \pm 1.0$  | $12.6 \pm 2.0$   |

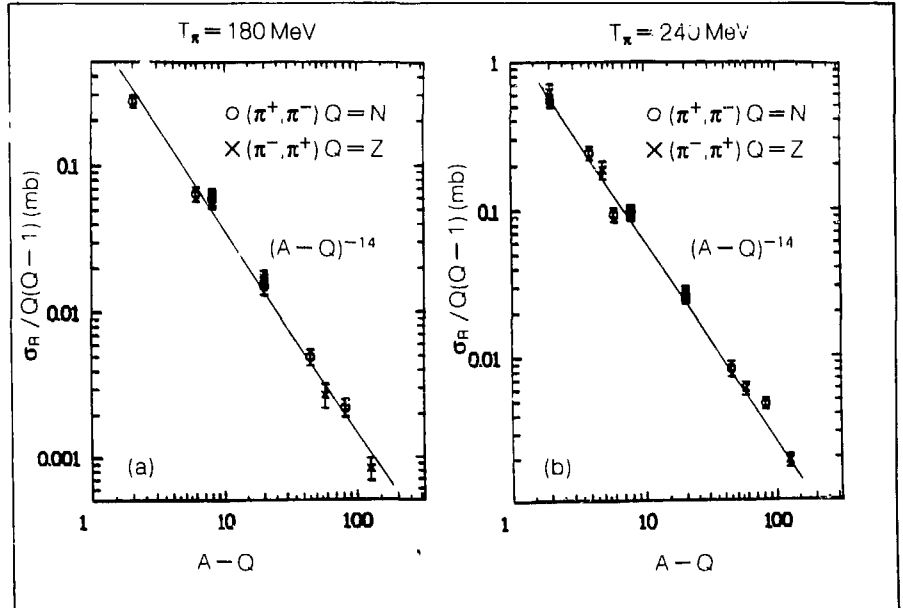


FIGURE 3. Total inclusive DCX cross sections at (a) 180 MeV and (b) 240 MeV, divided by  $Q(Q-1)$  and plotted against  $(A-Q)$ , where  $Q=N$  for  $(\pi^+, \pi^-)$  and  $Q=Z$  for  $(\pi^-, \pi^+)$ . The lines correspond to fits of the form  $Q(Q-1)/(A-Q)^p$ . For both lines,  $p=1.4$ .

These qualitative ideas suggest an empirical parameterization of DCX total cross sections by the simple form  $\sigma \sim Q(Q-1)/(A-Q)^p$ , where  $A-Q$  represents the number of spectator nucleons on which competing reactions can occur. Figure 3 displays the cross sections for both  $(\pi^+, \pi^-)$  and  $(\pi^-, \pi^+)$  plotted according to this simple organizing principle for 180 and 240 MeV. The vertical axis is  $\sigma/Q(Q-1)$  and the horizontal axis is  $(A-Q)$ . In these graphs, cross sections for both charges of incident pion occur at the same values of  $(A-Q)$  for  $N=Z$  nuclei, but at different values of  $(A-Q)$  for  $N \neq Z$

nuclei. Nevertheless, all the cross sections at a particular energy, including those for  ${}^9\text{Be}$ , lie acceptably close to a straight line, which has a slope of  $-1.4$  for both energies. Thus for the  $N=Z$  nuclei this parameterization implies that  $\sigma \sim A^{0.6}$ , rather close to the  $A^{2/3}$  dependence characteristic of reactions that occur on the surface of the nucleus.

We are a long way from comprehension of the reaction mechanisms at work in DCX, but the success of this simple classical picture suggests that sequential SCX scattering operating in competition with the much more probable quasi-free scattering process is a useful idea with which to begin.

---

## References

1. M. Baumgartner et al., *Physics Letters* **112B**, 35 (1982).
2. J. L. Matthews, in "Proceedings of the LAMPF Workshop on Pion Double Charge Exchange," Los Alamos National Laboratory report LA-10550-C (September 1985).
3. S. A. Wood, Los Alamos National Laboratory report LA-9932-T (1984).
4. S. A. Wood et al., *Physical Review Letters* **54**, 635 (1985).
5. E. R. Kinney et al., *Bulletin of the American Physical Society* **29**, 1051 (1984).
6. P. A. M. Gram et al., *Bulletin of the American Physical Society* **30**, 783 (1985).



EXPERIMENT 804 — P<sup>3</sup>-East

### Measurement of the Analyzing Power In $\pi^-p \rightarrow \gamma n$ and $\pi^-p \rightarrow \pi^0 n$ Using a Transversely Polarized Target

UCLA, George Washington Univ.,  
Catholic Univ. of America, Abilene  
Christian Univ., Los Alamos

Spokesman: B. M. K. Nefkens (UCLA)

The experimental setup is shown in Fig. 1. The major components are two sets of 15 neutron detectors, two sets of 15 gamma detectors, and the Los Alamos P-Division polarized proton target. The incident beam was centered on the target using two steering magnets in the beam line 5 m upstream of the target. These magnets were used to correct for the bending of the beam at the target by the "C" magnet of the polarized target. A pair of thin scintillation counters  $S_1$  and  $S_2$ , located 60 cm upstream of the target, defined the beam. The beam flux was typically  $0.9 \times 10^6 \pi^-/s$  on a 2-cm-diam spot on

the target. The central momenta and respective momentum bites of the incident beam were  $427 \pm 2$ ,  $471 \pm 2$ ,  $547 \pm 4$ , and  $625 \pm 6$  MeV/c.

The target consisted of 1-mm-diam ethylene glycol beads contained in a truncated sphere 4.6 cm in diameter and 2.8 cm high. The target polarization, typically 80%, was measured with a nuclear magnetic resonance (NMR) system.

The final-state neutron and gamma were detected in coincidence. The gamma detector consisted of 15 counters arranged in a 5 (vertical)  $\times$  3 (horizontal) rectangular array. Each counter was a 15- by 15- by 25-cm-deep lead-glass block optically isolated from its neighbors and viewed by a 12.7-cm Amperex XP2941 photomultiplier tube. The neutron detector also consisted of 15 counters, each a cylindrical plastic scintillator 7.6 cm in diameter and 45.7 cm long, viewed by an RCA 8575 photomultiplier tube.

An important consideration in designing the experiment was the clean separation between the REX (radiative-exchange),  $\pi^-p \rightarrow \gamma n$ , and the CEX (charge-exchange),  $\pi^-p \rightarrow \pi^0 n$ , events. Experimentally, the REX and CEX events have identical neutral particles in their final states, but the CEX reaction has a cross section very much larger than that for REX. The gammas from the REX reaction are kinematically restricted to a small area on the gamma detector. The  $\pi^0$  yields two back-to-back gammas in the  $\pi^0$  rest frame that are folded forward in the laboratory frame by the Lorentz transformation and that illuminate the entire area covered by the gamma detector.

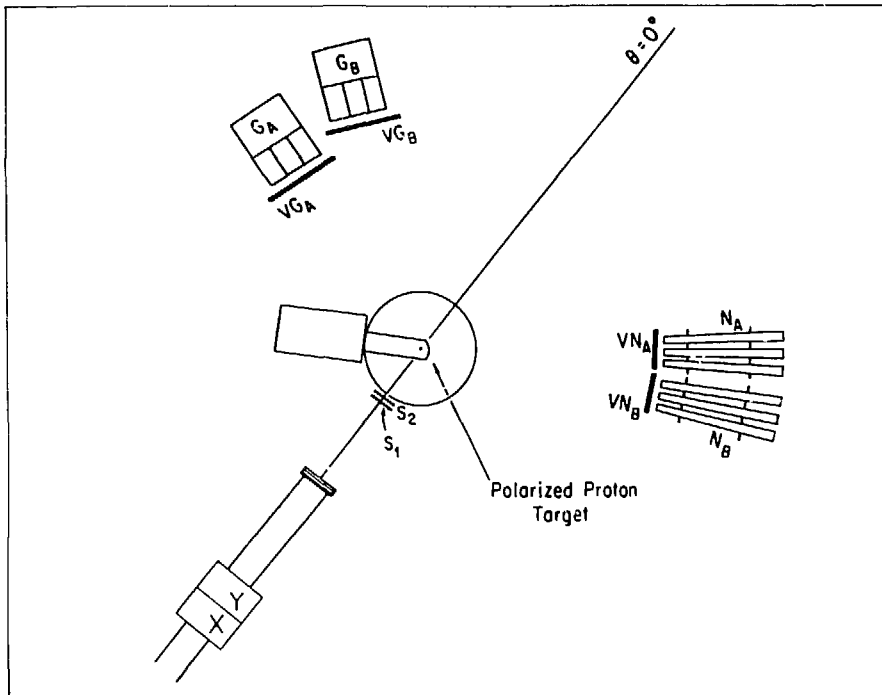


FIGURE 1 Layout of the experimental setup. The beam was centered on the target with the help of  $x$ - and  $y$ -steering magnets.  $S_1$  and  $S_2$  are the beam-defining scintillation counters.  $N_A$  and  $N_B$  are two sets of neutron detectors, and  $G_A$  and  $G_B$  are two sets of corresponding gamma detectors.  $VN_A$  and  $VN_B$  are charged-particle veto counters in front of the neutron detectors, and  $VG_A$  and  $VG_B$  are veto counters for the gamma detectors.

The neutron counters were arranged such that each counter was matched to a unique gamma counter, as dictated by the kinematics of the two-body final state of the REX reaction. Figure 2 shows the front faces of a gamma detector and the matched neutron counter array. The radial distances of the detectors, between 2 and 3 m, were chosen on the basis of a Monte Carlo study in which we optimized the REX-signal-to-CEX-background ratio within a matched neutron-counter-gamma-counter pair. Radial distances of both the neutron and gamma detectors were changed for different scattering angles and incident pion momenta, and the neutron counters were also rearranged to preserve the one-to-one neutron-counter-to-gamma-counter matching.

Charged-particle veto counters, *VN* and *VG*, were in front of the neutron and gamma detectors. There were two pairs of neutron-gamma detectors, each pair with a completely separate set of electronics. This arrangement allowed the measurement of two angular intervals simultaneously. For each event we recorded the pulse heights and time of flights from all neutron and gamma counters and the time of  $S_1$ ,  $S_2$ , and the 200-MHz rf pulse on which the accelerator was timed. All times were measured relative to the gamma counter that triggered the event. The rf timing signal was used to correct for small timing differences caused by different gamma counters starting an event, and to remove any timing

jitter caused by different gamma interaction points and the transmission of light within a gamma counter.

In the data analysis the neutron time of flight and the gamma pulse height were very useful in eliminating a large fraction of the background events from the 90%-by-weight nonhydrogenic parts of the polarized target. The neutron time of flight could not be used to completely separate the REX and CEX events except at low energies or at very forward gamma angles; a fraction of the CEX events was removed by the use of a narrow window on the neutron time of flight while retaining most of

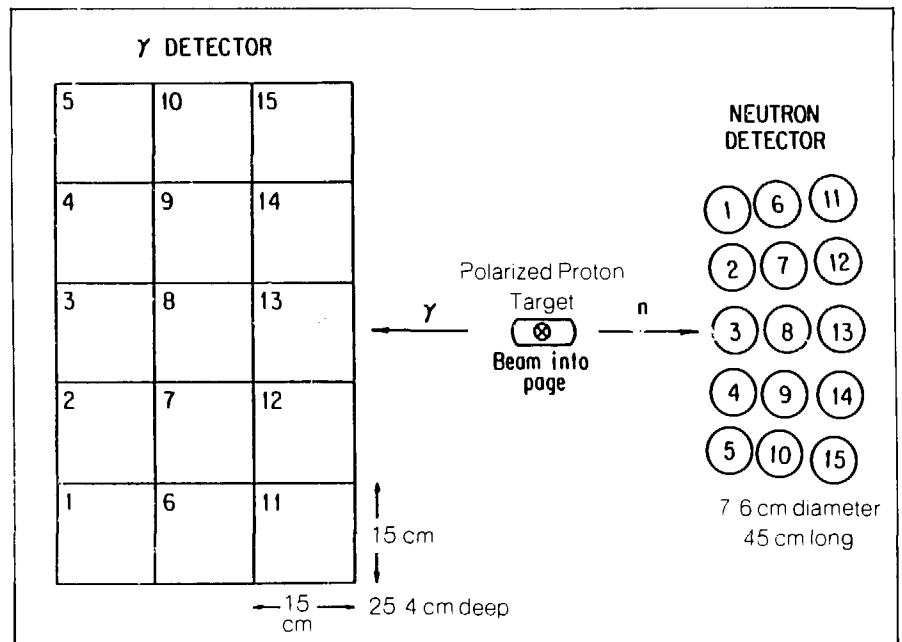


FIGURE 2 The neutron counters and gamma counters arranged in one-to-one matching prescribed by REX kinematics

the REX events. The major challenge of the data analysis was the clean separation between the small REX events and the preponderant CEX events. The key to handling the problem was to exploit as much as possible the two-body character of the REX compared with that of the three-body CEX reaction.

After applying the neutron time-of-flight and gamma pulse-height cuts, we constructed a scatter plot displaying the event distribution from all neutron-counter-gamma-counter combinations. Using the one-to-one neutron-counter-to-gamma-counter matching prescribed by the REX kinematics, the counters were numbered such that neutron

counter 1 corresponded with gamma counter 1, etc. (see Fig. 2). Figure 3 displays a two-dimensional histogram of the number of events in each neutron-counter-gamma-counter combination; the REX events ideally lie only on the diagonal whereas the CEX events are distributed over the entire histogram. Because the neutron-counter-gamma-counter matching was not perfect, there was a slight REX enhancement in the adjacent counters.

The analyzing power is given by the expression

$$A_N = \frac{1}{P_i} \frac{Nu - Nd}{Nu + Nd - 2B}$$

where  $P_i$  is the known target polarization,  $Nu$  is the normalized yield of events that passed the gamma pulse-height and neutron time-of-flight cuts of the spin-up target,  $Nd$  is similar for the spin-down target, and  $B$  is the normalized background yield.

The background yields were measured in separate runs in which the target material was replaced by Teflon ( $C_2F_4$ ) beads. The number of events is normalized by the beam flux. Only the events that lie on the diagonal of the 2D histogram are considered REX candidates. The difficult problem in calculating the REX asymmetry is the reliable subtraction of the CEX contamination among the REX candidates to yield the true REX events. A 2D histogram of the CEX distribution was produced using a Monte Carlo code. From this Monte

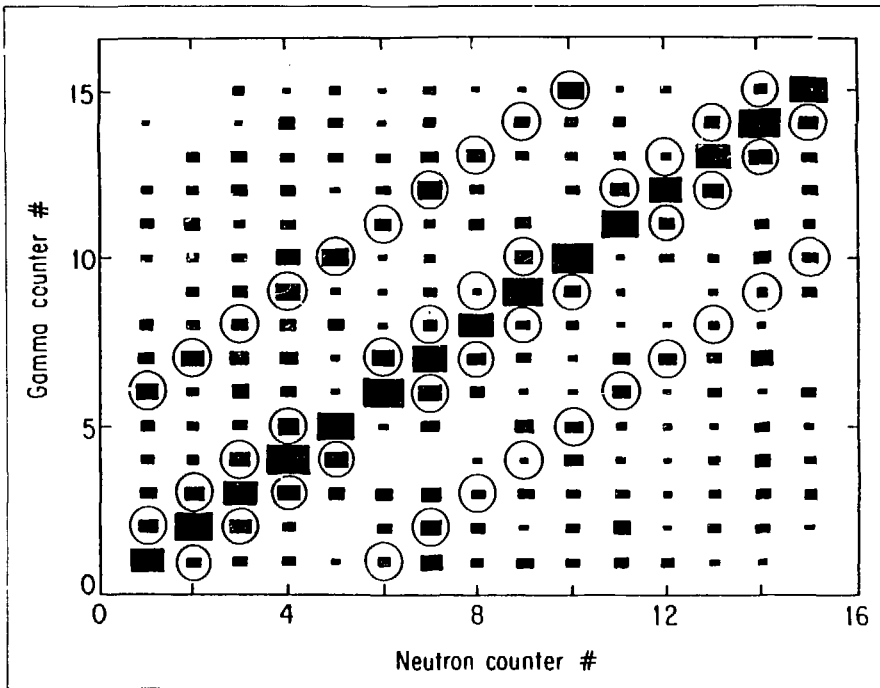


FIGURE 3. A two-dimensional neutron-counter-gamma-counter event distribution. The diagonal elements of this 2D histogram are events from the matched neutron-counter-gamma-counter pairs. The circled elements are events from neutron- and neighboring gamma-counter pairs. A slight REX enhancement can be seen in neighboring elements.

Carlo CEX distribution, the number of CEX background events in the diagonal elements of the 2D histogram was calculated from the numbers of CEX events from the non-diagonal and the nonadjacent elements. Typically, the background was 30%, of which 90% of the background was CEX events and the rest came from the nonhydrogenic material in the target.

Some preliminary results of the analyzing power  $A_N$  in the REX reaction at 427, 471, 547, 586, and 625 MeV/c are shown in Figs. 4-6.

The solid lines are the predictions from the most recent energy-dependent partial-wave analysis of single-pion photoproduction by Arai and Fujii.<sup>1</sup> The agreement is poor, which leads us to question their value for the radiative decay amplitude of the Roper resonance,  $A_{1/2}^{\pi} = 23 \pm 9 \times 10^{-3} \text{ GeV}^{-1/2}$ . Comparison is also made with the prediction of a 1977 partial-wave analysis (PWA) by Noelle<sup>2</sup>; the agreement with our data is good. The only other existing measurements of the asymmetry are a few points at 427 MeV/c by a SIN group.<sup>3</sup> Within their sizable error of about 0.2, there is good agreement with our results, as shown in Fig. 5.

As a consequence of time-reversal invariance,  $A_N$  must be the same in sign and magnitude as the recoil proton polarization  $P$  measured in  $\pi^-$  photoproduction from a neutron target. Some results obtained with a deuterium target<sup>4,6</sup> at  $90^\circ$ , shown in

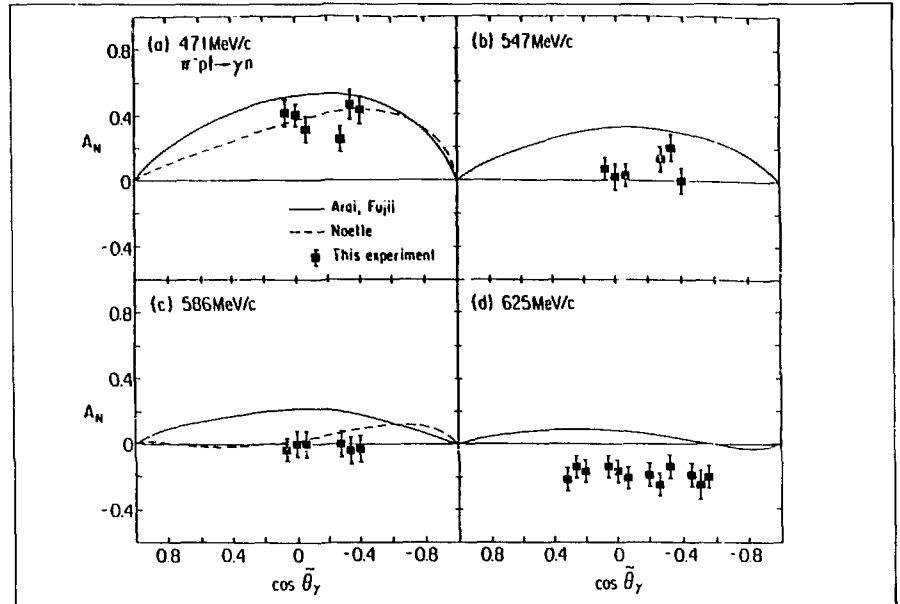


FIGURE 4 Asymmetry parameter  $A_N$  measured in  $\pi^- p \rightarrow \gamma n$ , using a transversely polarized target. The incident pion momenta are (a) 471, (b) 547, (c) 586, and (d) 625 MeV/c. The solid lines are the predictions from the energy-dependent partial-wave analysis of single-pion production by Arai and Fujii (Ref. 1). The dashed lines in (a) and (c) are the predictions by Noelle (Ref. 2) of (a)  $p_\pi = 471 \text{ MeV}/c$  and (c)  $p_\pi = 575 \text{ MeV}/c$ . The statistical and systematic uncertainties were summed in quadrature.

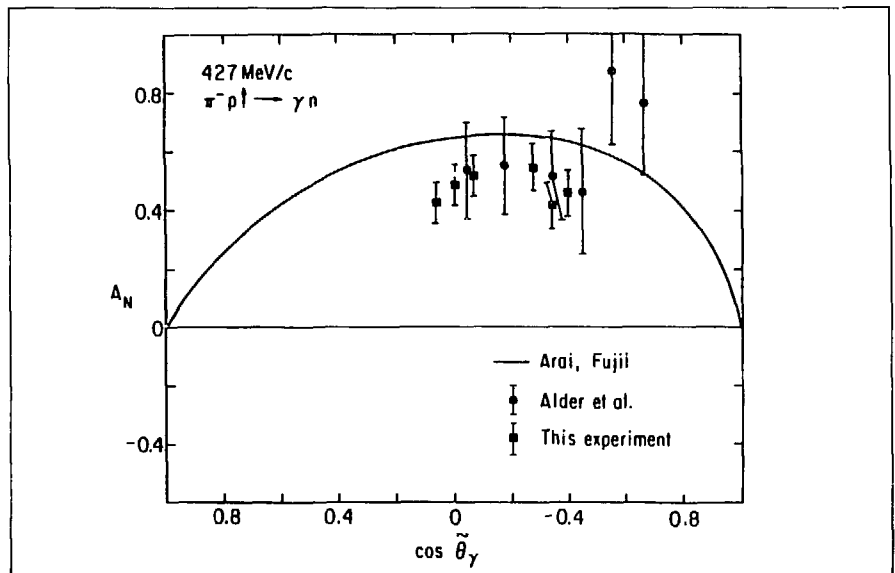


FIGURE 5 Asymmetry parameter  $A_N$  measured in  $\pi^- p \rightarrow \gamma n$ . Results of the present experiment are compared with the data of Adler et al. (Ref. 3) at 427 MeV/c.

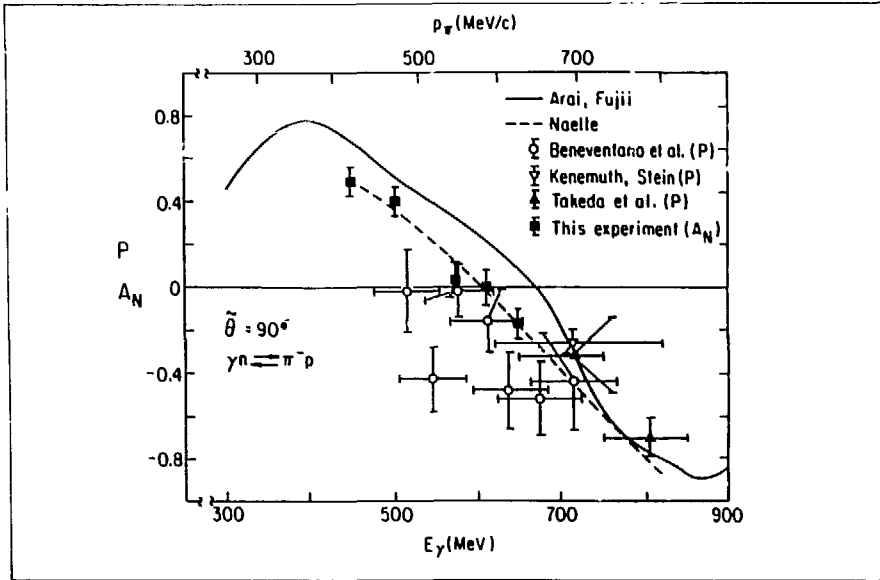


FIGURE 6 The asymmetry parameter obtained in  $A_N$  in this experiment compared with the recoil proton polarization data  $p$  measured in a  $\pi^-$  photoproduction reaction at  $90^\circ$  using a deuterium target by Beneventano et al. (Ref. 4), J. Kenemuth and P. C. Stein (Ref. 5), and H. Takeda et al. (Ref. 6)

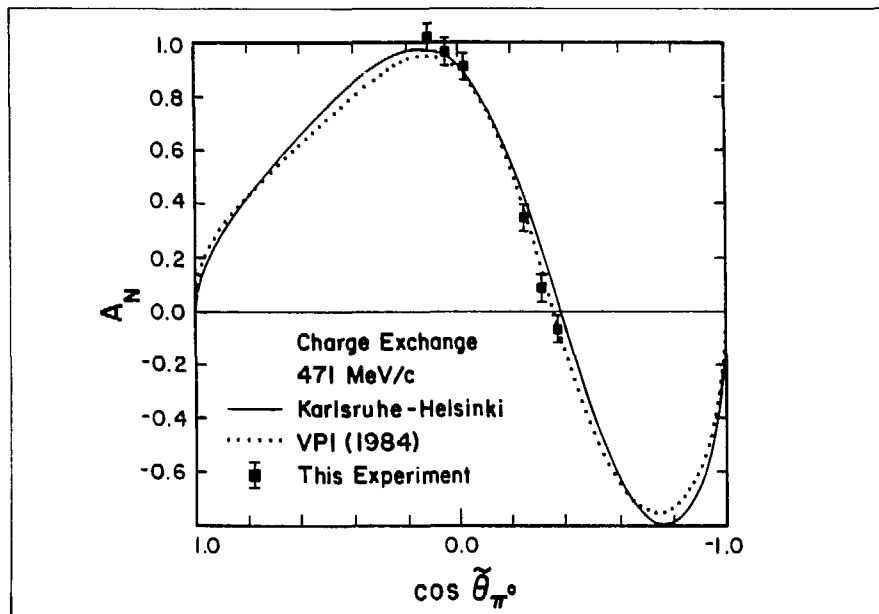


FIGURE 7 Asymmetry parameter  $A_N$  measured in  $\pi^- p \rightarrow \pi^0 n$  using a transversely polarized target. The solid curve is the prediction by the Karlsruhe-Helsinki (K-H) group (Ref. 7) and the dotted curve is the prediction by VPI (Ref. 9)

Fig. 6, are compared with our work. Because there is currently no reason to doubt the applicability of time-reversal invariance in this process, we conclude from the poor agreement between our data and that of the inverse reaction measured with a deuterium target that the deuterium corrections are not well understood. Hence the radiative decay amplitude of neutral resonances based on deuterium-target data should be re-evaluated.

Easily obtainable and very valuable by-products of our REX experiment are some accurate data on the analyzing power of the CEX reaction. These data have become very important for checking the correctness of the double Roper resonance pole, which is the outcome of the 1984 Virginia Polytechnic Institute and State University (VPI) partial-wave analysis. Our preliminary CEX data at  $p_r = 471$  and  $625$  MeV/c are shown in Figs. 7 and 8 together with the predictions of the partial-wave analyses by the Karlsruhe-Helsinki (K-H), Carnegie-Mellon University/Lawrence Berkeley Laboratory (CMU-LBL), and VPI groups (Refs. 7, 8, and 9, respectively). The predictions of the partial-wave analyses are in good agreement with our  $A_N$  data at  $471$  MeV/c. At  $625$  MeV/c the predictions of various partial-wave analyses diverge at backward angles and our  $A_N$  data agree best with the 1984 VPI solution. This is very interesting because the VPI solution shows the  $P_{11}$  wave having two nearby poles in the complex plane at  $(1359, -100i)$  and  $(1410, -80i)$  MeV/c.

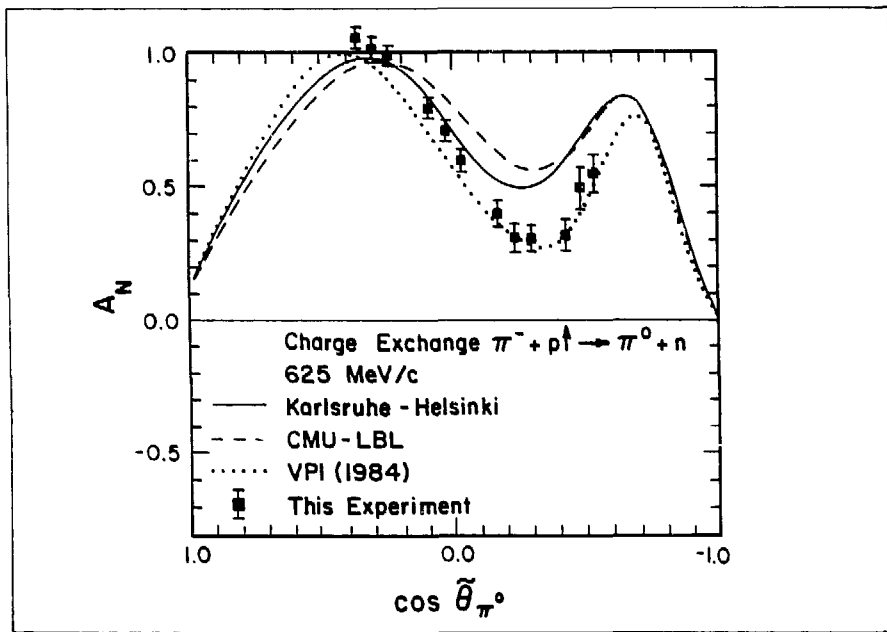


FIGURE 8 Asymmetry parameter  $A_N$  measured in  $\pi^- p \rightarrow \pi^0 n$ . The solid curve is the prediction by K. H. (Ref. 7), the dashed curve, CMU-LBL (Ref. 8), and the dotted curve, VPI (Ref. 9)

## References

1. I. Arai and H. Fujii, *Nuclear Physics* **B194**, 251 (1982).
2. P. Noelle, Ph.D. thesis, University of Bonn report Bonn-IR-75-20 (1977); and P. Noelle, *Progress of Theoretical Physics* **60**, 778 (1978).
3. J. C. Adler et al., *Physical Review D* **27**, 1040 (1983).
4. M. Beneventano et al., *Lettere al Nuovo Cimento* **3**, 840 (1970).
5. J. R. Kennemuth and P. C. Stein, *Physical Review* **129**, 2259 (1963).
6. H. Takeda et al., *Nuclear Physics* **B168**, 17 (1980).
7. G. Hohler et al., "Handbook of Pion-Nucleon Scattering," *Physics Data* **12-1** (1979).
8. R. E. Cutkosky et al., *Physical Review D* **20**, 2804 and 2839 (1979).
9. R. Arndt et al., *Physical Review D* **32**, 1085 (1985).

EXPERIMENT 827 — P<sup>3</sup>**Study of Isobaric-Analog-State Transitions with Pion Single Charge Exchange in the 300- to 500-MeV Region**

Los Alamos, Tel Aviv Univ., Utah State Univ., Arizona State Univ., Univ. of Colorado, SIN

Spokesmen: J. Alster (Tel Aviv Univ.), H. W. Baer and E. Piasezky (Los Alamos), and U. Sennhauser (SIN)

This was the first experiment performed with the  $\pi^0$  spectrometer mounted in the P<sup>3</sup> channel. The purpose of the experiment is to extend the empirical systematics of isobaric-analog-state (IAS) differential cross sections to energies above the  $\Delta(P_{33})$  resonance. Questions of particular interest are whether the 0° cross sections are well represented by the form  $g(N-Z)A^{-\alpha}$  and, if so, whether the values of  $g$  and  $\alpha$  continue the trends observed at energies between 100 and 300 MeV. These trends show  $\alpha$  to be a decreasing function of energy, going from 1.40 at 100 MeV to 1.10 at 295 MeV. The energy dependence of  $g$  follows approximately the shape of the free cross section  $d\sigma/d\Omega(\pi^-p \rightarrow \pi^0n)$  at 0°. From the preliminary analysis of the data, given below, we see large surprises relative to expectations based on these trends.

Another goal of this experiment is to provide a test of pion-nucleus scattering theory at an energy where this theory is expected to work best. At energies around 500 MeV the reaction mechanism is generally expected to be simplified considerably because of the lesser role of isolated resonances in the  $\pi N$  system, the weaker optical potential, and the smaller pion de Broglie wavelength. Thus the data should give a less-ambiguous evaluation of the theory than at lower energies.

In a 22-day data run in August-September 1985, we measured the  $(\pi^+, \pi^0)$  forward-angle differential cross sections (0 to 8°) at four energies on various targets (Table I).

The resolution in the  $\pi^0$  spectra measured at P<sup>3</sup> was not as good as that in the LEP measurements because of the poorer momentum analysis of the P<sup>3</sup> beam. The smallest value of  $\Delta p/p$  we were able to obtain was approximately 1% (even if the momentum slits were set for smaller values). This corresponds to  $\Delta E = 4$  MeV at 300-MeV incident energy and  $\Delta E = 6.6$  MeV at 550 MeV. In addition, it was necessary to put thick degraders into the beam (11.5-cm graphite at 550 MeV) to reduce the proton contamination; this degrader further broadened the incident pion energy distribution. The final energy resolutions we obtained in the  $\pi^0$  spectra were approximately 8 MeV at 425 MeV and 11 MeV at 500 MeV.

The  $\pi^0$  spectrometer was mounted in its two-post configuration to allow for large target-to-detector distances ( $R$ ). All data were taken with  $R = 2.0$  m and with a nominal setup angle of 0°. This gave a finite acceptance for  $\pi^0$  scattering angles in the range from 0 to 10°. In the off-line analysis the data were binned into three groups according to measured scattering angles.

The incident  $\pi$  flux was measured using the scintillator activation tech-

TABLE I Measurements of  $(\pi^+, \pi^0)$  Forward-Angle Differential Cross Sections

| $T_\pi$ (MeV) | Targets  |
|---------------|--|
| 300           | ${}^7\text{Li}$ , ${}^{27}\text{Al}$ , ${}^{60}\text{Ni}$  |
| 425           | ${}^7\text{Li}$ , ${}^{14}\text{C}$ , ${}^{27}\text{Al}$ , ${}^{60}\text{Ni}$ , ${}^{90}\text{Zr}$ , ${}^{120}\text{Sn}$ , ${}^{208}\text{Pb}$ |
| 500           | ${}^7\text{Li}$ , ${}^{14}\text{C}$ , ${}^{27}\text{Al}$ , ${}^{60}\text{Ni}$  |
| 550           | ${}^7\text{Li}$ , ${}^{14}\text{C}$  |

nique. Because the protons in the beam also induce  $^{11}\text{C}$  activity, a correction had to be applied based on the measured proton contaminations and known proton activation cross sections. The proton/pion ratios at each energy were measured using a sampling-grid scintillator. Typical beam conditions at which data were taken are given in Table II.

Figure 1 shows the  $\pi^0$  spectra at  $T_\pi = 425$  MeV at the most-forward scattering angle for targets from  $^7\text{Li}$  to  $^{208}\text{Pb}$ . The IAS peaks can be well identified at the expected energies. The measurement for the  $\pi^-p \rightarrow \pi^0n$  reaction, also shown in Fig. 1, was performed with a  $\text{CH}_2$  target. The carbon contribution was subtracted out using a measured carbon spectrum. The solid curve represents a Monte Carlo calculation for the line shape and gives a good description of the data. The curves shown with the  $(\pi^+, \pi^0)$  data represent fits done with a single peak plus a polynomial function for the background. We see that this model gives a fair representation of the data.

At 500 MeV we took data only on  $^7\text{Li}$ ,  $^{14}\text{C}$ ,  $^{27}\text{Al}$ , and  $^{60}\text{Ni}$  because of the limited run time. The most-forward-angle spectra are shown in Fig. 2. Again, the IAS is clearly discernible at the expected energies, and one can see that the line shapes calculated by Monte Carlo simulation describe the data quite well.

TABLE II Typical Beam Conditions During Data Taking for Exp. 827.

| $T_\pi$ (MeV) | $\pi^+$ Flux ( $\text{s}^{-1}$ ) | $\Delta\rho/\rho$ (%) | Proton/Pion Flux |
|---------------|----------------------------------|-----------------------|------------------|
| 300           | $1 \times 10^7$                  | 0.2                   | $\sim 0$         |
| 425           | $5 \times 10^6$                  | 0.2                   | 0.02             |
| 500           | $2.5 \times 10^6$                | 0.4                   | 0.16             |
| 550           | $8 \times 10^4$                  | 0.5                   | 4.0              |

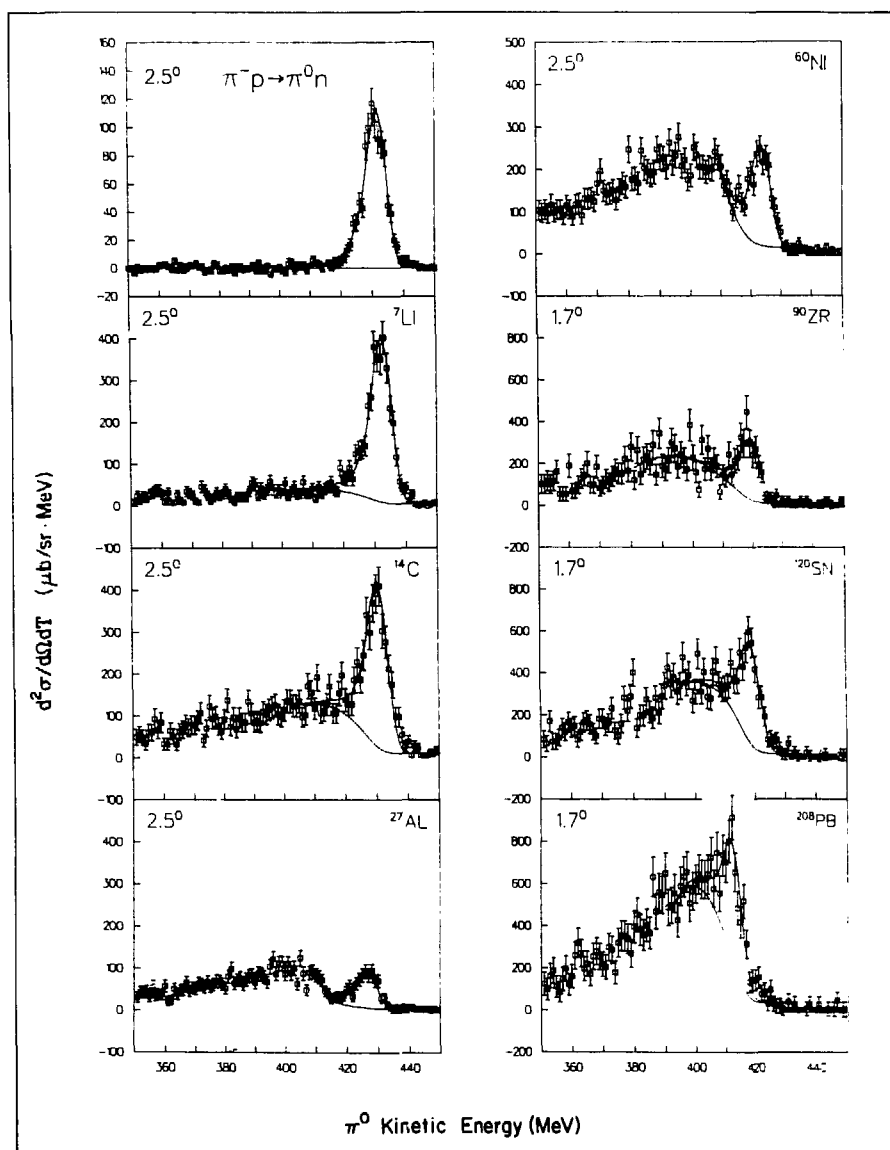


FIGURE 1 Spectra for the  $(\pi^+, \pi^0)$  reaction at 425 MeV for various nuclear targets. These spectra were measured at the P<sup>3</sup> channel with the LAMPF  $\pi^0$  spectrometer. The peaks occur at the expected energies for the IAS transitions.



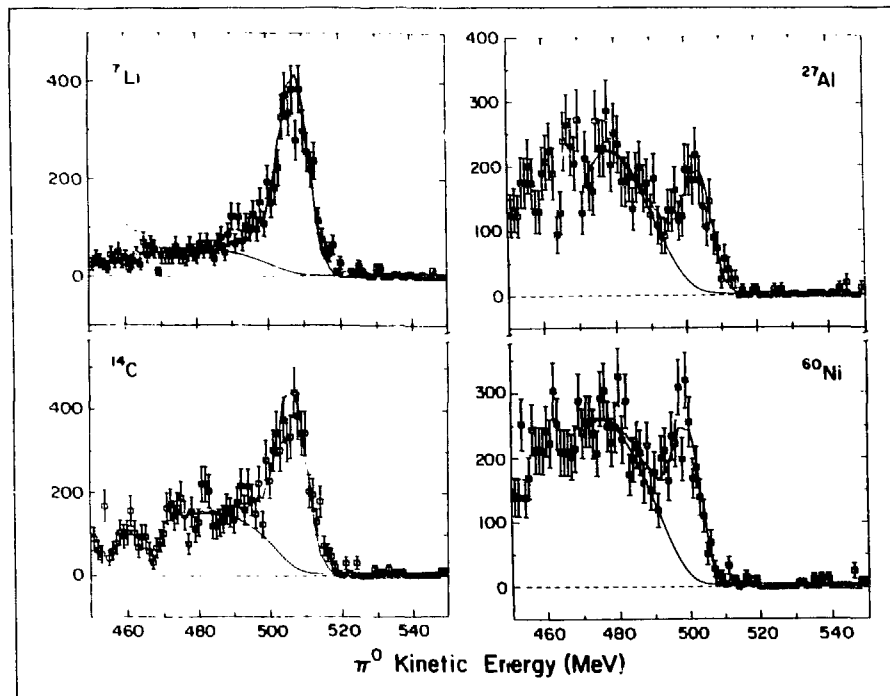


FIGURE 2 Spectra for the  $(\pi^+, \pi^0)$  reaction at 500 MeV for various nuclear targets. The peaks occur at the expected energies for the IAS transitions.

In Fig. 3 we show the data on  $^{60}\text{Ni}$  at 425 MeV for three values of scattering angle. These show the IAS to be a very sharp forward-angle feature. At  $7^\circ$  the IAS is hardly visible in the spectrum. We expect these angular distributions to follow a  $J_0^2(qR)$  shape. The first zero of a Bessel function of order 0 is 2.405. For an inter-

action radius  $\bar{R} = 1.25 A^{1/3}$  and a beam energy of 425 MeV, this would give a first minimum for  $^{60}\text{Ni}$  at  $10^\circ$ , which is consistent with the data. We will analyze the data to obtain both the  $0^\circ$  cross sections and the rate of falloff versus  $q^2$  (or  $\theta^2$ ).

In Fig. 4 we give preliminary  $0^\circ$  cross sections for  $^7\text{Li}$  and  $^{14}\text{C}$  at 425 and 500 MeV. Also shown are published cross sections at lower energies. The factor of 2 rise in cross section between 300 and 425 MeV is surprising. Certainly this is not a feature that exists in the elementary  $\pi^- p \rightarrow \pi^0 n$  cross section. Its energy dependence (Fig. 4) is such that the cross section drops by approximately 25% between 300 and 500 MeV. It will be interesting to understand the origin of the sharp rise in the nuclear cross sections.

The near equality of the  $^7\text{Li}$  and  $^{14}\text{C}$  cross sections between 230 and 500 MeV is consistent with an  $(N-Z)/A$  dependence in the cross sections. In a plane-wave model one expects an  $(N-Z)$  dependence for the  $0^\circ$  cross sections. In a strong-absorption model one expects an  $(N-Z)/A^{4/3}$  dependence.

When we complete the data analysis, the excitation functions between 165 and 425 MeV will be known for  $^7\text{Li}$ ,  $^{14}\text{C}$ ,  $^{27}\text{Al}$ ,  $^{60}\text{Ni}$ ,  $^{90}\text{Zr}$ ,  $^{120}\text{Sn}$ , and  $^{208}\text{Pb}$ . For the lighter nuclei,  $^7\text{Li}$  to  $^{60}\text{Ni}$ , the excitation functions will be determined up to 500 MeV. For  $^7\text{Li}$  and  $^{14}\text{C}$  they will be determined from 20 to 550 MeV.

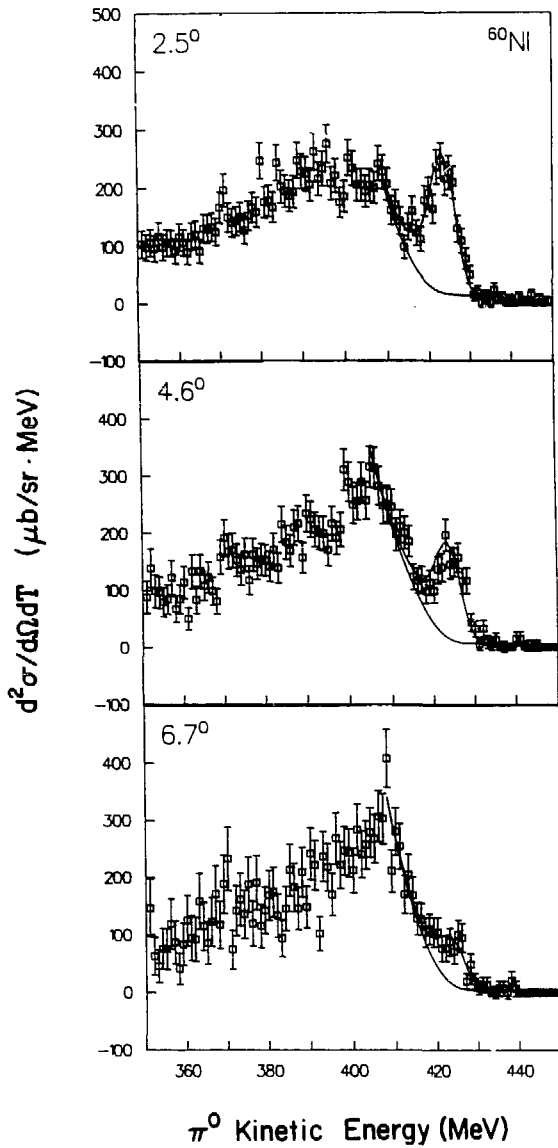


FIGURE 3 Spectra for the  $^{60}\text{Ni}(\pi^+, \pi^0)$  reaction at 420 MeV at three forward angles. The IAS transition has a sharp forward-peaked angular distribution.

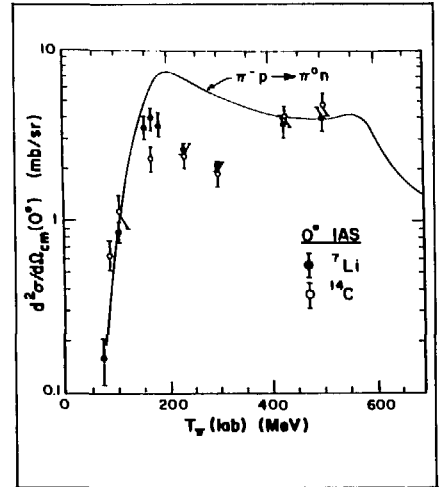


FIGURE 4. Excitation function of the  $0^+$  IAS cross sections for  $^7\text{Li}$  and  $^{14}\text{C}$ . The new (preliminary) data at 425 and 500 MeV show that the cross section rises sharply above 300 MeV. The free cross section  $d\sigma/d\Omega_{\text{cm}}(\pi^-p \rightarrow \pi^0n)$  versus  $T_\pi(\text{lab})$  is shown as a solid line. Between 300 and 500 MeV it is a gradually decreasing function of energy, in sharp contrast to the shape of the excitation functions for the nuclear targets.

EXPERIMENT 852 — P<sup>3</sup>

## Measurements of ( $\pi^\pm, \eta$ ) Reactions on Nuclear Targets to Study the Production and Interaction of $\eta$ Mesons with Nuclei

Los Alamos, Univ. of Virginia

Spokesman: J. C. Peng (Los Alamos)

Participants: J. E. Simmons, M. J. Leitch, J. Kapustinsky, J. M. Moss, C. Lee, S. Tang, J. C. Peng, J. D. Bowman, F. Irom, Z. F. Wong, T. K. Li, C. Smith, and R. R. Whitney

Discussion on the physics motivations of Exp. 852 and results from a test run appeared in the 1984 Progress Report.

This experiment has received beam time in 1985 for the following measurements:

1. the  ${}^3\text{He}(\pi^-, t)\eta$  reaction. Tritons are detected with the large-aperture spectrometer (LAS) at forward angles ( $5^\circ < \theta_{\text{lab}} < 15^\circ$ ) with 620- and 680-MeV/c  $\pi^-$  beam.
2. the  ${}^3\text{He}(\pi^-, \eta)t$  reaction. The LAMPF  $\pi^0$  spectrometer and the University of Virginia  ${}^3\text{He}$  target have been used to measure this reaction through the detection of  $\eta \rightarrow 2\gamma$  decays. Cross sections at forward angles ( $0^\circ < \theta_{\text{lab}} < 30^\circ$ ) have been

measured at six beam momenta ( $590 \text{ MeV}/c \leq p(\pi^-) \leq 700 \text{ MeV}/c$ ).

3. the ( $\pi^+, \eta$ ) reaction on  ${}^7\text{Li}$ ,  ${}^9\text{Be}$ , and  ${}^{13}\text{C}$ . Energy resolution in these measurements is optimized to examine whether isobaric-analog states (IASs) can be strongly excited in the ( $\pi^+, \eta$ ) reaction.
4. the inclusive ( $\pi^+, \eta$ ) reaction on  ${}^3\text{He}$ ,  ${}^4\text{He}$ ,  ${}^7\text{Li}$ ,  ${}^9\text{Be}$ ,  ${}^{12}\text{C}$ ,  ${}^{27}\text{Al}$ ,  ${}^{40}\text{Ca}$ ,  ${}^{120}\text{Sn}$ , and  ${}^{208}\text{Pb}$  at 620, 650, and 680 MeV/c.

The data are currently being analyzed. Some of the preliminary results are presented in this report.

Figure 1 shows the triton spectrum obtained in the  ${}^3\text{He}(\pi^-, t)$  measurement using the LAS. A peak is observed in the triton spectrum at a

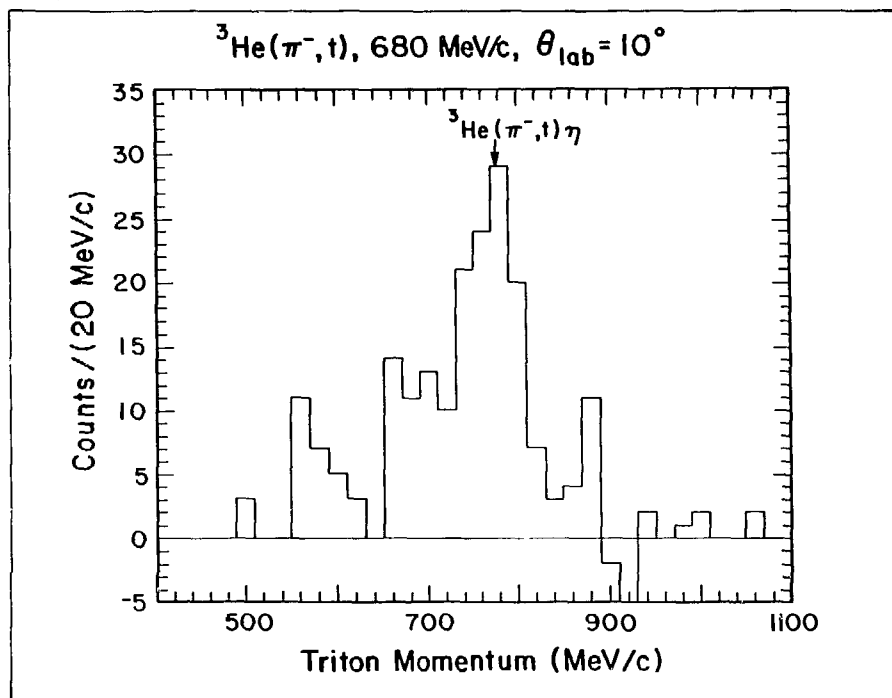


FIGURE 1. Energy spectrum of the  ${}^3\text{He}(\pi^-, t)$  reaction. The arrow indicates the expected location of the  ${}^3\text{He}(\pi^-, t)\eta$  peak.

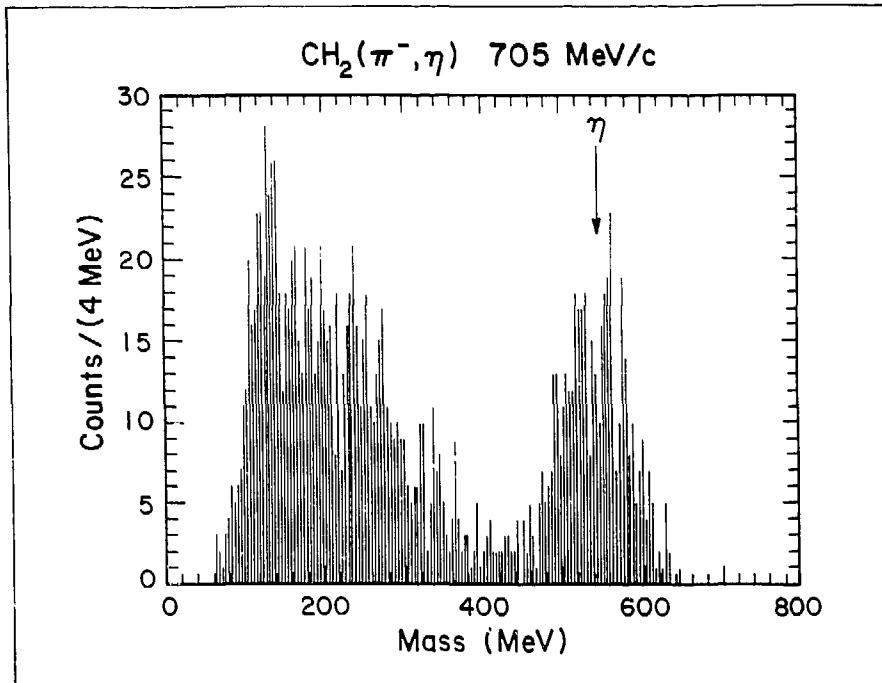


FIGURE 2 Invariant mass plot for the two photons detected in the  $\pi^- + \text{CH}_2$  reaction using the LAMPF  $\pi^0$  spectrometer

location expected for the  ${}^3\text{He}(\pi^-, t)\eta$  binary reaction. Note that this peak stands out rather clearly above some other possible backgrounds, such as the  ${}^3\text{He}(\pi^-, t)\pi^+\pi^-\pi^0$  reaction that contributes a continuum triton background. Preliminary analysis gives a cross section of  $1 \mu\text{b}/\text{sr}$  for the  ${}^3\text{He}(\pi^-, t)\eta$  reaction. Because tritons are detected at very forward angles, the measured cross section corresponds to the backward angle in the  ${}^3\text{He}(\pi^-, \eta)t$  reaction. This is the first time that a discrete final state has been observed in the  $(\pi, \eta)$  reaction on nuclear targets.

The LAMPF  $\pi^0$  spectrometer, moved to the P<sup>3</sup>-East area from the LEP channel during 1985, was used for the  $(\pi, \eta)$  measurements. Figure 2 shows that the  $\eta$  mesons are clearly identified from the invariant mass plot. The  $\eta$ -energy spectra are shown in Fig. 3 for the  ${}^3\text{He}(\pi^-, \eta)$  reaction at three pion beam momenta. At 680 MeV, which is near the free  $\rho(\pi^-, \eta)n$  threshold, the  ${}^3\text{He}(\pi^-, \eta)t$  reaction appears as a shoulder of the quasi-free  ${}^3\text{He}(\pi^-, \eta)$  reaction. As the beam momentum is lowered to

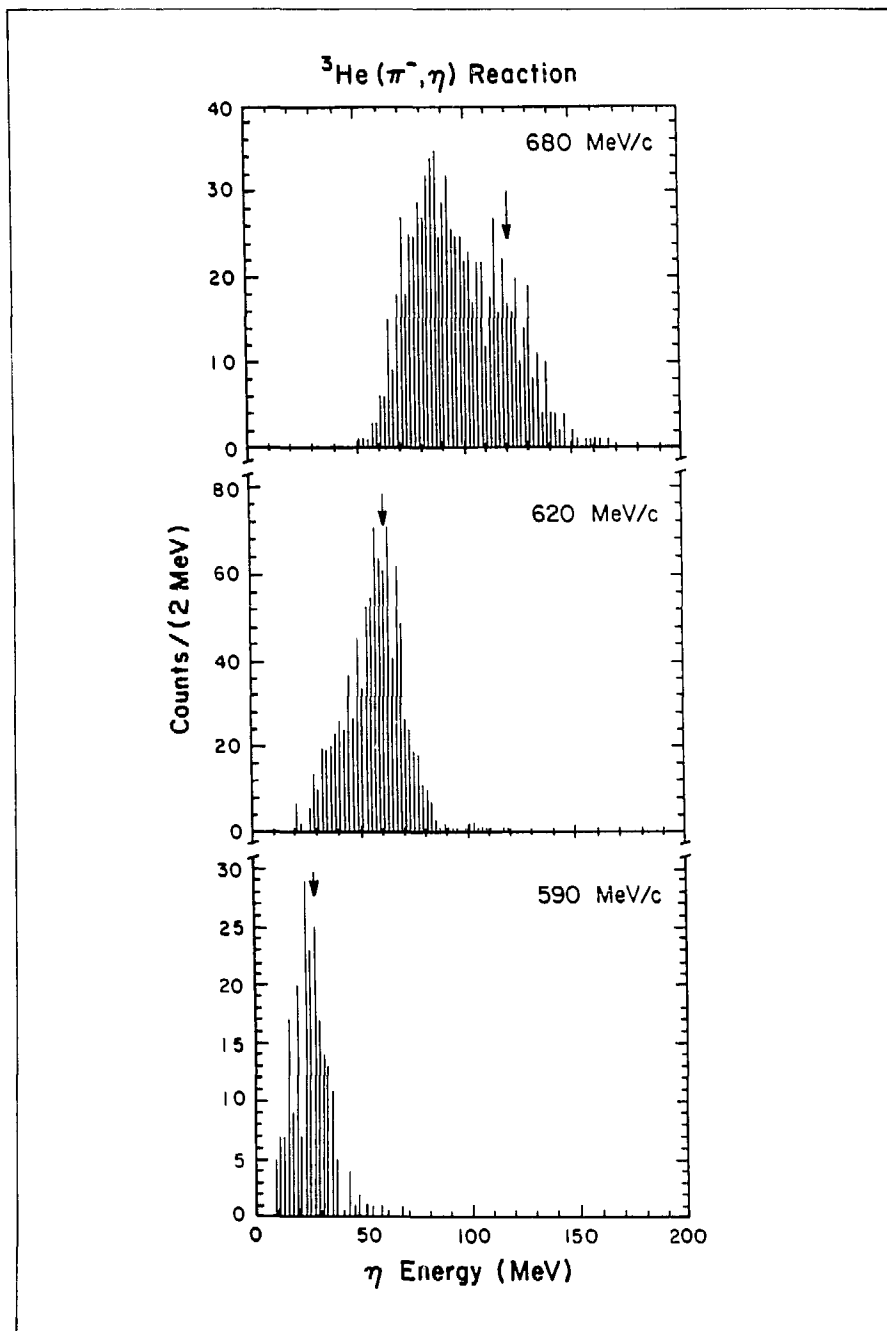


FIGURE 3 The  $\eta$ -energy spectra measured in the  ${}^3\text{He}(\pi^-, \eta)$  reaction with three different  $\pi^-$  momenta. The arrows indicate the locations of the  ${}^3\text{He}(\pi^-, \eta)t$  transition.

620 MeV/c, the separation between the ground-state transition and the quasi-free continuum improves greatly. At 590-MeV/c pion momentum, which is just above the absolute threshold of the  ${}^3\text{He}(\pi^-, \eta)t$  reaction and below the threshold of any other  ${}^3\text{He}(\pi^-, \eta)$  channels, the  ${}^3\text{He}(\pi^-, \eta)t$  reaction is unambiguously detected. We expect to study the mechanism of the  $(\pi, \eta)$  reaction and the  $\eta$ -nucleus interaction through the energy dependence and angular distribution of this reaction. It is intriguing that the subthreshold  $(\pi, \eta)$  reaction has appreciable cross sections.

Preliminary results also show that IASs are excited in the  $(\pi^\pm, \eta)$  reaction on  ${}^7\text{Li}$ ,  ${}^9\text{Be}$ , and  ${}^{13}\text{C}$ . This is surprising because the momentum transfer in the  $(\pi, \eta)$  reaction, unlike the situation in the  $(\pi, \pi^0)$  reaction, is rather unfavorable for exciting the IASs. We note that the  $(\pi^\pm, \eta)$  reaction can be considered as an unconventional charge-exchange reaction. The conventional charge-exchange reactions, such as  $(p, n)$ ,  $({}^3\text{He}, t)$ , and  $(\pi^\pm, \pi^0)$ , involve a pair of particles belonging to the same isospin multiplets. In contrast, the  $(\pi^\pm, \eta)$  reaction involves a pair of mesons belonging to different isospin multiplets. We expect that the  $(\pi, \eta)$  reaction could also shed new light on the mechanism of charge-exchange reactions.

An experiment was performed using the Crystal Box detector to study the rare radiative pion decay  $\pi \rightarrow e\nu\gamma$ . The distribution of energy sharing between the three particles in the decay yields information about the ratio of axial-vector-to-vector form factors that describe the structure-dependent part of the pion decay amplitude. This information is important for nonperturbative quantum chromodynamics (QCD) calculations of low-energy sum rules and for providing important information on the current quark masses. Two previous experiments obtained similar results for the magnitude of the ratio but had conflicting results for the sign.

The experiment used a beam of  $\sim 10^5 \pi^+$ /s stopped in a thin target at the center of the Crystal Box detector. The trigger required a coincidence between one charged and one neutral particle, each with a minimum energy of  $\approx 15$  MeV. The

effective branching ratio for  $\pi \rightarrow e\nu\gamma$  is  $\sim 10^{-8}$ . We collected several hundred events covering a broad region of the allowed phase space; the data should easily resolve the ambiguity among results of previous experiments.

The data analysis is proceeding. The absolute energy calibration of each of  $\approx 400$  crystals has been determined using the known energy spectrum from normal muon decay. The data tapes have been processed to select candidate events. The most difficult part of the analysis is the separation of the signal from accidental coincidences in the region of low electron energy and high photon energy. Results are expected in a few months.

## EXPERIMENT 888 — SMC

### Study of the Decay $\pi^+ \rightarrow e^+\nu_e\gamma$

Los Alamos, Stanford Univ., Univ. of Chicago, Temple Univ.

*Spokesman:* Aksel Hallin (Los Alamos)

*Participants:* R. D. Bolton, M. D. Cooper, J. S. Frank, A. L. Hallin, P. Heusi, C. M. Hoffman, G. E. Hogan, F. G. Mariam, R. E. Mischke, L. Piilonen, V. D. Sandberg, R. Werbeck, R. A. Williams, S. L. Wilson, M. Ritter, D. Grosnick, S. C. Wright, V. L. Highland, and J. McDonough

## EXPERIMENT 969 — SMC

**MEGA: Search for the Rare Decay** **$\mu^+ \rightarrow e^+\gamma$** 

Argonne, UCLA, Univ. of Chicago, Univ. of Houston, Los Alamos, Stanford Univ., Texas A&M Univ., Univ. of Virginia, Univ. of Wyoming, Yale Univ.

*Spokesman: M. D. Cooper (Los Alamos)*

*Participants: K. F. Johnson, D. Barlow, B. M. K. Nefkens, C. Pillai, S. C. Wright, E. V. Hungerford, III, D. Kodayh, B. W. Mayes, II, L. Pinsky, J. F. Amann, R. D. Bolton, M. D. Cooper, W. Foreman, C. M. Hoffman, G. E. Hogan, T. Kozlowski, R. E. Mischke, D. E. Nagle, F. J. Naivar, M. A. Oothoudt, L. E. Piilonen, R. D. Werbeck, E. B. Hughes, R. H. Burch, Jr., C. A. Gagliardi, R. E. Tribble, K. O. H. Ziock, A. R. Kunselman, P. S. Cooper, R. Lauer, and J. K. Markey*

The search for processes that violate conservation of muon number continues to be a subject of high interest because these reactions must occur through processes outside the minimal Standard Model of weak interactions. In placing the observed fermions in the group representations of the model, the assignments are repeated three times and the particles are assigned to generations or families in the order of their mass. However, the minimal Standard Model is aesthetically incomplete because it contains many unknown parameters and the family replication is not explained. The apparent need for an extension to the Standard Model and the requirement that muon-number nonconservation be outside the model have driven experimentalists to redouble their efforts to find such a process. Furthermore, its nondiscovery at increasingly better limits restricts the types of models that can be built.

The future of this field at LAMPF is called MEGA, an acronym standing for **M**uon decays into an **E**lectron and a **G**amma ray, and is a search with a branching-ratio sensitivity of  $9 \times 10^{-14}$ . The MEGA collaboration, formed in the spring of 1985, submitted the experiment proposal to LAMPF last summer. The experiment was approved but awaits final DOE funding approval, we hope by February 1986. Meanwhile, substantial ac-

tivity has begun at most of the 10 collaborating institutions. Our reasons for beginning a new search for  $\mu^+ \rightarrow e^+\gamma$  follow.

1. The search addresses some of the most compelling physics issues of the 1980s—that is, physics beyond the Standard Model. Many of the possible extensions of the Standard Model would make  $\mu^+ \rightarrow e^+\gamma$  observable. In many models the mass scale probed would be well above the energies expected, even at the Superconducting Super Collider (SSC).

2. MEGA will have a factor of 500 improved sensitivity compared with that of the Crystal Box, which is currently the best detector for  $\mu^+ \rightarrow e^+\gamma$ . The factor of 500 improvement is the largest that can be made on any of the reactions that have already been studied at a significant level.

3. The  $\mu^+ \rightarrow e^+\gamma$  is the easiest to tackle at LAMPF. A  $\mu^-$  beam of sufficient intensity to warrant undertaking the  $\mu^- A \rightarrow e^- A$  conversion experiment does not exist, and the cost of a new beam line is prohibitive. Each of the muon branches has been pushed to the limit of acceptable background, and the technical improvements required for a three-particle final-state decay are more complex at a low-duty-factor accelerator.

4. Substantial expertise already exists at LAMPF from the  $\mu e \gamma I$  and Crystal Box experiments for detecting this process.

5. The new technology used in this experiment will raise the technical expertise available at LAMPF.

MEGA will

- be the first with a large cryogenic magnet,
- demonstrate the ability to take data in a very high intensity environment,
- use a multicrate FASTBUS system, and
- use low-cost microcomputer technology, both in data acquisition and in replay, to achieve 5 times the computing power of the Data Analysis Center.

6. There is a window of time for the next 5 years when LAMPF will have the most intense beam for doing a high-sensitivity experiment.

In the design of the experiment several features are considered.

First, the sought-after process is identified through the measurement of kinematical variables, that is, conservation of the four-momentum. The  $\mu^+ \rightarrow e^+\gamma$  decay has the signature of back-to-back electrons and photons that are in-time, each 52.8 MeV and from a common vertex.

To reach the very high sensitivity, the second requirement is a large number of useful muon decays,

$$M = \frac{\Omega_0}{4\pi} \epsilon RT,$$

where  $\Omega_0$  is the solid angle,  $\epsilon$  is the detection efficiency, and  $RT$  is the stopping rate times the running time.

MEGA is designed for 50% acceptance, high efficiency, and the highest stopping rate consistent with detector performance. The detector uses a low-energy stopped-muon beam and a thin target to achieve its required stopping density.

A third requirement is good resolution, which stresses technology in high-rate environments and which is needed to suppress backgrounds of either allowed processes or accidental coincidences. The experiment must be background free so that sensitivity will improve inversely as the running time, rather than inversely as the square root of the running time when background is present. There are two sources of backgrounds: prompt-allowed processes and random coincidences. These backgrounds are suppressed with good resolution.

Fourth, the data processing is a search for a rare process in a very great number of decays. Hence, a clever trigger is designed to control data-encoding and tape-writing rates, and sophisticated analysis is used to select any possible candidates.

Finally, to understand the detector response, the allowed process  $\mu^+ \rightarrow e^+\gamma\nu\bar{\nu}$  is measured to prove that the instrument can observe what it should.



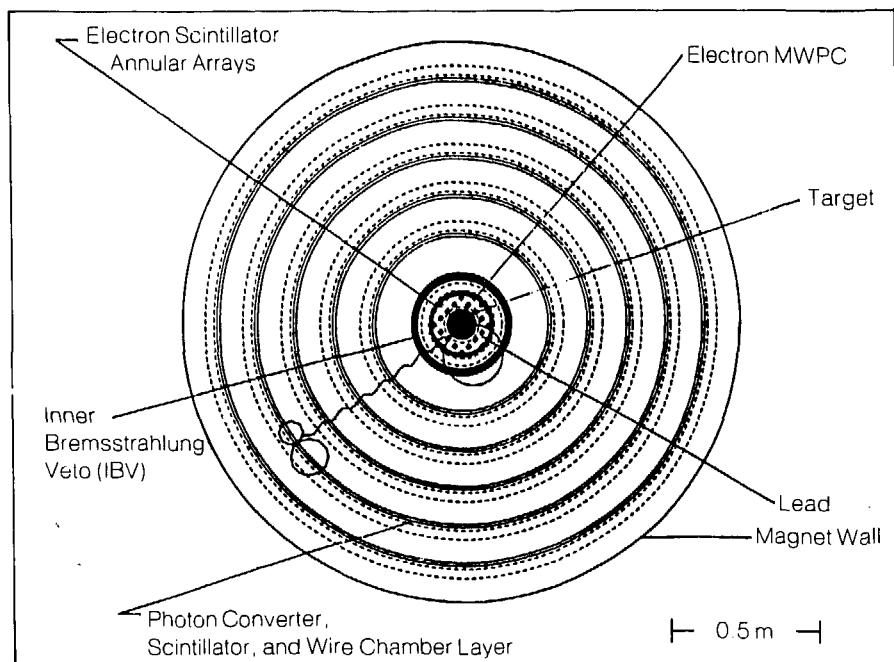


FIGURE 1. End view of the MEGA apparatus with an idealized  $\mu^+ \rightarrow e^+\gamma$  decay shown.

The MEGA apparatus is shown in Figs. 1 and 2 and is designed to find the decay  $\mu^+ \rightarrow e^+\gamma$  in a background-free experiment if its branching ratio is greater than  $10^{-13}$ . The apparatus is contained in a large magnet that will be obtained from SLAC; it has a field of 1.5 T, a clear bore of 1.85 m, and a length of 2.2 m. The central region of the magnet contains the target, which is a thin planar ellipse canted at a large angle relative to the beam. This orientation provides adequate stopping power in the beam direction to contain the muons and presents a minimal thickness to the decay products. The expected stopping rate is  $3 \times 10^7$  Hz (average).

The detector is divided into an electron spectrometer and a series of photon pair-spectrometers. All the charged particles arising from muon decay are confined to a maximum radius of 29 cm, leaving the photon detectors in a relatively quiet environment. A low-rate photon arm is essential to the success of the experiment. The design philosophy of the electron arm is to optimize the resolution of the electron detectors without producing photon backgrounds.

The electron arm consists of two parts. The electrons from muon decay first pass through a multiwire proportional chamber (MWPC) with three layers of sense wires at radii of 6, 11, and 14 cm. The chamber,

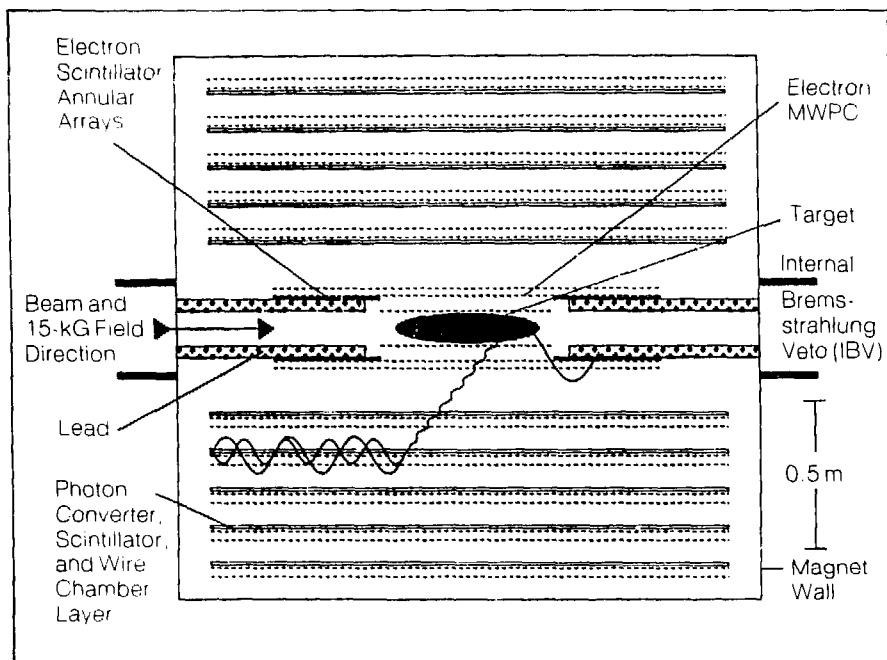


FIGURE 2 A sectioned plan view of the MEGA apparatus with the same idealized  $\mu^+ \rightarrow e^+\gamma$  event shown that was displayed in Fig. 1.

which is built of the thinnest possible materials to minimize multiple scattering and positron annihilation in flight, also acts as a  $180^\circ$  spectrometer to measure the helical paths of the electrons in the uniform magnetic field. The parallel components of the momenta are derived from the measured coordinates of chamber intersections along the beam direction. These measurements are achieved with spiral cathode strips. The wire spacing in the chamber is 1 mm, a pitch that makes the chamber efficient at high rates. The chamber is gated with a short coincidence pulse to limit its sensitivity to the periods of interest.

The very high rate makes a serious pattern-recognition problem. A typi-

cal event is illustrated in Fig. 3. The key to identifying candidate electrons is that in the end view they make almost perfect circles. The symmetry in a circle, plus redundancy in the cathode strips, makes for a highly efficient selection of candidates that still rejects useless events. Figure 4 illustrates the expected resolutions from the electron arm.

The second part of the electron spectrometer consists of banks of scintillators arranged in a cylindrical geometry about the beam near the pole faces. After at least one revolution in the chamber, the electrons enter the scintillators, which measure the time of the electron.

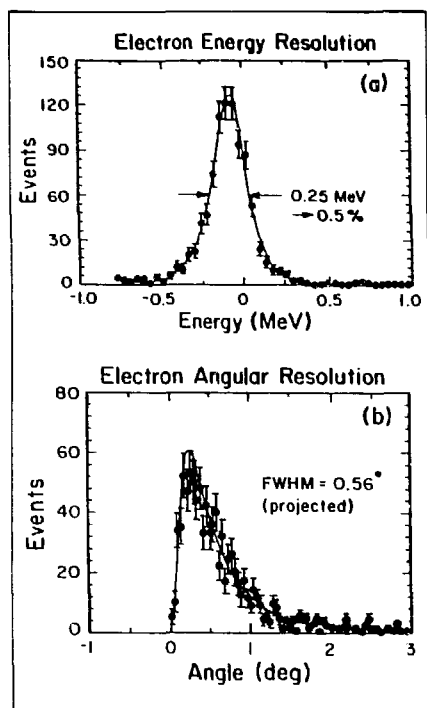


FIGURE 4 The expected resolutions from the MEGA electron arm in (a) energy and (b) angle. The simulation includes resolutions of the MWPC and multiple scattering in the chambers and target

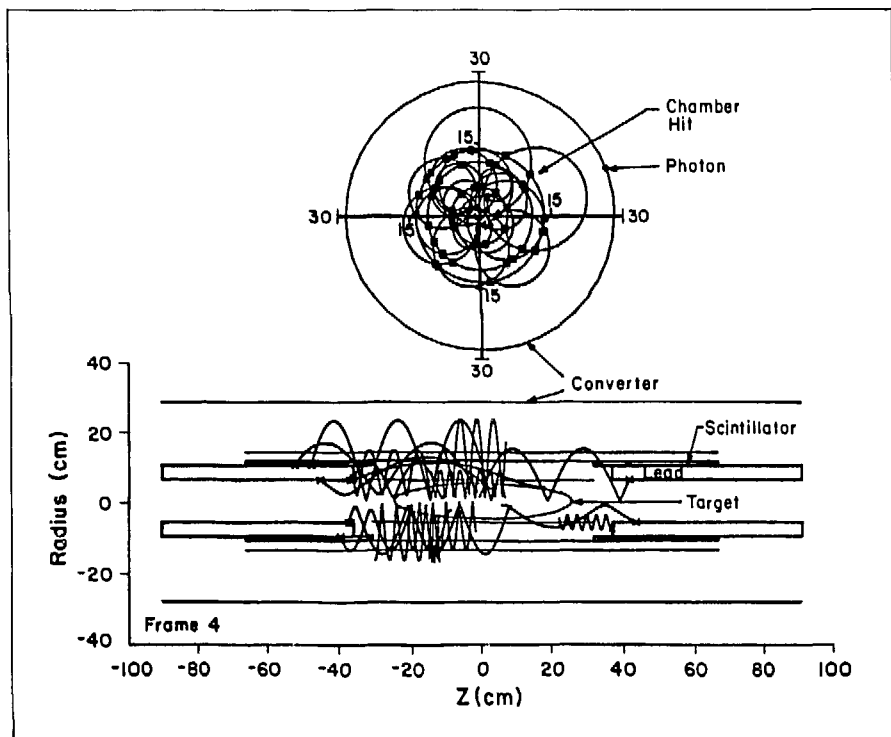


FIGURE 3 A typical event in the electron spectrometer

Electrons trapped in the field for more than eight loops are rejected by their relative time with respect to the photon. Each bank is divided into 100 elements to keep the individual counter rates manageable. After passage through the scintillators, the electrons are stopped in a 4-cm-thick annulus of lead.

The photon arm consists of concentric pair-spectrometers of essentially identical construction. A blowup of a section of one spectrometer is shown in Fig. 5. Each pair-spectrometer is made of lead converters, MWPCs, drift chambers,

and scintillators. The converters are divided into three sheets and are separated by the MWPCs. Each sheet is thin enough to maintain good resolution (1.2% at 50 MeV). The MWPCs determine in which sheet the incident photon is converted, allowing a correction for the mean energy loss in subsequent sheets to be made. The electron and positron from the conversion have most of their energy measured by the drift chambers as they move along helical paths whose radii are proportional to their perpendicular momenta. The parallel components of momenta are

measured with spiral cathodes. Finally, the particles recross the converters into a cylindrical hodoscope of scintillators of 4-cm arc length. These scintillators, with photomultiplier tubes at both ends, measure the time of the photon conversion. Contributions from energy-loss straggling and chamber resolution degrade the resolution to 2%. Bremsstrahlung produces a low-energy tail for 50% of the spectrum. The expected response function of the pair-spectrometer is shown in Fig. 6.

The most serious background for the experiment is a 52.8-MeV electron from normal muon decay in accidental, back-to-back, and time coincidence with a 52.8-MeV photon. The most copious source of 52.8-MeV photons comes from internal bremsstrahlung or radiative muon decay ( $\mu^+ \rightarrow e^+ \gamma \nu \bar{\nu}$ .) We intend to veto these photons by detecting the normally present low-energy electrons with which the photons are associated. These electrons are below 2.5 MeV and follow the field lines to the magnet pole faces. Relevant parts of the pole faces will be lined with scintillators set to veto on these electrons.

The very high instantaneous rates require a sophisticated trigger. The primary trigger relies on the fact that all electrons from muon decay are contained in the central region of the detector. If the trigger requires a photon of at least 42 MeV, the number of firings will be reduced by a factor of roughly 700 relative to the muon stopping rate.

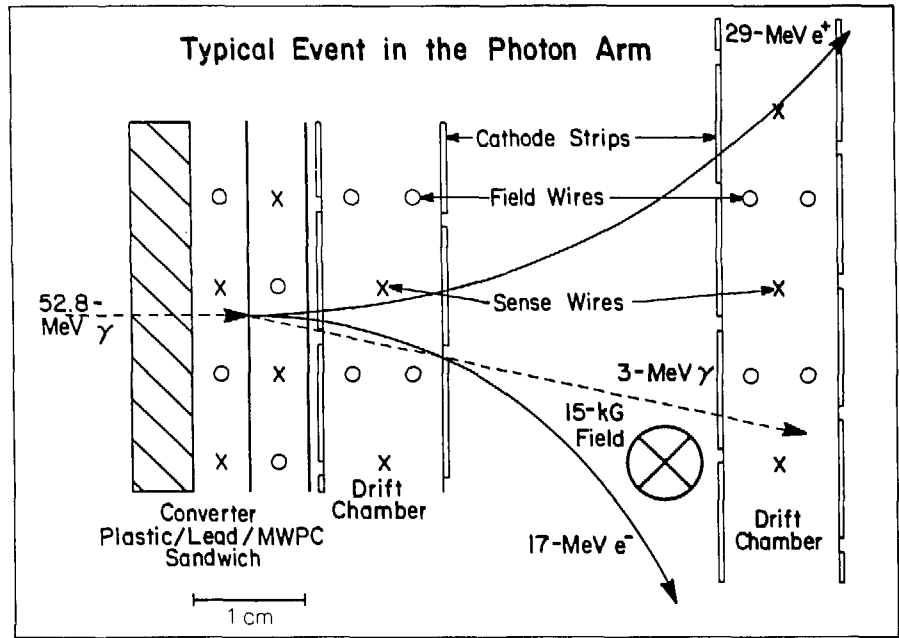


FIGURE 5 A blown-up view of one pair-spectrometer showing the multiple layers of converters and the chambers and scintillators

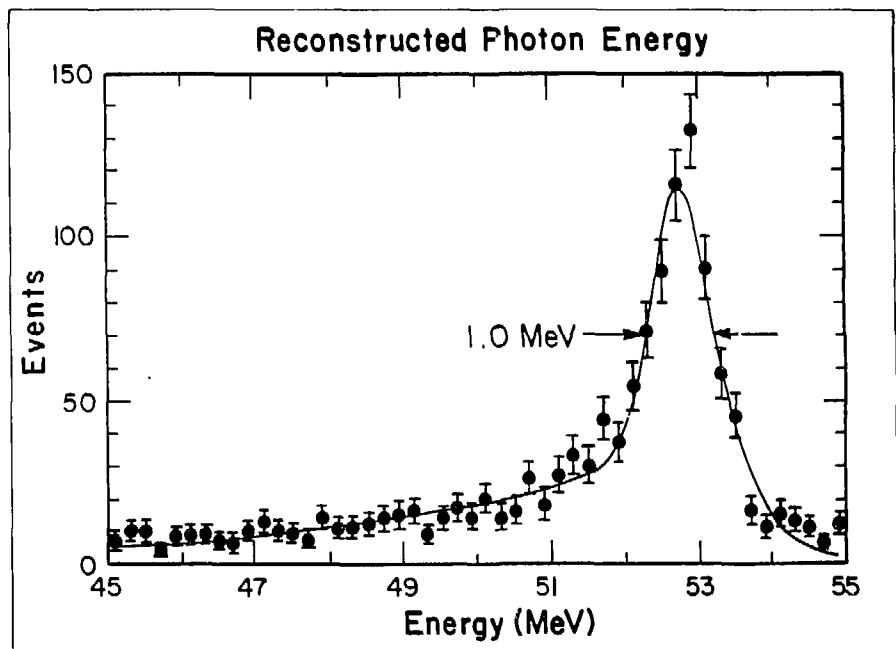


FIGURE 6 The energy resolution expected from the pair-spectrometers

TABLE I Parameters of  $\mu^+ \rightarrow e^+\gamma$  Experiments <sup>a</sup>

| Properties   | MEGA                | $\mu e\gamma$         | Crystal Box         |
|--|---------------------|-----------------------|---------------------|
| Fractional electron energy resolution                          | 0.005               | 0.09                  | 0.08                |
| Fractional photon energy resolution                            | 0.02                | 0.08                  | 0.08                |
| Photon-electron timing (ns)                                    | 0.5                 | 2.0                   | 1.1                 |
| Electron position resolution at the target (mm)                | 2.0                 | 3.0                   | 2.0                 |
| Electron angular resolution, including target scattering (deg) | 0.6                 | 1.3                   | 1.3                 |
| Photon conversion point resolution (mm)                        | 3                   | 76                    | 25                  |
| Electron-photon angle (deg)                                    | 0.6                 | 3.8                   | 8.0                 |
| Photon angle (deg)   | 10                  | ---                   | ---                 |
| inefficiency of bremsstrahlung veto                            | 0.2                 | ---                   | 0.5                 |
| Fractional solid angle times detection efficiency              | 0.1                 | 0.018                 | 0.2                 |
| Muon-stopping rate ( $s^{-1}$ )                                | $3 \times 10^7$     | $2 \times 10^6$       | $5 \times 10^5$     |
| Running time (s)   | $1.2 \times 10^7$   | $1.1 \times 10^6$     | $2 \times 10^6$     |
| Branching-ratio sensitivity                                    | $8 \times 10^{-14}$ | $1.7 \times 10^{-10}$ | $4 \times 10^{-11}$ |
| Number of background events with $\pm 2\sigma$ cuts            | 0.4                 | $\sim 10$             | $\sim 50$           |

<sup>a</sup>All resolutions are FWHM

On average, there will be 36  $\mu s$  between triggers, which is sufficient time for modern electronics to encode, compact, and read the data into memories. A typical event will contain about 700 data words. The dead-time will be kept small by using substantial parallel processing. At the end of a LAMPF macropulse, the data from the events will be read into one of 32 microprocessors for further selection.

The additional criteria will require the electron energy to be 49 MeV, to pass some restrictions on its relative time to the photon, and to be within  $10^0$  of back-to-back to the photon. The surviving events will be written to tape at a rate of 11/s for further analysis, which will use the complete calibrations and refined algorithms

to sharpen the detector response functions, thus kinematically isolating any  $\mu^+ \rightarrow e^+\gamma$  events from all backgrounds. The replay of the tapes will be done with the data-acquisition microprocessors.

The parameters of MEGA are summarized in Table I, where they are compared with earlier experiments since 1975. In almost every category MEGA makes significant improvements over the previous efforts. The product of these improvements leads to an experiment with an ultimate sensitivity that is 500 times greater than that expected in results from the Crystal Box.

To dramatize the sensitivity, Fig. 7 displays the 90% confidence limit versus running time that can be achieved with MEGA. The current limit and the curve for the Crystal Box are also shown. In the background-free region, the curves drop inversely as the running time, and in

the background-limited region they drop inversely as the square root of the running time. The desirability of a background-free experiment is clear.

The collaboration has estimated the cost of MEGA to be \$2.9 million if the magnet is made available by SLAC. The Director of SLAC has just given his approval for the move. If the funding is available to allow for rapid procurement, debugging of the experiment can begin in the spring of 1988. The collaboration is very enthusiastic about the experiment and is working hard to keep it on schedule.

MEGA is a world-class effort to search for muon-number non-conserving decays, and it comple-

ments experiments at SIN (muon-electron conversion<sup>1</sup>) and at Brookhaven (rare kaon decays<sup>2</sup>), to find a violation of the Standard Model. We must explore all the possible channels because theory gives very little guidance as to which process will be easiest to observe. Unfortunately, there are so many possible extensions to the Standard Model, each containing unconstrained parameters, that no definitive predictive power exists. Most of the models introduce new particles of large mass. Therefore, the new experiments will continue to restrict the model builders and give insight on what to expect at the new generation of accelerators.

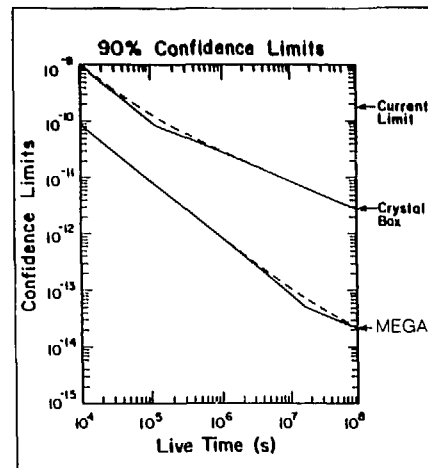


FIGURE 7. The branching-ratio sensitivity as a function of running time for MEGA and the Crystal Box.

## References

1. A. Badertscher et al., "Search for  $\mu^- \rightarrow e$  Conversion," SIN letter of intent R-85-07.0, Villigen, Switzerland, 1985.
2. R. D. Cousins et al., "Study of Very Rare  $K_L$  Decays," Brookhaven National Laboratory Alternating Gradient Synchrotron (AGS) Proposal 791, 1984.

## EXPERIMENT 914 — SMC

LAMPF

## EXPERIMENT 791 — Beam B5

Brookhaven

**Study of Very Rare  $K_L$  Decays**

Los Alamos, Stanford Univ., Univ. of Pennsylvania, UCLA, Temple Univ., College of William & Mary

Spokesmen (LAMPF Exp. 791): G. H. Sanders and W. W. Kinnison (Los Alamos)

Spokesman (Brookhaven Exp. 791): S. Wojcicki (Stanford Univ.)

As part of a major program of research in very rare  $K_L$  decays, LAMPF Exp. 914 was proposed to measure the analyzing power of a segmented muon polarimeter, a measurement essential to the design of the  $K_L$  experiment and to the analysis of the subsequent data.

The program of rare  $K_L$  decay research is an approved experiment at the Brookhaven National Laboratory Alternating Gradient Synchrotron (AGS). In a 2500-h exposure to a beam of  $10^{13}$  protons per pulse (with a 30 to 40% macroscopic duty factor) we will search for the decay  $K_L \rightarrow \mu e$  with a branching-ratio sensitivity of  $\sim 1 \times 10^{-12}$ , bettering existing limits by many orders of magnitude. In addition, the known decay  $K_L \rightarrow \mu^+ \mu^-$  will be simultaneously measured. This decay has a branching ratio of

$9.1 \times 10^{-9}$ , and 27 events constitute the world sample. The new experiment should collect  $\sim 10\,000$  of these events. We will search for the decays  $K_L \rightarrow ee$  and  $K_L \rightarrow \pi^0 e^+ e^-$  as well.

The physics motivations for these studies address frontier particle-physics problems, and all are among the high-priority experiments that would be pursued at a LAMPF II facility. The  $K_L \rightarrow \mu e$  experiment is a search for nonconservation of muon number, competitive with and complementary to the Crystal Box experiments and the MEGA (Muon decays into an Electron and a GAMMA ray) project. The measurement of 10 000 events for  $K_L \rightarrow \mu \mu$  would far exceed the precision of previous studies. However, the unique and exciting aspect of this new study will be our search for polarization of the  $\mu^+$  from the  $K_L \rightarrow \mu^+ \mu^-$  decay. The Standard Model predicts no polarization, and the present world sample provides no limit on the polarization. Therefore, observation of any nonzero polarization would signify the presence of entirely new physics, beyond the Standard Model and most likely involving charge-parity (CP) violating mechanisms. This subject has been considered extensively by the theoretical community, which includes Peter Herczeg at Los Alamos.

The measurement of polarization is the motivation for LAMPF Exp. 914. In the Brookhaven detector, Los Alamos will provide the largest detector component, a 300-ton, fully active muon range finder/polarimeter. Figure 1 shows the kaon-decay

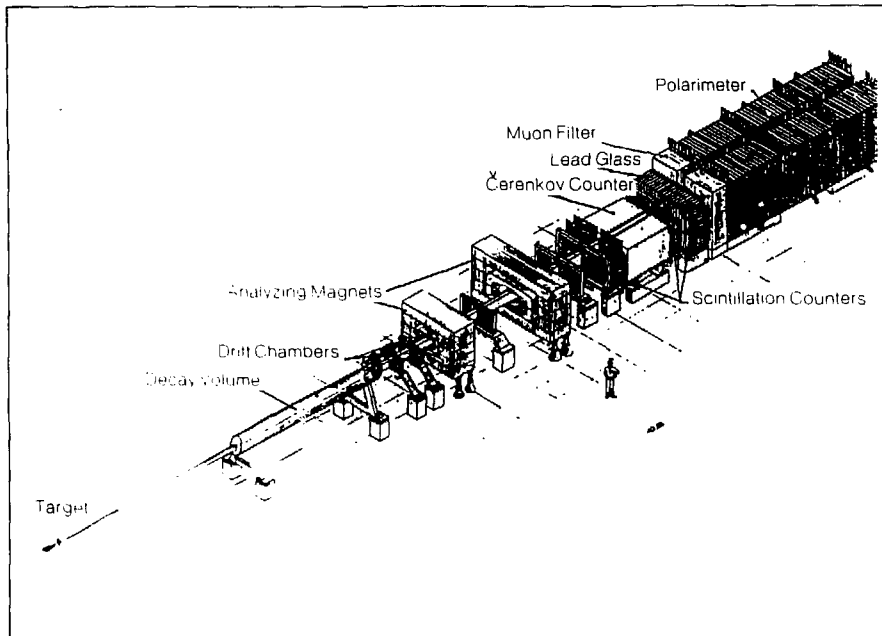


FIGURE 1 The rare kaon decay spectrometer.

spectrometer, with the Los Alamos polarimeter at the downstream end. This module will measure the muon range in real time, essential to the experiment trigger. In addition, when fully instrumented it will locate the stopping position of each muon and detect the time and direction of corresponding decay electrons. The entire volume of the module will be in a vertical 60-G magnetic field. The muon polarization will be unfolded from the decay asymmetry observed.

To carry out the polarization measurement, the range finder/polarimeter must be constructed of materials that induce no  $\mu^+$  depolarization at the stopping point. For this reason, the 300 tons of absorber plates will be made of Carrara marble and the active tracking detectors will be  $\sim 40\,000$  extruded aluminum proportional tubes. This combination is the lowest-cost system that meets the performance requirements, and these choices follow the developments in earlier experiments at CERN.

The polarization analyzing power has been carefully calculated using Monte Carlo simulations. However, validation of these design calculations requires empirical verification. In addition, the key parameter, the analyzing power, must be measured because many subtle, but significant, systematic effects cannot be reliably included in any simulation. For these reasons, LAMPF Exp. 914 was proposed to determine the polarization analyzing power, using the precision control of  $\mu^+$  polarization available at the SMC.

The prototype polarimeter module used is shown in Fig. 2. It was constructed jointly at the College of William & Mary and LAMPF. It consists of 256 channels of proportional tubes and provision for 3 absorber plates. The sensitive region of the polarimeter is housed within a Helmholtz coil that provides the

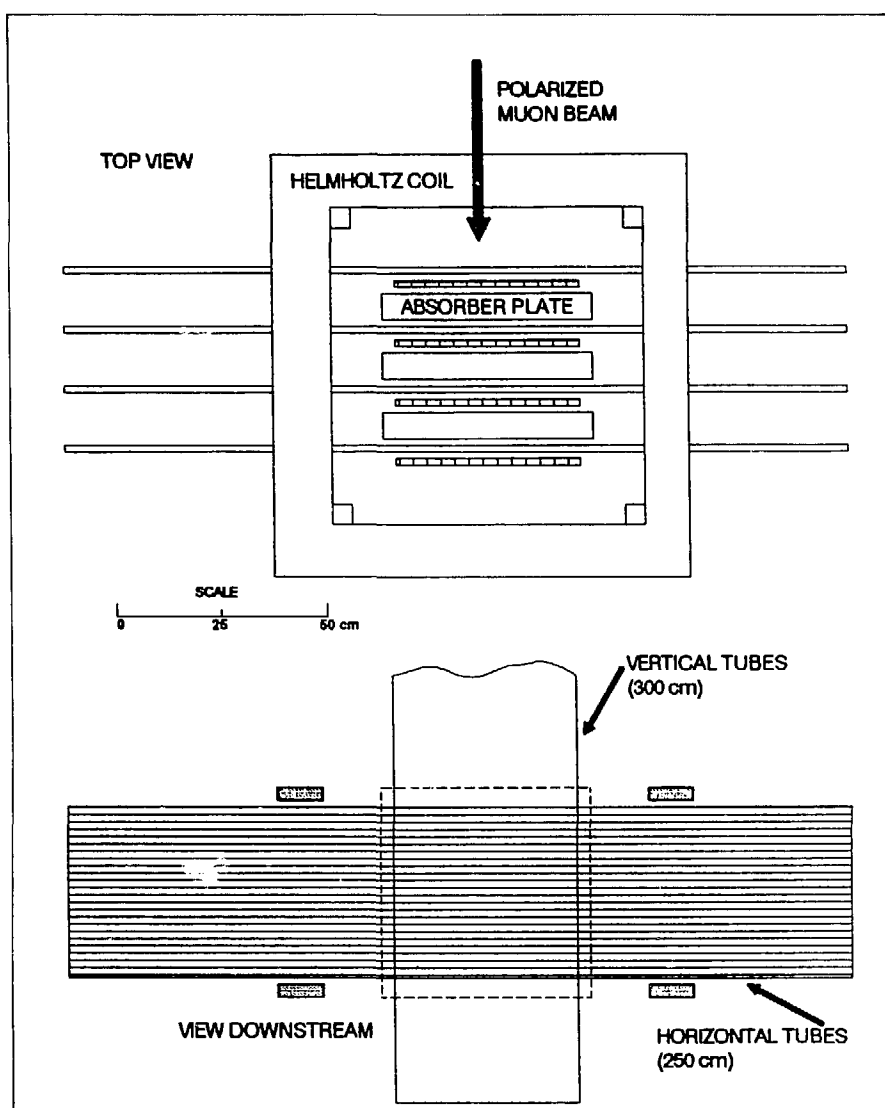


FIGURE 2. The test polarimeter used in LAMPF Exp. 914



necessary 60-G muon precession field. The incoming muon beam is measured by upstream trigger scintillators, and tracks are defined by two sets of multiwire proportional chambers. The polarimeter proportional-tube planes are read out into 128-word-deep buffer memories, clocked at 10 MHz. The trigger is such that for each stopped muon the entire history of the polarimeter module is digitized for 6.4  $\mu$ s before and 6.4  $\mu$ s following the muon stop. This provides a complete measurement of the muon stops and decays.

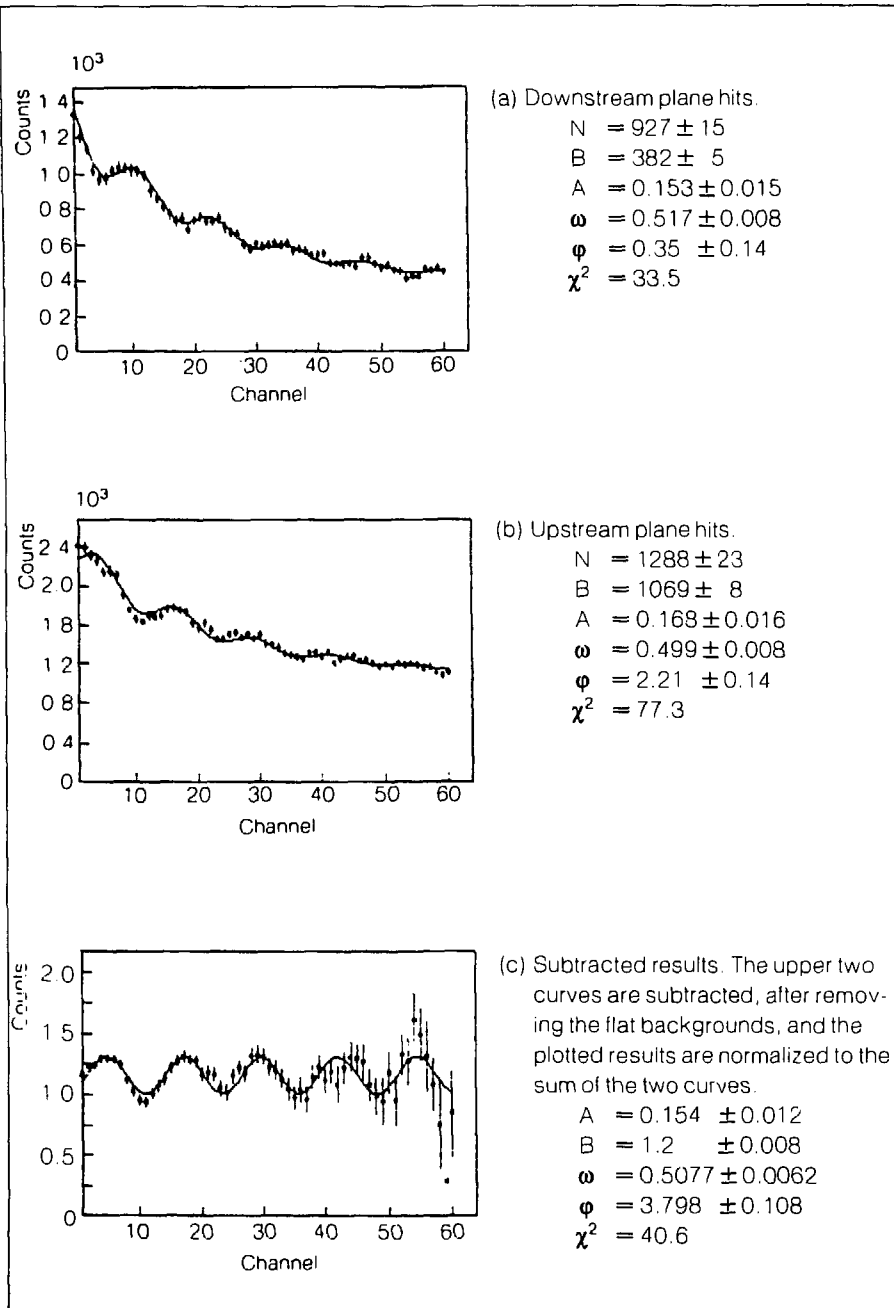
The first of two data runs has been carried out, using 133-MeV/ $c$  polarized  $\mu^+$  at the SMC. By varying the source pion momentum in the collection section of the SMC, the polarization of the  $\mu^+$  beam was ad-

justed between full forward and full backward polarization. A total of  $10^6$  stopped  $\mu^+$  events was recorded, with data taken under varying beam rates, absorber plate thicknesses, choices of absorber material (6061 aluminum and Carrara marble), and magnetic-field settings.

Figure 3 shows the observed decay-electron counting rate in a selected proportional-tube region as a function of time after the muon stop. The data clearly show the  $\mu^+$  decay rate and the modulation resulting from  $\mu^+$  polarization. The decay asymmetry from a preliminary fit to these data is shown. The final analysis of all the data taken and the comparison of the fit results with the Monte Carlo results will yield the measurement of the analyzing power under the conditions studied. A second data run for Exp. 914 will be requested when the final detector version is constructed.

During 1986 a major part of the absorber system and a significant part of the active detectors will be constructed for use at Brookhaven in autumn 1986.

FIGURE 3. Preliminary results from analysis of the test polarimeter data. The raw precession spectrum is from chambers upstream and downstream of the muon stopping point. Marble absorbers (3.8 cm thick) were located in each gap. Fit results are shown below.



## EXPERIMENT 745 — SMC

***E2 and E4 Deformations in  $^{232}\text{Th}$ ,  $^{233,234,235,236,238}\text{U}$ , and  $^{239,240,242}\text{Pu}$*** 

Los Alamos, Princeton Univ., Purdue Univ., Oak Ridge

Spokesmen: E. B. Shera (Los Alamos) and J. D. Zumbro (Princeton Univ./Univ. of Pennsylvania)

Participants: C. E. Bemis, Jr., M. V. Hoehn, R. A. Naumann, W. Reuter, E. B. Shera, R. M. Steffen, Y. Tanaka, and J. D. Zumbro

Muonic x-ray spectra of  $^{232}\text{Th}$ ,  $^{233,234,235,236,238}\text{U}$ , and  $^{239,240,242}\text{Pu}$  have been studied over the past 3 years.\* The primary purpose of the measurements was to make precise determinations of the nuclear electric hexadecapole moments in these heavy nuclei. The quadrupole (*E2*) moments, as revealed in this sequence of experiments, show a smooth systematic increase with increasing atomic mass [Fig. 1(a)]. The electric-quadrupole deformations inferred from the muonic hyperfine splittings are in good agreement with results<sup>2</sup> obtained by other workers using an independent experimental technique, Coulomb excitation. The agreement supports the validity of the interpretations of both experiments.

The precise new experimental values for the hexadecapole (*E4*) moments of these nuclei are the most significant results of our program [Fig. 1(b)]. These values, 2 to 5 times more precise than the results from Coulomb excitation, provide important new benchmarks for Hartree-Fock and Strutinsky-type calculations of the shapes of heavy nuclei. The regular systematic trend of the *E4* deformations in this region, like that for *E2*, is again evident. Note also the generally good agreement between the present results and Coulomb excitation work by Bemis et al.<sup>2</sup> (The older muonic-atom work of Close et al.<sup>3</sup> yielded much smaller *E4* values—the result, we believe, of an improper analysis formalism.)

Figure 2 shows sample muonic-K x-ray spectra measured in our experiments. The complex hyperfine pattern and isotope shift is clearly evident.

With the exception of  $^{237}\text{Np}$ , we have studied all the actinide nuclei that are available in sufficient quantity ( $\sim 10$  g) for our experiments.

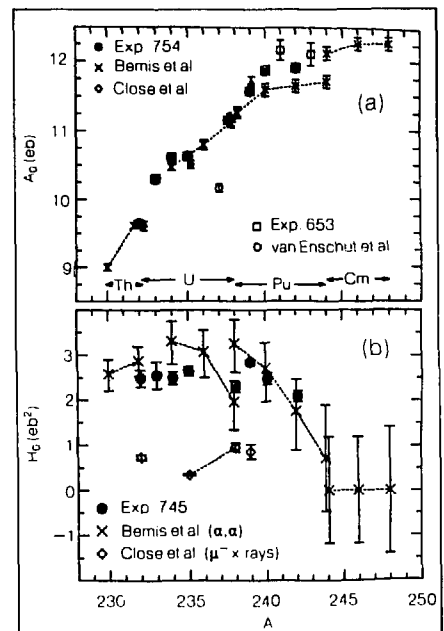


FIGURE 1.

- (a) The intrinsic quadrupole moment ( $Q_0$ ) versus  $A$ . Values from the present experiment are compared to results from other experiments. Also shown is the value of van Enschut et al. (Refs. 4 and 5) for  $^{237}\text{Np}$  and the values of Johnson et al. (Ref. 6) for  $^{241,243}\text{Am}$  measured in Exp. 653.
- (b) The intrinsic hexadecapole moment ( $H_0$ ) versus  $A$ . Values for isotopes of the same element are connected by dashed lines.

\*Reference 1 gives the results for  $^{232,234,235,236,238}\text{U}$ . The results for  $^{239,240,242}\text{Pu}$  will be published in *Physics Letters B*.

Many of these nuclei are, of course, intensely radioactive and require special techniques to obtain spectra of the quality shown in Fig. 2.

At the February 1985 meeting of the Program Advisory Committee (PAC), Exp. 745 requested time to measure  $^{237}\text{Np}$ . Almost simultaneously the SIN data for  $^{237}\text{Np}$  were

presented.<sup>4</sup> In Fig. 1 we show the intrinsic quadrupole moment of  $^{237}\text{Np}$  from the SIN work.<sup>5</sup> Because the result is quite different from the systematic trend of the other isotopes in this region, a verification of the SIN result clearly would be worthwhile.

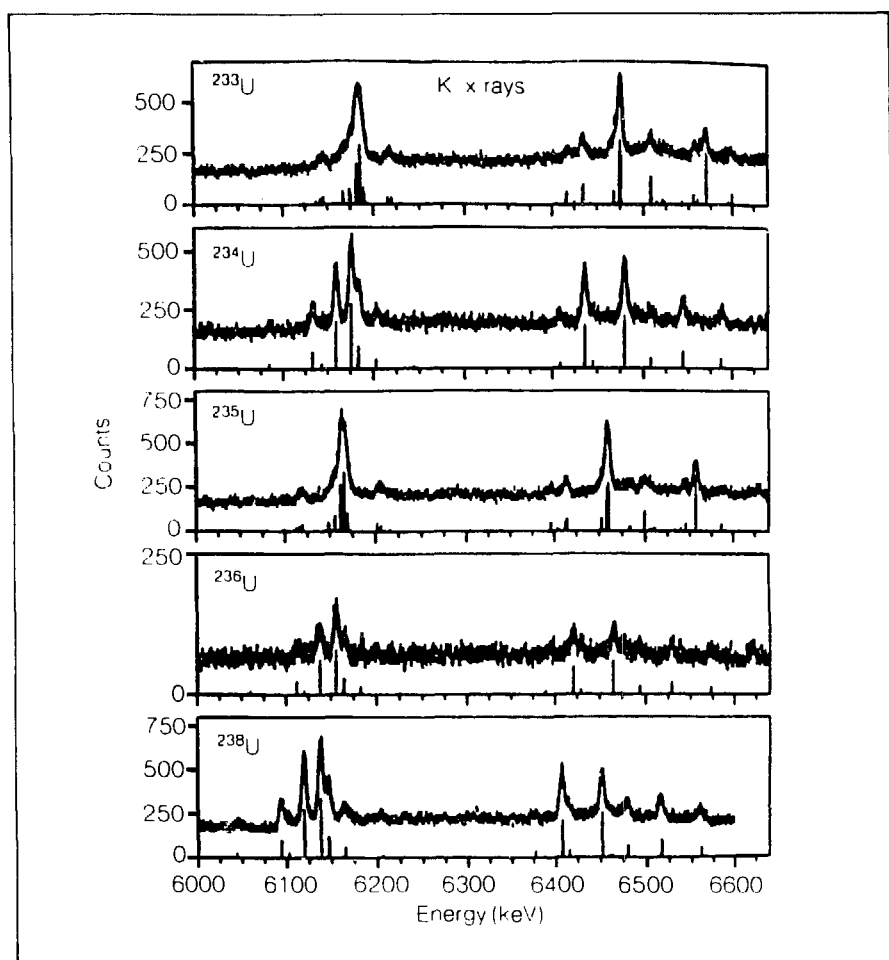


FIGURE 2 The  $^{233,234,235,236,238}\text{U}$  muonic-K x rays and the computed (fitted) spectra. The latter is shown as a continuous line through the data points. The vertical lines below each spectrum indicate the computed (fitted) energies and relative intensities of the individual x-ray transitions. The excellent fit of the computed spectra to the experimental data is evident; on the scale of these drawings the computed and experimental spectra cannot be distinguished.

---

**References**

1. J. D. Zumbro et al., *Physical Review Letters* **53**, 1888 (1984).
2. C. E. Bemis et al., *Physical Review C* **8**, 1466 (1973).
3. D. A. Close, J. J. Malanify, and J. P. Davidson, *Physical Review C* **17**, 1433 (1978).
4. J. F. M. d'Achard van Enscht et al., *SIN Newsletter* **17**, 44 (January 1985).
5. J. F. M. d'Achard van Enscht et al., *Helvetica Physica Acta* **58**, 925 (1985).
6. M. W. Johnson et al., *Physics Letters* **161B**, 75 (1985).

Experiment 726, a search for the  $C$ -violating decay of the neutral pion into three gamma rays, completed taking data at the end of August. The experiment used the Crystal Box as the photon detector. The central drift chamber was replaced by a liquid-hydrogen target in which negative pions stopped and produced neutral pions by charge exchange. A suitable tune of the SMC for a negative-pion beam had already been developed by us in preliminary studies and for Exp. 888. A momentum of 157 MeV/ $c$  was used, where we found the beam to be approximately 40% pions, 10% muons, and 50% electrons. The intensity was more than adequate to deliver 80 kHz of negative pions. The only drawback of the channel was that control of the momentum bite was primitive. Range straggling and multiple scattering limited the fraction of pions stopping in the 20-cm-long by 10-cm-diam liquid-hydrogen target to 50%. From a study of the stopping distribution, we tentatively deduce a momentum width of about 6% FWHM.

Minimal changes to the elaborate Crystal Box electronics system were required to adapt it to the new trigger. The principal source of triggers was expected to be the spreading of one of the showers from a two-gamma decay of a pion to look like a three-gamma decay. Three different hardware devices were included in the trigger to insist on a minimum separation between gammas and to require a geometry consistent with a three-gamma decay. Another source of triggers was expected to be three gammas from multiple neutral pion production by two or more pions in the same or adjacent LAMPF beam buckets. These were indeed copious, but were almost entirely eliminated

EXPERIMENT 726 — SMC

**A Search for the  $C$ -NonInvariant Decay  $\pi^0 \rightarrow 3\gamma$**

Temple Univ., Los Alamos, Univ. of Chicago

*Spokesmen: Virgil Highland (Temple Univ.) and Gary Hogan (Los Alamos)*

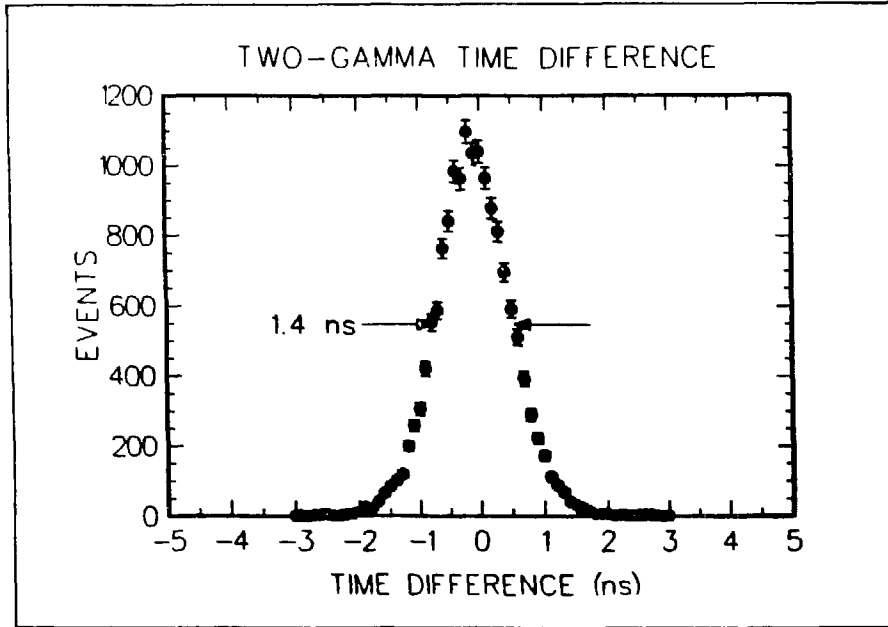


FIGURE 1 Measured photon time difference from  $\pi^0 \rightarrow 2\gamma$

by a hardware rejection of high pulse height in the beam counters and a subsequent on-line rejection of anomalous beam-counter pulse heights as measured by the CAMAC analog-to-digital converters (ADCs).

The experiment accumulated approximately 3 million events on tape, and the analysis is under way. The experience accumulated from previous Crystal Box experiments facilitates the analysis considerably. A first pass through the data has reduced the data set by a factor of 10, based on loose time and energy criteria on three adequately defined gamma shower clusters. At the same time, a sample of 3000 candidates for four-gamma decay was identified for further study. Time and energy calibration constants for all runs have been determined. The two-gamma events have a time resolution of 1.4 ns FWHM (see Fig. 1) and an energy resolution of 10 MeV FWHM at 137 MeV.

The events remaining after the first pass are completely dominated by the spread of two-gamma showers to look like three, as mentioned above. The geometry of the events clearly suggests this to the eye, the kinematics supports the interpretation, and a systematic time shift of the split-off gamma is observable. It is clear that considerable effort will be needed to understand this phenomenon in detail as the data analysis proceeds.

Extensive discussions of these experiments have appeared in the past several Progress Reports. The aim of these experiments is to search for several rare decay modes of the muon and to study these decay modes should they be observed. The muon-number-nonconserving decays  $\mu^+ \rightarrow e^+ e^+ e^-$ ,  $\mu^+ \rightarrow e^+ \gamma$ , and  $\mu^+ \rightarrow e^+ \gamma \gamma$  are being sought with a sensitivity to branching ratios of about  $4 \times 10^{-11}$  relative to ordinary muon decay. The data also will be analyzed to search for the decay  $\mu^+ \rightarrow e^+ \gamma f$ , where  $f$  is the familon.

A schematic diagram of the Crystal Box is shown in Fig. 1. The detector consists of a modular array of 396 NaI(Tl) crystals that surround an array of plastic scintillation counters and a high-resolution, narrow-stereo-angle drift chamber. Approximately  $5 \times 10^5 \mu^+$ /s (average) are stopped in a thin polystyrene target located in the center of the detector. Electron and positron trajectories are measured in the drift chamber and their arrival times are measured in the plastic scintillation counters. The energies of electrons, positrons, and photons are measured in the NaI(Tl). The energy is determined from the local high-pulse-height crystal and its surrounding 24 neighboring crystals. The photon-conversion points are also determined in the NaI(Tl). Photons do not register in either the drift chamber or the plastic scintillation counters.

In the search for all three decay modes, data were acquired simultaneously during summer 1984. The past year has been spent calibrating the detector and analyzing the data. The major source of backgrounds is the random coincidence of  $e^+$ 's and  $\gamma$ 's from the uncorrelated decays of several muons. This background is eliminated by requiring that the detected particles be in time coincidence and that they satisfy conservation of energy and momentum. For the  $\mu^+ \rightarrow e^+ e^+ e^-$  mode there is the additional constraint that the three tracks must emerge from a common vertex. To reject the backgrounds to an adequate level, excellent resolutions in timing, energy, and position are required.

The primary calibration of the NaI(Tl) is accomplished by removing the drift chamber, inserting a small liquid-hydrogen target in the center of the apparatus, and retuning the beam to stop  $\pi^-$ 's in the hydrogen. Calibration photons are produced in the reactions  $\pi^- p \rightarrow \pi^0 n$ ,  $\pi^0 \rightarrow \gamma \gamma$  ( $55 \text{ MeV} < E_\gamma < 83 \text{ MeV}$ ), and  $\pi^- p \rightarrow n \gamma$  ( $E_\gamma = 129 \text{ MeV}$ ). Figure 2 shows the total energy for the two photons from  $\pi^0$  decay after calibration. The energy resolution is  $\Delta E/E = 7.2\%$ .

## EXPERIMENTS

400/445 — SMC

### Crystal Box Experiments

Los Alamos, Stanford Univ., Univ. of Chicago, Temple Univ.

Spokesman: C. M. Hoffman (Los Alamos)

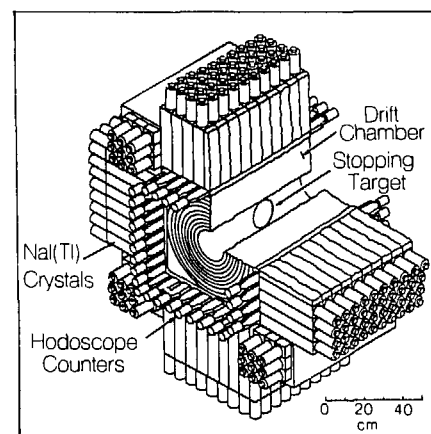


FIGURE 1 Schematic diagram of the Crystal Box detector.



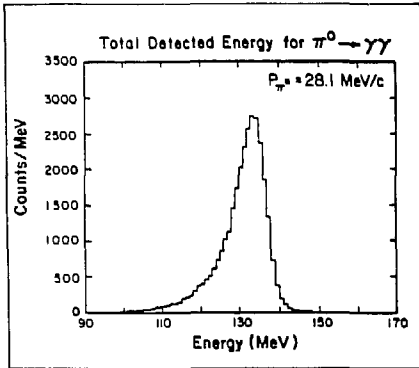
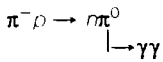


FIGURE 2 The sum of the photon energies from the reaction



(at rest) as measured with the NaI(Tl)

Once the crystals are calibrated with the pion data, we must track drifts in the gain of each crystal (and its associated electronics) over the course of the data taking. The gain of each crystal relative to the average for the entire array is tracked with a xenon flash tube that is connected to each crystal with fiber optics cables. Flasher runs were taken every 2 h. Although the flasher system is quite useful in tracking gain shifts and malfunctions in individual channels, it is not stable enough to determine the absolute gain shift of the entire crystal array. For this purpose the NaI(Tl) spectrum for positrons in each quadrant, accumulated for each data run (every 2 h), is used. The stability of the sodium iodide gains is checked with daily calibration runs triggered by single positrons. The resulting Michel spectrum is then fitted with the expected shape from the Monte Carlo program, as shown in Fig. 3. Analysis of this procedure indicates that the gain of the crystal array in each run is constant to within 0.5% and that the overall gain is correct to better than 0.25%.

The energy deposited in each NaI(Tl) crystal is measured by integrating for 200 ns the pulse from a photomultiplier coupled to the crystal. It is necessary to eliminate pileup, which is energy present during the integration gate from additional early or late pulses. This was accomplished with a second system that integrated the pulse over a 50-ns

gate that included the leading edge of the pulse. If a crystal has no pileup, the ratio of these two integrations is a constant that reflects the pulse shape:

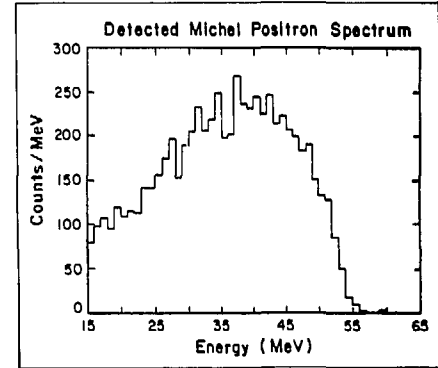


FIGURE 3 The measured energy spectrum for ordinary muon decay ( $\mu \rightarrow e^+ \nu_e \bar{\nu}_\mu$ ).

piled-up crystals have ratios either larger or smaller than this constant, depending on whether the pileup pulse occurs before or after the prompt pulse. If any crystal in a clump of 25 crystals has more than 2.5 MeV and pileup, the clump is discarded. Any piled-up crystal with less than 2.5 MeV is removed from the clump but the clump is retained. Approximately one-third of the data was taken without the pileup rejector working. For these data, the measured pileup spectrum is added to the Monte Carlo. For the data taken with the pileup rejector, no residual pileup can be detected, as evidenced by the complete agreement of data taken with instantaneous muon-stopping rates differing by a factor of 2.

The analysis of the  $\mu \rightarrow e\gamma$  data is nearly complete. The trigger condition for these data required a positron quadrant [a scintillator firing

plus  $\approx 35$  MeV in the NaI(Tl)] in coincidence with an opposite photon quadrant [ $\approx 35$  MeV in the NaI(Tl) with no scintillator firing]. Approximately 10% of the data were taken with higher energy thresholds. The resulting events can come from  $\mu \rightarrow e\gamma$ , inner bremsstrahlung ( $\mu \rightarrow e\gamma\nu\bar{\nu}$ , a process that conserves muon number), and random  $e^+\gamma$  coincidences. There were about  $10^7$  triggers. To determine the number of each kind of event, a maximum-likelihood analysis was performed on the 24 850 events, satisfying

$$|t_e - t_\gamma| < 2.0 \text{ ns} ,$$

$$E_\gamma > 40.0 \text{ MeV} ,$$

$$E_e > 44.0 \text{ MeV} ,$$

and

$$\theta_{e\gamma} > 160^\circ .$$

The likelihood function is defined as

$$L(\alpha, \beta) = N^{-1} \prod \left[ \alpha P(\vec{x}) + \beta Q(\vec{x}) + (N - \alpha - \beta) R(\vec{x}) \right] ,$$

where  $\alpha$ ,  $\beta$ , and  $(N - \alpha - \beta)$  are the number of  $\mu \rightarrow e\gamma$ , inner bremsstrahlung, and random coincident events, respectively, and  $P$ ,  $Q$ , and  $R$  are the probability density distributions for these kinds of events as a function of the variables  $E_e$ ,  $E_\gamma$ ,  $\theta_{e\gamma}$ , and  $t_e - t_\gamma$ . In the maximum-likelihood method, the maximum of the likelihood func-

tion in  $\alpha, \beta$  space is found. Figure 4 shows the likelihood function and its projections on the  $\alpha$  and  $\beta$  axes. The observed number of inner bremsstrahlung events ( $3475 \pm 75$ ) agrees with the expected number within errors. The likelihood function peaks at  $\alpha = 0$ , with a 90% confidence level upper limit of  $\alpha < 11$ ; this corresponds to a branching ratio of approximately  $5 \times 10^{-11}$ . The final result awaits a full analysis of the detection efficiency and the number of muon decays observed.

Preliminary results for  $\mu \rightarrow eee$  and  $\mu \rightarrow e\gamma\gamma$  were presented in last year's Progress Report. The full analysis of these data will be completed in early 1986. An additional preliminary result was presented at the Washington American Physical Society meeting in April 1985 for the decay  $\mu \rightarrow e\gamma f$ , where  $f$  is a familon, a massless scalar boson associated with family symmetry (this work was done with T. Goldman of Group T-5). The preliminary result was

$$\frac{\Gamma(\mu \rightarrow e\gamma f)}{\Gamma(\mu \rightarrow e\nu\bar{\nu})} < 1.2 \times 10^{-8} \text{ (90\% C.L.)} ,$$

corresponding to a lower limit on the scale of family symmetry breaking of  $9 \times 10^8$  GeV. The final result should be roughly an order of magnitude more sensitive to the symmetry-breaking scale.

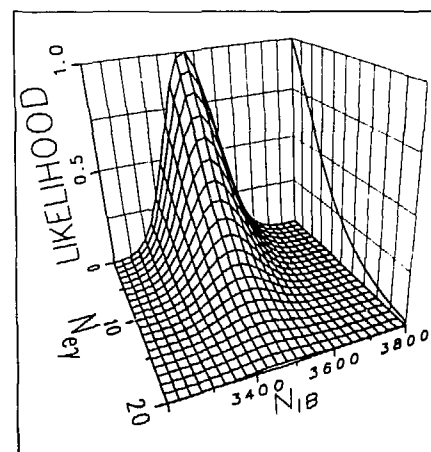


FIGURE 4 The normalized likelihood function plotted as a function of the number of muon inner bremsstrahlung events and the number of  $\mu^+ \rightarrow e^+\gamma$  events. The projected distribution on the  $N_{e\gamma}$  likelihood plane is also shown.

## ATOMIC AND MOLECULAR PHYSICS

### Theory of Muon-Catalyzed Fusion

James S. Cohen and M. Leon (Los Alamos)

The remarkable ability of a single negative muon to catalyze many  $dt$  fusions is now firmly established, and systematic research is under way to disentangle the intricacies of the catalysis cycle.<sup>1,4</sup> An essential contributor to the rapidity of the cycle is the resonant molecular-formation mechanism, in which the colliding  $t\mu + d$  form the loosely bound  $J=1$ ,  $v=1$   $dt\mu$  mesomolecular ion, with the energy released going into the vibration and rotation of the resulting compound molecule  $\{[(dt\mu)d_2e]^*$ , etc.}. The kinetic energies (and therefore the target temperatures for thermalized  $t\mu$  atoms for which the collisions are resonant) are readily determined once the  $dt\mu$  binding energy, the hyperfine splittings, and the compound-molecule "rovibrational" energies are known.

Recently, Breunlich et al.<sup>2</sup> reported a catalysis experiment at SIN using a low-density (1%  $LH_2$ ) DT target (with tritium fraction  $C_T = 0.88$ ) in which a rapidly decaying transient was seen in the appearance of the 14-MeV neutrons from  $dt$  fusion. In analogy with earlier experimental results on  $dd\mu$  fusion,<sup>5</sup> they interpret this transient in terms of a triplet-quenching hypothesis<sup>2</sup> in which (i) the thermalization time of the  $t\mu$  atoms is neglected, (ii) the molecular-formation rate for triplet  $t\mu$  is very large ( $\sim 10^9$  s<sup>-1</sup>) for a rather low temperature (30 to 300 K), and (iii) the quenching rate for the triplet  $t\mu$  depends strongly on temperature.

However, in regard to (i), by using the cross sections calculated by Melezhik et al.<sup>6</sup> for the scattering of 1-eV ground-state  $t\mu$  atoms from  $d$  and  $t$ , one finds for  $C_T = 0.88$  an elastic-scattering rate of only  $\sim 2 \times 10^9 \phi$  s<sup>-1</sup>, where  $\phi$  is the density in units of  $LH_2$  density ( $4.25 \times 10^{22}$  atoms cm<sup>-3</sup>), so that the thermalization time is clearly not negligible for  $\phi = 1\%$ .

An objection to (ii) comes from considering the energy balance: If we ignore the rotational contributions, the resonance energy for triplet  $t\mu$  collisions with  $D_2$  is about 219 meV; for DT, 107 meV. Hence neither channel can contribute for a  $t\mu$  atom thermalized at 30 K. One need not have confidence in the theory of resonant molecular formation<sup>7,8</sup> to subscribe to this conclusion, because it follows directly from the energy-balance equation [see Eq. (7) below].

An objection to (iii) is that so large a temperature dependence is not expected for the triplet-quenching rate, the process being dominated by triton exchange<sup>9</sup> [ $t\mu(\uparrow\uparrow) + t(\downarrow) \rightarrow t\mu(\downarrow\uparrow) + t(\uparrow)$ ]. Breunlich et al.<sup>2</sup> point out this disagreement, but an even more serious discrepancy is suggested by data reported earlier for 10% tritium,<sup>10</sup> which has the transient falling off much more rapidly. The triplet-quenching model then implies that the quenching cross section is greater for  $t\mu + d$  collisions than for  $t\mu + t$  collisions, a situation that clearly contradicts the well-founded idea that  $t$  exchange dominates the  $t\mu - t$  quenching.

For these reasons, therefore, we cannot accept the triplet-quenching

hypothesis. (Breunlich et al.<sup>2</sup> included the  *caveat*  that different theoretical explanations of their data should be considered, too.)

Instead, we believe that the transient in the neutron appearance observed by Breunlich et al.<sup>2</sup> is due to a new phenomenon with significant implications: epithermal molecular formation.\* Specifically, we propose that the observed time dependence actually represent the population of  $t\mu$  atoms passing through the energy region of rapid (resonant) mesomolecular formation during thermalization. Several elements contribute to the argument:

1. the population of energetic ( $\sim 1$ -eV) ground-state  $t\mu$  atoms grows as the target density  $\phi$  is reduced;
2. thermalization slows as the tritium fraction or the target temperature is increased;
3. the molecular-formation rates fall rapidly as the effective temperature of the  $t\mu$  kinetic-energy distribution falls below  $\sim 10^3$  K; and, furthermore,
4. the dipole-formation mechanism, in which the  $t\mu + d$  system makes a dipole transition to

the loosely bound  $J=1, l=1$   $dt\mu$  state, is actually less important than direct formation, in which  $t\mu$  and  $d$  approach in a relative  $p$  wave and form the bound state with no dipole transition involved.

We now deal with these four points in detail.

1. The influence of the target density on the population of energetic  $t\mu$  atoms comes from the role that radiation plays in  $t\mu$  deexcitation. The relevant rates for  $n=4$  and 3 are shown in Table I. (Stark mixing is strong enough for  $\phi \geq 1\%$  that we do not have to consider the different  $\ell$  levels separately.<sup>12</sup>)

Ponomarev<sup>1</sup> has pointed out the importance of elastic scattering of excited  $t\mu$  atoms to the thermalization process. Adopting the  $d\mu + d$  excited-state elastic-scattering rates  $\lambda_{e\ell}(n)$  of Menshikov and Ponomarev<sup>13</sup> for  $t\mu + t$  (for 1-eV kinetic energy) gives the products of rate times lifetime  $\lambda_{e\ell}\tau$  shown in Table I. Because about half the kinetic energy is lost at each collision, a rough measure of the surviving fraction of kinetic energy is given by  $(1/2)^{\lambda_{e\ell}\tau}$ .

Thus we see from Table I that the fractional energy surviving the  $n=3$

\*The possibility of epithermal molecular formation has been raised before—especially by J. Rafelski (Ref. 11).

TABLE I. Deexcitation and Elastic-Scattering Rates for Excited  $t\mu$  Atoms.<sup>a</sup>

| $\phi$ | $n=4$       |                  |                       | $n=3$       |                  |                       |
|--------|-------------|------------------|-----------------------|-------------|------------------|-----------------------|
|        | $\lambda_e$ | $\lambda_\gamma$ | $\lambda_{e\ell}\tau$ | $\lambda_3$ | $\lambda_\gamma$ | $\lambda_{e\ell}\tau$ |
| 1.0    | 9.5         | 0.06             | 1.9                   | 1.2         | 0.19             | 6.7                   |
| 0.1    | 0.95        | 0.06             | 1.8                   | 0.12        | 0.19             | 3.1                   |
| 0.01   | 0.10        | 0.06             | 1.1                   | 0.01        | 0.19             | 0.5                   |

<sup>a</sup>External Auger ( $\lambda_e$ ) and radiative ( $\lambda_\gamma$ ) deexcitation rates and the product  $\lambda_{e\ell}\tau$  for excited  $t\mu$  atoms. The  $\lambda_e$  and  $\lambda_{e\ell}$  are taken from Menshikov and Ponomarev, Ref. 13.  $\lambda_{e\ell}$  is from their  $d\mu-d$  rates. Units are  $10^{11} \text{ s}^{-1}$ .

state increases drastically as  $\varphi$  is decreased. Although the kinetic energy upon arrival at  $n = 3$  is not known with any degree of confidence, it has long been thought<sup>12</sup> to be  $\sim 1$  eV (the exact value is not critical to our arguments as long as it is  $\gg kT$ ). For definiteness we assume that the population of epithermal ground-state  $t\mu$  atoms is Maxwell-distributed, with an average energy of 1 eV.

2. Elastic scattering of (ground-state)  $t\mu$  atoms by  $d$  and  $t$  has been calculated by Melezhik et al.<sup>6</sup> A striking result is that the cross section for scattering from  $t$  is an order of magnitude smaller than that from  $d$ . This implies much faster thermalization for lower tritium fraction and thus, according to the epithermal hypothesis, a much faster decay of the transient, as observed by Breunlich et al.<sup>10</sup> Furthermore, thermalization through the region of  $\sim 10^3$  K clearly must take longer as the target temperature is increased, explaining the temperature dependence of the transients.<sup>2,10</sup>

The time evolution of the non-equilibrium  $t\mu$  energy-distribution function  $f(E, t)$  is determined (for arbitrary target temperature and composition) by a Monte Carlo simulation of the time-dependent Boltzmann equation.<sup>14</sup> We use the cross sections of Ref. 6 and some less-accurate values for  $t\mu + t$  scattering above the 0.24-eV inelastic threshold<sup>15</sup> (adjusting the latter to be consistent with the former). As an approximation we separate the calculation of the slowing from that of

molecular formation and ignore the effect of molecular formation on  $f(E, t)$ . Time  $t = 0$  corresponds to the arrival of the  $t\mu$  atom at its 1s ground state. According to the calculations of Markushin,<sup>16</sup> the cascade from a free  $\mu^-$  with 2-keV kinetic energy to the 1s state takes only  $\sim 0.1$  ns for  $\varphi = 1\%$ . Thus the unexplained rise seen in the SIN experiment,<sup>2</sup> which takes  $\sim 50$  ns, is presumably because the  $t = 0$ ,  $t\mu$  kinetic-energy distribution is significantly above the energy at which the (epithermal) molecular-formation rate is maximum. Hence the low-density muon-catalyzed  $dt$  fusion experiments present an opportunity to gain unprecedented knowledge of the  $t\mu$  cascade.

3. The dipole molecular-formation rates are calculated following Vinitzky et al.<sup>7</sup> and Leon,<sup>8</sup> but include the electron-shielding correction pointed out by Cohen and Martin.<sup>17</sup> As long as the resonances involved (for a given vibrational excitation) are not close to threshold, we can, rather than include the many different individual resonances, sum to a good approximation over all the final molecular rotational states, ignoring the rotational energy differences. Then, instead of the many partial-wave terms of Ref. 8, the sum rule gives

$$\begin{aligned} \sum_{K_f} F(K_i, K_f) &\approx \int d\rho y_0(\rho) y_v(\rho) \mathcal{E}(\rho) \\ &\times \int d\rho' y_0(\rho') y_v(\rho') \mathcal{E}(\rho') j_0 \\ &\times [\eta k_2(\rho - \rho')] , \end{aligned} \quad (1)$$

where the  $y_i$  are the vibrational wave functions,  $j_0$  is the zero-order spherical Bessel function,  $k_2$  is the  $t\mu + D_2$  (DT) relative momentum,  $\eta = 1/2(3/5)$  for  $D_2$  (DT) collisions, and  $\mathcal{E}(\rho)$  is the electric field from the spectator nucleus plus electrons.<sup>17</sup> For  $D_2$  collisions we include contributions from  $v = 2$  through 5; for DT,  $v = 3$  through 6. We use the sum rule for all but the lowest  $v$  value. The results for singlet  $t\mu$  atoms are shown in Fig. 1. In general,  $v = 3$  gives the dominant contribution, but for  $D_2$  collisions at low temperature the  $v = 2$  contribution is largest. The weighted sum of these contributions appropriate to  $C_i = 0.88$  does indeed fall for temperature  $< 10^3$  K.

The temperature in Fig. 1 is not that of the target, but rather it characterizes the kinetic-energy distribution in the  $t\mu + D_2$  (or DT) c.m. system. As one can readily show, when the projectile ( $t\mu$ ) Maxwell distribution (with temperature  $T_a$ ) is combined with the target-molecule ( $D_2$  or DT) Maxwell distribution ( $T_b$ ), the result in the c.m. system is also a Maxwell distribution, with temperature  $T_{c.m.} = (m_a T_b + m_b T_a) / (m_a + m_b)$ , where  $m_a$  is the projectile mass and  $m_b$  is the target mass.

4. The direct molecular-formation process has not previously been considered. We approximate it by making use of some results of Melezhik et al.<sup>6</sup> and by assuming that the  $p$ -wave  $t\mu + d$  elastic scattering is dominated by the  $J = 1, v = 1$  state

with binding energy<sup>1</sup>  $\epsilon_b \approx 0.64$  eV. In the present formulation we need to deal with collisions of  $t\mu$ , both with a deuteron and with the  $D_2$  (or DT) molecule. We follow the convention of using  $M_1, k_1$ , and  $E_1$  for the reduced mass, relative wave number, and c.m.-system collision energy, respectively, for the former, and  $M_2, k_2$ , and  $E_2$  for the latter. We write the  $p$ -wave elastic-scattering cross section as

$$\sigma_p^{el} = \frac{12\pi}{k_1^2} \frac{\Gamma_{el}^2(k_1)/4}{(E_1 + \epsilon_b)^2 + \Gamma_{el}^2(k_1)/4}, \quad (2)$$

with the elastic width  $\Gamma_{el}(k_1)$  (in electron volts) being given by

$$\Gamma_{el}(k_1) = a_3 k_1^3 + a_2 k_1^2 = 0.65 E_1^{3/2} + 0.049 E_1 \quad (3)$$

( $E_1$  is also expressed in electron volts). The  $a_3 k_1^3$  term is due to the bound state at  $-\epsilon_b$ , and  $a_3$  is chosen to fit the calculated values of Melezhik et al.<sup>6</sup> The  $a_2 k_1^2$  term comes from the known long-range polarization potential.<sup>18</sup> Equations (2) and (3) describe the results of Ref. 6 extremely well.

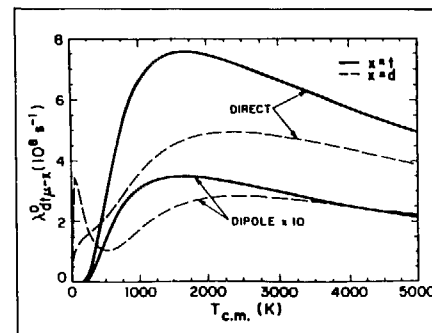


FIGURE 1. Epithermal molecular-formation rates as functions of c.m. temperature. The upper curves are the direct process; the lower, the dipole (times 10) for  $D_2$  (broken curves) and DT (solid curves) collisions (normalized to  $C_d = \phi = 1$ ).

We make the jump from elastic  $t\mu + d$  scattering to resonant mesomolecular formation in  $t\mu + D_2$  (or DT) collisions using the impulse approximation. This method has previously been applied to rovibrational excitation in collisions of atoms with diatomic molecules,<sup>19</sup> a process that is closely related to direct mesomolecular formation. The basic assumption is appropriate for  $t\mu + D_2$  collisions, even at relatively low energy, because the small neutral  $t\mu$  atom interacts significantly with a deuteron only at distances that are small when compared with typical internuclear distances of  $D_2$ . In the impulse approximation (with approximate treatment of the internal target momentum, as shown below), the molecular-formation cross section can be written as the product

$$\sigma_{direct}^{mf} \approx \left(\frac{M_2}{M_1}\right)^2 \tilde{\sigma}_p | \langle v, K_f; 0, K_i \rangle |^2 \quad (4)$$

In this expression,  $\langle v, K_f; 0, K_i \rangle \equiv \langle v, K_f | \exp(i\eta \vec{k}_2 \cdot \vec{p}) | 0, K_i \rangle$  is the molecular bound-state form factor. We define the quantity  $\tilde{\sigma}_p$  to be the result of taking the  $p$ -wave amplitude off the energy shell; as the molecular binding is turned off,  $\tilde{\sigma}_p \rightarrow \sigma_p^{e\bar{e}}$ .

In approximating  $\tilde{\sigma}_p$  in Eq. (4), we are guided by the fact that the scattering is strongly dominated by the bound state. Expressing the energy denominator in Eq. (2) in terms of  $E_2$

to describe the molecular collision, we write the final result

$$\sigma_{direct}^{mf} \approx \left(\frac{M_2}{M_1}\right)^4 \left(\frac{12\pi}{k_1^2}\right) \times \frac{\Gamma_{en}(k_1)\Gamma_{deex}/4}{(E_2 - E_{res})^2 + \Gamma_{tot}^2/4} \quad (5)$$

In this expression,

$$\Gamma_{en}(k_1) \equiv | \langle v, K_f; 0, K_i \rangle |^2,$$

$\Gamma_{en}(k_1)$  is the "entrance width,"  $\Gamma_{deex}$  is the deexcitation rate for all processes (from the compound-molecule state formed in the collision to states with too little energy for the system to "back decay"<sup>20</sup>), and  $\Gamma_{tot}$  is the total width of the compound-molecule state. Presumably,  $\Gamma_{deex}$  is dominated by Auger deexcitation,<sup>21</sup> but collisional deexcitation may contribute at large  $\phi$ .

We take the internal target motion into account in an approximate way by averaging over the deuteron momentum in the initial molecular state; this gives the relation between  $E_1$  and  $E_2$ ,

$$E_1 = \frac{M_1}{M_2} E_2 + \eta \frac{M_1}{m_d} \left( \frac{1}{2} E_0' + E_{K_i}' \right), \quad (6)$$

where  $m_d$  is the deuteron mass and

$$\frac{1}{2} (E_0^i + E_{K_i}^i)$$

is the initial rovibrational kinetic energy. The resonance energy  $E_{res}$  is given by the energy balance equation,

$$E_{res} = E_v^f - E_0^i + E_{K_f}^f - E_{K_i}^i - \Delta\epsilon_{bf} - \epsilon_b \quad (7)$$

Here,  $E_v^i$  ( $E_v^f$ ) and  $E_{K_i}^i$  ( $E_{K_f}^f$ ) are the initial (final) vibrational and rotational energies and  $\Delta\epsilon_{bf}$  gives the difference in hyperfine energies in the  $t\mu$  and  $dt\mu$  states.

Because we expect that  $\Gamma_{deex} \approx \Gamma_{tot}$  and that  $\Gamma_{tot} \ll E_2$ , the integral over energy,

$$\int dE_2 f(E_2, t) \sigma_{direct}^{mf}(E_2), \quad (8)$$

becomes a sum over resonances and the dependence on  $\Gamma_{tot}$  disappears. Furthermore, we can with sufficient accuracy use the sum-rule result [analogous to Eq. (1) but with the electric-field  $\mathcal{E}(\rho)$  factors missing] for all but the lowest vibrational contribution to the direct process. The same  $v$  values are included as for the dipole mechanism; the dominant contribution is from  $v = 3$ . Considerations of the initial  $D_2$  rotational states are also the same as for the dipole mechanism.<sup>22</sup>

The resultant direct contributions to the singlet  $D_2$  and DT molecular-formation rates as functions of  $T_{c.m.}$  are shown in Fig. 1. The direct process is more than 20 times stronger than that for the dipole, and the weighted sum falls for  $T_{c.m.} < 10^3$  K. (The triplet rates are similar to the singlet ones, allowing us to avoid explicit treatment of triplet contributions and quenching.)

With the above four elements in hand, we combine the energy-distribution function  $f(E_2, t)$  with the total molecular-formation cross section  $\sigma_{mf}(E_2)$  to give the time-dependent molecular-formation rate  $\lambda_{dt\mu}(t)$ , shown in Fig. 2, for target temperatures 30 and 300 K and  $C_t = 0.88$ . As expected, more-rapid  $t\mu$  energy loss for the 30 K target results in faster decay of the transient, in agreement with the SIN experiment.<sup>2</sup> Furthermore, the time scale of both the rise and decay of the molecular-formation rate is in good agreement with the experiment. The magnitude of the peak in  $\lambda_{dt\mu}(t)$  also agrees fairly well with the values  $(8.9) \times 10^8 \text{ s}^{-1}$ , quoted by Breunlich et al.<sup>2</sup> (which they call triplet).

In addition, on the basis of the present epithermal molecular-formation hypothesis, we predict that the amplitude of the transient signal will decrease as the target density is increased (see Table I). The triplet-quenching hypothesis implies no such dependence.

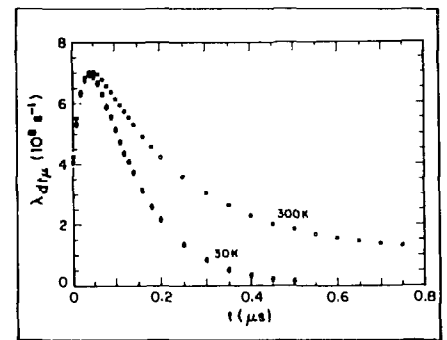


FIGURE 2 Time dependence of the molecular-formation rate for  $C_t = 0.88$  and  $\phi = 1\%$  ( $\lambda_{dt\mu}$  normalized to  $C_d = \phi = 1$ , muon decay is not included)



In conclusion:

1. The triplet-quenching hypothesis is probably not a viable explanation of the SIN experimental results.
2. The epithermal molecular-formation hypothesis appears to be in good agreement with experiment and with theoretical expectations.
3. Observation of the density dependence of the amplitude of the transient in neutron production would provide additional evidence for choosing between the two hypotheses.\*
4. Direct mesomolecular formation is more important than the dipole mechanism.
5. The detailed time dependence of the transient offers us valuable and hitherto unavailable information on the  $t\mu$  cascade and collision processes.

\*Evidence for such density dependence has been seen in the LAMPF  $dt$  catalysis data (information is from A. N. Anderson, Jackson, Wyoming, 1985).

---

## References

1. L. I. Ponomarev, *Atomkernenergie Kerntechnik* **43**, 175 (1983).
2. W. H. Breunlich et al., *Physical Review Letters* **53**, 1137 (1984).
3. S. E. Jones et al., *Physical Review Letters* **51**, 1757 (1983); S. E. Jones, "Some Surprises in Muon-Catalyzed Fusion," *Atomic Physics IX*, R. S. Van Dyck, Jr., and E. N. Fortson, Eds. (World Scientific Co., Seattle, Washington, 1985), p. 99; and "Progress at LAMPF," Los Alamos National Laboratory report LA-10429-PR (April 1984), p. 89.
4. V. M. Bystritsky et al., *Zhurnal Eksperimental'noi i Teoreticheskoi Fiziki* **80**, 1700 (1981) [*Soviet Physics-JETP* **53**, 877 (1981)].
5. P. Kammel et al., *Physical Review A* **28**, 2611 (1983).
6. V. S. Melezhik, L. I. Ponomarev, and M. P. Faifman, *Zhurnal Eksperimental'noi i Teoreticheskoi Fiziki* **85**, 434 (1983) [*Soviet Physics-JETP* **58**, 254 (1983)].
7. S. I. Vinitsky et al., *Zhurnal Eksperimental'noi i Teoreticheskoi Fiziki* **74**, 849 (1978) [*Soviet Physics-JETP* **47**, 444 (1978)].
8. M. Leon, *Physical Review Letters* **52**, 605 and 1655 (1984).
9. A. V. Matveenko and L. I. Ponomarev, *Zhurnal Eksperimental'noi i Teoreticheskoi Fiziki* **59**, 1593 (1970) [*Soviet Physics-JETP* **32**, 871 (1971)].

10. W. H. Breunlich et al., "New Experimental Results on Muon Catalyzed Fusion in Low Density Deuterium-Tritium Gas," *Fundamental Interactions in Low-Energy Systems*, P. Dalpiaz, G. Fiorentini, and G. Torelli, Eds. (Plenum Press, New York, 1985), pp. 449-457.
11. J. Rafelski, *Exotic Atoms '79*, K. Crowe et al., Eds. (Plenum Press, New York, 1980), p. 203.
12. M. Leon and H. A. Bethe, *Physical Review* **127**, 636 (1962); and M. Leon, *Physics Letters* **35B**, 413 (1971).
13. L. I. Menshikov and L. I. Ponomarev, USSR preprints IAE-4006/12 and IAE-4041/12.
14. K. Koura, *Journal of Chemical Physics* **65**, 3883 (1976).
15. A. V. Matveenko and L. I. Ponomarev, *Zhurnal Eksperimental'noi i Teoreticheskoi Fiziki* **58**, 1640 (1970) [*Soviet Physics-JETP* **31**, 880 (1970)]; and A. V. Matveenko et al., *Zhurnal Eksperimental'noi i Teoreticheskoi Fiziki* **68**, 437 (1975) [*Soviet Physics-JETP* **41**, 212 (1975)].
16. V. E. Markushin, *Zhurnal Eksperimental'noi i Teoreticheskoi Fiziki* **80**, 35 (1981) [*Soviet Physics-JETP* **53**, 16 (1981)].
17. J. S. Cohen and R. L. Martin, *Physical Review Letters* **53**, 738 (1984).
18. T. F. O'Malley, L. Spruch, and L. Rosenberg, *Journal of Mathematical Physics* **2**, 491 (1961).
19. A. Bogan, *Physical Review A* **9**, 1230 (1974).
20. A. M. Lane, *Physics Letters* **98A**, 337 (1983).
21. L. N. Bogdanova et al., *Zhurnal Eksperimental'noi i Teoreticheskoi Fiziki* **83**, 1615 (1982) [*Soviet Physics-JETP* **56**, 931 (1982)].
22. M. Leon and J. S. Cohen, *Physical Review A* **31**, 2680 (1985).

EXPERIMENT 727 — Biomed  
and SMC**Measurement of the Efficiency of  
Muon Catalysis in Deuterium-  
Tritium Mixtures at High Densities**Brigham Young Univ., Idaho National  
Engineering Laboratory, Los Alamos

Spokesman: S. E. Jones (Brigham Young Univ.)

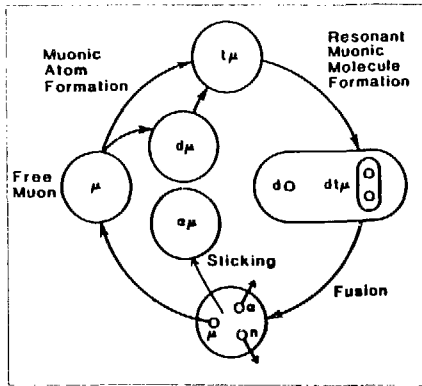
Participants: A. N. Anderson, J. N. Bradbury, A. J.  
Calfrey, J. S. Cohen, P. A. M. Gram, M. Leon,  
H. R. Maltrud, M. A. Paciotti, C. D. Van Siclen,  
and K. D. Watts

FIGURE 1 The main  $dt\mu$ -catalysis cycle. Other channels (not shown) are discussed in the text.

The study of muon catalysis of  $dt$  fusion (see Fig. 1) has now entered a period of rapid development,<sup>1,3</sup> just a few years after the experimental confirmation by Bystritsky et al.<sup>4</sup> that  $dt\mu$  molecular formation is indeed fast on the scale of the muon lifetime (2.2  $\mu$ s). In the 1983 and 1984 LAMPF Progress Reports and in Refs. 1 and 2, we reported the first measurements of some of the basic parameters of this fascinating process. In particular, the sticking probability  $\omega_s$  was measured and the  $dt\mu$  formation rates  $\lambda_{d\mu-d}$  and  $\lambda_{d\mu-t}$  for collisions of  $t\mu$  atoms with  $D_2$  and  $DT$  molecules were determined as functions of target temperature  $T$ . Targets of widely varying tritium fraction  $C_t$  (but only two values of density  $\phi$ ) were used, where  $\phi = 0.45$  and  $0.60$  (relative to liquid-hydrogen density,  $4.25 \times 10^{22}$  atoms/cm<sup>3</sup>). We have now made measurements over a much larger range of  $\phi$  and have consequently discovered some new and unexpected phenomena: both  $\omega_s$  and  $\lambda_{d\mu-d}$  vary strongly with density  $\phi$ . These observations indicate clearly that in spite of extensive theoretical efforts<sup>5</sup> our understanding of muon-catalyzed  $dt$  fusion is still incomplete.

The experiment was performed using the methods described in the earlier reports.<sup>1,2</sup> In Fig. 2 we show the  $\phi$  dependence of the normalized muon-cycling rate  $\lambda_c \equiv \lambda_c^{obs}/\phi$  (where  $\lambda_c^{obs}$  is the observed cycling rate) for a

variety of temperatures and tritium fractions. It is conventional to normalize to liquid-hydrogen density because of the expectation that all relevant rates scale linearly with density. The cycling time ( $\equiv 1/\lambda_c^{obs}$ ) is dominated by the time the negative muon spends in the  $d\mu$ -atom ground state waiting to transfer to a triton (rate  $\phi\lambda_{dt}C_t$ ), and that spent in the  $t\mu$  ground state waiting for molecular formation to occur (rate  $\phi\lambda_{d\mu}C_d$ , where  $C_d$  is the deuterium fraction). Thus we write\*

$$\frac{\phi}{\lambda_c^{obs}} \equiv \frac{1}{\lambda_c} \simeq \frac{q_{1s}C_d}{\lambda_{dt}C_t} + \frac{1}{\lambda_{d\mu}C_d} \quad (1)$$

The product  $q_{1s}C_d$  is the probability that the muon will reach the  $d\mu$  ground state;  $q_{1s}$  will deviate from unity, both because of muon transfer to  $t$  from excited states of  $d\mu$  (Ref. 6) and because the initial atomic-capture ratio might differ somewhat from the ratio  $C_d/C_t$ .

At the time of the present experiment the only predicted source of  $\phi$  dependence was the factor  $q_{1s}$ . However, Fig. 2 shows clearly that, contrary to expectation, the  $\phi$  dependence is least at small  $C_t$ , where the first term of Eq. (1) is dominant, and is most when striking at large  $C_t$ , where the second term dominates. Hence we are forced to conclude that the normalized molecular-formation rate  $\lambda_{d\mu}$  increases with  $\phi$ . Thus  $dt\mu$  formation, which occurs via the resonance mechanism,<sup>7-10</sup> is probably not a purely two-body collision process as previously assumed.

\*Here all  $t\mu$  atoms are treated alike and hyperfine quenching effects are ignored.

Separating the contributions of the two terms in Eq. (1) is complicated by the possibility that  $q_{1s}$  may depend on both  $C_i$  and  $\phi$  and require further assumptions. Our procedure is first to estimate  $\lambda_{dt}$  from the high- $C_i$  data and  $\lambda_{dt}/q_{1s}$  from the low- $C_i$  data, and then to use these values as the starting point for a global fit.\* We assume that  $\lambda_{dt}$  depends only on  $T$  and that all residual dependence of  $\lambda_{dt}/q_{1s}$  on  $\phi$  and  $C_i$  is due to  $q_{1s}$ . In contrast to recent calculations of Menshikov and Ponomarev<sup>6</sup> (MP), who predict values  $q_{1s}^{MP}$  that fall precipitously with increasing  $C_i$  and  $\phi$ , our results suggest a relatively weak dependence on  $C_i$  and negligible dependence on  $\phi$ . For example, for  $C_i = 0.5$  and  $T = 300$  K, we obtain  $\lambda_{dt}/q_{1s} = (446 \pm 93) \times 10^6 \text{ s}^{-1}$  at  $\phi = 0.12$  and  $\lambda_{dt}/q_{1s} = (457 \pm 58) \times 10^6 \text{ s}^{-1}$  at  $\phi = 0.72$ , whereas MP predict an increase by over a factor of 2 ( $q_{1s}^{MP}$  decreasing from 0.195 to 0.085). Similarly, for  $C_i = 0.04$ ,  $T = 300$  K, and  $\phi = 0.72$ , we obtain  $\lambda_{dt}/q_{1s} = (328 \pm 25) \times 10^6 \text{ s}^{-1}$ . This is only a factor of  $\sim 1.5$  less than that at the higher  $C_i = 0.5$ , compared with the predicted decrease by a factor of  $\sim 7$  ( $q_{1s}^{MP} = 0.62$  for  $C_i = 0.04$ ).\*\*

On the other hand, our results for  $q_{1s}$  are consistent with recent experimental findings<sup>12</sup> for  $\pi^-$  capture in mixtures of hydrogen and deuterium at  $\phi \lesssim 0.11$ . Extrapolating from those results, which show no density dependence, we infer that  $q_{1s} \approx [1 - (1 - \gamma_1) C_x](\gamma_2)^{2C_x}$ , with  $\gamma_1 = 0.81 \pm$

$0.01$ ,  $\gamma_2 = 0.83 \pm 0.01$ , and  $x = d$  for a chemically equilibrated mix of  $\text{H}_2/\text{HD}/\text{D}_2$ . Then, using the same functional form to analyze our data, we find (now with  $x = t$ ) that  $\gamma_1 \approx \gamma_2 = 0.75 \pm 0.20$  and that  $\lambda_{dt} \approx [1 + (6 \pm 1) \times 10^{-4} T] (280 \pm 40) \times 10^6 \text{ s}^{-1}$  for the temperature range from 20 to 500 K. This value of  $\lambda_{dt}$  agrees with the low- $\phi$ , low- $C_i$  experiment of Bystritsky et al.<sup>4</sup> The temperature dependence is not quite as strong as that predicted,<sup>13</sup> but it shows the same trend.

The rate  $\lambda_{dt}$  has contributions from  $t\mu$  collisions with both  $\text{D}_2$  and  $\text{DT}$ , so that  $\lambda_{dt} = C_d \lambda_{dt-d} + C_t \lambda_{dt-t}$ .

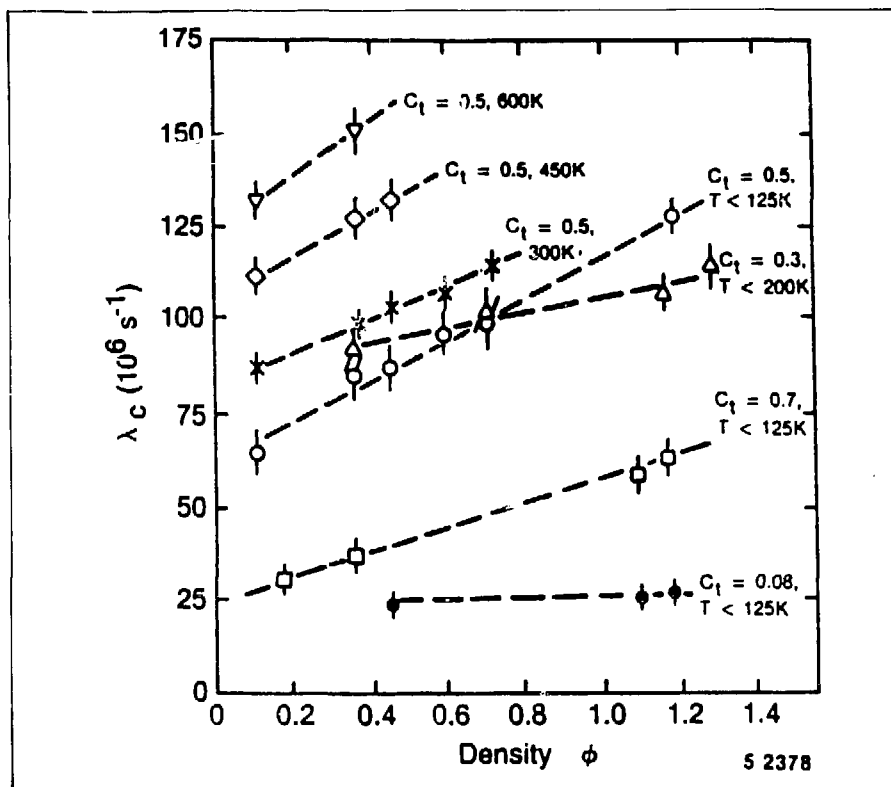


FIGURE 2. Dependence of the normalized cycling rate  $\lambda_c$  on the density  $\phi$  of the  $dt$  mixture. The data presented here and below may change slightly upon further data analysis.

\*Quoted errors reflect statistical uncertainty. A further 13% systematic uncertainty arises mainly from the uncertainty in neutron detection efficiency.

\*\*Including a three-body transfer mechanism gives values of  $q_{1s}$  that vary more drastically and hence worsen the discrepancy (see Ref. 11).

TABLE I Fitted Contributions to the  $dt\mu$  Formation Rate<sup>a</sup> (in units of  $10^6 \text{ s}^{-1}$ ). We assume that  $\lambda_{dt\mu} = C_d[\lambda_{dt\mu-d}^{(1)} + \lambda_{dt\mu-d}^{(2)}\phi] + C_t\lambda_{dt\mu-t}^{(1)} [C_t\lambda_{dt\mu-t}^{(2)}\phi \text{ is fixed at zero}]$ .

| $T$ (K) | $\lambda_{dt\mu-d}^{(1)}$ | $\lambda_{dt\mu-d}^{(2)}$ | $\lambda_{dt\mu-t}^{(1)}$ | $\lambda_{dt\mu-t}^{(2)}$ |
|---------|---------------------------|---------------------------|---------------------------|---------------------------|
| <130    | $206 \pm 29$              | $450 \pm 50$              | $26 \pm 6$                | ...                       |
| 300     | $306 \pm 43$              | $287 \pm 67$              | $92 \pm 19$               | ...                       |
| 400-500 | $347 \pm 52$              | $275 \pm 120$             | $225 \pm 21$              | ...                       |

<sup>a</sup>Quoted errors reflect statistical uncertainty. A further 13% systematic uncertainty arises mainly from the uncertainty in neutron detection efficiency.

We write  $\lambda_{dt\mu-x} = \lambda_{dt\mu-x}^{(1)} + \lambda_{dt\mu-x}^{(2)}\phi$ , the superscripts indicating the power of  $\phi$  appearing in the observed (rather than normalized)  $dt\mu$  formation rates. A global fit with all four terms present shows that the  $\lambda_{dt\mu-t}^{(2)}$  values are consistent with zero. Fitting with  $\lambda_{dt\mu-t}^{(2)}$  constrained to be zero gives the values shown in Table I and the  $\lambda_{dt\mu-d}(\phi)$  for  $T < 130$  K shown in Fig. 3. We conclude that our data show a strong linear  $\phi$  dependence for (normalized)  $\lambda_{dt\mu-d}$ , but not for  $\lambda_{dt\mu-t}$ . The large values of  $\lambda_{dt\mu-d}^{(2)}$  are

evidence of significant resonant  $dt\mu$  formation via three-body collisions.

Menshikov and Ponomarev<sup>14</sup> have recently discussed a mechanism for three-body resonant molecular formation—for example,  $t\mu + D_2 + D_2 \rightarrow [(dt\mu)d2e]^* + D_2 + \Delta E$ . The singlet  $t\mu + D_2$  collisions are special, in having their strongest resonances just below threshold where they are not accessible in two-body collisions.<sup>9</sup> By absorbing some kinetic energy, the spectator molecule ( $D_2$ ,  $DT$ , or  $T_2$ ) moves

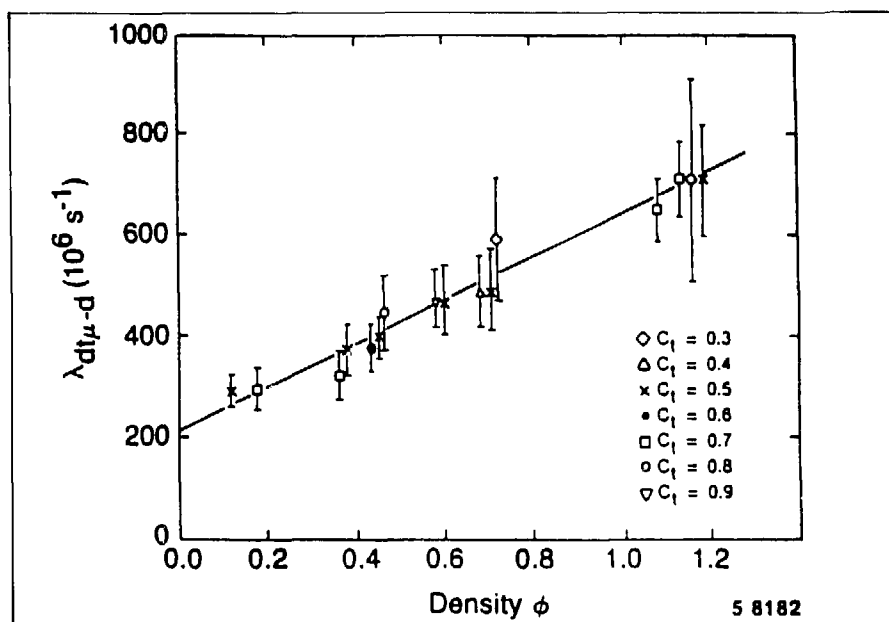


FIGURE 3. Density dependence of the normalized molecular formation rate  $\lambda_{dt\mu-d}$  for  $T < 130$  K, assuming that  $\lambda_{dt\mu-t}$  is density independent. The solid line is a fit to the data (see Table I).

these strong resonances above threshold, allowing them to contribute to molecular formation.

We turn now to the mechanisms of muon loss from the catalysis cycle. The muon may be captured and retained by a helium nucleus synthesized during  $dt\mu$ ,  $dd\mu$ , or  $tt\mu$  fusion, with sticking probabilities  $\omega_s$ ,  $\omega_d$ , and  $\omega_t$ , respectively. The muon may also be scavenged by  ${}^3\text{He}$  introduced by tritium decay (normally  $C_{\text{He}} \ll 0.01$ ). The total muon-loss probability per cycle can be written as<sup>1,5</sup>

$$\begin{aligned}
 w \approx & \frac{q_{15} C_d}{\lambda_{dt} C_t + \lambda_{dd\mu} C_d} \\
 & \times \left\{ 0.58 \lambda_{dd\mu} C_d \omega_d + \lambda_{d\text{He}} C_{\text{He}} \right\} \\
 & + \frac{1}{\lambda_{dt\mu} C_d} \left\{ \lambda_{tt\mu} C_t \omega_t + \lambda_{t\text{He}} C_{\text{He}} \right\} \\
 & + C_{\text{He}} \omega_{\text{He}} + \omega_s^{\text{eff}}, \quad (2)
 \end{aligned}$$

where  $\lambda_{dd\mu}$  and  $\lambda_{tt\mu}$  are the rates for  $dd\mu$  and  $tt\mu$  molecular formation,  $\lambda_{d\text{He}}$  and  $\lambda_{t\text{He}}$  are the rates for transfer to  ${}^3\text{He}$  from the  $d\mu$  and  $t\mu$  ground states, and  $\omega_{\text{He}}$  is the probability for initial capture by  ${}^3\text{He}$ . The  $\omega_s^{\text{eff}}$  is then the effective sticking probability for the  $dt\mu$  fusion reaction.

It follows from Eq. (2) that  $dd\mu$  fusion shows up in our experiment as an increase in  $w$  for low- $C_t$  targets, permitting us to evaluate the product  $\lambda_{dd\mu} \omega_d$  at different temperatures. Because  $\omega_d$  has been measured independently,\* we are able to extract

$\lambda_{dd\mu}$  as a function of temperature, as shown in Fig. 4. Our results agree well with the room-temperature measurement of  $\lambda_{dd\mu}$  of Balin et al.<sup>15</sup> and, except for normalization, with earlier data<sup>15</sup> over the range from 50 to 400 K. Similarly, assuming that the observed temperature dependence of  $w$  for high- $C_t$  targets is due to the temperature dependence of  $\lambda_{dd\mu}$ , we evaluate the corresponding product for  $tt\mu$  fusion,  $\lambda_{tt\mu} \omega_t = (0.4 \pm 0.1) \times 10^6 \text{ s}^{-1}$ . Muon losses resulting from scavenging by  ${}^3\text{He}$  are evaluated by noting the increase in  $w$  with time as  ${}^3\text{He}$  builds up from tritium decay.

Subtracting from  $w$  the contributions discussed above yields  $\omega_s^{\text{eff}}$ , which depends on density and tritium fraction, as shown in Fig. 5. The striking variation with  $\phi$  and  $C_t$  was completely unexpected. Furthermore, the observed value of  $\omega_s^{\text{eff}}$ , as small as 0.3% and still decreasing

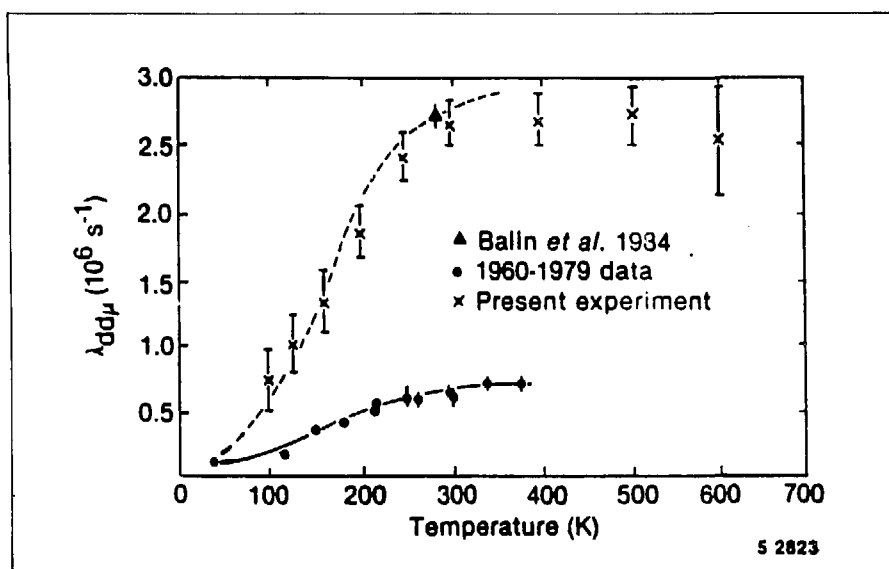


FIGURE 4 Temperature dependence of the  $dd\mu$  formation rate  $\lambda_{dd\mu}$  (using  $\omega_d \approx 0.122$  from Ref. 15), from data with  $C_t < 13\%$ . The solid line is a theoretical fit (Ref. 7) to earlier data (circles); renormalization yields the dashed curve.

\*For earlier measurements of  $\lambda_{dd\mu}$ , see Ref. 15

at high density, is much smaller than the calculated value<sup>16</sup> of 0.9% for  $\alpha$  sticking accepted before the present experiment. (The calculated sticking fraction is the product of the probability that the muon is initially captured by the recoiling-fusion  $\alpha$  particle,  $\omega_s^0 \approx 1.2\%$ , with the conditional probability that the muon is not subsequently stripped,  $1 - R \approx 0.75$ .) More accurate calculations<sup>17</sup> of initial sticking have very recently reduced this estimate by 25 to 33%, but the resulting values still significantly exceed our high-density  $\omega_s^{\text{eff}}$  results.\*

The variation of  $\omega_s^{\text{eff}}$  could come from events (1) preceding or (2) following the nuclear fusion. Under (2), the most likely origin is the muon-stripping process. Although the value of  $R$  is somewhat uncertain, it is not expected<sup>19</sup> to have nearly as much dependence on  $\phi$  or  $C_t$  as implied by Fig. 5. Under (1), a certain fraction of the muons may be delayed after molecular formation but before fusion, thus increasing  $\omega_s^{\text{eff}}$  above a small initial sticking value.<sup>20</sup> The  $dt\mu$  system, initially formed in the ex-

cited  $J=1, v=1$  state, needs to cascade via Auger transitions to a  $J=0$  state for fusion to be rapid. Possibly this cascade may be facilitated by electrons supplied by ionization induced by tritium decay.<sup>21</sup> The sensitivity to  $\phi$  and  $C_t$  could then come from the ion-electron recombination process, whose rate is proportional to  $\phi\sqrt{C_t}$ . This model also encounters some difficulties.<sup>20</sup> Clearly, further study is needed to determine which, if either, of these ideas can explain the observed dependence of  $\omega_s^{\text{eff}}$ .

With the experimental  $\omega_s^{\text{eff}}$  well below predicted values, 300 or more fusions per muon might be possible. We have already detected an average value of  $160 \pm 4$  (statistical)  $\pm 20$  (systematic) fusions per muon, releasing about 3 GeV of energy, in a liquefied  $dt$  target with  $C_t = 0.3$ .

In summary, we have discovered some completely unexpected target density dependences in both the  $dt\mu$  molecular-formation rate  $\lambda_{dm-d}$  and the effective sticking probability  $\omega_s^{\text{eff}}$ . The former is presumably due to three-body contributions to resonant mesomolecular formation. The origin of the latter is much less clear.

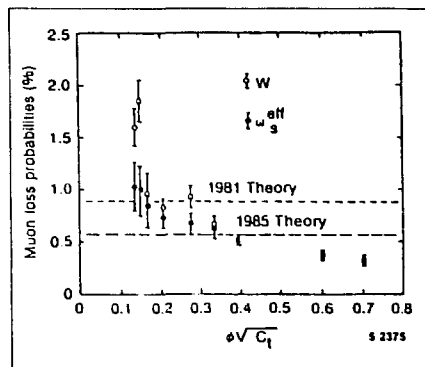


FIGURE 5. Dependence of  $\omega_s^{\text{eff}}$  on  $\phi\sqrt{C_t}$  for  $C_t \leq 0.3$ . The uncorrected values  $\omega_s^0$  are also shown. The data are consistent with  $\omega_s^{\text{eff}} = (23 \pm 10) + (419 \pm 34)\phi\sqrt{C_t}$  for  $\phi \leq 1.3$ .

\*Rafelski and Müller have suggested that the energy dependence of the nuclear absorption amplitude leads to a small value of the initial sticking (see Ref. 18).

---

## References

1. S. E. Jones et al., *Physical Review Letters* **51**, 1757 (1983).
2. A. J. Caffrey et al., "Experimental Investigation of Muon-Catalyzed Fusion in High-Density Deuterium-Tritium Mixtures," *Muon-Catalyzed Fusion Workshop*, Jackson Hole, Wyoming, June 7-8, 1984, pp. 53-67; and A. N. Anderson, "Muon Catalyzed Fusion Data Analysis," *Muon-Catalyzed Fusion Workshop*, Jackson Hole, Wyoming, June 7-8, 1984, pp. 68-74.
3. W. H. Breunlich et al., *Physical Review Letters* **53**, 1137 (1984).
4. V. M. Bystritsky et al., *Zhurnal Eksperimental'noi i Teoreticheskoi Fiziki* **80**, 1700 (1981) [*Soviet Physics-JETP* **53**, 877 (1981)].
5. L. I. Ponomarev, *Atomkernenergie Kerntechnik* **43**, 175 (1983).
6. L. I. Menshikov and L. I. Ponomarev, *Pis'ma Zhurnal Eksperimental'noi i Teoreticheskoi Fiziki* **39**, 542 (1984) [*JETP Letters* **39**, 663 (1984)].
7. S. I. Vinitsky et al., *Zhurnal Eksperimental'noi i Teoreticheskoi Fiziki* **74**, 849 (1978) [*Soviet Physics-JETP* **47**, 444 (1978)].
8. M. Leon, *Physical Review Letters* **52**, 605 (1984).
9. J. S. Cohen and R. L. Martin, *Physical Review Letters* **53**, 738 (1984).
10. J. S. Cohen and M. Leon, *Physical Review Letters* **55**, 52 (1985).
11. L. I. Menshikov and L. I. Ponomarev, *Pis'ma Zhurnal Eksperimental'noi i Teoreticheskoi Fiziki* **42**, 12 (1985) [*Soviet Physics-JETP* **42**, 13 (1985)].
12. K. A. Aniol et al., *Physical Review A* **28**, 2684 (1983).
13. A. V. Matveenko and L. I. Ponomarev, *Zhurnal Eksperimental'noi i Teoreticheskoi Fiziki* **59**, 1593 (1970) [*Soviet Physics-JETP* **32**, 871 (1971)].
14. L. I. Menshikov and L. I. Ponomarev, "Quasi-Resonant Formation of  $d\mu$  Mesic Molecules in Triple Collisions" (submitted to *Physics Letters B*).



15. D. V. Balin et al., *Pis'ma Zhurnal Eksperimental'noi i Teoreticheskoi Fiziki* **40**, 318 (1984) [*JETP Letters* **40**, 1112 (1984)], and references therein.
16. S. S. Gershtein et al., *Zhurnal Eksperimental'noi i Teoreticheskoi Fiziki* **80**, 1690 (1981) [*Soviet Physics-JETP* **53**, 872 (1981)]; and L. Bracci and G. Fiorentini, *Nuclear Physics* **A364**, 383 (1981).
17. D. Ceperley and B. J. Alder, *Physical Review A* **31**, 1999 (1985); and L. N. Bogdanova et al., JINR preprint E4-85-425, Dubna, USSR (1985).
18. J. Rafelski and B. Müller, *Physics Letters* **164B**, 223 (1985).
19. L. I. Menshikov and L. I. Ponomarev (to be published in *Pis'ma Zhurnal Eksperimental'noi i Teoreticheskoi Fiziki*).
20. J. S. Cohen and M. Leon, "Target Dependence of the Effective Sticking Probability in Muon-Catalyzed *dt* Fusion," *Physical Review A* **33**, 1437 (1986).
21. P. C. Souers, E. M. Fearon, and R. T. Tsugawa, *Journal of Vacuum Science and Technology A* **3**, 29 (1985).

## MATERIALS SCIENCE

EXPERIMENT 842 — SMC

**Muon-Spin-Relaxation and Knight-Shift Studies of Itinerant Magnets and Heavy-Fermion Materials**

Los Alamos Univ. of California at  
Riverside, Texas Technol. Univ. of  
Columbing Univ. of Alaska Fair

Spokesmen: D. W. Cooke and R. H. Heffner (Los  
Alamos) and D. E. MacLaughlin (Univ. of  
California, Riverside)

**Introduction**

**Heavy Fermions.** The focus of Exp. 842 during the last year has been on measurements of the Knight-shift and zero-field relaxation rate in the heavy-fermion (HF) materials  $U_{1-x}Th_xBe_{13}$  ( $x = 0.00$  and  $0.033$ ) and  $UPt_3$ . These materials belong to a larger class of heavy-electron systems (including rare earth compounds) that exhibit a number of fascinating new properties,<sup>1</sup> a few of which are mentioned here.

1. HF materials possess a large low-temperature susceptibility ( $\chi$ ) and a large linear coefficient of electronic specific heat ( $\gamma$ ), indicating an effective mass of  $\sim 200 m_e$ , where  $m_e$  is the free-electron mass. Curiously, the Wilson ratio ( $\sim \chi/\gamma$ ), which is identically 1 for free electrons, is also  $\approx 1$  for the heaviest HF systems.
2. At high temperatures most of the HF materials exhibit a Curie-law susceptibility with a nonintegral number of Bohr magnetons, suggesting itinerant magnetism.
3. By contrast, the total entropy per uranium atom is large ( $S/R \sim \ln 2$  in  $UBe_{13}$ ), suggesting highly localized electronic excitations.
4. "Clean" HF systems have a resistivity that is relatively small near  $T = 0$  and that increases with increasing temperature, indicating the formation of a coherent electronic state involving hybridized  $f$  and conduction-band electrons.

These HF properties seem related to those of the single-impurity Kondo and mixed-valence systems, and single-impurity models are often used as a starting point for theories of heavy-electron materials.<sup>2</sup> The major challenge is to understand what new physics is required in the HF state.

In addition to having unusual normal-state properties, three HF systems ( $CeCu_2Si_2$ ,  $UPt_3$ ,  $UBe_{13}$ , and related compounds) undergo superconducting transitions that are unique in themselves. Because the discontinuity in the specific heat at  $T_c$  is comparable to that of the electronic specific heat, it is believed that the heavy electrons themselves become superconducting and thus are delocalized at low temperatures. In conventional BCS superconductors the energy gap is only weakly anisotropic; therefore, transport, specific heat, and spin-relaxation measurements are exponentially activated below  $T_c$ . By contrast, HF superconductors exhibit power-law ( $\sim T^n$ ) behaviors<sup>3,5</sup> below  $T_c$ , indicating a finite quasi-particle density of states at the Fermi level even at  $T = 0$ ; that is, the gap vanishes in certain regions of the Fermi surface. In analogy with  $^3He$ , one suspects that HF superconductors may exhibit both unconventional pairing and, further, that the superconducting interaction is purely electronic rather than electron-phonon in nature. Theories of HF superconductivity are complicated by a presumably strong spin-orbit interaction, band-structure effects, and strong coupling.<sup>2</sup> Regarding the last point, the characteristic energy ( $kT_0$ ) for the onset of the HF

state is in the range from 10 to 100 K, so that  $T_c/T_0 > 10^{-2}$  and  $\theta_D/T_0 \sim 1$ , where  $\theta_D$  is the Debye temperature. In normal metals the Fermi temperature  $T_F$  is large, so that  $T_c/T_F < 10^{-3}$  and  $\theta_D/T_F < 10^{-2}$ .

**Muon-Spin Relaxation ( $\mu$ SR) as a Probe of the HF State.** Measurements of the muon Knight shift allow a microscopic determination of the local-spin susceptibility  $\chi$  and thus are an excellent probe of both the normal ( $\chi_n$ ) and superconducting ( $\chi_s$ ) properties of the HF state. In the superconducting state, for example,  $\chi$  is sensitive to the type of spin pairing present.<sup>6</sup> For an even-parity (BCS) state, one has spin-singlet pairing, and thus  $\chi_s(T=0)$  vanishes in the absence of spin-orbit coupling. For odd-parity spin-triplet superconductivity,  $\chi_s(0) = \chi_n$  (as in anisotropic  $^3\text{He} - A$ ), or  $\chi_s(0) < \chi_n$  (as in isotropic  $^3\text{He} - B$ ). It is also known that, for  $^3\text{He}$ , strong Fermi-liquid corrections<sup>7</sup> reduce  $\chi_s(0)$ . Below, we discuss our measurements of the Knight shift in  $\text{U}_x\text{Th}_{1-x}\text{Be}_{13}$ . Measurements on  $\text{UPt}_3$  are in progress.

In addition to probing the spin susceptibility, muon-spin relaxation ( $\mu$ SR) is a sensitive tool to measure local magnetic field distributions and can therefore be used to detect the onset of magnetic order. Zero-field  $\mu$ SR was reported last year in  $\text{UPt}_3$ ; this year these studies have been extended to  $\text{U}_{1-x}\text{Th}_x\text{Be}_{13}$ .

## Sample Materials and Experimental Technique

The samples were prepared by J. L. Smith (Los Alamos, Group MST-5).  $\text{UBe}_{13}$  exhibits a superconducting transition at  $T_c \sim 0.86$  K, as determined for our samples by ac susceptibility.  $\text{U}_{1-x}\text{Th}_x\text{Be}_{13}$  shows<sup>8</sup> two superconducting transitions for  $0.02 < x < 0.05$ . For  $x = 0.033$ ,  $T_c \simeq 0.60$  and  $0.40$  K. Ultrasound attenuation measurements have been interpreted<sup>9</sup> in terms of an itinerant antiferromagnetism (AFM) transition that sets in below  $T_c$ . Nuclear magnetic resonance (NMR) measurements<sup>5</sup> have not detected such a transition, however, and place an upper limit of  $\simeq 0.01$  Bohr magnetons for any possible magnetism.

The data were collected with the LAMPF  $\mu$ SR spectrometer using 80-MeV/ $c$ -momentum backward-decay muons and applied transverse fields  $H$  between 0 and 5000 Oe. In the zero-field configuration the field at the sample was zeroed to within 10 mOe using earth coils. The  $\mu$ SR dilution refrigerator<sup>10</sup> was used for the temperature range from 0.33 to 3 K, and a conventional helitron cryostat was used for  $T > 3$  K.

The  $\mu$ SR time histograms were collected over the time range of 8 to 12  $\mu$ s, depending on the experiment, and the Knight-shift spectra were analyzed in both time and frequency (Fourier transform) domains. A standard copper sample at room temperature was used as an absolute frequency standard, and copper runs

were usually taken before and after runs on  $U_{1-x}Th_xBe_{13}$  (copper has a measured<sup>11</sup> Knight shift of +60 ppm). In addition, the field stability during each run was monitored with an NMR probe located near, but outside, the vacuum jacket of the cryostat. The shunt voltage for the magnet power supply was also monitored during each run. Nonlinearities and drifts in the time-to-amplitude and analog-to-digital converters used to histogram the time spectra were monitored before and after each data run. As a result of these checks, systematic uncertainties in the measured absolute frequency shifts were less than  $1:10^{-4}$  in the frequency range of interest, about 65 MHz. The statistical uncertainties were in the range from 200 to 400 ppm.

In transverse field a two-line frequency spectrum was observed, one line-shifted and one unshifted. It was determined in auxiliary experiments that the unshifted line was due largely to muon stops in the cryostat. At high transverse magnetic fields the momentum spread for the muons entering the sample region is such that some muons miss or are scattered from the sample because of differing radii of curvature in the applied field. This problem should be completely eliminated next year when the spin rotator is installed, because the beam will enter the spectrometer parallel to the field axis.

In addition to the frequency calibrations, the Knight-shift data must be corrected for demagnetization effects in both the normal and the superconducting states. In the

normal state, one has for an ellipsoidal sample

$$K_0^j = K_i^j - 4\pi\chi^j(1/3 - n^j), \quad (1)$$

where  $K_0^j$  and  $K_i^j$  are the observed and intrinsic shifts, respectively,  $\chi^j$  is the bulk susceptibility, and  $n^j$  is the demagnetization factor ( $n = 1/3$  for a sphere). The superscript  $j$ 's refer to the Cartesian coordinates of the ellipsoidal axes  $x$ ,  $y$ , and  $z$ . Our samples roughly approximate ellipsoids, so that by using the measured  $\chi_{bulk}$  and approximating  $n$  we find that  $4\pi\chi(1/3 - n) < 10^{-4}$  in dimensionless units ( $UBe_{13}$  is a cubic material, so that  $\chi^x \sim \chi^y \sim \chi^z$ ).

In the superconducting state a diamagnetic shift is produced due to circulating superconducting currents. The effect of this is to always reduce the measured Knight shift; however, a quantitative estimate of this shift can only be made if the magnetization in the superconducting state has been measured. To date no such experiments have been published for  $U_{1-x}Th_xBe_{13}$ . The correction depends on the sample shape, as in the normal state. These effects are discussed further under Results.

Finally, we note that the intrinsic Knight shift itself may be anisotropic, either because of an anisotropic local susceptibility (produced by lattice or crystal-field structure, for example) or because of an anisotropic  $\mu^+$  ion interaction, such as for dipolar coupling. For our preliminary analysis, we ignore the former, noting the  $UBe_{13}$  is a cubic material.

## Results

**Zero-Field Studies.** The zero-field linewidth in  $UBe_{13}$  for  $0.3 \text{ K} < T < 10 \text{ K}$  was temperature independent, with a value of  $\sigma \sim 0.20 \mu\text{s}^{-1}$ . We have performed lattice-sum calculations for nuclear dipolar broadening, assuming several sites, and find that the calculations are consistent with the  $\mu^+$  occupying a single site of octahedral symmetry in the  $UBe_{13}$  lattice. For the  $x = 0.033$  sample,  $\sigma \approx 0.23 \mu\text{s}^{-1}$  for  $0.33 < T < 0.7 \text{ K}$ , as shown in Fig. 1. The origin of the slightly higher value for  $x = 0.033$  is not known (thorium is mono-isotropic with no nuclear moment). It may be that the addition of a few per cent thorium causes a slight shift in the  $\mu^+$  equilibrium site position.

**Knight Shifts.** An analysis of the  $\mu^+$  Knight shifts is shown in Figs. 2 and 3. Several results are apparent: (1) the shift is large and negative; (2) the shift tracks our measured susceptibilities for  $4 < T < 100 \text{ K}$ , but deviates for  $T > 100 \text{ K}$ ; and (3) there is a pronounced temperature dependence of the shift in the superconducting state for  $x = 0.00$  but not for  $x = 0.033$ . We discuss these results in turn.

The large ( $>0.1\%$ ) Knight shift means that all the corrections to the raw data in the normal state are of the order of 10% or less. Thus we feel confident that we have measured  $K_\mu$  reasonably well. (The error bars shown in the figures are statistical.) The negative value is probably due to core-polarization effects produced by different radial dependences in the

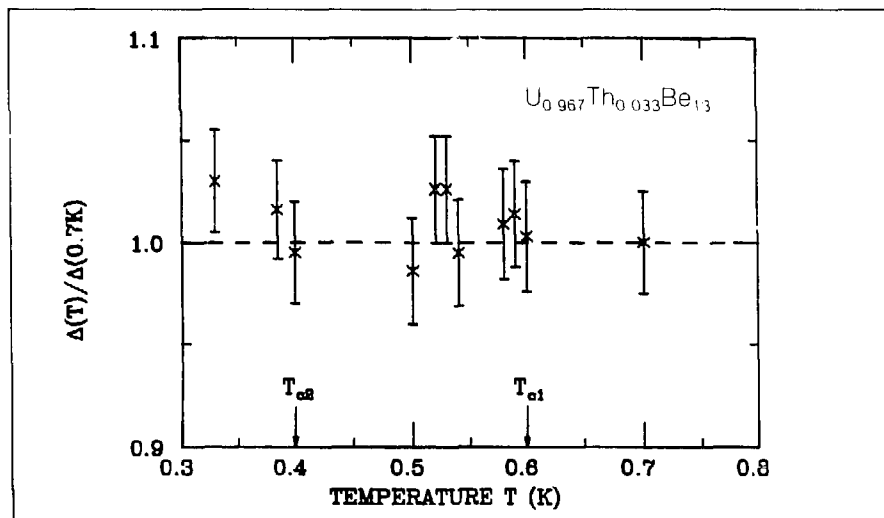


FIGURE 1 Temperature dependence of the zero-field  $\mu^+$  Gaussian relaxation rate  $\Delta$  relative to the value  $0.23 \pm 0.03 \mu\text{s}^{-1}$  at  $T = 0.7 \text{ K}$ . The transition temperatures  $T_{c1}$  (superconducting) and  $T_{c2}$  are indicated by arrows. An upper bound of  $\sim 0.1 \text{ Oe}$  is placed by these data on any increase in  $\mu^+$  local field between  $0.3 \text{ K}$  and  $T_{c2}$ .

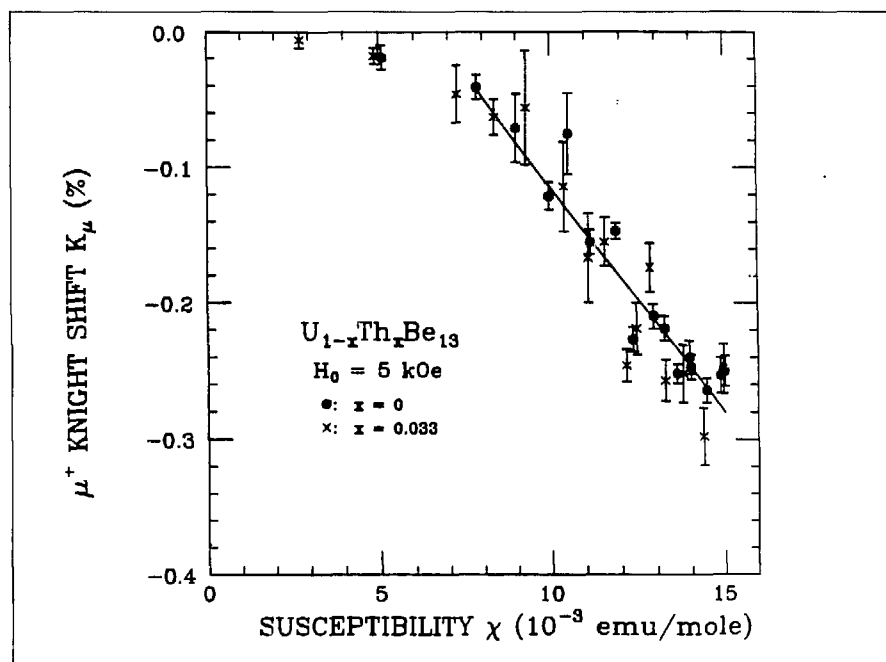


FIGURE 2 Dependence of  $\mu^+$  Knight shift  $K_\mu$  on bulk paramagnetic susceptibility  $\chi$  in  $U_{1-x}Th_xBe_{13}$ ,  $x = 0$  and  $0.033$ , applied field  $H_0 = 5 \text{ kOe}$ . Temperature is an implicit variable. The straight line is a least-squares fit to the data for  $\chi \geq 8 \times 10^{-3} \text{ emu/mole}$ , and yields a hyperfine field  $H_{hf} = -1.84 \pm 0.13 \text{ kOe}/\mu_B$ .

spin-up and spin-down densities at the  $\mu^+$  site. Negative  $\mu^+$  shifts have been seen in other materials—palladium, for example.<sup>11</sup> Although the diamagnetic corrections in the superconducting state have not been made, we note that, because they must be negative, the increasingly positive Knight shift below  $T_c$  in  $\text{UBe}_{13}$  must be intrinsic and thus the diamagnetic corrections are small. Moreover, both specimens ( $x = 0$  and  $x = 0.033$ ) are extreme

type II superconductors for which mixed-state diamagnetism is small, so that the differences seen in the Knight shifts in these two materials below  $T_c$  are intrinsic.

The temperature dependence of  $K_i$  can be modeled as

$$K_i(T) = \alpha\chi_1 + \beta\chi_{orb} + \delta\chi_f(T), \quad (2)$$

where  $\chi_1$  is the contribution from  $s$ -like electrons,  $\chi_{orb}$  is an orbital term (analogous to the Van Vleck susceptibility), and  $\chi_f(T)$  is due to the heavy ( $5f$ -like) electrons. Both  $\chi_1$  and  $\chi_{orb}$  are taken to be temperature-independent. The fact that  $K_i(T)$  tracks the bulk susceptibility for  $T < 100$  K ( $\chi_{bulk} > 8$  emu/mole) means that we are sampling the heavy electrons in this regime. From the slope of the  $\chi_{bulk}$  versus  $K_i(T)$ , we obtain a hyperfine field of  $-1.84 + 0.13$  kOe/ $\mu_B$ . We do not understand, however, why  $K_i(T)$  breaks away from  $\chi_{bulk}(T)$  at the higher temperatures ( $\chi_{bulk} < 8$  emu/mole). A plot of  $\chi_{bulk}$  versus  $1/T$  reveals a temperature-independent contribution of  $\approx 1 \times 10^{-3}$  emu/mole. We note that a similar value was obtained<sup>10</sup> years ago, from  $^{27}\text{Al}$  NMR on  $\text{UAl}_2$ , and associated with  $\chi_{orb}$ .

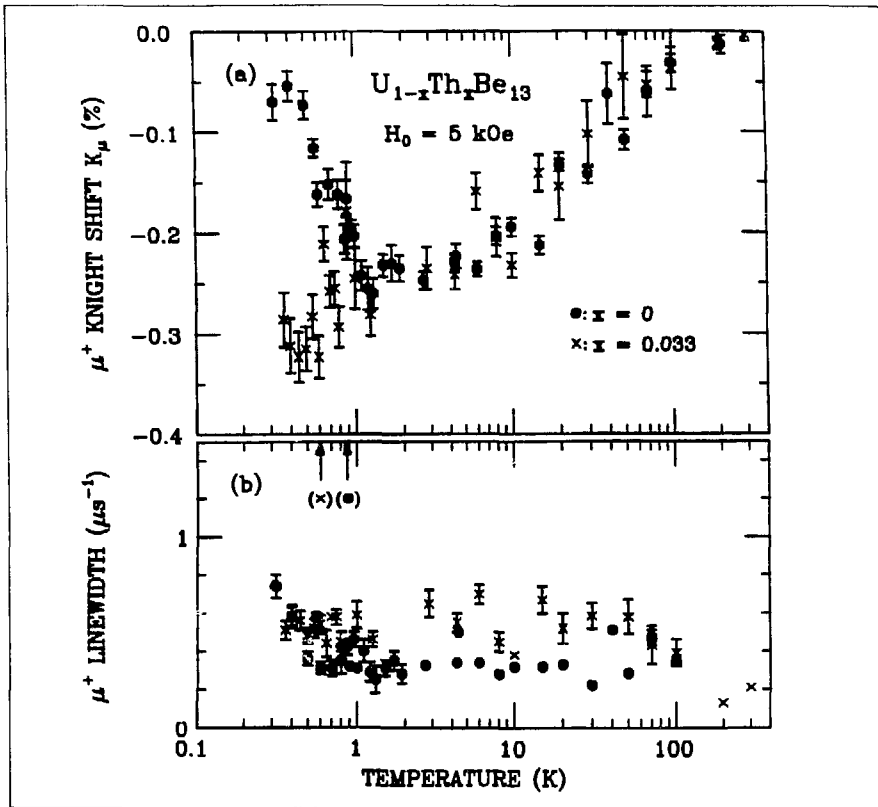


FIGURE 3.

- (a) Temperature dependence of the  $\mu^+$  Knight shift  $K_\mu$  between 0.3 and 300 K in  $\text{U}_{1-x}\text{Th}_x\text{Be}_{13}$ ,  $x = 0$  and 0.033, applied field  $H_0 = 5$  kOe. The superconducting transition temperatures are indicated by arrows, labeled by the symbols in parentheses.
- (b) Temperature dependence of  $\mu^+$  Gaussian linewidth  $\sigma$ ; conditions are the same as in (a).

## Discussion

**Zero-Field Relaxation.** In  $\text{UBe}_{13}$  the magnitude of the linewidth  $\sigma$  allows a determination of the likely  $\mu^+$  site, as discussed above. The fact that the width is independent of temperature means that the  $\mu^+$  is stationary. In  $\text{U}_{0.967}\text{Th}_{0.033}\text{Be}_{13}$  the absence of a change in  $\sigma$  down to  $T/T_{c2} \approx 0.83$  allows one to set an upper bound to the magnitude of any quasi-static local field produced by itinerant antiferromagnetism (AFM). A commensurate AFM order of wavelength equal to the muon site spacing could cancel the local field by symmetry, but an ordinary commensurate spin-density wave requires both a particular balance of electron/atom ratio with band structure<sup>12</sup> and a perfectly symmetric  $\mu^+$  site. These cannot be completely ruled out, but seem unlikely *a priori*. In the absence of such cancellation we find that any AFM moment must be less than  $10^{-4} \mu_B$ . This limit is about 100 times lower than the upper bound<sup>5</sup> set by  $^9\text{Be}$  NMR.

**Knight Shifts.** The most unambiguous and important fact derived from these data is that the two superconducting states in the  $(\text{U,Th})\text{Be}_{13}$  system (one for  $x = 0$  and one for

$x = 0.033$ ) seem to be qualitatively different, as reflected in the different temperature dependences of  $K_{\mu}$  below  $T_c$ . This fact leads directly to the conclusion that the superconducting-order parameter in the  $(\text{U,Th})\text{Be}_{13}$  system is not likely to be of the conventional, isotropic BCS type, which does not allow two distinct superfluid phases.

We now address the temperature dependence of the Knight shift in pure  $\text{UBe}_{13}$ . The earliest NMR Knight shifts<sup>6</sup> in the BCS superconductors aluminum and mercury showed  $\chi_s(0)/\chi_n \approx 0$  and  $\chi_s(0)/\chi_n \approx 0.7$  to 0.8, respectively, the difference being attributed to a large spin-orbit interaction in mercury, coupled with samples whose geometrical dimensions were smaller than the superconducting coherence length. Thus, Cooper pairs reflected from the sample surfaces had their spins flipped by the spin-orbit interaction, and so the zero-temperature susceptibility remained large. Because spin-orbit coupling is strong in uranium-derived wave functions, spin-orbit scattering would be expected to increase  $\chi_s(0)$  substantially, if this material exhibits conventional BCS pairing. This was not observed, which suggests unconventional pairing.

---

## References

1. G. R. Stewart, *Reviews of Modern Physics* **56**, 755 (1984).
2. P. A. Lee, T. M. Rice, J. W. Serene, L. J. Shan, and J. W. Wilkins, "Theories of Heavy-Electron Systems" (to be published in *Comments on Solid State Physics*).
3. D. Jaccard, J. Flouquet, P. Lejay, and J. L. Tholence, *Journal of Applied Physics* **57**, 3062 (1985).
4. H. R. Ott et al., *Physical Review Letters* **52**, 1915 (1984).
5. D. E. MacLaughlin, C. Tien, W. C. Clark, M. D. Lan, Z. Fisk, J. L. Smith, and H. R. Ott, *Physical Review Letters* **53**, 1833 (1984).
6. R. Meservey and B. B. Schwartz, in *Superconductivity*, R. D. Parks, Ed. (Marcel Dekker, Inc., New York, 1969), p. 118; and D. E. MacLaughlin, *Solid State Physics* **31**, 1 (1976).
7. A. J. Leggett, *Review of Modern Physics* **47**, 331 (1975).
8. H. R. Ott, H. Rudigier, Z. Fisk, and J. L. Smith, *Physical Review B* **31**, 1651 (1985).
9. B. Batlogg, D. Bishop, B. Golding, C. M. Varma, Z. Fisk, J. L. Smith, and H. R. Ott, *Physical Review Letters* **55**, 1319 (1985).
10. D. W. Cooke, J. K. Hoffer, M. Maez, W. A. Steyert, and R. H. Heffner, "A Dilution Refrigerator for a Muon-Spin Relaxation Experiment" (to be published in *Review of Scientific Instruments*).
11. A. Schenck, *Helvetica Physica Acta* **54**, 471 (1981).
12. W. C. Koehler, R. M. Moon, A. L. Trego, and A. R. Mackintosh, *Physical Review* **151**, 405 (1966).



The results of muon-spin-relaxation ( $\mu$ SR) experiments in the magnetic oxides, including oxide spin glasses, have been particularly fruitful this past year, resulting in several refereed publications and conference contributions. The effort has been directed into three main areas:

1.  $\mu$ SR study of the dynamics of the magnetic environment in magnetite ( $\text{Fe}_3\text{O}_4$ ) in the temperature region near 247 K where the reported anomalous transition in the local muon field and depolarization rate occurs,
2. a new experimental study on the oxide spin-glass  $\text{Fe}_2\text{TiO}_5$  (pseudobrookite), and
3. further theoretical work on the muon site in karelianite ( $\text{V}_2\text{O}_3$ ).

Details of these investigations are given below. These show clearly that the muon provides a sensitive probe of the dynamic processes in magnetic materials on the atomic scale and that, particularly in magnetite, it is one of the most sensitive experimental tools available.

### Magnetite ( $\text{Fe}_3\text{O}_4$ )

As described in detail in our latest publications,<sup>1,2</sup> the Mott-Wigner glass state in  $\text{Fe}_3\text{O}_4$  has been firmly established for temperatures above the Verwey transition (125 K). Much of the work this year was devoted to a study of the muon hyperfine field and depolarization anomaly at 247 K. The origin of this anomaly has been of considerable interest since its discovery<sup>3</sup> by  $\mu$ SR measurements.

We have now come much closer to an understanding of this effect. Data taken over a year ago<sup>4</sup> showed that the dynamical fluctuation of the magnetic environment is slower than the muon precession frequency below 247 K, and faster above that temperature (see also the LAMPF Progress Report for 1984, Ref. 4). This result prompted additional external-field measurements, which were performed this year.

Figure 1 shows the results of the application of a field of 2500 and 720 Oe as the temperature was varied across the anomaly at 247 K. As can be seen for  $B_{\text{ext}} \parallel \langle 110 \rangle$  above 247 K, only one frequency (that is, one magnetic muon site) is observed, whereas below this temperature two frequencies (sites) are observed.

EXPERIMENTS 639 and  
854 — SMC

### Muon-Spin Relaxation ( $\mu$ SR) in Select Magnetic Oxides and Oxide Spin Glasses

Texas Tech Univ., Univ. of Wyoming, Los Alamos, Technical Univ. of Eindhoven in The Netherlands

Spokesmen (Exp. 639): C. Boekema (Texas Tech Univ.), A. B. Denison (Univ. of Wyoming), and D. W. Cooke (Los Alamos)

Spokesmen (Exp. 854): C. Boekema and R. L. Lichti (Texas Tech Univ.) and D. W. Cooke (Los Alamos)

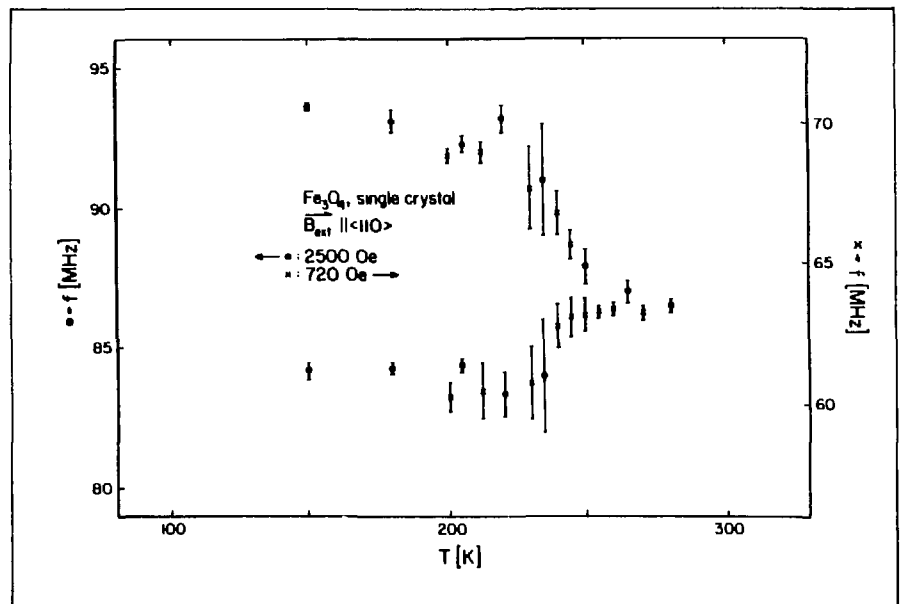


FIGURE 1. Temperature dependence for the  $\mu$ SR signal at  $B_{\text{ext}} = 720$  and 2500 Oe ( $B_{\text{ext}} \parallel \langle 110 \rangle$ ).

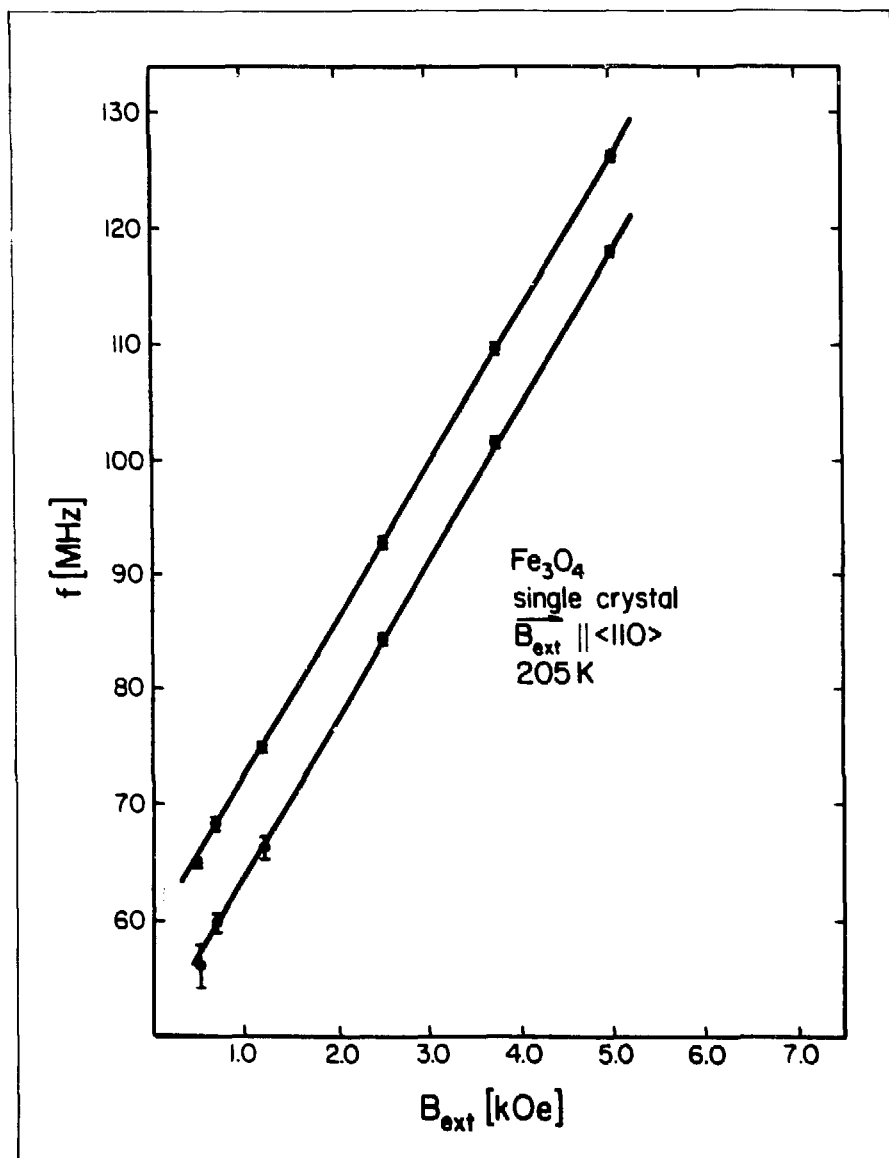


FIGURE 2 External field dependence of the  $\mu$ SR signal in  $\text{Fe}_3\text{O}_4$  at 205 K.  $B_{\text{ext}}$  is parallel to the  $\langle 110 \rangle$  direction

The dependence on external-field strength at a constant temperature (205 K) is shown in Fig. 2. Above the demagnetization field ( $\sim 200$  Oe) the iron moments are parallel to the applied-field direction. The slope of the field dependence (13.5 kHz/Oe) indicates that the effective local muon fields are parallel to the applied field. The interpretation of these results, along with the earlier cross-relaxation work,<sup>4</sup> is that a breakdown of short-range (atomic-cluster) order occurs above 247 K. Two types of magnetic sites exist below this temperature that are correlated with the characteristics of the short-range order. New, selectively doped (nickel and zinc) crystals are currently being investigated in hopes of altering the motion of the atomic clusters' range and, therefore, of shifting or destroying the anomaly observed at 247 K in pure magnetite.

### Pseudobrookite ( $\text{Fe}_2\text{TiO}_5$ )

A new research direction began this year with the  $\mu$ SR study of oxide spin glasses. Initial experiments were conducted on modified pseudobrookite ( $\text{Fe}_{1.75}\text{Ti}_{1.25}\text{O}_5$ ) prepared by V. A. M. Brabers (Eindhoven). Zero-field measurements were made to obtain the asymmetry and depolarization rate as a function of temperature. As observed

from Fig. 3, the depolarization rate shows a marked increase at the glass transition temperature ( $\approx 45$  K), with another smaller increase near 8 K. The shape of the depolarization versus temperature curve just above the glass transition can be used to compare two competing theories of spin dynamics, namely the standard power law<sup>5</sup> versus the Vogel-Fulcher law.<sup>6,7</sup> The change in depolarization rate near 8 K is associated with the suggested onset<sup>8</sup> of the transverse spin ordering. Further analysis will determine the validity of this interpretation.

### Karelionite ( $V_2O_3$ )

The main thrust this year of the  $\mu$ SR results on  $V_2O_3$  (see the LAMPF Progress Report, Ref. 4) has been the interpretation of our previous measurements.<sup>9,10</sup> The data showed a clear jump in the local field at the magnetic and metal-insulator transition temperature ( $T_i \approx 134$  K) for our oxygen-deficient sample. Because of the electronic configuration of the vanadium ion, the source of the local magnetic field is mainly of point-dipole origin from the  $V^{3+}$ . Calculations based on dipole sums have been performed to search for and identify the muon-stopping site. The

original calculations<sup>9</sup> found a set of sites that satisfied the experimental results for the 15-MHz  $\mu$ SR signal with respect to the magnitude and direction of the local field when an external field was applied. However, in the original search, sites appeared to be missing, as deduced from experimental asymmetries. Recent work by Chan et al.<sup>10</sup> indicated additional sites, explaining the 0-MHz  $\mu$ SR signal. Summarizing for  $V_2O_3$ , Bates muon sites, as well as Rodriguez muon sites (similar to those found in  $\alpha$ - $Fe_2O_3$ ), have been found. Comparing  $V_2O_3$ ,  $Fe_3O_4$ , and  $\alpha$ - $Fe_2O_3$   $\mu$ SR studies, we conclude that muon-oxygen bonding occurs in insulating as well as (semi)metallic oxides.

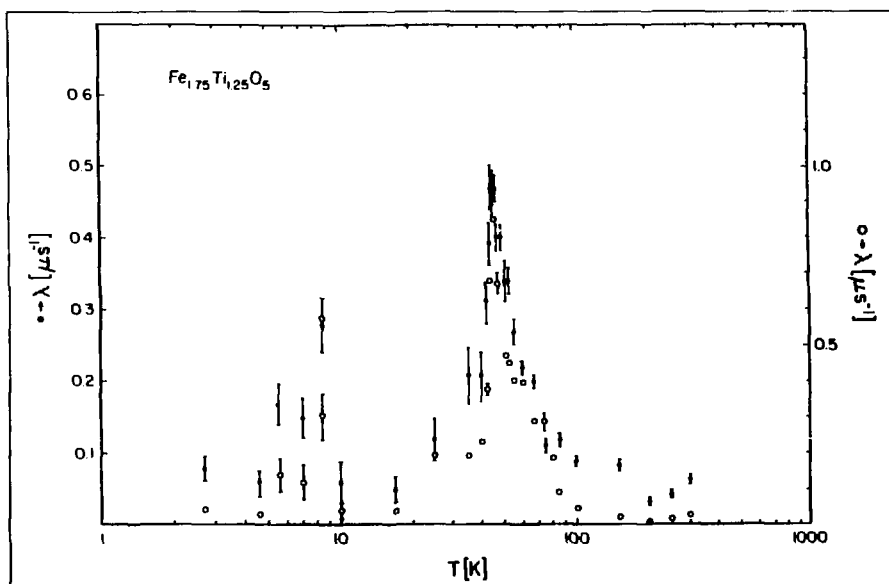


FIGURE 3 Depolarization rate measured as a function of temperature for  $Fe_{1.75}Ti_{1.25}O_5$ . The open circles represent the fit with the standard power law (Ref. 5), the solid circles, that for the Vogel-Fulcher law (Refs. 6 and 7).

---

## References

1. C. Boekema, R. L. Lichti, K. C. B. Chan, V. A. B. Brabers, A. B. Denison, D. W. Cooke, R. H. Heffner, R. L. Hutson, and M. E. Schillaci, *Physical Review B* **33**, 210 (1986).
2. N. F. Mott, *Metal-Insulator Transitions* (Taylor Francis, Ltd., London, 1974).
3. C. Boekema, *Philosophical Magazine* **B42**, 409 (1980).
4. C. Boekema, R. L. Lichti, V. A. M. Brabers, A. B. Denison, D. W. Cooke, R. H. Heffner, R. L. Hutson, M. Leon, and M. E. Schillaci, *Physical Review B* **31**, 1233 (1985); and "Progress at LAMPF," Los Alamos National Laboratory report LA-10429-PR (April 1985), pp. 105-108.
5. R. Rammel and J. Souletie, "Spin Glasses," in *Magnetism of Metals and Alloys*, M. Cyrot, Ed. (North Holland Publishing Co., Amsterdam, 1982), Chap. 4, pp. 379-486; R. H. Heffner et al., *Journal of Applied Physics* **53**, 2174 (1982); and J. Uemura et al., *Physical Review B* **31**, 546 (1985).
6. J. L. Tholence, *Solid State Communications* **35**, 113 (1980).
7. H. Vogel, *Zeitschrift fuer Physik* **22**, 645 (1921); and G. S. Fulcher, *Journal of the American Ceramic Society* **8**, 339 (1925).
8. Y. Yeshuran and H. Somplinsky, *Physical Review B* **31**, 3191 (1985).
9. A. B. Denison, C. Boekema, R. L. Lichti, K. C. B. Chan, D. W. Cooke, R. H. Heffner, R. L. Hutson, M. Leon, and M. E. Schillaci, *Journal of Applied Physics* **57**, 3745 (1985).
10. K. C. B. Chan, C. Boekema, R. L. Lichti, D. W. Cooke, M. E. Schillaci, and A. B. Denison, "Muon-Spin-Rotation Study of  $V_2O_3$ ," *Journal of Applied Physics* **57(1)**, 3743 (1985).

A wide variety of magnetically disordered materials exhibit two magnetic transitions: (1) a ferromagnetic transition at a Curie temperature  $T_c$  and (2) a transition to a spin-glass state at a lower temperature  $T_g$ . We have studied both the freezing and the spin dynamics in one such system,  $PdFe_{0.0035}Mn_{0.05}$ , using zero-field muon-spin relaxation ( $\mu$ SR). The freezing processes have been considered in a previous report,<sup>1</sup> so we discuss here the recent improvements in our analysis of zero-field data and the use of the  $\mu$ SR dilution refrigerator, which have led to a better understanding of the spin dynamics near and below  $T_c$ .

Time-dependent fluctuations of the impurity moments contribute to the muon depolarization through the magnetic dipole coupling to the muon moment. The dynamic contribution to the depolarization dominates the observed relaxation at long times for  $T < T_c$ . Above  $T_c$  there is no quasi-static field and the observed relaxation is entirely dynamic in origin. The resulting relaxation function  $P(t)$  is usually assumed to be either exponential or root exponential,  $P(t) \propto \exp[-(\lambda t)^{1/2}]$ . We argue below that neither form adequately describes our data, so we briefly review the calculation of the depolarization function in the case of no muon diffusion. More complete discussions have been given by McHenry et al.<sup>2</sup> and by Seymour and Sholl.<sup>3</sup>

In the motional-narrowing limit, which is appropriate here, a muon at site  $j$  has an exponential depolarization function

$$P_j(t) = \exp \left[ -t \sum_i' \frac{1}{T_1(r_{ij})} \right], \quad (1)$$

where the sum is restricted to the occupied impurity sites surrounding the muon site  $j$ . The overall depolarization function  $P(t)$  observed in a  $\mu$ SR experiment is an average of the  $P_j(t)$  over all muon sites. Because the  $P_j(t)$  may depend strongly on  $j$ , the average  $P(t)$  will in general be nonexponential. For dipolar or RKKY coupling,  $1/T_1(r_{ij})$  can be approximated<sup>3</sup> by an angle-averaged relaxation rate  $1/T_1(r) = K/r^6$ , where  $K$  is a temperature-dependent quantity containing the impurity fluctuation time and the coupling strength. Note that any concentration dependence observed in  $K$  is due to the concentration dependence of the impurity dynamics. All direct concentration dependence in the muon relaxation function has been removed through the sum in Eq. (1) and the average over muon sites.

When  $1/T_1(r) = K/r^6$ , the average relaxation function is given by<sup>2,3</sup>

$$P(t) = \prod_i \left[ (1-c) + c \exp(-tK/r_i^6) \right], \quad (2)$$

where  $c$  is the impurity concentration and  $r_i$  are the possible impurity site locations relative to the muon site. The general behavior of the relaxation function is determined by  $c$

## EXPERIMENT 941 — SMC

### Muon-Spin-Relaxation Studies ( $\mu$ SR) of Disordered Spin Systems

Rice Univ., Los Alamos, Univ. of California at Riverside

Spokesmen: S. A. Dodds (Rice Univ.), R. H. Heffner (Los Alamos), and D. E. MacLaughlin (Univ. of California, Riverside)

and by  $t_0 = r_0^6/K$ . The parameter  $r_0$  is the minimum muon-impurity distance, so  $t_0^{-1}$  is the maximum muon relaxation rate from a single impurity. When  $c \rightarrow 1$ , the  $P(t)$  is exponential at all times, but at the concentrations of interest here,  $c \leq 0.1$ , the  $P(t)$  is exponential for  $t \ll t_0$  and root exponential for  $t \gg t_0$ . In practice, it may be difficult to observe the exponential region at low concentration because very little depolarization will occur for  $t \leq t_0$ . The root exponential will then be a good approximation to the observable depolarization function.

An explicit calculation of  $K$  is straightforward in the dipolar coupling case, yielding<sup>2</sup>

$$K = 1.33 (\hbar \gamma_\mu \gamma_s)^2 S(S+1) \tau_{eff}, \quad (3)$$

where  $\gamma_\mu$  and  $\gamma_s$  are the muon and impurity gyromagnetic ratios,  $S$  is the impurity spin, and  $\tau_{eff}$  is an effective impurity correlation time. The numerical factor arises from the angular averaging of the dipolar coupling.

Equation (2) is clumsy to use for fitting data because evaluation of the lattice sum is lengthy. In the limit of small concentrations it is convenient to use a continuum approximation, replacing the lattice sum by an integral to obtain<sup>2</sup>

$$P(t) = \exp \left\{ -\frac{4\pi}{3} r_0^3 \rho c \left[ e^{t/t_0} - 1 + \left( \frac{\pi t}{t_0} \right)^{1/2} \operatorname{erf} \left( \frac{t}{t_0} \right)^{1/2} \right] \right\}, \quad (4)$$

where  $\rho$  is the number density of host sites. The quantity  $r_0$  is an inner cutoff radius for evaluation of the integral. In terms of these parameters, the limiting root-exponential rate is  $\lambda = (16\pi^3/9)\rho^2 c^2 K$ , obtained when  $r_0 = 0$ . By taking  $r_0$  as an adjustable parameter, one can also approximate the exact  $P(t)$  for the case where the near-neighbor sites are excluded.

The muon-relaxation data above  $T_c$  were initially fit with both exponential and root-exponential functions. The resulting  $\chi^2$  per degree of freedom suggests a change from an exponential form at the highest temperature (low relaxation rate) to a root-exponential form at lower temperature. Neither function fits the entire range well. The more general form of Eq. (4) requires a two-parameter fit to the data in a region where the relaxation function does not have either limiting form. The  $P(t)$  data at  $T = 10$  K fulfill this requirement. Accordingly,  $P(t)$  from Eq. (4) was fit to the data by adjusting  $K$  and  $r_0$ . We find that  $r_0/a_0 = 0.72 \pm 0.08$ , where  $a_0$  is the palladium fcc lattice parameter. This value of  $r_0$  was then held fixed for the fits at other temperatures. The resulting  $\chi^2$  values demonstrate that this procedure accurately describes our depolarization data.

Comparing the value of  $r_0$  [deduced from fitting the data to Eq. (4)] with the exact lattice-sum results when various sites are excluded, we infer that there is no contribution to  $P(t)$  from the interstitial sites nearest the impurities. In a normal resonance experiment with a large applied field, this might be due to the shift of the muon-resonance frequency produced by the polarized impurity moment. The shift would also entail a loss of signal amplitude relative to the pure host signal by a factor of  $(1 - c)^n = 0.63$ , because the six near-neighbor sites would not contribute to the intensity of the observed signal. Here, the muon  $P(t)$  is measured in zero field and the full asymmetry is observed above  $T_c$ , so this mechanism cannot be significant.

We suggest instead that the muon is physically excluded from the octahedral interstitial sites nearest the manganese impurities. This could be caused by a contraction of the host lattice around the manganese or by a repulsive muon-manganese interaction of electronic origin. X-ray lattice parameter measurements on a series of  $PdMn$  alloys containing 2 to 10% manganese do not show any significant deviation from the pure palladium lattice parameter, leading us to infer that the effect is electronic. Presumably, muons are also excluded from near-neighbor sites in the other  $PdMn$  alloys previously studied<sup>4,5</sup> by  $\mu$ SR.

The spin-lattice-relaxation rate constants  $K$ , obtained from fitting Eq. (4) to the  $PdFeMn$  data with  $r_0$

fixed, are plotted in Fig. 1. Above  $T_c$  the fits have the full muon asymmetry, and the whole time range is included in the fit. Below  $T_c$  the initial damping from the quasi-static fields reduces the initial asymmetry for the dynamic part to one-third, and only the time range beyond the initial falloff is included in the fit.

Two additional data points (triangles) were taken in an applied longitudinal field. The significance of these data is discussed below. For comparison, we have also reanalyzed earlier data<sup>4,5</sup> on ferromagnetic  $PdMn_{0.02}$  and on spin-glass  $PdMn_{0.07}$ , using Eq. (4) with  $r_0 = 0.72 a_0$ . These results, scaled by their respective ordering temperatures, are plotted as the solid and dashed lines. Figure 1 also presents the temperature dependence of the low-frequency (21.7-Hz) ac susceptibility on the same  $PdFeMn$  sample.

The onset of dynamic broadening above  $T_c$  is similar to that seen in ferromagnetic  $PdMn$ , as shown by the solid curve in Fig. 1. Furthermore, application of a longitudinal magnetic field strongly suppresses the muon relaxation for  $T \geq T_c$ , in agreement with previous results<sup>4</sup> in ferromagnetic  $PdMn$ . By contrast, a field has only a modest effect on muon relaxation in a spin glass.<sup>5</sup> It seems reasonable to conclude that the transition at  $T_c$  is to a ferromagnetic state, as previously reported.<sup>6</sup> It is not known why the

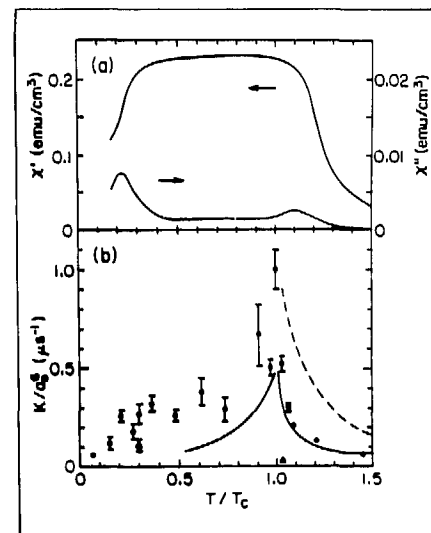


FIGURE 1.

- Temperature dependence of the real ( $\chi'$ ) and imaginary ( $\chi''$ ) parts of the low-field ac susceptibility of the  $\mu$ SR sample, showing  $T_g \approx 1.9$  K from the peak of  $\chi''$ .
- Temperature dependence of the zero-field muon spin-lattice relaxation parameter (defined in the text), scaled by the palladium lattice parameter. Here,  $T_c = 8.25$  K, from the peak of the  $\mu$ SR rate (circles represent the zero-applied field; triangles, the 1-kOe longitudinal field).

The solid line represents muon-relaxation rates in ferromagnetic  $PdMn_{0.02}$ , with temperatures scaled by  $T_c = 5.8$  K (Ref. 4). The dashed line represents muon-relaxation rates in spin-glass  $PdMn_{0.07}$  with temperatures scaled by  $T_g = 5.0$  K (Ref. 5).

Curie temperature determined from the peak of the  $\mu$ SR rate,  $T_c = (8.25 \pm 0.1)$  K, is somewhat lower than the temperature of the peak in  $\chi''$  or the inflection in  $\chi'$ .

The transition to the spin-glass state is marked by the lower-temperature peak in  $\chi''$  and the falloff in  $\chi'$ . No comparable signal in the muon relaxation exists, although the relaxation rate gradually decreases below  $T_g$  and is much less sensitive to applied fields near  $T_g$  than it is near  $T_c$ . A nonreentrant spin glass (for example,  $PdMn_{0.07}$ ) would display an increase in relaxation rate over a wide temperature range as  $T \rightarrow T_g$  from above (indicated by the dashed line in Fig. 1). The rate near  $T_g$  would be similarly insensitive to applied fields.<sup>5</sup>

In the temperature region between  $T_c$  and  $T_g$  the relaxation-rate constant remains substantially elevated, in contrast to the ferromagnet where the rate constant falls to unmeasurably low values at comparable reduced temperatures. This indicates the continued presence of slow fluctuations in this temperature range. From Eq. (3) we can deduce effective correlation times  $\tau_{eff} \approx 10^{-10}$  to  $10^{-11}$  s for these fluctuations. At the same time, the lack of an increase of  $K/a_0$  (Ref. 6) near  $T_g$  in  $PdFeMn$  implies that the ferromagnet to spin-glass transition is not accompanied by critical fluctuations in the frequency range  $\omega \approx 10^{10}$  s<sup>-1</sup> probed by  $\mu$ SR. The low-frequency spin fluctuations of this reentrant system are therefore unlike those of either a disordered ferromagnet or a spin glass.

---

## References

1. "Progress at LAMPF," Los Alamos National Laboratory report LA-10429-PR (April 1985).
2. M. R. McHenry, B. G. Silbernagel, and J. H. Wernick, *Physical Review B* **5**, 2958 (1972).
3. E. F. W. Seymour and C. A. Sholl, *Journal of Physics C: Solid State Physics* **18**, 4521 (1985).
4. S. A. Dodds, G. A. Gist, D. E. MacLaughlin, R. H. Heffner, M. Leon, M. E. Schillaci, G. J. Nieuwenhuys, and J. A. Mydosh, *Physical Review B* **28**, 6209 (1983).
5. R. H. Heffner, M. Leon, M. E. Schillaci, S. A. Dodds, G. A. Gist, D. E. MacLaughlin, J. A. Mydosh, and G. J. Nieuwenhuys, *Journal of Applied Physics* **55**, 1703 (1984).
6. B. H. Verbeek, G. J. Nieuwenhuys, H. Stocker, and J. A. Mydosh, *Physical Review Letters* **40**, 586 (1978).



Progress toward increasing the LAMPF muon-spin-relaxation ( $\mu$ SR) capabilities occurred in three areas: (1) construction of an addition to the SMC-West cave to provide space for the permanent installation of the  $\mu$ SR spectrometer and the muon-spin rotator, (2) construction of a muon-spin rotator, and (3) continuing development studies of the muon beam-chopping system. These three items will enable  $\mu$ SR experiments to be done with more convenience and efficiency, at higher data rates, at lower temperatures, and with thin samples.

During 1985, Group MP-7 constructed an addition to the SMC-West cave to accommodate the  $\mu$ SR spectrometer. This improvement will greatly enhance the efficiency of doing  $\mu$ SR experiments by eliminating the necessity of setting up and dismantling the spectrometer for every run and by reducing the probability of damage to fragile spectrometer and cryogenics components during moving, assembly, and dismantling of the experimental setup.

Plans in 1986 are to install and test a spin rotator that will give the capability of rotating the muon spin  $90^\circ$  before the muon enters the  $\mu$ SR sample. A spin rotator will allow both transverse- and longitudinal-field  $\mu$ SR measurements to be done without turning the  $\mu$ SR spectrometer magnet to orient the magnetic field appropriately for each type of measurement. Group MP-13 has refurbished a 3-m-long particle

separator to be used as the rotator and has undertaken the procurement of power supplies that will provide high voltage to the separator.

The successful muon beam-chopping feasibility studies carried out in 1984, using rudimentary electronics, were followed this year by test runs using a more complete system comprising newly designed high-voltage and control electronics and a beam-line-component layout closely approximating the configuration to be used for the final installation. The chopper control electronics worked as expected and the high-voltage system switched the beam on and off faster and operated with much higher reliability than the old system.

To transport the beam to the  $\mu$ SR spectrometer in the new SMC-West cave addition, beam-line components were arranged so that the muon beam, after exiting QM21 in the west cave, passes through the beam chopper box containing the crossed electric and magnetic fields and into a  $20^\circ$  bending magnet. It is then refocused by a quadrupole doublet to form a spot at the  $\mu$ SR sample position in the spectrometer. A drift space between the doublet and the spectrometer will eventually be occupied by the spin rotator.

### **Improvements to the Muon-Spin-Relaxation ( $\mu$ SR) Experimental Facility**

R. L. Hutson (Los Alamos)

## EXPERIMENT 787 — Biomed

**Muon Channeling for Solid-State Physics Information**

Los Alamos, Max Planck Institute at Stuttgart, Texas Tech Univ., Technical Univ. of Munich, Univ. of Mississippi

*Spokesmen:* G. Flik (Max Planck Institute at Stuttgart), K. Maier (Max Planck Institute at Stuttgart), and M. Paciotti (Los Alamos)

*Participants:* C. Boekema, J. Bradbury, W. Cooke, H. Daniel, G. Flik, R. Heffner, M. Leon, K. Maier, M. Paciotti, J. Reidy, H. Rempp, and M. Schillaci

The most interesting muon-channeling results obtained at LAMPF came from light-on/light-off experiments in germanium and gallium arsenide along the  $\langle 110 \rangle$  direction. A large concentration of excess-charge carriers was produced in these high-quality single crystals by directing the radiation from a tungsten lamp onto the sample surface. Taking advantage of the structure of the LAMPF pion beam (pulse repetition period 8.3 ms, pulse length  $\approx 750 \mu\text{s}$ ), the light was chopped so that each pulse overlapped alternate pion pulses striking the crystal. This resulted in a high carrier concentration when the light was on and, because of rapid surface and bulk recombination, an intrinsic concentration when the light was off. This technique allowed us to (1) reduce the heat load on the sample, (2) observe the effects of different carrier concentrations at the same sample temperature, and (3) minimize the effects of any small shift in crystal orientation or drifts in electronics with time.

Most of the photons produced by the lamp ( $T = 3400 \text{ K}$ ) and transmitted through the Lucite light guide have energies exceeding the germanium ( $E_g = 0.67 \text{ eV}$ ) and gallium arsenide ( $E_g = 1.43 \text{ eV}$ ) band gaps. Upon illumination, the carriers are produced at the surface within a depth  $\alpha \sim 1 \mu\text{m}$  ( $\alpha$  being the absorption coefficient), whereupon they rapidly diffuse into the bulk. For typical bulk recombination times, this distance far exceeds the  $50\text{-}\mu\text{m}$  depth

from which the channeled muons emanate. Thus, within this depth the carrier concentration resulting from illumination is constant, a typical value being  $10^{15} \text{ cm}^{-3}$  for germanium.

In Fig. 1 we show radial averages of the relative muon yield for germanium as a function of the angle  $\psi$  measured with respect to the  $\langle 110 \rangle$  direction. Data are presented for light-on and light-off conditions at two different temperatures. The radial average is obtained by dividing the two-dimensional channeling data by a random spectrum—that is, one obtained by putting a scattering foil between the sample and the muon detector—and subsequently averaging the relative number of muons that lie within a fixed radius of the center. By increasing this radius, one obtains a radial average distribution (channeling profile) of the channeled muons.

At 100 K there are striking differences between the muon-channeling profiles taken with light off and light on [compare Figs. 1(a) and 1(b)]. For example, with light off we see both a center peak (that is,  $\psi = 0^\circ$ ) and an off-center one ( $\psi = 0.22^\circ$ ), whereas with light on we observe only an off-center peak ( $\psi = 0.1^\circ$ ). At 200 K [see Figs. 1(c) and 1(d)], we do not observe any appreciable difference (within statistical error) between light-off and light-on conditions. Each profile exhibits a center peak with hints of possible off-center peaks. Thus, we conclude that the differences in the muon-channeling profiles observed at 100 K can be attributed to the

occupation of different pion sites, resulting from an increased carrier concentration during the light-on condition. Furthermore, we note that pion sites at 200 K are different from those at 100 K and are essentially unaffected by light.

Figures 2(a) and 2(b) contrast the light-off/light-on differences in the muon-channeling profiles of gallium arsenide taken at room temperature.

Qualitatively, these results are similar to those of germanium at 100 K [Figs. 1(a) and 1(b)], that is, we observe both a center and an off-center peak for light off, but only an off-center peak for light on. These results are consistent with our conclusion that for some temperatures a pion site change occurs when the free-carrier concentration is increased (light on).

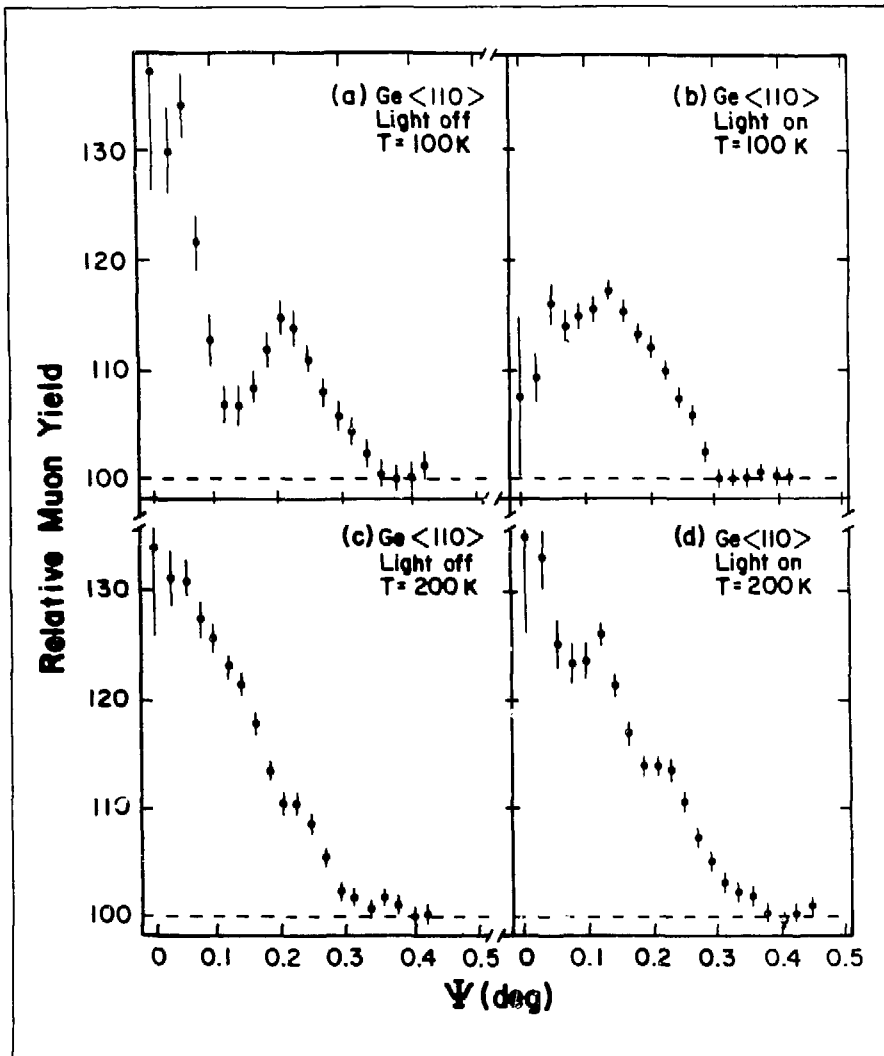


FIGURE 1 Radial averages of relative muon yields for germanium.

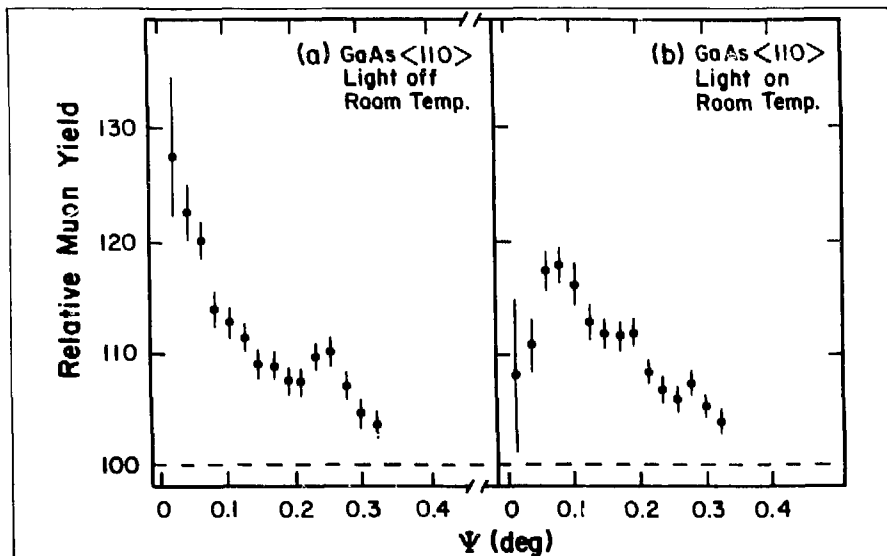


FIGURE 2 Radial averages of relative muon yields for gallium arsenide.

For a qualitative interpretation of the data in terms of specific site occupancy we refer to Fig. 3, which represents the projection of a diamond-type lattice onto a (110) plane. The positions of hexagonal (*H*) and tetrahedral (*T*) sites are shown with respect to the  $\langle 110 \rangle$  channel. Other sites of interest are bond-centered (*BC*) and  $\langle 111 \rangle$  antibond (*AB*) sites.

Figures 1 and 2 illustrate muon-flux enhancement exclusively, that is, channeling rather than blocking, so one can immediately exclude substitutional sites as candidates for possible pion locations. Moreover, channeling theory<sup>1</sup> predicts that pion sites located in or very near a channel center produce muon-channeling

peaks centered at  $\psi = 0$ , whereas off-center sites yield off-center ( $\psi < 0$ ) peaks. Unfortunately, theoretical efforts have not shown definitively that one can in fact resolve the *T* and *H1* sites in a muon-channeling experiment. Thus, we cannot currently make an unambiguous correlation of observed channeling peaks with specific pion sites based on the data along  $\langle 110 \rangle$  directions alone. For a true site determination, we need additional data along  $\langle 100 \rangle$  and/or  $\langle 111 \rangle$  directions. Therefore, we discuss the two different possibilities that are left.

If *H*-site occupancy is preferred when the light is off, the center peak could be due to a pion residing at *H1* whereas the off-center peak could be attributed to *H2-H5* occupancy. For

light on, the pion would preferentially occupy the *T* site. This interpretation seems plausible based on the angular position of the off-center peaks for both germanium and gallium arsenide during light on. That is, we note that the off-center peak occurs at a smaller angle during light on than during light off. One must be somewhat careful with this conclusion, however, because it might be possible to generate an off-center peak [as shown in Figs. 1(b) and 2(b)] by appropriately weighting two peaks such as those shown in Figs. 1(a) and 2(a). This fact, coupled with our lack of knowledge regarding *T*- and *H*-site resolution, suggests a second equally plausible interpretation of the observed muon-channeling profiles.

The center peaks observed in Figs. 1(a) and 2(a) are associated with pions occupying *H*1 and/or *T* sites, whereas the off-center peaks represent *AB* site occupancy. With light on [Figs. 1(b) and 2(b)], a larger portion of the pions occupy *AB* sites than *H* and/or *T* sites.

At 200 K, germanium exhibits a rather broad center peak for both light on and light off, indicative of possible multiple-site occupancy.

Regardless of the ambiguity in elucidating specific pion sites from the observed channeling profiles, it is clear that for certain temperature intervals a pion site change occurs when the carrier concentration is increased (light on). This is qualitatively understood in terms of

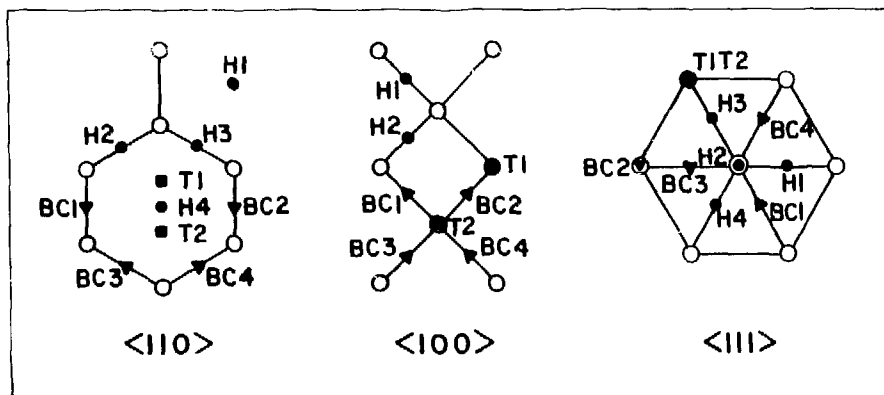


FIGURE 3 Pion sites with respect to low-index channels in diamond-type structures (*H*1-*H*4 hexahedral sites, *T*1, *T*2, tetrahedral sites, *BC*1-*BC*4, bond-centered sites)

differently structured electronic states of the pion. From muon-spin-relaxation ( $\mu$ SR) experiments, where positive muons ( $\mu^+$ ) are implanted into semiconductors, it is known that muons form different electronic states, namely diamagnetic (bare)  $\mu^+$ , "normal" muonium ( $Mu = \mu^+ + e^-$ ), and "anomalous" muonium.<sup>2</sup> We suggest that pionium ( $Pi = \pi^+ + e^-$ ), an analog state to normal muonium and also to atomic hydrogen with a meson nucleus, is formed because it seems highly unlikely that a bare pion would change sites when the carrier concentration is increased.

Hartree-Fock and Hückel calculations<sup>3,4</sup> demonstrate that the lattice potential for 1s hydrogen isotopes at *T* sites  $E_T^*$  is an absolute minimum. Thus, we conclude that *Pi* formation occurs at *T* sites, which is consistent with either of the aforementioned interpretations of pion site location. Furthermore, it is known<sup>3,4</sup> that the lattice potential  $E_H^*$  of 1s hydrogen isotopes occupying *H* sites represents an absolute maximum, with  $E_H^* - E_T^* \gtrsim 1.2$  eV for atomic hydrogen in silicon. For muonium in diamond, Sahoo et al.<sup>4</sup> find that  $E_H^* - E_T^* \sim 0.8$  eV.

We conclude from these calculations that *H* sites are unstable for *Pi*. Thus *H*-site occupancy seems plausible only if one assumes that *Pi* forms bonds with each nearest-neighbor germanium atom. Likewise, if *Pi* sits at an *AB* site, one must conclude that a chemical bond is formed with the nearest-neighbor germanium atom on which the *AB* site exists. Regardless of which interpretation is viewed as the correct one, *Pi* states appear to exist that cannot be explained by the formation of normal pionium on *T* sites. In analog to  $\mu$ SR terminology, we associate these sites with anomalous *Pi*.

---

## References

1. G. Gemmell, *Reviews of Modern Physics* **46**, 1 (1974).
2. A. Weidinger et al., *Physical Review B* **24**, 6185 (1981); and B. Patterson, *Hyperfine Interactions* **17-19**, 517 (1984).
3. V. A. Singh et al., *Physica Status Solidi* **B81**, 637 (1977).
4. N. Sahoo et al., *Physical Review Letters* **50**, 913 (1983).

## RADIATION-EFFECTS STUDIES

### Operating Experience at the Los Alamos Spallation Radiation-Effects Facility (LASREF) at LAMPF

W. F. Sommer, I. K. Taylor, and R. M. Chavez (Los Alamos) and W. Lohmann (KFA, Jülich)

Operation of a new irradiation facility at the beam stop (Target Station A-6) at LAMPF began in May 1985. The facility is now fully operational. A closed-loop water system, a closed-loop helium system, remote-handling procedures for activated materials, experimental change-out procedures, and experimental control equipment are all in place.

Experience dictated a change in irradiation capsules from a system that used metal seals to a system that is completely welded. The seals were found to be unreliable and difficult to replace by remote means.

Several materials have been irradiated in the direct 760-MeV proton beam. Material property changes, as well as helium production in a variety of materials, are being investigated.

A special sample holder that can accommodate transmission-electron-microscopy (TEM) specimens, isolate them from the cooling medium, maintain a fixed temperature, and retain essentially a stress-free state has been developed. Remote-handling retrieval of these specimens is being developed.

Activation-foil measurements are being made in order to determine the secondary-particle flux and spectrum (charged particles and neutrons) that result from interaction of the direct proton beam with targets at the beam stop. Twelve independent irradiation ports, each with an irradiation volume 0.12 by 0.25 by 0.50 m, are available for exposing material to this particle flux (primarily neutrons). Two irradiations were completed in this area during the period from May to December 1985. The neutron spectrum here resembles a fission spectrum with the addition of neutrons in the million-electron-volt energy range (high-energy tail). The neutron flux, which at a maximum is about  $6 \times 10^{13} \text{ n/cm}^2 \text{ s}$  at one of the 12 ports, drops down by a factor of about 10 at a minimum.

Three independent ports for proton irradiations are in place. Each has an irradiation volume of about  $150 \text{ cm}^3$ . The proton beam has a Gaussian intensity profile; the maximum proton flux at the center of the beam is  $1.2 \times 10^{14} \text{ p/cm}^2 \text{ s}$ . The beam spot has a size of approximately  $2\sigma = 5 \text{ cm}$ . Four irradiations were completed in this area during the period from May to December 1985.

Four separate irradiations in the direct proton beam at Los Alamos Spallation Radiation-Effects Facility (LASREF) at the LAMPF beam stop were completed. The irradiation capsules contained sample material of aluminum alloys, pure aluminum, Zircalloy, and tungsten—materials that had been slated as candidates for the German Spallation Neutron Source (SNQ) target wheel structure, vacuum-to-air window, and target element cladding. Extensive investigations aimed at determining mechanical and physical property changes induced by the irradiation will now be conducted at Jülich.

Control equipment, including a closed-loop helium heat sink, a closed-loop water heat sink, and attendant instrumentation, was made operational. In addition, components required for a complex *in situ* testing device were irradiated in the neutron environment to determine their reliability. We found that components such as a stepping motor, a load cell, and a linear-variable-differential transformer can acceptably tolerate the environment. The *in situ* measurements will proceed next year.

#### EXPERIMENT 769 - Beam Stop Area

### **Proton-Irradiation Effects on Candidate Materials for the German Spallation Neutron Source (SNQ)**

KFA at Jülich, Los Alamos

*Spokesmen: W. Lohmann and K. Graf (KFA, Jülich) and W. Sommer (Los Alamos)*



## EXPERIMENT 769 — Beam Stop Area

### Quantitative Study, by Field-Ion Microscopy, of Radiation Damage in Tungsten After Neutron and Proton Irradiation

Los Alamos, New Mexico Institute of Mining and Technology, Institute of Atomic Energy in China, KFA at Jülich

Spokesmen: W. Lohmann (KFA, Jülich) and W. Sommer (Los Alamos)

Participants: O. T. Inal and J. Yu

The defects that result from proton and neutron irradiation of tungsten were studied using the field-ion microscope (FIM). The initial stages of radiation damage can be examined by noting the configuration, density, and type of defect. This study used medium-energy protons as well as a spallation neutron flux for the irradiation.

Annealed tungsten, in an un-irradiated and an irradiated condition, was examined in the FIM. Irradiations were conducted using protons and spallation neutrons at LAMPF. Proton energies were 650 and 800 MeV. The neutron spectrum resembled a fission spectrum with the addition of substantial numbers of neutrons in the 10- to 100-MeV range. In the proton irradiations, temperature was controlled (by water cooling) to less than 50 °C; the temperature for the neutron irradiations was measured at 125 °C.

The calculated diffusion coefficients of vacancies at 323 and 398 K in tungsten are  $10^{-54}$  and  $10^{-44}$  cm<sup>2</sup>/s, respectively, which means that the vacancies are essentially immobile. The interstitials at this temperature are mobile and should diffuse to a sink, leaving few interstitials in the matrix; this was confirmed by the FIM

in this study. The concentration of vacancies that survived recombination and were observed with the FIM was 1 to 3% of the calculated displacements per atom (dpa). We suspect that the remainder have undergone vacancy-interstitial recombination or have found a sink. The vacancy concentrations resulting from fluences of  $10^{22}$  and  $10^{24}$  p/m<sup>2</sup> were  $2.5 \times 10^{-3}$  and  $1.0\text{--}1.6 \times 10^{-2}$ , respectively. The neutron-irradiated samples contained a vacancy concentration of  $4 \times 10^{-3}$  after a fluence of  $10^{23}$  n/m<sup>2</sup>. Depleted zones containing a thousand or more vacant lattice sites along with smaller zones containing from 30 to 300 vacant lattice sites were observed in the irradiated samples. The shape of the smaller zones was uniform and rounded; the larger depleted volumes split into nodes.

Un-irradiated samples of the same stock were examined for defects. The calculated equilibrium vacancy concentration at 300 K is  $10^{-56}$ ; therefore, vacancies should not be found. This proved correct for the samples examined, as no vacancies or void volumes were found.

The data indicated that the number of vacancies increases with increasing fluence and that the number surviving recombination is from 1 to 3% of the calculated dpa. The most numerous defect for both the proton and neutron irradiations was the single vacancy. Depleted zones were of two basic sizes: (1) 30 to 300 vacant lattice sites or (2) over 1000 vacant lattice sites.

A new irradiation facility, LASREF (Los Alamos Spallation Radiation-Effects Facility), has been completed at the beam stop area at LAMPF. Irradiations are possible in the primary proton beam and in the secondary neutron flux resulting from interactions of the primary beam with the isotope production targets and with the copper beam stop. High-purity activation foils are being irradiated, the gamma spectrum is being analyzed to determine the activity of the spallation products, and the measured activity is being used as input in a computer code to unfold the proton and neutron energy spectrum at LASREF. This analysis will also aid in developing a simplified dosimetry package that will be irradiated with each experiment.

Measurements are being made at locations where proton irradiations are possible in order to determine the energy spectrum and flux of the secondary neutrons that would impinge on peripheral experimental equipment. Aluminum samples are placed directly in the proton beam to analyze the beam spot size, beam degradation, and the proton flux.

A pneumatic rabbit system has been built to measure the flux of secondary neutrons and protons in the neutron-irradiation ports. Four rabbit tubes allow measurements in radial locations 0.12, 0.18, 0.27, and

0.38 m off the beam center line. Disk-shaped foils of titanium, nickel, zinc, iron, copper, vanadium, scandium, gold, cobalt, and aluminum, each with a center hole, are strung on an aluminum center wire inside an aluminum capsule to assure identification. Capsules are pneumatically placed in the neutron-irradiation port using helium gas as a propellant, and the foils are irradiated for 3 to 24 h. Because of the high activation of short-lived isotopes, the capsules and foils are allowed to decay for 48 h before analysis begins. Results of the irradiations give the effect of isotope production target loading on the secondary neutron energy spectrum in the neutron-irradiation ports.

Five irradiations have been made at the neutron-irradiation port outside the isotope production targets. After the irradiations were completed, the insert was moved to a neutron-irradiation port outside the copper beam stop, where seven measurements were made.

## EXPERIMENT 936 — Radiation Damage

### **Additional Measurements of the Radiation Environment at the Los Alamos Spallation Radiation-Effects Facility (LASREF) at LAMPF**

Los Alamos, Iowa State Univ.

*Spokesmen: D. R. Davidson and W. F. Sommer  
(Los Alamos)*

*Participants: R. C. Reedy and M. S. Wechsler*

## EXPERIMENT 943 — Radiation Damage

**Microstructural Evolution Under Particle Irradiation**

Institute of Atomic Energy, China, Los Alamos

Speckesmen: J. Yu (Institute of Atomic Energy, China) and W. F. Sommer (Los Alamos)

Participant: J. N. Bradbury

Structural materials for advanced energy sources, such as magnetically and inertially confined thermonuclear reactors, are subjected to (1) a radiation environment that produces high-energy displacement cascades and (2) transmutation products that include helium. A similar environment exists at the Los Alamos Spallation Radiation-Effects Facility (LASREF), where a spallation neutron flux is available as well as the direct proton beam. The major differences among the three environments—fusion, LAMPF spallation neutrons, and 800-MeV protons—are the details of point-defect production rates, transmutation-product production rates, and the recoil energy of displaced atoms.

In preparation for an experiment that addresses the relative effects of the above parameters by exposing control materials to both the spallation neutron flux and the direct proton beam, we have formulated a theory that predicts the microstructural evolution that should proceed under the two different conditions. The ratio of the helium production rate to the atomic-displacement rate is predicted to be 10 times greater in the direct proton beam than in the neutron flux. If the prediction and experiment can be brought into

agreement, it may be possible to extrapolate data for microstructural evolution and the attendant mechanical property changes to the fusion case, in which the ratio is similar to that for the spallation neutron case but the recoil atom energy spectrum is different.

For the theory, we consider that immediately after a high-energy cascade event a vacancy-rich region exists near the primary event site, and that an interstitial-rich zone, formed by collision chains, exists some distance from the primary event site. Transmutation-product helium can diffuse into the vacancy-rich zone and stabilize bubble nuclei, which will later grow if sufficient vacancies and helium atoms diffuse to the nucleus. These bubbles are the sinks for excess radiation-produced vacancies. The excess radiation-produced interstitials migrate and bond. If the binding energy is high enough, a di-interstitial is considered to be a stable dislocation loop nucleus. The loop nuclei grow if they receive more interstitials than vacancies; this represents material swelling because the bubbles do not cause a lattice contraction to offset the dilation caused by the growing dislocation loops.

We consider further that the interstitial loop growth process can be represented by a Langevin equation. If the growth process at time  $t$  is assumed to be dependent only on the instantaneous interstitial concentration and the instantaneous

microstructural state (dislocations, bubbles, and grain boundaries) and independent of previous history, the growth process can be considered to be a Markov process. Application of an equivalent Fokker-Plank equation allows deduction of an interstitial-loop nucleation and growth equation, the solution of which yields an interstitial-loop distribution function.

Use of appropriate material parameters gives the incubation and growth regimes of swelling and also allows a determination of the maximum swelling temperature. These results predict a maximum swelling temperature of 117°C for aluminum, 550°C for stainless steel, and 1100°C for molybdenum, in good agreement with experimental results.

Basically, the maximum swelling temperature is a function of only  $s_v$ ,  $\epsilon_v^f/\epsilon_v^m$ ,  $(\rho_N + \rho_R)$ , and  $N_p$ . The maximum swelling temperature increases as  $(\rho_N + \rho_R)$ ,  $N_p$ , and  $\epsilon_v^f/\epsilon_v^m$  increase, and decreases as  $s_v$  increases. Here,  $s_v$  is the vacancy-formation entropy,  $\epsilon_v^f$  is the vacancy-formation energy,  $\epsilon_v^m$  is the vacancy-mobility energy,  $\rho_N$  is the network-dislocation density,  $\rho_R$  is the dislocation loop density, and  $N_p$  is the production rate of vacancies and interstitials per unit volume under irradiation.

Further, the resolution characteristics for interstitial dislocation loops have a strong bearing on their

evolution because the threshold for the resolution of an interstitial loop is lower than that for the helium in the bubbles. As vacancies also condense at interstitial loops, the resolution is enhanced.

The above treatment also gives a set of equations for the evolution of bubbles and an approximate solution of a distribution function for bubble size as a function of fluence and temperature. The distribution function gives the number of bubbles of size  $r$  at time  $t$ ,  $N(r,t)dr$ , as a function of size  $r$ .

We found that  $N(r,t)dr$  increases with fluence. Also, the peak value of  $N(r,t)dt$  shifts to higher  $r$  with increasing fluence. Nucleation depends mainly on helium concentration and defect cluster concentration, whereas bubble growth is controlled mainly by the vacancy concentration and a fluctuation coefficient.

If suitable parameters are chosen, a reasonable distribution function for bubble size can be obtained. The helium diffusion coefficient is less than that for vacancies by five orders of magnitude. The fraction of helium remaining in matrix is less than  $10^{-2}$ ; the majority of the helium is associated with the bubbles.

## BIOMEDICAL RESEARCH AND INSTRUMENTATION

### Radiobiology of Ultrasoft X Rays

M. R. Raju, S. G. Carpenter, J. J. Chmielewski, M. E. Schillaci, P. L. Schor, and M. E. Wilder (Los Alamos)

The objective of this program is to provide evidence to further constrain and test assumptions used in models for the biological effect of radiation. Ultrasoft x rays (with energies less than a few kiloelectron volts) are of interest in radiobiology because they deposit energy over spatial dimensions comparable with those of critical structures within the cell, such as DNA strands and metaphase chromosomes.

During the past year, we completed the initial phase of our investigations using V-79 hamster cells. Our first experiments confirmed the earlier Harwell results<sup>1</sup> for cell killing. We found relative-biological-effectiveness (RBE) values for C-K $\alpha$  (0.28-keV), Al-K $\alpha$  (1.5-keV), and Cu-K $\alpha$  (8.0-keV) x rays, referenced to 250-keV-peak x rays of 3.0, 1.7, and

1.3, respectively, at 20% survival. In addition, we performed new studies of the increased sensitivity of cells to radiation in the presence of oxygen. We found oxygen-enhancement-ratio (OER) values for carbon, aluminum, and copper x rays of 1.8, 2.1, and 2.5, respectively, at 20% survival. Also, we measured variations in cell killing with cell volume, which correlates with age in the cell cycle. The cell-cycle responses after exposure to carbon and aluminum x rays were very similar to those for 250-keV-peak x rays.

Computer simulations<sup>2</sup> show that nearly one-third of the energy of 250-keV-peak x rays is deposited by terminal low-energy secondary electrons having a concentrated, short-track structure characteristic of ultrasoft x rays. Our results show that the effectiveness of hard x rays is primarily due to these terminal electron tracks; however, oxygen has a greater influence on the more widely spaced lesions associated with the major share of the energy deposition for hard x rays, but produced to a lesser extent with ultrasoft x rays.

---

### References

1. R. Cox, J. Thacker, and D. T. Goodhead, *International Journal of Radiation Biology* **31**, 561 (1977); and D. T. Goodhead, J. Thacker, and R. Cox, *International Journal of Radiation Biology* **36**, 101 (1978).
2. D. J. Brenner and M. Zaider, *Radiation Research* **99**, 492 (1984).

A completely implantable (passive) hyperthermia applicator is being developed. Tests in gel phantoms indicate that heat can be localized in depth without a significant temperature increase near the implanted subdermal-receiving antenna. It has also been demonstrated that the average temperature increase in the treatment region can be regulated by control of the voltage-current phase at the transmitting antenna. We have formed a collaboration with the Washington University (Mallinckrodt Institute of Radiology) for animal tests and, eventually, trials on deep-seated malignant tumors in humans. The DOE has filed a patent application on this instrument.

Javier Magrina at the Truman Medical Center in Kansas City reports that all of the six initial patients with cervical intraepithelial neoplasia (CIN) have responded with remission of their disease following hyperthermia treatment using the Los Alamos apparatus. He has found virtually no complications with this technique, including those commonly experienced with surgical, cryosurgical, or laser therapy.

The software for calculating transient temperature distribution in tissue has been expanded to incorporate user-defined models for simulation of the hyperthermia generator specifications, including power output, temperature monitor location, and temperature-feedback loop characteristics.

A hyperthermia probe capable of heating larger tissue volumes has been supplied to our collaborators at the Ren Ji Hospital in Shanghai, where treatments of brain cancer continue, and an electrosurgical device has been developed that combines cutting and coagulating capability in one instrument. A patent application has been filed.

Another patent application has been filed on a dissolvable stent, which is intended for use in blood vessel surgery.

## Instrumentation

J. D. Doss and C. W. McCabe (Los Alamos)

## NUCLEAR CHEMISTRY

EXPERIMENT 897 — LEP

**Pion Single Charge Exchange in  ${}^7\text{Li}$  to the Isobaric-Analog Ground State of  ${}^7\text{Be}$** 

Los Alamos, Institute of Atomic Energy at Beijing, China

Spokesman: B. J. Dropesky (Los Alamos)

Participants: B. J. Dropesky, G. C. Giesler, M. J. Leitch, L. C. Liu, C. J. Orth, R. J. Estep, L. E. Ussery, and A. Cui

In this study we are particularly interested in the interference between  $s$ - and  $p$ -wave  $\pi N$  amplitudes as manifested in the cross section for the pion single-charge-exchange (SCX) reaction. Evidence for this interference was first observed by the dramatic and unexpected drop in the forward-angle cross sections for the  ${}^{14}\text{N}(\pi^+, \pi^0){}^{15}\text{O}$  isobaric-analog-state (IAS) reactions measured at 48 MeV with the LAMPF  $\pi^0$  spectrometer.<sup>1</sup> The theoretical model of Kaufmann and Gibbs,<sup>2</sup> which includes the  $s$ - and  $p$ -wave  $\pi N$ -amplitude cancellation, predicts a deep minimum in the forward-angle cross section at about 50 MeV for such an SCX reaction. This was confirmed for the reaction  ${}^{14}\text{C}(\pi^+, \pi^0){}^{14}\text{N}$  (IAS) by measurements<sup>3</sup> with the  $\pi^0$  spectrometer that extended the  $0^\circ$  excitation function for this reaction down to near 30 MeV.

Our activation measurements<sup>4</sup> in Exp. 553 of the angle-integrated cross section as a function of energy for the SCX reaction  ${}^{13}\text{C}(\pi^+, \pi^0){}^{13}\text{N}$  (10 min, IAS) showed a dip in the excitation function at about 70 MeV. This dip is another manifestation of the interference between  $s$  and  $p$  waves. The Kaufmann-Gibbs calculation for this angle-integrated cross section predicted a minimum in the excitation function near 60 rather than 70 MeV.

In this experiment we have investigated another example of an SCX reaction that leads to an isobaric-analog ground state, namely  ${}^7\text{Li}(\pi^+, \pi^0){}^7\text{Be}$  (53 days, IAS). This study is complicated by the fact that one other bound state, the first excited state in  ${}^7\text{Be}$  at 429 keV resulting from a nonanalog spin-flip transition, is also involved. However, very recently at TRIUMF we measured the cross section to this nonanalog state using the prompt  $\gamma$  technique over the energy range from 50 to 90 MeV, and at LAMPF we measured the yield of 53-day  ${}^7\text{Be}$  over the energy range from 35 to 90 MeV. These measurements give us the sum of the cross sections to both the analog and nonanalog states. By subtraction we obtain the excitation function for the IAS transition alone and look for a dip caused by  $s$ - and  $p$ -wave interference. Of particular interest is whether this dip, if observed, is shifted upward in energy when compared with theory, as we saw for  ${}^{13}\text{C}$ . Because the spin-flip transition should not have any sharp structure

in its energy dependence, such a dip should also appear in the cross section for the sum of the two transitions.

The cross sections for these reactions in  ${}^7\text{Li}$  were measured several years ago by Shamai et al.<sup>7</sup> at LAMPF (70 to 250 MeV) and by Altman et al.<sup>8</sup> at SIN (90 to 210 MeV). They noted that the cross section to the nonanalog state is about one third that of the analog transition. At LAMPF, the  $\pi^0$  spectrometer measurements<sup>7</sup> of the 0<sup>-</sup> cross section for the  ${}^7\text{Li}(\pi^+, \pi^0){}^7\text{Be}$  (IAS) reaction have been made from about 30 to 100 MeV, and a distinct minimum at  $\approx 42$  MeV was observed. The Kaufmann-Gibbs calculation puts the interference minimum at  $\sim 50$  MeV, a canonical energy that appears to be independent of the nuclear size in their model.

To determine the excitation function for the  ${}^7\text{Li}(\pi^+, \pi^0){}^7\text{Be}$  (53-day, IAS) reaction over the energy range from 35 to 90 MeV, we irradiated disks of natural lithium metal, sealed in thin-windowed containers, in the  $\pi^+$  beam of the LEP channel for an appropriate number of hours. The electron-free pion flux emerging from the 15-ft particle beam separator,<sup>10</sup> which was coupled to the LEP channel, ranged from  $4 \times 10^6$  to  $1 \times 10^8 \pi^+$ /s. After irradiation, the lithium disks were transferred, in an inert atmosphere, to new containers, and the induced 53-day  ${}^7\text{Be}$   $\gamma$ -ray (478-keV) activity was measured with our low-background, high-resolution germanium or Ge(Li)  $\gamma$  spectrometers in the Nuclear Chemistry Laboratory at LAMPF.

The absolute cross section for the sum of the contributions of the  ${}^7\text{Li}(\pi^+, \pi^0)$  reactions to the first-excited and ground states of  ${}^7\text{Be}$  will come from relating the yield of  ${}^7\text{Be}$  to the activity of 15-h  ${}^{24}\text{Na}$  induced in thin aluminum flux monitor foils coupled with the lithium targets and the cross sections for the  ${}^{27}\text{Al}(\pi^+, \pi N){}^{24}\text{Na}$  reaction we determined previously,<sup>8</sup> down to 50 MeV. For this experiment, therefore, it was necessary for us to make a few 40-min irradiations, at 35 and 45 MeV, of packets of aluminum foil plus Pilot-B scintillator disks to determine the  ${}^{27}\text{Al}(\pi^+, \pi N){}^{24}\text{Na}$  cross sections relative to our well-established  ${}^{12}\text{C}(\pi^+, \pi N){}^{11}\text{C}$  (20.4-min) primary cross sections at these energies.<sup>9</sup>

For the lithium targets, which are  $\approx 100 \text{ mg/cm}^2$ , secondary ( $p, n$ ) reactions from protons generated by pion interactions in the target can contribute to the yield of 53-day  ${}^7\text{Be}$ . Because of target fabrication and oxidation problems, it was not feasible to consider an experimental study of these secondary effects as a function of target thickness. Therefore, we intend to calculate the magnitude of these corrections by means of the formalism developed in our group by J. J. H. Berlijn and the computer program written by W. R. Gibbs of Group T-5.



Our preliminary cross sections for the reaction  ${}^7\text{Li}(\pi^+, \pi^0){}^7\text{Be}$  to the sum of the analog plus nonanalog states over the energy range from 35 to 90 MeV are shown in Fig. 1. No corrections have yet been made for secondary ( $p, n$ ) contributions to the measured cross sections. Also, subtraction of the contribution to the 53-day  ${}^7\text{Be}$  by transitions to the nonanalog 429-keV excited state will have to wait until the recent TRIUMF data can be processed. However, we can point out that the present data show that our measured cross section for the sum of the analog and nonanalog transitions at 90 MeV is in agreement with the earlier measurement of Altman et al.<sup>6</sup> On the other hand, our 70-MeV cross section ( $1.16 \pm 0.19$  mb) is in disagreement with the earlier value of Shamai et al.<sup>5</sup> ( $\approx 2.7 \pm 1$  mb).

Our preliminary excitation function shows a monotonic decrease in cross section as the energy is lowered from 90 to  $\approx 50$  MeV, and then an increase in going to 35 MeV. This would appear to reflect the interference between  $s$  and  $p$ -wave  $\pi N$  amplitudes<sup>1</sup> that accounted for the minimum (at 42 MeV) observed in the  $0^\circ$  excitation function for this reaction measured with the  $\pi^0$  spectrometer.<sup>7</sup> Despite the missing value at 50 MeV, the minimum in our excitation function is quite broad, as was noted for the  $0^\circ$  measurements, particularly when compared with the minimum observed for the SCX reactions in  ${}^{14}\text{C}$  and  ${}^{15}\text{N}$ , for example.<sup>7</sup> Likewise, this minimum is much broader than the one we observed in the excitation function of the angle-integrated cross sections for the  ${}^{13}\text{C}(\pi^+, \pi^0){}^{13}\text{N}$  (IAS) reaction.<sup>4</sup>

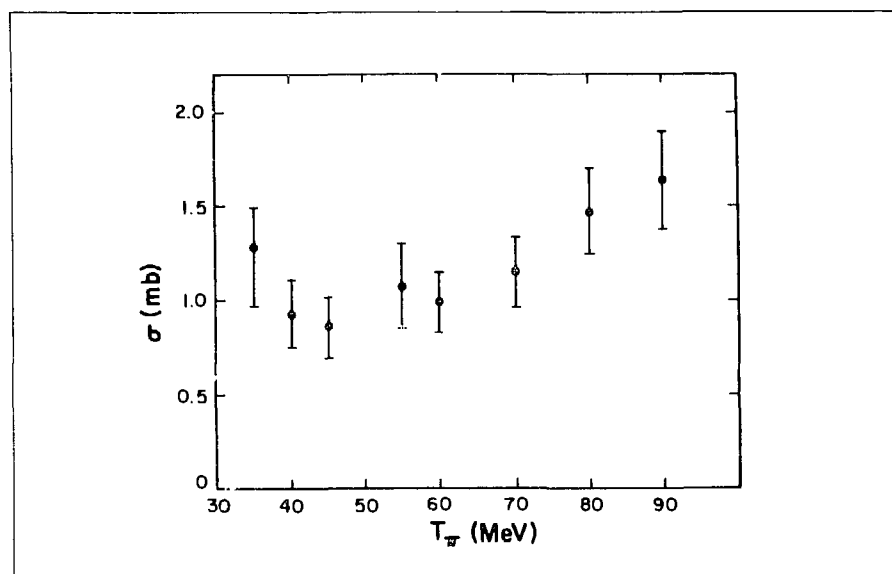


FIGURE 1 Energy dependence of the angle-integrated cross section for the sum of the transitions to the analog and nonanalog states for the single-charge-exchange reaction  ${}^7\text{Li}(\pi^+, \pi^0){}^7\text{Be}$ .

---

## References

1. M. D. Cooper, H. W. Baer, R. Bolton, J. D. Bowman, F. Cverna, N. S. P. King, et al., *Physical Review Letters* **52**, 1100 (1984).
2. W. B. Kaufmann and W. R. Gibbs, *Physical Review C* **28**, 1286 (1983).
3. J. L. Ullman, P. W. F. Alons, J. K. Kraushaar, J. M. Mitchell, R. J. Peterson, R. A. Ristinen, et al., "Pion Single Charge Exchange on  $^{13}\text{C}$  from 35 to 295 MeV" (submitted to *Physical Review C*).
4. L. E. Ussery, D. J. Vieira, J. J. Berlijn, G. W. Butler, B. J. Dropesky, G. C. Giesler, N. Imanishi, M. J. Leitch, and R. S. Rundberg, "Excitation Function for the Pion Single Charge Exchange Reaction  $^{13}\text{C}(\pi^+, \pi^0)^{13}\text{N}$  (g.s.)" (to be submitted to *Physical Review C*).
5. Y. Shamaï, J. Alster, D. Ashery, S. Cochavi, M. A. Moïnestor, and A. I. Yavin, *Physical Review Letters* **36**, 82 (1976).
6. A. Altman, J. Alster, D. Ashery, I. Navon, H. J. Pfeiffer, H. K. Walter, et al., *Physical Review Letters* **39**, 864 (1977).
7. F. Irom, H. W. Baer, J. D. Bowman, M. D. Cooper, E. Piasezky, U. Senthauser, et al., *Physical Review C* **31**, 1464 (1985); and F. Irom, M. J. Leitch, H. W. Baer, J. D. Bowman, M. D. Cooper, B. J. Dropesky, E. Piasezky, and J. N. Knudson, *Physical Review Letters* **55**, 1862 (1985).
8. B. J. Dropesky, G. W. Butler, G. C. Giesler, C. J. Orth, and R. A. Williams, *Physical Review C* **32**, 1305 (1985).
9. G. W. Butler, B. J. Dropesky, C. J. Orth, R. E. L. Green, R. G. Korteling, and G. K. Y. Lam, *Physical Review C* **26**, 1737 (1982).

Physics Department, Lawrence Livermore National Laboratory, Livermore, California 94550

## Time-of-Flight Isochronous (TOFI) Spectrometer

Lawrence Livermore National Laboratory, Livermore, California 94550

J. M. Wouters, K. Vaziri, D. J. Vieira, F. K. Wohn, R. H. Kraus, H. Wollnik, G. W. Butler, J. R. Sims, J. W. van Dyke, S. Archuleta, M. Mays, J. R. Zerwekh, D. D. Kercher

## Introduction

This report is the third in a series of progress reports describing the design, construction, and testing of the time-of-flight isochronous (TOFI) spectrometer and its associated secondary beam line. TOFI, which is being constructed jointly by INC and MP Divisions, is designed to measure in a systematic fashion the ground state masses of the light neutron rich nuclei with  $A \leq 70$  that lie far from the valley of  $\beta$  stability. Three major goals were achieved during the past year:

1. the second half of the transport line was installed and the entire line was tested;
2. the four dipole magnets that constitute the spectrometer were field mapped and optimized; and

3. the spectrometer was installed and tested, and an initial set of data was acquired.

Here we describe these major accomplishments. For a summary of the scientific goals and overall design of the TOFI spectrometer, see the two previous LAMPF Progress Reports.<sup>1,2</sup>

## Secondary Beam Transport Line

The secondary beam line for the TOFI spectrometer was completed in March of 1985 with the installation of the second half of the line. This transport line consists of four quadrupole-triplet focusing magnets, a mass-to-charge filter, and several x,y steering magnets (see Fig. 1). The purpose of the transport line is threefold:

1. to provide a focused image of the target at the entrance to TOFI while capturing the largest solid angle possible from the production target;
2. to reduce the transmission of high-yield light ions (that is, protons, deuterons, alphas, and neutral particles) that would normally saturate the first timing detector; and
3. to physically remove the spectrometer from the LAMPF high-intensity beam line in such a way that easy access to the system is obtained.

To achieve these goals the transport-line optics is arranged as two almost identical quasi-telescopic sections using four quadrupole triplets. The first section incorporates an electrostatic deflector and dipole magnet located immediately in front of the second quadrupole triplet to act as a

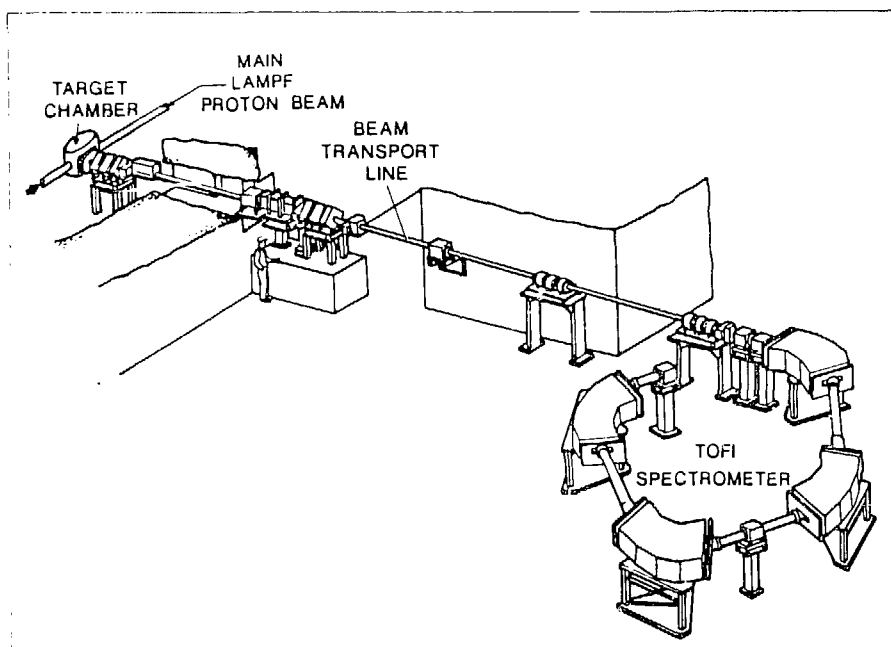


Fig. 1. TOFI spectrometer and its associated transport line.

crude mass-to-charge filter to eliminate most of the high yield light ions. A collimator is placed at an intermediate focal position between the two telescopic sections to define the mass-to-charge transmission. Several tests were carried out to characterize and optimize the transport line performance with respect to solid angle and momentum and mass-to-charge transmission properties, as well as overall image quality.

The transport line was tuned using various alpha sources and light reaction products originating from 800-MeV proton bombardments of a natural thorium target. Each quadrupole triplet was characterized separately in point-to-point focusing tests using  $\alpha$  particles. These imaging studies used a position sensitive multiwire proportional counter<sup>2</sup> located at the intermediate and final focusing positions. Further focusing studies using some or all of the triplets were carried out with  $\alpha$  sources located in the scattering chamber or at positions along the transport line. Figure 2 shows the type of images obtained at the final focusing position (1) for a source located at the target position and (2) for a projected image of a collimator located in the transport line 40 cm from the target.

To deliver a large solid angle to the spectrometer, the transport line reduces the angular spread of the reaction products. This presents an enlarged image of the target region to the spectrometer. Using the general ion optical systems code (GIOS), the  $x$  and  $y$  magnifications were calculated<sup>3</sup> to be 2.0 and 2.3, respectively, which agrees with our

measurements exactly. Using various sized collimators to define the solid angle acceptance of the line, we studied transmission versus solid angle. Only a 5% intensity loss from the target to the final focus was measured for the design solid angle acceptance of 2.5 msr.

Using a multienergy, mixed  $\alpha$  source of  $^{106}\text{Gd}$  and  $^{229}\text{Th}$  and a large area (1000 mm<sup>2</sup>) silicon detector, the momentum transmission of the line was determined in the same fashion as that reported previously for the first half of the line.<sup>2</sup> This momentum transmission curve is basically Gaussian in shape, with a width of  $\delta p/p = 28\%$  (FWHM). This is more than sufficient to fill the spectrometer, which has a design acceptance of  $\delta p/p = 4\%$ . Additional tests showed that the optimized tune developed for one particular  $\alpha$  energy gives good solutions at other energies if scaled according to momentum.

Finally, to investigate the filtering properties of the mass-to-charge ( $m/q$ ) filter, a  $\Delta E$ - $E$  silicon telescope was used to identify proton, deuteron, triton,  $^3\text{He}$ , and  $\alpha$  reaction products. For these tests the transport line was set for a particular momentum-to-charge value (190 MeV/c/ $q$ ) and then the electric field of the ( $m/q$ ) filter was tuned to various values in order to select different ( $m/q$ ) ratios. By comparing the intensity of identified alphas and tritons at different ( $m/q$ ) settings, the ( $m/q$ ) transmission of the trans-

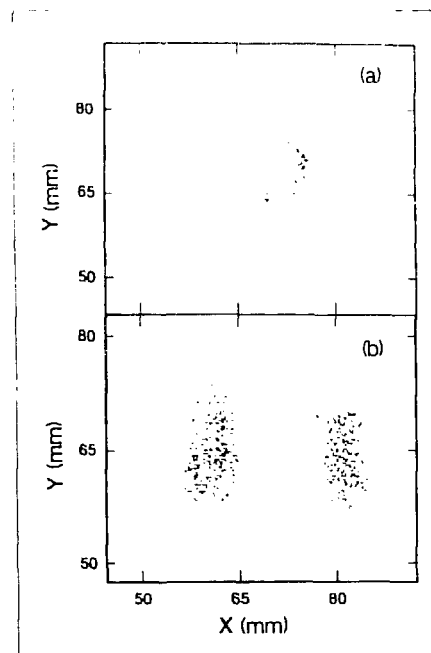


FIGURE 2. Images observed (a) at the end of the transport line for a  $^{241}\text{Am}$   $\alpha$  source located at the production target position and (b) at the intermediate focusing position approximately half way through the transport line for a double slit collimator located 40 cm downstream of the  $\alpha$  source target location. In (a) a circular image is obtained that reflects the source shape.

port line was determined. A clear filtering of the neighboring ( $m, q$ ) species was observed. The  $A/Q$  transmission curve is semi-Gaussian with a width of  $(\delta A/Q)/(A/Q) = 14\%$  (FWHM) and a tail extending to the high  $A/Q$  side of the peak. More specifically, at a setting optimized for tritons (that is,  $A/Q = 3$ ), the intensity of  $\alpha$  particles ( $A/Q = 2$ ) was reduced by more than three orders of magnitude. This filtering is particularly important in our future experiments because the yields of the exotic nuclei of interest will be several orders of magnitude lower than those of  $p, d, \alpha$ , and other recoils with  $A/Q \leq 2$ .

In conclusion, all these measurements agreed with the expected design performance of the transport line.

### Magnet Mapping and Optimization

Mapping of the spectrometer dipole magnets was divided into three separate tasks:

1. optimizing the size of the Rose shims used to extend the radial width of the uniform field region,
2. determining the shape and size of iron wedges used to tilt and straighten the effective field boundaries (EFBs) at the entrance and exit of each magnet, and
3. mapping the uniform portion of the magnetic field in order to build surface inhomogeneity coils.

These measurements and trimming procedures were developed using the first magnet. The optimized design for the Rose shims and wedges determined for the first dipole were duplicated, installed, and checked on the remaining three magnets. Because the four dipoles were nearly identical, no reoptimization of these shims was required. However, the surface coils were custom designed for each magnet in order to remove field non-uniformities that were unique to each dipole magnet. After spending nearly 5 months measuring and optimizing the first dipole, we completed work on the remaining three dipoles in only 2 months.

Optimization of the Rose shims was done using a simple iterative technique in which several radial scans across the pole face were obtained using a Hall probe attached to an  $x, y$  plotter. From these scans the shape of the field could be determined to a relative accuracy of 0.2 G out of an overall field of 5.7 kG. Absolute calibration of the probe was unnecessary and drift corrections could be ignored because of the short (30-s) scan period. The width of the Rose shims (curved segments of 2.5-mm-thick magnet steel attached to the inner and outer radii of the top and bottom poles) was changed after each scan until the widest uniform field region was obtained. The final field shape introduced a slight (0.5-G) field hump

at both the inner and outer radii to compensate for the natural decrease in the magnetic field as the distance from the central radius increases. A complication to the trimming of the Rose shims arose in the region of the top pole piece supports. A noticeable narrowing of the uniform field region was observed at these locations. This effect was corrected by mounting small iron rings around the supports. With these optimization procedures the radial width of the uniform field region (defined here as  $\pm 0.5$  G) was increased from 15 to 20 cm for a pole width of 30 cm and a magnetic gap of 9.6 cm.

Trimming the entrance and exit effective field boundaries of the magnet was done using an iterative technique that determined these boundaries at equal spacings across the width of the pole. Ten Hall-probe scans taken parallel to the particle trajectory at the entrance and exit of each magnet and going from the field-free region outside the magnet to the uniform field region were obtained. Using an interactive analysis code, we transformed these individual scans from the measurement coordinates to magnet coordinates, which we then used to calculate the location of the EFB along each scan to an accuracy of 0.25 mm.

Steel shims placed on the sloped portions of the entrance/exit poles were designed so that all scans resulted in the same EFB location. Four types of shims were finally constructed for each magnet. The outer radius shims were simple 2.5-mm-thick, 2.5- and 5.0-cm-long metal

strips that were bolted in place. The inner radius shims were fairly complicated wedges that had to be optimized using many iterations. These wedges countered the tendency of the field to fall off too quickly near the corners of the poles and thus produce a curved EFB. Two types of wedges and two types of straight shims were required because of the difference between the end of the magnet that had the current leads and the end that did not. The final effective field boundaries were flat (to 0.76 mm over half the central arc length of 78 cm) across the usable portion of the magnet pole width (20 cm).

The final step in the dipole optimization was to produce complete field maps taken near the top and bottom pole pieces in order to construct top and bottom surface coils to reduce the remaining field inhomogeneities unique to each magnet. This step was especially difficult because of the dual requirements for obtaining 0.1-G accuracy in the homogeneous portion of the field and for extending the map into the fringing field regions of the magnet with lower resolution. A new field-mapping technique that acquires two field maps simultaneously was developed to accomplish this dual goal.

The first map used a nuclear magnetic resonance (NMR) magnetometer to measure the field, and the second map used a temperature-stabilized Hall probe. The NMR field

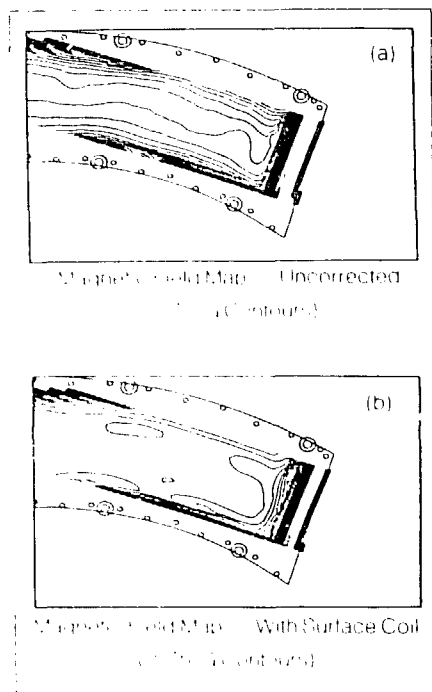


Figure 3. The magnetic field maps that were used to design the inhomogeneity coils. The map in (a) was the uncorrected field map, and the map in (b) was the field map with the surface coil energized.

map was accurate to considerably better than 0.05 G, but could not obtain data in the fringe fields of the magnets. The Hall map covered the entire region that needed to be mapped, but was accurate to only 5 G absolute.

A composite field map was produced by using the NMR map where the magnetometer was stable and by filling the remaining regions with a corrected Hall map. This correction consisted of finding the two most recent data points where both the NMR and Hall maps were valid and then normalizing the Hall data to the NMR data. In this fashion the Hall-probe data were continuously recalibrated on an absolute scale, yielding fringing field data with an accuracy of 0.5 G.

The resulting field maps for the top and bottom poles were modified in several ways in order to create the final contour maps needed to design the surface inhomogeneity coils.

First, the maps had to be extended, using a linear-extrapolation routine, to regions that could not be reached by the field-mapping probes because of obstructions.

Second, a boundary region was defined around the map that was 3.2 cm wide and located 3.2 cm away from the effective surface coil outer edge. Outside this boundary region the map was set to a constant value; inside, the map was set to the final field

value. The values of the data points within the boundary region itself were determined by doing a linear interpolation across the boundary. In this fashion the contour lines of the field map could be smoothly closed.

Third, the maps were smoothed several times using a technique that looked at adjacent data points and averaged over them to redetermine the central data point.

Finally, the maps were drawn full size. The contours were cut by hand in one place and reconnected to form a spiral, permitting current to be fed in at one point of the circuit board and returned at another. The final contour spacing was 0.75 G, producing a field of approximately that uniformity. The field-uniformity improvement resulting from these surface coils can be seen in Fig. 3(a), which shows an uncorrected field map, and Fig. 3(b), which shows the same field map after the surface coil has been energized. The field homogeneity has been improved by approximately a factor of 3.

## Spectrometer Installation and Tuneup

After the magnetic-field optimization of each dipole was completed, the magnets underwent final assembly. This involved the installation of the inhomogeneity surface coils, the quadrupole/hexapole surface coils, and the vacuum tank. (The quadrupole/hexapole surface coils were included to adjust the first- and

second field indices to optimize the isochronous and focusing properties of the spectrometer.) The dipoles were assembled and moved into the TOF experimental area where they were aligned and connected to the cooling water supply and the spectrometer power supply. By the end of October 1985, the installation of the vacuum system was completed and the spectrometer was under vacuum.

After the momentum collimator and fast timing detectors were installed, the spectrometer was turned on for the first time on November 11, 1985. Within the first day the spectrometer had achieved its mass resolving power design goal of  $M/\Delta M = 2000$ , with the measurement of  $^{241}\text{Am}$   $\alpha$  particles showing a timing accuracy of 500 ps out of a total transit time of 600 ns. After 2 weeks of further off line and on line testing, data collection for the first experiment was begun. Data collection continued until mid-December, when the LAMPF production run ended.

The purpose of this initial tuneup experiment was to provide a preliminary data set to develop the data-analysis procedures and to define any remaining improvements needed before the next beam period starts in the summer of 1986. At that time the first experiment will be completed. The experiment seeks to measure the masses of neutron rich nuclei in the  $Z = 10$  to 12 region in an attempt to further understand the appearance of a rapid nuclear shape transition occurring in these nuclei.

---

## References

1. "Progress at LAMPF," Los Alamos National Laboratory report LA-10070-PR (April 1984), pp. 121-124.
2. "Progress at LAMPF," Los Alamos National Laboratory report LA-10429-PR (April 1985), pp. 189-192 and 192-195.
3. J. M. Wouters, D. J. Vieira, H. Wollnik, H. Enge, S. Kowalski, and K. L. Brown, *Nuclear Instruments & Methods* **A240**, 77-90 (1985), and references therein.



**RADIOISOTOPE PRODUCTION****Isotope Production and Separation****Radioisotope Production**

K. E. Peterson, A. N. Herring, M. J. Segura, F. H. Seurer, W. A. Taylor, J. Steinkruger, M. A. Ott, J. A. Barnes, and P. M. Wanek  
(Group INC-3, Los Alamos)

The medical radioisotopes research program in INC-11 (formerly INC-3) continues to supply radioisotopes to the medical research community. Several of these radioisotopes are uniquely produced here and many others can only be produced in quantity at LAMPF. Two new isotopes were made available this year:  $^{32}\text{Si}$  for inhalation studies

and  $^{44}\text{Ti}$  to be used in the  $^{44}\text{Ti}/^{44}\text{Sc}$  generator. The  $^{44}\text{Sc}$  is a positron-emitting isotope that concentrates in the bone. Both of these new radioisotopes were obtained from initial research targets. Additional information will be presented as procedures are finalized.

In 102 shipments, 45.6 Ci of 13 radioisotopes were distributed during FY 1985. These data are summarized in Table I.

Table 1. Medical Radioisotope Shipments, FY 1985

| Isotope        | Supplier/Institution  | Number of Shipments | Amount (mCi)       |                    |
|----------------|---|---------------------|--------------------|--------------------|
|                |   |                     | Shipped            | Received           |
| Technetium-99m | Los Alamos National Laboratory  | 1                   | $5 \times 10^{-4}$ | $5 \times 10^{-4}$ |
| Technetium-99m | Los Alamos National Laboratory  | 1                   | 150.00             | 150.00             |
| Technetium-99m | Los Alamos National Laboratory  | 8                   | 188.59             | 188.59             |
| Technetium-99m | Robert H. Lurie College of Medicine<br>Cook County Hospital, Chicago<br>University of Illinois at Chicago<br>University of Michigan<br>Los Alamos National Laboratory<br>Los Alamos National Laboratory<br>Los Alamos National Laboratory<br>Oak Ridge Y-12 Plant<br>General Electric Health Institute<br>Royal Children's Hospital, Melbourne, Australia<br>University of California, Davis<br>University of New Mexico<br>USDA, Beltsville, Maryland<br>USDA, Grand Forks, North Dakota | 44                  | 2,555.68           | 1,802.00           |
| Technetium-99m | University of Nebraska Medical Center   | 2                   | 617.90             | 441.73             |
| Technetium-99m | Argonne National Laboratory<br>Atomic Energy of Canada, Ltd.<br>Brookhaven National Laboratory<br>E. I. DuPont, NEN Products (New England Nuclear Corp.)<br>Isotope Products Labs<br>Oak Ridge Associated Universities<br>Office des Rayonnements Ionisants, France<br>University of Chicago<br>University of Liege, Belgium<br>University of Wisconsin<br>Washington University via DuPont, NEN<br>Washington University   | 19                  | 792.31             | 790.00             |
| Technetium-99m | Benedict Nuclear Pharmaceuticals, Inc.  | 1                   | 52.79              | 16.00              |
| Sodium-22      | E. I. DuPont/NEN Products<br>New England Nuclear Corp.  | 3                   | 1,328.60           | 1,328.60           |
| Scandium-46    | Los Alamos Group INC-DO   | 1                   | 1.00               | 1.00               |
| Strontium-82   | E. R. Squibb & Sons<br>Medical Research Council (MRC) Cyclotron,<br>Hammermith Hospital, London   | 10                  | 2,966.31           | 2,765.00           |
| Titanium-44    | University of California, Donner Laboratory<br>Los Alamos Group INC-DO<br>Oak Ridge Associated Universities   | 3                   | 0.06               | 0.06               |
| Yttrium-90     | Brookhaven National Laboratory  | 6                   | 36,820.00          | 31,650.00          |
| Yttrium-90     | E. I. DuPont/NEN Products<br>Isotope Products Labs  | 2                   | 90.00              | 90.00              |
| TOTALS         |   | 102                 | 45,563.24          | 39,222.98          |

## Electrolytic Separation of Selenium Isotopes from Proton-Irradiated Targets

P. M. Grant<sup>1</sup>, D. A. Miller<sup>1</sup>, J. S. Gilmore<sup>1</sup>, and H. A. O'Brien, Jr.<sup>1</sup>  
<sup>1</sup>Department of Physics, University of Tennessee,  
 Knoxville, TN 37996, USA

Arsenic-72 has many applications in medicine and environmental toxicology. It is a positron emitter, making it a potentially valuable isotope in positron emission tomography (PET); it might be conjugated to appropriate monoclonal antibodies for use in cancer therapy; and it can be used as a tracer in biochemical studies to evaluate the environmental impact of arsenic produced in coal combustion and geothermal emissions. For many applications it is important to have the radioarsenic in very high specific activity.

Probably the best approach for the production of  $^{72}\text{As}$  is by use of a  $^{72}\text{Sc}/^{72}\text{As}$  radiochemical generator system. Selenium-72 can be produced in reasonable yield by irradiating RbBr targets with 800-MeV protons.<sup>1</sup> We are developing a novel procedure to separate selenium isotopes from the RbBr target material.

The process is based on the electrolytic deposition of the selenium as Cu(I) selenide from a solution containing a Cu(I) ion and selenious acid onto a platinum-gauze electrode. A strongly adherent precipitate of Cu(I) selenide is produced. Virtually quantitative deposition is observed after 1 h; however, several plate/strip steps are required to remove trace radiochemical impurities. The final product contains approximately equal quantities of  $^{76}\text{Se}$  and  $^{72}\text{Se}$  and is suitable for generator development. We usually produce 200- to 300-mCi  $^{72}\text{Se}$  from a 2-day irradiation of a 30-g RbBr target, with an overall recovery of  $\approx 80\%$ .

The success of the electrolytic separation process suggests a novel approach to the construction of a  $^{72}\text{Se}/^{72}\text{As}$  generator system. In developing the separation process we observed that arsenic does not deposit to any appreciable extent under conditions necessary to deposit Cu(I) selenide. Thus it should be possible to develop an electrochemical generator system that would be relatively simple to use. One such system currently under investigation involves concentric cylindrical platinum-gauze electrodes. By reversing the current on these electrodes a series of plate/strip operations should release the  $^{72}\text{As}$  to the solution of electrolyte. This system is currently being tested and results are promising.

## Reference

1. P. M. Grant, D. A. Miller, J. S. Gilmore, and H. A. O'Brien, Jr., "Medium-Energy Spallation Cross Sections. 1. RbBr Irradiation with 800-MeV Protons," *International Journal of Applied Radiation and Isotopes* **33**, 415 (1982).

The goal of our research is to develop methods of attaching radio-nuclides to monoclonal antibodies and antibody fragments for use in tumor imaging and internal radiation therapy. Monoclonal antibodies and their fragments are of interest because they enable the selective targeting of tumors. The labeled antibodies could be used as carriers to transport radioisotopes to tumors,<sup>1</sup> thus minimizing total-body radiation dose and radiation damage to normal tissue. We have developed methods to label antibodies with <sup>67</sup>Cu, a potentially useful medical radioisotope having a suitable half-life (62 h) and nuclear decay properties<sup>2</sup> for use in tumor imaging and therapy. This radioisotope is produced in high specific activity (17 000 Ci/g) at LAMPF. Porphyrins were chosen as <sup>67</sup>Cu chelating agents to be conjugated to antibodies for two reasons:

(1) metalloporphyrins, which are ubiquitous in nature, present little problem of toxicity and (2) copper porphyrins are very stable to loss of copper ions in human serum under simulated *in vivo* conditions.<sup>3</sup> We have adopted the synthetic strategy of coupling activated chelating agents, N-benzyl porphyrins, to antibodies before labeling with <sup>67</sup>Cu. This has the advantage of being a "cold kit," a purified porphyrin-antibody preparation that can be radiometalated as the final step in the synthesis.

## Radio pharmaceutical Labeling Research

### Preparation of Radiolabeled Monoclonal Antibodies

D. Moody (Group II), U. I. Los Alamos

## Radiometalation of N-Benzyl Porphyrins

J. A. Mercer Smith, S. D. Figard, W. A. Taylor, and D. K. Lavallee (City Univ. of New York - Hunter College and Los Alamos)

The remarkable ability of porphyrins to retain bound copper ions and the great stability that synthetic porphyrin ring systems have against degradation make them desirable chelators of  $^{67}\text{Cu}$  for antibody labeling. There are two possible strategies to radiolabel antibodies with  $^{67}\text{Cu}$  using porphyrins:

1. Radiometalate the porphyrin first, purify the copper porphyrin, and then covalently link the metalloporphyrin to the antibody. This method presents the usual difficulties that are inherent whenever short-lived radioisotopes are used.
2. Attach the porphyrin to the antibody, then purify the porphyrin-antibody conjugate before radiometalation of the porphyrin. This strategy has the advantage of being a cold-kit type of synthesis in which radiolabeling is the final step of the preparation.

We are investigating the second strategy as a means of preparing radiolabeled antibodies. A major drawback to the use of porphyrins has been the slow rates at which the relatively inflexible planar porphyrins incorporate metal ions. Although  $\text{Cu}(\text{II})$  is one of the most

rapidly incorporated metal ions, the rate in aqueous solutions in the pH and temperature range where proteins are stable is too slow to make the reactions of  $^{67}\text{Cu}$  with porphyrin-antibody conjugates feasible. The only route available for typical porphyrins is the synthesis of the  $^{67}\text{Cu}$  complex in refluxing dimethylformamide and purification,<sup>4</sup> followed by coupling of the radiolabeled porphyrin complex to the antibody (strategy 1). To achieve the rapid metal-complexation rates that are necessary for a procedure in which a prepurified porphyrin-antibody adduct could be labeled with  $^{67}\text{Cu}$  immediately before use, the porphyrin itself must be synthetically modified.

Lavallee<sup>5</sup> has previously shown that N-substitution of synthetic porphyrins of the *meso*-tetraaryl type leads to greatly increased metal-complexation rates and that the rate is especially favorable for  $\text{Cu}(\text{II})$ . Once the  $\text{Cu}(\text{II})$  ion is bound, the N-substituent must be removed to give a highly stable porphyrin complex because metal ions are readily removed from the N-substituted metalloporphyrins.<sup>6</sup> Simple N-substituents such as the methyl group are not removed by water as a nucleophile under mild conditions, but require such strong nucleophiles as amines.<sup>7</sup> The strong nucleophiles necessary to remove the N-methyl

substituent require reaction conditions too harsh to be used for porphyrin-antibody conjugates; however, N-benzyl substituents are easily removed.<sup>8</sup> The rate for the overall reaction of metal complexation and N-benzyl group removal in buffered aqueous solution is rapid and independent of Cu(II) concentration.<sup>9</sup>

For this study we selected water-soluble, N-benzyl-substituted porphyrins that can be readily coupled to antibodies. Because the coupling of a carboxylate to an amine site on a protein is a common strategy for antibody conjugation reactions, we examined two N-benzyl porphyrins with carboxylic acid functionalities. These two porphyrins are N-benzyl-5,10,15,20-tetrakis(4-carboxyphenyl) porphine, denoted N-bzHTCPP, and N-4-nitrobenzyl-5(4-carboxyphenyl)-10,15,20-tris(4-sulfophenyl) porphine, denoted N-bzHCS<sub>3</sub>P.

The four carboxylate groups of the N-bzHTCPP molecule present the potential problem of crosslinking to amine groups on the antibody. Because several identical carboxylate groups are available, crosslinking between antibodies or multiple attachment on a single antibody is possible. Therefore we decided to include in our studies a synthetic N-benzylporphyrin, N-bzHCS<sub>3</sub>P, that would have several peripheral anionic groups to provide water solubility, but only a single carboxy-

late among them that could be used for coupling. We have described the syntheses of these compounds elsewhere.<sup>3</sup>

In a borate buffer at pH 8.0, the progress of the reaction of Cu(II) with N-bzHTCPP can be followed spectrophotometrically. With the porphyrin concentration at  $10^{-5}$  to  $10^{-3}$  M and Cu(II) concentrations from stoichiometric to  $10^{-2}$  M, the half-life for the reaction at 40°C is less than 5 min and is independent of Cu(II) concentration, demonstrating that metal complexation is faster than debenzylation. With <sup>67</sup>Cu at less than  $10^{-6}$  M (no carrier added) and other conditions as above, ion exchange after separation shows that 95% or more of the <sup>67</sup>Cu is incorporated after 10 min.

The results with cold Cu(II) and uncoupled N-bzHTCPP support our results, which indicate rapid binding of <sup>67</sup>Cu to porphyrin-antibody adducts. Thus the N-benzyl porphyrins can be metalated with <sup>67</sup>Cu readily under conditions that do not denature proteins. Therefore, the attachment of N-benzyl porphyrins to antibodies followed by rapid metalation with radiocopper appears to be a very promising method to radiolabel antibodies with copper.

## Coupling Porphyrins to Antibodies for Radiolabeling with Copper-67

Richard L. A. Marder, with E. N. Cuthbert, M. H. Harner, and D. K. Johnson, Los Alamos City Univ. of New York, State College, and Univ. of W. Virginia

We are developing methods to attach porphyrins as chelating agents to antibodies that retain the antigen-binding capacity of the antibody. Copper-67, a radioisotope with a half-life and nuclear decay properties particularly suitable for tumor imaging and therapy, is chelated very tightly by porphyrins. If antibodies can be labeled with  $^{67}\text{Cu}$  while retaining their immunological activity, they would have great potential as agents for transporting of the copper isotope to cancerous tissue with minimum radiation damage to normal tissue.

The two porphyrins we have used are N-benzyl-5,10,15,20-tetrakis(4-carboxylphenyl) porphine, denoted N-bzHTCPP, and N-4-nitrobenzyl-5-(4-carboxyphenyl)-10,15,20-tris(4-sulfophenyl) porphine, denoted N-bzHCS<sub>3</sub>P. The N-benzyl group on each porphyrin permits rapid metalation of the porphyrin under very mild conditions that are compatible with antibody integrity. The carboxylate groups on the N-benzyl porphyrins can be used to form a covalent linkage to antibodies. In addition to the possibility of crosslinking of the antibody by the coupling reagents used, the potential to preactivate more than one carboxylate and subsequently to crosslink the antibody with the porphyrin exists with the N-bzHTCPP. This problem was addressed by examining the same

conjugation reactions for N-bzHCS<sub>3</sub>P with its single carboxylate. In all cases when crosslinking was observed with the N-bzHTCPP, substituting the N-bzHCS<sub>3</sub>P under identical conditions eliminated the crosslinking.

The porphyrin-antibody system presents problems for the analysis of porphyrin-coupling reactions. First, porphyrins have an inherent nonspecific affinity for proteins in general,<sup>10</sup> the "sticky-porphyrin" problem. Second, copper has its own affinity for protein, and this is the basis for the Biuret reaction, a standard protein assay.<sup>11</sup> Gel filtration by high-performance liquid chromatography (HPLC) cannot separate nonspecifically bound porphyrin from the antibody and antibody-porphyrin conjugates. HPLC was also inadequate in removing nonspecifically bound copper from the antibody when  $^{67}\text{Cu}$  was added to metalate the porphyrin after coupling. A different method of analysis was needed.

We developed sodium dodecylsulfate polyacrylamide gel electrophoresis<sup>12</sup> as an analytical method that removes all the nonspecifically associated porphyrin. Gel-scanning spectroscopy at wavelengths appropriate for either protein (280 nm) or porphyrin (405/435 nm) permits accurate measurement of the porphyrin covalently attached to the protein after completion of the electrophoresis.

Thus the use of a radiotracer is unnecessary. Gel filtration at very slow techniques was also developed for preparative scale purification of the conjugates and for the removal of nonspecifically bound copper. The latter is of importance for the preparation of porphyrin antibody conjugate kits that can be easily labeled with short lived isotopes by hospital personnel for clinical use.

The porphyrins we are studying have carboxylate functional groups; consequently, we have examined reagents commonly used to form amide bonds between carboxylate and amino groups. The first reagent to be studied was 1-ethyl-3-(3-dimethylamino-propyl) carbodiimide hydrochloride (EDAC), a water-soluble carbodiimide. We also examined N-hydroxysuccinimide used in conjunction with EDAC (NHS/EDAC). The third reagent we tested was a peptide synthesis reagent, 1,1'-carbonyldiimidazole (CDI). Because all these reagents react with carboxylate-function groups on the protein as well as those on the porphyrin, we have used one basic strategy in our attempts at conjugation. The porphyrin is first preactivated with the coupling reagent before the addition of the antibody. The antibody is then added to the reactive intermediate, the preactivated porphyrin, and allowed to couple to the protein's amino groups, which are pri-

marily lysine residues.

Reaction with EDAC proved to be unsuccessful. A study of the NHS/EDAC reaction as a function of preactivation time, preactivation pH, coupling time, coupling pH, and reagent concentrations gave an optimum coupling yield of 22% (average of 2.2 porphyrins/antibody) for non-cross-linked N-bzHTCPP-antibody conjugates. Under identical conditions, the N-bzHCS<sub>3</sub>P had an optimum coupling yield of 20% (average of 2.0 porphyrins/antibody) in non-cross-linked conjugates, and crosslinking was eliminated. A similar study for CDI gave an optimum coupling yield of 30% (average of 3 porphyrins/antibody) for non-cross-linked N-bzHTCPP-antibody conjugates. Similar conditions gave a yield of 15% (average of 1.5 porphyrins/antibody) for N-bzHCS<sub>3</sub>P antibody conjugates.

We have shown that N-benzyl porphyrins can be attached covalently to antibodies, and we have developed methods to quantify the amount coupled. The ease of radiometallation of the N-benzyl porphyrin with <sup>67</sup>Cu both before and after conjugation has been demonstrated. Our future work will determine the effect the coupling reactions have on the antigen-binding capacity of the porphyrin-antibody conjugates while examining the possibility of using other conjugation methods.



---

## References

1. D. E. Yelton and M. D. Scharff, "Monoclonal Antibodies: A Powerful New Tool in Biology and Medicine," *Annual Review of Biochemistry* **50**, 657 (1980).
2. S. Raman, and J. j. Pinajian, "Decay of  $^{67}\text{Cu}$ ," *Nuclear Physics A* **131**, 393 (1969).
3. J. A. Mercer-Smith, S. D. Figard, Z. V. Svitra, S. M. Fehrenbach, and D. K. Lavalley, "Techniques of Radiolabeling Antibodies with Copper-67 Utilizing Porphyrin Chelators," Los Alamos National Laboratory document LA-UR-85-3748, proceedings of the Radiochemical Labeling and Characterization of Proteins Symposium, Society of Nuclear Medicine Annual Meeting, Houston, Texas, May 31-June 5, 1985 (in press).
4. J. A. Mercer-Smith, R. Scott Rogers, N. J. Segura, and W. A. Taylor, "Synthesis of  $^{67}\text{Cu}$  *meso*Tetra(4-Carboxyphenyl) Porphine for Conjugation to Monoclonal Antibodies," Los Alamos National Laboratory report LA-10366-PR (April 1985), p. 69.
5. General Mechanism of Prophyrin Metallation," *Inorganic Chemistry* **18**, 3358 (1979).
6. D. K. Lavalley and A. E. Gebala, "Facile Dissociation of a Copper Porphyrin: Chlorocopper (II) N-Methyltetraphenylporphine," *Inorganic Chemistry* **13**, 2004 (1974).
7. D. Kuila and D. K. Lavalley, "Kinetics and Mechanisms of Reactions of N-Alkylporphyrin Complexes 3: The Effect of Porphyrin Ring Substituents and Reaction Media," *Inorganic Chemistry* **22**, 1095 (1983).

8. D. K. Lavalley and D. Kuila, "Kinetics of Dealkylation Reactions of N-Alkylporphyrin Complexes 4: Effect of the N-Alkyl and N-Aryl Substituents on the Dealkylation Process," *Inorganic Chemistry* **23**, 3987 (1984).
9. D. K. Lavalley, K. Liddane, A. Diaz, D. Mansuy, and J. P. Battioni, "N-Benzylporphyrins as Precursors for the Rapid Synthesis of Metalloporphyrins" (submitted to *Inorganic Chemistry*).
10. G. R. Parr and R. F. Pasternak, "The Interaction of Some Water-Soluble Porphyrins and Metalloporphyrins with Human Serum Albumin," *Bioinorganic Chemistry* **7**, 277 (1977).
11. A. G. Gornall, C. J. Bardawill, and M. M. Davis, "Determination of Serum Proteins by Means of the Biuret Reaction," *Journal of Biological Chemistry* **177**, 751 (1949).
12. U. K. Laemmli, "Cleavage of Structural Proteins During the Assembly of the Head of Bacteriophage T4," *Nature (London)* **227**, 680 (1970).

## Radioisotope Production Publications

### Publications (INC-3)

K. E. Peterson, M. A. Ott, F. H. Seurer, N. J. Segura, W. A. Taylor, J. W. Barnes, F. J. Steinkruger, K. E. Thomas, and Philip M. Wanek, "INC-3 Isotope Production Activities in FY 1984," in "Isotope and Nuclear Chemistry Division Annual Report FY 1984," Los Alamos National Laboratory report LA-10366-PR (April 1985), pp. 66-69.

J. A. Mercer-Smith, R. S. Rogers, N. J. Segura, and W. A. Taylor, "Synthesis of Copper-67 meso-Tetra-(4-Carboxyphenyl) Porphine for Conjugation to Monoclonal Antibodies," in "Isotope and Nuclear Chemistry Division Annual Report FY 1984," Los Alamos National Laboratory report LA-10366-PR (April 1985), pp. 69-71.

P. M. Wanek, Z. V. Svitra, R. S. Rogers, and W. A. Taylor, "Imaging and Biodistribution Capabilities at INC-3," in "Isotope and Nuclear Chemistry Division Annual Report FY 1984," Los Alamos National Laboratory report LA-10366-PR (April 1985), pp. 76-77.

P. M. Wanek and F. J. Steinkruger, "Rubidium-86 Production," in "Isotope and Nuclear Chemistry Division Annual Report FY 1984," Los Alamos National Laboratory report LA-10366-PR (April 1985), p. 73.

F. J. Steinkruger, P. M. Wanek, and D. C. Moody, "Cadmium-109 → Silver-190m Biomedical Generator," in "Isotope and Nuclear Chemistry Division Annual Report FY 1984," Los Alamos National Laboratory report LA-10366-PR (April 1985), pp. 73-75.

M. A. Ott, J. W. Barnes, F. H. Seurer, N. J. Segura, W. A. Taylor, H. A. O'Brien, Jr., and D. C. Moody, "Improved Targeting System for  $^{123}\text{Xe} \rightarrow ^{123}\text{I}$  Production and Recovery," in "Isotope and Nuclear Chemistry Division Annual Report FY 1984," Los Alamos National Laboratory report LA-10366-PR (April 1985), pp. 71-72; and ———, "New Stringer and Targeting System for  $^{123}\text{Xe} \rightarrow ^{123}\text{I}$  Production and Recovery," in "Progress at LAMPF," Los Alamos National Laboratory report LA-10429-PR (April 1985), p. 139.

K. E. Thomas, N. J. Segura, and J. W. Barnes, "Isotope Separations from a ZnO Target," in "Progress at LAMPF," Los Alamos National Laboratory report LA-10429-PR (April 1985), p. 139.

F. J. Steinkruger, P. M. Wanek, and D. C. Moody, " $^{109}\text{Cd} \rightarrow ^{109\text{m}}\text{Ag}$  Biomedical Generator," in "Progress at LAMPF," Los Alamos National Laboratory report LA-10429-PR (April 1985), pp. 143-144.

J. A. Mercer Smith, N. J. Segura, F. J. Steinkruger, Z. V. Svitra, W. A. Taylor, and P. M. Wanek, "Synthesis and Biodistribution of Copper-67 meso-Tetra (4-Carboxyphenyl) Porphine," in "Progress at LAMPF," Los Alamos National Laboratory report LA-10429-PR (April 1985), pp. 145-146.

J. A. Mercer Smith, S. D. Figard, and D. K. Lavalley, "Reactions to Conjugate Porphyrins to Antibodies," in "Progress at LAMPF," Los Alamos National Laboratory report LA-10429-PR (April 1985), pp. 146.

Z. V. Svitra, R. S. Rogers, and D. S. Wilbur, "Synthesis of Small Molecules Labeled with Bromine-77," in "Progress at LAMPF," Los Alamos National Laboratory report LA-10429-PR (April 1985), pp. 146-147.

P. M. Grant and P. M. Wanek, "Radiation-Induced Redox Speciation of  $^{77}\text{Br}$  in Aqueous Solution as Determined by Anion Chromatography," Los Alamos National Laboratory document LA-UR-84-3868 (submitted to *Radiochimica Acta*).

J. A. Mercer Smith, A. Raudino, and D. C. Mauzerall, "A Model of the Origin of Photosynthesis. III. The Ultraviolet Photochemistry of Uroporphyrinogen," *Photochemistry and Photobiology* **42**, 239-244 (1985).

J. A. Mercer Smith, S. D. Figard, D. K. Lavalley, and Z. V. Svitra, "Techniques of Radiolabeling Antibodies with Copper-67 Utilizing Porphyrin Chelators," Los Alamos National Laboratory document LA-UR-85-536 (submitted to the *Journal of Nuclear Medicine*).

F. J. Steinkruger, P. M. Wanek, and D. C. Moody, "Cadmium-109/Silver-109m Biomedical Generator," Los Alamos National Laboratory document LA-UR-84-4029 (submitted to the *Journal of Nuclear Medicine*).

F. T. Avignone, III, W. C. Barker, H. S. Miley, H. A. O'Brien, Jr., F. J. Steinkruger, and P. M. Wanek, "Near Threshold Behavior of Pair-Production Cross Sections in a Lead Target" (submitted to *Physica Review A*).

M. D. Hylarides, P. L. Buksa, F. A. Mettler, and D. S. Wilbur, "Radiobromination of the 1-Position of Estradiol Using No-Carrier-Added Bromine-77," *Journal of Labelled Compounds and Radiopharmaceuticals* **22**, 437 (1985).

M. D. Hylarides, A. A. Leon, F. A. Mettler, and D. S. Wilbur, "Radiolabeling of the B- and C-Ring of Estradiol Using No-Carrier-Added Bromine-77," *Journal of Labelled Compounds and Radiopharmaceuticals* **22**, 443 (1985).

M. Speranza, C. Y. Shiue, A. P. Wolf, D. S. Wilbur, and G. Angelini, "Regiospecific Radiofluorination of Arylpentafluorosilicates as a General Route to Fluorine-18-Labeled Aryl Fluorides," *Journal of the Chemical Society, Chemical Communication* **21**, 1448 (1984).

D. S. Wilbur, S. R. Garcia, M. J. Adam, and T. J. Ruth, "An Evaluation of the Introduction of Stable Nuclides of Bromine into High Specific Activity Radiobrominations," *Journal of Labelled Compounds and Radiopharmaceuticals* **21**, 767 (1984).

D. S. Wilbur and Z. V. Svitra, "Electrophilic Radiobrominations of Hippuric Acid: An Example of the Utility of Aryltrimethylsilane Intermediate," *Journal of Labelled Compounds and Radiopharmaceuticals* **21**, 415 (1984).

D. S. Wilbur, "Structural Determination of Some Chloroazepine-2,5-diones Using a Lanthanide Shift Reagent," *Journal of Heterocyclic Chemistry* **21**, 801 (1984).

M. D. Hylarides, A. A. Leon, F. A. Mettler, and D. C. Wilbur, "Synthesis of 1-Bromoestradiol," *Journal of Organic Chemistry* **49**, 2744 (1984).

### Patents (INC-3)

H. A. O'Brien, Jr., J. W. Barnes, W. A. Taylor, K. E. Thomas, and G. E. Bentley, "Method of Producing <sup>67</sup>Cu," U.S. Patent No. 4,487,738, December 1984.

P. M. Wanek, F. J. Steinkruger, and D. C. Moody, "Biomedical Silver-109m Isotope Generator," patent submitted, 1985.

## THEORY

### Nonanalog Pion Double Charge Exchange Through the $\Delta_{33}$ -Nucleon Interaction

Results are presented for the calculation of the nonanalog pion double charge exchange cross section through the  $\Delta_{33}$ -nucleon interaction. The calculation is done in the distorted-wave impulse approximation framework. The transition density was constructed microscopically for transitions between specific shell model configurations. The reaction dynamics suggested by the data is DCX through the  $\Delta_{33}$  resonance, as shown in Fig. 1. A model of the force including  $\pi + \rho$  exchange was used.

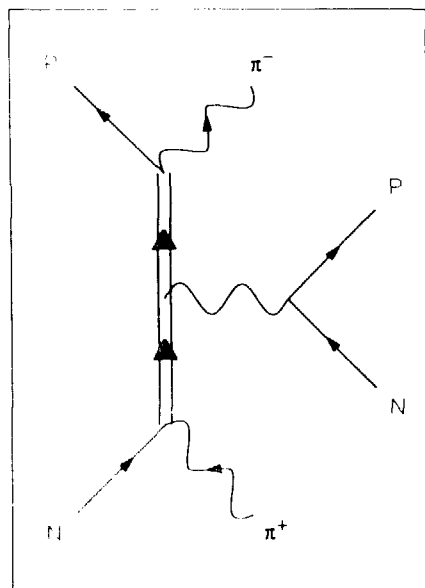


FIGURE 1. Reaction mechanism for the nonanalog  $\Delta_{33}$ -nucleon interaction.

Double-charge-exchange (DCX) cross sections were calculated within a distorted-wave impulse approximation framework.<sup>1</sup> The transition density was constructed microscopically for transitions between specific shell model configurations. The reaction dynamics suggested by the data is DCX through the  $\Delta_{33}$  resonance, as shown in Fig. 1. A model of the force including  $\pi + \rho$  exchange was used.

Results for the angular distribution (Fig. 2) and energy dependence of the  $0^\circ$  cross section (Fig. 3) are shown. Although the magnitude of the  $0^\circ$  cross section depends sensitively on the range parameter of the pion-nucleon form factor, the angular distribution does not, suggesting that the  $\Delta$ -nucleon interaction is the important physical mechanism underlying the DCX.

## Reference

1. R. Gilman, H. T. Fortune, M. B. Johnson, E. R. Siciliano, H. Toki, and A. Wirzba, *Physical Review C* **32**, 349 (1985).

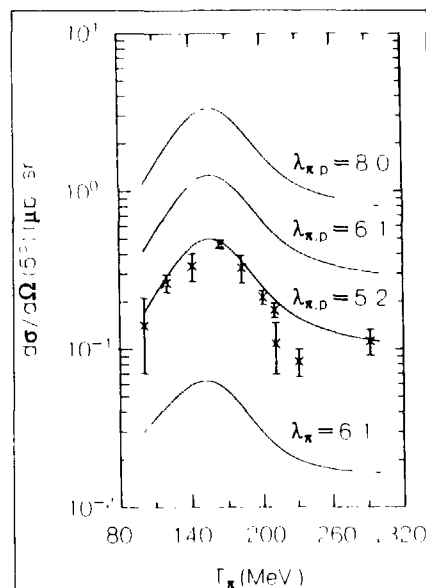


FIGURE 2. Energy dependence of calculations of  $^{16}\text{O}(\pi^+\pi^-)^{16}\text{Ne}$  (g.s.) for several values of  $\lambda_\pi$  and  $\lambda_\rho$  (values given in  $\text{fm}^{-1}$ ) contrasted with data. The curve labeled  $\lambda_\pi = 6.1$  was calculated without an intermediate  $\rho$  meson.

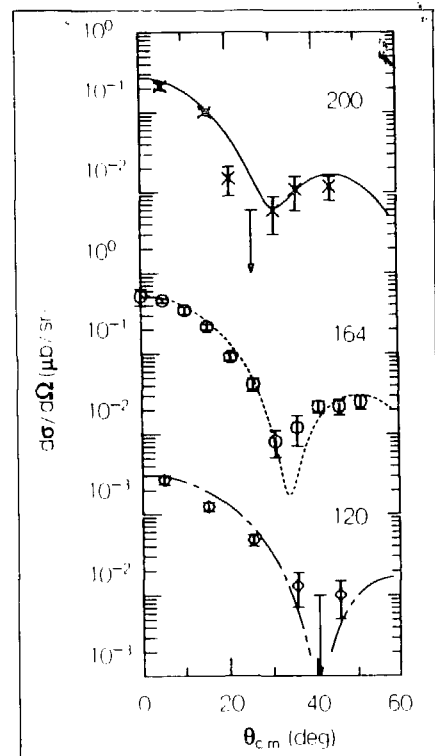


FIGURE 3. Angular distribution of calculations of  $^{16}\text{O}(\pi^+\pi^-)^{16}\text{Ne}$  (g.s.) contrasted with angular distributions plotted against  $\theta_{c.m.}$  in degrees. The calculations used  $\lambda_\pi = \lambda_\rho = 5.2 \text{ fm}^{-1}$ . The incident pion energy,  $T_\pi$  (MeV) is denoted beside each curve.

It has been recognized that the  $\eta(548)$  meson plays almost no role in traditional nuclear structure physics<sup>1</sup> because the  $\eta NN$  coupling constant is very small<sup>2</sup> when compared with the  $\pi NN$  and  $\pi N\Delta$  coupling constants. The situation, however, is quite different in medium- and high-energy nuclear reactions where  $\eta$  production becomes possible. In a recent LAMPF experiment,<sup>3</sup> a significant amount of pion-induced  $\eta$  production in  $^4\text{He}$  and  $^{12}\text{C}$  has been detected at pion kinetic energies near 500 MeV. A recent theoretical model<sup>4</sup> for  $\pi N \rightarrow \eta N$  reactions indicates that threshold pionic  $\eta$  production on a nucleon proceeds mainly through the formation of the  $N^*(1535)$  resonance and that the  $\eta NN^*$  coupling constant is not small. Production of the  $\eta$  meson has also been observed in proton-nucleus collisions at proton kinetic energies of  $\sim 1$  GeV. In addition, experimental evidence of  $\pi^0\text{-}\eta^0$  mixing in nuclear reactions has also been reported.<sup>5</sup> Clearly, medium-energy nuclear reactions create new opportunities for studying the interaction between a nucleon and the short-lived ( $\sim 10^{-18}$  s)  $\eta$  meson.

The work of Bhalerao and Liu<sup>4</sup> indicates that the realistic  $\eta N \rightarrow \eta N$  interaction, which is compatible with the  $\pi N \rightarrow \eta N$  data, is attractive at low energies. We have used the model of Ref. 4 to generate an  $\eta$  nucleon and then a covariant  $\eta$ -nucleus optical potential. Our result is that this optical potential can lead to the formation of nuclear bound states of the  $\eta$  meson.<sup>6</sup>

Because the  $\eta$  has no electric charge, these bound states of  $\eta$  are not caused by the Coulomb force. They are solely the result of the strong interaction between the  $\eta$  meson and the nucleons in the nucleus. In these bound systems, which we call  $\eta$ -mesic nuclei, the  $\eta$  meson is bound in a nuclear orbit.

In Table I we present the predicted bound-state levels in various nuclei.<sup>6</sup> These bound states are obtained with full ( $s$ ,  $p$ , and  $d$ -wave)  $\eta N$  interaction as well as with Fermi-averaging over the nucleon motion. In our full off-shell calculation, all

## Theoretical Evidence for the Existence of the $\eta$ -Mesic Nucleus

© Haider and L. C. Liu (Los Alamos)

TABLE I. The Binding Energies and Half Widths (in Millions of Electron volts) of  $\eta$ -Mesic Nuclei. The parameter sets I and II refer to the parameters of Ref. 4 determined from the  $\pi N$  phase shifts of Arndt and the CERN theoretical group, respectively.

| Nucleus           | Orbit | Set I               | Set II              |
|-------------------|-------|---------------------|---------------------|
| $^{208}\text{Pb}$ | 1s    | $-(22.20 + 11.43i)$ | $-(19.74 + 11.21i)$ |
|                   | 2s    | $-(2.68 + 5.99i)$   | $-(0.95 + 5.44i)$   |
|                   | 1p    | $-(13.74 + 9.53i)$  | $-(11.32 + 9.11i)$  |
|                   | 1d    | $-(4.38 + 6.89i)$   | $-(2.51 + 6.44i)$   |
| $^{90}\text{Zr}$  | 1s    | $-(17.27 + 9.72i)$  | $-(14.86 + 9.39i)$  |
|                   | 1p    | $-(5.12 + 6.39i)$   | $-(3.54 + 5.80i)$   |
| $^{40}\text{Ca}$  | 1s    | $-(10.44 + 7.11i)$  | $-(8.38 + 6.63i)$   |
| $^{16}\text{O}$   | 1s    | $-(4.10 + 5.17i)$   | $-(2.66 + 4.55i)$   |
| $^{12}\text{C}$   | 1s    | $-(1.75 + 3.60i)$   | $-(0.76 + 2.96i)$   |

subthreshold  $\eta N$  interactions enter (see Ref. 6 for details). From Table I we see that the  $\eta$ -mesic nucleus can exist for nuclei ranging from  $^{12}\text{C}$  to  $^{208}\text{Pb}$ . The fact that a nucleus of sufficient size is required to develop bound states, which are absent in

few-nucleon systems, is easily understood from basic quantum mechanical principles.<sup>7</sup>

It is instructive to compare the binding energies of  $\eta$ -mesic nuclei with those of  $\Lambda$  hypernuclei. This is done in Fig. 1, where we show the  $A$  dependence of the predicted binding energies of the 1s-state of the  $\eta$ -mesic nuclei (solid circles) together with the extrapolated  $A$  dependence of the  $\Lambda$ -hypernuclei binding energies<sup>8</sup> (dashed curve). We note that the difference in the binding energies,  $(B.E.)_{\Lambda} - (B.E.)_{\eta}$ , is nearly equal to half the separation energy of the nucleons in these nuclei. This difference can be qualitatively understood from the fact that a  $\Lambda$  hypernucleus is formed after con-

verting an already bound neutron, whereas to form an  $\eta$ -mesic nucleus the  $\eta$  meson has to be captured into a bound orbit.

We have further noted that only the  $s$ -wave  $\eta N$  interaction is important. Pauli blocking and the density-square dependent interaction have very small effects on the calculated binding energies and widths. Deviations of measured binding energies and widths from the predicted ones, therefore, could be due mainly to the medium effects on other dynamical quantities such as the self-energies of the  $\eta$ .

As the work continues we shall extend our calculations to identify the experimental signatures of  $\eta$ -mesic nuclei.

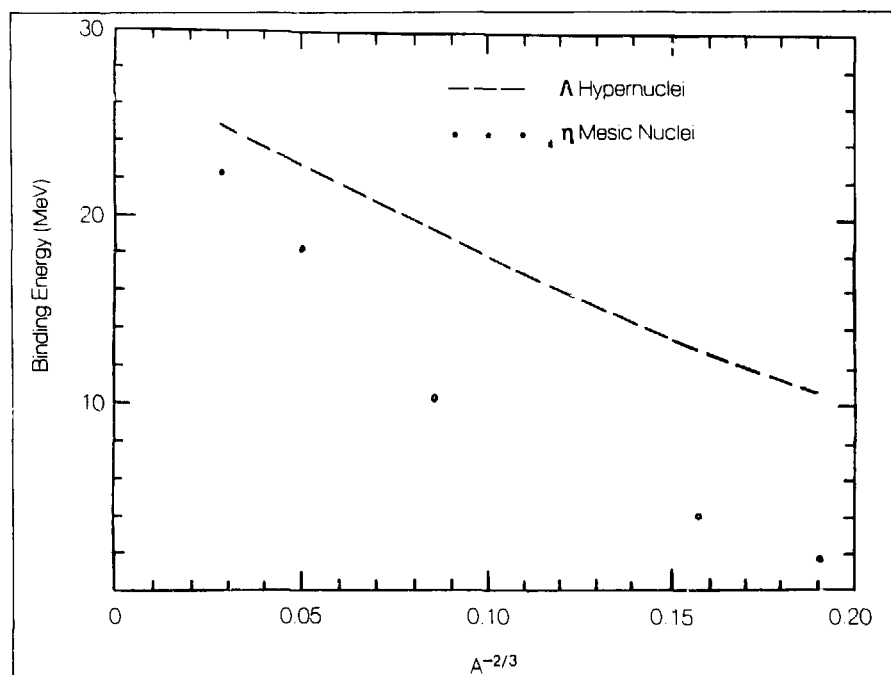


FIGURE 1 The  $A$  dependence of the binding energies of the 1s-state  $\eta$ -mesic nuclei (solid circles) and of the  $\Lambda$  hypernuclei (dashed curve). The  $\eta$ -mesic nuclear-binding energies are the set I results of Table I. The  $\Lambda$ -hypernuclei binding energies are extrapolated from those determined in light nuclei by using the formula given in Ref. 8.



---

## References

1. H. Pilkuhn, *The Interactions of Hadrons* (North-Holland, Amsterdam, 1967).
2. W. Grein and P. Kroll, *Nuclear Physics* **A338**, 332 (1980).
3. J. C. Peng et al., *AIP Conference Proceedings* **133**, 255 (1985).
4. R. S. Bhalerao and L. C. Liu, *Physical Review Letters* **54**, 865 (1985).
5. P. Berthet et al., *Nouvelle de Saturne* (Laboratoire National Saturne, Saclay, France, 1984), Vol. 9A, p. 28.
6. Q. Haider and L. C. Liu, "Formation of Eta-Mesic Nucleus," Los Alamos National Laboratory document LA-UR-85-3361 (submitted to *Physics Letters B*).
7. L. I. Schiff, *Quantum Mechanics*, 3rd ed. (McGraw-Hill, Tokyo, Japan, 1968).
8. B. Povh, *Annual Review of Nuclear and Particle Science* **28**, 1 (1978).

## A Self-Consistent Calculation of One-Gluon Exchange in the Friedberg-Lee Soliton Model

John M. Rusk and Richard A. Arndt

Department of Physics, University of Maryland, College Park, Maryland 20742

Received 12 October 1983

Revised 12 December 1983

Abstract

One-gluon exchange (OGE) is included in the Friedberg-Lee soliton model.

The masses of the ground-state baryons and mesons in the octet of flavor SU(3) are calculated.

The parameters are given in Part I of this series of papers.

The masses of the  $\Delta$  and  $\Omega$  are used to determine the parameters. All other masses are predicted.

| Particle   | Calculated | Experiment |
|------------|------------|------------|
| $\Lambda$  | 1146       | 1116       |
| $\Sigma$   | 1185       | 1193       |
| $\Xi$      | 1267       | 1313       |
| $\Delta$   | 1230       | 1232       |
| $\Sigma^*$ | 1244       | 1244       |
| $\Xi^*$    | 1254       | 1253       |
| $\Omega$   | 1213       | 1212       |
| $\pi$      | 117        | 135        |
| $\rho$     | 737        | 770        |
| $\omega$   | 767        | 782        |
| $\eta^*$   | 1021       | 995        |
| $\eta$     | 549        | 549        |

It is well known that static bag models<sup>1,2</sup> have been relatively successful in reproducing the spectra and properties of low-lying hadronic states involving light quarks (up, down, and strange). A central difficulty with all such models is the handling of the dynamics of the confinement mechanism. A field-theoretical approach to this dynamics has been formulated by Friedberg and Lee in their nontopological soliton bag model.<sup>3</sup>

Numerical solutions to the Friedberg-Lee model involving only quark and scalar fields have been obtained by many authors.<sup>4-7</sup> The model was first applied to the nucleon and the delta by Goldflam and Willets.<sup>8</sup> It was later extended to the study of mesons by Celenza et al.<sup>9</sup> In all these calculations<sup>4-9</sup> the exchange of gluons between the quarks was neglected.

The effects of one-gluon exchange (OGE) have been investigated recently by Bickeböllner et al.<sup>10</sup> In their work the gluon field is treated perturbatively to lowest order in the strong-coupling constant  $\alpha_s$ . The effects of OGE on hadron masses have also been studied by the MIT group using a perturbative approach.<sup>1</sup> The perturbative OGE assumes that the interior of the bag belongs, presumably, to the region where asymptotic freedom holds; consequently, the gluonic interactions can be treated perturbatively. However, there is no convincing argument to support the idea that the asymptotically free region is indeed attained everywhere inside the bag, which can have a

spatial extension as large as 1 to 2 fm. Furthermore, the effective strong-coupling constant, as determined from perturbative calculations of OGE,<sup>1,10</sup> is rather large ( $\sim 2$ ) and therefore should cause concerns about the soundness of evaluating OGE perturbatively.

Over the past year we have developed a self-consistent procedure for calculating OGE effects in the Friedberg-Lee model.<sup>11,12</sup> This procedure takes into account the iteration of OGE to all orders as opposed to the more commonly used first-order perturbative calculations. The procedure developed by us is quite general and can be easily adapted to other bag models.

TABLE II Magnetic Moments (in Units of Nuclear Magnetons) of the Baryon Octet Calculated with the Parameters Listed in Table I

| Particle    | Calculated | Experiment |
|-------------|------------|------------|
| $p$         | 2.62       | 2.79       |
| $n$         | -1.74      | -1.91      |
| $\Lambda^0$ | -0.55      | -0.61      |
| $\Sigma^+$  | 2.57       | 2.38       |
| $\Sigma^0$  | 0.79       | ...        |
| $\Sigma^-$  | -1.02      | -1.10      |
| $\Xi^0$     | -1.40      | -1.25      |
| $\Xi^-$     | -0.50      | -0.69      |

In Table I we present our results for the ground-state masses of the baryons (octet and decuplet) and mesons (pseudoscalar and vector nonets). The most striking feature of the self-consistent calculation is the prediction for the pion mass ( $\sim 117$  MeV). It should be mentioned that the perturbative OGE cal-

calculations<sup>1,12</sup> predict the pion mass to be  $\sim 350$  MeV.

In Table II we present the results for the magnetic moments of the baryon octet and compare them with the available experimental data. Our predicted value of  $g_A/g_V$  for the proton is 1.01, to be compared with the experimental value of 1.25. Because chiral symmetry and other related dynamics have not been taken into account in our calculations, we consider the level of agreement between our results and the data quite satisfactory.

In Fig. 1 we compare the measured proton and pion form factors with the theoretical predictions. It is worth noting that a self-consistent treatment of OGE improves considerably the calculated form factors for momentum-transfer  $q < 600$  MeV/c, indicating that it represents a significant component of physics at low-momentum transfer. The discrepancy between the calculated form factors (perturbative and self-consistent) and the experimental data at very large  $q$  is of no surprise because the behavior of the form factor at large  $q$  depends on dynamics beyond OGE that have not been considered in this work.

In conclusion, we believe that one-gluon exchange has to be treated self-consistently in quark models before applying these models to nuclear physics.

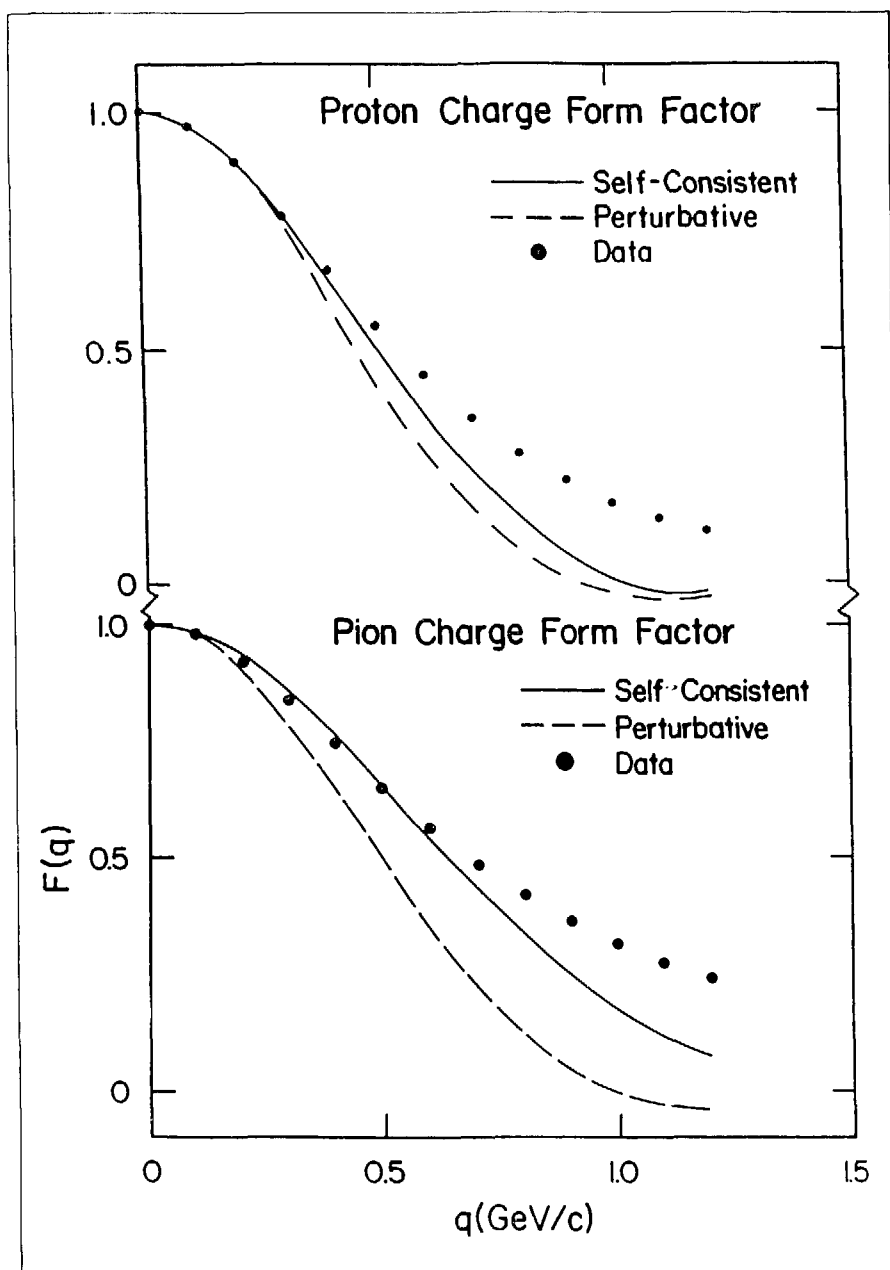


FIGURE 1. The measured proton and pion form factors compared with the predictions of the perturbative (Ref. 12) and self-consistent calculations

---

## References

1. T. DeGrand, R. L. Jaffe, K. Johnson, and J. Kiskis, *Physical Review D* **12**, 2060 (1975).
2. A. W. Thomas, *Advances in Nuclear Physics* **13**, 1 (1983).
3. R. Friedberg and T. D. Lee, *Physical Review D* **18**, 2623 (1978); and T. D. Lee, *Physical Review D* **19**, 1802 (1979).
4. R. Goldflam and L. Wilets, *Physical Review D* **25**, 1951 (1982).
5. R. Saly and M. K. Sundaresan, *Physical Review D* **29**, 525 (1984).
6. T. Köppel and M. Harvey, *Physical Review D* **31**, 171 (1985).
7. L. R. Dodd and M. A. Lohe, *Physical Review D* **32**, 1816 (1985).
8. R. Goldflam and L. Wilets, *Comments on Nuclear and Particle Physics* **12**, 191 (1984).
9. L. S. Celenza, A. Rosenthal, and C. M. Shakin, *Physical Review C* **31**, 212 (1985), and **31**, 232 (1985).
10. M. Bickeböller, M. C. Birse, H. Marschall, and L. Wilets, *Physical Review D* **31**, 2892 (1985).
11. Q. Haider and L. C. Liu, "The Effect of Self-Consistent Treatment of One-Gluon Exchange in the Friedberg-Lee Nontopological Soliton Model," *Journal of Physics G (Letter)* (in press).
12. Q. Haider and L. C. Liu, Los Alamos National Laboratory document LA-UR-85-1360 (1985).

## I. Introduction

The pion-nucleon interaction below 100 MeV has been a focal point of interest in hadronic physics for many years. For many the desire for better data was motivated by the possibility of being able to compare data with the predictions of PCAC. More generally, however, this system provides a laboratory for testing, in some depth, our basic concepts of hadronic interactions. The electromagnetic coupling, through the photoproduction and photoabsorption reactions, is expected to play an important role in this endeavor. This program has recently seen concrete realization with calculations of pion-nucleon scattering being performed in both meson exchange and QCD (cloudy bag) models.

The recent observation of the very deep minimum in the  $0^\circ$  cross section for analog pion charge exchange from nuclei has given even more impetus to research in this area. It was found that the position of this minimum was better known in the nuclear case than in free pion-nucleon charge exchange. Of course only the  $\pi^-p \rightarrow \pi^0n$  reaction is directly accessible in the laboratory while the  $\pi^+n \rightarrow \pi^0p$  cross section is needed to perform the nuclear calculations. Because of the cancellations involved, methods must be used which take into account the necessary isospin-breaking corrections when transforming between the two systems.

For these reasons we have recently performed an analysis of low-energy pion-nucleon scattering with emphasis on the new charge-ex-

change data taken by Fitzgerald *et al.*<sup>1</sup> at LEP.

Briefly, the technique employs a three-channel system of coupled potentials. The three channels are  $\pi^-p$ ,  $\pi^0n$ , and  $\gamma n$ . For most of the analysis the third channel was not needed. The strong interaction part of these potentials was obtained from a rotation in isospin space of the diagonal  $I = 3/2$  and  $I = 1/2$  potentials. Using this method the specific effects of the Coulomb potential and the pion and nucleon mass differences were included. These are important corrections at the low pion kinetic energies considered here. The potentials are chosen to have a separable form:

$$V(r,r') = g \frac{e^{-ar}}{r} \frac{e^{-ar'}}{r'}$$

for each  $\ell^j$  channel, except the  $P_{11}$ , which is taken to be the sum of two such terms. While this choice of potential form is directed toward application to the nuclear problem, the codes employed are able to use any well behaved non-local (or local) potential.

The results of this investigation are interesting in several respects. First, a comparison is possible with existing  $\pi^+$  and  $\pi^-$  elastic scattering data based on the charge exchange data and the conservation of isospin (after the isospin breaking corrections mentioned above have been removed). Our findings in this area are reported in section II.

## The Pion-Nucleon System at Low Energy\*

W. R. Gibbs and P. B. Siegel (Los Alamos)

\*The present report is a summary of a paper submitted for publication in *Physical Review C*, LA-UR-85-3915

Second, it is possible to use isospin conservation to determine the  $\pi^+n \rightarrow \pi^0p$  cross section, correcting for the mass differences and Coulomb effects. We find significant differences between this cross section and the measured cross section, particularly with respect to the cancellation in the zero degree cross section. These results are discussed in section III.

Finally, in section IV, the low-energy behavior of the s-wave phase shifts is discussed, and the value of the "odd" scattering length is extracted. The relation to the photoabsorption data can be seen and some insight into the reaction mechanism obtained.

## II. Data Analysis

Since the  $\pi^+$ -proton data is moderately self-consistent, we started from conventional phase shifts for this system. Even after some adjustments, our scattering parameters are very similar to those found in the literature<sup>2</sup> (Figure 1). Note that it was the strength and range of the isospin 3/2 potentials that was actually adjusted to give the fit to the data; we deal with phase shifts only as an intermediate step. By fitting the  $\pi^-p \rightarrow \pi^0n$  charge exchange data, which consists of the new forward angle data of ref. 1 along with three back-angle points<sup>3</sup> and two integrated cross sections<sup>4</sup>, we were able to obtain a fit with a  $\chi^2/N$  of the order of 1. The isospin 1/2 potentials (and hence the corresponding phase

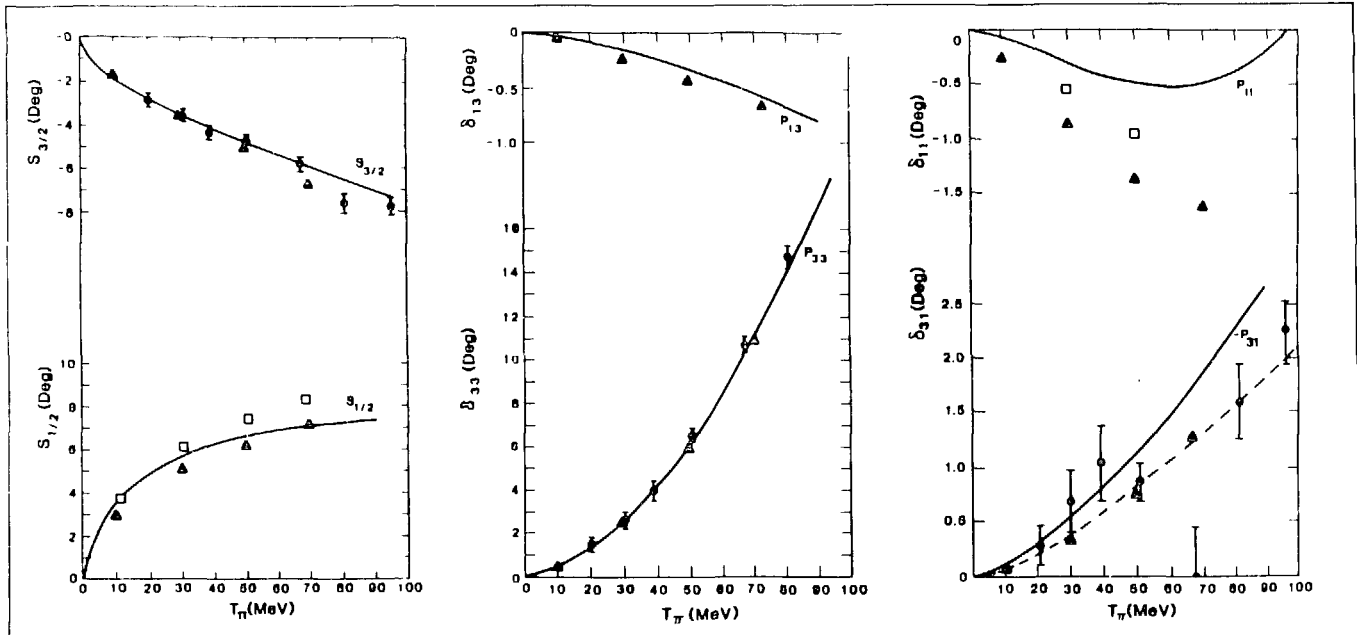


FIGURE 1. Comparison of the presently derived phase shifts with world data. It was verified that the use of the dotted curve for  $P_{31}$  (as well as the inclusion of  $\delta_{11}$  values) does not alter the conclusion of this work, although it does lead to a slightly better fit for the  $\pi^+p$  data in the forward direction.

TABLE 1. Values for the interaction scattering lengths and the  $P_{11}$  phase shift at 95 MeV

|          | $a_{11}^+$ | $a_{11}^-$ | $a_{11}^0$ | $a_{11}^+$ | $a_{11}^-$ | $a_{11}^0$ | $\delta_{11}^+$ | $\delta_{11}^-$ | $\delta_{11}^0$ |
|----------|------------|------------|------------|------------|------------|------------|-----------------|-----------------|-----------------|
| $\pi^+p$ | $-1.7$     | $-1.1$     | $-1.8$     | $0.0$      | $1.8$      | $0.7$      | $-93$           | $0.8$           | $0.8$           |
| $\pi^-p$ | $-1.7$     | $-1.1$     | $-1.8$     | $0.0$      | $1.8$      | $0.7$      | $-93$           | $0.8$           | $0.8$           |
| $\pi^+n$ | $-1.7$     | $-1.1$     | $-1.8$     | $0.0$      | $1.8$      | $0.7$      | $-93$           | $0.8$           | $0.8$           |
| $\pi^-n$ | $-1.7$     | $-1.1$     | $-1.8$     | $0.0$      | $1.8$      | $0.7$      | $-93$           | $0.8$           | $0.8$           |
| $\pi^+d$ | $-1.7$     | $-1.1$     | $-1.8$     | $0.0$      | $1.8$      | $0.7$      | $-93$           | $0.8$           | $0.8$           |
| $\pi^-d$ | $-1.7$     | $-1.1$     | $-1.8$     | $0.0$      | $1.8$      | $0.7$      | $-93$           | $0.8$           | $0.8$           |

shifts) were the only quantities varied in the process. The resulting phase shifts are shown in Fig. 1, and the potential strengths and ranges are to be found in the table. Most of these scattering parameters are consistent with previous determinations.

A notable exception to this agreement is the  $P_{11}$  phase shift, which has a less negative value than that usually ascribed to it. This result was forced by the charge exchange data, primarily the Fitzgerald data, by the limited amount of spin flip cross section allowed. This has possible consequences with regard to the calculation of pion true absorption, on the deuteron especially, since it is this channel which drives the process. Note that our analysis is valid only up to 70 MeV so the crossing point at 95 MeV (Fig. 1) cannot be considered meaningful.

We may now reverse the normal procedure (using  $\pi^+$  and  $\pi^-$  scattering data to calculate charge exchange cross sections) to predict the  $\pi^-p$  elastic scattering. We find that excellent agreement is obtained with the three highest energies of the Frank *et al.* data<sup>5</sup> (Fig. 2). This is

most interesting since, when published, this data disagreed with the available phase shifts based on world data. On closer inspection we found that, in fact, only one data set<sup>6</sup> determined those low energy isospin 1/2 phase shifts, and we conclude that this data<sup>6</sup> is inconsistent with the charge exchange data and isospin symmetry, while the Frank data (at least the three highest energies) is indeed consistent with these requirements.

On the other hand, the  $\pi^+$  and  $\pi^-$  scattering for the lowest energy (29.4 MeV) Frank data appear to be inconsistent. Actually a stronger statement can be made: There appear to be no strong phase shifts which can reproduce the three sets of data (the low energy  $\pi^\pm p$  elastic scattering from ref. 5 and our charge exchange data base<sup>1,3,4</sup>) and still conserve isospin.

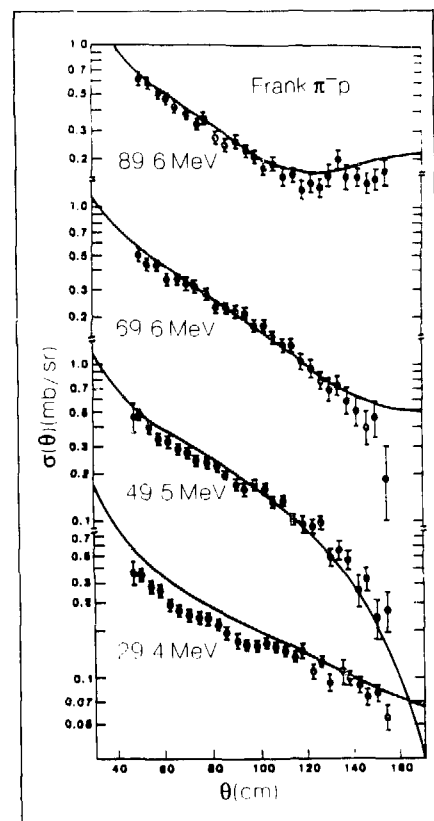


FIGURE 2. Comparison of the present predicted elastic  $\pi^-p$  scattering with the Frank *et al.* data<sup>5</sup>

### III. The Charge Exchange Cross Section

The reactions  $\pi^-p \rightarrow \pi^0n$  and  $\pi^+n \rightarrow \pi^0p$  have a difference in  $Q$ -value of twice the neutron-proton mass difference. This difference (and the Coulomb potential present in the first reaction) leads to a noticeable displacement in the position of the  $s$ - $p$  interference minimum as can be seen (fig. 3), when plotted as a function of pion laboratory energy. Note that this causes a significant difference in the  $0^\circ$  cross section for

energies as high as 55 or 60 MeV.

The importance of knowing the precise position of this minimum is that the charge exchange reaction ( $\pi^+n \rightarrow \pi^0p$ ) in a nuclear environment shows a remarkably similar behavior<sup>7</sup>. The existence of such a sharp feature in the nuclear reaction provides a handle on possible medium corrections to the  $\pi$ -nucleon  $t$ -matrix, either in the transition operator or in the remainder of the reaction mechanism. However, such a tool is useful only if the free space properties are well understood.

An example of the importance of the free space information follows. The minimum in the zero degree cross section for charge exchange on nuclei occurs at higher pion energies as the mass number increases. This phenomenon can be understood in terms of increasing Coulomb repulsion and greater  $Q$ -value for heavier nuclei. For the lightest nucleus measured however, <sup>7</sup>Li, the minimum falls somewhat below the free  $\pi^-p \rightarrow \pi^0n$  minimum. We now see that the minimum in the free  $\pi^+n \rightarrow \pi^0p$  reaction (the relevant comparison) falls at lower energies, and this fact presumably explains some of this displacement. The rest of the shift is probably due the attractive potential seen by the pion due to the strong interaction. The comparison of the nuclear charge exchange with nucleon charge exchange provides us with an excellent way to test our calculations of the effective pion-nucleus interaction, but only if the position of the "free" minimum is precisely known.

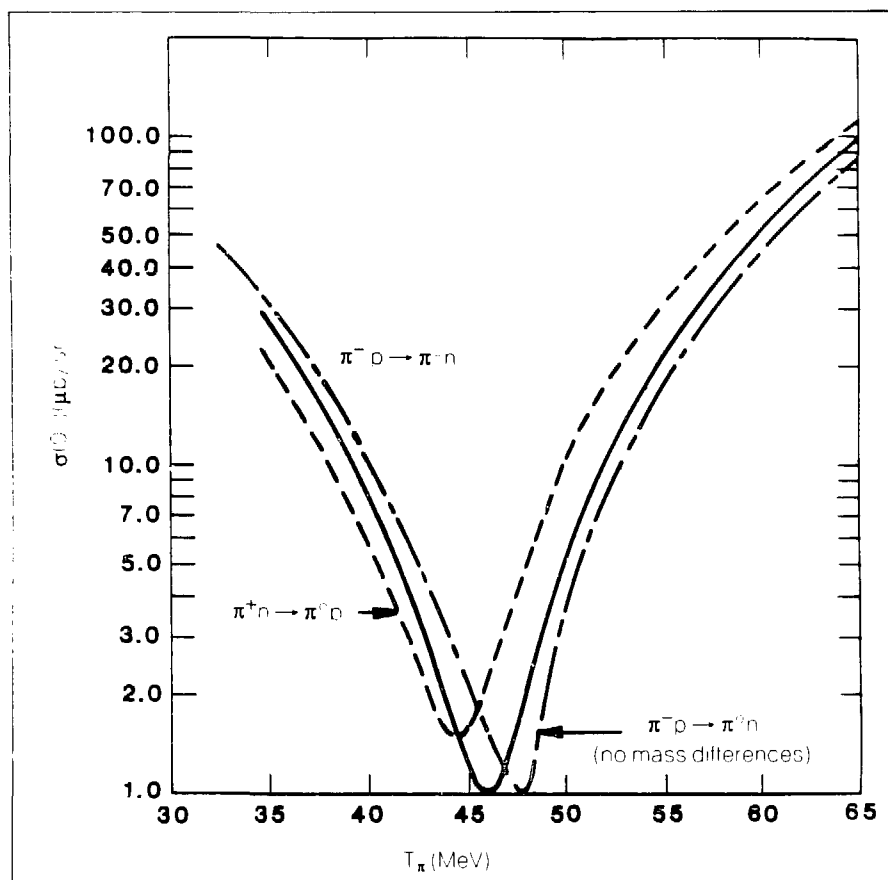


FIGURE 3. The  $\pi^-p \rightarrow \pi^0n$  and  $\pi^+n \rightarrow \pi^0p$  zero degree cross sections obtained in this work. The  $\pi^-p \rightarrow \pi^0n$  reaction with Coulomb effects only is also included to demonstrate that mass differences, and the Coulomb potential lead to partially cancelling effects.



We present a polynomial approximation to these amplitudes which gives a representation of our fits to the data around the minimum ( $\sim 30$ -60 MeV). These amplitudes have the form

$$f_{NF}(\theta) = f_0 + f_1 \cos\theta$$

$$f_{SF}(\theta) = \tilde{f}_1 \sin\theta$$

$$\sigma(\theta) = 10( |f_{NF}(\theta)|^2 + |f_{SF}(\theta)|^2 )$$

The functions,  $f$ , are given in fm and the cross section is in mb/sr.

The coefficients are

$$\pi^- p \rightarrow \pi^0 n$$

$$f_0 = -0.1983 + 0.0810k^2 - 0.0068i$$

$$f_1 = 0.6554k^2 - 0.34k^4 + 0.4325ik^5$$

$$\tilde{f}_1 = 0.3826k^2 + 0.2025ik^5$$

$$\pi^+ n \rightarrow \pi^0 p$$

$$f_0 = -0.2000 + 0.0848k^2 - 0.0054i$$

$$f_1 = 0.7037k^2 - 0.119k^4 + 0.5016ik^5$$

$$\tilde{f}_1 = 0.3905k^2 + 0.2411ik^5$$

where  $k$  is the charged pion momentum in the center of mass in units of  $\text{fm}^{-1}$ . The amplitudes can also be written in a separable form:

$$f = \lambda_0 (\sqrt{s}) + \lambda_1 (\sqrt{s}) \vec{k} \cdot \vec{k}'$$

where  $k'$  is the  $\pi^0$  momentum in the center of mass, and  $\sqrt{s}$  is the total invariant energy. In this form, the  $\lambda$  functions are nearly the same for the two systems.

#### IV. Low Energy Results and Photoabsorption

It has been known for many years that the isospin 1/2 pion-nucleon s-wave phase shift is not well represented by a pure scattering length approximation (i.e., it is not proportional to pion-nucleon momentum) except at very low energies ( $< 30$  MeV)<sup>8</sup>. Until the recent charge exchange data became available, this energy dependence had not been mapped out in detail. In contrast to the isospin 1/2 amplitude, the corresponding isospin 3/2 phase shift is well described by a scattering length approximation, even at energies as high as 100 MeV. This can be taken as a direct indication that the interaction range of the 1/2 channel is much longer than that of the 3/2 channel. The present work makes this statement quantitative in terms of the range of the potentials needed to fit the data. We will return to discuss the underlying physics of this difference at the end of this section.

By using the potentials obtained above and removing the mass differences and Coulomb effects to restore isospin conservation, we can calculate the "odd" scattering length in a world in which isospin is absolutely conserved. We obtain for "a" ( $= a_1 - a_3$ )

$$a = 0.290 \pm .008 \mu^{-1}$$

[Fitzgerald]

If we use the three highest energies of the Frank data to perform the corresponding, but independent, analysis we obtain

$$a = 0.284 \pm .005 \mu^{-1}$$

[Frank]

in complete agreement with the charge exchange result. These values are also in good agreement with the results of many dispersion theory analyses.

There are several references in the literature which quote values of "a" around  $0.26 \mu^{-1}$ . Traditionally<sup>9</sup> the charge exchange and dispersion relations tend to give the higher number;  $\pi^-p$  elastic scattering and pion photoproduction give the lower number. The result from Frank's data is clearly an exception to the  $\pi^-p$  elastic "rule". Perhaps the previous data did not extend to sufficiently low energies.

An exception to the charge exchange "rule" is a recent value obtained by Salomon *et al.*<sup>4</sup> In extracting this result the authors assumed, however, that the scattering length limit had been reached at 28 MeV. If we use the energy dependence obtained from our analysis, we find agreement with their cross section (in fact this data is included in our charge exchange data base). It should be clear that the energy dependence of the  $S_{1/2}$  phase shift (and hence of the charge exchange cross section) is a crucial feature of low energy  $\pi$ -nucleon scattering.

A persistent discrepancy has existed for many years between the odd scattering length obtained from pion charge exchange and that obtained with the use of the Panofsky ratio<sup>10</sup>,  $P$ . In order to make this comparison one must know the value of  $P$  and the zero energy limit of the cross section for  $\pi^-p \rightarrow n + \gamma$  (with Coulomb effects removed). In practice this limit is inferred from the principle of detailed balance, measurements of  $R$  (the ratio of  $\gamma + n \rightarrow \pi^- + p$  to  $\gamma + p \rightarrow \pi^+ + n$ ) from deuteron targets and the extrapolation to zero energy of the photoproduction cross section on the proton. While there may be some problem with extrapolating  $R$  to zero energy (Coulomb and deuteron effects must be removed) we will assume (along with ref. 10) that the number  $R = 1.34 \pm .02$  is correct. The value of  $P$  is accurately known to be  $1.546 \pm .009$ <sup>10</sup>.

The relevant photoproduction cross section is considerably less well known. The needed quantity is actually the cross section with the phase space ratio removed:

$$\sigma'(q_\pi) = \frac{k_\gamma}{q_\pi} \sigma(\gamma p \rightarrow \pi^+ n) .$$

In figure 4  $\sigma'$  is plotted as a function of pion momentum. The data is that of Adamovich *et al.*<sup>11</sup> The dotted curve is their fit, based on a polynomial in pion momentum, which represents these points and higher energy data (which is primarily p-wave) as well. This extrapolation is essentially the same one used

to get the zero energy value of  $\sigma'$  ( $193 \mu\text{b}$ ) employed in ref. 11 to obtain  $a_1 = a_3 = .263 \pm .005 \mu^{-1}$ .

The solid curve shows our calculation for the cross section using a range of 200 MeV/c for the  $V_{13}$  coupling potential and a strength adjusted to give the correct Panofsky ratio. For these low energy data points we obtain a better  $\chi^2/N$  than ref. 11. Note that we fit the recently measured point of Salomon *et al.*<sup>1</sup> at 27.4 MeV. Since our calculations are s-wave only, and we have not performed a multipole analysis, our results may be slightly too high at  $q = .4 \text{ fm}^{-1}$ . Two different analyses by Berends *et al.*<sup>12</sup> (shown also in Figure 4) have a very similar energy dependence but a slightly smaller magnitude.

Another recent value of  $\sigma'$  at zero energy is that of Noelle and Pfeil<sup>13</sup>:  $223 \mu\text{b}$ . If we compare this with our value of  $232 \pm 13 \mu\text{b}$ , we note agreement with their extrapolation of the photoproduction cross sections.

Our conclusion with respect to the Panofsky ratio is that there is no discrepancy within the quoted errors (even not including errors in R) if recent photoproduction analyses, with a substantial energy dependence, are used.

This energy dependence is perhaps the most interesting aspect of low energy  $\pi$  nucleon scattering and photoproduction. We find that it arises naturally from the inclusion of a finite size for the pion-nucleon system of the order of 1 fm. This length is a natural fundamental scale of the pion-nucleon system. We note that a  $\pi$  nucleon scattering mechanism in

which the pion interacts with one of the pions in the pionic cloud of the nucleon can proceed, to a very good approximation, only through the  $l = 1/2$  channel. This is because the  $\pi$ - $\pi$  interaction at low energies is predominately isospin zero (the  $l = 2$  scattering length is an order of magnitude smaller). The photoproduction reaction can also proceed directly via the pion cloud. Therefore, in this simple picture, the  $S_{1/2}$  and  $\gamma$ -N potentials would have roughly the same range (about 1 fm, or  $\alpha \sim 200 \text{ MeV}$ ) and both longer than the  $l = 3/2$  channel for which

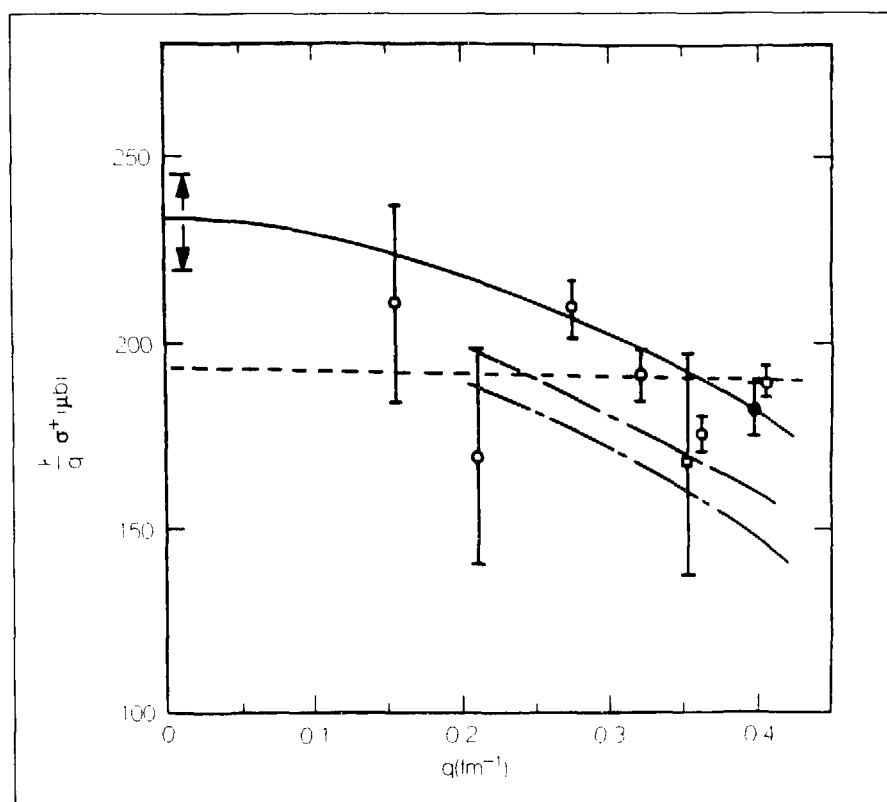


FIGURE 4. The extrapolation of the  $\gamma p \rightarrow \pi^+ n$  data to zero energy. The open circles are from Agardou *et al.*<sup>11</sup> and the solid circles from Salomon *et al.*<sup>1</sup>. The arrows give the range allowed in the extrapolation using our extrapolation  $a_1 = a_3 = (.263 \pm .005) \mu^{-1}$  and the Panofsky ratio.

the  $\pi$ - $\pi$  interactions must go through the much smaller  $I = 2$  interaction. Thus we might expect the  $3/2$  length scale to correspond to the confinement range or bag size.

To get some feeling for how the range is related to the energy dependence of the phase shift it is only necessary to consider the solution to the separable potential problem. If the potential has the form

$$V(\vec{r}, \vec{r}') = \lambda v(r) v(r')$$

then the scattering amplitude is given by

$$f(q, q', E) = \lambda v(q) v(q') D(E)$$

The factor  $D(E)$  is slowly varying in this case so that the main energy dependence comes from the momentum dependence of the functions  $v$ , i.e.,

$$f(k, k, E) \sim v(k)^2 \sim \frac{1}{(\alpha^2 + k^2)^2}$$

where  $\alpha$  is the range of the potential. This analysis assumes that the system is described by an energy independent potential (i.e. that  $\lambda$  is independent of  $E$ ) since there is no reason to expect a strong energy dependence on this scale.

The resultant picture is that of a nucleon consisting of two components: one of long range and rich in pionic components and one of short range and containing primarily non-pionic components. While this picture has often been considered before, it is interesting to be led to it along a new route. The novel feature of this work is that the energy dependence of the  $S_{1/2}$  and  $S_{3/2}$  phase shifts can be used to measure the spatial extent of these two components, allowing us to inferentially separate quark and pionic degrees of freedom.

## References

1. D. H. Fitzgerald *et al.* To be published.
2. R. A. Arndt, SAID on line program *Handbook of Pion-Nucleon Scattering*, Fach information zentrum, Karlsruhe.
3. J. Duclos *et al.* Phys. Lett. **B43**, 245 (1973).
4. M. Salomon, D. F. Measday, J. M. Poutissou and B. C. Robertson, Nucl. Phys. **A414**, 493 (1984).
5. J. S. Frank *et al.*, Phys. Rev. **D28**, 1569 (1983).
6. K. M. Crowe *et al.*, Phys. Rev. **180**, 1349 (1969).
7. F. Irom *et al.*, LA UR-85-2668.
8. G. Källén, *Elementary Particle Physics* (Addison-Wesley Publishing Co., Inc. 1964, page 88.
9. Adamovich *et al.*, Soviet Journal of Nuclear Physics, **8**, 685 (1969).
10. J. Spuller *et al.*, Phys. Lett. **67B**, 479 (1977).
11. M. I. Adamovich *et al.*, Sov. Jour. Nucl. Phys. **7**, 360 (1968).
12. F. A. Berends and A. Donnachie, Nucl. Phys. **B84**, 342 (1975).
13. P. Noelle and W. Pfeil, Nucl. Phys. **B31**, 1 (1971).

## Report of the T-5 Theoretical Group

1985-1986

Briefly summarized here are a few of the research topics considered during 1985 by members of the Medium-Energy Physics Theory Group (T-5) of the Theoretical Division at Los Alamos. These topics span a very wide range of subject matter, from conventional low energy nuclear physics to physics of direct interest to LAMPF and to problems that could be addressed by LAMPF II.

### Three-Body Forces in the Trinucleon System

Traditional nuclear physics has been primarily an investigation of applications of nuclear Hamiltonians which are nonrelativistic, entail only pairwise (two-body) forces, and ignore subnuclear degrees of freedom. Such models have been relatively successful in describing the properties of nuclear ground states, as well as nuclear scattering and reactions. The implication is that forces depending upon the simultaneous coordinates and quantum numbers of three nucleons (three body forces) are relatively unimportant. Such forces are intimately linked to the Dirac approach to proton nucleus scattering at intermediate energies and may play a substantial role in the still not entirely understood spin-orbit splittings in nuclei. Their smallness, however, hinders our effort to observe three-body force effects in many-body systems, where we lack the ability to generate accurate wave functions. Therefore, the trinucleon system plays an extremely important

role in the search for three body force effects, because we are now able to calculate numerically accurate solutions for nonrelativistic Hamiltonians.

The three nucleon system provides (together with the  $\alpha$ -particle) nontrivial tests of the traditional model. There is no guarantee that a nucleon-nucleon force model constructed to reproduce the deuteron binding energy and nucleon-nucleon scattering phase shifts can account for the trinucleon observables. Indeed, systematic investigation of the low-energy trinucleon properties, which determine the size and energy scales of the  $^3\text{H}$  and  $^3\text{He}$  bound states as well as the scattering of neutrons and protons from deuterons, has revealed the inadequacy of the pairwise force assumption. The benchmark solutions of the Los Alamos Faddeev Group have demonstrated that "realistic" two-body force models underbind the triton by approximately 1 MeV (out of 8.5 MeV), possibly indicating the presence of three-body forces. The corresponding theoretical  $^3\text{H}$  charge radius is too large by some ten percent, and the (zero energy) neutron-deuteron spin-doublet scattering length is too large by a factor of 2. In addition, the  $^3\text{He}$  elastic electron scattering charge form factor does not exhibit its first zero at small enough momentum transfer, and the second maximum is not large enough to explain the data.

Our recent nonperturbative, configuration-space Faddeev calculations employing contemporary three

body force models indicate that three nucleon forces may indeed be of sufficient size to bring the theoretical values of the low energy trinucleon observables into reasonable agreement with experiment. The modelling of the nuclear three body force is in its infancy; much work remains before three nucleon force models will approach the sophistication of today's realistic nucleon-nucleon force models. Nonetheless, utilizing current two pion exchange three nucleon ( $2\pi, 3N$ ) force models, we obtain an increase in the triton binding energy of roughly 1.5 MeV over that obtained using only a two body force. That is,  $^3\text{H}$  is slightly overbound, with too small a radius, and the neutron deuteron scattering length is smaller than the data would indicate. By varying model parameters, we have been able to establish a simple relationship between the trinucleon binding energy and the corresponding rms radius, and to confirm the relation (Phillip's Line) between the  $^3\text{H}$  binding energy and the neutron-deuteron doublet scattering length. Calculation of the trinucleon charge form factors is still in progress.

It is clear from our investigation that a more sophisticated three nucleon force model could correct the underbinding of the triton, reduce the  $^3\text{H}$  and  $^3\text{He}$  charge radii to values in agreement with experiment, and lower the doublet neutron deuteron scattering length to its measured value. In addition, we have established that first-order perturbation theory is inadequate to obtain

even qualitatively reliable numbers for the additional binding from the three body forces, that the nucleon-nucleon odd parity partial waves contribute substantially to the wave function when a three nucleon force is included in the Hamiltonian (which is not true for the two-body force case), and that all existing contemporary three-nucleon force models require that a large number of three body channels (viz., 34, all two nucleon potential components corresponding to partial waves with  $J \leq 4$ ) be included to ensure that the calculation has produced a converged answer.

### Pion Charge Exchange

The pion single and double charge-exchange cross sections from light nuclei (in particular,  $^{12}\text{C}$ ) have been calculated. Using a three-body model ( $^{12}\text{C}$  core plus 2 neutrons) or a semiphenomenological wave function fit to (t,p) reactions, the qualitative features of the reaction can be understood. A detailed examination of the model shows substantial sensitivity to nucleon-nucleon separations between 0.5 and 1.0 fm. This distance is such that some explicit quark effects might be seen for large bag sizes. No evidence for quark degrees of freedom is seen in the present work, but the need for intermediate range nucleon-nucleon correlations (beyond that coming merely from angular momentum coupling in the shell model) is clearly evident.

## Light Hypernuclei

$\Lambda$  hypernuclei provide an opportunity for exploring the consequences of depositing a strange (s) quark in a sea of nonstrange (u and d) quarks which are confined within the finite volume of a nucleus. One might predict that in  ${}^5_{\Lambda}\text{He}$  only the s quark of the  $\Lambda$  could coexist with the 12 u and d quarks of the  ${}^4\text{He}$  core in the 1s state, and that the u and d quarks are Pauli blocked from the 1s shell. The consequence of such a quark shell model picture is that  ${}^5_{\Lambda}\text{He}$  should be less bound than a simple  $\Lambda\text{N}$  baryon potential picture would predict. Experimentally,  ${}^5_{\Lambda}\text{He}$  does exhibit anomalously small binding compared to  $\Lambda\text{N}$  central-force model predictions. However, it appears that quarks cluster into hadrons more strongly than occurs in such a naive quark shell-model picture. Otherwise, substituting an s quark for a d quark in the unbound  ${}^5\text{He}$  system could not produce a bound  ${}^5_{\Lambda}\text{He}$ , while substituting an s quark for a d quark in  ${}^4\text{He}$  to form  ${}^4_{\Lambda}\text{He}$  reduces the total binding energy from 28 MeV ( ${}^4\text{He}$ ) to 10 MeV ( ${}^4_{\Lambda}\text{He}$ ). The quark-gluon picture of nuclei must be more complex than the naive quark shell model.

One would like to know whether it is more economical to describe nuclei as systems of interacting baryons or as quark-gluon composites. (Clearly one does not wish to be in a position similar to that of calculating superconductivity starting from quantum electrodynamics.) Few-body hypernuclei offer an ideal

means to investigate this question. One has a "tagged" quark or baryon with which to work.

## Improved Quark Potential

One approach to understanding the structure of nuclei in terms of quarks is to treat the nucleus as a collection of  $3A$  quarks interacting via a potential energy. In this way one tries to build nuclei from their constituents by calculating the wave function for the quarks. Once this wave function is known, many questions can be answered, such as: what is the probability that the quarks are clustered into distinct nucleons? This would replace by an actual dynamical scheme the guesswork that is used today.

A prerequisite for this program is a knowledge of the potential energy for a system of quarks. An improved static potential that is better than those currently in use has been derived from the MIT bag model Lagrangian by fixing the positions of the quarks and solving for the shape of the glue field and the shape of the bag surface. This potential consists of a sum of two-body color Coulomb terms and a many-body confining term, and the latter differs significantly from the popular, but theoretically unfounded, sum of two-body potentials. The potential from the bag model also shows that the string limit is not approached until the distance exceeds  $\sim 2$  fm.

When this potential is specialized to the  $Q\bar{Q}$  system, it consists of a Coulomb term and a linear confining



term, but the slope of the latter (at small and medium distances) is only  $\sqrt{2/3}$  of its ultimate value at large distances (i.e., the string tension). When this potential was applied to heavy mesons such as  $\Upsilon(b\bar{b})$  and  $\psi(c\bar{c})$  it gave a good fit to their spectra. A successful prediction of the mass of the  $F^*(c\bar{s})$  was also made.

This potential is currently being applied to the simplest "nucleus" that is not a single hadron:  $Q^2\bar{Q}^2$ . Preliminary indications are that there may be a true bound state of this system (a dimeson) if the quarks are sufficiently heavy. Extensions of this approach to hadrons composed of light quarks, u and d, are being considered.

## CP Violation

Some aspects of the phenomenology of general  $SU(2)_L \times SU(2)_R \times U(1)$  electroweak models were studied. In particular the effects of CP-violation in the mixing of the two charged intermediate vector bosons ( $W_L - W_R$  mixing) and in the quark sector on some CP-conserving observables in muon decay, beta decay and double beta decay were investigated. It was found that in the presence of CP-violation the ratio of the positron longitudinal polarization in a Fermi beta transition and the positron longitudinal polarization in a Gamow-Teller beta transition (measured in a recent experiment) provides no limit on the right-handed boson mass,  $m_2$ , even for a

given value of the  $W_L - W_R$  mixing angle  $\zeta$ . Similarly, there is no bound on  $\zeta$  even for a given  $m_2$ . It has also been shown that in  $SU(2)_L \times SU(2)_R \times U(1)$  models the rates for double beta decays depend on two, rather than one, independent complex phases.

## NN $\rightarrow$ NN $\pi$ Reaction Studies

For certain exclusive kinematics situations (resembling those for the  $pp \rightarrow d\pi^+$  reaction), experiment shows strong enhancements in the proton momentum spectrum for very low relative nucleon-nucleon (NN) energies in the final state. NN final state interactions (FSI) in the PIPROD program are now treated by multiplying the three-body model amplitude by a Watson-Migdal factor. (Only the  $P_{11}$  and  $P_{33}$   $\pi$ -nucleon partial waves in this model are interacting.) Up to an overall normalization factor, those exclusive differential cross sections for  $pp \rightarrow np\pi^+$  which show the FSI effects are very well reproduced. Interaction in the  $^3S_1$  NN partial wave turns out to be more important than the (stronger)  $^1S_0$  interaction, because of the special set of selection rules that apply to this production process. We have also examined various spin observables, such as polarization asymmetries, for FSI effects. They are usually small, which is a fair representation of the present experimental situation.

Heretofore only one of the unitary-unified models for the coupled NN, NN $\pi$  system has been applied to computation of two- to three-body reaction observables. Recently, the isobar amplitudes of the Tjon-van Faassen coupled-two-body-channels model have been incorporated into the PIPROD code for calculating NN $\rightarrow$ NN $\pi$  observables. Comparison with previous three-body model predictions is now in progress. Surprisingly small differences result from the Tjon-van Faassen model  $\rho$ -meson exchanges (e.g., changes in spin observables on the order of 0.05 or less). Although differences between the Tjon-van Faassen and our models are often of a size to be discerned experimentally (0.2 or more), there appears to be substantial model independence. Detailed comparisons of the two models are currently being made.

### Parity Violation

A difference between the total cross sections for positive and negative helicity protons scattered from nuclear targets is parity violating. Theory and experiment agree on a small negative value for the ratio of this difference to the sum, for proton energies of a few tens of MeV. Theories based on sums of meson exchanges predict a zero near the maximum JAMPF energy. Beyond that, analyses extending to higher energies which include more and more meson exchanges produce a set of curves with increasingly positive

maximum values. A quark model calculation fitted to the positive experimental asymmetry found at 5 GeV was extended to lower energies. The quark model curve matches the envelope of the meson exchange model curves above 1 GeV, and agrees with the LAMPF result at 800 MeV. Furthermore, the quark model predicts an increase in the effect by roughly a factor of 100 as the energy increases from 5 to 500 GeV. A crucial test of the model may be made using the polarized beam at Brookhaven, where a "large" value ( $\sim 10^{-5}$ ) is predicted.

### The Family Problem

The three charged leptons differ only in mass, and no other apparent property. Yet something distinguishes them, since decays such as  $\mu \rightarrow e + \gamma$  have not been observed at all, let alone at the rate one would expect from the weak interaction. This pattern is repeated for the quarks, and leads us to define families of quarks and leptons, such as e, up-quark, and down-quark, where the lightest remaining of each type of fermion is assigned to each successive family. The family problem is that we still do not know why there are three (or more) families, nor what distinguishes them, other than mass. Proposed solutions fall into two categories: symmetry groups, or substructures of quarks and leptons. All predict that the unseen family-changing decays, such as the one above, or  $K^- \rightarrow \mu + e$ , do occur, however rarely. They also predict

neutrino mixing similar to that known to occur for the weak interactions of quarks. This leads to nonzero neutrino masses, and to neutrino oscillations, but the size of these effects is highly model dependent.

Finally, in some cases, a light or massless scalar or pseudoscalar boson is predicted, with coupling strengths to Fermions related to the scale of family symmetry breaking. A signal for producing such a scalar boson,  $f$ , is  $\mu \rightarrow e+f$ , but this can be difficult to detect because the electron signal at  $E_e = m_\mu/2$  is overwhelmed by electrons from the edge of the Michel spectrum. Instead, one can look more easily for the radiatively corrected process,  $\mu \rightarrow e+\gamma+f$ , with  $f$  carrying off significant undetected momentum and zero missing mass. The differential cross section for this process for one particular type of  $f$  boson coupling has been calculated, and the XTAL BOX collaboration has searched for the reaction; preliminary data analysis indicates a significant lower bound on the symmetry breaking scale. Work is continuing on the general class of processes.

## Quarkleis

An attempt has been made to describe nuclei directly in terms of single particle wavefunctions for quarks moving in a mean potential in a nucleus. This mean potential has considerable local structure, similar to that of an egg carton. Preliminary results of detailed calculations show

nucleons are little distorted in nuclei, justifying the traditional meson plus nucleon approach as a very good approximation. The binding energy and matter distributions may be fairly well described, and the model exhibits an EMC effect. An immediate result of this quark picture is the expectation of significant  $\Sigma \Lambda$  mixing in hypernuclei, with specific effects at shell closures. Progress has been made on efficient inclusion of Pauli exclusion effects, in an attempt to calculate the binding energy of  ${}^3\text{He}$  directly in terms of quark interactions.

## Medium Energy Probes and the Interacting Boson Model of Nuclei

The interacting boson model of nuclei (IBM) has been successful in describing the spectra and transition rates of many types of collective nuclei in a unified manner. This model is an approximation to the nuclear shell model. The basic assumption is that the low-lying collective states of nuclei are composed primarily of pairs of protons and pairs of neutrons coupled to angular momentum zero and two, and these coherent pairs are approximated as bosons. The IBM also contains a natural way for classifying nuclear states with the same isospin but with different neutron-proton symmetries.

The LAMPF high resolution spectrometer can resolve many excited states of collective nuclei. However, the extraction of nuclear structure in

formation from the proton differential cross sections for exciting specific states is complicated by the fact that coupled channel effects might be important at momentum transfers achievable at LAMPF, and hence the simple DWBA cannot be used. On the other hand, the Glauber model has been successful in describing medium energy proton scattering from nuclei, and affords a mechanism for including such effects in a simple manner.

The Glauber multiple scattering series can be approximated by an exponentiated first-order optical operator. If this operator is written in terms of Interacting Boson Model coordinates, coupled channel effects are included to all orders. Because the Glauber transition operator is a linear transformation on the bosons in the nucleus, and because the number of such bosons is finite, the effect of the Glauber optical operator for scattering to any state can be calculated in closed form. Analytic expressions for this operator have been derived as a function of impact parameter for a spherical vibrator, a  $\gamma$ -unstable rotor, and an axially symmetric prolate or oblate deformed rotor. For these types of nuclei it has been shown that coupled-channel effects are important at large momentum transfers, and for the axially symmetric rotor, at all momentum transfers.

For nuclei which are transitional between these extreme limits, the profile function must be calculated numerically. A computer program available at LAMPF has been im-

plemented which calculates the proton differential cross section for excitation to a specific nuclear state in the IBM, and which includes scattering to intermediate states. This means that it is now possible to extract meaningful nuclear structure information from medium energy proton scattering to the many collective states in nuclei where the IBM is applicable. Since the IBM includes explicitly both neutron and proton degrees of freedom, we can learn about the different roles played by neutrons and protons in collective motion by analyzing both electron and proton scattering in terms of the IBM.

## LAMPF II

The following T-5 staff members made contributions to the LAMPF II project: B. F. Gibson, T. Goldman, R. R. Silbar, W. R. Gibbs, P. Herczeg and S. P. Rosen.

## Group T-5

Anyone wishing further information on these matters may contact T-5 members J. L. Friar, W. R. Gibbs, B. F. Gibson, V (Group Leader), J. N. Ginocchio, T. Goldman, L. Heller, P. Herczeg, and R. R. Silbar. H. Hoffman, G. Faldt, and J. Speth were long-term visitors in T-5 during 1985. T. Otsuka, M. K. Singham, K. Maltman and G. Wenes held postdoctoral appointments in T-5, and D. Frazer and P. Siegel are Associated Western University students who worked in T-5 during 1985.

---

## Group T-5 Publications

J.-P. Auger, C. Lazard, R. J. Lombard, and R. R. Silbar, "Spin Observables in the  $NN \rightarrow N\Delta$  Transition," *Nucl. Phys.* **A442**, 621 (1985).

W. A. Beyer and L. Heller, "A Steiner Tree Associated with Three Quarks", submitted for publication.

C. R. Chen, G. L. Payne, J. L. Friar, and B. F. Gibson, "Nucleon-Deuteron Doublet Scattering Lengths with Three-Nucleon Potentials", *Phys. Rev. C* (to appear).

C. R. Chen, G. L. Payne, J. L. Friar, and B. F. Gibson, "Convergence of Faddeev Partial-Wave Series for Triton Ground State," *Phys. Rev. C* **31**, 2266 (1985).

C. R. Chen, G. L. Payne, J. L. Friar, and B. F. Gibson, "Faddeev Calculations of Three-Nucleon Force Contribution to Triton Binding Energy," *Phys. Rev. Lett.* **55**, 374 (1985).

A. E. L. Dieperink and G. Wenes, "Recent Developments in the Interacting Boson Model", *Ann. Rev. Nucl. Part. Sci.* **35** (1985).

J. Dubach, W. M. Kloet, and R. R. Silbar, "Nucleon-Nucleon Final State Interactions in  $NN \rightarrow NN\pi$ ", *Phys. Rev. C* (to appear).

J. L. Friar and W. C. Haxton, "Current Conservation and the Transverse Electric Multipole Field," *Phys. Rev. C* **31**, 2027 (1985).

J. L. Friar, "Configuration Space Methods in the Three-Nucleon Problem", Invited lecture at the "International Symposium on Few-Body Methods", Nanning, People's Republic of China, August 4 - 10, 1985, (World Scientific, Singapore, 1986).

J. L. Friar, "The Three-Nucleon Problem: Trinucleon Bound States and Trinucleon Interactions," Invited lectures at "New Vistas in Electronuclear Physics", Banff, Canada, August 22 - September 4, 1985 (NATO Advanced Study Institute), (Pienum, 1986).

J. L. Friar, B. F. Gibson, C. R. Chen, and G. L. Payne, "Scaling Relations for Triton Ground-State Observables," *Phys. Lett.* **161B**, 241 (1985).

W. R. Gibbs, W. B. Kaufmann, and P. B. Siegel, "The ABC's of Pion Charge Exchange", Invited talk at the "LAMPF Workshop On Pion Double Charge Exchange," January 10-12, 1985. (LA-10550C).

W. R. Gibbs and D. Strottman, "High Nuclear Temperatures by Antimatter-Matter Interaction," Invited talk at the "Telluride Meeting on Proton- and Antiproton Nucleus Physics," March, 1985.

"Proceedings of Hadronic Probes and Nuclear Interactions", March 11-14, 1985, *AIP Conf. Proc.* **133**, ed. by J. R. Comfort, W. R. Gibbs, and Barry G. Ritchie.

B. F. Gibson and R. R. Silbar, "Report on Steamboat Springs Conference," *Comments Nucl. Part. Phys.* **14**, 57 (1985).

B. F. Gibson, " $^3\text{He}$ : Hadrons or Quarks," at "International Conference on Hadronic Probes and Nuclear Interactions," *AIP Conference Proceedings No. 133*, ed. by J. Comfort, W. Gibbs, and B. Schneider, p. 390.

J. N. Ginocchio, "A Class of Exactly Solvable Potentials. II. Three-Dimensional Schrödinger Equation," *Ann. of Physics* **159**, 467 (1985).

J. N. Ginocchio, "Low-Lying Isovector Excitations in Heavy Nuclei," at "International Symposium on the Nuclear Shell Model," ed. by M. Vallieres and B. H. Wildenthal, (World Scientific, Singapore, 1985).

J. N. Ginocchio and P. Van Isacker, "Determination of the Neutron and Proton Effective Charges in the Quadrupole Operator of Nuclear Collective Models," *Phys. Rev. C* (to appear).

J. N. Ginocchio, T. Otsuka, R. Amado, and D. Sparrow, "Medium Energy Probes and the Interacting Boson Model of Nuclei," *Phys. Rev. C* (to appear).

T. Goldman and M. M. Nieto, "Gravitational Properties of Antimatter", Proceedings of the 3rd LEAR Workshop (Tignes-Savoie, France, Jan. 1985), "Physics with Antiprotons at LEAR in the ACOL Era," ed. by V. Gastaldi, R. Klapisch, J. M. Richard, and J. Tran Thanh Van (*Editions Frontieres*, 1985), p. 639.

T. Goldman and M. M. Nieto, editors, "Proceedings of the Santa Fe Meeting", Division of Particles and Fields, American Physical Society, 1984 (World Scientific, Singapore, 1985).

T. Goldman, "Quark Structure of Nuclei", at "Hadronic Probes and Nuclear Interactions", (Tempe, Arizona, March 1985), *AIP Conf. Proc.* **133**, ed. by J. R. Comfort, W. R. Gibbs, and B. G. Ritchie, p. 203.

T. Goldman, "Do Nucleons Dissolve?", Proceedings of the Santa Barbara Workshop on Nuclear Chromodynamics, (UC-Santa Barbara, August 1985).

L. Heller and J. A. Tjon, "On Bound States of Heavy  $Q^2\bar{Q}^2$  Systems", *Phys. Rev. D* **32**, 755 (1985).

L. Heller and J. A. Tjon, "Heavy Dimesons", Proceedings of the Santa Fe Meeting of the Division of Particles and Fields, American Physical Society, 1984, ed. by T. Goldman and M. M. Nieto, (World Scientific, Singapore, 1985), p. 290.

L. Heller, "A Better Potential for Quarks", at "Hadronic Probes and Nuclear Interactions", (Tempe, Arizona, March 1985), *AIP Conf. Proc.* **133**, ed. by J. R. Comfort, W. R. Gibbs, and B. G. Ritchie.

L. Heller, "The Potential Energy for Quarks," to be published in the Proceedings of the Workshop on Nuclear Chromodynamics: Quarks and Gluons in Particles and Nuclei, the Institute for Theoretical Physics, University of California, Santa Barbara, CA, August 12-23, 1985.

P. Herczeg, "Some Effects of CP-Violation in  $SU(2)_L \times SU(2)_R \times U(1)$  Electroweak Models", invited talk at the Third Telemark Miniconference on Neutrino Mass and Low Energy Weak Interactions, October 25-27, 1984, Telemark Lodge, Wisconsin, LA UR 85 1345, Proceedings, (World Scientific, Singapore, 1986).

P. Herczeg, "On Muon Decay in Left-Right Symmetric Electroweak Models." LA UR 85 2761, submitted to Nuclear Physics B.

C. L. Hollas, K. H. McNaughton, P. J. Riley, Shen-Wu Xu, B. E. Bonner, O. B. van Dyck, J. McGill, M. W. McNaughton, J. C. Peng, J. Dubach, W. M. Kloet, and R. R. Silbar, "Wolfenstein Polarization Observables for the Reaction  $pp \rightarrow p^+n$  at 800 MeV", *Phys. Rev. Lett.* **55**, 29 (1985).

C. Milner, M. Barlett, G. W. Hoffmann, S. Bart, R. E. Chrien, P. Pile, P. D. Barnes, G. B. Franklin, R. Grace, H. S. Plendl, J. F. Amann, T. S. Bhatia, T. Kozlowski, J. C. Peng, R. R. Silbar, H. A. Thiessen, C. Glashauser, J. A. McGill, R. Hackenburg, E. V. Hungerford, and R. L. Stearns, "Observation of  $\Lambda$ -Hyper nuclei in the  $^{12}\text{C}(\pi^+, K^+)_{\Lambda}^{13}\text{C}$  Reaction", *Phys. Rev. Lett.* **54**, 1237 (1985).

T. Otsuka and J. N. Ginocchio, "Low Lying Isovector Collective States and the Interacting Boson Model," *Phys. Rev. Lett.* **54**, 777 (1985).

T. Otsuka and J. N. Ginocchio, "Renormalization of g-boson Effects in the Interacting Boson Hamiltonian," *Phys. Rev. Lett.* **55**, 276 (1985).

P. B. Siegel, W. B. Kaufmann, and W. R. Gibbs, "K<sup>+</sup> as a Probe of Partial Deconfinement in Nuclei", *Phys. Rev.* **C31**, 2184 (1985).

P. B. Siegel, W. B. Kaufmann, and W. R. Gibbs, " $K^+$  as a Probe of Partial Deconfinement in Nuclei," at "Hadronic Probes and Nuclear Interactions", Tempe, Arizona, March, 1985.

P. B. Siegel and W. R. Gibbs, "Pion-Nucleon Charge Exchange and Scattering at Low Energies", (Submitted to *Phys. Rev. C.*) (LA UR-85-3915.)

E. L. Tomusiak, M. Kimura, J. L. Friar, B. F. Gibson, G. L. Payne, and J. Dubach, "Trinucleon Magnetic Moments", *Phys. Rev. C* (to appear).

S. Y. Van der Werf, N. Blasi, M. N. Harakeh, G. Wenes, A. D. Bacher, G. F. Emery, C. W. Glover, W. P. Jones, H. J. Karwowski, H. Nana, C. Olmer, P. den Heijer, C. W. de Jager, H. de Vries, J. Ryckebusch, M. Waroquier, "High Spin  $1p-1h$  Configurations in  $^{116}\text{Sn}$  and their Fragmentation as Seen in the Reaction  $^{116}\text{Sn}(\vec{p}, p')$ ,  $^{116}\text{Sn}(e, e)$ ,  $^{115}\text{In}(^3\text{He}, d)$  and  $^{115}(\alpha, t)$ ." (*Phys. Lett.*, to be published).

G. Wenes, A. E. L. Dieperink and N. Yoshinaga, "Algebraic Treatment of Multi step Excitation Processes in Collective Nuclei (II) Electromagnetic Excitation of Collective Nuclear States", *Nucl. Phys.* **A443**, 472 (1985).



## MP-DIVISION PUBLICATIONS

## Publications

## Nuclear and Particle Physics Research

L. Adiels, G. Backenstoss, I. Bergstrom, S. Carius, S. Charalambous, M. Cooper, C. Findeisen, D. Hadjifotiadou, A. Kerek, K. Papastefanou, P. Pavlopoulos, J. Repond, L. Tauscher, D. Troster, M. C. S. Williams, and K. Zioutas, "Investigations of Baryonium and Other Rare  $pp$  Annihilation Modes Using High-Resolution  $\pi^0$  Spectrometers (PS 182)," *Institute of Physics Conference Series* **73**, 297-304 (1984).

L. Adiels, G. Backenstoss, I. Bergstrom, S. Carius, S. Charalambous, M. D. Cooper, C. Findeisen, D. Hadjifotiadou, A. Kerek, K. Papastefanou, P. Pavlopoulos, J. Repond, L. Tauscher, D. Troster, M. C. S. Williams, and K. Zioutas, "A  $\pi^0$  and  $\eta$  Spectrometer of Lead Glass and BGO for Momenta up to 1 GeV/c," CERN report EP/85-140 (submitted to *Nuclear Instruments & Methods*).

R. C. Allen, V. Bharadwaj, G. A. Brooks, H. H. Chen, P. J. Doe, R. Hausamann, W. P. Lee, H. J. Mahler, M. E. Potter, A. M. Rushton, K. C. Wang, T. J. Bowles, R. L. Burman, R. D. Carlini, D. R. F. Cochran, J. S. Frank, E. Piasezky, V. D. Sandberg, D. A. Krakauer, and R. L. Talaga, "First Observation and Cross-Section Measurement of  $\nu_e + e^- \rightarrow \nu_e + e^-$ ," *Physical Review Letters* **55**, 2401 (1985).

H. W. Baer, "Pion Single- and Double-Charge-Exchange Scattering: General Features of Analog and Double-Analog Transitions," "Proceedings of the LAMPF Workshop on Pion Double Charge Exchange," Los Alamos National Laboratory report LA-10550-C (September 1985), pp. 45-89.

H. W. Baer, "Pion-Nucleus Double Charge Exchange: The Modern Era" (to be published in *Comments on Nuclear and Particle Physics*), Los Alamos National Laboratory document LA-UR-85-2308-R (1985).

G. S. Blanpied, B. G. Ritchie, M. L. Barlett, G. W. Hoffmann, J. A. McGill, M. A. Franey, and M. Gazzaly, "Elastic Scattering of 0.8-GeV Protons from the Non-Zero-Spin Nuclei  $^{13}\text{C}$  and  $^{14}\text{N}$ ," *Physical Review C* **32**, 2152 (1985).

R. D. Bolton, J. D. Bowman, R. Carlini, M. D. Cooper, M. Duong-Van, J. S. Frank, A. L. Hallin, P. Heusi, C. M. Hoffman, F. G. Mariani, H. S. Matis, R. E. Mischke, D. E. Nagle, V. D. Sandberg, G. H. Sanders, U. Sennhauser, R. L. Talaga, R. Werbeck, R. A. Williams, S. L. Wilson, E. B. Hughes, R. Hofstadter, D. Grosnick, S. C. Wright, G. E. Hogan, and V. L. Highland, "Search for the Muon-Number-Nonconserving Decay  $\mu \rightarrow e^+ e^+ e^-$ ," *Physical Review Letters* **53**, 1415 (1984).

R. D. Bolton, J. D. Bowman, M. D. Cooper, J. S. Frank, A. L. Hallin, P. Heusi, C. M. Hoffman, G. E. Hogan, F. G. Mariani, H. S. Matis, R. E. Mischke, D. E. Nagle, L. E. Pilonen, V. D. Sandberg, G. H. Sanders, U. Sennhauser, R. Werbeck, R. A. Williams, S. L. Wilson, R. Hofstadter, E. B. Hughes, M. W. Ritter, D. Grosnick, S. C. Wright, V. L. Highland, and J. McDonough, "Search for the Decay  $\mu^+ \rightarrow e^+\gamma$ " (submitted to *Physical Review Letters*).

R. D. Bolton, M. D. Cooper, J. S. Frank, V. E. Hart, H. S. Matis, R. E. Mischke, V. D. Sandberg, J. P. Sandoval, and U. Sennhauser, "Performance of the Cylindrical Drift Chamber for the Crystal Box at LAMPF," *Nuclear Instruments & Methods* **A241**, 52 (1985).

R. L. Boudrie, J. R. Shepard, and C. Y. Cheung, Eds., "Proceedings of the LAMPF Workshop on Dirac Approaches to Nuclear Physics," Los Alamos National Laboratory report LA-10438-C (May 1985).

J. D. Bowman, "Isovector Resonances in Pion Charge Exchange," Proceedings of the Symposium on Nuclear Structure, *Niels Bohr Centennial Conference*, Ricardo Broglia Gdrunhagemann and Bent Herskind, Eds. (North-Holland, Amsterdam, 1985), p. 549.

K. A. Brown, R. J. Bruni, P. R. Cameron, D. G. Crabb, R. L. Cummings, F. Z. Khiari, A. D. Krisch, A. M. T. Lin, R. S. Raymond, T. Roser, K. M. Terwilliger, G. T. Danby, L. G. Ratner, D. C. Peaslee, J. R. O'Fallen, J. B. Roberts, T. S. Bhatia, L. C. Northcliffe, and M. Simonius, "Spin-Spin Effects in  $pp \rightarrow pp$  at 16.5 GeV/c," *Physical Review D* **31**, 3017 (1985).

R. L. Burman, "Neutrino-Electron Scattering," *Physics Today* **S-50** (January 1986).

P. R. Cameron, D. G. Crabb, G. E. DeMuth, F. Z. Khiari, A. D. Krisch, A. M. T. Lin, R. S. Raymond, T. Roser, K. M. Terwilliger, K. A. Brown, G. T. Danby, L. G. Ratner, J. R. O'Fallen, D. C. Peaslee, J. B. Roberts, T. S. Bhatia, and M. Simonius, "Measurement of the Analyzing Power for  $p + \vec{p}p + p$  at  $p_{\perp}^2 = 6.5$  (GeV/c)<sup>2</sup>," *Physical Review D* **32**, 3070 (1985).

R. Carlini, C. Friedrichs, and H. A. Thiessen, "A Transversely Biased Ferrite-Tuned Cavity for the SSC Booster," Proceedings of the Superconducting Super Collider Injector Workshop, Berkeley, California, November 18-20, 1985.

R. Carlini, V. Sandberg, and H. A. Thiessen, "Idea for a Variable Impedance Beam Pipe," Proceedings of the Superconducting Super Collider Impedance Workshop, Berkeley, California, June 26-27, 1985.

- J. Chalmers, W. R. Ditzler, T. Shima, H. Shimizu, H. Spinka, R. Stanek, D. Underwood, R. Wagner, A. Yokosawa, J. E. Simmons, G. Burleson, C. Fontenla, T. S. Bhatia, G. Glass, and L. C. Northcliffe, "Measurements of  $K_{LL}$  and  $K_{NV}$  in  $\vec{p}d \rightarrow \vec{n}pp$  at 500, 650, and 800 MeV," *Physical Letters* **153B**, 235 (1985).
- E. P. Colton, "Acceleration Simulation in the LAMPF II Booster," *IEEE Transactions on Nuclear Science* **NS-32(5)**, 2567-2569 (1985).
- E. P. Colton, "Longitudinal Tune Control in Synchrotrons," *IEEE Transactions on Nuclear Science* **NS-32(5)**, 2570-2572 (1985).
- E. P. Colton, "Slow Extraction at LAMPF II," *IEEE Transactions on Nuclear Science* **NS-32(5)**, 2441-2443 (1985).
- E. P. Colton, "Slow Extraction at the SSC," *IEEE Transactions on Nuclear Science* **NS-32(5)**, 2442-2443 (1985).
- E. P. Colton, "The rf Program for LAMPF II," *IEEE Transactions on Nuclear Science* **NS-32(5)**, 2573-2575 (1985).
- E. P. Colton and H. A. Thiessen, "Some Thoughts on  $H^-$  Injection into SSC," Proceedings of the Superconducting Super Collider Injector Workshop, Berkeley, California, November 18-20, 1985.
- E. P. Colton and T. F. Wang, "SSC Kicker Impedances," Proceedings of the Superconducting Super Collider Injector Workshop, Berkeley, California, November 18-20, 1985.
- M. D. Cooper, "Muon Number Violating Rare Decays," Proceedings of the International Europhysics Conference on High-Energy Physics, Bari, Italy, July 18-24, 1985.
- K. S. Dhuga, G. R. Burleson, J. A. Faucett, R. L. Boudrie, W. B. Cottingham, S. J. Greene, C. L. Morris, N. Tanaka, Z. F. Wang, S. Nanda, D. Dehnhard, J. D. Zumbro, S. Mordechai, C. F. Moore, and D. J. Ernst, "Large-Angle Elastic Scattering of  $\pi^+$  and  $\pi^-$  from  $^{16}\text{O}$  at 14 MeV" (submitted to *Physical Review*), Los Alamos National Laboratory document LA-UR-85-2798 (1985).
- J. A. Faucett, B. E. Wood, D. K. McDaniels, P. A. M. Gram, M. E. Hamm, M. A. Oothoudt, C. A. Goulding, L. W. Swenson, K. S. Krane, A. W. Stetz, H. S. Plendl, J. Norton, H. Funsten, and D. Joyce, "Kinematically Complete Measurement of the  $(\pi^+, \pi^+p)$  Reaction on  $^{12}\text{C}$  at 220 MeV," *Physical Review C* **30**, 1622 (1984).

R. W. Ferguson, M. L. Barlett, G. W. Hoffmann, J. A. Marshall, E. C. Milner, G. Pauletta, L. Ray, J. F. Amann, K. W. Jones, J. B. McClelland, M. Gazzaly, and G. J. Igo, "The Spin Rotation Parameter  $Q$  for 800-MeV Proton Elastic Scattering from  $^{16}\text{O}$ ,  $^{40}\text{Ca}$ , and  $^{208}\text{Pb}$ ," *Physical Review C* **33**, 1 (1986), Los Alamos National Laboratory document LA-UR-85-2486 (1985).

R. W. Ferguson, "The Spin Rotation Parameter  $Q$  for Elastic Scattering of 800-Million Electron Volt Protons from Oxygen-16, Calcium-40, and Lead-208," Thesis, Los Alamos National Laboratory report LA-10554-T (October 1985).

D. H. Fitzgerald, H. W. Baer, J. D. Bowman, F. Irom, N. S. P. King, M. J. Leitch, E. Piasezky, W. J. Briscoe, M. E. Sadler, K. J. Smith, and J. N. Knudson, "Forward-Angle Cross Sections for Pion-Nucleon Charge Exchange Between 100 and 150 MeV/ $c$ " (submitted to *Physical Review C*).

J. S. Frank, T. J. Bowles, R. L. Burman, R. D. Carlini, D. R. F. Cochran, E. Piasezky, V. D. Sandberg, R. C. Allen, V. Bharadwaz, H. H. Chen, P. J. Doe, R. Hausammann, H. J. Mahler, K. C. Wang, D. A. Krakauer, and R. C. Talaga, "Observation of  $\nu_e$ - $e$  Elastic Scattering," *Proceedings of the Twenty-Second International Conference on High-Energy Physics* (Leipzig, DDR, 1984), Vol. 1, p. 231.

F. C. Gaille, V. L. Highland, L. B. Auerbach, W. K. McFarlane, G. E. Hogan, C. M. Hoffman, R. J. Macek, R. E. Morgado, J. C. Pratt, and R. D. Werbeck, "Precise Measurement of the Pion Charge-Exchange Forward Differential Cross Section at 522 MeV/ $c$ ," *Physical Review D* **30**, 2408 (1984).

S. Gilad, W. J. Burger, G. W. Dodson, S. Hoibraten, L. D. Pham, R. P. Redwine, E. Piasezky, H. W. Baer, J. D. Bowman, F. H. Cverna, M. J. Leitch, U. Sennhauser, T. S. Bawer, C. H. Q. Ingram, G. S. Kyle, D. Ashery, S. A. Wood, and Z. Fraenkel, "Measurement of the  $^{16}\text{O}(\pi^+, \pi^0 p)$  Reaction" (submitted to *Physical Review C*).

R. Gilman, H. T. Fortune, J. D. Zumbro, P. A. Seidl, C. F. Moore, C. L. Morris, J. A. Faucett, G. R. Burleson, S. Mordechai, and K. S. Dhuga, "Angular Distributions for  $^{13}\text{C}^{26}\text{Mg}(\pi^+, \pi^-)$ " (submitted to *Physical Review C*), Los National Laboratory document LA-UR-85-2750 (1985).

R. Gilman, H. T. Fortune, J. D. Zumbro, C. M. Laymon, G. R. Burleson, J. A. Faucett, W. B. Cottingham, C. L. Morris, P. A. Seidl, C. F. Moore, L. C. Bland, R. R. Kiziah, S. Mordechai, and K. S. Dhuga, "Mass Dependence of Pion Double Charge Exchange" (submitted to *Nuclear Physics*), Los Alamos National Laboratory document LA-UR-85-3218 (1985).

R. Gilman, H. T. Fortune, M. B. Johnson, E. R. Siciliano, H. Toki, and A. Wirzba, "Nonanalog Pion Double Charge Exchange Through  $A_{33}$ -Nucleon Interaction," *Physical Review C* **32**, 349 (1985).

R. Gilman, "Systematics of Pion Double Charge Exchange," Thesis, Los Alamos National Laboratory document LA-10524-T (October 1985).

G. Glass, T. S. Bhatia, J. C. Hiebert, R. A. Kenefick, S. Nath, L. C. Northcliffe, W. B. Tippens, D. B. Barlow, A. Saha, K. K. Seth, J. G. J. Boissevain, J. J. Jarmer, J. E. Simmons, R. H. Jeppesen, and G. E. Tripard, "Measurements of Spin-Correlation Parameters  $A_{LL}$  and  $A_{SL}$  for  $pp \rightarrow \pi d$  Between 500 and 800 MeV," *Physical Review C* **31**, 288 (1985).

R. W. Harper, V. Yuan, H. Frauenfelder, J. D. Bowman, R. Carlini, R. E. Mischke, D. E. Nagle, R. L. Talaga, and A. B. McDonald, "Parity Nonconservation in Proton-Water Scattering at 1.5 GeV/c," *Physical Review D* **31**, 1151 (1985).

C. J. Harvey, H. W. Baer, J. A. Johnstone, C. L. Morris, S. J. Seestrom-Morris, D. Dehnhard, D. B. Holtkamp, and S. J. Greene, "Elastic  $\pi^+$  and  $\pi^-$  Scattering on  $^{14}\text{C}$  at 164 MeV," *Physical Review C* (in press).

R. S. Hicks, R. A. Lindgren, M. A. Plum, G. A. Peterson, H. Crannell, D. I. Sober, H. A. Thiessen, and D. J. Millener, " $M4$  Excitations in  $^{14}\text{C}$ " (submitted to *Physical Review*).

C. M. Hoffman, R. D. Bolton, M. D. Cooper, J. S. Frank, A. L. Hallin, P. Heusi, G. E. Hogan, L. E. Piilonen, F. G. Mariam, H. S. Matis, R. E. Mischke, D. E. Nagle, V. D. Sandberg, G. H. Sanders, U. Sennhauser, R. Werbeck, R. A. Williams, S. L. Wilson, R. Hofstadter, E. B. Hughes, M. Ritter, D. Grosnick, S. C. Wright, V. L. Highland, and J. McDonough, "Search for Rare Muon Number-Non-Conserving Decays of the  $\mu^+$ ," in the Proceedings of the 1985 International Symposium on Lepton and Photon Interactions at High Energy, Kyoto, Japan, August 19-24, 1985.

G. E. Hogan, R. D. Bolton, J. D. Bowman, R. Carlini, M. D. Cooper, M. Duong-Van, J. S. Frank, A. L. Hallin, P. Heuse, C. M. Hoffman, F. G. Mariam, H. S. Matis, R. E. Mischke, D. E. Nagle, V. D. Sandberg, G. H. Sanders, U. Sennhauser, R. L. Talaga, R. Werbeck, R. A. Williams, S. L. Wilson, E. B. Hughes, R. Hofstadter, G. Grosnick, S. C. Wright, and V. L. Highland, "A Progress Report on Recent Rare Muon Decay Experiments at the Los Alamos Meson Physics Facility," *Nuclear Physics A* **434**, 475c (1985).

D. B. Holtkamp, S. J. Seestrom-Morris, D. Dehnhard, H. W. Baer, C. L. Morris, S. J. Greene, C. J. Harvey, D. Kurath, and J. A. Carr, "Pion Scattering to  $4^-$  States in  $^{14}\text{C}$ ," *Physical Review C* **31**, 957 (1985).

D. J. Horen, F. E. Bertrand, E. E. Gross, T. P. Sjoreen, D. K. McDaniels, J. R. Tinsley, J. Lisantti, L. W. Swenson, J. B. McClelland, T. A. Carey, S. J. Seestrom-Morris, and K. Jones, "Cross Sections and Analyzing Powers for Quenched Spin Excitations in  $^{40,48}\text{Ca}$  at  $E_p = 33\text{--}4\text{ MeV}$ ," *Physical Review C* **31**, 2049 (1985).

F. Irom, H. W. Baer, J. D. Bowman, M. D. Cooper, E. Piassetzky, U. Sennhauser, H. J. Ziock, M. J. Leitch, A. Erell, M. A. Moinester, and J. R. Comfort, "Pion Single Charge Exchange on  $^7\text{Li}$  at Low Energies," *Physical Review C* **31**, 1464 (1985).

F. Irom, H. W. Baer, J. D. Bowman, M. D. Cooper, E. Piassetzky, M. J. Leitch, B. J. Dropesky, and J. N. Knudson, "The Energy and Mass Dependence of Low-Energy Pion Single Charge Exchange to the Isobaric Analog State," *Physical Review Letters* **55**, 1862 (1985).

M. W. Johnson, E. B. Shera, M. V. Hoehn, R. A. Naumann, J. D. Zumbro, and C. E. Bemis, Jr., " $^{241}\text{Am}$  and  $^{243}\text{Am}$  Charge Distributions from Muonic X-Ray Spectroscopy and the Quadrupole Moment of the  $^{240}\text{Am}$  Fission Isomer," *Physical Review Letters* **161B**, 75 (1985).

K. W. Jones, C. Glashauser, R. de Swiniarski, S. Nanda, T. A. Carey, W. Cornelius, J. M. Moss, J. B. McClelland, J. R. Comfort, J.-L. Escudie, M. Gazzaly, N. Hintz, G. Igo, M. Haji-Saeid, and C. A. Whitten, "Energy Dependence of Deformation Parameters in the  $^{12}\text{C}(\vec{p}, p')^{12}\text{C}$  Reaction," *Physical Review C* **33**, 17 (1986), Los Alamos National Laboratory document LA-UR-85-2483 (1985).

G. J. Krausse, "A 10-MHz High-Voltage Modulator with Pulse Width and Repetition Rate Agility," submitted to the 5th IEEE Pulsed Power Conference, Arlington, Virginia.

M. J. Leitch, H. W. Baer, J. D. Bowman, M. D. Cooper, E. Piassetzky, U. Sennhauser, H. J. Ziock, F. Irom, J. R. Comfort, P. B. Siegel, and M. A. Moinester, "Pion Single Charge Exchange Angular Distribution at  $T_\pi = 48\text{ MeV}$ ," *Physical Review C* **33**, 278 (1986).

M. J. Leitch, E. Piassetzky, H. W. Baer, J. D. Bowman, R. Burman, B. J. Dropesky, P. A. M. Gram, F. Irom, D. Roberts, G. A. Rebka, Jr., J. N. Knudson, J. R. Comfort, V. A. Pinnick, D. H. Wright, and S. A. Wood, "Double Analog Transition  $^{14}\text{C}(\pi^+, \pi^-)^{14}\text{O}$  at 50 MeV," *Physical Review Letters* **54**, 1482 (1985).

D. E. Lobb, "A 0.8 GeV/c Kaon Channel for LAMPF II," Los Alamos National Laboratory report LA-10599-MS (1985).

D. W. MacArthur, "Device to Generate Intensity Modulation in a Pulsed Particle Beam" (submitted to *Nuclear Instruments & Methods A*).

D. W. MacArthur, "Special Relativity: Understanding Experimental Tests" (submitted to *Physical Review A*).

D. W. MacArthur, K. B. Butterfield, D. A. Clark, J. B. Donahue, P. A. M. Gram, H. C. Bryant, C. J. Harvey, and W. W. Smith, "Test of the Special Relativistic Doppler Formula at  $\beta = 0.84$ ," *Physical Review Letters* **56**, 282 (1985).

D. W. MacArthur, K. B. Butterfield, D. A. Clark, J. B. Donahue, P. A. M. Gram, H. C. Bryant, C. J. Harvey, W. W. Smith, and G. Comtet, "Energy Measurement of the Lowest  $^1P_0$  Feshbach Resonance in  $H^-$ ," *Physical Review A* **32**, 1921 (1985).

D. W. MacArthur, R. E. Mischke, and J. P. Sandoval, "Fast Integrating Multi-wire Beam Profile Monitor with Digital Readout" (submitted to *Nuclear Instruments & Methods A*).

Robert J. Macek, "LAMPF II Capabilities from an Experimenter's Viewpoint," invited talk at the Workshop on Nuclear and Particle Physics at Intermediate Energies with Hadrons, International Center for Theoretical Physics, Trieste, Italy, April 1-3, 1985 (to be published in the proceedings).

Robert J. Macek, "Review of Proposed Kaon Factory Facilities," *AIP Conference Series* **133**, 346-376 (1985).

C. J. Martoff, J. A. Bistirlich, C. W. Clawson, K. M. Crowe, M. Koike, J. P. Miller, S. S. Rosenblum, W. A. Zajc, H. W. Baer, A. H. Wapstra, G. Strassner, and P. Fruöl, "Spin-Flip Transitions in  $^{13}\text{C}$  and  $^{19}\text{F}$  Probed with the  $(\pi^-, \gamma)$  Reaction," *Physical Review C* **27**, 1621 (1983).

W. K. McFarlane, L. B. Auerbach, F. C. Gaille, V. L. Highland, E. Jastrzembski, R. J. Macek, F. H. Cverna, C. M. Hoffman, G. E. Hogan, R. E. Morgado, J. C. Pratt, and R. D. Werbeck, "Measurement of the Rate for Pion Beta Decay," *Physical Review D* **32**, 547 (1985).

C. Milner, M. Barlett, G. W. Hoffmann, S. Bart, R. E. Chrien, P. Pile, P. D. Barnes, G. B. Franklin, R. Grace, H. S. Plendl, J. F. Amann, T. S. Bhatia, T. Kozłowski, J. C. Peng, R. R. Silbar, H. A. Thiessen, C. Glashauser, J. A. McGill, R. Hackenburg, E. V. Hungerford, and R. L. Stearns, "Observation of  $\Lambda$  Hypernuclei in the Reaction  $^{12}\text{C}(\pi^+, K^+)_{\Lambda}^{12}\text{C}$ ," *Physical Review Letters* **54**, 1237 (1985).

R. E. Mischke, "Parity Nonconservation in Light Hadronic Systems," Proceedings of the Particles and Nuclei Tenth International Conference, Heidelberg, Germany, July 30-August 3, 1984, pp. 505c-514c.

C. S. Mishra, B. G. Ritchie, R. S. Moore, M. Blecher, K. Gotow, R. L. Burman, M. V. Hynes, E. Piasezky, N. S. Chant, P. G. Roos, T. Sjoreen, F. E. Obenshain, and E. E. Gross, "Isospin Effect in  $\pi^+$   $^{12}\text{C}$  Elastic Scattering at 50 MeV," *Physical Review C* **32**, 995 (1985).

S. Mordechai, P. A. Seidl, C. F. Moore, L. C. Bland, R. Gilman, K. S. Dhuga, H. T. Fortune, C. L. Morris, and S. J. Greene, "Systematics of Continuum Pion Double Charge Exchange on  $T = 0$  Nuclei," *Physical Review C* **32**, 999 (1985), Los Alamos National Laboratory document LA-UR-85-1178 (1985).

D. E. Nagle, R. D. Bolton, R. L. Burman, K. B. Butterfield, R. D. Carlini, J. S. Frank, W. Johnson, V. D. Sandberg, G. B. Yodh, G. A. Goodman, R. L. Talaga, B. Dingus, X. Chang, R. W. Ellsworth, J. Linsley, H. Chen, R. C. Allen, P. J. Doe, and W. T. Lee, "The 'Cygnus' Experiment at LAMPF," Proceedings of the Workshop on a Gamma-Ray Air Shower Detector, San Diego, California, August 30, 1985.

S. Nanda, "Spin Excitations in  $^{48}\text{Ca}$  and  $^{90}\text{Zr}$  with 319-MeV Protons," Thesis, Los Alamos National Laboratory report LA-10368-T (May 1985).

H. W. Baer and M. J. Leitch, Eds., "Proceedings of the LAMPF Workshop on Pion Double Charge Exchange," Los Alamos National Laboratory report LA-10550-C (September 1985).

R. S. Raymond, K. A. Brown, R. J. Bruni, P. R. Cameron, D. G. Crabb, R. L. Cummins, F. Z. Khiari, A. D. Krisch, A. M. T. Lin, K. M. Terwilliger, G. T. Danby, Y. Y. Lee, L. G. Ratner, J. R. O'Fallen, D. C. Peaslee, T. S. Bhatia, G. Glass, and L. C. Northcliffe, "Analyzing Power Measurements for  $pp$  Elastic Scattering at High  $P_{\perp}^2$ " (submitted to *Physical Review Letters*).

L. B. Rees, J. M. Moss, T. A. Carey, K. W. Jones, J. B. McClelland, N. Tanaka, A. D. Bacher, and E. Esbensen, "Continuum Polarization Transfer in 500 MeV Proton Scattering and Pionic Collectivity in Nuclei" (submitted to *Physical Review*), Los Alamos National Laboratory document LA-UR-86-35 (1986).

R. Rieder, P. D. Barnes, B. Bassalleck, R. A. Eisenstein, G. Franklin, R. Grace, C. Maher, P. Pile, J. Szymanski, W. R. Wharton, F. Takeuchi, J. F. Amann, S. A. Dytman, and K. G. R. Doss, "Triple-Differential Cross Sections of the ( $\pi^+$ ,  $pp$ ) Reaction on Lithium Isotopes" (submitted to *Physical Review C*), Los Alamos National Laboratory document LA-UR-85-586 (1985).



V. D. Sandberg, L. S. Bayliss, M. P. Dugan, J. S. Frank, T. Gordon, G. W. Hart, C. M. Hoffman, G. E. Hogan, H. S. Matis, G. H. Sanders, and H. P. von Gunten, "A Fast Analog Mean-Timer," *Nuclear Instruments & Methods* **A234**, 512-516 (1985).

P. A. Seidl, C. F. Moore, S. Mordechai, R. Gilman, K. S. Dhuga, H. T. Fortune, J. D. Zumbro, C. L. Morris, J. A. Faucett, and G. R. Bureson, "The Energy Dependence of  $^{18}\text{O}(\pi^+\pi^-)^{18}\text{Ne}$  (g.s.)," *Physics Letters* **154B**, 255 (1985), Los Alamos National Laboratory document LA-UR-84-3373 (1984).

P. A. Seidl, "The Measurement of Pion Double Charge Exchange on Carbon-13, Carbon-14, Magnesium-26, and Iron-56," Thesis, Los Alamos National Laboratory report LA-10338-T (February 1985).

E. R. Siciliano, M. D. Cooper, M. B. Johnson, and M. J. Leitch, "Effect of Nuclear Correlations on Low-Energy Pion Charge-Exchange Scattering" (submitted to *Physical Review C*), Los Alamos National Laboratory document LA-UR-86-406 (1986).

W. W. Smith, C. Harvey, J. E. Stewart, H. C. Bryant, K. B. Butterfield, D. A. Clark, J. B. Donahue, P. A. M. Gram, D. MacArthur, G. Comtet, and T. Bergeman, "Simple Atomic Systems in Strong External Fields," in *Atomic Excitation and Recombination in External Fields*, M. H. Nayfeh and C. W. Clark, Eds. (Gordon and Breach, New York, 1985).

W. R. Smythe, T. G. Brophy, R. D. Carlini, C. C. Friedrichs, D. L. Grisham, G. Spalek, and L. C. Wilkerson, "rf Cavities with Transversely Biased Ferrite Tuning," *IEEE Transactions on Nuclear Science* **NS-32(5)**, 2951 (1985).

D. A. Sparrow, J. Piekarewicz, E. Rost, J. R. Shepard, J. A. McNeil, T. A. Carey, and J. B. McClelland, "Relativistic Impulse Approximation, Nuclear Currents, and the Spin-Difference Function," *Physical Review Letters* **54**, 2207 (1985).

H. A. Thiessen, "A Review of Kaon Factory Proposals," *IEEE Transactions on Nuclear Science* **NS-32(5)**, 1601-1606 (1985).

C. Tschalär, "Multiple Scattering: A General Formalism for Small Angles," Los Alamos National Laboratory report LA-10620 (1985).

J. L. Ullman, P. W. F. Alons, J. J. Kraushaar, J. H. Mitchell, R. J. Peterson, R. A. Ristinen, J. N. Knudson, J. R. Comfort, H. W. Baer, J. D. Bowman, D. H. Fitzgerald, F. Ironi, M. J. Leitch, and E. Piassetzky, "Pion Single Charge Exchange on  $^{14}\text{C}$  from 35 to 295 MeV" (submitted to *Physical Review C*).

S. L. Wilson, "A Search for the Neutrinoless Decay  $\mu^+ \rightarrow e^+\gamma$ ," Thesis, Los Alamos National Laboratory report LA-10471-T (1985).

V. Yuan and J. D. Bowman, "Study of LAMPF  $H^-$  Beam-Position Motion and a Predictive Algorithm for Noise Reduction," *IEEE Transactions on Nuclear Science* **NS-32(5)**, 1979-1981 (1985).

### Applications-Oriented Research

C. Boekema, K. C. B. Chan, R. L. Lichti, V. A. M. Brabers, A. B. Denison, D. W. Cooke, R. H. Heffner, R. L. Hutson, and M. E. Schillaci, "A  $\mu$ SR Study of Valence Fluctuation in  $Fe_3O_4$ ," *Proceedings of the International Conference on Magnetism* (North Holland, Amsterdam, 1985) (to be published in the *Journal of Magnetism and Magnetic Materials*).

C. Boekema, R. L. Lichti, V. A. M. Brabers, A. B. Denison, D. W. Cooke, R. H. Heffner, R. L. Hutson, M. Leon, and M. E. Schillaci, "Magnetic Interactions, Bonding, and Motion of Positive Muons in Magnetite," *Physical Review B* **31**, 1223 (1985).

C. Boekema, R. L. Lichti, K. C. B. Chan, V. A. M. Brabers, A. B. Denison, D. W. Cooke, R. H. Heffner, R. L. Hutson, and M. E. Schillaci, "Experimental Evidence for a Mott-Wigner Glass Phase of Magnetite Above the Verwey Temperature," *Physical Review B* **33**, 210 (1986).

R. D. Brown, "Power Deposition Measurements at the LAMPF Neutron Radiation Effects Facility," Los Alamos National Laboratory report LA-10448-MS (May 1985).

R. D. Brown, J. R. Cost, and J. T. Stanley, "Irradiation-Induced Decay of Magnetic Permeability of Metglas 2605S-3 and Mumetal," *Journal of Nuclear Materials* **131**, 37 (1985).

K. C. B. Chan, C. Boekema, R. L. Lichti, D. W. Cooke, M. E. Schillaci, and A. B. Denison, "Magnetic Interaction Localization and Motion of Positive Muons in  $V_2O_4$ ," (to be published in the *Journal of Magnetism and Magnetic Materials*).

J. S. Cohen and M. Leon, "New Mechanism for Resonant  $d\mu$  Formation and Epithermal Effects in Muon-Catalyzed Fusion," *Physical Review Letters* **55**, 52 (1985).

J. S. Cohen and M. Leon, "Target Dependence of the Effective Sticking Probability in Muon-Catalyzed  $d-t$  Fusion," *Physical Review A* **33**, 1437 (1986).

D. W. Cooke, J. K. Hoffer, M. Maez, W. A. Steyert, and R. H. Heffner, "A Dilution Refrigerator for Muon-Spin Relaxation Experiments," *Review of Scientific Instruments* (in press).

D. R. Davidson, W. F. Sommer, and R. C. Reedy, "Measured Radiation Environment at the Clinton P. Anderson Los Alamos Meson Physics Facility Irradiation Facility," *Effects of Radiation on Materials*, Proceedings of the Twelfth International Symposium ASTM STP 870, F. A. Garner and J. S. Perrin, Eds. (American Society for Testing and Materials, Philadelphia, 1985), pp. 1199-1208.

D. R. Davidson, W. F. Sommer, I. K. Taylor, R. D. Brown, and L. Martinez, "'Rabbit' System for Activation Foil Irradiations at the Los Alamos Spallation Radiation Effects Facility at LAMPE," Second International Conference on Fusion Reactor Materials, Chicago, Illinois, April 13-17, 1986, Los Alamos National Laboratory document LA-UR-85-3630 (1985).

D. R. Davidson, W. F. Sommer, and M. S. Wechsler, "Additional Measurements of the Radiation Environment at the Los Alamos Spallation Radiation Effects Facility at LAMPE," Thirteenth International Symposium on the Effects of Radiation on Materials, Seattle, Washington, June 23-25, 1986, Los Alamos National Laboratory document LA-UR-85-3502 (1985).

A. B. Denison, C. Boekema, R. L. Lichti, K. C. Chan, D. W. Cooke, R. H. Heffner, R. L. Hutson, M. Leon, and M. E. Schillaci, "Muon-Spin-Rotation Study of  $V_2O_5$ ," *Journal of Applied Physics* **57**, 3743 (1985).

J. F. Dicello, M. E. Schillaci, C. W. McCabe, J. D. Doss, M. Paciotti, P. Berardo, and J. F. Dicello, III, "Meson Interactions in NMOS and CMOS Static RAMs," 1985 Annual Conference on Nuclear and Space Radiation Effects, San Francisco, California, July 22, 1985 (to be published in *IEEE Transactions on Nuclear Science*).

J. D. Doss, "Simulation of Automatic Temperature Control in Tissue Hyperthermia Calculations" (to be published in *Medical Physics*), Los Alamos National Laboratory document LA-UR-85-216 (1985).

2. J. Farnum, W. F. Sommer, O. T. Inal, and J. Yu, "Quantitative Study, by Field Ion Microscopy, of Radiation Damage in Tungsten After Neutron and Proton Irradiation," Thirteenth International Symposium on the Effects of Radiation on Materials, Seattle, Washington, June 23-25, 1986, Los Alamos National Laboratory document LA-UR 85-3918 (1985).
3. J. Flik, J. N. Bradbury, D. W. Cooke, R. H. Heffner, M. Leon, M. A. Paciotti, M. E. Schillaci, K. Maier, H. Rempp, J. J. Reidy, C. Boekema, and H. Daniel, "Muon Channeling in Semiconductors: Evidence for Pionium Formation" (submitted to *Physical Review Letters*).
4. G. A. Gist, S. A. Dodds, D. E. MacLaughlin, D. W. Cooke, R. H. Heffner, R. L. Hutson, M. E. Schillaci, C. Boekema, J. A. Mydosh, and G. J. Nieuwenhuys, "Ferromagnetism in Reentrant PdFeMn" (submitted to *Physical Review B*).
5. R. Heffner, W. Cooke, Z. Fisk, R. Hutson, M. Schillaci, J. Smith, J. Willis, D. MacLaughlin, C. Boekema, R. Lichti, A. Denison, and J. Oostens, "Anomalous Muon Knight Shift and Absence of Magnetic Order in Superconducting  $U_{1-x}Th_xBe_{1-x}$ " (submitted to *Physical Review Letters*).
6. R. H. Heffner, D. W. Cooke, R. L. Hutson, M. E. Schillaci, J. L. Smith, P. M. Richards, D. E. MacLaughlin, S. A. Dodds, and J. A. Oostens, "Holmium-Ion Dynamics in  $Ho_xLu_{1-x}Rh_4B_{1-x}$ ," *Applied Physics* **57**, 3107 (1985).
7. R. H. Heffner, D. W. Cooke, R. L. Hutson, M. E. Schillaci, S. A. Dodds, G. A. Gist, and D. E. MacLaughlin, "Muon-Spin-Relaxation Study of Exchange Coupling in Dilute AgMn Alloys" (to be published in the *Journal of Magnetism and Magnetic Materials*).
8. R. H. Heffner and D. G. Fleming, "Muon Spin Relaxation: The Technique and Its Applications to Condensed Matter Physics," *Physics Today* **37**, 38-46 (1984).
9. K. H. Hicks, R. G. Jeppesen, J. J. Kraushaar, P. D. Kunz, R. J. Peterson, R. S. Raymond, R. A. Ristinen, J. L. Ullmann, F. D. Becchetti, J. N. Bradbury, and M. Paciotti, "Fission of Heavy Nuclei Induced by Energetic Pions," *Physical Review C* **31**, 1323 (1985).
10. S. E. Jones, A. N. Anderson, A. J. Caffrey, C. D. Van Siclen, K. D. Watts, J. N. Bradbury, J. S. Cohen, P. A. M. Gram, M. Leon, H. R. Maltrud, and M. A. Paciotti, "Observation of Unexpected Density Effects in Muon-Catalyzed  $d-d$  Fusion," *Physical Review Letters* **56**, 588 (1986).

M. Leon, "Back Decay and Resonant Hyperfine Quenching in  $dd\mu$  Fusion" (submitted to *Physical Review Letters*).

M. Leon and J. S. Cohen, "Ortho- and Para-Deuterium Effects in Muon-Catalyzed Fusion," *Physical Review A* **31**, 2680 (1985).

W. Lohmann, A. Ribbens, W. F. Sommer, and B. Singh, "Microstructure and Mechanical Properties of 800-MeV Proton-Irradiated Commercial Aluminum Alloy," Workshop on the Relation Between Mechanical Properties and Microstructure Under Fusion Irradiation Conditions, Riso National Laboratory, Roskilde, Denmark, June 27-July 2, 1985, Los Alamos National Laboratory document LA-UR-85-2296 (1985).

B. N. Singh, W. Lohmann, A. Ribbens, and W. F. Sommer, "Microstructural Changes in Commercial Aluminum Alloys After Proton Irradiation," Thirteenth International Symposium on the Effects of Radiation on Materials, Seattle, Washington, June 23-25, 1986, Los Alamos National Laboratory document LA-UR-85-4074 (1985).

W. F. Sommer, W. Lohmann, I. K. Taylor, and R. M. Chavez, "Operating Experience at the Los Alamos Spallation Radiation Effects Facility at LAMPF," Thirteenth International Symposium on the Effects of Radiation on Materials, Seattle, Washington, June 23-25, 1986, Los Alamos National Laboratory document LA-UR-85-3917 (1985).

M. S. Wechsler, D. R. Davidson, L. R. Greenwood, and W. F. Sommer, "Calculation of Displacement and Helium Production at the Clinton P. Anderson Meson Physics Facility (LAMPF) Irradiation Facility," *Effects of Radiation on Materials*, Proceedings of the Twelfth International Symposium ASTM STP 870, F. A. Garner and J. S. Perrin, Eds. (American Society for Testing and Materials, Philadelphia, 1985), pp. 1189-1198.

J. Yu, W. F. Sommer, and J. N. Bradbury, "Interstitial Dislocation Loop Nucleation and Growth and Swelling Produced by High-Energy Cascades," Thirteenth International Symposium on the Effects of Radiation on Materials, Seattle, Washington, June 23-25, 1986, Los Alamos National Laboratory document LA-UR-86-679 (1986).

## Accelerator Operations

- F. R. Gallegos, L. J. Morrison, and A. Browman, "The Development of a Current Monitor System for Measuring Pulsed-Beam Current over a Wide Dynamic Range," *IEEE Transactions on Nuclear Science* **NS-32(5)**, 1959-1961 (1985).
- G. R. Swain and A. A. Browman, "Proposed Bunching Scheme for a Polarized  $H^-$  Injector," *IEEE Transactions on Nuclear Science* **NS-32**, 3024-3026 (1985).
- H. S. Butler, A. A. Browman, D. C. Hagerman, and M. J. Jakobson, "New 750-keV  $H^-$  Beam Transport Line For LAMPF," *IEEE Transactions on Nuclear Science* **NS-32(2)**, 3086-3088 (1985).
- J. W. Hurd, "Measurement and Resulting First- and Second-Order Approximations for a  $90^\circ$  Bending Magnet in LAMPF's 750-keV Transport," *IEEE Transactions on Nuclear Science* **NS-32(5)**, 3637-3639 (1985).
- S. C. Schaller, J. K. Corley, and P. A. Rose, "Optimizing Data Access in the LAMPF Control System," *IEEE Transactions on Nuclear Science* **NS-32(5)**, 2080-2082 (1985).
- S. K. Brown, S. C. Schaller, E. A. Bjorklund, G. P. Carr, R. A. Cole, J. K. Corley, J. F. Harrison, T. Marks, P. A. Rose, G. A. Pedicini, and D. E. Schultz, "The Status of the LAMPF Control System Upgrade," poster session, 1985 Particle Accelerator Conference, Vancouver, British Columbia, Canada, May 13-16, 1985.
- G. Pedicini and J. Corley, "A Central Message Processing Facility" (to be published in the Proceedings of the Digital Equipment Computer Users Society, December 1985).
- G. W. Swift, A. Migliori, J. Wheatly, C. R. Waller, and G. Suazo, "Fabrication and Leak-Tight Furnace Brazing of Intricate Objects," *Brazing and Soldering* **8**, 32 (1985).
- R. L. York, R. R. Stevens, Jr., R. A. DeHaven, J. R. McConnell, E. P. Chamberlin, and R. Kandarian, "The Development of a High-Current  $H^-$  Injector for the Proton Storage Ring at LAMPF," *Nuclear Instruments & Methods in Physics Research* **B10**, 891-895 (1985), Los Alamos National Laboratory document LA-UR-84-3043 (1984).

## Experimental Facilities and Research Support

R. D. Brown, D. L. Grisham, and J. E. Lambert, "Beam-Line Windows at LAMPF," *IEEE Transactions on Nuclear Science* **NS-32(5)**, 3812-3814 (1985), Los Alamos National Laboratory document LA-UR-85-1737 (1985).

G. R. Burlison, W. B. Cottingame, K. S. Cottingame, K. S. Dhuga, J. A. Faucett, C. P. Fontenla, J. F. Amann, R. L. Boudrie, S. J. Greene, C. L. Morris, N. Tanaka, Z. F. Wang, D. Yusnukis, M. Brown, R. R. Kiziah, E. C. Milner, C. F. Moore, S. Mordechai, D. Oakley, P. A. Seidl, C. L. Blilie, D. Dehnhard, S. Nanda, S. J. Seestrom-Morris, J. D. Zumbro, and M. Maeda, "A Large Angle Pion Nucleus Scattering Facility for EPICS at LAMPF" (submitted to *Nuclear Instruments & Methods*), Los Alamos National Laboratory document LA-UR-86-274 (1986).

A. M. Gonzales, "Implementation of a Local Area Network at Los Alamos Meson Physics Facility (LAMPF)," in the Proceedings of the Digital Equipment Computer Users Society (May 1985).

D. L. Grisham, J. E. Lambert, and W. F. Sommer, Jr., "Major Facility Overhauls at LAMPF," *IEEE Transactions on Nuclear Science* **NS-32(5)**, 3095-3097 (1985), Los Alamos National Laboratory document LA-UR-85-1736 (1985).

D. L. Grisham and J. E. Lambert, "Application of Teleoperator Expertise to Robotics," to be presented at the Robotics 1986 Conference, Chicago, Illinois, April 20-24, 1986, Los Alamos National Laboratory document LA-UR-85-4066 (1985).

J. E. Lambert and D. L. Grisham, "Recent Advances in Remote Handling at LAMPF," *IEEE Transactions on Nuclear Science* **NS-32(5)**, 3098-3100 (1985), Los Alamos National Laboratory document LA-UR-85-1735 (1985).

D. M. Lee, J. R. Bilskie, and G. H. Sanders, "The Response of Drift Tubes to Variations in Wire Diameter and Gas Fillings," submitted to the Wire Chamber Conference, Vienna, Austria, Los Alamos National Laboratory document LA-UR-85-4100 (1985).

M. W. McNaughton, "Proton Polarimeters for Spin Transfer Experiments," Continuous Electron Beam Accelerator Facility (CEBAF) Summer Workshop, Newport News, Virginia, June 3-7, 1985, Los Alamos National Laboratory document LA-UR-85-2161 (1985).

Z. F. Wang, S. J. Greene, and M. J. Plum, "High-Precision Floating-Wire Measurements of Large Dipole Magnets at LAMPF," submitted to *Nuclear Instruments & Methods*, Los Alamos National Laboratory document LA-UR-85-3449 (1985).

## **Facilities Services and Program Management**

L. Rosen, "LAMPF - Its History and Accomplishments," Los Alamos National Laboratory document LA-UR 85-3437 (1985).

## **Patents**

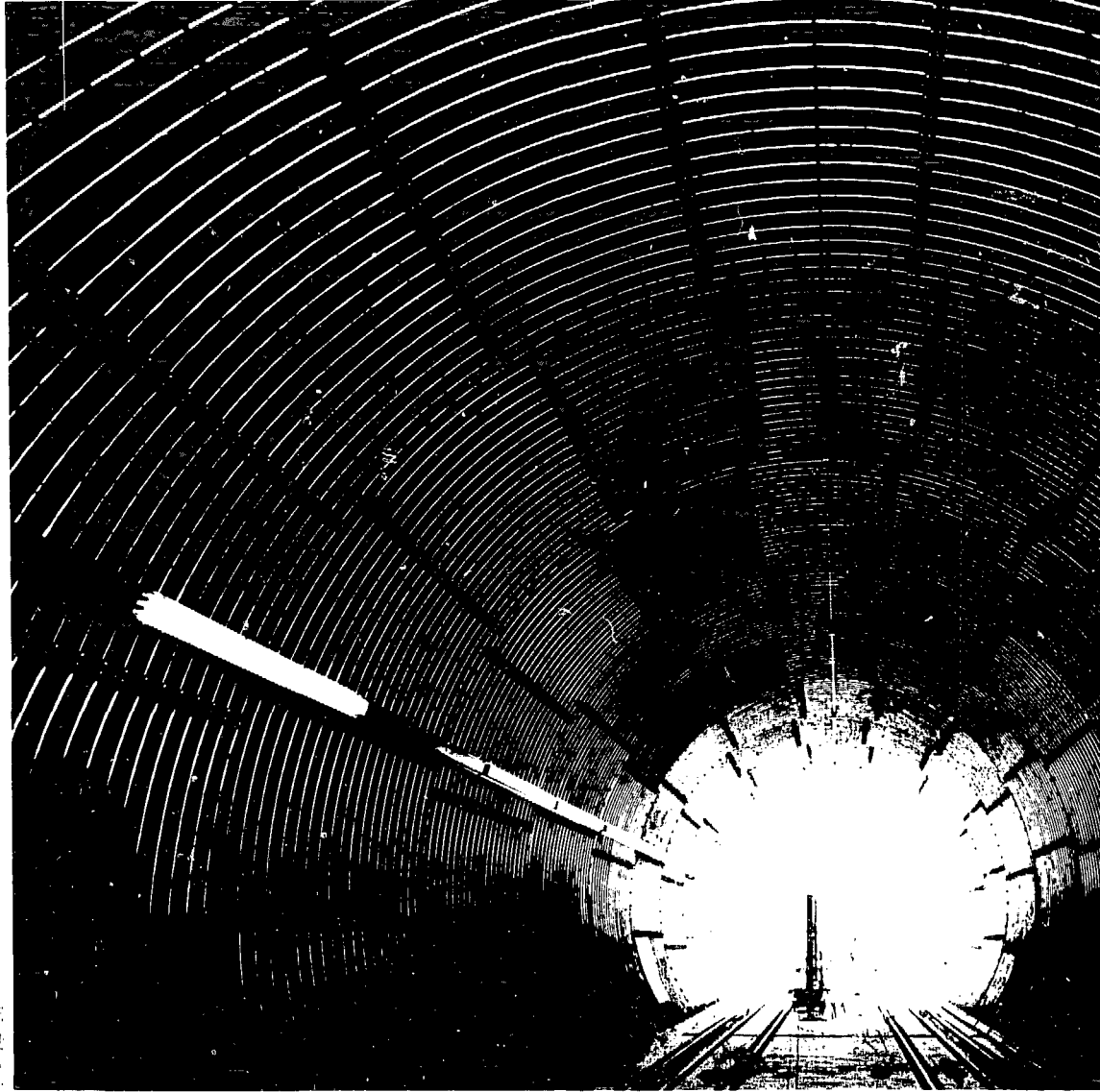
C. Morris, G. Idzorek, and L. Atencio, "Gated Strip Proportional Detector," U.S. Patent pending, submitted January 1985.

J. D. Doss and C. W. McCabe, "Electrosurgical Device for Both Mechanical Cutting and Coagulation of Bleeding," U.S. Patent pending, submitted February 1985.

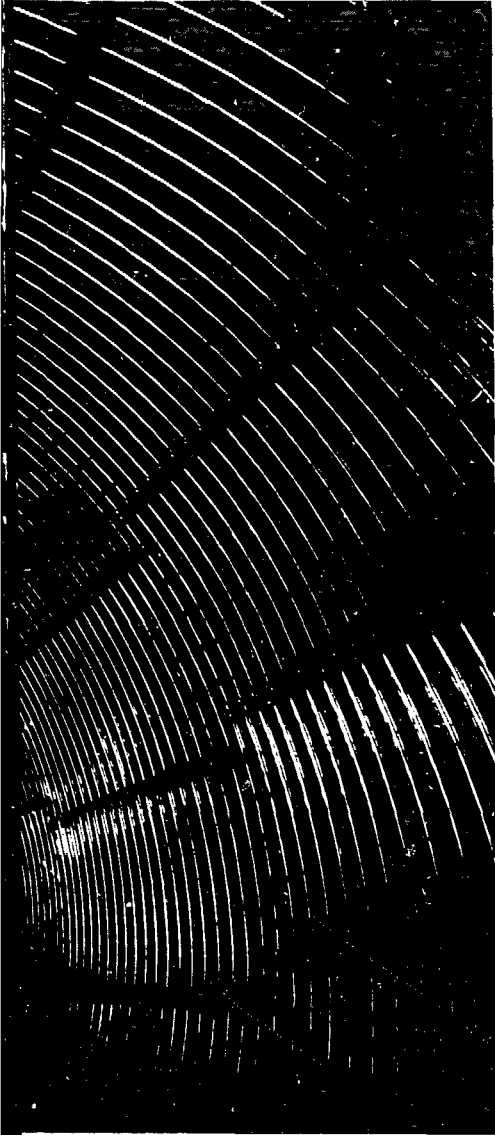
J. D. Doss, "Implantable Apparatus for Localized Heating of Tissue," U.S. Patent pending, submitted May 1985.

J. D. Doss, "Method and Device for Supporting Blood Vessels During Anastomosis," U.S. Patent pending, submitted May 1985.





**Status of LAMPF II**



**Accelerator Studies**

H. A. Friesinger et al.

**Summary of Proposed Accelerator Complex**

We propose to accelerate protons from 0.8 to 45 GeV in two steps.

1. The first synchrotron, a 60-Hz rapid-cycling booster, is injected by every second macro pulse of 797-MeV  $H^-$  ions from the existing LAMPF linac and accelerates  $1.5 \times 10^{13}$  protons per pulse to 6 GeV. The booster provides only fast-extracted beams. Fourteen of eighteen of the 6-GeV pulses (78%) are provided to experimental Area N for neutrino physics. The remaining four booster pulses (22%) are injected into the main ring. The proposed layout of the accelerator and experimental areas on the LAMPF site is shown in Fig. 1.

2. The second synchrotron accelerates  $6.0 \times 10^{13}$  protons per pulse (four booster batches) from 6 to 45 GeV at 3.33 Hz. The main ring has slow extraction only, with a 50% macroscopic duty factor. The slow spill can be done in two modes, fully debunched with a microscopic duty factor of 100%, or with rf on, giving 1.75-ns pulse (FWHM) every 16.7 ns (59.8 MHz). A summary of the parameters of the proposed LAMPF II accelerators is given in Table I.

The experimental areas of LAMPF II fall naturally into two classes. The secondary hadron beams are all produced by the 45-GeV proton beam and are located in the existing high-energy experimental hall, Area A. In the upstream thin-

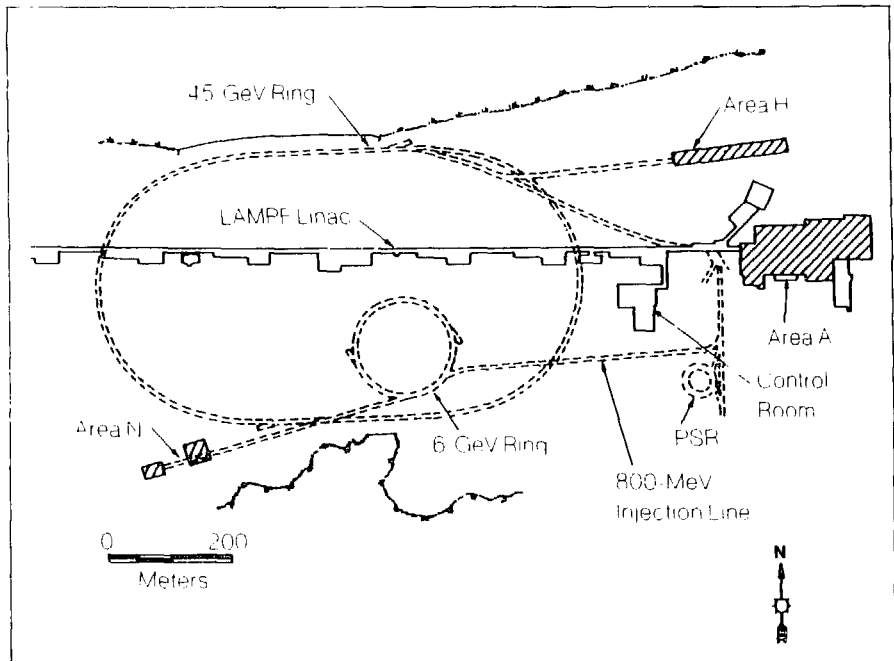


FIGURE 1 Site plan of the proposed LAMPF II accelerators and experimental areas

target portion of Area A, facilities are provided for Drell-Yan experiments with 45 GeV protons. Neutrino experiments will be performed in a new experimental area, Area N.

The proposed LAMPF II accelerators are simple and conventional. High intensity is obtained by rapid cycling. This "brute-force" technique requires larger rf voltages and more rapid transfer of energy to magnets than in other high-energy accelerators. However, the circulating current is similar to existing machines, allowing reliable extrapolation of accelerator physics to the LAMPF II design. Technology development is limited to producing efficient and cost-effective designs; no new ground needs to be broken in control of high-intensity phenomena. Our choice of operating the main ring above its transition energy makes the beam stable against microwave instabilities without an artificial increase of the longitudinal phase space.

Our accelerator and experimental area parameters are the result of an extensive discussion in which physics output and cost were the most important factors. Our basic strategy is to build a full set of experimental facilities in a single slow-extracted beam area. We have proposed a simple high-energy accelerator that has the possibility of significant upgrades in the future. This strategy more than doubles our efficiency in using protons to produce secondary beams, allows maximal physics output in the early years, and promises upgrades later to the less-activated portion of the facility, namely the accelerator.

TABLE I. Parameter List for LAMPF II

|                         | Booster              | Main Ring               |
|-------------------------|----------------------|-------------------------|
| Energy, range (GeV)     | 0.70-6.0             | 6.0-45.0                |
| Repetition rate (Hz)    | 60                   | 3-33(6-67) <sup>a</sup> |
| Number of protons/pulse | $1.5 \times 10^{13}$ | $6.0 \times 10^{13}$    |
| Current ( $\mu$ A)      | 144                  | 32(64)                  |
| Circumference (m)       | 430.97               | 1333.13                 |
| Number of superperiods  | 6                    | 2                       |
| Horizontal tune         | 5.22                 | 7.15                    |
| Vertical tune           | 4.08                 | 6.45                    |
| Transition gamma        | 1.153                | 6.4                     |
| Dipoles                 |                      |                         |
| Number                  | 24                   | 80                      |
| Length (m)              | 5.7                  | 8.0                     |
| Field (T)               | 0.224-1.053          | 0.225-1.503             |
| Quadrupoles             |                      |                         |
| Number                  | 48                   | 72                      |
| Magnet waveform         | Sinusoidal           | Linear                  |
| Rise time (ms)          | 11-75                | 50                      |
| Fall time (ms)          | 3-97                 | 50                      |

<sup>a</sup>The beam current and repetition rate for the main ring are shown for the slow-extraction mode. Operation in the fast-extraction mode doubles the repetition rate.

Two types of upgrade to the LAMPF II accelerator are possible in the future. The intensity can be increased by a factor of 3 to 100  $\mu$ A by the addition of a collector ring and a stretcher ring. No changes to the booster or main ring will be required by this intensity upgrade. The second possibility is to raise the final energy to 60 GeV. The nominal 1.5-T bending magnets of the main ring are designed for later operation at 2.0 T at a cost of a factor of 2 in magnet power.

New features are presented in this proposal that represent significant changes from the previous version.

- The users of LAMPF II will notice most the fully debunched slow-extraction option with 100% microscopic duty factor.

- The fast feedback around the rf amplifier will lower the effective cavity impedance to enable debunched slow extraction, and it will also allow higher beam loading, which will reduce rf costs (both capital and operating) by 30% or more.
- The newly proposed separated-function lattices have more flexibility for unforeseen operating modes, can be upgraded to higher final energy, and have a lower operating cost than the previous combined-function versions.
- We have increased the length of the straight sections of the main ring, allowing the possibility of Siberian snakes to avoid altogether the problems of crossing depolarizing resonances.
- And finally, the new single high-energy experimental area uses the available protons more efficiently, which is the equivalent of a 2-times-higher beam current than that in our previous version.

Also, technical improvements in the accelerator design have been made that will be less visible to the users but will contribute to more reliable operation or greater flexibility in the future.

To begin with, we considered many alternative designs. Because none of these was more cost effective than the proposed two-ring design,

we now have greater confidence that we are moving in the right direction.

The lattice designs have been changed from combined function to separated function. This change allows the use of more symmetric magnets with smaller undesired multipole errors, reduces stored energy in the dipoles, and enables us to better predict the expected field errors. We have tracked both rings using realistic error estimates and found that the dynamic aperture is larger than the worst-case phase space, even with 4 times the expected magnetic field errors.

The injection scheme has been studied in more detail. Simulations now include "plural scattering" and the long tails of energy loss caused by delta-ray production in the stripper foil. Experience with the Proton Storage Ring (PSR) shows that the lifetime of 300- $\mu\text{g}/\text{cm}^2$  carbon foils is not a problem, even with a much larger circulating current, more foil hits, and a smaller foil than that proposed for LAMPF II. The halo factor has been raised from 2 to 4 because simulations showed that this would be necessary to keep losses down to a few tenths of a per cent.

We have made significant progress in our study of instabilities. We now have a calculation of the expected longitudinal and transverse impedance of both rings, using realistic elements that include kickers, rf cavities, and beam monitors. Bunched-beam instabilities have been considered in addition to the

coasting beam instabilities discussed in the previous proposal. Numerical simulations have been done, both for thresholds and for growth times of important modes.

Our work on the rf system has progressed in several important areas:

- we have calculated the mode spectrum with two- and three-dimensional codes and have compared the calculations with measurements on a full-scale prototype cavity;
- the rf test stand has been completed;
- full peak power has been delivered to a dummy load; and
- a full-scale cavity has been constructed and all components, including ferrite and BeO cooling rings, are on site. First tests of this cavity with ferrite are expected by April 1986.

We have begun a study to determine feedback-control requirements for the rf system and to see how this system interacts with beam stability. We have selected fast feedback around the final rf stage because this gives the best stability. Our design includes the capability of operating the cavities with very low fundamental voltage, as would be required during extraction from both rings and injection into the main ring.

The ac power system has been investigated in further detail. Clearly, an additional power supply to Los Alamos County is required. The Labo-

ratory grid is adequate to distribute the power on the Lab site, but a new 115- to 13.8-kV substation is needed for the additional average power. The large pulsed load of the main-ring magnets must be filtered locally. We have commissioned Brown Boveri to study the capability of a generator to handle the pulsed load. A 1300-MVA Brown Boveri generator was chosen for the design study because Group CTR is planning to install that generator in Los Alamos for a compact torus experiment and it therefore may be available to us when LAMPF II goes on line in late 1994.

### Control of High-Intensity Beams

High initial intensity is of little operational use unless beam spills are acceptably small. We intend to keep general losses to a level of 0.1% so that hands-on maintenance of the accelerators will be possible. For losses that cannot be prevented, such as those in the injection and extraction hardware, local shielding and special remote-maintenance facilities will be provided. One-turn, fast-abort dumps will protect the machines from accidental spill of the entire beam, and emittance-defining collimators downstream of the extraction systems will protect the re-

maintaining hardware from scattering in the extraction system, emittance growth, and general halos.

A number of design features are built into the machines to facilitate minimum loss operation. Above all, good diagnostics will be provided throughout the facility, including the possibility of full measurement of the phase space and orientation in both rings and all transfer lines. The  $H^-$  injection system allows full control of filling of the injected phase space in all six dimensions. Halo strippers are provided to clean up the long tails of the linac beam, and dumps will catch any unstripped  $H^-$  or  $H^0$  beam.

Our bunch-to-bunch transfer from linac to booster and from booster to main ring will minimize capture losses. By filling less than 50% of the rf bucket, we can prevent losses during the nonadiabatic transition from coasting to acceleration in both machines. Gaps in the beam ( $\sim$  six empty buckets) will be provided so that single-turn transfer between rings and fast extraction will be possible without losses.

Large apertures and conservative low-tune shifts early in the acceleration cycle will minimize space-

charge problems. Low  $R_s/Q$  (shunt-impedance/resonant  $Q$ ) cavities with fast rf feedback around the final amplifier and cavity will prevent losses associated with the Robinson instability. The proposed ceramic beam pipe with conducting strips eliminates troubles from multipoles produced by eddy currents of the rapid-cycling guide field and the need for a low-impedance beam pipe. Active dampers will be provided to eliminate the coupled-bunch instabilities that cannot be stabilized by control of the beam environment. The special high-beta straight sections of the main ring are designed to minimize losses at the slow-extraction septum and also at the magnetic septum, which will be placed  $90^\circ$  downstream of the electrostatic septum.

The minimization of losses is a continuing process of attention to detail, training of staff, and possibly the uncovering of new accelerator physics problems. The experience to be gained at the Los Alamos PSR, which recently set a new record of  $30\text{-}\mu\text{A}$  average current delivered to experimenters, will be invaluable in minimizing the commissioning time and beam losses of a high-intensity facility such as LAMPF II. The continuing beam-availability record of LAMPF indicates that the Laboratory infrastructure, the staff, and the injector are ready to meet the challenges of high-intensity at LAMPF II.

## Comparison with Existing and Proposed Accelerators

The parameters of a number of existing and proposed high-intensity machines are shown in Table II.

The circulating current of both LAMPF II machines (2.2 A) is only slightly above the CERN Proton Synchrotron (1.6 A) and is considerably less than that already achieved at the Los Alamos PSR (9 A). The circulating current is a good measure of the trouble to be expected with  $H^-$  injection foil lifetime and scattering,

and is also important in determining the instabilities to be expected.

LAMPF II looks like a reasonable choice based on this criterion.

The users' measures of machine performance are secondary beam flux and duty factor. Averaged over the past few years, the typical operating mode for high-energy machines, such as the Brookhaven AGS, has been, roughly, 50% slow-extracted beam and 50% fast-extracted beam. For this kind of schedule, the LAMPF II proposal of simultaneous 6-GeV fast-extracted beam and 45-

TABLE II. Parameters of Proton Synchrotrons

| Name of Facility  | Proton Energy (GeV)                    | Protons/Pulse ( $\times 10^{13}$ ) | Duty Factor (%) | Circulating Current (A) | Repetition Rate (Hz) | Average Current ( $\mu$ A) |
|---|--|------------------------------------|-----------------|-------------------------|----------------------|----------------------------|
| Argonne Intense Pulsed Neutron Source (IPNS)                                      | 0.5                                    | 0.17                               | 0.00057         | 2.3                     | 30                   | 8                          |
| Rutherford Appleton Laboratory (RAL) Scattering Neutron Source (SNS) <sup>a</sup> | 0.5(0.8)                               | 0.5(2.5)                           | 0.0032          | 0.5(6.1)                | 50                   | 17(200)                    |
| Los Alamos PSR <sup>a</sup>   | 0.8                                    | 1.5(5)                             | 0.00032         | 9(27)                   | 12                   | 30(100)                    |
| Fermilab Booster  | 8                                      | 0.3                                | 0.0024          | 0.3                     | 15                   | 7.2                        |
| KEK Proton Synchrotron  | 12                                     | 0.4                                | 18              | 0.6                     | 0.6                  | 0.32                       |
| CERN Proton Synchrotron   | 26 <sup>b</sup><br>26 <sup>b,c</sup>   | 2.2<br>0.5                         | 0.00014<br>50   | 1.6<br>0.4              | 0.67<br>0.38         | 2.3<br>0.5                 |
| Brookhaven Alternating Gradient Synchrotron (AGS)                                 | 27.5 <sup>b</sup><br>27.5 <sup>a</sup> | 1.64<br>1.2                        | 0.00018<br>50   | 1.0<br>0.7              | 0.67<br>0.38         | 1.8<br>0.73                |
| TRIGA-Kaplan Facility, <sup>d</sup>   | 30 <sup>b</sup><br>30 <sup>a</sup>     | 6<br>6                             | 0.0036<br>1     | 2.8<br>2.8              | 10<br>10             | 100<br>100                 |
| LAMPF II  | 6 <sup>a</sup><br>45 <sup>a</sup>      | 1.5<br>6                           | 0.0067<br>50    | 2.2<br>2.2              | 60<br>10             | 144<br>32                  |

<sup>a</sup>In commissioning stage (design goals are in parentheses)

<sup>b</sup>Operating modes not available simultaneously

<sup>c</sup>No longer available for experiments

<sup>d</sup>Similar to the European Hadron Facility

<sup>e</sup>Dual-energy beams available simultaneously



TABLE III Normalized yield from Existing and Proposed Kaon Factories

|                                    | Yield per Year     |                    |                        |                           |
|------------------------------------|--------------------|--------------------|------------------------|---------------------------|
|                                    | $K^-$<br>(1 GeV/c) | $K^-$<br>(7 GeV/c) | $\bar{p}$<br>(7 GeV/c) | $\nu_\mu$<br>(Integrated) |
| Brookhaven AGS (1984) <sup>a</sup> | 1                  | 1                  | 1                      | 1                         |
| TRIUMF Kaon Factory <sup>a,b</sup> | 139                | 161                | 176                    | 68                        |
| LAMPF II <sup>c</sup>              | 100                | 187                | 290                    | 61                        |

<sup>a</sup>Assumes 50% slow extraction, 50% fast extraction

<sup>b</sup>Identical to the European Hadron Facility

<sup>c</sup>Simultaneous slow and fast extraction

GeV slow-extracted beam would yield essentially the same duty factor and beam flux as the TRIUMF Kaon Factory. In addition, the high-energy (45-GeV) LAMPF II beam is more favorable for Drell-Yan physics, high-energy kaons, and antiproton production. The low-energy (6-GeV) fast-extracted beam is preferred for neutrino oscillation experiments. A comparison of the expected yield of secondary and tertiary beams from several kaon factories is shown in Table III.

In comparing the LAMPF II and other kaon factory proposals, one should take note of the following technical points:

- The LAMPF II magnet apertures include a factor of 4 increase in acceptance for clearance of the beam halo. Experience at LAMPF indicates that large apertures are necessary to ensure low losses.
- The LAMPF II rf buckets will be filled to no more than 50% in order to avoid longitudinal losses that begin at 65%. The 33%

bunching factor used in the space-charge calculation is the result of a Monte Carlo simulation of the proposed injection scheme with 50% bucket filling.

- The LAMPF II cavities will be tuned with perpendicular biased ferrites that have extremely low losses. The natural  $R_s/Q$  of the cavities, which is approximately  $35 \Omega$ , minimizes beam-loading problems. Because of the perpendicular bias, a much higher bandwidth is possible in the bias field (Fermilab cavities would have trouble providing the rapid tuning required in a 60-Hz machine). Thus, the proposed LAMPF II rf system is the best choice from the point of view of efficiency, beam loading, and tuning bandwidth.
- The low- $\gamma$ , main ring proposed for LAMPF II results in better stability at extraction time than an infinite- $\gamma$ , main ring.
- The linear-ramp power supply proposed for the LAMPF II main ring is more flexible than the resonant system. In particular, front porches and variable repetition

rates can be easily obtained. Also, we have calculated that this system is cheaper initially and uses less operating power.

- The two ring machine proposed for LAMPF II will be easier to operate than any other kaon factory machine. LAMPF II will also have smaller beam losses because of fewer transitions between rings, which cause significant operating problems, emittance growth, and beam losses at all existing high energy facilities.

## Alternatives

The proposed two ring design for LAMPF II is the most cost-effective of many scenarios considered. We enumerate here those alternative versions that were studied to the level of a cost estimate and the factors that led to their rejection.

Early designs for LAMPF II used one ring. These designs had to contend with a large phase-space acceptance, crossing transition, and very high rf voltage with broadband tuning. The best version was the 45-GeV variable transition-energy design of Franczak.<sup>1</sup> Our cost estimate indicated that the one-ring design is \$50 million more expensive than the adopted design.

Another scheme for eliminating the booster involved building a new high-energy linac to replace LAMPF as an injector. A cost-optimized injector that would fit into the LAMPF tunnel is a 3.7-GeV linac. This linac would have to deliver 797-MeV beam to the PSR, 200  $\mu\text{A}$  to a neutrino target (the same beam power as that from a 6-GeV booster) and 34  $\mu\text{A}$  (chopped) to the LAMPF II main ring. The installed cost of a 3.7-GeV linac is estimated at \$88 million (1985 dollars without contingency), compared with the \$42 million booster replacing it in the current proposal. The use of 3.7-GeV  $\text{H}^-$  causes some problems that have not yet been solved, it requires a large radius-of-curvature switchyard that makes reuse of Area A impossible, and it requires a much longer shut-down of the PSR than would our two-ring proposal.

One of the reasons that the high-energy linac option is expensive is that it must give a high duty factor and serve several users simultaneously. A way around these problems is to provide a linac in the injection

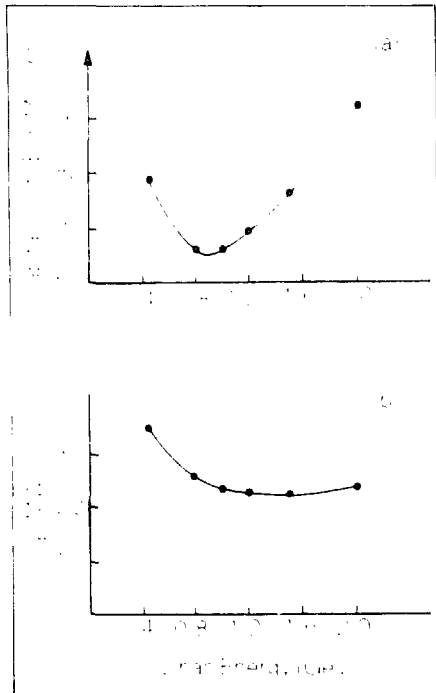


Fig. 2. (a) Material cost of LAMPF linac generators versus linac energy. (b) Power consumption of LAMPF linac generators versus linac energy.

tunnel to raise the injection energy of LAMPF II. We have done a cost trade off study of this option. The total cost of linac, booster, and main ring is shown in Fig. 2(a); the linac power consumption is shown in Fig. 2(b). The optimum energy for injection into the booster is so close to 800 MeV that it is not worthwhile to consider the complications of an additional linac in the injection chain.

Both the TRIUMF and European Hadron Facility groups have proposed accelerators with a dc collector ring between the booster and main ring and a stretcher ring to achieve 100% duty factor. We have studied this scheme for LAMPF II and find that to achieve 67  $\mu\text{A}$  at 45 GeV costs about \$30 million more for material than would the two-ring, 34- $\mu\text{A}$  design. Because the dc rings use components (magnets, rf, vacuum, etc.) that are different from the rapid-cycling rings, at least a 200 man-year per ring cost would be incurred in engineering design and inspection (ED&I) and installation. The dc rings not only will raise the initial cost but also will make rapid construction of the machines very difficult and extend the commissioning process. We have chosen, instead, to make provision for a later upgrade by adding collector and stretcher rings. With these additions, the output current of LAMPF II at 45 GeV can be raised to 100  $\mu\text{A}$  without booster or main ring changes.

Recently, the suggestion has been made that a superconducting linac might be an attractive alternative. Proven designs at 5 MeV/m gradient exist, with greater than 20 MeV/m demonstrated in single cavities. Recirculation of protons looks difficult below velocities of 0.9999 times the speed of light (65 GeV). Thus we consider a single linac of 45 GeV. At 20 MeV/m, a 2.25-km linac would be required. At \$100 thousand per meter, the structure alone would cost \$225 million. This amount equals the approximate cost of the two proposed synchrotrons, including buildings, installation, ED&I, project management, and contingency. Thus, at the present time a superconducting linac appears to be more than twice as expensive as the proposed rapid-cycling synchrotrons. Should a major breakthrough in superconducting linac technology occur, we will reevaluate this option.

One possibility for a cost-effective machine is still to be evaluated. Superconducting magnets for the main ring might allow a shorter tunnel and lower operating cost than would the proposed room-temperature main ring. A careful study is needed to determine whether the superconducting magnet alternative is more cost effective than room-temperature magnets. We expect to study the superconducting magnet option in the next year.

Reference

1. B. J. Franczak, "Transitionless Lattices for LAMPF II," Los Alamos National Laboratory report LA-10260-MS (October 1984).



## Facility Development



Nucleon Physics Laboratory Upgrade

Spectrometer Calibration at EPICS

Radiation-Effects Facility

Data Analysis Center

LAMPF Computer-Control System

## Nucleon Physics Laboratory (NPL) Upgrade

J. B. McClelland, P. E. France, and R. Werbeck, Brookhaven National Laboratory

### Introduction

LAMPF has embarked on a major 3 year development program to enhance ongoing experimental programs and to provide facilities for new physics research in nucleon charge-exchange reactions<sup>1</sup> in the Nucleon Physics Laboratory (NPL, Area B). Central to this development is a high-intensity polarized-ion source, a medium resolution proton

spectrometer for  $(p,p')$  and  $(n,p)$  reactions, a 600 m neutron flight path with a beam swinger for  $(p,n)$  reactions, a high-resolution atomic-beam facility, and beam-line modifications to deliver beam to these areas.

General management responsibility for the upgrade project lies with L. Agnew, Associate Division Leader for Experimental Areas, and the Experimental Area Development Committee will review progress. R. Werbeck is the Technical Coordinator, with the following project managers:

- J. Donahue (MP-7) — Beam-Line Modifications and High-Resolution Atomic Beam (HIRAB);
- J. B. McClelland (MP-10) — Neutron Time of Flight (NTOF); and
- R. Boudrie (MP-10) — Medium-Resolution Spectrometer (MRS).

User advisory panels have been formed to provide input from the scientific community and to serve as a board of review for plans and options. Advisors for NTOF are S. Austin, A. Bacher, C. Goodman, J. Moss, and C. Zafiratos; advisors for MRS are G. Crawley, C. Glashausser, G. Glass, D. Lind, and J. Rapaport.

### Facility Upgrade

**The  $(p,n)$  Facility.** One of the earliest possible additions to the NPL could be a beam swinger and neutron time-of-flight (NTOF) facility for  $(p,n)$  reactions. The primary proton beam would be directed into the beam swinger area by a switching magnet (Fig. 1). Quadrupole

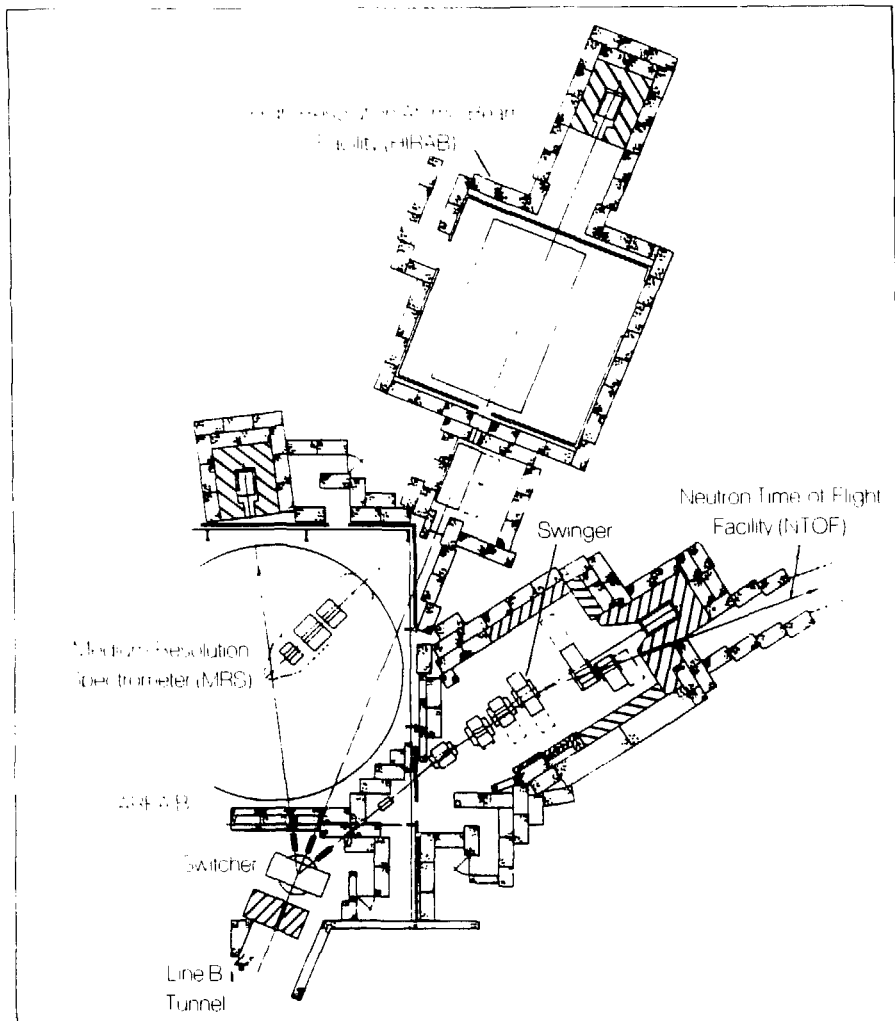


FIGURE 1. Proposed modifications of the NPL area.

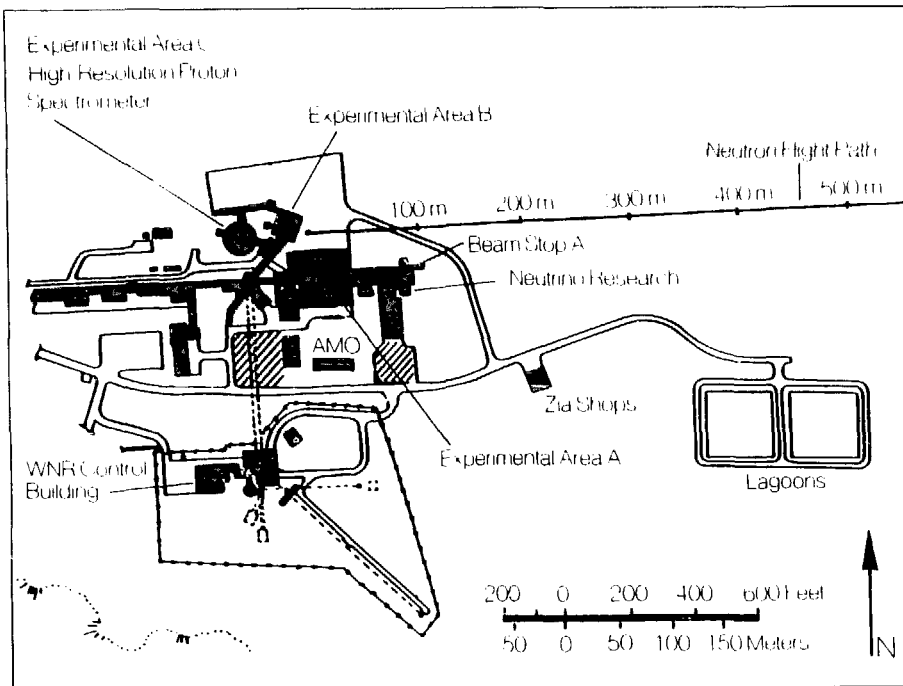


Figure 1. Schematic of the facility area showing neutron time-of-flight (NTOF) path and end stations.

magnets will maintain the focus on the  $(p, n)$  target as the swinger angle is varied. Beam-line instrumentation will be similar to the existing inventory—wire chambers, ionization chambers, and polarimeters for determining beam profile, intensity, and polarization.

The beam swinger would be a five magnet system for varying the incident angle of the proton beam on the  $(p, n)$  target, effectively changing the neutron scattering angle while keeping the neutron flight path and detectors stationary. As currently envisioned, this system will allow for momentum transfers greater than  $3 \text{ fm}^{-1}$  at all energies between 200 and 800 MeV. The fourth magnet of the swinger would aim the proton

beam into a beam dump capable of stopping and shielding up to 600 nA of 800-MeV protons. The swinger,  $(p, n)$  target, and beam dump will reside in a shielded crypt appended to the EPB room, as shown in Fig. 1.

A flight path of up to 600 m would be possible with some excavation (see Fig. 2). Given the expected timing performance of the accelerator and detectors, this will yield neutron energy resolutions of 1 to 2 MeV at 800 MeV. This is consistent with  $(p, n)$  work being carried out at other laboratories at lower energies. Beam timing characteristics will be monitored using beam microstructure pickoffs, such as those used at the Weapons Neutron Research (WNR) facility. These were tested in

Line C during the 1985 production period. Polarized beam would usually be chopped at 100 ns for neutron timing.

The detector hut will be a 4- by 10 m<sup>2</sup> portable house, on a carriage so that it can be positioned at three or four predetermined locations along the 600-m flight path. It would be a self-contained unit, housing the detectors and their support systems, electronics, and the computer-acquisition area. Alternatively, the acquisition station could be separate, but move in tandem with the detector station.

**Medium-Resolution Spectrometer (MRS).** A medium-resolution spectrometer,  $\Delta E \sim 1$  MeV, would have several roles. It would

1. complement the HRS with high acceptance where 1 MeV resolution is adequate, possibly serving about half the HRS queue;
2. serve as a home base for polarized-target and light-nuclei experiments that cannot exploit the HRS energy resolution; and

3. serve as a detector for  $(n,p)$  studies with resolution well matched to the narrowest available neutron spectrum.
- The MRS would occupy the present EPB area most of the time.

Design work has proceeded for the optical performance of such a spectrometer. The design goals that were considered are listed in Table 1. Because the instrument will be used to measure the polarization of the scattered particles, the net angle of deflection should be small, ideally about 15°. This will ensure that for all momenta considered there will be no dead spots in the polarization analyzed (that is, the outgoing polarization will not be precessed significantly into the longitudinal component at the focal-plane detectors). The demands for a large solid angle and reasonable resolution, taken together with the small net deflection angle and focal-plane angle, will be difficult to meet.

Four different layouts were tried, each with a large number of variations:

1. a QQDQQ system,

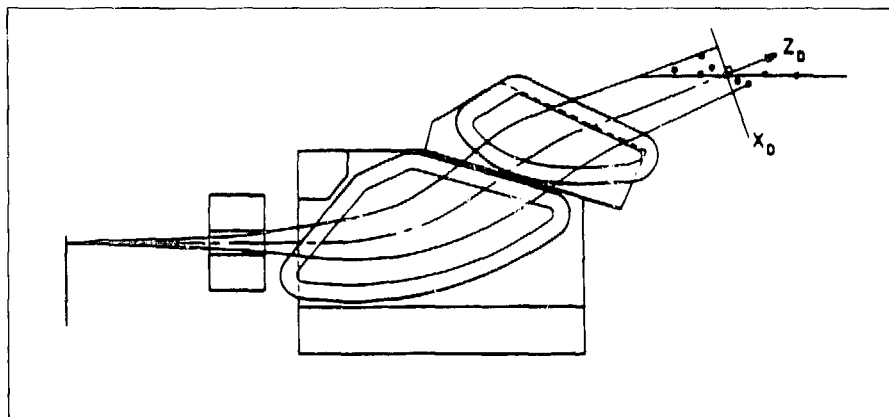


FIGURE 3 Layout for the QD(-D) system of Medium-Resolution Spectrometer (MRS)



TABLE 1. Medium-Resolution Spectrometer Design Requirements

|                              |              |                    |
|------------------------------|--------------|--------------------|
| Maximum momentum             | 1900 MeV/c   | (800 MeV deuteron) |
| Angular range                | 0-160        |                    |
| Overall length               | 9 m          |                    |
| Full Acceptance (at 500 MeV) |              |                    |
| Momentum                     | $\pm 1.0\%$  | ( $\pm 150$ MeV)   |
| Resolution                   | 0.4%         | (5 MeV)            |
| Solid angle                  | 15 mrad      |                    |
| Reduced Acceptance           |              |                    |
| Momentum                     | $\pm 1.5\%$  | ( $\pm 20$ MeV)    |
| Resolution                   | 0.04%        | (0.5 MeV)          |
| Solid angle                  | 10 mrad      |                    |
| Angular resolution           | $\pm 2$ mrad |                    |

2. a QDQ system with a strong negative  $n$  value,
3. a QD(D) system with strong wedge focusing, and
4. a QDS system with a strong negative  $n$  value.

The QD(D) system is the most promising (a layout is shown in Fig. 3). Ray-tracing calculations are in progress. One issue is performance with a large target area ( $\sim 25$  cm<sup>2</sup>) for the  $(n,p)$  capability. Additional requirements to be addressed are improved small-angle scattering coverage, localized target shielding, a generalized second arm, a focal-plane polarimeter, and a non-magnetic pivot to accommodate a polarized target. The spectrometer facility will require a permanent counting house.

The first expected use would be on  $(p,p')$  reactions. During this time the effects of a large target area associated with the  $(n,p)$  reaction would be studied. The initial implementation of a neutron source for

$(n,p)$  experiments might best be done using the existing BR neutron channel, replacing the LD<sub>2</sub> target with a thin lithium target. This would produce a nuclear-physics-grade neutron beam with an energy width less than 1 MeV, and implies moving the MRS between EPB and BR, which is an advantage from another point of view. It would allow the MRS to be used in nucleon-nucleon programs in the BR, for which a keen interest was demonstrated during the NPL upgrade workshops. Because the wall separating EPB and BR is movable, it would be reasonable to move the MRS on air pads between the two areas on a cycle basis. When the initial phase of the  $(n,p)$  program in BR is completed, a decision can be made as to the best targeting scheme for the program in general. A possibility exists to target the proton beam in EPB about 2 m upstream of the  $(n,p)$  target, then "dogleg" it around the MRS and restore it in the EPB dump.

This is similar to the system being developed at TRIUMF for a similar application at lower energies. The required shielding configuration is not yet clear.

Future studies involving polarization transfer might use the rather large values of  $D_{LL}$  for lithium ( $\sim 0.5$  at 800 MeV) in conjunction with neutron spin precession and the MRS focal-plane polarimeter. However, the reduced counting rates associated with polarimeter efficiencies may require further development. This facility—a polarized monoenergetic neutron beam, a proton spectrometer, and a polarimeter—would be a powerful and unique tool for spin-isospin nuclear physics, highly complementary to the  $(\vec{p}, \vec{n}')$  program being proposed, as well as to the  $(\vec{p}, \vec{p}')$  program at HRS.

**High-Resolution Atomic-Beam Facility.** The prime goal of the neutral particle-beam program is to assess the feasibility of using neutral particle beams as directed energy weapons outside the earth's atmosphere. This initiative calls for a significantly enhanced program of technological feasibility demonstrations. The High-Resolution Atomic-Beam (HIRAB) facility will provide the capability to study beam sensing and control. A wide range of basic atomic physics issues can also be investigated with unprecedented precision.

The project will provide for the construction of a 1600-sq-ft air-conditioned building, 20- by 40- by 4-ft-thick concrete pad, isolated from the NPL building slab, will provide vibra-

tion isolation for the laser and optics. A movable beam plug upstream of the facility will allow it to be occupied while the other areas are being used.

**Beam-Line Modifications.** As shown in Fig. 1, HIRAB will receive undeflected  $H^-$  ( $P^-$ ) along the present EPB line. A switching magnet will direct the beam toward the MRS or NTOF; thus use ordinarily will be exclusive. The only interference with personnel access to areas not receiving beam will come from the transport of the HIRAB beam near MRS.

A shielded extension of the Line B tunnel into the EPB area will enclose the switching magnet and beam plugs for each line. Upstream of the switching magnet, the EPB line will remain much the same.

The 52-in. cyclotron magnet acquired from the University of Colorado will be the switcher, bending the beam  $29^\circ$  to the left toward MRS or  $28^\circ$  to the right toward NTOF. The NTOF line will continue through a  $7^\circ$  bend to the right into the new NTOF swinger crypt to be built east of the EPB area. The undeflected beam will pass through the MRS shielding enclosure into the new HIRAB building that is to be constructed northeast of Area B (at the present EPB beam-stop location).

The switching magnet and beam plugs will be enclosed in a minimum-thickness concrete house. The shielding will be kept to a minimum to reduce the amount of floor space lost to the MRS area in the building. This effort to maximize floor space for the MRS precludes space for the

installation of phase-space tailoring collimators for MRS and NTOF. Future collimator installation would reduce the angular range for the MRS.

Once beyond the Line B tunnel extension, each of the three transport lines will contain beam instrumentation, a quadrupole doublet (available from surplus), and a vacuum system. Each beam line will ultimately terminate in a beam stop capable of stopping several hundred nanoamperes of protons.

The MRS enclosure will be lightly shielded along its sides and will have no shield roof above it. Thus, even thin MRS targets will need to be locally shielded in order to run a few nanoamperes of beam into them. The HIRAB enclosure also will be thinly shielded along its walls and will have no shielding in the roof. However, HIRAB will not use solid targets, so not much shielding is required. The swinger crypt for the NTOF facility will be a relatively well-shielded enclosure (including a shielded roof) that will permit several hundred nanoamperes of protons to strike targets up to  $1 \text{ g/cm}^2$  thick. The crypt will be quite large (12 by 7.5 m) to accommodate the motion of the large swinger magnets. Much of the shielding will be reused surplus shielding from the University of Colorado 52-in. cyclotron facility and from Area A of LAMPF.

Experiments also can be run in the EPB area, more or less as done currently. During such periods, the MRS would have to be rotated out of the way of the experimental setups. A movable beam stop upstream of HIRAB will allow HIRAB to be an open area.

Implementation of the new facilities will be staged over several years. During the 1986 shutdown (January to mid-June 1986) the switching magnet and the three movable beam plugs will be installed and enclosed in shielding. Some of the modifications to the Area B building needed for the completed NPL upgrade project will be started (for example, the addition of personnel access doors and the removal/relocation of electrical breaker panels and transformers). The present EPB beam stop will be moved, and work on the HIRAB area will start. During the 1986 production cycles, the EPB main area will be available for experimental use.

## Workshops

On December 16 and 17 of this past year, a second workshop dealing with these major upgrades of the NPL at LAMPF was held, with 60 participants representing 22 universities and national laboratories. The purpose of the workshop was to review the extensive planning and design that had taken place within the last year and to make final criteria and designs for completion of the project. Working groups were established for long-term projects such as detector

development, beam-diagnostic instrumentation, and spin-precession systems. There was general agreement on work done to date on beam-line modifications, the Medium-Resolution Spectrometer, and the beam swinger and flight path for the Neutron Time-of-Flight facility.

Within the funding schedule and manpower for this project, it is expected that the neutron flight path and swinger will be available in 1987, and that the spectrometer and neutron source will be available in 1988.

---

## Reference

1. J. B. McClelland, A. Bacher, R. L. Boudrie, T. A. Carey, J. Donahue, C. D. Goodman, et al., "Development Plan for the Nucleon Physics Laboratory (NPL) Facility at LAMPF," Los Alamos National Laboratory report LA-10278-MS (February 1986).

The floating-wire technique has been used to measure the particle momentum versus magnetic-field calibration of the spectrometer at EPICS.<sup>1</sup> Orbits through the dipoles were measured *in situ* over the range from 233 to 659 MeV/c. The measurements were corrected for gravitational and frictional effects.

If a thin, flexible wire of negligible mass carrying a current  $i$  is suspended with a tension  $T$  in a magnetic field  $B$ , it will follow a path described by the differential equation of motion for a particle with charge  $q$  and momentum  $P$  in the same field, provided no other forces act on the wire. The relationship

### Spectrometer Calibration at EPICS

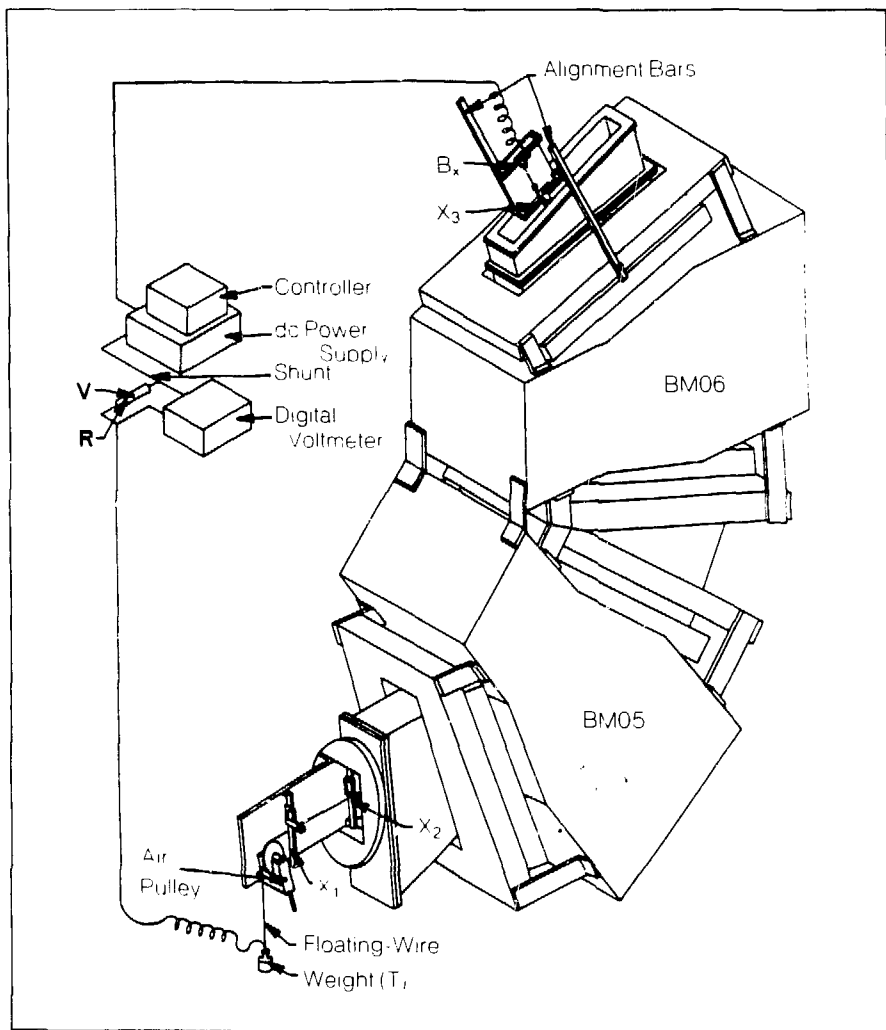


FIGURE 1 Sketch of the spectrometer dipoles at EPICS and schematic of the floating-wire system. The vertical bend angle is  $120^\circ$ . DCPS is the direct-current power supply, and DVM is the digital voltmeter.

among the quantities is

$$\frac{P(\text{MeV}/c)}{q(\text{electron charge})} = \frac{T(\text{grams})}{i(\text{amperes})}$$

Because the spectrometer bend plane is vertical, the path of the wire must be corrected for distortion induced by gravity.

An apparatus, shown in Fig. 1, was designed to measure the entrance and exit trajectories of a 0.025-mm CuBe wire with measured tension and current for magnetic field  $B$  from 6 to 17 kG. A frictionless air-bearing pulley was used for accurate tensioning. The wire weight distortion is shown in Fig. 2. The distance  $DS$  in the figure is the calculated

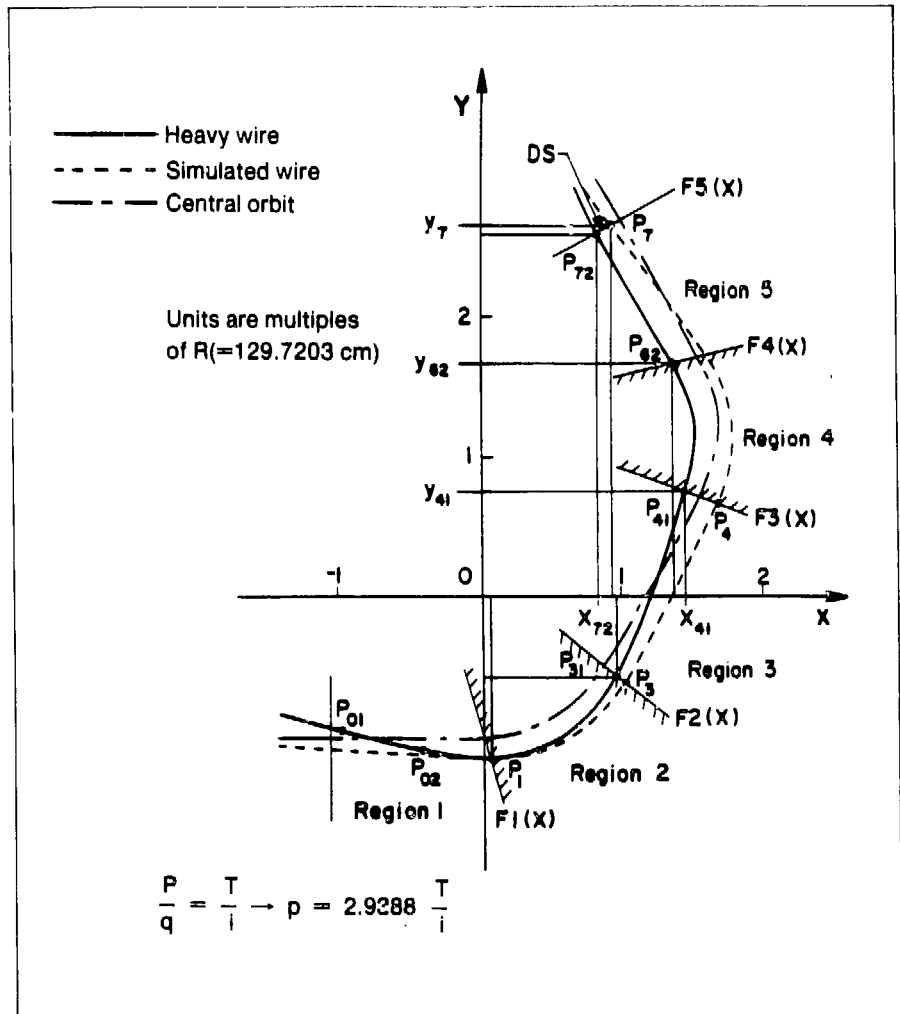


FIGURE 2 Schematic diagram of the spectrometer divided into five regions, and the paths of the central ray, simulated wire, and heavy wire from the image plane through the spectrometer to the focal plane

difference, in the midplane, between the actual wire location and that for a massless wire. Measurements of this distance as a function of tension compared well with predictions.

From these measurements the quantity  $B/Pc$  for the central ray was determined. This quantity is used by the kinematic routines in determining magnet settings for the spectrometer. The momentum dependence of this quantity is neither constant nor linear, as currently implemented in the kinematics calculations. The method of measurement and the implications of the results are under consideration. The average value of the redetermined  $B/Pc$  is 25.725 G/MeV/c with  $\sigma(B/Pc) = 0.005$ , to be compared with the previously determined value of 25.63 G/MeV/c. The comparison is shown in Fig. 3.

This new calibration is currently being used for development scanning of the channel output momentum at EPICS with respect to magnet settings.

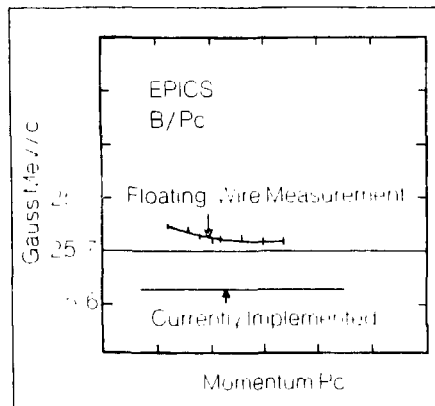


FIGURE 3 Comparison of  $B/Pc$

## Reference

1. Z. F. Wang, S. J. Greene, and M. A. Plum, "High-Precision Floating-Wire Measurements of Large Dipole Magnets at LAMPE," *Nuclear Instruments & Methods* (in press).

## Radiation Effects Facility

### New Facility at Beam Stop

M. F. Sommer, L. K. Taylor, and R. M. Chavez (Los Alamos)

Installation of new hardware at Target Station A-6 for radiation-damage-effects studies was completed in May 1985. Experiment capsules may be introduced into the secondary particle flux emanating from the interaction of the primary proton beam with the isotope production targets and the beam stop. Twelve independent inserts are available for irradiations in

the secondary particle flux. Figure 1 shows eight of the inserts and their relation to the isotope production targets and the beam stop. Also, three inserts allow positioning of irradiation capsules into the direct proton beam. Figure 2 shows the position of these capsules in the overall layout of Target Station A-6.

During the period from May to December 1985, four proton irradiations (LAMPF Exp. 769) and two neutron irradiations (Exps. 936 and 769) were completed. Control equipment, a

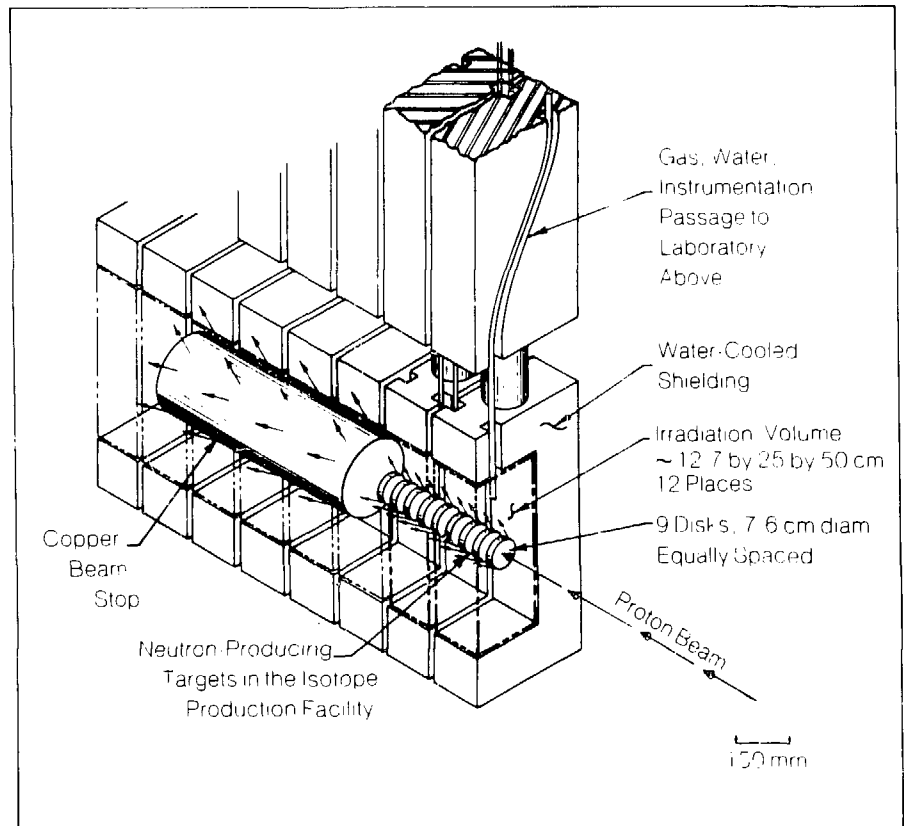


FIGURE 1. Neutron irradiation inserts at LAMPF Target Station A-6 and their relation to the isotope production targets and the beam stop. Shown are 8 of the 12 inserts, each with a usable experiment volume of about 0.02 m<sup>3</sup>.



closed-loop helium heat sink, and a closed-loop water heat sink for temperature control were made operational. Instrumentation racks for this equipment are located directly outside the Target Station A-6 concrete hut and are accessible during

beam-on operation.

Experiment changes were made during periods between cycles as well as on a maintenance day. It was demonstrated that an experiment change can be accomplished in 6 h.

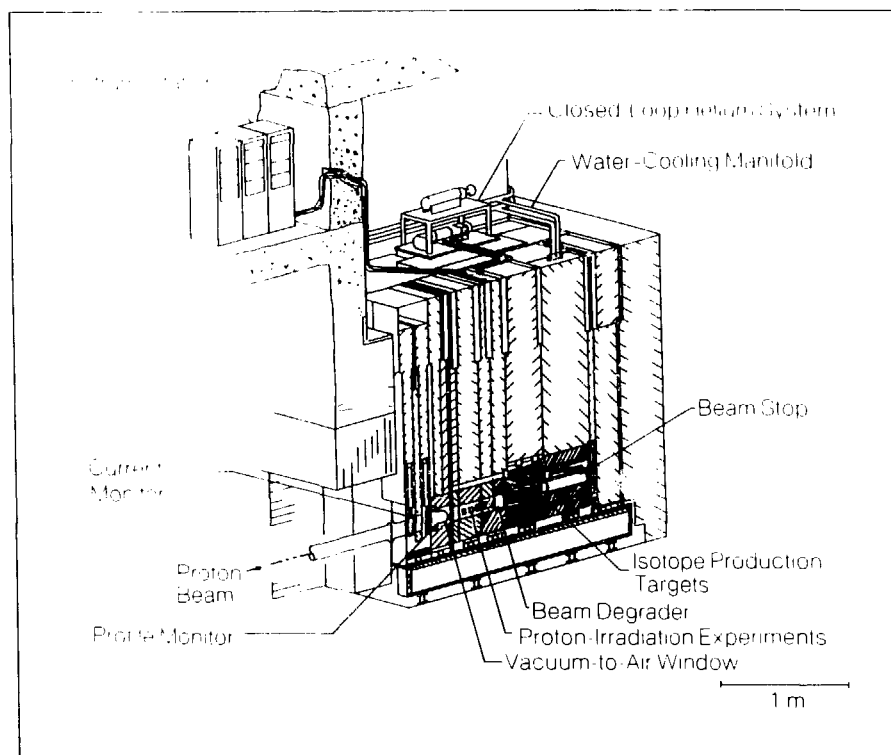


FIGURE 2. Overall layout of Target Station A-6. Note the relation among the proton irradiation experiment, the cooling systems, and the instrumentation racks.

## Measurements of Power Deposition at the LAMPF Neutron Radiation Effects Facility

R. D. Brown (Los Alamos)

As part of the effort to characterize the LAMPF neutron Radiation Effects Facility (REF), measurements have been made of the power deposition in a copper calorimeter located in the spallation neutron flux about 20 cm beneath the isotope production stringers. Calculations<sup>1,2</sup> of the neutron flux showed that the flux should be peaked near this location and that the heat flux should therefore be at a maximum here.

A calorimeter was constructed of two copper cylinders with electrical heaters on the inside and outside cylinders. The heaters allowed us to supply measured power levels to the calorimeter and thereby to calibrate it. The temperatures in the calorimeter were modeled using a time-dependent equation. To determine the

power deposition, we needed to know the emissivity of the inner cylinder, the heat-transfer coefficient between the cylinders, and the thermal mass of the inner cylinder. All these coefficients were determined from the initial calibration runs. The calorimeter was inserted into REF stringer 3 and irradiated for 2 days. Temperatures were recorded using thermocouples attached to an automated data-collection system, and the beam current was monitored using graphs of the beam current obtained from the central control room. Analysis of the data showed that the power density plotted versus time was approximately a constant, equal to about 2 W/cm<sup>3</sup>/mA.

The power deposition, which has been measured at one position at the REF, is in reasonable agreement with calculated values. Further measurements are needed to determine the variation in power deposition with position along the beam line and with radial distance from the beam line.

---

## References

1. D. R. Davidson, L. R. Greenwood, R. C. Reedy, and W. F. Sommer, "Measured Radiation Environment at the LAMPF Irradiation Facility," 12th International Symposium on Effects of Radiation on Materials, Williamsburg, Virginia, June 18-20, 1984, Los Alamos National Laboratory document LA-UR-84-1050 (June 1984).
2. D. R. Davidson, W. F. Sommer, J. N. Bradbury, R. E. Prael, and R. C. Little, "Characterization of the LAMPF Beam Stop Area Radiation Environment," Los Alamos National Laboratory document LA-UR-83-33 (January 1983).

## 800-MeV Proton Irradiation of Materials for the SIN Beam Stop

R. D. EISENBERG, R. J. ALLEN, and C. E. TRACY  
 Fusion Energy Research Center, University of  
 California, and LLNL, Livermore, California, State  
 University

SIN has been studying the possibility of constructing a neutron source/beam stop that uses a vertical cylinder of liquid lead-bismuth. At the design current, the proton beam current density will be about  $20 \mu\text{A}/\text{cm}^2$ , essentially the same as that now available (at 800 MeV) at the LAMPF A-6 radiation effects area. The window in the cylinder base must be made of an alloy that is chemically compatible with the molten lead bismuth and that can

maintain reasonable ductility and strength following proton irradiation to fluences of about  $10^{21} \text{p}/\text{cm}^2$  at a temperature of about  $400^\circ\text{C}$ . Initial examination of materials for chemical compatibility with the lead bismuth indicated that iron based alloys and tantalum could both be candidates. Materials selected for irradiation included Fe, Fe-2.25Cr-1Mo, Fe-12Cr-1Mo (HT-9), and Ta.

Tensile samples were heat treated and encapsulated in a lead-bismuth eutectic alloy, sealed in an outer steel capsule and proton irradiated. A set of high-fluence samples received about  $5.4 \times 10^{20} \text{p}/\text{cm}^2$ ; a set of low-fluence samples, about  $4.8 \times 10^{19} \text{p}/\text{cm}^2$ . In pure iron, these results

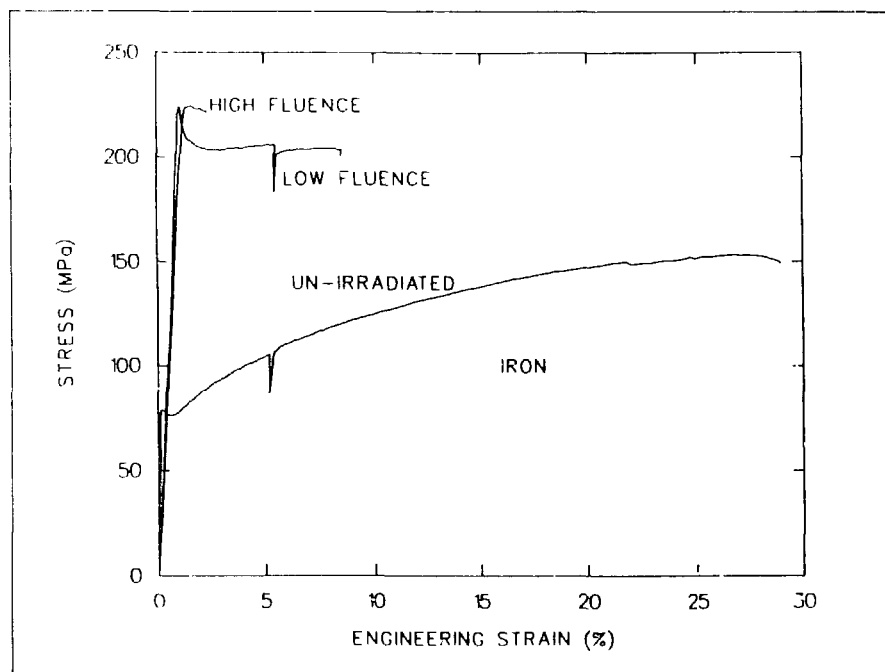


FIGURE 1. Stress-strain curves for iron as a function of proton fluence.

correspond to about 1.6 and 0.14 dpa, respectively.\* Examination of the samples following removal from their capsules showed no corrosion caused by contact with the molten lead-bismuth. The samples were then dipped in acid to remove alpha contamination and tensile tested in the hot cells (at another site in the Laboratory) at a strain rate of  $9 \times 10^{-4}$ /s.

The yield and ultimate strengths increased in all materials following irradiation, whereas the ductility, as

measured by the uniform plastic strain, generally decreased. Figure 1 shows stress-strain curves for iron as a function of fluence. The pure metals, iron and tantalum, exhibited the greatest radiation hardening and embrittlement; the HT-9 alloy showed the smallest changes in strength and ductility. Additional work is under way to study the radiation modified microstructures using transmission electron microscopy.

\*Reference 1 and information provided by D. R. Davidson, Los Alamos National Laboratory, June 1985.

---

## Reference

1. C. A. Coulter, D. M. Parkin, and W. V. Green, "Calculation of Radiation Damage Effects of 800-MeV Protons in a 'Thin' Copper Target," *Journal of Nuclear Materials* **67**, 140 (1977).

## VAX Cluster

Computing capacity at the Data Analysis Center (DAC) was significantly enhanced during 1985 with the addition of a VAX 8600, a new machine equivalent to approximately four VAX 11/780 computers. One of the DAC VAX 11/780s was transferred to the Central Control Room (CCR) to support the operations programming section, leaving the DAC with a cluster of three VAX 11/780s and a VAX 8600.

The VAX 8600 considerably increased the computing capacity at the DAC, and that capacity was used almost instantly (see Fig. 1). The VAX 8600 also increased disk space, both for scratch space (1.4 Gbyte) and for system storage, because the VAX 8600 uses a separate system disk for optimum operation. In addition, one TU78 tape unit (6250/1600 bpi) was upgraded to a TA78 and is controlled through the HSC50 cluster controller; this means that the tape unit is available to any machine in the cluster, not simply to a specific machine. Another TU78 tape unit was purchased in 1985 and slaved to the TA78 so that it is also available to the cluster.

## Other Support

The tape library at the DAC was expanded in 1985, from a capacity of about 7000 to about 12 500 tapes. The tape library racks are currently about 70% filled.

Several Digital Equipment Corporation (DEC) LN03 desk-top laser printers were purchased during 1985. Some units are supported from printer ports off specific terminals and some are set up as spooled devices in the DAC and in the Laboratory Office Building. Support is provided for word processing, including Greek and mathematical characters.

Some effort was expended evaluating a terminal replacement for the outdated VT640 terminals now in use around LAMPE. The new terminal requirements included higher-resolution graphics and compatibility with the DEC terminal VT100-style keypad (a favorite for use with the DEC EDT editor). Specifications are being prepared to send to various vendors for bids. Note that the hardcopy units (Tektronix 4612) will not be able to support higher-resolution terminals.

## Data-Analysis Center

McPherson and DeAngelis (1987) (p. 101)

### Networking

The LAMPF local area network cable currently runs from the DAC to Areas B and C, throughout Area A, and to the new neutrino experiment at the far-east end of the accelerator. The total length of the coaxial cable comprising the network is 764 m. Currently 10 nodes are connected, with capability for growth to 200 to 300 nodes. The Ethernet network has proved to be a highly reliable and cost effective means for information exchange.

With the advent of the network, experimenters are now better able to make efficient use of the resources at the DAC and throughout the experimental areas. This network, coupled with the connection over the Laboratory broadband network to the C-Division computers and through those computers to worldwide networks such as Telenet and Arpanet gives LAMPF experimenters almost direct access to home institutions and other collaborators.

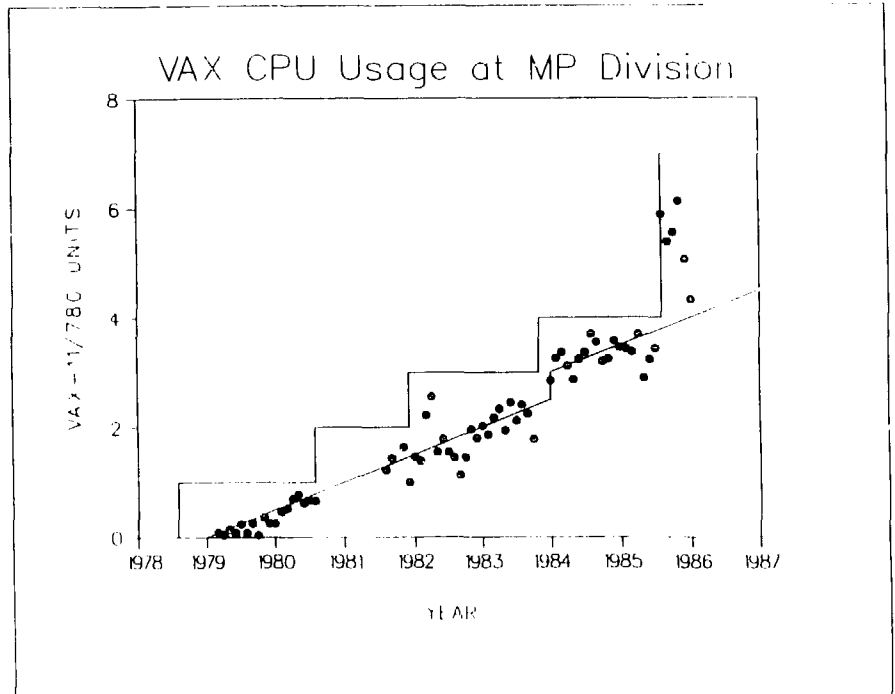


Figure 1. VAX-11/780 computer MP Division from 1979 to 1986. The equipment is the same as the year 1981 computer, but the capacity is increased to the total capacity. The trends are the same as the previous computer. The jump in straight line in 1984 is due to the commitment to provide computer for group 12, and the same jump in units (the equivalent of four VAX-11/780 units) which results from the acquisition of the VAX-8600. The six-monthly acquisition of the VAX-8600 shows a cost in terms of about 30%.

## LAMPF Control System

The Central Control Room (CCR) VAX computer control system<sup>1</sup> was used for tune-up of the new H<sup>-</sup> injector and transport lines during the spring 1985 accelerator startup. Applications program conversion from the SEL 810 to the VAX 11-780 is largely complete. A second VAX is used in the CCR for system development, and clustering of the two VAXes is under way. When LAMPF beam is turned on in the late spring of 1986, we will be using the new control system software exclusively. The SEL 810 will probably remain through that operating cycle as a security blanket or to cover the chance that a program has been omitted. Following this cycle, the SEL 810 will be removed. With the vital work done, essential improvements and future growth can be considered.

## Software Optimization Issues

Once an applications program is complete, we evaluate its responsiveness. If it is too slow, several tools are used to determine where it is spending its time. We find that most programs spend the majority of their time in very limited areas of the code. These areas are then made more efficient. In some cases these areas are in subroutines that are used on a system-wide basis, such as those supporting plotting and data taking, and attacking these inefficiencies therefore increases responsiveness on a system-wide basis.

Several graphics applications proved to be quite slow. We were using a set of routines supplied and

supported by the Laboratory Computing Division. We discovered that they had taken one high-level set of routines, the package supported by the National Center for Atmospheric Research (NCAR), and laid it on top of the set of routines C Division has supported for years (CGS). By removing this bottom layer, we doubled the plotting speed while keeping the standard NCAR interface.

We also found that programs that acquire accelerator data spent more time than expected managing space for global data structures. By preallocating memory for some of these structures, we reduced data acquisition CPU usage by a factor of 2 without sacrificing the diagnostic capabilities afforded by these globally accessible structures. Because data-taking routines are part of the control system run-time library, optimizations in this area provided improvements in most of the applications programs.

Several applications programs acquire data from a large number of accelerator devices on a repetitive basis. Programs that support monitoring, as well as the program that displays the status of the system and accelerator operational status, are examples. The latter program, for instance, acquires data from approximately 300 different devices once every 3 s. Because applications programs must use symbolic device names for data acquisition, they are unable to make direct use of the hardware organization to optimize their data access. We provided a data acquisition routine that allows an application to combine a group of disparate devices into an aggregate de-

## LAMPF Computer-Control System

DAVID FROST, Lawrence Livermore National Laboratory, University of California, Livermore, California 94550; and JOHN W. HARRIS, Lawrence Livermore National Laboratory, University of California, Livermore, California 94550

vice. Reading the aggregate device, the data-acquisition routines acquire data for each component device, thereby minimizing the number of hardware references required. This optimization has decreased the CPU time needed for the rf status program by a factor of 3 while retaining the hardware independence afforded by symbolic device naming. (More details on data-acquisition optimizations can be found in Ref. 2.)

Another interesting optimization also involves this status program. During production, the operators often run the program from several different consoles, which initially meant running a separate copy of the program at each console, substantially loading the system resources. Now, additional requests for the status display are met by a slaved copy at negligible cost.

### **VMS Environment**

Some of the jobs done by operations personnel are more efficiently implemented by the VAX/VMS operating system than by the control system. By using a VMS interface for these tasks, we do not need special applications programs. Examples of these tasks include displaying VMS and accelerator status information, displaying file directories, updating applications-program data files, and generating reports from the accelerator device-description data base.

However, if operators are logged in as normal users, accidental file deletions are possible. To prevent this, VMS access is limited by an indirect command file that is activated when an operator logs in on a touch panel. The command file allows the operator to execute a small subset of VMS commands, and the only way to leave the indirect command procedure is by logging out. This simplifies and protects the operator interaction.

### **Remote Computer Network**

Five small PDP-11 computers are located throughout the facility (Areas A and B, the switchyard, transition region, and the ion-source test stand) for remote data acquisition and control through CAMAC data links directed by a communications-node computer (NET-11) in the CCR. Several other small PDPs are also in place for special tasks. This network was built up over the years largely with customized hardware and software, leading to problems with maintenance and development.

The planned upgrade will replace the PDP-11s with micro-VAXes and the network with Ethernet. Ethernet will allow straightforward network expansion and can be driven by the CCR VAXes without the NET-11 relay node. Four of the data-acquisition micro-VAXes will not have disks. We will probably install the VAXELN memory-resident operating system, which can be down-loaded from the



CCR over Ethernet. VAXELN is written and supports EPASCAL, an International Standards Organization PASCAL with extensions for real-time processing.

Programs running on the micro VAXes will access data through symbolic device names, as is currently done by the VAX-11/780 programs. The device description data base will be maintained on the VAX-11/780s and downloaded as needed by the remote computers.

Access between computers will be supported through a paradigm for calling procedures for remote computers. The computer at the ion source test stand (ISTS) is an exception in that it is essentially a stand-alone system with no direct connection to the accelerator. We are considering adding local disk storage to the ISTS micro VAX and running the micro VMS operating system. We expect that portions of the VAX-11/780 control system can be used to handle the ISTS environment. The Ethernet connection will be used to transfer software and data bases.

At the present time the Ethernet cable has been purchased and is in place. Micro VAXes have been purchased for the switchyard, the master timer, and the ISTS computers, but are not yet installed.

### Summary

The upgrade from the SEL 840 to the VAX-11/780 is all but complete. Most of the applications program software is now in production. This software has been monitored to uncover response bottlenecks. Some optimizations have been implemented with good results. We intend to continue to monitor performance and make additional changes where they make sense. We have been able to provide a limited VMS environment for the operators so that those tasks most easily accomplished by using VMS can be done safely. Finally, the control-system network upgrade is well under way. We project that this task will be completed in about one more year.

---

### References

1. D. E. Schultz and S. K. Brown, "On-Line Replacement of a Particle Accelerator Control Computer," IEEE Real-Time Systems Symposium, Miami Beach, Florida, December 8-10, 1981, IEEE Catalog No. 81CH1700-4, pp. 78-82.
2. S. C. Schaller, J. K. Corley, and P. A. Pose, "Optimizing Data Access in the LAMPF Control System" (to be published in *IEEE Transactions on Nuclear Science*).



## Accelerator Operations



## Accelerator Operations

This report covers operating cycles 42, 43, and 44. The accelerator was in operation from April 22 through December 22, 1985. Beams were provided for research use for 187 days, and for facility development for 25 days. Almost all the facility development time was used for Proton Storage Ring (PSR) commissioning. A summary of information on beams provided for research is given in Table 1.

A new high intensity  $H^+$  ion source was brought into operation to provide beam for the PSR. With the exception of three shifts for a nuclear chemistry experiment, beam from the new source was used exclusively for operation and development in the PSR and Line E. Peak  $H^+$  beam currents in excess of 6 mA and average beam currents as high as 33  $\mu A$  were delivered to the PSR.  $H^+$  beam availability was 77, 85, and 79% for cycles 42, 43, and 44, respectively.

TABLE 1. Beam Statistics for Cycles 42 Through 44

|                              |                                   | Cycle 42 | Cycle 43 | Cycle 44 |
|------------------------------|-----------------------------------|----------|----------|----------|
| Number of experiments served |                                   | 30       | 38       | 41       |
| $H^+$                        | scheduled beam (h)                | 1599     | 1366     | 1504     |
| $P^-$                        | scheduled beam (h)                | 1911     | 1338     | 1491     |
| $H^+$                        | beam availability (%)             | 73       | 89       | 86       |
| $P^-$                        | beam availability (%)             | 66       | 71       | 80       |
| $H^+$                        | average current ( $\mu A$ )       | 700      | 830      | 900      |
| $P^-$                        | average current (nA) <sup>a</sup> | 10       | 6        | 22       |
| $H^+$                        | beam duty factor (%)              | 6.9      | 6.9      | 6.9      |
| $P^-$                        | beam duty factor (%)              | 3.9      | 3.9      | 3.9      |

<sup>a</sup>Averaged over entire cycle

The low availability of  $P^+$  beams during cycles 12 and 13 was directly related to problems with the ion source. A change in source operating parameters during the latter part of cycle 11 resulted in a significant improvement in stability and a five-fold increase in  $P^+$  beam current.

Accelerator operation was smooth and reliable, easily providing  $H^+$  beam intensities of 1 mA at 9% duty factor and 950  $\mu A$  at 6%. Poor  $H^+$  availability during cycle 12 was

largely due to failure of a quadrupole triplet in an A-2 target cell; ground faults and a resultant large water leak required replacement of coolant lines and cost over a week of unscheduled downtime.

A summary of unscheduled facility downtime during research shifts is given in Table II. Because some of the outages are concurrent, and because some affected only one of three beams, the total is much greater than the beam downtime.

TABLE II. Unscheduled Machine Downtime During Shifts in 1985

| Category   | Downtime | Per Cent of Total |
|--|----------|-------------------|
| 201 MHz amplifiers and transmission lines              | 255      | 14                |
| 805 MHz amplifier systems                              | 90       | 5                 |
| Vacuum systems   | 70       | 4                 |
| Magnets  | 223      | 12                |
| Magnet power supplies                                  | 65       | 4                 |
| Interlock systems                                      | 29       | 2                 |
| Ion sources and Cockcroft-Walton high voltage supplies | 798      | 44                |
| Cooling water systems                                  | 33       | 2                 |
| Computer control and data acquisition                  | 22       | 1                 |
| Production targets                                     | 30       | 4                 |
| Pulse timing systems                                   | 19       | 1                 |
| Miscellaneous (utilities, lightning, etc.)             | 118      | 7                 |
| TOTAL  | 1802     |                   |



## Milestones



## MILESTONES

## 1968

|  |                   |
|--|-------------------|
| Official Ground Breaking   | February 15, 1968 |
| Spinoff: Adoption of LAMPF Accelerating Structure for X-Ray Therapy and Radiography Machines | ca 1968           |

## 1970

|  |               |
|--|---------------|
| 5-MeV Beam Achieved                                  | June 10, 1970 |
| Adoption of a LAMPF-Standard Data-Acquisition System | August 1970   |

## 1971

|                       |                 |
|-----------------------|-----------------|
| 100-MeV Beam Achieved | June 21, 1971   |
| 211-MeV Beam Achieved | August 27, 1971 |

## 1972

|  |                    |
|--|--------------------|
| 800-MeV Beam Achieved  | June 9, 1972       |
| Spinoff: First Use of Electrosurgical Forceps in Open-Heart Surgery (University of New Mexico) | September 13, 1972 |
| Discovery of $^{236}\text{Th}$ (Experiment Zero)   | September 25, 1972 |
| Dedication to Senator Clinton P. Anderson  | September 29, 1972 |
| Spinoff: First Hyperthermic Treatment of Animal Tumors   | October 1972       |

## 1973

|  |                 |
|--|-----------------|
| First $\text{H}^-$ Injector Beam                       | March 28, 1973  |
| First Simultaneous $\text{H}^+$ and $\text{H}^-$ Beams | May 4, 1973     |
| Beam to Area B   | July 15, 1973   |
| First Experiment (#56) Received Beam                   | August 24, 1973 |
| First Meson Production, Beam to Area A                 | August 26, 1973 |

## 1974

|  |                   |
|--|-------------------|
| Beam to Area A-East                          | February 6, 1974  |
| First Medical Radioisotope Shipment          | July 30, 1974     |
| Usable 100- $\mu\text{A}$ Beam to Switchyard | September 5, 1974 |
| Pi-Mesic Atoms with "Ticklish" Nuclei        | October 13, 1974  |
| First Experimental Pion Radiotherapy         | October 21, 1974  |
| First Tritium Experiment (80 000 Ci)         | November 1974     |
| Start of Great Shutdown                      | December 24, 1974 |



## 1975

---

|   |                    |
|---|--------------------|
| New Precise Measurements of Muonium Hyperfine-Structure Interval and $\mu^+$ Magnetic Moment                                | 1975-77-80         |
| Q Data Acquisition Software Operational   | June 1975          |
| Spinoff: First Use of $^{82}\text{Rb}$ for Myocardial Imaging in Humans (Donner Lab, Lawrence Berkeley National Laboratory) | June 1975          |
| Spinoff: First Hyperthermic Treatment of Human Cancer (University of New Mexico)  | July 11, 1975      |
| Accelerator Turnon  | August 1, 1975     |
| Acceptable Simultaneous 100- $\mu\text{A}$ $\text{H}^+$ and 3- $\mu\text{A}$ $\text{H}^-$ Beams to Switchyard               | September 14, 1975 |
| Production Beam to Area B   | October 7, 1975    |

## 1976

---

|  |                  |
|--|------------------|
| First Pions Through EPICS  | March 18, 1976   |
| Production Beam in Areas A and A-East:<br>End of Great Shutdown  | April 5, 1976    |
| Muon-Spin-Rotation Program   | June 1976        |
| Spinoff: First Hyperthermic Treatment of Cancer Eye in Cattle (Jicarilla Reservation)                                      | June 3, 1976     |
| 100- $\mu\text{A}$ Production Beam in Area A   | August 1976      |
| Experiment in Atomic Physics ( $\text{H}^-$ + laser beam):<br>Observation of Feshbach and Shape Resonances in $\text{H}^-$ | October 1976     |
| Double Charge Exchange in $^{16}\text{O}$ : LEP Channel  | October 5, 1976  |
| Startup of Isotope Production Facility   | October 15, 1976 |
| HRS Operation Begins   | November 1976    |
| Maintenance by "Monitor" System of Remote Handling   | Fall 1976        |

## 1977

---

|   |                |
|---|----------------|
| Proton Beam to WNR  | March 12, 1977 |
| Polarized Proton Beam Available   | April 1977     |
| Spinoff: First Practical-Applications Patent Licensed to Private Industry | April 12, 1977 |
| Pion Radiotherapy with Curative Intent                                    | May 1977       |
| Proton-Computed Tomography Program  | June 1977      |
| Experimental Results at Neutrino Facility                                 | July 1977      |
| Cloud and Surface Muon Beams: SMC   | July 1977      |
| EPICS Operation Begins  | August 1977    |
| 300- $\mu\text{A}$ Production Beam in Area A                              | Fall 1977      |

**1978**

---

|  |                 |
|--|-----------------|
| AT Division Established                            | January 1, 1978 |
| $\pi^0$ Spectrometer Begins Operation              | February 1978   |
| Operation of Polarized-Proton Target               | Spring 1978     |
| Successful Water-Cooled Graphite Production Target | November 1978   |

**1979**

---

|  |               |
|--|---------------|
| Spinoff: First Thermal Modification of Human Cornea (University of Oklahoma) | July 11, 1979 |
| 600- $\mu$ A Production Beam in Area A                                       | November 1979 |
| New Limit on $\mu \rightarrow e\gamma$                                       | December 1979 |

**1980**

---

|   |                  |
|---|------------------|
| Experimental Measurement of the Strong-Interaction Shift in the $2p-1s$ Transition for Pionic Hydrogen              | 1980-81-82       |
| Commercial Production of Radioisotopes  | January 1980     |
| Spin Precessor Begins Operation   | February 1980    |
| Data-Analysis Center Operational  | April 1980       |
| Variable-Energy Operation   | June 1980        |
| Single-Isobaric-Analog States in Heavy Nuclei   | June 1980        |
| Spinoff: First Use of $^{82}\text{Rb}$ for Brain Tumor Imaging in Humans (Donner Lab, Lawrence Berkeley Laboratory) | September 1980   |
| Production of Fast Muonium in Vacuum  | Fall 1980        |
| Double-Isobaric-Analog States in Heavy Nuclei   | October 1980     |
| Focal-Plane Polarimeter Operational at HRS  | October 1980     |
| Safety Award to LAMPF Users Group, Inc. for Working One Million Man-Hours Since 1975 Without a Disabling Injury     | October 27, 1980 |
| New Measurement of Pion Beta Decay—Improved Test of Conserved-Vector Current  | November 1980    |

**1981**

---

|   |                |
|---|----------------|
| First Excitation of Giant Dipole Resonance by Pion Single Charge Exchange   | March 1981     |
| First Excitation of Isovector Monopole Resonance in $^{120}\text{Sn}$ and $^{90}\text{Zr}$ by Pion Single Charge Exchange | March 1981     |
| Search for Critical Opalescence in $^{40}\text{Ca}$   | September 1981 |

## 1982

---

|  |               |
|--|---------------|
| Average Beam Current of LAMPF Accelerator<br>Established at 750 $\mu\text{A}$  | 1982          |
| Staging Area Constructed   | 1982          |
| Particle Separator Installed at SMC  | 1982          |
| "Dial a Spin" Capability on Line B Permits Different<br>Spin Orientations for HRS, Line B, and EPB<br>Simultaneously | 1982          |
| Time Projection Chamber in Operation   | 1982          |
| Improved Test of Time-Reversal Invariance in<br>Strong Interactions  | January 1982  |
| Search for Parity Nonconservation in $pp$ Scattering   | November 1982 |
| $d\bar{t}$ Fusion Catalyzed by Muons   | November 1982 |

## 1983

---

|   |                  |
|---|------------------|
| LAMPF Accelerator Produces Proton Beam<br>of 1.2 mA   | February 7, 1983 |
| First Observation of $\nu_e e^-$ Scattering   | October 1983     |
| Result for Asymmetry in $\vec{p}p$ Scattering Caused by<br>Parity Violation: $A_L = (2.4 \pm 1.1) \times 10^{-7}$<br>at 800 MeV | November 1983    |

## 1984

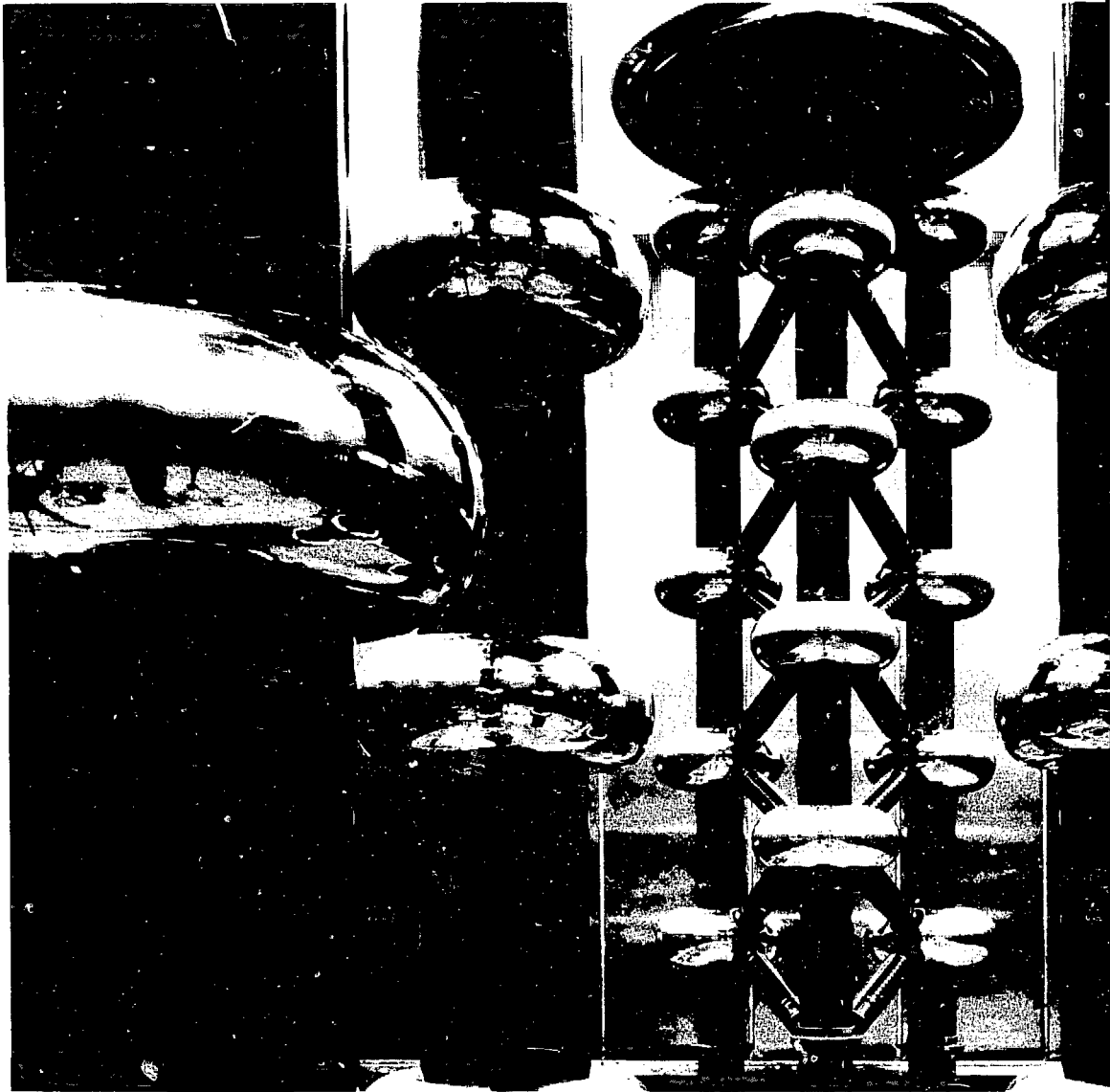
---

|  |                |
|--|----------------|
| Duty Factor $\geq 9\%$ Achieved  | February 1984  |
| Total Cross Section for $\nu_e e^-$ Scattering:<br>$\sigma_T = 10^{-44} E_\nu (\text{GeV}) \text{ cm}^2$ | May 1984       |
| Clamshell Spectrometer On Line   | June 1984      |
| High-Intensity $\text{H}^-$ Source Operational   | September 1984 |
| Branching Ratio for $\mu^+ \rightarrow e^+ e^+ e^-$ Probes Mass<br>Range to 10 TeV                       | October 1984   |

**1985**

---

|   |                |
|---|----------------|
| New Beam Stop Installed by Remote-Handling System   | Spring 1985    |
| High-Intensity H <sup>-</sup> Injector Operational  | April 1985     |
| New Switchyard Permits Three-Beam Operation   | April 1985     |
| Proton Beam to Proton Storage Ring (PSR)  | May 1985       |
| Routine Production at Beam Current of 1 mA  | Summer 1985    |
| $\pi^- p \rightarrow \pi^0 n$ Reaction Observed   | July 1985      |
| $\eta$ -Meson Production Near Threshold   | August 1985    |
| 17-mA Peak Current Achieved   | September 1985 |
| Time-of-Flight Isochronous Spectrometer (TOFI) On Line  | November 1985  |
| Test of the Relativistic Doppler Effect at 0.84 c by Collision of an Atomic Beam with Laser Light | 1985           |



## Appendixes



**APPENDIX A**

Experiments Run in 1985

**APPENDIX A:  
Experiments Run in 1985**

| No. | Channel    | Beam Hours | Experiment Title  |
|-----|------------|------------|---|
| 225 | NEUTRINO-A | 3653       | A Study of Neutrino Electron Elastic Scattering   |
| 267 | ISORAD     | 3628       | Preparation of Radioisotopes For Medicine and The Physical Services Using The LAMPF Isotope Production Facility   |
| 294 | AB-NUCCHEM | 18         | High Energy Nuclear Reactions   |
| 455 | P3         | 774        | High Precision Study of The $\mu^-$ Decay Spectrum  |
| 533 | HRS        | 126        | The Asymmetry in The (P, $\pi$ ) Reaction on ${}^6\text{Li}$ at 800 MeV   |
| 572 | EPICS      | 200        | A-Dependence of The ( $\pi^+$ , $\pi^-$ ) Reaction and The Width of a Double Isobaric Analog State in Heavy Nuclei  |
| 588 | EPB        | 321        | A Search For Long-Lived States of The $\text{H}^-$ Ion  |
| 589 | BR         | 343        | Free Forward NP Elastic Scattering Analyzing Power Measurements at 800 MeV  |
| 601 | EPICS      | 246        | Determination of Isoscalar and Isovector Transition Rates For Low Lying Collective States in ${}^{90}\text{Zr}$ and ${}^{208}\text{Pb}$ By $\pi^+$ and $\pi^-$ Inelastic Scattering |
| 623 | HRS        | 152        | Measurement of Cross Section, Analyzing Power and Depolarization Parameters in The ${}^{28}\text{Si}(p,p'){}^{28}\text{Si}$ (6- T = 0 AND T = 1) Reaction at 400 MeV                |
| 639 | SMC        | 177        | Muon Spin Rotation Study of Muon Bonding and Motion in Select Magnetic Oxides   |
| 657 | EPICS      | 189        | Inelastic $\pi^\pm$ Scattering From The N = 26 Isotones   |

| No. | Channel    | Beam<br>Hours | Experiment Title  |
|-----|------------|---------------|---|
| 665 | BR         | 418           | The Measurement of The Initial State Spin Correlation Parameters $C_{LL}$ AND $C_{SL}$ In N-P Scattering At 500, 650, and 800 MeV         |
| 687 | HRS        | 96            | Measurement of The Spin Rotation Parameters In $^{208}\text{Pb}$ and In $^{40}\text{Ca}$ at 400 Mev                                       |
| 705 | P3         | 568           | Study of Pion Absorption In $^3\text{He}$ on and Above The (3,3) Resonance*   |
| 722 | HRS        | 96            | Measurement of Cross Sections and Analyzing Powers for Elastic and Inelastic Scattering of 400 to 500 MeV Protons From $^{14}\text{C}$    |
| 723 | EPICS      | 199           | Measurement of The Neutron and Proton Contributions to Excited State in $^{39}\text{K}$ By $\pi^+$ and $\pi^-$ Inelastic Scattering       |
| 726 | SMC        | 570           | Search for The C-Noninvariant Decay $\pi^0 \rightarrow 3\gamma$   |
| 727 | SMC        | 252           | Measurement of The Efficiency of Muon Catalysis in Deuterium-Tritium Mixtures at High Densities   |
| 742 | SMC        | 258           | Search for The Negative Muonium Ion   |
| 752 | TTA        | 958           | Tuneup of The Time-of-Flight Spectrometer For Direct Atomic Mass Measurements   |
| 769 | RADAMAGE-1 | 3173          | Proton Irradiation Effects on Candidate Materials For The German Spallation Neutron Source (SNQ)  |
| 770 | BR         | 1953          | The Measurement of NP Elastic Scattering Spin Correlation Parameters With L- and S-Type Polarized Beam and Target Between 500 and 800 MeV |



**APPENDIX A**

Experiments Run in 1985

| No. | Channel | Beam Hours | Experiment Title  |
|-----|---------|------------|---|
| 773 | EPICS   | 286        | Measurements of $(\pi^+, \pi^-)$ Angular Distributions on $^{56}\text{Fe}$ at 164 and 292 MeV                                     |
| 799 | HRS     | 120        | Large Momentum Transfer Measurements of $A_y$ for 800 MeV $P + ^{208}\text{Pb}$ Elastic Scattering                                |
| 800 | EPICS   | 277        | Inelastic Pion Scattering From $^{22}\text{Ne}$   |
| 807 | P3      | 344        | Test of The LAMPF Recoil Polarimeter (JANUS) in Measurements of The $\pi^- p$ Elastic Scattering Proton Polarization at 625 MeV/c |
| 811 | LEP     | 248        | Study of Unnatural Parity States in Nuclei Using Low-Energy Pions   |
| 813 | LEP     | 131        | Pion Charge Asymmetries for $^{13}\text{C}$ at Low-Beam Energies on The LEP Spectrometer  |
| 814 | LEP     | 155        | $\pi^\pm$ Nuclear Elastic Scattering From Ni and Sn Isotopes at Energies Between 30 and 80 MeV                                    |
| 815 | EPB     | 1256       | Measurements of $A_{NO}$ , $S_{SL}$ , and $A_{LL}$ in $\bar{p}p \rightarrow p\pi^+$ at 500, 580, 650, 720, and 800 MeV            |
| 827 | P3      | 383        | Study of Isobaric Analog States in Pion Single Charge Exchange Reactions in The 300- to 500-MeV Region                            |
| 828 | LEP     | 258        | Total and Differential Cross Sections for $\pi^+ d \rightarrow pp$ Below 20 MeV   |
| 832 | EPB     | 588        | Gamma Ray Angular Correlation for $^{12}\text{C}(P, P')^{12}\text{C}(15.11)$  |
| 833 | EPICS   | 250        | Continuation of The Investigation of Large-Angle Pion-Nucleus Scattering  |

| No. | Channel | Beam Hours | Experiment Title  |
|-----|---------|------------|---|
| 836 | EPICS   | 209        | Energy Dependence of Pion Scattering to The Giant Resonance Region of $^{208}\text{Pb}$   |
| 837 | HRS     | 127        | Measurement of Spin-Flip Cross Sections Up to 40 MeV Excitation in $^{58}\text{Ni}$ and $^{90}\text{Zr}$  |
| 841 | EPICS   | 171        | Forward-Angle Pion Inelastic Scattering on Light Nuclei   |
| 842 | HRS     | 488        | " $\mu\text{SR}$ Shift and Relaxation Measurements in Itinerant Magnets"  |
| 848 | LEP     | 69         | In-Flight Absorption of Low Energy Negative Pions   |
| 851 | HRS     | 388        | Search for Recoil Free $\Delta$ Production and High Spin States in the $^{208}\text{Pb}(p,t)^{205}\text{Pb}$ Reaction at $E_p \approx 400$ MeV  |
| 852 | P3      | 700        | Measurements of $(\pi^+,n)$ Reactions on Nuclear Targets to Study The Production and Interaction of $\eta$ Mesons With Nuclei                   |
| 853 | HRS     | 214        | Measurement of Wolfenstein Parameter at 650 MeV and $d\Sigma/d\Omega$ at 500, 650, and 800 MeV for $\bar{p}d \rightarrow pd$ Elastic Scattering |
| 854 | SMC     | 177        | Muon Spin RsearchH in Oxide Spin Glasses  |
| 855 | HRS     | 151        | Measurement of $^{206}\text{Pb}$ - $^{208}\text{Pb}$ Ground State Neutron Density Difference  |
| 856 | P3      | 140        | Comparison of Double Charge Exchange and Inclusive Scattering in $^3\text{He}$  |
| 859 | P3      | 170        | Study of The A Dependence of Inclusive Pion Double-Charge-Exchange in Nuclei  |

**APPENDIX A**

Experiments from 1985-

| No. | Channel | Beam<br>Hours | Experiment Title   |
|-----|---------|---------------|--|
| 860 | LEP     | 256           | Inelastic $\pi^+$ Scattering to Excited $O^+$ States at Energies Between 30 and 80 MeV                     |
| 866 | EPB     | 278           | Neutrino Source Calibration  |
| 869 | SMC     | 145           | Higher Precision Measurement of the Lamb Shift in Muonium  |
| 877 | SMC     | 113           | The Microdosimetry of Error Induction in Microelectronics  |
| 879 | HRS     | 184           | Characteristic Dirac Signature in Large-Angle $\vec{p} + {}^{40}\text{Ca}$ Elastic Scattering at 500 MeV   |
| 882 | LEP     | 855           | Measurement of the Differential Cross Section for $\pi^-p \rightarrow \pi^0n$ at 10, 20 and 40 MeV         |
| 883 | HRS     | 177           | A Study of the Reaction Mechanism for the ${}^2\text{H}(\vec{p}, \gamma){}^3\text{He}$ Reaction at 800 MeV |
| 884 | LEP     | 415           | Pion Double Charge Exchange on ${}^{14}\text{C}$ at Low Energies   |
| 885 | HRS     | 157           | Measurement of $K_{SS}$ for the $\vec{p}p \rightarrow d\pi^+$ Reaction at 650 and 800 MeV                  |
| 888 | SMC     | 494           | Study of the Decays $\pi^+ \rightarrow e^+\nu_e\gamma$ and $\pi^+ \rightarrow e^+e^+e^-\nu_e$              |
| 891 | HRS     | 150           | Development of Zero Degree Spin-Flip Measurements at HRS   |
| 896 | HRS     | 231           | A Test of the Dirac Treatment of Proton-Nucleus Inelastic Scattering                                       |
| 897 | LEP     | 52            | Pion Single Charge Exchange in ${}^7\text{Li}$ to the Isobaric Analog Ground State of ${}^7\text{Be}$      |

| No. | Channel | Beam<br>Hours | Experiment Title  |
|-----|---------|---------------|---|
| 898 | EPICS   | 102           | Pion Elastic Scattering from ${}^4\text{He}$<br>- A Test of Charge Symmetry   |
| 899 | LEP     | 60            | A Measurement of the Neutron<br>Deformation of ${}^{165}\text{Ho}$ by Pion<br>Single Charge Exchange  |
| 902 | HRS     | 72            | Inelastic Scattering of 500 MeV<br>Polarized Protons from ${}^{88}\text{Sr}$ :<br>Determination of Neutron Transition<br>Densities  |
| 903 | HRS     | 64            | A Study of Transition Nuclei in the<br>Rare Earth Region by Proton<br>Inelastic Scattering  |
| 905 | EPICS   | 329           | Elastic and Inelastic Scattering of<br>$\pi^{\pm}$ on ${}^3\text{H}$ and ${}^3\text{He}$ to Test<br>Charge Symmetry, Compare Form<br>Factors, and Investigate the<br>Reaction Mechanism |
| 906 | EPICS   | 240           | DCX on ${}^{44}\text{Ca}$   |
| 907 | HRS     | 241           | Spin Excitations in ${}^{40}\text{Ca}$ and<br>${}^{48}\text{Ca}$  |
| 908 | EPICS   | 114           | Angular Distribution for the<br>${}^{42}\text{Ca}(\pi^+, \pi^-){}^{42}\text{Ti}$<br>(g.s.) Reaction at 290 MeV  |
| 914 | SMC     | 137           | Measurement of the Analyzing Power<br>of a Muon Polarimeter for Use in a<br>Search for Muon Polarization in the<br>Decay $K_1 \mu\mu$   |
| 917 | P3      | 70            | Pion Charge Exchange to Delta-Hole<br>States of Complex Nuclei  |
| 927 | LEP     | 106           | Investigation of Non-Analog Double<br>Charge Exchange Between 50 MeV and<br>120 MeV   |
| 928 | EPB     | 490           | $\vec{p} + n$ quasielastic Scattering<br>from Deuterium   |

**APPENDIX A**

Experiments from 1980

| No. | Channel    | Beam Hours | Experiment Title  |
|-----|------------|------------|---|
| 933 | LEP        | 158        | Study of the Mass and Energy Dependence of Ultra Low Energy Pion Single Charge Exchange                   |
| 936 | RADAMAGE-1 | 2053       | Dosimetry Experiment to Characterize the Radiation Environment at LAMPF Target Station A-6                |
|     | RADAMGE-1  | 2053       | Dosimetry Experiment to Characterize the Radiation Environment at LAMPF Target Station A-6                |
| 941 | SMC        | 149        | Muon Spin Relaxation Studies of Disordered Spin Systems   |
| 942 | LEP        | 69         | Measurement of Low Energy Cross Sections for the $^{12}\text{C}(\pi^{\pm}, \pi N)^{11}\text{C}$ Reactions |
| 944 | SMC        | 384        | Feasibility Study for an Experiment to Search for Muonium & Antimuonium Conversion                        |
| 945 | EPICS      | 100        | DCX on Nickel   |
| 947 | EPICS      | 100        | Measurements of Large-Angle Pion-Deuteron Scattering  |
| 950 | EPICS      | 200        | Mass of the Extremely Neutron Rich $^{48}\text{Ar}$   |
| 957 | P3         | 204        | "Inclusive Pion Double-Charge-Exchange in Light p-Shell Nuclei,"  |
| 963 | SMC        | 280        | "Experimental Investigation of Muon Catalysis,"   |
| 979 | LEP        | 169        | "A Search for T=2 Dibaryon Production in the $d(\pi^+, \pi^-)X$ Reaction,"                                |

**APPENDIX B:  
New Proposals During 1985**

| No. | Spokesperson   | Title  |
|-----|--|--|
| 954 | R.J. Peterson<br>Univ. of Colorado   | "Isospin Amplitudes For Giant Resonances In $^{58}\text{Ni}$ and $^{64}\text{Ni}$ ,"                                     |
| 955 | G.W. Hoffmann<br>Univ. of Texas, Austin<br><br>J.J. Jarmer<br>Los Alamos<br>M.L. Barlett<br>Univ. of Texas, Austin<br>R.L. Ray<br>Univ. of Texas, Austin | "Search for Experimental Proof of the Existence of Lower Components in the Nuclear Wave Function,"                       |
| 956 | A. Saha<br>Univ. of Virginia<br>J.J. Kelly<br>Univ. of Maryland  | "Microscopic Structure of the Calcium Isotopes,"   |
| 957 | G.A. Rebka, Jr.<br>Univ. of Wyoming<br>J.L. Matthews<br>MIT<br>P.A.M. Gram<br>Los Alamos   | "Inclusive Pion Double-Charge-Exchange in Light p-Shell Nuclei,"   |
| 958 | G.W. Hoffmann<br>Univ. of Texas, Austin<br><br>J.B. McClelland<br>Los Alamos   | "Study of the $^{90}\text{Zr}(\vec{p}, \vec{n})^{90}\text{Nb}$ <small>g.s.</small> Charge-Exchange Reaction at 500 MeV," |
| 959 | C.F. Moore<br>Univ. of Texas, Austin<br>H.T. Fortune<br>Univ. of Pennsylvania<br>S. Mordechai<br>Univ. of Texas, Austin                                  | "Inelastic Pion Scattering from $^{20}\text{Ne}$ ,"  |
| 960 | G.R. Burlison<br>New Mexico State Univ.<br><br>K.F. Johnson<br>Argonne Nat. Lab.<br>L.C. Northcliffe<br>Texas A&M  | "Measurement of $\Delta\sigma_L$ and $\Delta\sigma_T$ in Free Neutron-Proton Scattering Between 300 and 800 MeV,"        |

**APPENDIX B**

New Proposals During 1985

| No. | Spokesperson  | Title   |
|-----|---|---|
| 961 | L.C. Northcliffe<br>Texas A&M   | "Measurement of the Spin-Correlation Parameter $A_{NN}(\theta)$ for n-p Elastic Scattering at 800 MeV," |
| 962 | S.J. Seestrom-Morris<br>Univ. of Minnesota                                    | "Target Mass Dependence of the Isovector Contribution to the Giant Quadrupole Resonance,"               |
| 963 | A.N. Anderson<br>EG&G, Idaho<br>M. Leon<br>Los Alamos<br>S.E. Jones<br>BYU    | "Experimental Investigation of Muon Catalysis,"   |
| 964 | G.S. Blanpied<br>Univ. of South Carolina<br>J.-P. Egger<br>SWISS INST         | "Study of $(\pi^-, p)$ , and $(\pi^+, p)$ Reactions with EPICS,"  |
| 965 | E.L. Chupp<br>Univ. of New Hampshire<br>P.P. Dunphy<br>Univ. of New Hampshire | "Test and Calibration of Detector for Solar Neutrons and Gamma Rays,"                                   |
| 966 | B.G. Ritchie<br>ASU   | "Pion Absorption on Quasideuterons in $^{10}\text{B}$ ( $\pi^+, 2p$ ),"                                 |
| 967 | D.R. Tieger<br>Univ. of Washington<br>I. Halpern<br>Univ. of Washington       | "Inclusive $\pi^-$ Scattering at 100 MeV on C, Ca, Sn, and Pb,"   |
| 968 | F. Irom<br>Los Alamos<br><br>R.J. Peterson<br>Univ. of Colorado               | "Study of Inelastic Scattering of $\pi^\pm$ from $^7\text{Li}$ and $^{14}\text{C}$ at Low Energies,"    |
| 969 | M.D. Cooper<br>Los Alamos   | "MEGA - Search for the Rare Decay $\mu^+ \rightarrow e^+\gamma$ ,"                                      |

| No. | Spokesperson   | Title  |
|-----|--|--|
| 970 | C.F. Moore<br>Univ. of Texas, Austin<br>C.L. Morris<br>Los Alamos<br>R.J. Peterson<br>Univ. of Colorado    | "Measurement of the Delta-Nucleus Interaction by Pion Inelastic Scattering to the $1^+$ Doublet in $^{12}\text{C}$ ,"                                |
| 971 | R.W. Fergerson<br>Rutgers Univ.  | "Measurement of the Spin-Rotation Parameter Q for the 200 MeV $\vec{p} + ^{208}\text{Pb}$ ,"   |
| 972 | C.L. Morris<br>Los Alamos<br>J.A. McGill<br>Los Alamos   | "Low-Momentum Delta Production Via the Reaction $^{13}\text{C}(\pi^+, p)^{12}\text{C}_\Delta$ ,"   |
| 973 | G. Pauletta<br>Univ. of Texas, Austin<br><br>M.M. Gazzaly<br>Univ. of Minnesota<br>N. Tanaka<br>Los Alamos | "Search for Narrow Resonances in the B=2 Missing-Mass Spectrum From p+He Reactions and in the Excitation Functions of the pp Pion Production,"       |
| 974 | G. Pauletta<br>Univ. of Texas, Austin<br><br>M.M. Gazzaly<br>Univ. of Minnesota<br>N. Tanaka<br>Los Alamos | "A Search for Narrow Resonances in the B=2 System Using the $^3\text{He}(\pi^+, p)\text{MM}$ and the $^2\text{H}(\pi^+, \pi^+)\text{MM}$ Reactions," |
| 975 | L.-C. Liu<br>Los Alamos<br>M.J. Leitch<br>Los Alamos   | "Single Charge Exchange with Stopped Negative Pions,"  |
| 976 | J.D. Bowman<br>Los Alamos  | "Study of the Charged Particle Decay of the Giant Dipole Resonance Excited by Pion Single Charge Exchange on $^{13}\text{C}$ ,"                      |



| No. | Spokesperson  | Title  |
|-----|---|--|
| 977 | G.J. Igo<br>UCLA  | "Measurement of Wolfenstein Parameters for Proton-Deuteron Elastic Scattering at 800 MeV,"       |
| 978 | G.A. Rebka, Jr.<br>Univ. of Wyoming<br>J.L. Matthews<br>MIT<br>P.A.M. Gram<br>Los Alamos                              | "A Coincidence Measurement of Pion Double Charge Exchange: ${}^4\text{He}(\pi^+, \pi^-p)3p^-$ ," |
| 979 | C.L. Morris<br>Los Alamos<br><br>J.A. McGill<br>Los Alamos  | "A Search for T=2 Dibaryon Production in the $d(\pi^+, \pi^-)X$ Reaction,"                       |
| 980 | K.K. Seth<br>Northwestern Univ.   | "An Investigation of the Near-Stability of ${}^6\text{H}$ and ${}^7\text{H}$ ,"                  |
| 981 | K.K. Seth<br>Northwestern Univ.   | "Do Bound States of Real Pions Exist?"   |
| 982 | R.A. Loveman<br>Univ. of Colorado   | "The Measurement of Light Fragments from Pion True Absorption,"                                  |
| 983 | D. Wright<br>VPI and State Univ.<br><br>G.S. Blanpied<br>Univ. of South Carolina<br>M. Blecher<br>VPI and State Univ. | " $\pi^+$ -Tin and $\pi^-$ Lead Elastic Scattering at Energies Between 30 and 65 MeV,"           |
| 984 | R.J. Peterson<br>Univ. of Colorado  | "Pion Scattering to $8^-$ Stretched States of ${}^{60}\text{Ni}$ ,"                              |
| 985 | C.M. Hoffman<br>Los Alamos<br>J.R. Kane<br>Coll. of William & Mary<br>V.W. Hughes<br>Yale University                  | "Search for Muonium to Antimuonium Spontaneous Conversion,"                                      |

| No. | Spokesperson  | Title  |
|-----|---|--|
| 986 | J. Linke<br>KFA-JULICH  | "Spallation Neutron Irradiation of Non-Oxide Ceramics for First-Wall Fusion Reactor Application,"                            |
| 987 | J. Linke<br>KFA-JULICH<br><br>W. Delle<br>KFA-JULICH<br>W.F. Sommer<br>Los Alamos                     | "Fast Neutron Irradiation Screening Test of Polycrystalline Graphites Under First-Wall Fusion Conditions,"                   |
| 988 | C.L. Morris<br>Los Alamos<br>R. Gilman<br>Univ. of Pennsylvania                                       | "Double-Isobaric-Analog Resonance in Heavy Nuclei,"  |
| 989 | K.S. Dhuga<br>New Mexico State Univ   | "Investigation of Energy and Mass Dependence of Large-Angle Pion-Nucleus Elastic Scattering Across the Resonance Region,"    |
| 990 | M.A. Moinester<br>Tel-Aviv<br>R.A. Loveman<br>Univ. of Colorado<br>R.J. Peterson<br>Univ. of Colorado | "Pion Single Charge Exchange on the Deuteron,"   |
| 991 | G.R. Burleson<br>New Mexico State Univ  | "Continuation of the Investigation of the Energy, Mass, and Charge Dependence of Pion-Nucleus Elastic Scattering Near 180°," |
| 992 | M.A. Plum<br>Los Alamos   | "Excitation Functions for Magnetic Transitions in $^{24}\text{Mg}$ and $^{28}\text{Si}$ ,"                                   |
| 993 | C.L. Morris<br>Los Alamos<br>R.D. Ransome<br>Rutgers Univ.  | "Study of $\pi$ Absorption Below the $\Delta_{3/2,3/2}$ Resonance Region,"   |

| No.  | Spokesperson  | Title  |
|------|---|--|
| 994  | C.L. Morris<br>Los Alamos<br>R.D. Ransome<br>Rutgers Univ.  | "Study of $\pi$ Absorption Above the $\Delta_{3/2,3/2}$ Resonance Region,"   |
| 995  | C.F. Moore<br>Univ. of Texas, Austin<br><br>S.J. Seestrom-Morris<br>Univ. of Minnesota                            | "Energy Dependence of $\pi^+$ and $\pi^-$ Scattering to Low-Lying States in $^{208}\text{Pb}$ ,"   |
| 996  | J.D. Zumbro<br>Univ. of Pennsylvania  | "A Search for the $^5\text{Li}+\pi^-$ State in $^5\text{He}$ ,"  |
| 997  | F.T. Baker<br>Univ. of Georgia<br>G.L. Glashausser<br>Rutgers Univ.<br>K.W. Jones<br>Los Alamos                   | "Spin-Flip Cross Section for Inelastic Proton Scattering from $^{12}\text{C}$ and $^{16}\text{O}$ at 319 MeV,"   |
| 998  | C.L. Morris<br>Los Alamos<br>D.K. Dehnhard<br>Univ. of Minnesota  | "The $^4\text{He}(\pi, \pi'p)^3\text{He}$ Reaction - A Test of Charge Symmetry,"   |
| 999  | A. Fazely<br>Louisiana State Univ.<br><br>L.-C. Liu<br>Los Alamos   | "Study of Pion Double Charge Exchange Reactions $^{128}\text{Te}(\pi^+, \pi^-)^{128}\text{Xe}(\text{g.s.})$ and $^{130}\text{Te}(\pi^+, \pi^-)^{130}\text{Xe}(\text{g.s.})^-$ ," |
| 1000 | D.K. Dehnhard<br>Univ. of Minnesota<br><br>K.W. Jones<br>Los Alamos<br>S.J. Seestrom-Morris<br>Univ. of Minnesota | "Cross Sections for the $(p, \pi^+)$ Reaction on $^{12}\text{C}$ , $^{13}\text{C}$ , and $^{14}\text{N}$ ,"  |

| No.  | Spokesperson   | Title   |
|------|--|---|
| 1001 | E. Piassetzky<br>Los Alamos<br><br>H.W. Baer<br>Los Alamos<br>M.J. Leitch<br>Los Alamos                    | "Study of Double-Analog<br>Transitions at Pion Energies 20 to<br>80 MeV,"                         |
| 1002 | B.J. Dropesky<br>Los Alamos<br><br>L.-C. Liu<br>Los Alamos   | "Energy Dependence of the<br>( $\pi^+$ , $2\pi^+$ ) Reaction in Complex<br>Nuclei,"               |
| 1003 | R.C. Reedy<br>Los Alamos   | "Production of Long-Lived<br>Radionuclides by Stopped Negative<br>Muons,"                         |
| 1004 | J.C. Peng<br>Los Alamos<br>J.E. Simmons<br>Los Alamos  | "Measurements of $\eta$ -Meson Mass in<br>Free Space and in Nuclei,"                              |
| 1005 | J.M. Moss<br>Los Alamos  | "Relativistic Effective Mass<br>Renormalizations of Continuum<br>Polarization Observables,"       |
| 1006 | G. Pauletta<br>Univ. of Texas, Austin<br><br>M.W. Gazzaly<br>Univ. of Minnesota<br>N. Tanaka<br>Los Alamos | "A Search for a Narrow Resonance<br>in the B=2 System Using the<br>$\pi^+d\pi^+p$ Reaction,"      |
| 1007 | B.M.K. Nefkens<br>UCLA<br><br>W.J. Briscoe<br>George Washington Univ.                                      | "Comparison of NSF-Minimum in<br>$\pi^-^3\text{H}$ and $\pi^+^3\text{He}$ Elastic<br>Scattering," |

**APPENDIX B**

New Proposals During 1985

| No.  | Spokesperson  | Title   |
|------|---|---|
| 1008 | F. Irom<br>Los Alamos<br><br>J.D. Bowman<br>Los Alamos                  | "Study of the Mass and Energy Dependence of Low Energy Pion Single Charge Exchange at 180°,"              |
| 1009 | F.W. Hersman<br>Univ. of New Hampshire                                  | "Pion Scattering From $^{206}\text{Pb}$ --How Far Can Pions Probe Into The Nuclear Interior?,"            |
| 1010 | F.T. Baker<br>Univ. of Georgia<br><br>S.K. Nanda<br>Univ. of Minnesota  | "Measurements of Spin-Flip Cross Section Angular Distributions for $E_x < 40$ MeV in $^{124}\text{Sn}$ ," |
| 1011 | K.K. Seth<br>Northwestern Univ.   | "Non Analog DCX - Systematics in Heavy Nuclei,"   |
| 1012 | K.K. Seth<br>Northwestern Univ.   | "Study of Analog DCX on $^{88}\text{Sr}$ ,"   |
| 1013 | K.K. Seth<br>Northwestern Univ.   | "Pion Production in the Continuum with Polarized Protons,"  |
| 1014 | A. Horsewell<br>Riso Nat. Lab, Denmark<br><br>W.F. Sommer<br>Los Alamos | Proton, Spallation Neutron and Fission Neutron Irradiation of Copper                                      |

## APPENDIX C: LAMPF Visitors During 1985

**Bjarne Aas**, UCLA  
**David L. Adams**, UCLA  
**Gary S. Adams**, Univ. of South Carolina  
**Eric G. Adelberger**, Univ. of Washington  
**Steven D. Adrian**, UCLA  
**Wanda Alberico**, Univ. of Torino  
**Richard C. Allen**, UC, Irvine  
**John C. Allred**, Consultant, New Mexico  
**Peter W. F. Alons**, Univ. of Colorado  
**Jonas Alster**, Tel Aviv Univ.  
**Mohammed Ali Al-Solami**, Univ. of South Carolina  
**Alan N. Anderson**, EG&G, Idaho  
**Bryon D. Anderson**, Kent State Univ.  
**Mary E. Anderson**, Univ. of New Mexico  
**A. Ballard Andrews**, Univ. of Texas  
**Hans-Jurgen Arends**, Univ. of Bonn  
**Katsushi Arisaka**, Univ. of Pennsylvania  
**Richard A. Arndt**, Virginia Polytechnic Inst. & State Univ.  
**Klaus-Peter Arnold**, Univ. of Heidelberg  
**Marina Artuso**, Northwestern Univ.  
**Daniel Ashery**, Tel Aviv Univ.  
**Leonard B. Auerbach**, Temple Univ.  
**Naftali Auerbach**, Tel Aviv Univ.  
**David A. Axen**, TRIUMF  
**Mark G. Bachman**, Univ. of Texas  
**F. Todd Baker**, Univ. of Georgia  
**Leonce L. Barger**, Univ. of Pennsylvania  
**Barry Barish**, Caltech  
**Martin L. Barlett**, Univ. of Texas  
**David B. Barlow**, UCLA  
**Bernd Bassalleck**, Univ. of New Mexico  
**Michael E. Beddo**, New Mexico State Univ.  
**Barry L. Berman**, Lawrence Livermore Lab.  
**William W. Bewley**, UC, Riverside  
**Charles S. Bhatia**, Texas A&M Univ.  
**Louis Bimbot**, Univ. of Paris  
**Terry J. Black**, Abilene Christian Univ.  
**Leslie C. Bland**, Indiana Univ.  
**Gary S. Blanpied**, Univ. of South Carolina  
**Marvin Blecher**, Virginia Polytechnic Inst. & State Univ.  
**Marek Bleszynski**, UCLA  
**David J. Blevins**, Consultant, New Mexico  
**Carolus Boekema**, Texas Tech Univ.  
**Victor A. M. Brabers**, Eindhoven Univ. of Tech.  
**Jeffrey T. Brack**, Univ. of Colorado  
**Michael R. Braunstein**, Univ. of Colorado  
**Joseph L. Breeden**, Indiana Univ.  
**Nance L. Briscoe**, Nat. Bureau of Standards  
**William J. Briscoe**, George Washington Univ.  
**Michael A. Bryan**, Univ. of Texas  
**Howard C. Bryant**, Univ. of New Mexico  
**David V. Bugg**, Univ. of London  
**Michael G. Burlein**, Univ. of Pennsylvania  
**George R. Burleson**, New Mexico State Univ.  
**Mary J. Burns**, Univ. of New Mexico  
**Jiri Bystricky**, UCLA  
**Augustine J. Caffrey**, EG&G, Idaho  
**Vanice A. P. Carlson**, Argonne  
**Kwai-Chow Benjamin Chan**, Texas Tech Univ.  
**Chung-Yun Chang**, Univ. of Maryland  
**Herbert H. Chen**, UC, Irvine  
**Francis Chmely**, Yale Univ.  
**Katherine W. C. Choi**, Louisiana State Univ.  
**Steven B. Christo**, Louisiana State Univ.  
**Douglas E. Ciskowski**, Univ. of Texas  
**Benjamin L. Clausen**, Univ. of Colorado  
**Anthony S. Clough**, Univ. of Surrey  
**Stanley Cohen**, Drexel Univ.  
**Joseph R. Comfort**, Arizona State Univ.  
**Genevieve R. Comtet**, Centre Nat. de la Recherche Sci.  
**James P. Connelly**, Univ. of New Hampshire  
**David C. Cook**, Univ. of Minnesota  
**Peter S. Cooper**, Yale Univ.  
**Hall L. Crannell**, Catholic Univ. of America

- Gerard M. Crawley, Michigan State Univ.  
An-Zhi Cui, Inst. of Atomic Energy, PRC  
Stephen T. Cummings, Univ. of Texas  
Dian B. Curran, Univ. of Iowa  
Donald R. Cyborski, Argonne  
James A. Dalton, Abilene Christian Univ.  
Sunayana Datta, Temple Univ.  
Craig K. Davidson, Jomar Systems  
Charles A. Davis, TRIUMF  
Alfred R. de Angelis, Rutgers Univ.  
Dietrich K. Dehnhard, Univ. of Minnesota  
Peter P. Denes, Univ. of New Mexico  
Arthur B. Denison, Univ. of Wyoming  
Kalvir Singh Dhuga, New Mexico State Univ.  
John F. Dicello, Clarkson Univ.  
John F. Dicello III, Clarkson Univ.  
Paul T. Dicello, Clarkson Univ.  
Byron D. Dieterle, Univ. of New Mexico  
Brenda L. Dingus, Univ. of Maryland  
Ned S. Dixon, Franklin/Marshall Coll.  
Stanley A. Dodds, Rice Univ.  
Peter J. Doe, UC, Irvine  
Hermann J. Donnert, Kansas State Univ.  
Edward G. Donoghue, Rutgers Univ.  
David W. Dryer, Argonne  
Hendrik M. Duiker, Univ. of Colorado  
Morton Eckhause, Coll. of William & Mary  
Robert W. Ellsworth, George Mason Univ.  
Jon M. Engelage, UCLA  
Peter A. J. Englert, Univ. of Koln  
David J. Ernst, Texas A&M Univ.  
Jorge A. Escalante, Univ. of South Carolina  
John A. Faucett, New Mexico State Univ.  
Ali Fazely, Louisiana State Univ.  
Alan E. Feldman, Univ. of Maryland  
Raymond W. Ferguson, Rutgers Univ./Univ. of Texas  
William J. Fickinger, Case Western Reserve Univ.  
John M. Finn, Coll. of William & Mary  
Randall J. Fisk, Valparaiso Univ.  
Gottfried Flik, Max-Planck Inst.  
Carlos A. Fontenla, New Mexico State Univ.  
H. Terry Fortune, Univ. of Pennsylvania  
Michael A. Franey, Univ. of Minnesota  
Stuart J. Freedman, Argonne  
Linda S. Fritz, Franklin/Marshall Coll.  
Brian K. Fujikawa, Caltech  
Herbert O. Funsten, Coll. of William & Mary  
Raffaello Garfagnini, Univ. Degli Studi  
Juan R. Garza, Univ. of Texas  
M. Magdy Gazzaly, Univ. of Minnesota  
Donald F. Geesaman, Argonne  
Robert A. Giannelli, Arizona State Univ.  
Edward F. Gibson, California State Univ.  
Ronald A. Gilman, Univ. of Pennsylvania  
John F. Ginkel, Coll. of William & Mary  
Grant A. Gist, Rice Univ.  
Charles M. Glashausser, Rutgers Univ.  
George Glass, Texas A&M Univ.  
Roy J. Glauber, Harvard Univ.  
Eduardo Gonzalez-Hernandez, Univ. of Texas  
Jordan A. Goodman, Univ. of Maryland  
Jeffrey S. Gordon, UCLA  
Krishnaswamy N. Gounder, Univ. of South Carolina  
Scott C. Graessle, Abilene Christian Univ.  
Karl-Heinz Graf, KFA  
Andrew A. Green, Rutgers Univ.  
Chilton B. Gregory, Univ. of New Mexico  
David P. Grosnick, Univ. of Chicago  
Franz L. Gross, Coll. of William & Mary  
Sunil K. Gupta, Univ. of Maryland  
Paul P. Guss, Coll. of William & Mary  
William N. Haberichter, Argonne  
Stephen L. Hall, Abilene Christian Univ.  
Akşel L. Hallin, Princeton Univ.  
Ronnie W. Harper, Ohio State Univ.  
Erik K. Heide, Univ. of Minnesota  
John Walker Heimaster, Ohio State Univ.  
F. William Hersman, Univ. of New Hampshire  
Martin Hesche, Univ. of Innsbruck  
John C. Hiebert, Texas A&M Univ.

- Virgil L. Highland**, Temple Univ.  
**Daniel A. Hill**, Argonne  
**Roger E. Hill**, Univ. of New Mexico  
**Norton M. Hintz**, Univ. of Minnesota  
**Gerald W. Hoffmann**, Univ. of Texas  
**Steinar Hoibraten**, MIT  
**Bo R. Hoistad**, Gustaf Werner Inst.  
**Karl F. Holinde**, Univ. of Bonn  
**Charles L. Hollas**, Univ. of Texas  
**Barry R. Holstein**, Univ. of Massachusetts  
**James A. Holt**, Texas A&M Univ.  
**Andy Horsewell**, Riso National Lab.  
**Ying-Chiang David Huang**, Temple Univ.  
**E. Barrie Hughes**, Stanford Univ.  
**Vernon W. Hughes**, Yale Univ.  
**Charles R. Hummer**, Univ. of Connecticut  
**George J. Igo**, UCLA  
**Richard L. Imlay**, Louisiana State Univ.  
**Robert L. Jaffe**, MIT  
**Mark J. Jakobson**, Univ. of Montana  
**Randolph H. Jeppesen**, Univ. of Montana  
**Keneth F. Johnson**, Argonne  
**Carol J. Johnstone**, Univ. of New Mexico  
**Mark K. Jones**, Univ. of Minnesota  
**Steven E. Jones**, Brigham Young Univ./EG&G, Idaho  
**Jan Källne**, JET  
**John R. Kane**, Coll. of William & Mary  
**Ju Hwan Kang**, Univ. of New Mexico  
**Paul J. Karol**, Carnegie-Mellon Univ.  
**Thomas E. Kasprzyk**, Argonne  
**James J. Kelly**, Univ. of Maryland  
**Robert A. Kenefick**, Texas A&M Univ.  
**Christopher J. Kenney**, Coll. of William & Mary  
**Steve H. Kettell**, Yale Univ.  
**Edward R. Kinney**, MIT  
**Leonard S. Kisslinger**, Carnegie-Mellon Univ.  
**Amir Klein**, Soreq Nuclear Research Center  
**James N. Knudson**, Arizona State Univ.  
**Dale S. Koetke**, Valparaiso Univ.  
**Donald D. Koetke**, Valparaiso Univ.  
**Donald K. Kohl**, Consultant, New Mexico  
**Kathryn L. Kolsky**, Carnegie-Mellon Univ.  
**Daniel S. Koltun**, Univ. of Rochester  
**Michael A. Kovash**, Univ. of Kentucky  
**Robert S. Kowalczyk**, Argonne  
**Stanley B. Kowalski**, MIT  
**Heribert Koziol**, CERN  
**Daniel A. Krakauer**, Univ. of Maryland  
**Robert H. Kraus**, Clark Univ.  
**Laura L. Kropp**, Valparaiso Univ.  
**Yunan Kuang**, Yale Univ.  
**Barry D. Kuban**, Ohio State Univ.  
**Krishna S. Kumar**, Syracuse Univ.  
**A. Raymond Kunselman**, Univ. of Wyoming  
**Peter H. Kutt**, Univ. of Pennsylvania  
**Gary S. Kyle**, New Mexico State Univ.  
**Masoud R. Laghai**, Univ. of New Mexico  
**Robert A. Lamb**, Univ. of Surrey  
**K. Dean Larson**, Univ. of New Mexico  
**Nabil A.-F. Lasheen**, Univ. of South Carolina  
**Juergen F. Last**, Argonne  
**Christopher P. Leavitt**, Univ. of New Mexico  
**Wen-Piao Lee**, UC, Irvine  
**Paul A. Lennous**, Ohio State Univ.  
**Frieder Lenz**, SIN  
**Kevin T. Lesko**, Lawrence Berkeley Lab./Argonne  
**Jechiel Lichtenstadt**, Tel Aviv Univ.  
**Roger L. Lichti**, Texas Tech Univ.  
**B. Joseph Lieb**, George Mason Univ.  
**David A. Lind**, Univ. of Colorado  
**V. Gordon Lind**, Utah State Univ.  
**Richard A. Lindgren**, Univ. of Massachusetts  
**Alan G. Ling**, UCLA  
**Ta-Yung Ling**, Ohio State Univ.  
**John D. Linsley**, Univ. of New Mexico  
**Stanley Livingston**, Consultant, New Mexico  
**Vladimir M. Lobashev**, Inst. of Nuclear Research, USSR  
**Donald E. Lobb**, Univ. of Victoria  
**Wolfgang Lohmann**, KFA  
**David Lopiano**, UCLA



- William G. Love, Univ. of Georgia  
Robert A. Loveman, Univ. of Colorado  
Chris B. Luchini, New Mexico State Univ.  
Li-Ping Lung, Univ. of Minnesota  
Christopher R. Lyndon, Coll. of William & Mary  
Malcolm H. MacFarlane, Indiana Univ.  
Anthony M. Mack, Univ. of Minnesota  
John R. Mackenzie, Florida State Univ.  
Douglas E. Maclaughlin, UC, Riverside  
Maureen P. Madden, Argonne  
Richard Madey, Kent State Univ.  
Kazushige Maeda, Tohoku Univ.  
John H. Manley, Consultant, New Mexico  
Jeremy Margulies, SLAC  
John K. Markey, Yale Univ.  
Richard M. Marshall, Univ. of Virginia  
William G. Marterer, Louisiana State Univ.  
Howard S. Matis, Lawrence Berkeley Lab.  
June L. Matthews, MIT  
Bjorn E. Matthias, Yale Univ.  
Bill W. Mayes, Univ. of Houston  
Joseph W. McDonald, Univ. of Texas  
James E. McDonough, Temple Univ.  
W. Kenneth McFarlane, Temple Univ.  
Robert D. McKeown, Caltech  
James T. McKinley, Univ. of Montana  
Brent G. McMillan, Abilene Christian Univ.  
Kok-Heong McNaughton, Univ. of Texas  
Katie M. McShana, Argonne  
William J. Metcalf, Louisiana State Univ.  
Jason S. Meyer, Univ. of Maryland  
Daniel W. Miller, Indiana Univ.  
Ralph C. Minehart, Univ. of Virginia  
Chandrashekhara Mishra, Univ. of South Carolina  
Tanuja Mishra, Univ. of South Carolina  
Joseph H. Mitchell, Univ. of Colorado  
Joseph W. Mitchell, Ohio State Univ.  
Keith E. Mitchell, Abilene Christian Univ.  
William A. Mitchell, Ohio State Univ.  
Murray A. Moinester, Tel Aviv Univ.  
Alireza Mokhtari, George Washington Univ./UCLA  
William R. Molzon, Univ. of Pennsylvania  
C. Fred Moore, Univ. of Texas  
Troy D. D. Moore, Abilene Christian Univ.  
Shaul Mordechai, Univ. of Texas  
Sheila L. Morris, Univ. of Texas  
Leif K. Morton, Abilene Christian Univ.  
Moshi G. Moshi, UCLA  
Sanjoy Mukhopadhyay, Northwestern Univ.  
Takemi Nakagawa, Tohoku Univ.  
Sirish K. Nanda, Univ. of Minnesota  
James J. Napolitano, Argonne  
Subrata Nath, Texas A&M Univ.  
Itamar Navon, Tel Aviv Univ.  
Bernard M. K. Nefkens, UCLA  
James E. Nelson, Argonne  
Charles R. Newsom, Univ. of Iowa  
Benwen Ni, Yale Univ.  
Michael Nicholas, Univ. of Mississippi  
M. Edward Nieland, Iowa State Univ.  
Erik A. Nilsson, Gustaf Werner Inst.  
Kunihiko Nishiizumi, UC, San Diego  
Eric B. Norman, Lawrence Berkeley Lab.  
Lee C. Northcliffe, Texas A&M Univ.  
David S. Oakley, Univ. of Texas  
Yuji Ohashi, Argonne/UCLA  
Hajime Ohnuma, Tokyo Inst. of Tech.  
Jean M. Oostens, Univ. of Cincinnati/Illinois Inst. of Tech.  
Herbert Orth, Yale Univ.  
Brett L. Parker, Univ. of Massachusetts  
Gianni Pauletta, Univ. of Texas  
Seppo I. Penttila, Univ. of Turku  
Charles F. Perdrisat, Coll. of William & Mary  
Roy J. Peterson, Univ. of Colorado  
Anne M. Petrov, George Washington Univ.  
Eliazer Fiasetzky, Tel Aviv Univ.  
Gerard M. Pignault, Univ. of South Carolina  
Chandrasekhara T. G. Pillai, UCLA  
Dinko Pocaric, Stanford Univ.  
Norbert T. Porlie, Purdue Univ.

**Michael E. Potter**, UC, Irvine  
**Barry M. Freedom**, Univ. of South Carolina  
**Vina A. Punjabi**, Coll. of William & Mary  
**Michael J. Purcell**, Univ. of Texas  
**Thomas M. Putnam**, Consultant, New Mexico  
**Mohini W. Rawool**, New Mexico State Univ.  
**Glen A. Rebka**, Univ. of Wyoming  
**Robert P. Redwine**, MIT  
**Paul L. Reeder**, Battelle Pacific Northwest Lab.  
**Randolph A. Reeder**, Univ. of New Mexico  
**James J. Reidy**, Univ. of Mississippi  
**Horst Dieter Rempp**, Max-Planck Inst.  
**James H. Richardson**, Consultant, New Mexico  
**Joan A. Rifley**, Univ. of Texas  
**Peter J. Riley**, Univ. of Texas  
**Robert A. Ristinen**, Univ. of Colorado  
**Barry G. Ritchie**, Arizona State Univ.  
**Michael W. Ritter**, Stanford Univ.  
**Warren M. Roane**, Abilene Christian Univ.  
**Donald A. Roberts**, Univ. of Wyoming  
**Kathleen A. Roemheld**, UC, Irvine  
**Sayed H. Rokni**, Utah State Univ.  
**Thomas A. Romanowski**, Ohio State Univ.  
**Philip G. Roos**, Univ. of Maryland  
**Dennis Rothenberger**, Arizona State Univ.  
**Nadine A. Roy**, Argonne  
**Charles J. Rush**, Ohio State Univ.  
**Moustafa K. Saber**, Northwestern Univ.  
**Michael E. Sadler**, Abilene Christian Univ.  
**David P. Saunders**, Univ. of Texas  
**H. Reiner Schaefer**, Yale Univ.  
**John P. Schiffer**, Argonne  
**Karlheinz Schindl**, CERN  
**Stuart W. Schmidt**, Argonne  
**Susan J. Seestrom-Morris**, Univ. of Minnesota  
**Colin J. Seftor**, George Washington Univ./UCLA  
**Ralph E. Segel**, Northwestern Univ.  
**Peter A. Seidl**, Univ. of Texas  
**Urs J. Sennhauser**, SIN  
**Kamal K. Seth**, Northwestern Univ.  
**M. Hassan Sharifian**, Univ. of New Mexico  
**Tomikazu Shima**, Argonne  
**Hajime Shimizu**, Tokyo Inst. of Tech.  
**Karam Ali Shojaei**, Virginia State Univ.  
**Rickey L. Shypit**, Univ. of Surrey  
**Edward R. Siciliano**, Univ. of Georgia  
**Margaret L. Silbar**, Consultant, New Mexico  
**Elton S. Smith**, Ohio State Univ.  
**Kaleen J. Smith**, Abilene Christian Univ.  
**L. Cole Smith**, Univ. of Virginia  
**Winthrop W. Smith**, Univ. of Connecticut  
**Michael J. Smithson**, Univ. of Texas  
**W. Rodman Smythe**, Univ. of Colorado  
**Daniel I. Sober**, Catholic Univ. of America  
**Troy Soos**, MIT  
**Paul A. Souder**, Syracuse Univ.  
**Rayappu Soundranayagam**, Northwestern Univ.  
**Franz Sperisen**, UCLA  
**Joseph F. Speth**, KFA  
**Harold M. Spinka**, Argonne  
**Robert W. Stanek**, Argonne  
**Michael P. Staskus**, Univ. of Colorado  
**Mary Beth Stearns**, Arizona State Univ.  
**Rolf M. Steffen**, Purdue Univ.  
**George S. F. Stephans**, MIT  
**James E. Stewart**, Univ. of New Mexico  
**Noel M. Stewart**, Univ. of London  
**Carey E. Stronach**, Virginia State Univ.  
**Richard L. Talaga**, Univ. of Maryland  
**Peter C. Tandy**, Kent State Univ.  
**Robert L. Tanner**, Consultant, New Mexico  
**Morton F. Taragin**, George Washington Univ.  
**T. Neil Thompson**, UC, Irvine  
**James M. Thorne**, Brigham Young Univ.  
**Mark Timko**, Ohio State Univ.  
**W. Bradford Tippens**, Texas A&M Univ.  
**John A. Tjon**, Univ. of Utrecht  
**John W. Tobin**, New Mexico State Univ.  
**Gerald E. Tripard**, Washington State Univ.  
**Christoph Tschalär**, SIN

- R. Steven Turley, Hughes Research Lab.  
Jeff T. Ui, Louisiana State Univ.  
John L. Ullmann, Univ. of Colorado  
David G. Underwood, Argonne  
Gerrit Van Kalker, UC, Riverside  
Jay W. Van Orden, Univ. of Maryland  
Clinton D. Van Siclen, EG&G, Idaho  
Gordon J. Vandalen, UC, Riverside  
Kamran Vaziri, Utah State Univ.  
Bruce J. VerWest, Arco Oil & Gas Co.  
Victor E. Viola, Indiana Univ.  
Stephen Von Molnar, IBM Watson Research Center  
William F. Vulcan, Coll. of William & Mary  
Roberta J. Wade, Univ. of New Mexico  
John D. Walecka, Stanford Univ.  
Robert L. Walker, Consultant, New Mexico  
Angel T. M. Wang, UCLA  
Keh-Chung Wang, UC, Irvine  
Sou-Tien Wang, Wang NMR, Inc.  
Yea-Fei Wang, Wang NMR, Inc.  
Zhi-Fu Wang, Inst. of Atomic Energy, PRC  
Ray A. Warner, Battelle Pacific Northwest Lab.  
Douglas L. Watson, Univ. of Bradford  
John W. Watson, Kent State Univ.  
Monroe S. Wechsler, Iowa State Univ.  
Robert C. Welsh, George Mason Univ.  
Charles A. Wert, Univ. of Illinois  
C. Steven Whisnant, Univ. of South Carolina
- D. Hywel White, Brookhaven  
R. Roy Whitney, Univ. of Virginia  
Charles A. Whitten, UCLA  
Robert J. Whyley, Coll. of William & Mary  
Bryan H. Wildenthal, Drexel Univ.  
Allen L. Williams, Univ. of Texas  
Kentner B. Wilson, Consultant, New Mexico  
Robert R. Wilson, Columbia Univ.  
Andreas Wirzba, SUNY, Stony Brook  
Fred K. Wohn, Iowa State Univ.  
Stephen A. Wood, Tel Aviv Univ.  
Kim A. Woodle, Yale Univ.  
James N. Worthington, Jenworth Co.  
Bryan K. Wright, Univ. of Virginia  
Dennis H. Wright, Virginia Polytechnic Inst. & State Univ.  
S. Courtenay Wright, Univ. of Chicago  
Shen-Wu Xu, Univ. of Texas  
Ming-Jen Yang, Univ. of Chicago  
Sergei K. Yesin, Inst. of Nuclear Research, USSR  
Akihiko Yokosawa, Argonne  
Jinnan Yu, Inst. of Atomic Energy, PRC  
Chris D. Zafiratos, Univ. of Colorado  
Larry Zamick, Rutgers Univ.  
Benjamin Zeidman, Argonne  
Hans J. Ziock, UCLA  
Klaus O. H. Ziock, Univ. of Virginia  
Robert Ziock, UCLA  
John D. Zumbro, Univ. of Pennsylvania

## Information for Contributors

*Progress at LAMPF* is the progress report of MP Division of Los Alamos National Laboratory. In addition it includes brief reports on research done at LAMPF by researchers from other institutions and Los Alamos National Laboratory divisions.

*Progress at LAMPF* is published annually on April 1. This schedule requires that manuscripts be received by January 1.

Published material is edited to the standards of the *Style Manual* of the American Institute of Physics. Papers are not refereed, hence presentation in this report does not constitute professional publication of the material nor does it preempt publication in other journals. Readers should recognize that results reported in *Progress at LAMPF* are sometimes preliminary or tentative and that authors should therefore be consulted in the event that these results are cited.

Contributors can expedite the publication process by giving special care to the following specifics:

1. When possible, furnish computer files for text and MAPPER files for illustrations together with a hardcopy of your paper. *Progress at LAMPF* can accept files from computers, stand-alone word processors, and personal computers. TeX files are especially welcome.
2. Drawings and figures submitted should be of quality suitable for direct reproduction after reduction to single-column width, 55 mm (2-1/4 in.). MAPPER files should be printed on laser printers.
3. Figure captions and table headings must be furnished. The *AIP Style Manual* requires that every figure have a caption that is "complete and intelligible in itself without reference to the text."
4. References must be complete and accurate. If a reference cites a paper submitted for publication, the title of the paper must be given. Laboratory standards prefer six authors before et al. in reference lists.  
For legal reasons the term private communication cannot be used in *Progress at LAMPF*. Credit for unpublished information may be given in footnotes provided the name, organization, and date are cited.
5. Abbreviations and acronyms should be avoided if possible (in figures and tables as well as text), and when used must be defined.
6. All numerical data should be given in *Système International* (SI) units.
7. Authors are reminded that it helps the reader to have an introduction, which states the purpose(s) of the experiment, before presentation of the data.

Research reports should be brief but complete. A list of recent publications relating to the experiment, for separate tabulation in this report, is much appreciated.

Contributors are encouraged to include as authors all participants in experiments so that they may receive credit for authorship and participation.

Questions and suggestions should be directed to John C. Allred, Los Alamos National Laboratory, MS H850, Los Alamos, NM 87545.